

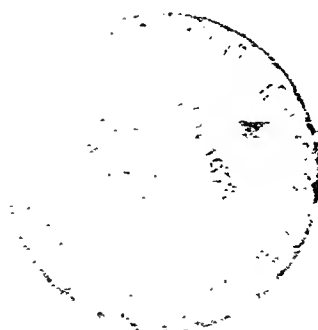
NASA TM X-2934

NASA TECHNICAL
MEMORANDUM



NASA TM X-2934

30



8TH AEROSPACE MECHANISMS SYMPOSIUM

Held at

Langley Research Center

Hampton, Virginia

October 18-19, 1973

NATIONAL AERONAUTICS AND SPACE ADMINISTRATION • WASHINGTON, D. C. • OCTOBER 1973

THE PROCEEDINGS OF THIS SYMPOSIUM ARE DEDICATED TO

Dr. George G. Herzl

Born April 28, 1926 – Died February 18, 1973

Senior Staff Engineer, Lockheed Missiles & Space Co., Inc.

Co-Founder, Aerospace Mechanism Symposia

General Chairman, Aerospace Mechanism Symposia 1966-1972

(PRECEDING PAGE BLANK NOT FURNISHED)

PREFACE

The 8th Aerospace Mechanisms Symposium, held at Langley Research Center, Hampton, Virginia, October 18 and 19, 1973, was sponsored jointly by the National Aeronautics and Space Administration, Lockheed Missiles and Space Company, Inc., and California Institute of Technology. This symposium is devoted exclusively to an interchange of ideas and information on aerospace mechanisms.

Contributions were from NASA Research Centers, U.S. universities, U.S. manufacturers, and European and British research groups.

PRECEDING PAGE BLANK NOT FILMED

8TH AEROSPACE MECHANISMS SYMPOSIUM

MORNING SESSION – October 18, 1973

Chairman: D. F. Welch
California Institute of Technology

1. OSO-7 SPECTROHELIOGRAPH MECHANISMS	1
Donald N. Matteo, General Electric Co.	
2. DEVELOPMENT OF AND DYNAMIC STUDIES CONCERNING A CABLE BOOM SYSTEM PROTOTYPE	15
G. Bring, European Space Research and Technology Centre, G. Schmidt, Dornier System, and D. Wyn-Roberts, British Aircraft Corp.	
3. A LASER INITIATED EXPLOSIVE DEVICE SYSTEM	25
L. C. Yang, V. J. Menichelli, and J. E. Earnest, Jet Propulsion Laboratory	

Chairman: R. J. Herzberg
Lockheed Missiles & Space Co., Inc.

4. PRINCIPAL AXES AND MOMENTS OF INERTIA OF DEFORMABLE SYSTEMS . . .	37
T. R. Kane, Stanford University	
5. CURRENT EUROPEAN DEVELOPMENTS IN SOLAR PADDLE DRIVES	49
R. H. Bentall, European Space Research and Technology Centre	
6. TELESCOPIC BOOMS FOR THE HAWKEYE SPACECRAFT	59
Roger D. Anderson, University of Iowa	
7. THE DEVELOPMENT AND TEST OF A LONG-LIFE, HIGH RELIABILITY SOLAR ARRAY DRIVE ACTUATOR	69
Don L. Kirkpatrick, General Electric Co.	

AFTERNOON SESSION

Chairman: O. H. Fedor
NASA Kennedy Space Center

8. HIGH PERFORMING ACTUATION SYSTEM FOR USE WITH A LOUVER ARRAY FOR SATELLITE THERMAL CONTROL	85
Peter U. Reusser and Jan A. F. Coebergh, Messrs. Peter U. Reusser Ltd.	

9. DEVELOPMENT OF THE ELEVATION DRIVE ASSEMBLY FOR ORBITING SOLAR OBSERVATORY I (EYE)	97
W. F. Sharpe, M. C. Olson, Hughes Aircraft Co., and B. W. Ward, NASA Goddard Space Flight Center	
10. A NEW APPROACH TO LONG-LIFE-NONCONTACTING ELECTROMECHANICAL DEVICES	109
Edward J. Devine, NASA Goddard Space Flight Center	
11. A REVIEW OF THE TECHNOLOGY OF NONCONTACTING SYSTEMS	117
Philip A. Studer, NASA Goddard Space Flight Center	
12. DESIGN AND DEVELOPMENT OF A MOMENTUM WHEEL WITH MAGNETIC BEARINGS	131
Leo J. Veillette, NASA Goddard Space Flight Center	
13. MODEL STUDIES OF CROSSWIND LANDING-GEAR CONFIGURATIONS FOR STOL AIRCRAFT	145
Sandy M. Stubbs and Thomas A. Byrdsong, NASA Langley Research Center	
14. MODEL SUPPORT ROLL BALANCE AND ROLL COUPLING	155
Roy E. Sharpes and William J. Carroll, NASA Langley Research Center	
15. SPACECRAFT SEPARATION SYSTEMS MECHANISMS: CHARACTERISTICS AND PERFORMANCE DURING HIGH-ALTITUDE FLIGHT TEST FROM NASA WALLOPS STATION, VA	165
J. D. Pride, Jr., NASA Langley Research Center	
16. DEVELOPMENT OF LOW-SHOCK-PYROTECHNIC SEPARATION NUTS	179
Laurence J. Bement, NASA Langley Research Center, and Vernon H. Neubert, Pennsylvania State University	
MORNING SESSION - October 19, 1973	
Chairman: A. C. Bond NASA Manned Spacecraft Center	
17. ROCKET ENGINE BIPROPPELLANT VALVE PROBLEMS AND CURRENT EFFORTS	213
Joseph Fries, NASA Johnson Space Center	
18. METEOROID-DETECTOR DEPLOYMENT AND PRESSURIZATION SYSTEMS	229
H. C. Halliday, NASA Langley Research Center	
19. CONTROL VALVE: HOT GAS FAST RESPONSE	237
J. T. Hollis, A. B. Killcbrew, and J. M. Smith, McDonnell-Douglas Astronautics	

20. THE VIKING SURFACE SAMPLER	245
Robert B. Seger, Martin-Marietta Aerospace, and Vernon P. Gillespie, NASA Langley Research Center	
21. VIKING LANDER ANTENNA DEPLOYMENT MECHANISM	257
Kenneth H. Hopper and Dean S. Monitor, Martin-Marietta Aerospace Corp.	
22. OPTICAL MODULE FOR THE INTEGRATED REAL-TIME CONTAMINATION MONITOR	271
E. H. Wrench, General Dynamics, Convair	

AFTERNOON SESSION - October 19, 1973

Chairman: R. W. Lester
Jet Propulsion Laboratory

23. TRANSDUCER TECHNOLOGY TRANSFER TO BIO-ENGINEERING APPLICATIONS	283
E. N. Duran, G. W. Lewis, C. Feldstein, Jet Propulsion Laboratory, and E. Corday, S. Meerbaum, Tzu-Wang Lang, Cedars-Sinai Medical Center	
24. HELICOPTER VISUAL AID SYSTEM	293
Ronald L. Baisley, NASA Jet Propulsion Laboratory	
25. A GRAVITY EXERCISE SYSTEM	311
William E. Brandt and Allen L. Clark, Gyrotrim Corporation	

OTHER SELECTED PAPERS

26. POLYURETHANE RETAINERS FOR BALL BEARINGS	317
R. I. Christy, Hughes Aircraft Company	
27. MULTI-POINT RELEASE MECHANISM	329
E. Groskopfs, Spar Aerospace Products, Ltd.	
28. VIKING ORBITER 1975 ARTICULATION CONTROL ACTUATORS	335
G. S. Perkins, Jet Propulsion Laboratory, California Institute of Technology, Pasadena, California	
29. THE REQUIREMENT FOR DESIGNING ANALYZABLE SPACE DEPLOYABLE STRUCTURES	351
Arthur A. Woods, Jr., Lockheed Missiles and Space Co., Inc.	

1. OSO-7 SPECTROHELIOGRAPH MECHANISMS

Donald N. Matteo

General Electric Company - Space Division
Valley Forge, Pa.

SUMMARY

The OSO-7 Orbiting Solar Observatory was launched on September 29, 1971. One of the two main sun pointing instruments aboard was the Goddard Space Flight Center Spectroheliograph for monitoring extreme ultraviolet (EUV) and X-ray radiation from the sun. The instrument, which was designed, built and tested by General Electric Company for NASA-GSFC, has been operating successfully in orbit for approximately two years.

The design solution to each of the mechanism tasks is described. Also described are certain developmental problems and their solutions which led to the ultimate mission success.

INTRODUCTION

Orbiting Solar Observatory-H (redesignated OSO-7 upon successful orbit injection) is an earth orbiting spacecraft which is the platform for several sun observing instruments. The spacecraft contains two experiments which are precisely pointed at the sun by a spacecraft provided orientation system. The EUV and X-ray spectroheliograph is the "right-hand" member of this pair of sun pointing instruments. Its position and relationship to the spacecraft and other scientific instruments are shown in Figure 1.

The instrument consists of five separate scientific experiments. These are:

- o Extreme Ultraviolet (EUV) Spectroheliograph
- o H-Alpha Spectroheliograph
- o Longwave (LW) X-Ray Spectroheliograph
- o Shortwave (SW) X-Ray Spectroheliograph
- o X-Ray Polarimeter

The locations of these five experiments within the instruments are shown in Figure 2. Figure 3 is a photograph of the instrument showing the same general arrangement as Figure 2.

EUV Spectroheliograph

The EUV spectroheliograph is designed to obtain spectropheliograms in the EUV region between 170 and 400 Å. The experiment consists of an imaging system (grazing incidence telescope), a variable aperture mechanism located at the focal plane of the telescope, a grating, and a carriage mechanism which scans the first order diffracted component from the grating, the scan being made along the spectrometer's focal curve. The variable aperture mechanism permits the selection of four different on-axis apertures and also provides the capability to scan the solar diameter when the instrument is center-sun pointing. The carriage mechanism contains three magnetic electron multipliers (MEM), a set of two selectable exit slits for each MEM, and associated drive motors and electronics. This arrangement permits three lines of radiation to be selected and observed at one time. Items of interest to the mechanism designer in this experiment are:

- o The carriage scan mechanism,
- o The variable aperture mechanism,
- o The exit slit selection mechanism.

Longwave X-Ray Spectroheliograph

The Longwave X-ray experiment provides spectropheliograms in selected spectral bands between 7.9 Å and 16 Å. The experiment consists of a collimator, a filter wheel mechanism, a double chambered proportional counter, and associated electronics. The filter wheel has 6 positions; five containing filter pairs and one "open" position which is used for calibration. Each filter pair consists of two side-by-side filters, each of which is common to only one of the two chambers of the proportional counter. With a filter pair placed in front of the proportional counter, it is possible to measure radiation in a very narrow spectral band by obtaining the difference in the outputs of the two proportional counter chambers.

Shortwave X-Ray Spectroheliograph

The Shortwave X-Ray experiment provides spectropheliograms in selected bands between 1.7 Å and 8 Å and operates in the same manner as the Longwave X-Ray system.

The filter wheel mechanism, which provides the filter selection functions for both the LW and SW X-Ray spectroheliographs, is a mechanism of interest which is described in this paper.

H-Alpha Spectroheliograph and X-Ray Polarimeter

Both of these experiments are passive from a mechanisms standpoint (after initial precision alignments are completed) and are not discussed in detail herein.

EUV EXPERIMENT MECHANISMS

EUV Variable Aperture Mechanism

The entrance aperture of the EUV Spectroheliograph is located at the focal surface of the EUV grazing incidence telescope.

The entrance aperture determines the size and location (relative to the solar disc image) of the image element entering the EUV Spectroheliogram. It thus contributes to the spectral resolution and the scanning capability of the instrument. The variable aperture assembly is required to:

- o Selectively admit to the spectroheliograph image elements of 10 x 20 arc-seconds, 20 x 20 arc-seconds, 40 x 20 arc-seconds, 20 x 60 arc-seconds (on-axis of the EUV telescope).
- o Provide for the scan of a 20 x 20 arc-second image element across the diameter of the solar disk in 90 equal steps.
- o During scan, the aperture slit must track the curved surface of focus of the telescope in the direction perpendicular to the scan along the line of sight of the telescope.
- o The mechanism must include an indexing feature to permit return of the image element to the optic axis upon ground command.

The variable aperture mechanism consists of a 20 arc-second wide (approximately 0.08 mm at focus of telescope) fixed slit located normal to the instrument baseplate and to the incoming radiation, and of a rotating slit assembly located just in front of the fixed slit. The rotating slit limits the height of the fixed slit to 10, 20, 40, or 60 arc-seconds on-axis and also scans across the solar disc along the fixed slit with a 20 arc-second wide aperture as a function of rotary position. The rotating assembly is driven by a stepper motor and gear reduction unit. Two microswitches provide position indication of the rotary assembly and advance the position to a fixed reference position. Figure 4 shows this arrangement.

Fixed Slit. The fixed slit is bonded to the entrance slit mounting base. The slit is fabricated by electroplating nickel on a 0.00762 cm thick electrolytic copper substrate to a thickness of 0.000762 cm around the desired slit configuration (which is held to \pm 0.00025 cm). The copper is then etched away in the area of the slit so that the desired slit configuration is formed by the nickel plating. This technique is used for all the slits in the instrument, including the rotating slit and the EUV exit slits.

Rotating Slit Assembly. The rotating slit assembly (which is mounted directly on the motor/gearhead output shaft) consists of the four central aperture slits and a single spiral slit. The central aperture slits are of constant radius from the center of rotation so as to always be on the optical centerline. They occupy approximately equal arc segments in 180 degrees of the disc. The blank space between the slits is bridged by an off-axis slit of larger radius so that a failure of the rotating slit drive cannot block the incoming radiation no matter what angular position the rotating slit assembly is in should a failure occur.

The spiral slit occupies the remaining 180 degrees of the disc. The radial distance of the spiral varies such that the spiral scans the diameter of the solar disc as the slit is rotated. When this arrangement of spiral slit rotating in front of a straight fixed slit was first conceived, the apertures were thought of as slits in simple flat foils arranged normal to the optical axis. However, upon more detailed investigation it was realized that the telescope focal surface was not a plane, but rather a body of revolution above the optical axis which approximated a portion of an ellipsoid. See Figure 5. Since the entrance aperture is required to be in or near the telescope focal surface, this development threatened to greatly complicate entrance aperture mechanism. After several complex design solutions were considered, however, the simple technique of mounting the spiral slit on a surface inclined to the axis of rotation was discovered to generate the required along-axis motion of the aperture as a function of off-axis scan position. As the disc rotates the axial position of that portion of the slit which defines the image element varies. By properly positioning the spiral slit on the inclined rotating member, that axial position can be made to be of longest focal length when the image element is on the center of the solar disc (optical axis) and to move to shorter focal lengths as the image element moves to either edge of the solar disc. Selecting the inclination angle controls the rate of axial travel as a function of off-axis scan. The actual angle used was $12^{\circ}28'$ from normal to optical axis in order to scan the profile shown in Figure 5.

Drive for the rotating slit assembly is provided by 13 VDC, size 8, 90° stepper motor driving a 60.75 to 1 ratio gearhead. Lubrication technique was dry film throughout motor/gearhead. All gearhead bearings and gears were lubricated with Lubeco 905. Each individual gear and

bearing element was individually inspected and lubricated prior to assembly. The gearhead bearings were lubricated on their races and the inner surfaces of their two piece ribbon retainers. All gearhead bearings were run-in individually and torque tested prior to assembly. The motor bearings were lubricated by means of an MoS_2 bearing ball retainer. They were torque tested and run-in at assembly. Each motor/gearhead set was green-run for 100 hours in a vacuum at nominal torque and speed; then torn down, inspected and re-assembled. This same technique was used for all motor/gearhead combinations in the instrument (including EUV carriage, EUV exit slit section mechanism, and X-Ray filter wheels. While the lubrication/run-in/test procedure was rigorous, the excellent performance in orbit justifies the effort expended.

The rotating portion of the variable aperture assembly was balanced about its center of rotation (by fine ballasting) and no launch lock mechanism was used.

A thermal shield was provided just forward of the rotating disc assembly. This shield intercepts radiation from those portions of the solar image which are not to be scanned in order to minimize thermal effects on the aperture mechanism.

EUV Carriage Scan Mechanism

The carriage assembly shown in Figure 6 is a machined beryllium frame containing the three Bendix magnetic electron multiplier detectors, six spectrometer exit slits positioned on the spectrometer focal circle, the movable mask to select the desired group of three exit slits, the two microswitches for selecting the exit slit mask position, and the motor/gearhead drive for the mask. The carriage is movable along the focal circle to cover the wavelength range of 170 Å to 400 Å in approximately 0.07 Å steps. At one unique position the six exit slits are aligned with six selected EUV lines, three of which can be viewed simultaneously by each of the three detectors as selected by positioning the mask.

Carriage Drive. The carriage is supported on a track fixed to the instrument base and curved to the focal circle radius (50 cm.). A recirculating ball bearing with the balls riding in "V" groove races in the track and carriage provides low friction and stiff support for the carriage motion. The "V" groove is machined into stainless steel inserts in the beryllium track and carriage. The carriage is driven by a motor/gearhead assembly fixed to the instrument baseplate with the output pinion driving a curved stainless steel rack on the carriage. The gearhead ratio and the pinion size are such that for each 90-degree step of the motor, the carriage travels a linear distance of 0.0028 cm., or approximately 0.07 Å. This compares to a specified maximum of 0.1 Å per step. The control logic provides for three separate speeds of travel, 6.25, 12.5, or

50 steps per second. At the longwave and shortwave limit of its travel, the carriage actuates separate microswitches which give an indication to the control logic that the limit has been reached. The logic reverses the direction of travel and, when so commanded, stops the travel. Whenever a specific carriage position is to be duplicated, it is approached from the same direction as first achieved by counting motor pulses from a reference position. In this way, gearhead backlash is trimmed out and carriage positions are duplicated within one motor step. The motor/gearhead combination is the same type as that described in the section on the variable aperture mechanism except that the gearhead ratio is 305.35 to 1.

The motor/gearhead assembly, the rack and pinion, the carriage bearing races, and the ball return slots are lubricated with the same solid film lubricant system as previously described.

Exit Slit Assembly. The six exit slits are precisely positioned on a single exit slit foil by the plating and etching process described previously. The foil is then mounted to a frame and the assembly is attached to the carriage. Particular care is taken in mounting the foil to the frame to maintain the slit leading and trailing edges in the same plane. Because of the shallow angle at which the radiation passes through the slit, any out of plane condition of the two edges would appear to be a change in width of the slit, thus affecting the spectral resolution. The spacing between the six slits is accurately held so that the six selected spectral lines appear simultaneously at the same carriage position. Because slits are tangent to the Rowland circle, their width is such that the projected width, in a plane perpendicular to the incident radiation, is 85 μm . Spectral width measurements show that the effective width is uniform within 0.1 \AA from slit to slit.

Flexprints. The electrical connection between the instrument electrical system and the movable carriage is made through two flexprints. One flexprint contains the two high voltage conductors and the second contains 21 low voltage conductors. The conductors are etched copper ribbons between Kapton substrates and an external coating of Teflon. The thicknesses of the copper conductors are 0.00686 cm for the low voltage flexprint and 0.01372 cm for the high voltage flexprint. The thickness of the Kapton is 0.005 cm in both cases.

The original thickness of the low voltage flexprint was 0.01372 cm. However, it was determined by life tests that this thickness was unsuitable for the bend configuration and flexing modes of the low voltage flexprint. The thickness was changed to 0.00686 cm and subsequent life tests show no failures after 43,000 cycles.

The high voltage flexprint with the 0.01372 cm thick conductors was life tested and withstood 41,000 cycles before failure. Forty-one thousand cycles represents a safety factor of approximately 4 based on the expected one-year operational mode of the instrument and was considered adequate. Actual number of flexure cycles logged in orbit as of June 1973 was 15,200

without failure. This is an actual rate of just over 9000 per year and shows the decision that the demonstrated life was adequate.

Launch Lock. The launch lock is a pyrotechnic operated device which secures the movable carriage to the track during the application of the vibration and acceleration loads of the launch environment. The launch lock is fired upon command after orbit has been achieved and spacecraft separation has occurred.

The launch lock housing is mounted externally on the instrument baseplate. A retractable pin projects through the baseplate into a close fitting hole in the carriage assembly. The locking pin is loaded by a combination torsion and compression spring. The torsion holds the pin in the locked position in a detent in the housing. The pin is rotated against this torsion load and out of the detent by dual pyrotechnically actuated pistons. The compression in the spring then retracts the pin from the carriage. The dual pistons are provided for redundancy. Both pistons are actuated by the one firing command. Each piston meets the requirements of 1 ampere, no fire, 3-1/2 amperes, all fire. Actuation of a single piston is adequate to release the locking mechanism. An advantage of this arrangement is that the locking pin can be manually engaged and disengaged by using a screw driver whether the pyrotechnic actuators are installed.

EUV Exit Slit Selection Mechanism

It is a requirement on the EUV system that there be a single position of the carriage assembly where six specific EUV lines be "visible" to the electron multipliers and that either of two groups of three of these lines each be selectable for detection by ground command, without carriage motion. As described above, the exit slits are positioned such that each of these EUV lines will pass through one of the six exit slits when the carriage is in the proper position along the track.

In order to select between the two groups of three lines, an exit slit mask is provided. This mask is positioned immediately in front of the exit slits and is configured such that it will block illumination from entering three exit slits while passing illumination to the other three exit slits. This mask travels in "V" grooves. As is the case with the carriage track, the 440C stainless steel balls roll on a 440C stainless steel "V" groove.

The mask is shuttled from one end of the track to the other by ground command and is stopped by the actuation of a microswitch at each travel extreme. At one end of its travel, the mask uncovers one group of three slits and, at the opposite end, the mask uncovers the other three slits while covering the original group. The slits are positioned in pairs such that energy entering either slit of a given pair enters one of the three detectors (electron multipliers). The mask is configured to uncover one slit of each of the three pairs at each end of its travel.

Mask drive is provided by a motor/gearhead unit which is mounted on and rides with the carriage. The output of the 48 to 1 ratio gearhead is delivered to the mask by means of an eccentric arm acting on a slot in the mask assembly. The output of the eccentric is delivered to the mask by means of ball bearing with its outer ring rolling in the slot. A 180 degree rotation of the eccentric arm (gearhead output shaft) results in mask travel from one end of its track to the other. In this way, extreme accuracy of output shaft position (as affected by backlash) is not required since mask position accuracy is a function of the difference in cosines of small angles.

The motor, gearhead, "V" groove track, and mask slot are lubricated by the same MoS_2 dry film system as described previously.

LW&SW X-RAY MECHANISMS

Both the longwave and the shortwave X-ray experiment designs consist of a collimator to provide the spatial selectivity and side lobe suppression, a set of five balanced filter pairs to provide the spectral bands of interest, a double channel proportional counter, and associated electronics. The filter pairs are mounted on a 6-position filter wheel which is motor-driven so that each of the 5 filter pairs and an open position may be placed in front of the double-channel proportional counter by command. The channels in the detector are side-by-side (A&B) as are the filters (A&B) in each filter pair; therefore, the output of each channel (A or B) is a function of the filter which is placed in front of the channel.

X-Ray Filter Wheel Mechanism

The filter wheel assembly, shown in Figure 7 contains the longwave and shortwave filter wheels which rotate independently about a common pedestal to insert wavelength selective filters in the X-ray path. Each wheel has provision for mounting six such filter pairs. One filter pair position is left open to provide a position where unfiltered X-ray energy will enter the detectors (X-ray proportional counters). The proportional counters and their associated electronic amplifiers are mounted internally within the pedestal.

The filter wheel rotates on a large diameter thin cross-section bearing. A large ring gear is attached to the wheel. Each wheel is driven independently through its ring gear by a separate motor/gearhead similar to the other motor/gearheads in the instrument. The gearhead ratio is 8.476 to 1. The rotation of the wheels is controlled by two microswitches for each wheel. One microswitch engages the detents when the filter is fully in front of the proportional counter. It provides an input to the control logic to stop the wheel in this position and to advance the filter position count. The second switch is actuated once each complete revolution by a

pin projecting from the wheel. This actuation resets the telemetered filter position count.

Each wheel also contains a radioactive source which comes into view of the detector once each revolution of the wheel. The source provides a calibration level for the system.

The filter wheel bearings, ring gear and gearhead output pinion are lubricated with the same solid film lubricant system described previously.

A unique feature of this mechanism is that, as a weight and space saving technique, each filter wheel is mounted on a single, large diameter, slim cross-section bearing. This was deemed tolerable due to the balanced nature of the wheel, its light weight, and high diameter to depth ratio. No launch lock mechanism was employed in the filter wheel. This technique has worked well through vibration tests and the flight program.

PROBLEMS ENCOUNTERED

During the development of the mechanisms described herein, the following problems were encountered:

- (1) Problem - Filter wheel motor/gearhead would move two steps on single step command, would slew instead of run in-synch.
Causes - High reflected inertia, voltage pulse being cut-off to motor winning at point of maximum step overshoot.
Solution - Voltage pulse increased from 15 mS to 40 mS to improve electrical detenting.
- (2) Problem - EUV variable entrance aperture wheel would not stop at reference position after qualification vibration.
Cause - Reference cam deformed by impacting of microswitch actuator arm during vibration.
Solution - Recontoured cam to increase bearing area. Implemented operational change which positions wheel in rotational position where actuator arm is not in contact with cam during vibration (launch).

- (3) Problem - EUV mask did not move upon command after qualification vibration.
- Cause - Brinelling of beryllium "V" groove by mask support balls.
- Solution - Changed "V" groove design to incorporate stainless steel insert (similar to main carriage track).
- (4) Problem - EUV mask did not stop at end of travel.
- Cause - Improper setting of microswitch.
- Solution - Widened actuation range of microswitch.
- (5) Problem - SW X-Ray filter wheel did not respond to commands.
- Cause - Torque output marginal to overcome 'O'-Ring drag and ramp effect on indexing cam.
- Solution - Removed 'O'-Ring (seal not required due to solid lubricant) and changed shape of indexing cam.
- (6) Problem - EUV carriage launch lock did not fully retract.
- Cause - Repeated firings of the same launch lock assembly raised a burr in the housing which hung-up retraction pin.
- Solution - Replaced launch lock after implementing design change which chamfers corner where burr was raised.

CONCLUDING REMARKS

The author wishes to thank Dr. Werner Neupert, NASA-GSFC Principal Investigator, and Mr. Milton Kalet, NASA-GSFC Technical Officer, for their contribution to the successful development of the hardware discussed. Particular note should be made of the fact that the original concept for the EUV entrance slit mechanism was provided by GSFC in the RFP specification.

The mechanisms discussed by no means represent all of the challenges presented to the mechanical system designer by the OSO-7 spectroheliograph instrument. Such items as telescope optics mounts, beryllium structure stabilization, maintenance of precision alignments through environments, X-ray mechanical collimation, and thermal control were of great importance in achieving the precision and reliability demonstrated by the instrument in orbit. However, those items discussed are representative of fully matured, space proven hardware of the type of interest to the mechanism designer. It is hoped that some of the techniques presented will be helpful in the design of future hardware of this type.

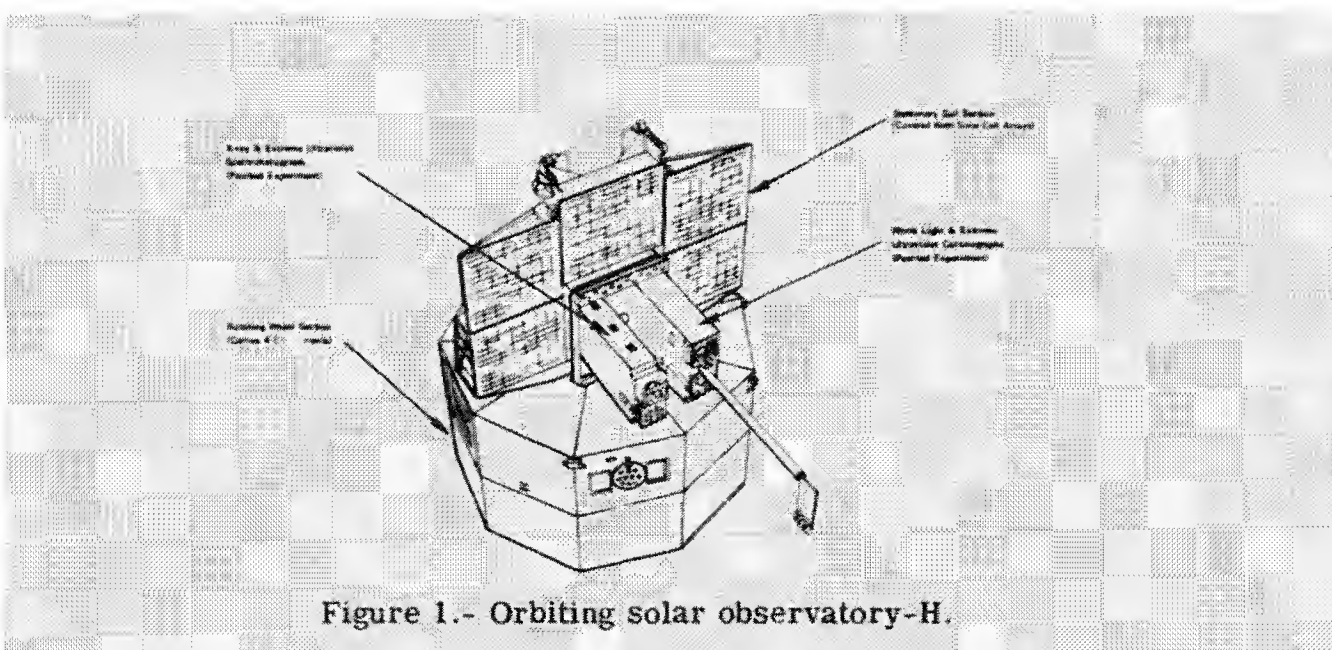


Figure 1.- Orbiting solar observatory-H.



Figure 2.- OSO-H spectroheliograph general arrangement.

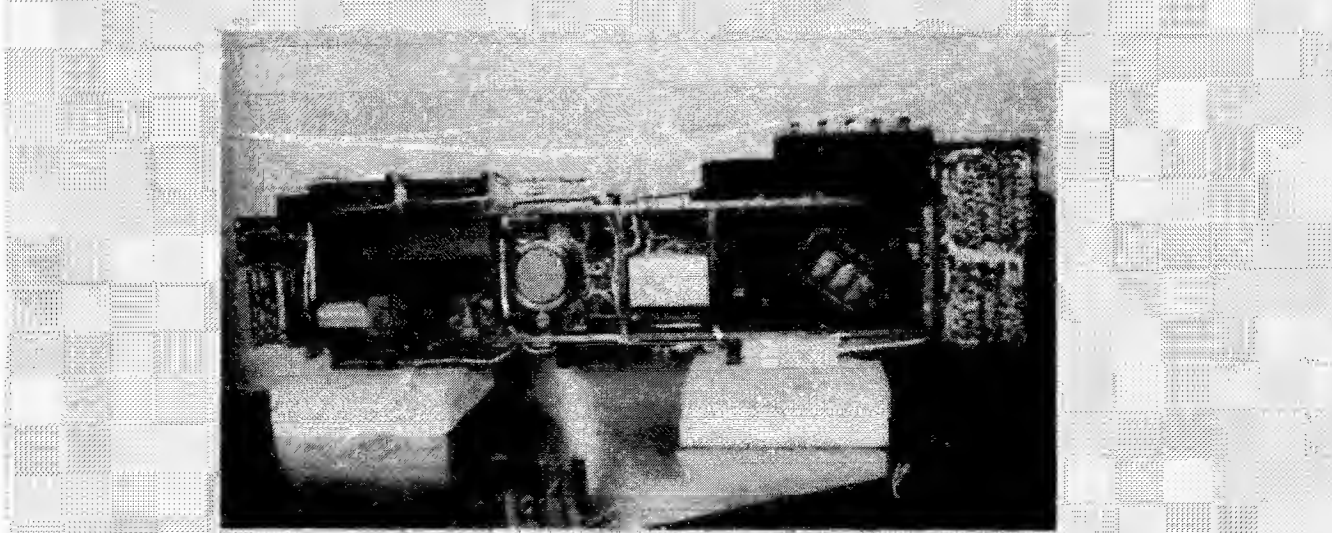


Figure 3.- OSO-II spectroheliograph general arrangement.

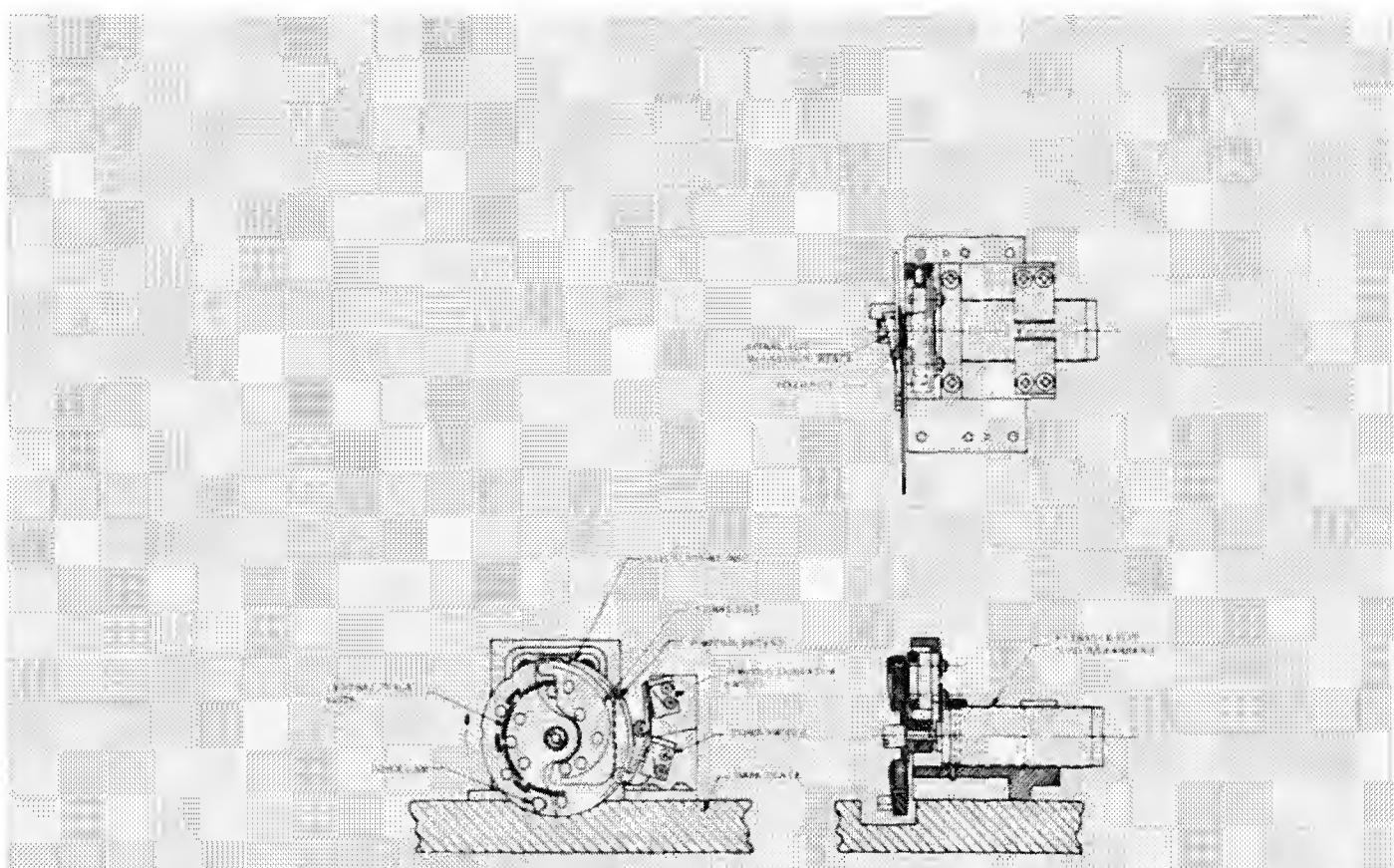


Figure 4.- EUV variable aperture mechanism.

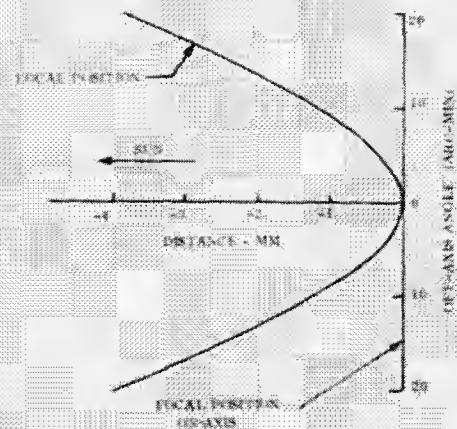


Figure 5.- Variation of curvature of focal surface with angle of off-axis radiation.

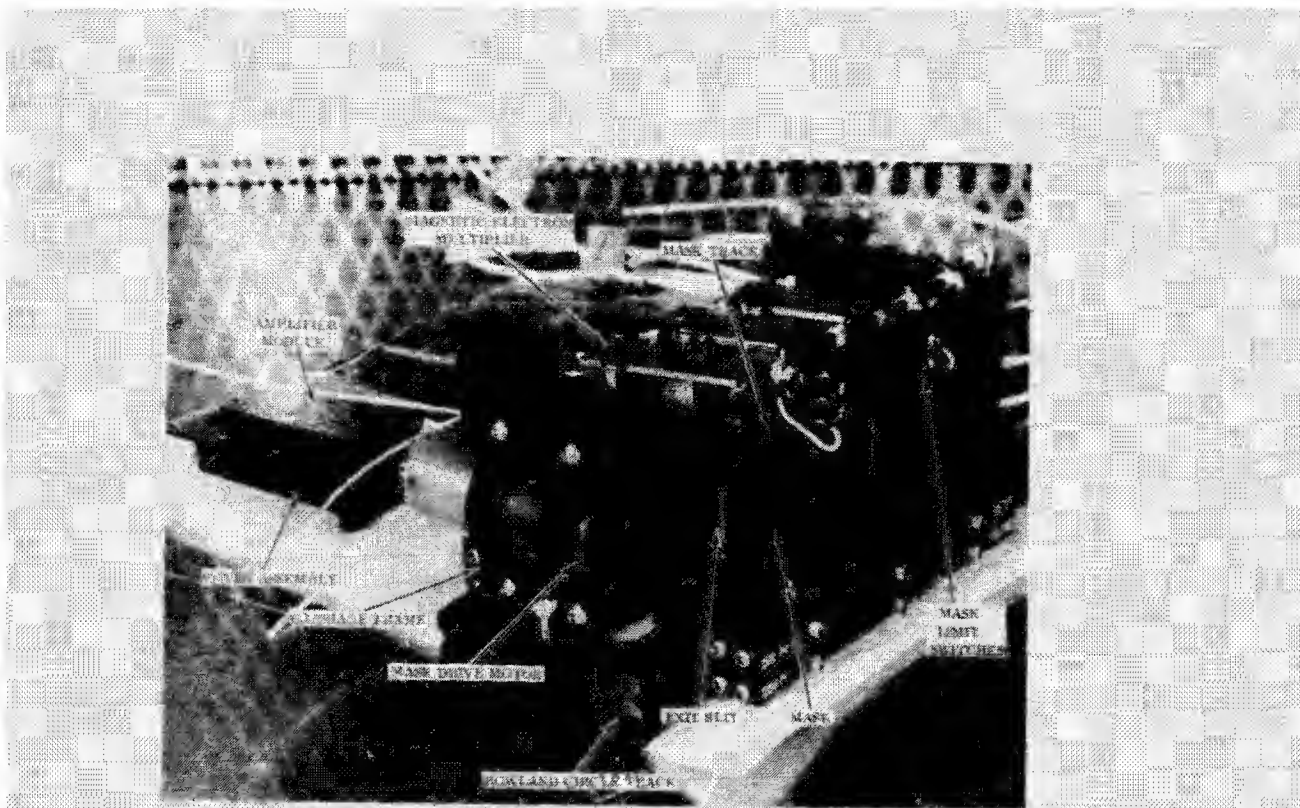


Figure 6.- EUV carriage mechanism.

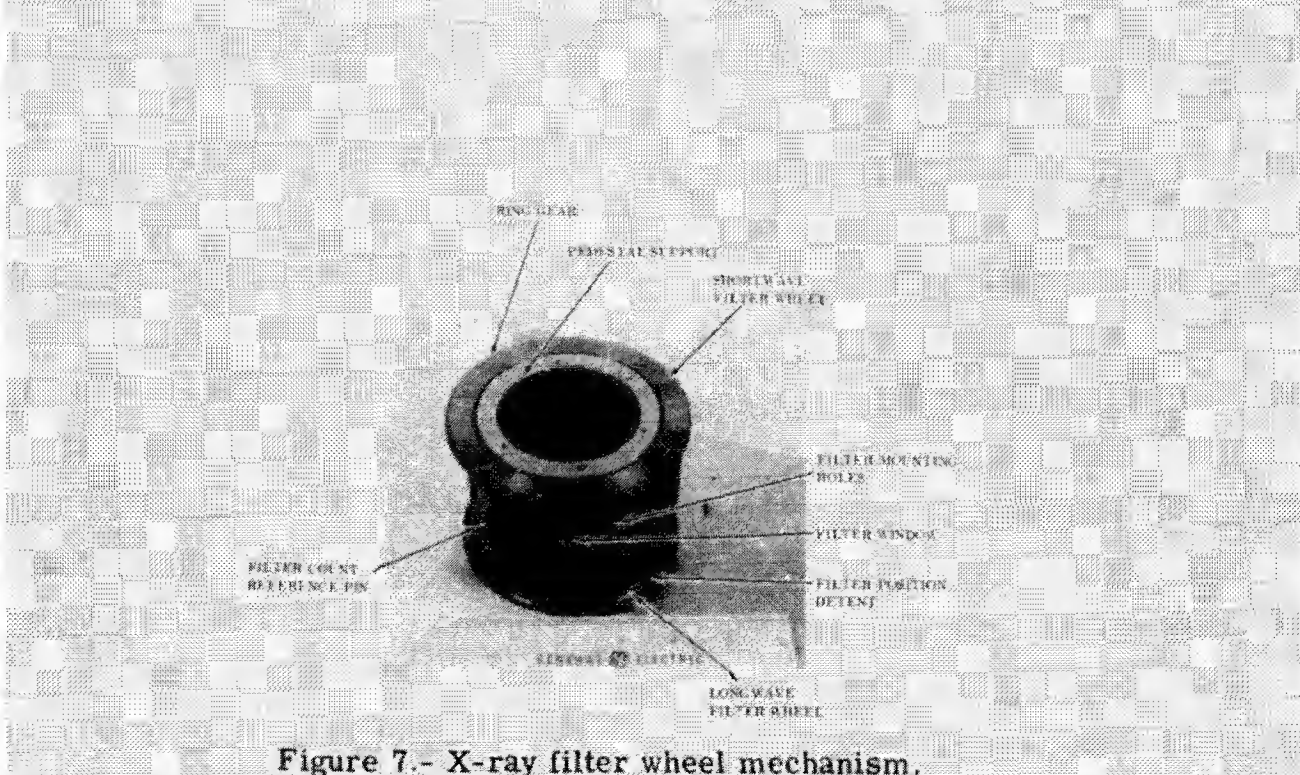


Figure 7.- X-ray filter wheel mechanism.

2. DEVELOPMENT OF AND DYNAMIC STUDIES CONCERNING A CABLE BOOM SYSTEM PROTOTYPE

By G. Bring (ESTEC, Noordwijk, Holland)
G. Schmidt (Dornier System, Friedrichshafen, Germany)
D. Wyn-Roberts (B.A.C., Bristol, England)

SUMMARY

The conception of a cable boom system for a scientific spin stabilized satellite led to a flat cable stowed on a drum with a "flexlead without conversion" to avoid slip rings and to facilitate automatic restowage from any state of deployment. Some dynamic features of the extended cable boom and especially the comparison between round and flat cables were investigated in a "phenomenological" study using a test rig capable of inducing lateral, torsional and thermal cycling disturbances separately or in any combination.

INTRODUCTION

The use of cable booms on spin stabilized spacecraft has been foreseen, with the object of providing the electrical and structural connection with scientific experimental packages having to be placed away from the satellite body. The cables may have to contain several wires which may be arranged to form a round or a flat cable. The flat cable arrangement has certain advantages for the stowage and deployment devices.

A development program was therefore started to have designed, built and tested a cable boom system including a storage container for the undeployed cable, a deployment control unit and the cable itself. The philosophy of the programme was to have a realistic system designed and built and the most interesting characteristics of the system evaluated, thus forming a firm starting point for the developments to more strict specifications.

An experimental programme was launched in parallel in which the phenomenological possibility was studied of pure or coupled vibrations of the deployed cable. This was done over a range of cable sections and other parameter combinations. Cyclic disturbances of types that can be expected in the case of radial booms on a spinning spacecraft were introduced.

SYMBOLS

d_i	inner diameter of cable drum
d_a	outer diameter of drum & cable
n	number of windings of cable
s	cable thickness
N_D	drum rotation speed

V cable deployment speed

L cable length

INVESTIGATION OF CABLE RESPONSE TO THERMAL AND MECHANICAL INPUTS

Introduction

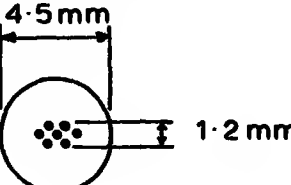
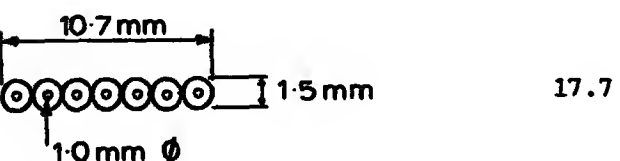
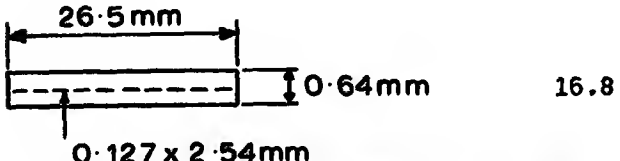
A qualitative investigation of thermal and mechanical responses of cables was carried out in order to obtain data relevant to the behaviour of a cable boom on a spinning satellite. The study phases were as follows:

1. Definition of Test Parameters
2. Equipment Set-up and Check-out
3. Test Programme

Test Parameters

In the first place, it was necessary to choose suitable cables for testing. Three cables of different cross section were specified, their overall properties being based on the GEOS satellite requirements and defined so that thermal and mechanical responses would be exaggerated. The cables finally obtained are shown in Table 1 and consist of silver plated copper wires insulated by a polytetrafluoroethylene (P.T.F.E.) outer sleeving.

Table 1 TEST CABLES

Cable Cross Section	Cross Sectional Area (mm ²)	Width/thickness Ratio
 4.5 mm 1.2 mm	16	1
 10.7 mm 1.5 mm 1.0 mm Ø	17.7	7.1
 26.5 mm 0.64 mm 0.127 x 2.54 mm	16.8	41.8

An analysis of the thermal properties of these cables was carried out by means of a small computer programme. The analysis was mainly confined to steady state conditions. A selection of the results is given in Table 2.

Table 2 PRINCIPAL RESULTS OF THERMAL ANALYSIS

Cable type	Environment	Heat input (W/m ²)	Mean Temp (°C)	Temp Gradient (°C)	Comment
Circular cross section	Space	445	-51.1	0.7	
	Laboratory	445	43.2	0.7	
Ribbon cable "	Space	445	-134.0	23.9)	Edge on
	Laboratory	890	32.5	23.3)	to sun
Flat cable	Space	445	-177.7	12.3)	Edge on
	Laboratory	1780	25.9	11.7)	to sun
Flat cable	Space	560	-16.6	0.3)	Flat side
	Laboratory	560	55.9	0.7)	to sun

Note: all results for an α of 0.7 and ϵ of 0.8.

The highest required laboratory heat load is for the flat cable where, in the worst case, a heat input of 4 solar constants is required in order to obtain the equivalent (space) thermal gradient. The experimental heat lamps were subsequently designed to give this output.

The heating equipment itself consisted of two parabolic reflectors 3 meters high which could be placed on either side of the test cable. The heat is provided by banks of 1 kW tungsten-quartz tubes mounted along the reflector length at the focus of the parabola. Steady state or oscillating heating can be provided by these lamps, the heat output in the oscillating mode being sinusoidal. This output is controlled over the range 0 - 3Hz by means of an external oscillator operating via a 3-phase AC controller connected to a thyristor switching unit.

In order to provide the cable with mechanical inputs, a mechanism was devised capable of providing translatory oscillations in two perpendicular directions in the plane normal to the cable longitudinal direction, together with torsional oscillations. The oscillations could be provided separately or in any combination over the range .03-2.5Hz. Motor speed readout was provided by means of a photocell arrangement, and control by means of manually operated potentiometers.

Equipment Set-Up and Check-Out

The equipment was assembled in a test area with safety doors. Initially, the heat output from the arrays was calibrated under steady state conditions using thermoplates. Fig. 1 shows the measured heat intensity distribution along the cable position. This was the most even distribution possible within the programme restraints and was achieved by a combination of re-distribution of lamps and tilting of the arrays.

Prior to each test, a disk-shaped mass of 1 kg was clamped to the end of the test cable. The mass was chosen on the basis of the calculated centrifugal force experienced by the satellite cable boom in orbit, whereas the inertia was chosen in order to produce a low torsion frequency and maximise the cross

coupling with the thermal inputs.

Test Programme

The test programme consisted of a parametric study of thermal and mechanical responses of the cables. The mechanical inputs were 15° for torsion and 16mm for lateral oscillations. Torsional output amplitude was measured by noting the position of scribed lines on the tip mass whereas lateral amplitudes were measured by viewing a grid scribed on a reflecting plate and placed below the cable.

The principal results were as follows:

- .. All cables exhibited well defined mechanical resonance characteristics. This can be seen from Fig. 2, for example, which shows the torsion resonances measured for all 3 cables. Further very high amplitude magnification was recorded, ranging from 9 to 30 for the torsion mode and 80 to 180 for the lateral modes.
- .. No induced movement could be achieved in any cables solely as a result of thermal inputs.
- .. The natural torsion frequencies of all cables were reduced by between 10% to 30% as a result of heat inputs.

Conclusions

The high amplitude magnifications, particularly for lateral oscillations, show that the intrinsic damping characteristics of the cables are very small. Also, the changes in natural torsional frequency with temperature indicate that quite a wide range of natural frequencies will be experienced in space, since the temperature will have an even larger variation than that experienced during our tests. The introduction of artificial damping i., therefore, of prime importance.

Finally, since no cable movements were induced as a result of oscillatory heat inputs only, despite the fact that an exaggeration of the conditions for inducing thermal gradients was aimed for in the tests, then the improvements in damping effects induced by the added damper should virtually eliminate any concern due to this effect.

DEVELOPMENT OF A CABLE BOOM MECHANISM

Introduction

A cable boom mechanism study was conducted in parallel with the investigation of cable response. The objective was to design a cable boom system, including storage container, development control unit and the cable itself, such that the system could be built and tested and exhibit a high degree of reliability. The design had to take into account the following constraints:

- .. The mechanism had to stow and deploy at least 10m of cable boom.
- .. It should be possible to stop the boom at any stage of deployment.
- .. No slip rings should be used.
- .. At least one metre of the end of the boom had to have a circular cross section.

System Study

This consisted, essentially, of an examination of system variations for one basic solution - that is, a cable stowed on a rotatable drum. A flat cable boom was chosen because of its compact storage characteristics. The requirements could be met by using 6 coaxial wires plus one central load wire surrounded by shielding and outer insulation. This arrangement could readily be converted to circular cross-section cable over the final 1 metre of length and is illustrated in Fig. 3.

The main problem with the rotating drum solution is the electrical connection. The latter was studied from the point of view of both a retractable and a non-retractable system.

Non-Retractable System

The electrical signals can be taken from the cable boom by means of a flexible cable, termed a flexlead, which can be positioned inside or next to the drum. For the non-retractable system, flexlead length can be minimised by using the conversion technique. The flexlead is backwound on the central shaft and unwinds during boom deployment. After passing the conversion point, it then rewinds onto the shaft in the opposite sense. The same cable could be used for both boom and flexlead.

Deployment can be performed by motor driven gears. Both a worm gear and a spur gear drive were considered. The worm gear has a self-locking capability and requires the motor power of about 3 watts during deployment. The spur gear solution is relatively straightforward but requires an auxiliary braking device. The power required by the motor would be about 12 watts and would cause more magnetic disturbance than the previous solution.

Retractable System

This imposes more stringent requirements on the flexlead, because it must work reliably in both directions. Tests were carried out on various configurations and the preferred solution was a single stage flexlead without conversion. This requires additional flexlead length so that, in order to minimise mass and volume, it is preferable not to use the cable boom cable itself as the flexlead but to use a special flexlead cable. This system has been successfully tested.

For the deployment drive unit, the retraction forces are higher than the deployment forces. Peak output motor power required would be 20W for the worm gear and 15W for the spur gear. The motor output power can be decreased by reduction of the retraction speed. The latter can be achieved by gear switching or by utilisation of induction motors with sharply decreasing torque/rotational speed characteristics.

Detailed Design Study

The retractable system was chosen for the detailed design study because this feature was considered desirable for ground testing. During this phase, detailed analysis of the various components was undertaken in order to provide

final dimensions to enable manufacturing drawings to be produced. The final drawing of the complete mechanism is given in Fig. 4.

For the flexlead, a stranded flat ribbon cable 0.7mm thick was chosen capable of being wound on an inner diameter of 25mm. A total length of 6.8m of flexlead was required for 10m of cable boom and its total weight is 102 g.

For the cable drum, a minimum diameter of 100mm, for 10m of cable, was calculated, the outer diameter of drum + cable being 200mm. For a constant drum rotation speed, the deployment speed of the cable will vary. However, no correction was made for this since the speed variation was within an acceptable range. Optimisation of the drum parameters was achieved by using the following drum equations:

1. $d_i + 2 \cdot n \cdot s. = d_a$
2. $d_a \leq 2 d_i$ (If $N_D \approx \text{const}$ and $V_{\max} \geq V_{\min}$)
3. $(d_i + d_a) \pi/2 = L$

The motor driven worm gear system was chosen for the drive. Sizing was based on the expected cable loads during deployment as shown in Fig. 5. This led to the choice of a Clifton Ash size 11 two phase A.C. motor of 27×10^{-3} Nm (4 oz-in.) stall torque and speed of 12000 r.p.m. together with a sterling size 11 gearhead. The pitch diameter of the worm gear was 18mm with a pitch angle of 8° . An A.C. motor was chosen because of electromagnetic cleanliness requirements, the remanent magnetic field being at least a factor of 10 better than for D.C. motors.

Dry lubricants and dry lubricated materials were used throughout.

The unit was successfully built and has undergone vacuum testing on the facility illustrated in Fig. 6.

Conclusions

A mechanism for storage and deployment control of a cable boom was successfully developed and tested.

A phenomenological study of cable boom vibrations indicated that some supplementary damping is most desirable.

A problem that has to be investigated for a certain geostationary scientific satellite application of the cable boom concept is the development of a cable that will withstand the severe radiation and eclipse thermal environments.

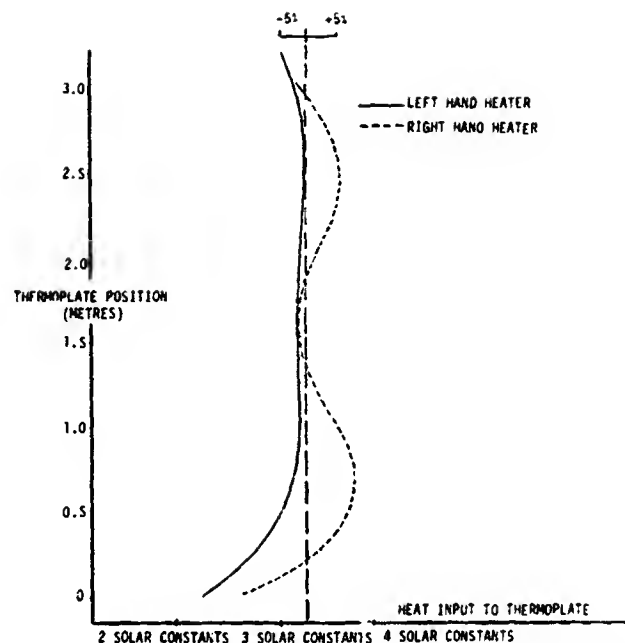


Figure 1.- Heat intensity distribution along length of cable position for both arrays.

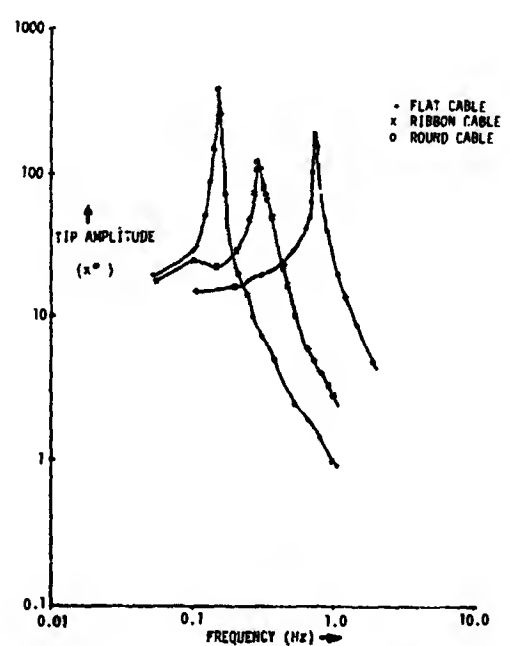
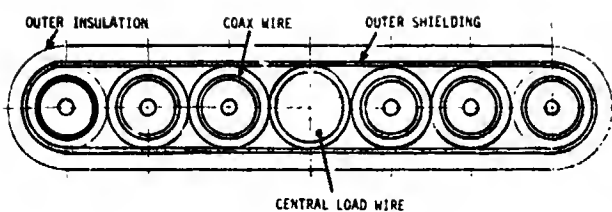
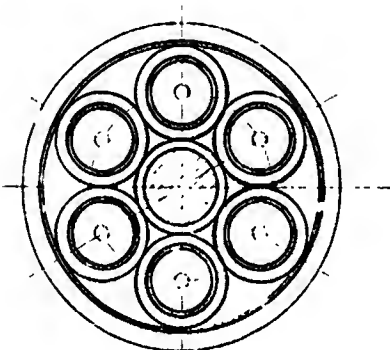


Figure 2.- Torsion resonance plots for three cable types. (Input amplitude, 15°).



(a) Flat arrangement.



(b) Round arrangement.

Figure 3.- Cable cross section.

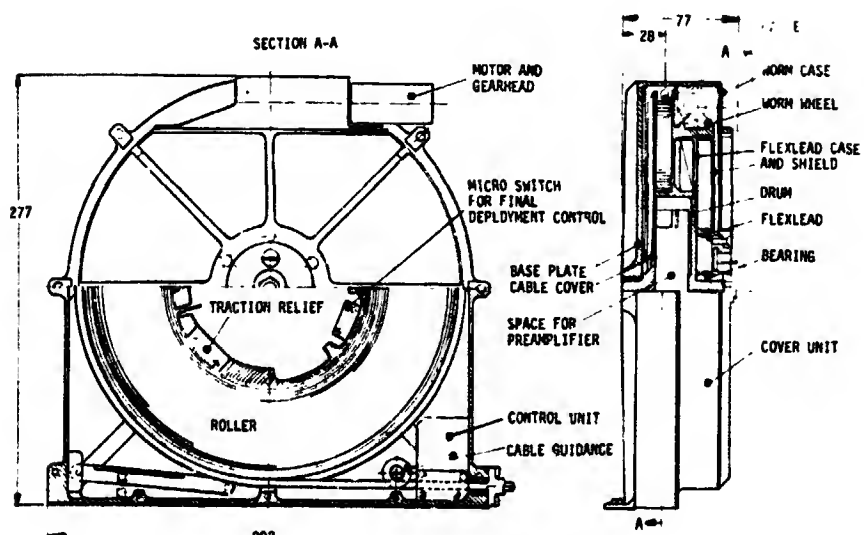


Figure 4.- GEOS cable boom system.

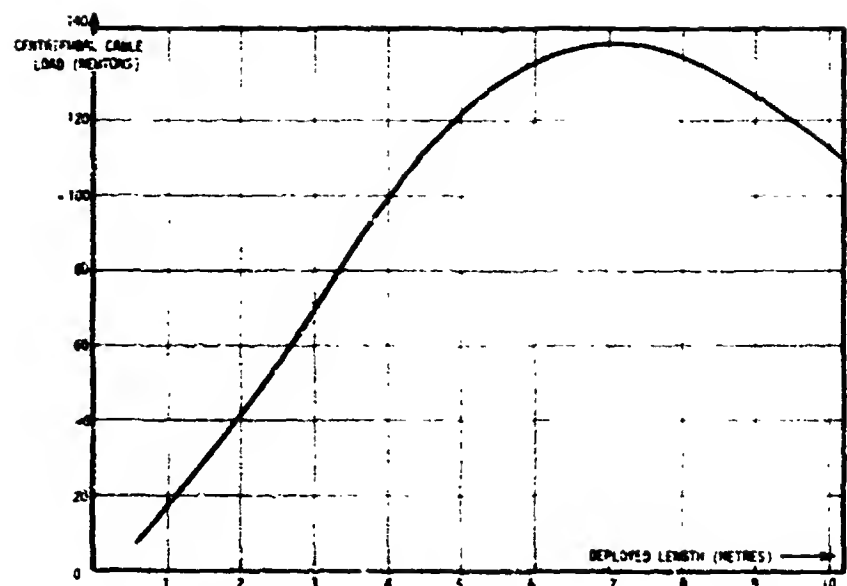


Figure 5.- Cable load during deployment.

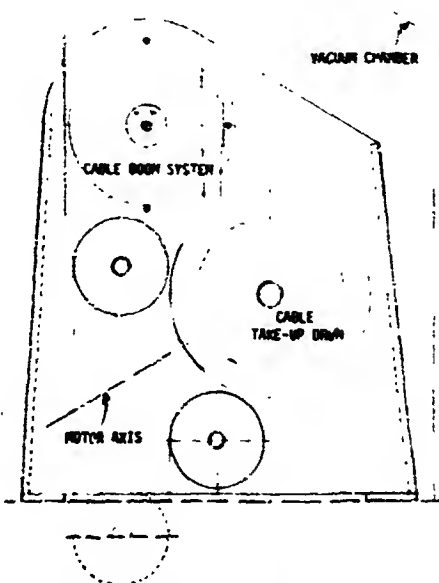


Figure 6.- Vacuum test facility.

3. A LASER INITIATED EXPLOSIVE DEVICE SYSTEM*

**By L. C. Yang, V. J. Menichelli,
and J. E. Earnest**

**California Institute of Technology
Jet Propulsion Laboratory
Pasadena, California 91103**

SUMMARY

A laser initiated explosive system has been recently developed which can simultaneously initiate multiple explosive devices. Advantages of this system over electrically initiated devices (EED's) are increased safety and reliability, simplicity of laser initiated devices, and increased weight efficiency. The system design with test data is presented and a comparison between laser initiation and electrical initiation is discussed.

INTRODUCTION

There are numerous applications for explosive devices aboard space-crafts and launch vehicles. In most cases these devices are electrically initiated. The mechanism in hot-bridgewire type electroexplosive devices (EED's) is quite simple. However, the electrical system (power supply, cabling, EED) is a complex work in design, fabrication, and testing because of severe requirements on safety, reliability, and weight efficiency. Inherent disadvantages of EED's are manifold. For example, EED's can be inadvertently initiated from electro-magnetic radiation, spurious electrical signals and/or static discharges. There have been approaches to remedy some of these problems; e.g., initiation sensitivity of EED's has been reduced with the well known 1 watt, 1 amp no-fire squibs using a ceramic header as a heat sink, antistatic gaps and breakdown conductive shunt materials to by-pass static discharges, and electrically nonconductive explosive materials. The bridgewire/header/explosive interface is the most critical area of an EED and has always been the main source of EED unreliability due to poor bridgewire welds, corrosion of the bridgewire, and poor contact between the wire and the explosive. Detailed quality control is necessary to minimize these

*This paper presents the results of one phase of research carried out at the Jet Propulsion Laboratory, California Institute of Technology, under contract NC NAS 7-100, sponsored by the National Aeronautics and Space Administration.

problems, but at very high cost. Nevertheless, there are areas which are so intrinsic that no adequate solution (such as the strain behavior of bridgewire under local heating of the wire or mismatch of its thermal expansion with respect to the bridgewire support) has been found.

A laser initiated explosive device system consists of three parts: A pulsed laser as the power source, fiber optics as the energy transmitter, and laser-initiated explosive devices. The advantages of a laser-initiated device are immediately apparent from Figure 1. It is constructed with the same dimensions as a typical 1 amp, 1 watt no-fire squib, except the electrical connector has been redesigned to accept a fiber-optics bundle. The bridgewire/header subassembly has been replaced with a glass-to-metal sealed window designed to withstand the maximum pressure generated by the explosion. The elimination of the bridgewire and the associated hazards is directly responsible for the elimination of at least 80% of the testing procedures normally required on an EED. These include fabrication of the header, pin to header seal, the spark gap, anti-static shunt, welding of bridgewire, application of explosive slurry to the bridgewire, bridgewire resistance test, pin to case and pin to pin insulation resistance test, electrostatic discharge test, 1 watt, 1 amp no-fire test, post-fire resistance test, temperature cycling test, and various non-destructive tests. To establish these procedures and the quality assurance at each step has been the main effort in the manufacture and qualification of aerospace squibs.

It is realized that laser initiation is energetically more efficient than a 1 watt, 1 amp no-fire hot wire ignition. The laser sensitivity (1 msec laser pulse) of a typical pyrotechnic mixture (Zr/NH_4ClO_4 , 50/50) is of the order of 0.93 J/cm^2 (6 J/in.^2) while millisecond firing sensitivity of typical 1 watt, 1 amp no-fire squibs are about 6 to 9.3 J/cm^2 (40 to 60 J/in.^2) average energy flux at the wire-explosive interface for a typical 1 ohm bridgewire, 2.54mm in length and 0.05mm in diameter (100 mil x 2 mil). The high flux rate required of the latter results from the fact that the header (alumina) which is a good thermal conductor is in contact with the wire and the heat transfer is more efficient. Reliabilitywise, the laser device has more advantages than the electrical hot-wire devices. The mechanism of heat conversion is directly on the explosive in the former case, while the latter has to rely on bridgewire heating and transfer to the explosive. There are possibilities of bridgewire burnout without the resultant explosive ignition. (This is an important mode of failure in a high current, low temperature firing or if an insensitive explosive is used.) When one considers the area of contact of the explosive and the energy it is seen that the laser initiation is less critical to pyrotechnic inhomogeneity. The interface in a laser initiation is typically a 2mm diameter (80 mils) or $32 \times 10^{-3} \text{ cm}^2$ ($5 \times 10^{-3} \text{ in.}^2$) in area of initiation, while for a bridgewire 0.05 mm diameter (2 mil) by 2.54 mm long (100 mil) the area is in the order of $20 \times 10^{-4} \text{ cm}^2$ ($3.2 \times 10^{-4} \text{ in.}^2$).

It is interesting to note that a laser initiation system can have a weight advantage over an electrical initiation system. At first glance, the laser technique appears to be inefficient in the energy storage. A pulsed solid state laser returns only of the order of 2 to 3% of the electrical energy

needed to excite a flash lamp for laser pumping. However, the specific efficiency of capacitors to store energy increases nonlinearly depending upon the charging voltage. For a typical 50 V tantalum electrolytic capacitor used on a spacecraft for an electrical initiation system the factor is about 11.0 J/Kg (5J/lb) while the aluminum-polyester type (5 kV) and aluminum electrolytic (500 V) energy storage capacitors for laser flash lamp discharge can be as high as 275 J/Kg (125J/lb) and 440 J/Kg (200J/lb), respectively. This fact alone is enough to make the weight efficiencies compatible. On the other hand, the switching and triggering circuitry of a laser initiation system can be made much simpler than an electrical system (especially for simultaneous multi-unit actuation) and be weight saving. This plus the inherently better sensitivity of laser initiation makes it possible for a properly designed laser initiation system to be lighter than an electrical initiation system of the same capability.

LASER SYSTEM DESIGN

Listed below are some of the state-of-the-art considerations in designing a laser initiation system:

1. For pyrotechnic initiation a pulsed neodymium laser operated in the free running mode with a pulse length from 0.2 to 2.0 milliseconds is best suited for laser and pyrotechnic initiation efficiency.
2. Pyrotechnic laser initiation sensitivity is assumed to be 0.93 J/cm^2 (6 J/in.^2) which can be achieved, e.g., with a mixture of $\text{Zr}/\text{NH}_4\text{ClO}_4$ (50/50).
3. The reflective losses of light energy on all optical interfaces such as the focusing lens surface and fiber optic ends, etc., can be reduced to a negligible amount by using anti-reflection coatings.
4. For better transmission of the laser wavelength (1.06μ), glass fiber optics is preferable to plastic fiber optics. The transmission factor I/I_0 is defined as:

$$I/I_0 = e^{-\alpha x}$$

where α is the attenuation constant, with a typical value of $0.4/\text{m}$ for fiber bundle containing 0.075 mm (3 mil) diameter individual glass fibers and x is the length of the fiber optics in meters.

5. For better reliability and ease of fabrication, the fiber bundle of conventional glass fiber optics should have a minimum diameter of 1.65 mm (65 mils).
6. The weight of such types of fiber optics is about 22.4 g/m (0.015 lb/ft) or less, including proper flexible metal cable protection.

7. The relevant quantity of the system is the energy flux density, J/cm^2 ($J/in.^2$); in general, in order to increase the initiation efficiency and to compensate for the rather large loss factor in the fiber optics, the laser beam should be focused to feed into the fiber optics. For a fixed laser beam divergence, the shorter the focal length of the lens, the higher energy flux density at the focal point. However, in practice, focal length of 12.7 to 25.4 mm (0.5 in. to 1.0 in.) is proper in order to match the beam diameter. Too sharp a focus usually will result in burning the input end of the fiber bundle and cause large insertion losses. It will also limit the transmission to only a few individual fibers thereby decreasing the reliability. It is always possible to match the laser spot with the input fiber bundle diameter by adjusting the distance between the lens and the input end of the fiber optics. A detailed study of the flux distribution at the input end is helpful. However, under this condition an average energy flux density Φ can be assumed as:

$$\Phi = \frac{\text{Energy}}{A}$$

where A is the area of the input fiber bundle of diameter 1.65 mm (0.065 in.) for a single fiber bundle, single device application. For multi-devices and a multi-bunched fiber bundle,

$$\Phi = \frac{\text{Energy}}{NA}$$

where N is the number of the devices or fiber bundle branches.

8. With proper design, pulsed neodymium laser may have specific efficiency, i.e., laser energy output per unit weight or volume, of the order of 3.3 J/Kg (1.5 J/lb) and $0.005 J/cm^3$ (0.08 J/in.³). (References 1 and 2).
9. With proper design, laser output energy should be about 2% of the electrical energy stored in the high voltage energy storage bank.
10. The required dc input power for the laser can be estimated as

$$\text{Average dc input power} = \frac{1}{e} \frac{\text{Electrical energy in the capacitor bank}}{\text{Required charging time}}$$

where e is the efficiency factor of a dc to dc high voltage converter. For a properly designed converter, $e > 50\%$.

11. The following is an example illustrating the use of these estimation procedures:

Requirements: Simultaneously initiate four devices over a distance of 3.05 m (10 feet).

Laser sensitivity of device = 0.93 J/cm^2 (6 J/in.^2)

Transmission factor of 3.05 m (10 ft) of fiber optic $\approx 20\%$

Energy flux density required at input end of the fiber optics, X

$$\Phi = 0.93 \text{ J/cm}^2 \div 20\% = 4.65 \text{ J/cm}^2 = 30 \text{ J/in.}^2$$

Laser energy required = $NA \Phi$

$$= 4 \times \pi \times \left(\frac{1.65 \text{ mm}}{2} \right)^2 \times 4.65 \text{ J/cm}^2$$

$$= 0.4 \text{ J}$$

Laser energy required to satisfy a performance margin of 3

$$= 0.4 \text{ J} \times 3 = 1.2 \text{ J}$$

Weight of laser = $1.2 \text{ J} \div 3.3 \text{ J/Kg} = 364 \text{ g} = 0.8 \text{ lb}$

Size of the laser = $1.2 \text{ J} \div 0.005 \text{ J/cm}^3 = 240 \text{ cm}^3 = 15 \text{ in.}^3$

Weight of the fiber optics = $4 \times 3 \text{ m} \times 22.4 \text{ g/m}$

$$= 269 \text{ g} = 0.6 \text{ lb}$$

It is evident that the procedure is quite simple and effective.

A PRACTICAL EXAMPLE OF THE SYSTEM

A miniaturized laser initiation system has been developed very recently in the Jet Propulsion Laboratory. The objective was to satisfy the requirements stated above. This type of functional requirement is very typical for spacecraft applications, e.g., the Viking Lander separation mechanism. At the beginning of the development it was not quite certain what values of specific efficiency would be achieved since, when the optical pumping level is low, it is known that the lasing threshold condition takes an important role. The optimization of a pulsed neodymium laser is a formidable problem, because the laser efficiency depends essentially on the total efficiency of each link in the chain of laser generation. After careful selection of components and a systematically optimized design and fabrication program, we were able to achieve high energy storage efficiency, good spectral range of the xenon flash lamp, and a laser head configuration for high laser output efficiency. The construction of the laser is shown in Figure 2. It has a dimension of $5.08 \times 7.62 \times 12.7 \text{ cm}$ (2 in. \times 3 in. \times 5 in.), weighs 774g (1.7 lb) and gives out a laser pulse, 2.8J in energy and 1.5 msec in duration. It requires 10 watts average dc input in a charging time of about 50 sec. The capacitor bank is a 520 V rated, 1200 μf , electrolytic capacitor $5.08 \times 11.9 \text{ cm}$ (2 in. \times 4.68 in.) in size and 340g (12 oz) in weight. The details of the design are reported elsewhere (Reference 2).

Figure 3 shows the test set-up to demonstrate the simultaneous initiation of four explosive devices (the type shown in Figure 1). The fiber optics for this particular type of test was fabricated to have a single input 3.3 mm in diameter (0.130 in.) and branched into four identical outputs (1.65 mm in diameter (0.065 in.)). The total length to each pyrotechnic device was 3.05 m (10 ft). Randomization of the individual fibers resulted in equal light splitting within $\pm 5\%$ at each output and independent of the light input distribution. The gas pressure generated by the burning pyrotechnic material was monitored by the same method as that used for spacecraft electroexplosive devices. The system consists of 1 cc pressure bomb, Kistler pressure transducers and charge amplifiers. The result of the test as recorded by an oscilloscope is shown in Figure 4. The sharp-rise peak pressure in each channel was reached within approximately 0.1 ms after the start of the laser pulse. This type of ignition characteristic is very desirable for the functioning of pyrotechnic devices. In comparison with the total laser pulse duration of 1.5 ms, the laser energy of 2.8J gives approximately a performance margin of 10. Therefore for a performance margin of three the laser can be further reduced more than 50% to the size and weight estimated in the last section. It is interesting to note that the pyrotechnic switching (firing) unit on the Viking Orbiter '75 spacecraft of the similar capability is 9.8 x 15.2 x 23.4 cm (3.875 in. x 6.0 in. x 9.2 in.) in size and weighs 3.18 Kg (7.0 lb).

CONCLUSION AND REMARKS ON THE FUTURE

The novel features of a laser initiated explosive device system, especially in comparison to an electroexplosive initiation system have been demonstrated. It is evident that the system has gone through a speculative stage since the late 60's and has materialized towards a realistic system. Further evaluations should be made with respect to specific needs. There are minor details such as developing a rotary electro-optical or mechanical scanning system of the laser beam or fiber optics for a programmed firing sequence of multi-events, a hermetically sealed fiber optic feed through connector, etc. They can be engineered to be weight efficient and reliable.

The results illustrated here are more or less oriented toward the pyrotechnic system for spacecraft-type application. The concept of laser initiation of explosive devices in general has also been proven to be effective. For example, zirconium doped PETN and RDX can be initiated by the same type of laser, resulting in a burn to detonation. The laser sensitivities are in the order of 3.1 J/cm² (20J/in.²). Primary high explosives such as lead azide and lead styphnate can be directly initiated. (Reference 3). Q-switched mode lasers can directly detonate PETN, RDX and Tetralyl in a properly designed device (References 4 and 5) and can be useful where micro-second simultaneity is important.

REFERENCES

1. Yang, L. C., and Menichelli, Vincent J.: A High-Efficiency, Small, Solid-State Laser for Pyrotechnic Ignition, JPL Quarterly Technical Review, Vol. 2, No. 4, January 1973, Page 29-37.
2. Yang, L. C.: The Design of High Efficiency, Small, Pulsed Solid-State Laser. Laser Focus Magazine, July, 1973.
3. Menichelli, Vincent J. and Yang, L. C.: Sensitivity of Explosives to Laser Energy. JPL Technical Report 32-1474, Jet Propulsion Laboratory, April, 1970.
4. Yang, L. C. and Menichelli, Vincent J.: Detonation of Insensitive High Explosives by a Q-switched Ruby Laser. Appl. Phys. Lett. Vol. 19, p 473-475, 1971.
5. Menichelli, Vincent J. and Yang, L. C.: Initiation of Insensitive Explosives by Laser Energy. JPL Technical Report 32-1557, Jet Propulsion Laboratory, June 1972.

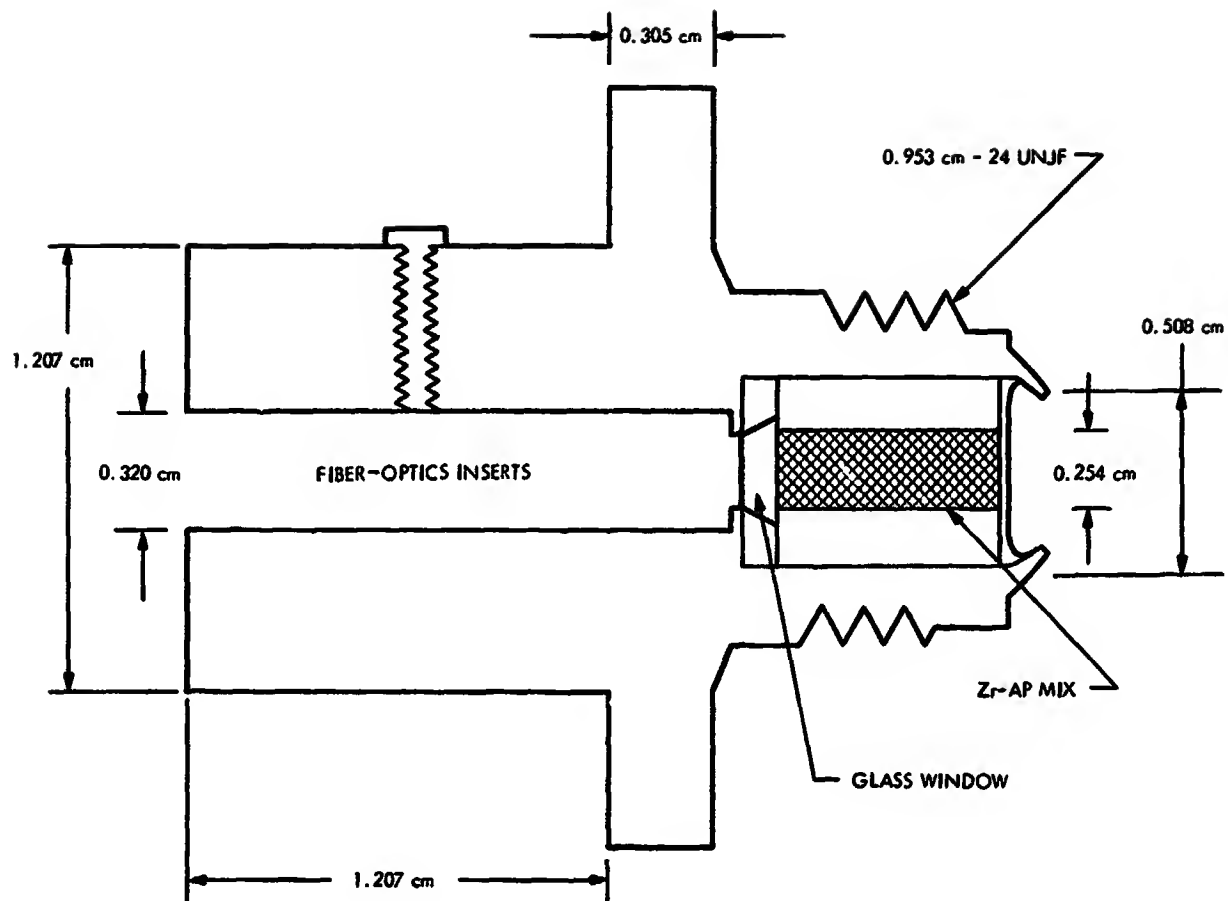


Figure 1.- Laser-initiated pyrotechnic device.

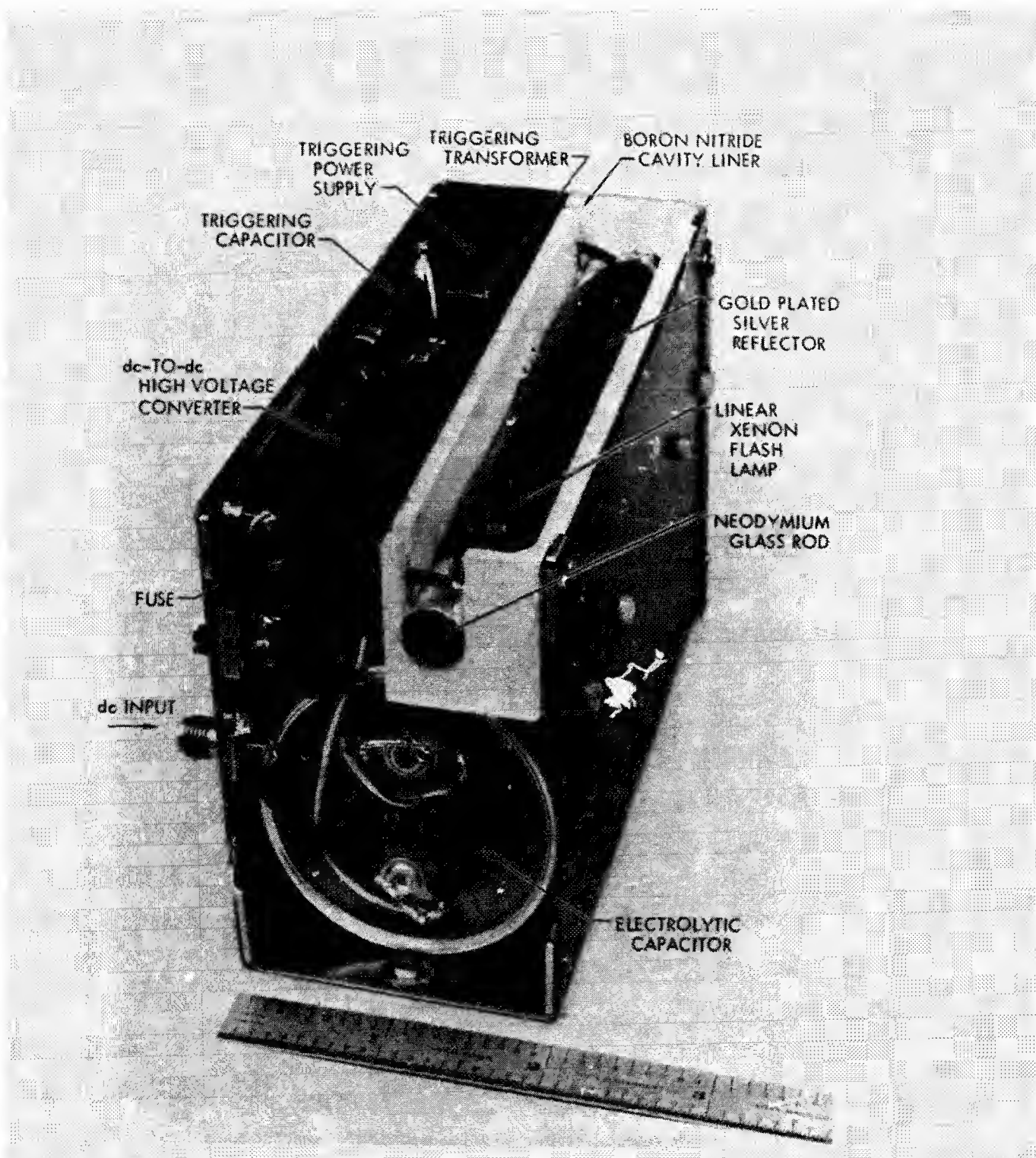


Figure 2.- Interior of a high-efficiency, small, pulsed neodymium laser showing the components and construction.

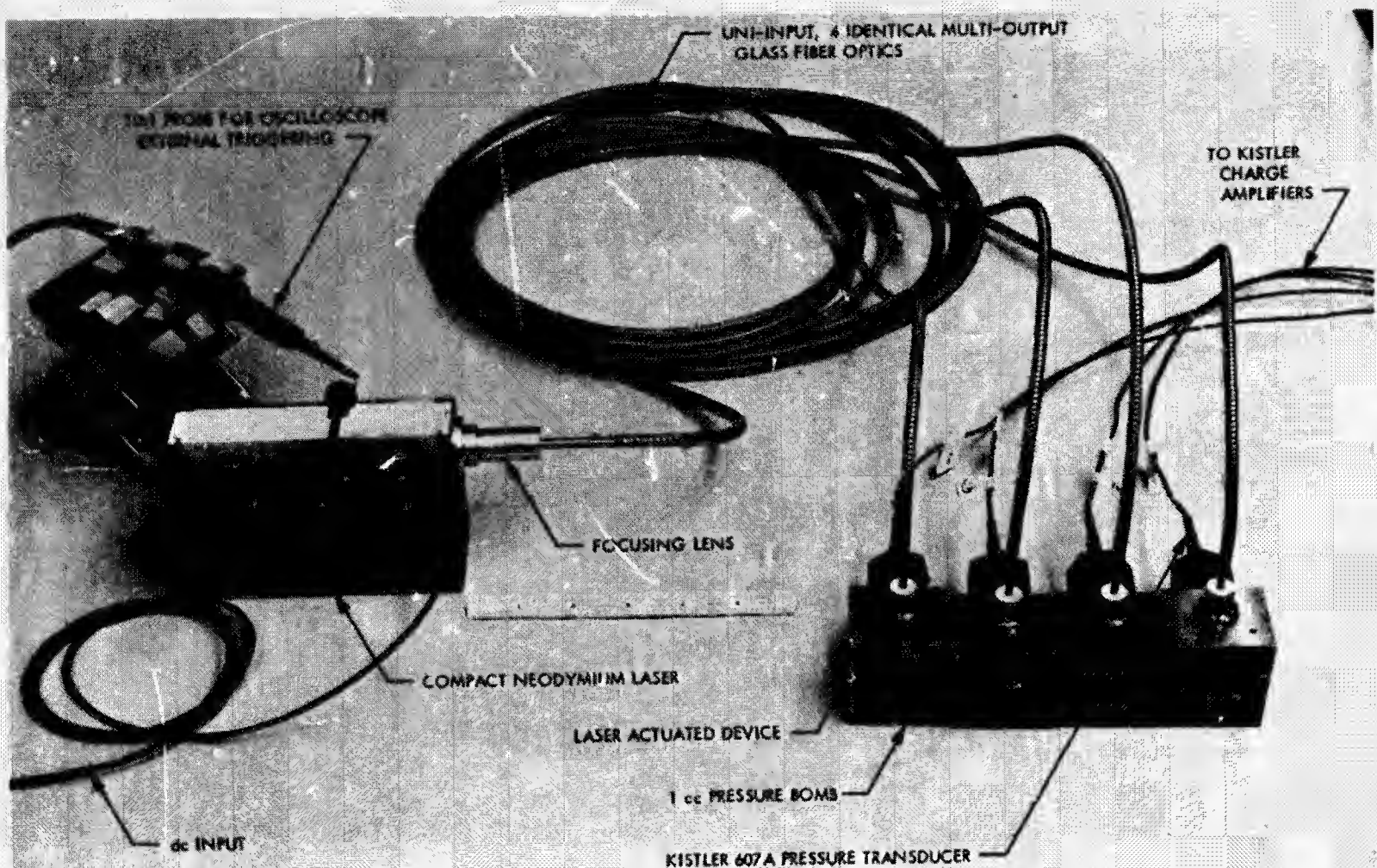
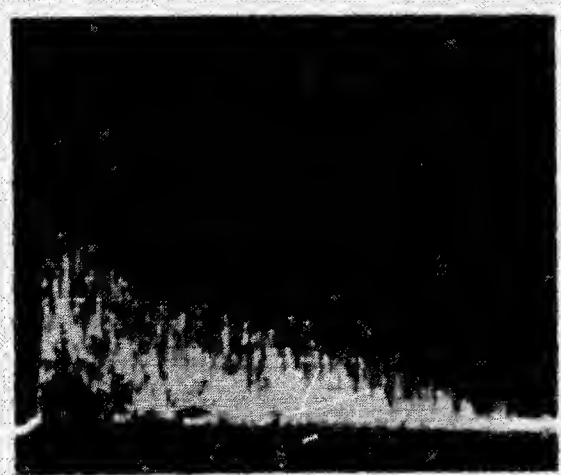
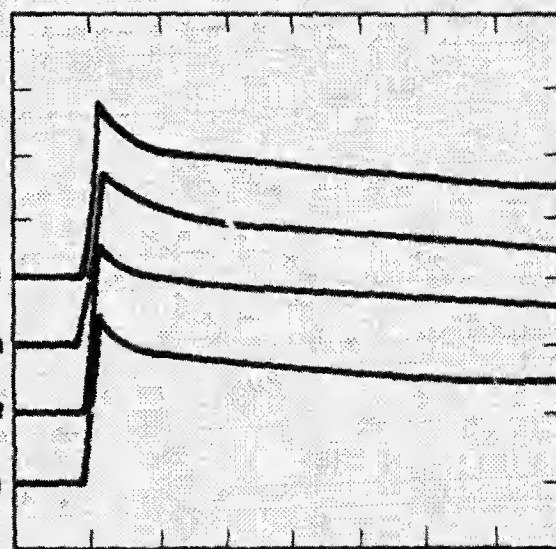


Figure 3.- The test set-ups of simultaneous initiation of multi-devices by a neodymium laser.



LASER OUTPUT

HORIZONTAL SCALE: 0.2 msec/DIVISION
VERTICAL SCALE: RELATIVE UNITS



PRESSURE OUTPUT

VERTICAL SCALE: $1.72 \times 10^7 \text{ N/m}^2/\text{UNIT}$
(2500 psi/UNIT)
HORIZONTAL SCALE: 0.2 msec/UNIT

LASER ENERGY: 2.8 J

LENGTH OF THE FIBER-OPTICS: 3.0 m (10 ft)

FOCUSING LENS: 75 mm FOCAL LENGTH
12 mm DIAMETER

FIBER-OPTICS CONFIGURATION: UNIT-INPUT-4-
IDENTICAL OUTPUTS

ZERO TIME: TRIGGERING PULSE TO FLASH LAMP

EXPLOSIVE DEVICE: JPL AP-Zr LASER SQUIB

VOLUME OF PRESSURE BOMB: 1 cc

Figure 4. Test record of simultaneous initiation of pyrotechnic devices by laser energy.

4. PRINCIPAL AXES AND MOMENTS OF INERTIA

OF DEFORMABLE SYSTEMS

By T. R. Kane

Professor of Applied Mechanics
Stanford University, Stanford, California

SUMMARY

Information about principal axes and moments of inertia is presented in terms of formulas involving solely quantities which can be expressed in literal form whenever central principal axes can be located by inspection for at least one state of a deformable system composed of particles and rigid bodies. Two illustrative examples are worked out in detail.

INTRODUCTION

Principal axes and moments of inertia play important physical roles in certain situations. For example, any completely free rigid body (or a deformable body moving as if it were rigid) can execute a simple rotational motion, that is, a motion during which the angular velocity vector remains parallel to a body-fixed line; but this is possible only if the line is parallel to a central principal axis of inertia, and the stability of the motion is affected by the relative magnitudes of the central principal moments of inertia.

Principal axes and moments of inertia are of interest also from an analytical point of view, for their use can lead to marked simplifications of expressions for kinetic energy, angular momentum, gravity torque, etc. Consequently, the following are natural questions: Are there any difficulties associated with the use of principal axes and principal moments of inertia? And, if so, how can they be overcome? The answer to the first question is "yes"; for, while the problem of locating principal axes and evaluating principal moments of inertia can always be solved in principle (it is simply the eigenvalue problem for a 3×3 symmetric matrix), the solution, in general, entails finding the roots of a cubic equation, and this can give rise to difficulties ranging from relatively minor ones, presenting themselves when one is dealing with numerical (rather than literal) values of system parameters, to apparently insurmountable ones, which arise when one seeks results expressed entirely in literal form. As to the second question, it is the purpose of this paper to supply a partial answer by presenting formulas containing information about principal axes and moments of inertia in terms of quantities which

PRECEDING PAGE BLANK NOT FILMED

are readily available in literal form whenever central principal axes can be located by inspection for at least one state of the system under consideration. These formulas are

$$\tilde{b}_{jj} = 1, \quad \tilde{b}_{jk} = 0 \quad (1)$$

$$\tilde{b}_{jj,r} = 0, \quad \tilde{b}_{jk,r} = \frac{\tilde{I}_{jk,r}}{\tilde{I}_{jj} - \tilde{I}_{kk}} \quad (2)$$

$$\tilde{I}_j = \tilde{I}_{jj} \quad (3)$$

$$\tilde{I}_{j,r} = \tilde{I}_{jj,r} \quad (4)$$

$$\tilde{I}_{j,rs} = \tilde{I}_{jj,rs} + 2 \left(\frac{\tilde{I}_{jk,r} \tilde{I}_{jk,s}}{\tilde{I}_{jj} - \tilde{I}_{kk}} + \frac{\tilde{I}_{jl,r} \tilde{I}_{jl,s}}{\tilde{I}_{jj} - \tilde{I}_{ll}} \right) \quad (5)$$

To explain the symbols appearing in Eqs. (1)-(5), it is helpful to refer to a schematic representation of the situation to which these equations apply, Fig. 1, where S designates a material system composed of particles and rigid bodies. The relative positions and orientations of the objects forming S are presumed to be governed by n scalar quantities q_1, \dots, q_n chosen in such a way that all vanish when S assumes a certain configuration called the reference state. S^* is the mass center of S . A_1, A_2, A_3 are mutually perpendicular axes intersecting at S^* and meeting two requirements: the orientation of each axis relative to S depends uniquely on the values of q_1, \dots, q_n ; and each axis is a principal axis of inertia of S for S^* when S is in the reference state. B_1, B_2, B_3 are instantaneous central principal axes of S ; that is, they are principal axes of S for S^* for all values of q_1, \dots, q_n . Finally, $\tilde{a}_1, \tilde{a}_2, \tilde{a}_3$ are unit vectors respectively parallel to A_1, A_2, A_3 and $\tilde{b}_1, \tilde{b}_2, \tilde{b}_3$ are unit vectors respectively parallel to B_1, B_2, B_3 .

In Eqs. (1)-(5), each of the subscripts j, k , and l may take on the values 1, 2, and 3, but no two may have the same value; the subscripts r and s assume the values $1, \dots, n$; tildes denote evaluations at $q_1 = \dots = q_n = 0$, that is, in the reference state; and the symbols appearing in the equations are defined as follows:

$$b_{jj} \triangleq b_j \cdot \tilde{a}_j, \quad b_{jk} \triangleq b_j \cdot \tilde{a}_k \quad (6)$$

$$I_{jj} \triangleq a_j \cdot \tilde{I} \cdot \tilde{a}_j, \quad I_{jk} \triangleq a_j \cdot \tilde{I} \cdot \tilde{a}_k \quad (7)$$

and

$$I_j \triangleq b_j \cdot \tilde{I} \cdot \tilde{b}_j \quad (8)$$

where \tilde{I} is the inertia dyadic of S for S^* . Finally, a comma followed by r or/and s indicates partial differentiation with respect to r or/and s , so that, for example,

$$\tilde{I}_{11,57} = \frac{\partial^2 I_{11}}{\partial q_5 \partial q_7} \quad |_{q_1 = \dots = q_n = 0}$$

EXAMPLES

One class of problems whose solution is facilitated by using Eqs. (1)-(4) involves questions regarding the sensitivity of principal axes orientations and principal moment of inertia values to small changes in the configuration of a deformable system. For example, consider the system S of three particles P , Q , and R shown in Fig. 2(a). If P and Q each have a mass m while R has a mass $2m$, the mass center S^* of S is situated as indicated, and X_1 and X_2 are central principal axes of S when the three particles form an equilateral triangle with sides of length $2L$. The associated moments of inertia have the values $2mL^2$ and $3mL^2$, respectively. In Fig. 2(b), S is shown in a state of distortion. The mass center S^* is again the midpoint of the line segment connecting R to O , the midpoint of $P-Q$, but lines passing through S^* and parallel to $O-R$ or to $P-Q$ are no longer central principal axes. Instead, two of the central principal axes of S are now the perpendicular lines B_1 and B_2 , the first of which forms with $O-R$ an angle θ that depends on the distortion, and the associated principal moments of inertia, I_1 and I_2 , differ from $2mL^2$ and $3mL^2$. To study such distortion effects, one can introduce coordinates q_j , axes A_j , and unit vectors a_j and b_j ($j = 1, 2, 3$) as shown in Fig. 2(b). [A_3 , a_3 , and b_3 are normal to the plane of the paper and are omitted from Fig. 2(b)]. The orientation of A_j relative to S then depends uniquely on the values of q_1 , q_2 , and q_3 , and A_j is a principal axis of S for S^* when $q_1 = q_2 = q_3 = 0$.

Next, express \tilde{b}_1 as

$$\tilde{b}_1 = \tilde{b}_{11} + \tilde{b}_{12}$$

or, in accordance with Eqs. (6), as

$$\tilde{b}_1 = b_{11}\tilde{a}_1 + b_{12}\tilde{a}_2 \quad (9)$$

Then b_{11} and b_{12} are functions of q_1 , q_2 , and q_3 . Expanding these in Taylor series, retaining only terms of degree lower than two, and using the summation convention for repeated subscripts, one can write

$$b_{11} \approx \tilde{b}_{11} + \tilde{b}_{11,r}q_r, \quad b_{12} \approx \tilde{b}_{12} + \tilde{b}_{12,r}q_r$$

or, after using Eqs. (1) and (2),

$$b_{11} \approx 1, \quad b_{12} \approx \frac{\tilde{I}_{12,r}}{\tilde{I}_{11} - \tilde{I}_{22}} q_r$$

Hence, from Eq. (9),

$$\tilde{b}_1 = \tilde{a}_1 + \frac{\tilde{I}_{12,r}}{\tilde{I}_{11} - \tilde{I}_{22}} q_r \tilde{a}_2 \quad (10)$$

Now, I_{11} , I_{22} , and I_{12} [see Eqs. (7)] can be formed readily since the A_1 and A_2 coordinates of P , Q , and R can be found by inspection:

$$I_{11} = 2m[(L + q_1) \cos q_3]^2 \quad (11)$$

$$I_{22} = m[3(L + q_2)^2 + 2(L + q_1)^2 \sin^2 q_3] \quad (12)$$

$$I_{12} = -2m(L + q_1)^2 \sin q_3 \cos q_3 \quad (13)$$

Setting $q_1 = q_2 = q_3 = 0$ in Eqs. (11) and (12), one obtains

$$\tilde{I}_{11} = 2mL^2, \quad \tilde{I}_{22} = 3mL^2$$

and partial differentiations of Eq. (13) yield

$$\tilde{I}_{12,1} = \tilde{I}_{12,2} = 0, \quad \tilde{I}_{12,3} = -2mL^2$$

Substituting into Eq. (10), one thus arrives at

$$b_1 = a_1 + 2q_3 a_2$$

which shows that during a sufficiently small distortion of S one can approximate θ [see Fig. 2(b)] with $2q_3$.

The principal moments of inertia I_1 and I_2 are also functions of q_1 , q_2 , and q_3 . Again resorting to series expansion, and using Eqs. (3) and (4), one can, therefore, write

$$I_1 \approx \tilde{I}_{11} + \tilde{I}_{11,r} q_r, \quad I_2 \approx \tilde{I}_{22} + \tilde{I}_{22,r} q_r$$

and, in view of Eqs. (11)-(13),

$$I_1 \approx 2mL^2 \left(1 + 2 \frac{q_1}{L} \right), \quad I_2 \approx 3mL^2 \left(1 + 2 \frac{q_2}{L} \right) \quad (14)$$

These results describe the effect of a small distortion on I_1 and I_2 in terms of the quantities q_1 , q_2 and q_3 , which characterize the distortion.

Eqs. (14), and, indeed, the corresponding exact expressions for I_1 and I_2 , could be obtained also without the use of Eqs. (3) and (4), for we are here dealing with a planar distribution of matter, so that one needs to solve only a quadratic, rather than a cubic, equation to determine I_1 and I_2 . However, exact expressions are actually of less value than those displaying leading terms of series expansions when one is concerned with questions of sensitivity; and the reader can easily convince himself that the method here employed requires considerably less labor than does the process of finding exact expressions for I_1 and I_2 and then expanding in series.

A problem illustrating the use of Eqs. (4) and (5) to generate an exact result arises when one seeks conditions under which a principal moment of inertia of a deformable system possesses an extreme value. For instance, consider a system S composed of two rigid bodies, α and β , which are connected to each other by means of a gimbal γ , as shown in Fig. 3. Point O is the common mass center of α and β ; X_1 , X_2 , X_3 are principal axes of α , and Y_1 , Y_2 , Y_3 are principal axes of β ; and the gimbal can rotate relative to α and β only about X_1 and Y_2 , respectively. The relative orientation of α and β thus depends solely

on the angles q_1 and q_2 , and the central principal axes of α and β are necessarily central principal axes of S when $q_1 = q_2 = 0$. Suppose now that B_3 is the central principal axis of S that coincides with X_3 and Y_3 when $q_1 = q_2 = 0$, and let I_3 be the associated central principal moment of inertia of S . Then I_3 has a (local) minimum value when $q_1 = q_2 = 0$ if the following conditions are satisfied:

$$\tilde{I}_{3,1} = \tilde{I}_{3,2} = 0 \quad (15)$$

$$\tilde{I}_{3,11} > 0, \quad \tilde{I}_{3,11}\tilde{I}_{3,22} - (\tilde{I}_{3,12})^2 > 0 \quad (16)$$

How must α_1 , α_2 , α_3 , the central principal moments of inertia of α , be related to β_1 , β_2 , β_3 , the central principal moments of inertia of β , in order that Eqs. (15) and the inequalities (16) be satisfied? To answer this question, one can take for A_1 , A_2 , and A_3 the axes X_1 , X_2 , and X_3 , in which case, from Eqs. (7),

$$\tilde{I}_{11} = \alpha_1 + \beta_1, \quad \tilde{I}_{22} = \alpha_2 + \beta_2$$

$$I_{31} = (\beta_3 - \beta_1)c_1 s_2 c_2$$

$$I_{32} = -\beta_1 s_1 c_1 s_2^2 + \beta_2 s_1 c_1 - \beta_3 s_1 c_1 c_2^2$$

$$I_{33} = \alpha_3 + \beta_1 c_1^2 s_2^2 + \beta_2 s_1^2 + \beta_3 c_1^2 c_2^2$$

where s_i and c_i denote respectively $\sin q_i$ and $\cos q_i$ ($i=1,2$). It follows that

$$\tilde{I}_{31,1} = 0$$

$$\tilde{I}_{32,1} = \beta_2 - \beta_3$$

$$\tilde{I}_{33,1} = 0$$

$$\tilde{I}_{31,2} = \beta_3 - \beta_1$$

$$\tilde{I}_{32,2} = 0$$

$$\tilde{I}_{33,2} = 0$$

$$\tilde{I}_{33,11} = 2(\beta_2 - \beta_3)$$

$$\tilde{I}_{33,12} = 0$$

$$\tilde{I}_{33,22} = 2(\beta_1 - \beta_3)$$

and Eq. (4) thus gives

$$\tilde{I}_{3,1} = \tilde{I}_{3,2} = 0$$

**

while Eq. (5) yields

$$\begin{aligned}\tilde{I}_{3,11} &= \tilde{I}_{33,11} + 2 \left[\frac{(\tilde{I}_{31,1})^2}{\tilde{I}_{33} - \tilde{I}_{11}} + \frac{(\tilde{I}_{32,1})^2}{\tilde{I}_{33} - \tilde{I}_{22}} \right] \\ &= \frac{2(\alpha_2 - \alpha_3)(\beta_2 - \beta_3)}{\alpha_2 - \alpha_3 + \beta_2 - \beta_3}\end{aligned}$$

and

$$\tilde{I}_{3,12} = 0, \quad \tilde{I}_{3,22} = \frac{2(\alpha_1 - \alpha_3)(\beta_1 - \beta_3)}{\alpha_1 - \alpha_3 + \beta_1 - \beta_3}$$

Eqs. (15) are thus seen to be satisfied automatically, and the inequalities (16) are equivalent to

$$\frac{(\alpha_2 - \alpha_3)(\beta_2 - \beta_3)}{\alpha_2 - \alpha_3 + \beta_2 - \beta_3} > 0$$

and

$$\frac{(\alpha_1 - \alpha_3)(\beta_1 - \beta_3)}{\alpha_1 - \alpha_3 + \beta_1 - \beta_3} > 0$$

Hence, when the central principal moments of inertia of α and β satisfy these two conditions, then I_3 has a (local) minimum at $q_1 = q_2 = 0$.

DERIVATIONS

To establish the validity of Eqs. (1)-(5), one may begin by observing that Eqs. (1) follow immediately from Eqs. (6) together with the fact that, by construction, $a_j = b_j$ when S is in the reference state. Next, use Eqs. (6) and the identity

$$b_{\sim 1} \equiv b_{\sim 1} \cdot a_{\sim 1} a_{\sim 1} + b_{\sim 1} \cdot a_{\sim 2} a_{\sim 2} + b_{\sim 1} \cdot a_{\sim 3} a_{\sim 3}$$

to write

$$b_{\sim 1} = b_{11} a_{\sim 1} + b_{12} a_{\sim 2} + b_{13} a_{\sim 3}$$

and, after expanding b_{11} , b_{12} , and b_{13} in Taylor series and using Eqs. (1),

$$\begin{aligned}\underline{b}_1 &= (1 + \tilde{b}_{11,r} q_r + \dots) \underline{a}_1 \\ &\quad + (\tilde{b}_{12,r} q_r + \dots) \underline{a}_2 + (\tilde{b}_{13,r} q_r + \dots) \underline{a}_3\end{aligned}\quad (17)$$

Similarly, Eq. (3) is an immediate consequence of Eq. (8) and the first of Eqs. (7), and I_1 can, therefore, be expressed as

$$I_1 = \tilde{I}_{11} + \tilde{I}_{1,r} q_r + 2^{-1} \tilde{I}_{1,rs} q_r q_s + \dots \quad (18)$$

Now make use of the fact that, by construction, \underline{b}_1 is parallel to a central principal axis of inertia of S for all values of q_1, \dots, q_n , so that

$$\underline{I} \cdot \underline{b}_1 = I_1 b_1$$

or, after scalar multiplication of both sides of this equation with \underline{a}_1 ,

$$\underline{a}_1 \cdot \underline{I} \cdot \underline{b}_1 = I_1 \underline{a}_1 \cdot \underline{b}_1 \quad (19)$$

Substitution for \underline{b}_1 and I_1 from Eqs. (17) and (18), together with Eqs. (7), then gives

$$\begin{aligned}I_{11} (1 + \tilde{b}_{11,r} q_r + \dots) + I_{12} (\tilde{b}_{12,r} q_r + \dots) + I_{13} (\tilde{b}_{13,r} q_r + \dots) \\ = (\tilde{I}_{11} + \tilde{I}_{1,r} q_r + 2^{-1} \tilde{I}_{1,rs} q_r q_s + \dots) (1 + \tilde{b}_{11,r} q_r + \dots)\end{aligned}\quad (20)$$

Moreover, I_{11} , I_{12} , and I_{13} can also be expanded in series:

$$I_{11} = \tilde{I}_{11} + \tilde{I}_{11,r} q_r + 2^{-1} \tilde{I}_{11,rs} q_r q_s + \dots$$

$$I_{12} = \tilde{I}_{12,r} q_r + \dots, \quad I_{13} = \tilde{I}_{13,r} q_r + \dots$$

Consequently, each side of Eq. (20) can be regarded as a power series in q_1, \dots, q_n , and it follows that the coefficients of like terms can be equated separately. Doing this for terms of the first degree in q_1, \dots, q_n , one finds that

$$\tilde{I}_{1,r} = \tilde{I}_{11,r} \quad (21)$$

and considering second degree terms, one obtains

$$\tilde{I}_{1,rs} = \tilde{I}_{11,rs} + 2(\tilde{I}_{12,r}\tilde{b}_{12,s} + \tilde{I}_{13,r}\tilde{b}_{13,s}) \quad (22)$$

Proceeding similarly, but using \tilde{a}_2 and \tilde{a}_3 in place of \tilde{a}_1 in Eq. (19), one finds that

$$\tilde{b}_{12,r} = \frac{\tilde{I}_{12,r}}{\tilde{I}_{11} - \tilde{I}_{22}}, \quad \tilde{b}_{13,r} = \frac{\tilde{I}_{13,r}}{\tilde{I}_{11} - \tilde{I}_{33}} \quad (23)$$

and substitution into Eq. (22) then leads to

$$\tilde{I}_{1,rs} = \tilde{I}_{11,rs} + 2\left(\frac{\tilde{I}_{12,r}\tilde{I}_{12,s}}{\tilde{I}_{11} - \tilde{I}_{22}} + \frac{\tilde{I}_{13,r}\tilde{I}_{13,s}}{\tilde{I}_{11} - \tilde{I}_{33}}\right) \quad (24)$$

Finally, since \tilde{b}_1 is a unit vector,

$$(\tilde{b}_{11})^2 + (\tilde{b}_{12})^2 + (\tilde{b}_{13})^2 = 1$$

Differentiation with respect to q_r gives

$$\tilde{b}_{11}\tilde{b}_{11,r} + \tilde{b}_{12}\tilde{b}_{12,r} + \tilde{b}_{13}\tilde{b}_{13,r} = 0$$

or, after using Eqs. (1),

$$\tilde{b}_{11,r} = 0 \quad (25)$$

For $j = 1$, the validity of Eqs. (2) is established by Eqs. (25) and (23), that of Eq. (4) by Eq. (21), and that of Eq. (5) by Eq. (24). Clearly, similar proofs can be carried out for $j = 2$ and $j = 3$.

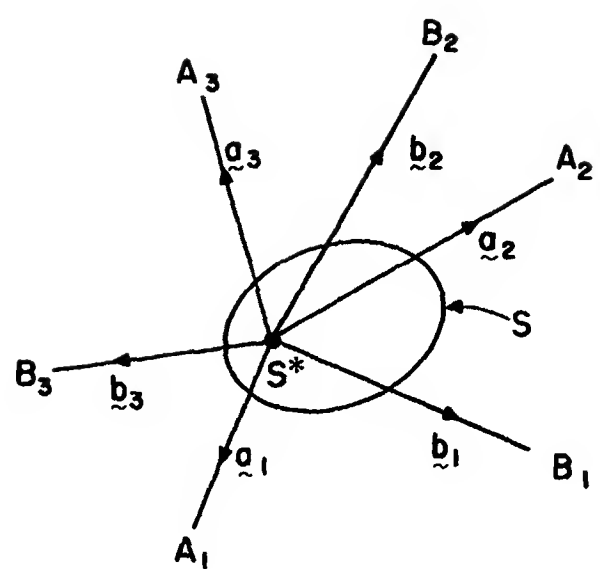
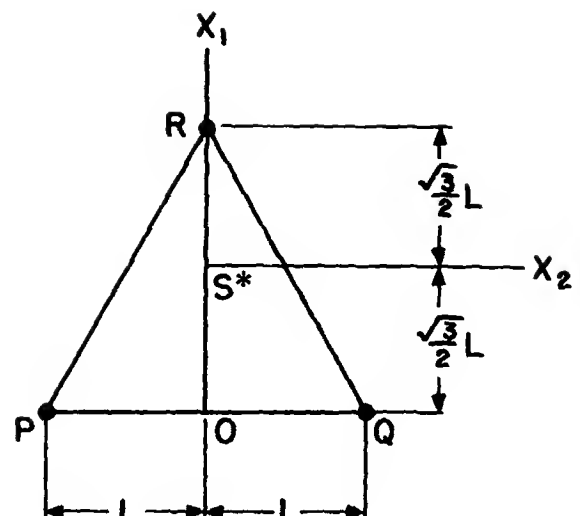
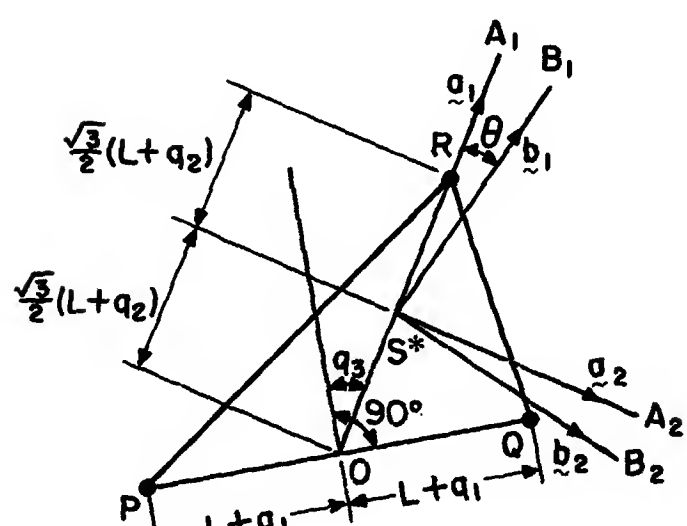


Figure 1.



(a)



(b)

Figure 2.

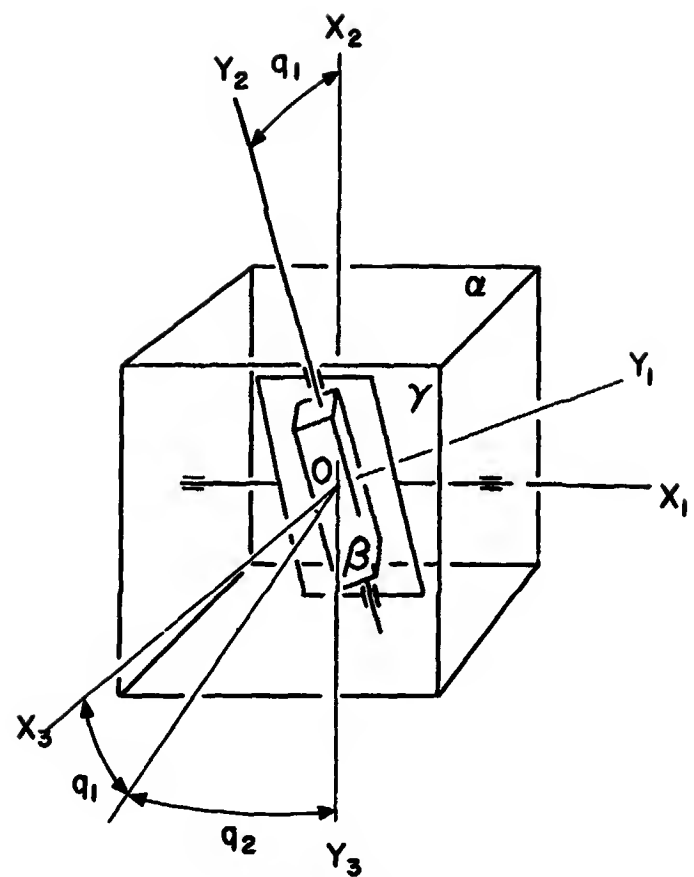


Figure 3.

5. CURRENT EUROPEAN DEVELOPMENTS IN SOLAR PADDLE DRIVES

By R.H. Bentall

EUROPEAN SPACE RESEARCH AND TECHNOLOGY CENTRE

SUMMARY

As part of its Supporting Technology Programme, the European Space Research and Technology Centre (ESTEC) is sponsoring the development of a number of critical spacecraft hardware items. The hardware under development includes two competing Solar Paddle Drives which are being produced to similar specifications by Hawker Siddeley Dynamics (HSD) and by Marconi Space and Defence Systems Ltd. (MSDS) in the U.K. Three mechanisms of each type are being produced and will undergo thermal vacuum testing at the newly commissioned European Space Tribology Laboratory (ESTL) at Risley, England. All mechanisms have lead lubricated bearings according to the process developed by MSDS.

INTRODUCTION

The growing acceptance of the three-axis-stabilized satellite as a vehicle suitable for future applications missions has intensified the need for light-weight solar paddles and a reliable means of orienting them towards the sun. Over the past 3 years ESTEC has been supporting various developments in European Industry in support of this activity and has laid particular emphasis on the provision of a versatile and thoroughly tested solar paddle drive, mainly because of the unavailability of reliability data on existing drives and the status of mechanisms generally as spacecraft single point failures. In September 1971 two competitive contracts were awarded to HSD and MSDS against strong international competition for the "design and build" of prototype solar paddle drives. Concurrently with these programmes the European Space Tribology Laboratory was commissioned, having a two-fold function, basic development on space tribology and vacuum life testing of the various ESTEC-sponsored mechanisms.

The mechanism specifications were intended for the development of an instrumented drive fabricated to a standard approaching that of flight hardware but were unconnected with the physical envelope constraints of a specific spacecraft structure. The designs were consequently derived by a series of trade-offs aimed primarily at mechanism reliability and with only passing deference to structural constraints; both designs were aimed at an "optimised" mechanism and, in fact, although the initial design phase was strictly competitive, both HSD and MSDS arrived at very similar concepts (2 bearing, direct drive). These designs are shown in Figures 1 (HSD) and 2 (MSDS/1).

Following their initial design MSDS were given a redesign contract which adapted their design concept to the specific requirements of a particular spacecraft installation. A controlling requirement was that the length of the mechanism should not exceed 10cm, about 1/3 that of the original design. The result, which is shown in Figure 3 (MSDS/2), was a significant improvement on the previous design and was chosen for further development.

The adoption of this mechanism over the previous "optimised" design is indicative of the stimulus of a challenging design goal.

As a result of the redesign, the characteristics of the two drives differ slightly. A summary is shown in Table 1.

DESCRIPTION OF SOLAR PADDLE DRIVES

During the design studies of both HSD and MSDS two main design considerations dictated the mechanical configuration chosen for the drive units.

The first was the requirement that the contributing loss of overall satellite pointing accuracy due to the motion of the paddle should not exceed 0.02°. Assuming, for example, a solar paddle inertia of 15 kg-m²/side and a relevant satellite inertia of 400 kg-m² and assuming also, as a worst case, that the satellite control system is unresponsive during the short time scale of the paddle movement dictates that the paddle should not step by more than 0.3°. This restriction can be met in a simple manner by a stepper motor driving the paddle through a gear reduction. However, this configuration introduces failure modes associated with the gearing and associated bearings and the second design consideration, that mechanism reliability was paramount and that sources of tribological failure were to be minimised, resulted in the adoption of a two bearing, direct drive configuration with a pancake motor mounted directly on the shaft and driving in a pulsed mode.

The exact form of pulsed drive differs in the two mechanisms but in both the result is that, in normal operation, the array steps through about 0.1° every 20 secs. If the mechanism fails to step, due to friction variation, the increasing error causes a progressively stronger motor pulse until the paddle continues its rotation. Obviously, a prime objective of the test programme is to ensure the evenness of operation and to assess variability of positioning error.

The choice of motor differs in the two designs; HSD, true to the philosophy of minimising wear surfaces, chose an Aeroflex Brushless DC motor, obtaining commutation and angular position information by means of an optical encoder referred to a read-only memory. MSDS, taking advantage of the limited number of revolutions required and the relative unimportance of wear life and wear debris, used a brushed Inland DC motor and a brushed transformer. The brushes of the motor were replaced with the Ag Cu MoS₂ composite used for the slip ring brushes.

Differential thermal expansions caused by overall temperature variations and internal gradients are compensated in part by the use of lead lubricated angular contact bearings and by mounting one of the races on a flexible seating, axially compliant but radially stiff. MSDS, in their first design, (Figure 2) used a bellows mounting but changed to a steel diaphragm in their later design (Figure 3) because of the length restriction. HSD used a titanium diaphragm. Further relief is obtained by HSD in the choice of Beryllium as shaft and housing material. The MSDS design uses a steel shaft and an aluminium housing.

In the case of the HSD drive, launch loads are taken by an off-loading mechanism which presses the shaft against a conical seating. Release is by

TABLE 1: Characteristics of Solar Paddle Drives

CHARACTERISTIC	HSD MECHANISM	MSDS MECHANISM	QUALIFICATION TEST LEVELS		
			TEST	HSD MECHANISM	MSDS MECHANISM
Operational Speed	1 rev/day	1 rev/day	Static Load (all axes)	1750N at shaft flange	900N 0.1m out- board of shaft flange
Acquisition Speed	1 deg/sec	2 deg/sec	Shock (all axes)	deleted	100g of 0.5msec duration with 6 Kg located 8cm outboard of shaft flange
Tracking Accuracy	± 2.5 deg	± 0.5 deg			
Typical Step Size	0.1 deg	0.1 deg			
Shaft Resolution	0.1 deg	0.1 deg			
Av. Friction Torque (estimated)	0.07 Nm	0.46 Nm	Sinusoidal Vibra- tion (all axes)	5 - 15 Hz 9mm o-p displacement 15 - 200 Hz 8g o-p acceleration at 2 octaves/minute	
Torque Margin	17:1	2.4:1	Random Vibration (all axes)	25 - 100 Hz 3dB/oct increasing to $0.2g^2/Hz$ 100 - 2000 Hz $0.2g^2/Hz$	
Power Required 'not including control)	<0.5 W average <10 W peak	<0.5 W average <10 W peak	<u>Thermal Vacuum</u>	Duration(hrs)	T1($^{\circ}$ C)
Slip Rings	12 Signal rings 12 Power rings (500 W) 1 Ground Ring	36 Signal rings 6 Power rings (460 W) 1 Ground Ring	T1=Shaft Flange T2=Housing Flange Mounting and Environment	8 8 8 8	-25 15 80 45
Envelope	25cm dia x 30cm	18cm dia x 10cm			
Weight	4.2 kg	3 kg			
				*	During this period four 72 min- ute eclipses will be simulated by decreasing the shaft temper- ature (T1) to -30° C while main- taining T2 at 45° C.

cable cutter. The bearings in the MSDS mechanism are unprotected during launch but are sized to withstand the severe requirements of the shock loading.

Both mechanisms use slip rings as a means for transferring power and signals and utilise a combination of a silver (82.5%) copper (2.5%) MoS₂ (15%) brush in conjunction with a silver ring. The use of these materials is consistent with the common design philosophy of dry lubrication, obviating the need for close tolerance sealing and eliminating the failure modes associated with contamination, lubricant degradation and lubricant loss through creep or evaporation. HSD use a modular design, with the slip ring unit cantilevered off the inboard bearing while the larger number of signal channels required for the MSDS mechanism led to a radial configuration for the signal rings with axially mounted power rings. MSDS limit outgassing contamination with the use of a Lithium Aluminosilicate glass ceramic as an insulating mount for the slip rings.

LUBRICANT

The lead lubricant chosen for both designs has been under development by MSDS for some years sponsored both by the Royal Aircraft Establishment (U.K.) and by ESTEC (References 1 and 2).

This method of lubrication has now reached a level of environmental testing giving a high degree of confidence in its use in long life spacecraft mechanisms. Figure 4 gives a summary of some test experience at speeds of 1/90 rpm, 100 rpm and 3000 rpm. The longest ongoing tests at these speeds have reached operating lives of 2.5 years, 2.8 years and 7 years, respectively.

Most relevant to the solar paddle application are the 1/90 rpm (10 revs/day) tests where the longest running rig has completed over 15000 revolutions without failure in a vacuum of 10^{-8} to 10^{-9} torr. Each rig was subjected to at least 50 hours air running and vibration testing before the life test in simulation of the pre-orbit environment. Unlike the liquid lubricants, where failure can be quite independent of the revolutions achieved, the concept of accelerated testing can, with care, be applied to solid lubricants. For example, Table 2 demonstrates the consistency of test results with accelerated operation. As an indication of torque noise, counts were made of the number of times the torque exceeded a certain level.

TABLE 2: Variation of torque performance with speed of 1/90 rpm test rig bearings (20N preload, average coefficient of friction ≈ 0.002).

Speed (rpm)	Average Torque (Nm)	Frequency of Peak Torque Levels (Counts/sec)				
		0.0011 Nm	0.0014 Nm	0.0017 Nm	0.0021 Nm	0.0023 Nm
1/90	0.00043	2.6	0.6	0.18	0.02	0.02
1/9	0.00040	2.1	0.5	0.10	0.04	0.00
1	0.00045	2.5	0.5	0.10	0.01	0.00

Unlike oil or grease lubricants, lead gives very little torque variation over the range of temperatures experienced by the drive. Figure 5 compares temperature characteristics for grease and lead as obtained in the 100 rpm test rigs.

TEST PROGRAMME

In order to simulate the operational environment foreseen for a flight model, each mechanism will undergo a period of air running which will be used to assess its performance when driving a load of inertia and stiffness representative of a solar paddle. Of the three mechanisms of each type, the first scheduled for delivery is the Accelerated Test Model which will be subjected to Qualification level testing for vibration and thermal vacuum (Table 1) prior to operation at an accelerated rate of 1 rev/hr over a period of about 7 months. During this time, the mechanism's performance under repeated eclipse conditions will be checked periodically at its normal rotational speed. The remaining two mechanisms, designated as Real Time Life Test Models, will undergo Acceptance Level testing and be operated for an extended period at 1 rev/day, again with periodic eclipse simulation. A controlled thermal environment will be maintained at all times.

Many past failures of BAPTA type mechanisms have been as a direct result of variations in thermal environment producing unforeseen degradations and increases in friction torque. The vacuum facilities at ESTL have been designed to simulate the mechanism environment with regard to both vacuum and thermal gradients. Figure 6 shows a typical installation. The chamber is fitted with an ion pump and, empty, can reach 10^{-10} torr. Thermal shrouds control the temperature of the mechanism mounting flange and surrounding environment (T_2). In addition, a thermally controlled pancake independently controls the shaft flange temperatures (T_1) by means of radiative coupling to a dished radiator. In this way, the mechanism can be tested in simulation of the temperature gradients enforced by the differing thermal environments of the paddle and the body of the satellite. A window is provided in the top flange for observation and, in the case of the MSDS mechanism, for control of the mechanism by the use of a mirror mounted on the shaft (see Figure 2).

Each mechanism is instrumented and temperatures, motor power, rotational movement, and slip ring voltage drops will be recorded via a data logger throughout life testing. Preload variation will also be monitored, although this is not expected to vary significantly in operation because of the flexibly mounted bearings.

PROGRAMME STATUS

The Accelerated Test Models of both mechanisms are expected to complete their life tests during the first quarter of 1974, when they will be stripped for examination. The first HSD mechanism began thermal vacuum testing in May 1973. All models are expected at ESTL by September 1973. The competitive nature of the design study is being maintained into the test phase since one of these mechanisms, or a close variant, will ultimately be chosen for use on the Orbital Test Satellite (part of the European Communication Satellite Programme) which is due for launch at the end of 1976.

ACKNOWLEDGEMENTS

Thanks are due to HSD and MSDS for their agreement to publish the information on their solar paddle drives and to ESTL for their cooperation. Thanks are also due to the Director of ESTEC for permission to publish the paper.

REFERENCES

1. C.L. Harris: Vacuum Evaluation of Lubricants and Techniques for Space Exposed Components. ASLE-ASME Lubrication Conference, Houston, Texas, 1969, (69-Lub-30).
2. P.J. O'Donnell, C.L. Harris & M.G. Warwick: The Lubrication of Bearings and Slip Rings in Vacuum. ESRO CR-91, September 1972.

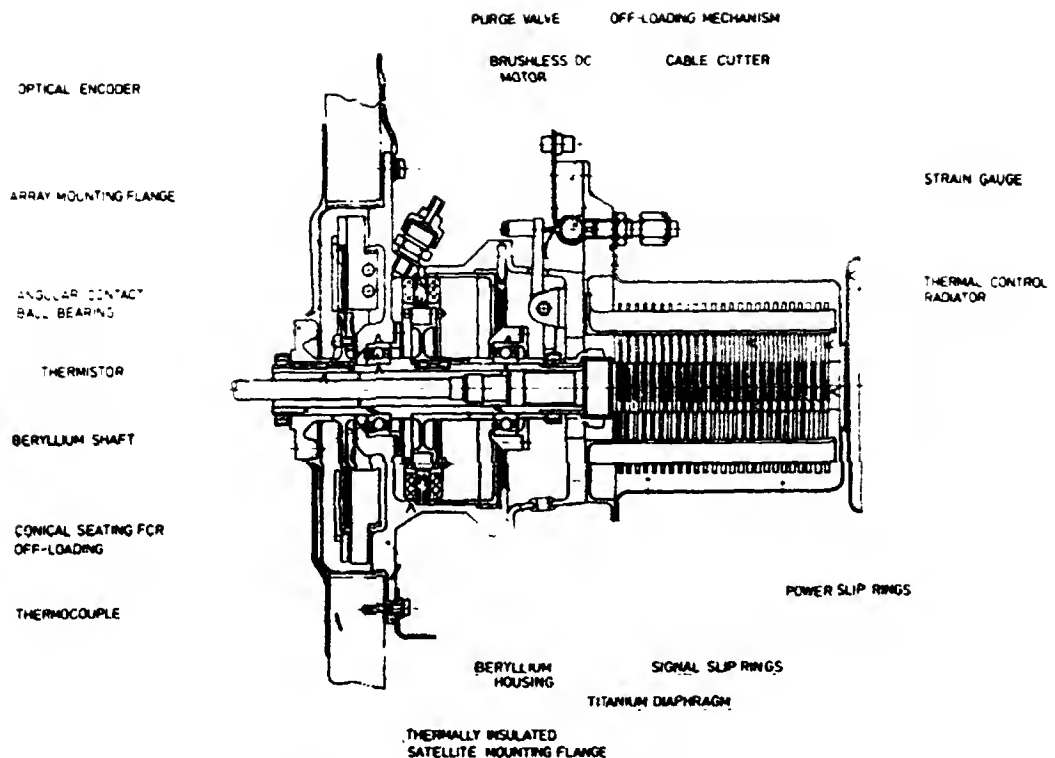


Figure 1.- HSD solar paddle drive.

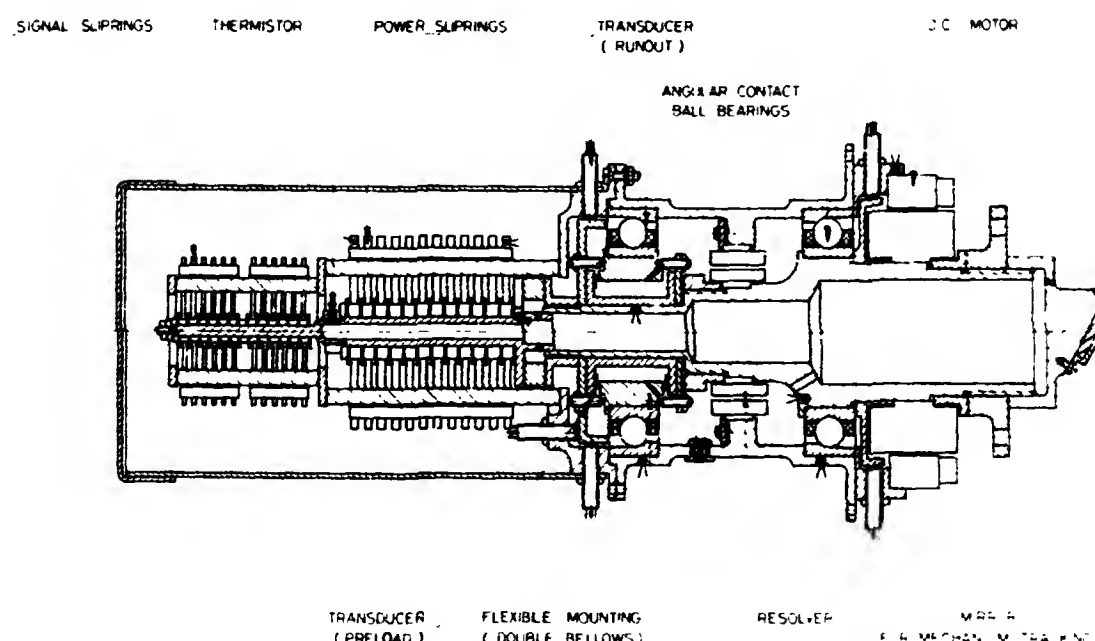


Figure 2.- MSDS solar paddle drive number 1.

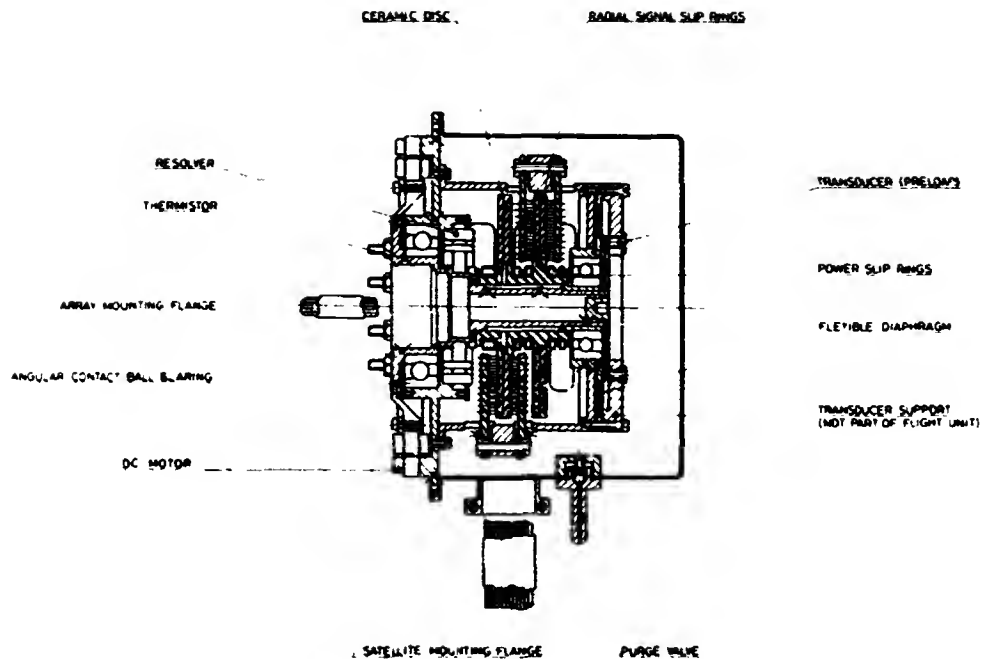


Figure 3.- MSDS solar paddle drive number 2.

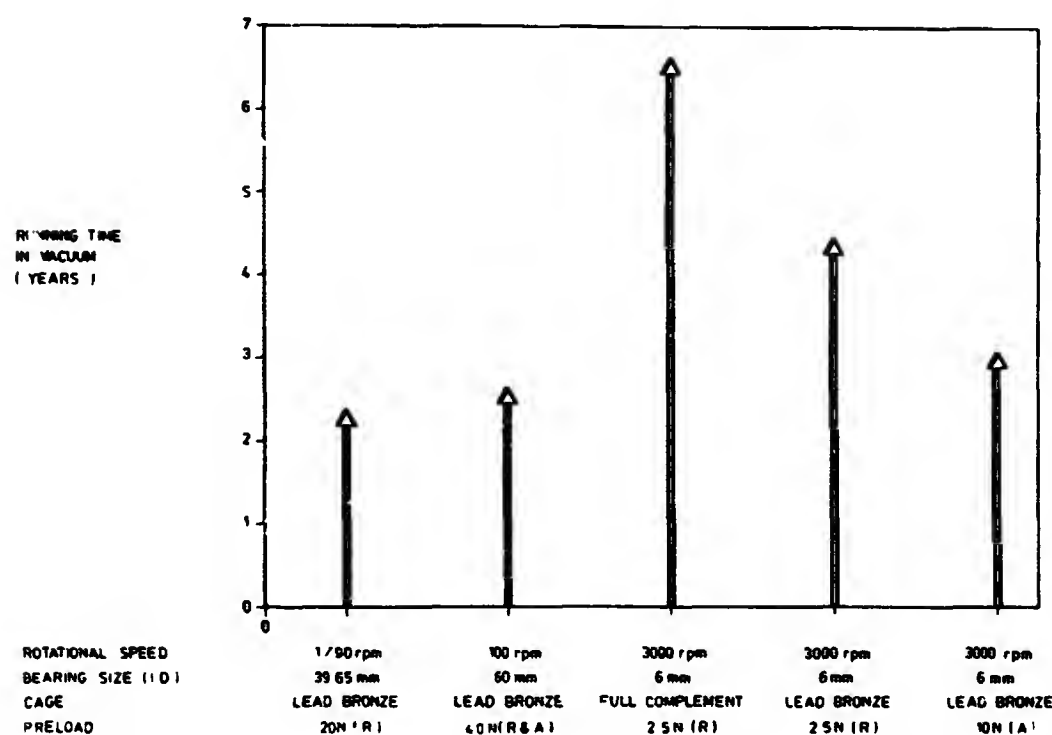


Figure 4.- Lifetimes achieved by lead lubricated bearings (all tests continuing)

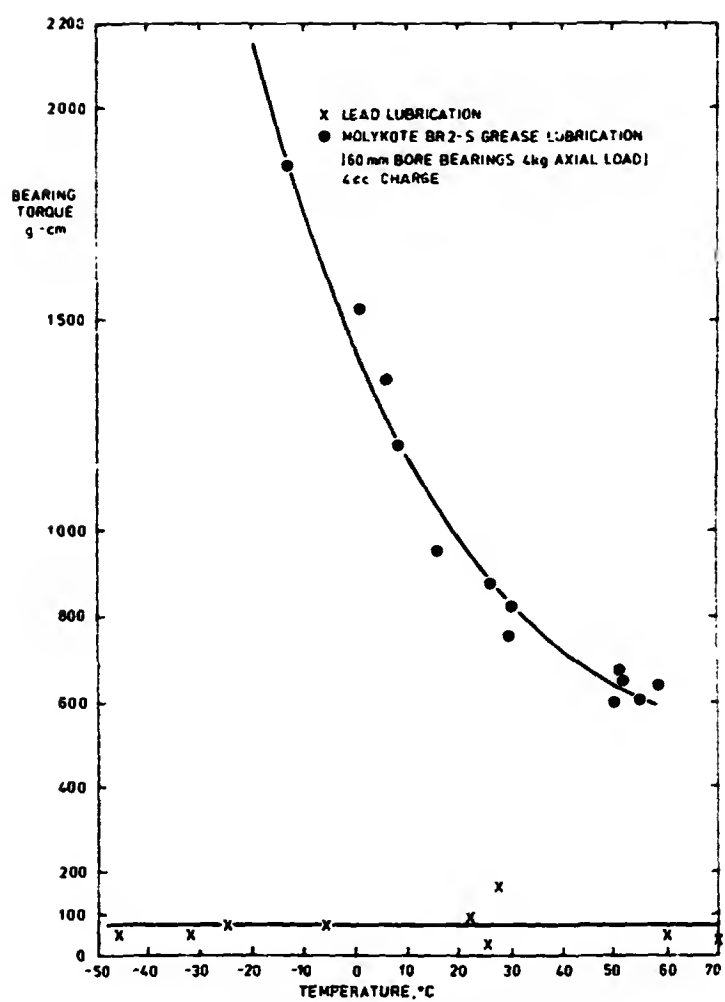


Figure 5.- Low-speed torque comparison for dry and liquid lubricated bearings at extremes of temperature.

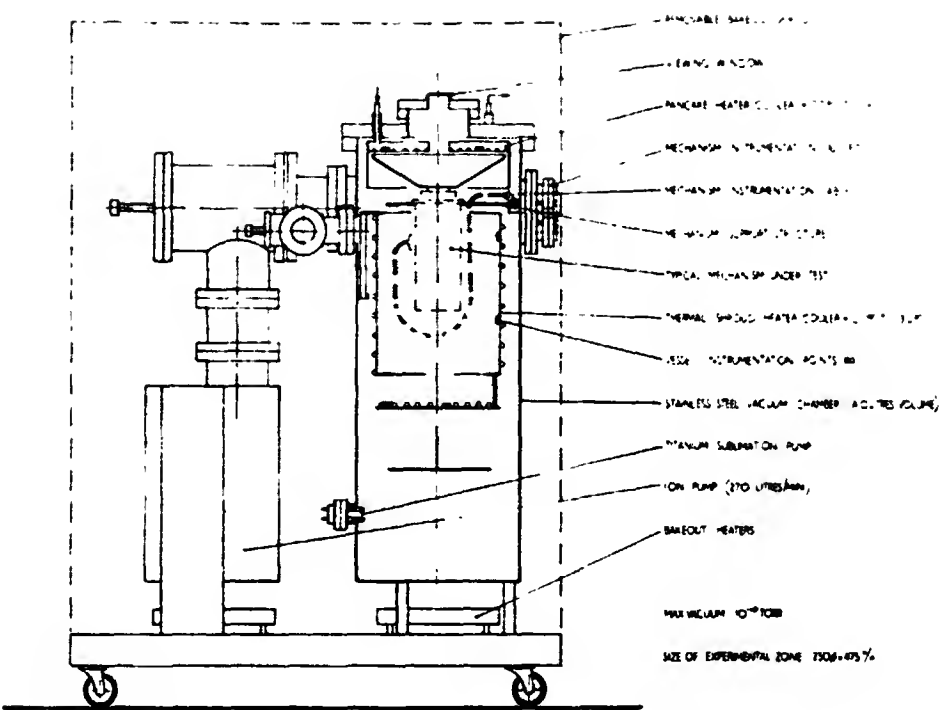


Figure 6.- Installation of typical mechanism in vacuum test chamber.

6. TELESCOPIC BOOMS FOR THE

HAWKEYE SPACECRAFT

by Roger D. Anderson

The University of Iowa, Department of Physics and Astronomy
Iowa City, Iowa 52242

INTRODUCTION

Several boom arrangements were proposed for the HAWKEYE spacecraft (formerly called the INJUN series of spacecrafsts).

The design chosen to fly consists of one pair of stem roll-out booms and a set of telescopic booms. Some of the advantages of choosing this boom configuration were that the booms could be stored in the belt line area, which is near the center of gravity of the spacecraft, and also with the approach the telescopic booms could be extended at the spacecraft's initial spin rate (180 rpm). By being able to extend these booms at the initial spin rate of the spacecraft the need for a despin system was eliminated, thus weight saving to the spacecraft. With the method of storage and extension employed by the telescopic design, the desirable sensor distance from the spacecraft could also be attained.

FIRST DESIGN

The first telescoping booms to be constructed were operated by hand, and from the first model a number of redesignings were made; a second redesigned unit was constructed with special Delrin brushings, weight-reduction methods, and a small DC motor. With this redesigned unit a number of successful deployment tests were conducted.

FINAL DESIGN

The final design employs three telescoping aluminum tubing sections which slide inside one another on special Delrin brushings. The outer section is made from $3/4" \times 3/4"$ square cornered tubing in which the outside dimensions are milled down to attain a wall thickness of .025". The middle section is made from $1" \times 1"$ square cornered tubing and milled to a wall

thickness of .025, and the largest section is 1-1/2 x 1-1/2 square tubing, which will have a final milled wall thickness of .030. So the final dimensions of these sections will be .675 x .675, .925 x .925, and 1.31 x 1.31, respectively.

These aluminum boom sections ride on brushings made from a Teflon-impregnated Delrin material, which encompasses the low frictional qualities of Teflon and the structural rigidity of Delrin. Figure 1. The aluminum sections are extended and retracted by reeling stainless steel cables in or out from aluminum storage drums.

This steel cabling is 3/128" in diameter and is strain hardened by pre-stretching. Figure 2. It has been found through tests that this cable will stay in the elastic portion of the stress-strain curve up to about 39 lb and has a breaking strength of ~ 60 lb. The maximum tensile load the cabling is expected to experience is about 13 lb, thus nearly a 5:1 safety factor.

Housed inside the telescoping boom sections are the sensor cabling harness for the search coil and magnetometer sensors. The cabling is stored inside the telescoping boom sections and, as the telescoping sections extend, the sensor harness also extends. Figure 1. The cables are fabricated by the "Cicoil Corp." and consist of 5 shielded and 1 twisted pair of #30 wires encased in silicon rubber, thus providing a flexible ribbon. The cables are then accordioned and surgical elastic rubber is attached to either side with lacing cord by personnel at the University of Iowa. This method of construction provides an essential 3.5 to 1 cabling elongation.

The boom's drive motor is fabricated by "MPC Products" and has mounted on the end a gearhead which gives an 84:1 gear reduction. The AC 2-phase motor has a rated torque of 7.6 in-oz @ 212 rpm and a no-load speed of 23,700 rpm. Curves of motor-gearhead characteristics of the two motors received are shown in Figure 3.

TESTING AND PROBLEMS

In order to do bench testing of these booms a centrifugal force simulator was constructed (fig. 4).

Since the building of this simulator many tests have been performed on the DVU (Design Variation Unit) and the protoflight booms.

When the DVU motor was received, it was mounted on the DVU boom. This boom was complete with the exception of not having the sensor harness installed (no cables were available at that time). Several boom extensions and retractions were performed on the simulator and on the spin table. It became apparent that some additional loading was occurring on the simulator. After some modifications were performed, the simulator provided loads necessary. A sketch of the simulator is provided in Figure 4. The simulator

force vs. boom extension curve is shown in Figure 5. Also on this same figure a plot of the calculated curve is provided.

Because it was felt that the antenna may be subjected to high coriolis forces during extension (from the combination of spin deceleration and extension speed) and, furthermore, that these forces may tend to bind the brushings during erection, the unit was installed on a spin table, which had inertias comparable to the proposed spacecraft. In this configuration, the antenna was extended and retracted successfully under various spin rates, while the power consumption of the motor was monitored. The booms were deployed at 40, 60, 100 and at 180 rpm. The approximate spin rate of the spacecraft before telescoping boom deployment is 180 rpm.

From calculations the bending loads on the boom sections were obtained, with the maximum bending occurring when a 1-G load is on the boom, during erection. This will occur only in ground testing and occurs in the largest section and is \approx 33 ft-lb (Fig. 6). The maximum stress in the booms takes place in the smallest section and is 1140 psi, which is a factor of \approx 35 below the yield point of the aluminum (Fig. 6). The other bending loads that occur on the boom are forces occurring from coriolis. The stress levels produced from these forces are very small, a factor of 50 below the G loading factors, so they are disregarded.

Because of some extension-retraction problems encountered during testing on the simulator, an investigation into the friction between worm and worm gear was undertaken. It was found that the friction changes considerably with environmental changes. The coefficient of friction of the dry stainless worm against the bronze worm gear could change from .25 to .55.

A lubrication expert was contacted on this problem and it was recommended to coat the gears with molybdenum disulfide. With this lubricant a coefficient of friction of .1 to .15 could be expected. From actual tests performed on the lubed gear, it was found that indeed the friction was a satisfactory .15. Calculations are shown in the appendix and in Figure 5.

To insure that no tooth shearing damage would take place in the gears of the aluminum storage drums, the loads in the gears were studied. With the maximum load of 28 lb, it was found that the maximum stress was \approx 356 psi. The shear strength of the 7075 aluminum used is 40,000 psi, resulting in a high safety factor. Calculations are shown in the appendix.

CONCLUSION

At the time of this writing, the DVU and protoflight boom units have gone through extensive testing. The flight telescopic boom is now in fabrication with additional testing planned for it.

APPENDIX

ALUMINUM GEAR DRUM CALCULATIONS

Aluminum Gears

The maximum centrifugal is $\approx 13 \times 2$ sides. With frictional losses, we assume a load of ≈ 28 lb.

CAL OF STRENGTH IN TOOTH

From Lewis formula (Ref. 1, p. 396):

$$W_E = \alpha_p F_y$$

$$\alpha = \frac{W_t}{\rho F_y} = \frac{28 \text{ lb}}{1.125 \times .2 \times .35}$$

$$\alpha = 355.5 \text{ psi}$$

Where

W_t = transmitted load = 28 lb

α = normal stress = ?

ρ = circular pitch dia. = 1.125

F = face width = .2

y = form factor $\approx .35$

From Barth equation (Ref. 1, p. 396):

$$\alpha_d = \alpha \frac{1200}{1200 + V}$$

$$\alpha_d = 355.5 \frac{1200}{1200 + 2.45}$$

$$\alpha_d = 354 \text{ psi}$$

Where

V = Velocity at pitch line
= 2.45 ft/min

α_d = stress due to dynamic
load = ?

The 7075 aluminum material used has a shear stress of 40,000 psi, so:
The safety factor is very high.

Worm and Worm Gear Efficiency

(Ref. 1, p. 455):

$$\text{eff} = \frac{\cos \phi_n - \mu \tan \lambda}{\cos \phi_n - \mu \cot \lambda} \quad \begin{aligned} \phi_n &= \text{pressure angle} \\ \lambda &= \text{lead angle} \end{aligned}$$

From measurements 7.6 in-oz at motor gearhead is 64 in-oz on pinion.

$$\text{so: } \text{eff} = \frac{64 \text{ in-oz}}{7.6 \text{ in-oz} \times 30:1 \text{ ratio}} = .28$$

$$\text{eff} = .28 = \frac{\cos \phi_n - \mu \tan \lambda}{\cos \phi_n - \mu \cot \lambda} = \frac{.9681 - \mu(.0627)}{.9681 - \mu(16.00)}$$

$\mu = .15$, so coefficient of friction = .15.

REFERENCE

1. Shigley, J.: Series in Mechanical Engineering. McGraw-Hill Book Co., Inc., 1963.

CABLE OPERATION OF ANTENNA BOOM

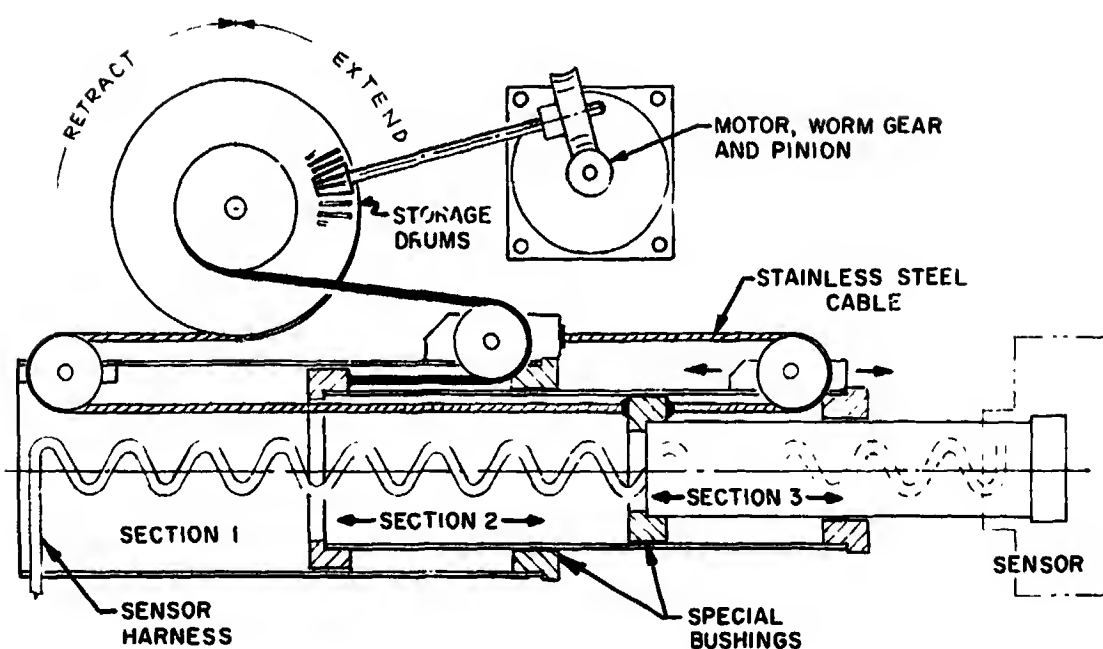


Figure 1.

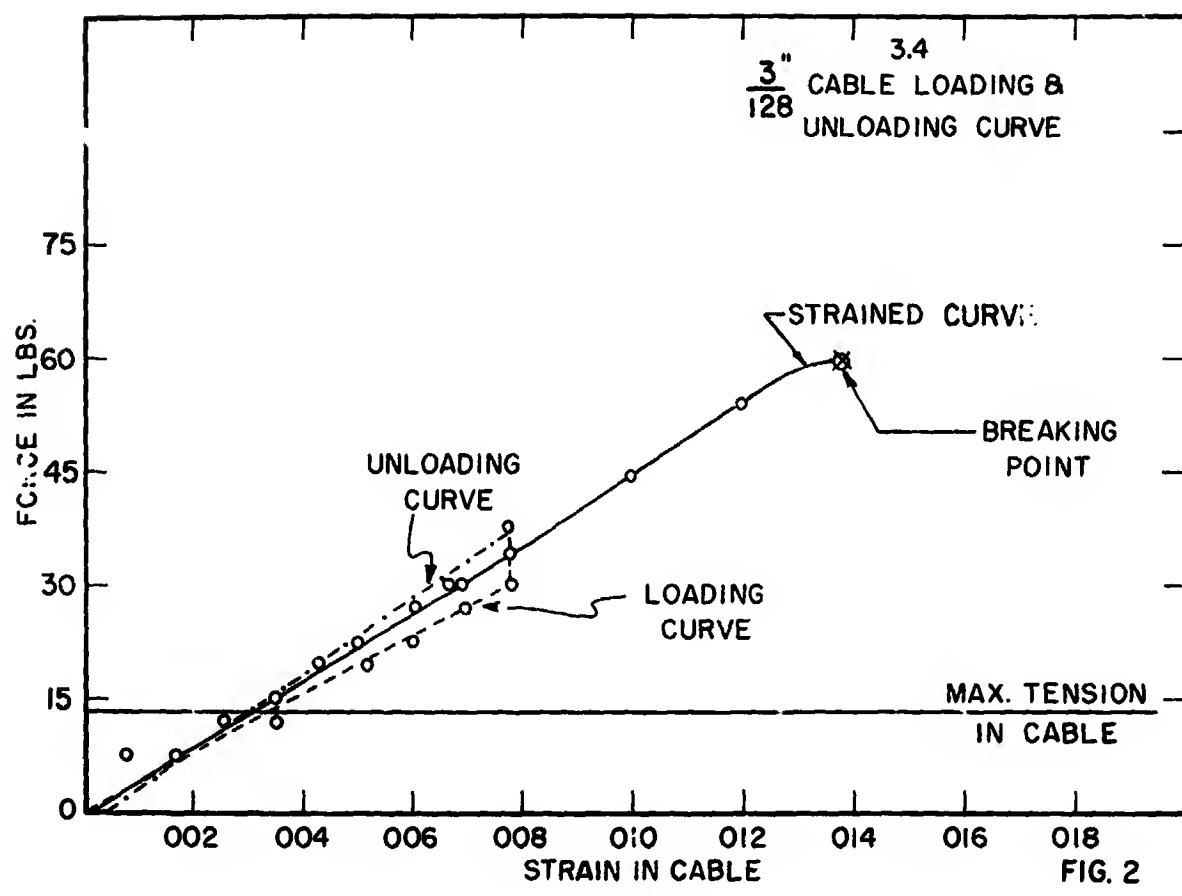


Figure 2.

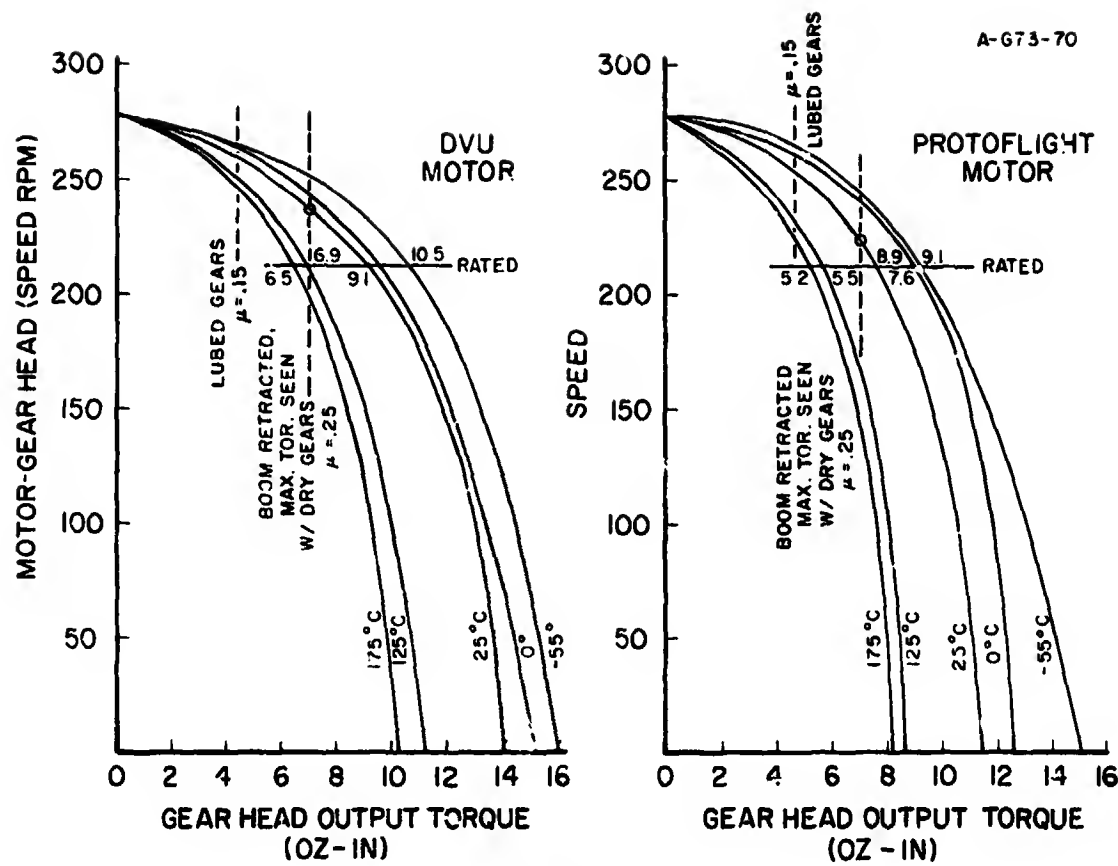


Figure 3.

CENTRIFUGAL FORCE SIMULATOR

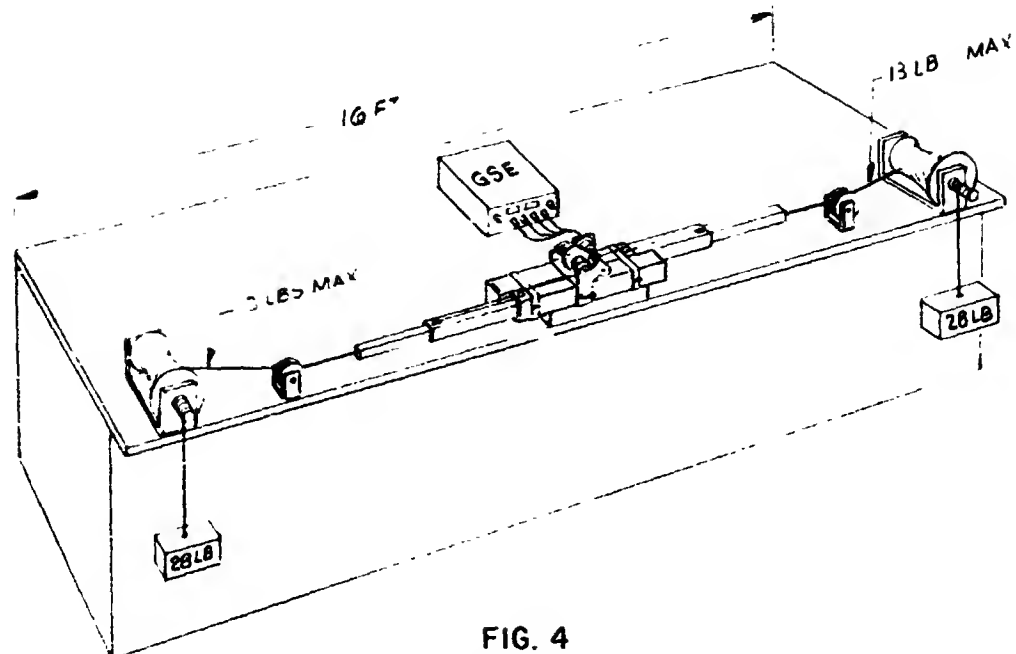


FIG. 4

Figure 4.

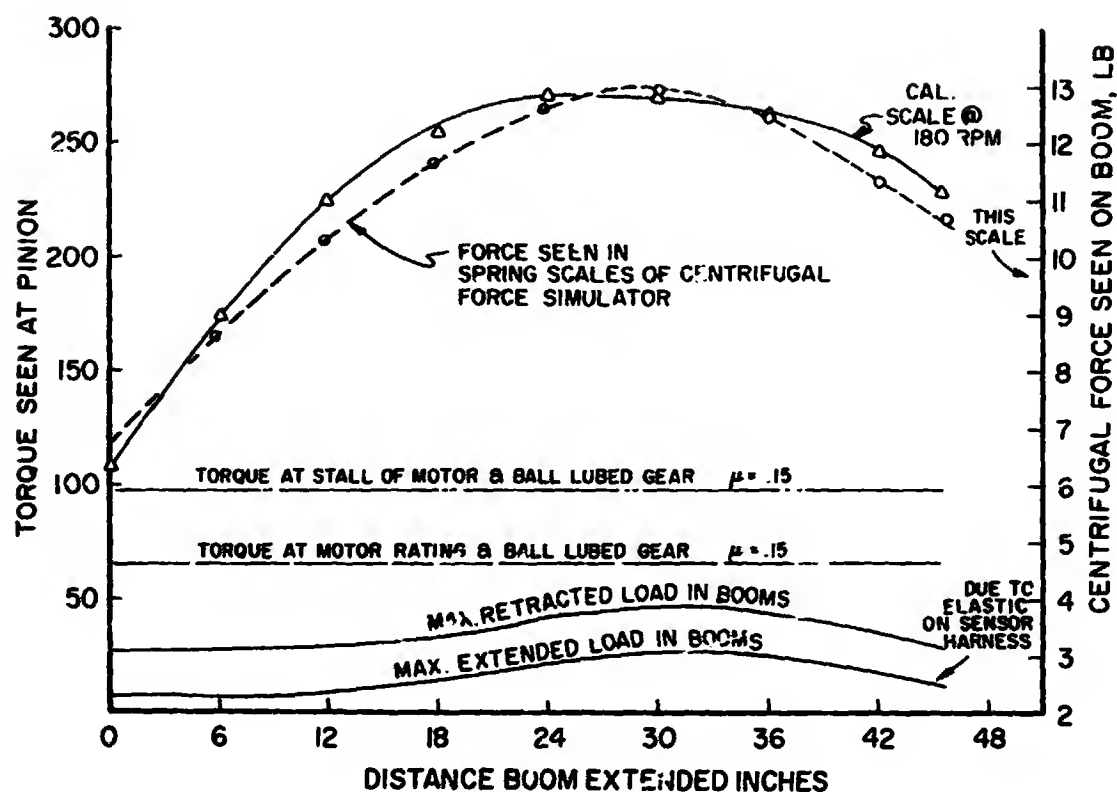


Figure 5.

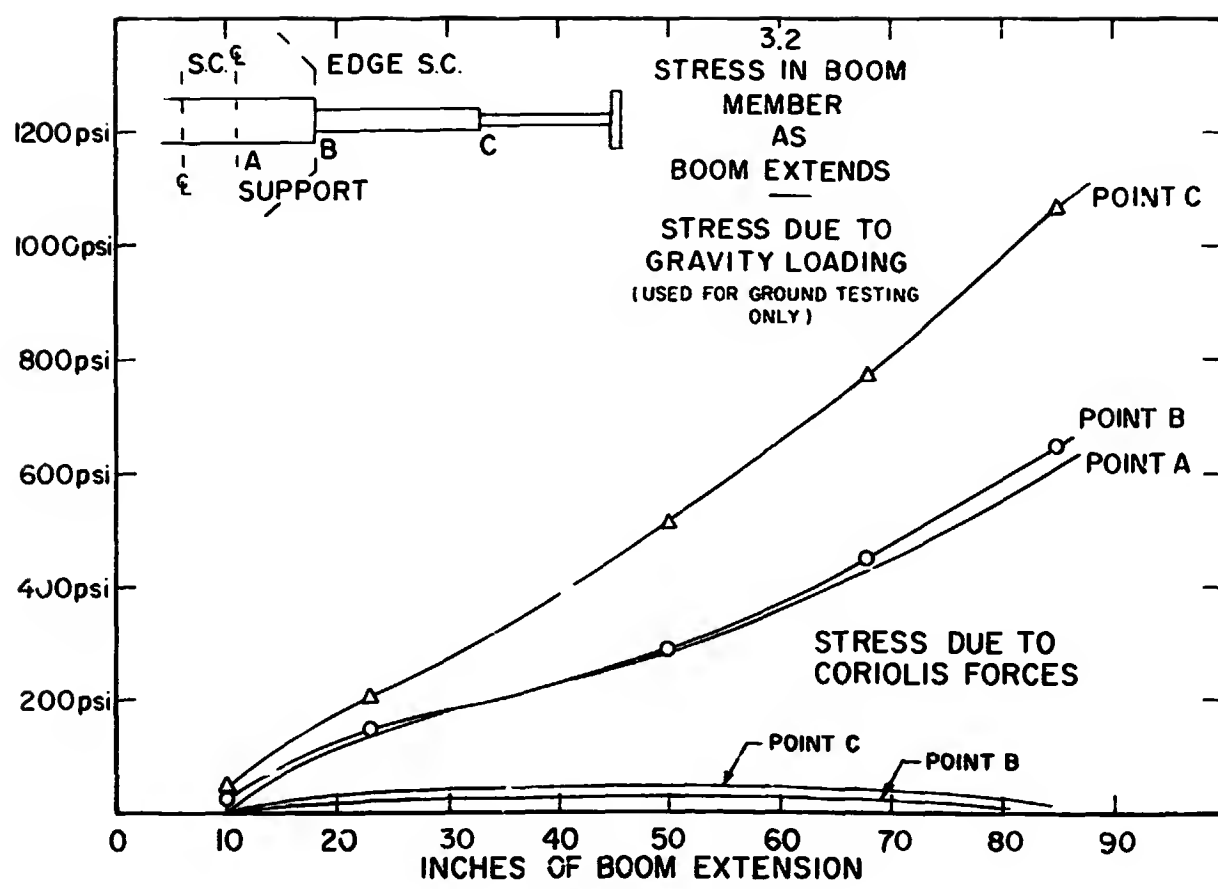


Figure 6.

7. THE DEVELOPMENT AND TEST OF A LONG-LIFE,
HIGH RELIABILITY SOLAR ARRAY DRIVE ACTUATOR

By Don L. Kirkpatrick*
General Electric Company

ABSTRACT

To meet the life and reliability requirements of five to ten year space missions, a new solar array drive mechanism for 3-axis stabilized vehicles has been developed and is undergoing life-test. The drive employs a redundant lubrication system to increase its reliability. An overrunning clutch mechanism is used to permit block-redundant application of two or more drives to a common array drive shaft. Two prototype actuator and clutch assemblies, in continuous vacuum life-test under load at 10^{-8} TORR for more than sixteen months, have each accumulated more than 34,000 output revolutions without anomaly, the equivalent of more than seven years of operation in a 1000 km (600 mm) orbit or nearly ninety-five years at synchronous altitude.

INTRODUCTION

This report discusses the design and test of a new high-reliability solar array orientation drive mechanism, under the auspices of the 1971 and 1972 GE Space Division IR&D Programs. Before proceeding to the discussion of the design features and test results of the new array drive, a brief background description of the vehicle system-level requirements which created the need for this device may be of interest to the reader.

In conjunction with preliminary design studies of a group of large, synchronous altitude communications satellites, a study of the suitability of existing solar array drives to meet vehicle and mission requirements was performed. These requirements included reliable operation throughout the ten-year missions planned; full functional redundancy to prevent mission termination as a result of any single-point failure; and the ability to drive large array inertias at acquisition slew rates as well as orbital rate; and to provide a torque margin of 10:1 relative to the expected beginning-of-life bearing and slip ring friction.

When it became apparent that no known flight-proven drive could be used without extensive modifications to either the drive itself, vehicle configurations

being studied, or both, new drive concepts and configurations were examined to determine whether an actuator more compatible with the vehicles' performance and reliability requirements and configurational constraints could be devised. One of the resulting drive design concepts showed sufficient promise of meeting all the major requirements of the class of vehicles under study, (and in addition, a broader applicability to any space vehicle requiring a reliable, long-life rotary actuator), that an IR&D program was formulated to further develop the new concept, build prototype drive mechanisms, and evaluate their performance through bench testing and vacuum life-test. To the extent that the two resulting prototype drive mechanisms have performed successfully throughout sixteen months of continuing bench and vacuum life-test, driving external loads alternately, and in parallel, the goals of the program have been met.

This success was achieved in large part as the result of the efforts of A. Schneider and R. Boileau. Their significant contributions are gratefully acknowledged.

PERFORMANCE REQUIREMENTS

Performance requirements which the Solar Array Drive Assembly (SADA) was designed to meet, and the actual capabilities/performance of the prototype drives built and life-tested, are given in Table 1.

Table 1. Large Synchronous Satellite Solar Array Drive - Summary of Requirements, Constraints and Actual SADA Capabilities

Parameter	Required Capability	Actual Capability
Rotation Rate Normal Slew (Minimum)	360 deg/day 0.5 deg/min	360 deg/day 9 deg/min
Nominal Output Torque	4.4 Nm (3.25 ft-lb)	54.2 Nm } minimum (40 ft-lb) }
Avail. Torque Margin	9X	11.3X
Load Inertia	13.6 kg-m ² (10 slug-ft ²)	
Drive Power Average Orbital Slew and Peak	2 watts 30 watts	0.3 watt 9.8 watts
Operating Temperature Range	20°F to 120°F	Meets: upper limit verified by test, lower limit verified by analysis

Table 1 (Continued)

Parameter	Required Capability	Actual Capability
Wear Life	10 years	95 years equivalent demonstrated in life-test of two drives
Redundancy	Full Functional	Meets: demonstrated by test
Reliability (10 years) Weight drive	0.998 2.7 kg (6.0 lb)	0.9997* 2.7 kg** (6.0 lb)

*Determined analytically for block redundant configuration.

**3.3 kg (7.2 lb) using aluminum gear case tested.

DRIVE CONFIGURATION DESCRIPTION

The SADA configuration which ultimately resulted from the design studies was created with simplicity and low cost as important goals, in addition to the requirements for high torque and performance margins, commensurate with reasonable input power and weight. The drive is comprised of a high torque, 1.8 degree/step, permanent magnet stepper motor; a 100:1 Harmonic Drive torque multiplier; a 6:05:1 spur gear output stage; and a fully redundant lubrication system. The single-active-element clutch which automatically couples the drive actuator to the solar array shaft during drive operation permits the use of two actuators on a spacecraft to provide full redundancy of the array drive function. A cross-sectional layout of this drive is shown in Figure 1 in the redundant (clutch coupled) configuration. This illustration also shows the type of spacecraft structural interface which this drive requires for proper mechanical alignment.

The motor drives the input of the 100:1 reduction harmonic drive, which in turn drives the pinion of the 6.05 spur gear reduction. The hollow-spur-gear shaft also serves as the input hub for the wrap-spring clutch, which drives the array shaft through the spring clutch driven hub when the motor is operating. These major drive train components of the SADA are shown sequentially in their order of operation in Figure 2. From right to left, they are:

1. The stepper motor with shaft position encoder
2. First reduction harmonic drive wave generator, circular spline, and flex-spline

3. Second reduction pinion, and output gear with integral clutch drive hub
4. Wrapspring clutch
5. Clutch driven hub, which attaches to the drive vacuum life-test fixture shaft

The second SADA prototype drive assembly is also shown in this photograph.

DRIVE DESIGN EVOLUTION

The initial SADA design configuration concept is shown in Figure 3. This basic actuator concept is extremely simple in comparison with its predecessors. The major active elements are the dc stepper motor, the harmonic drive, a single pair of output spur gears, and the wrapspring clutch. Support of all rotating elements requires only six ball bearings. By contrast, the solar array drives used on early Nimbus vehicles employed twenty gears, and twenty-two bearings, in addition to the motor and an internal slip clutch, which was necessary to protect the 85,000:1 gear train against damage from torques externally applied to the solar array shaft. (The earlier drives incorporated no provision for redundant application.) A schematic comparison between this design and the Nimbus I-III drive is shown in Figure 4. The prototype drive, ultimately developed from the aforementioned concept, is capable of withstanding high externally applied torques without damage, because of its relatively low (605:1) ratio, and the high strength of its gear train elements.

As originally conceived, the drive employed a frameless "pancake" stepper motor (comprised of a separable rotor and stator); and a Harmonic Drive (HD) 100:1 gear reduction (comprised of a wave-generator bearing, a circular spline, and a flex-spline), with two pairs of ball bearings mounted in a specially designed housing to support these elements. The smaller bearings supported the motor-rotor and the wave-generator (HD input), while the larger bearings supported a cylindrical shell to which the flex-spline (HD output) and the spur gear pinion of the second (6:1) gear reduction were attached. The output gear was mounted between a third pair of bearings. The hollow shaft of this gear extended to form the input hub of a wrapspring clutch, which would transmit the output torque of the drive mechanism to the solar array shaft through a hub pinned to that shaft whenever the drive was operating. In this configuration, the entire array drive was supported on the array shaft by a pair of self-lubricating sleeve bushings, and the drive torque was reacted into the vehicle through a pin or screw which attached the output gearcase to the vehicle structure. Comparison of this layout with the final concept, in Figure 1, will show that many significant design improvements were made over the initial concept in this phase of the program. The most significant changes and improvements incorporated in the prototype relative to the initial concept are:

1. The incorporation of a self-contained motor, which with its double-ended shaft supports the step-sensor (encoder) on one end, and the Harmonic Drive wave generator on the other
2. Straddle mounting of the drive pinion to ensure improved gear alignment and operation in smaller, stiffer bearings while still providing adequate support for the harmonic drive flex-spline.
3. Eliminating the need for the centering bushings between the drive output shaft and the array drive shaft by piloting the drive housing on the array shaft support bearing housing
4. Generally improving the overall housing structural design, ease of manufacture, assembly, alignment, and serviceability.

DESIGN PHILOSOPHY AND COMPONENT SELECTION RATIONALE

A major goal in the design of this device was to achieve long life and reliability through simplicity in both quantity and design of the basic mechanism elements. Further examination of the layout will show that this philosophy has been followed wherever possible in the design of the SADA. The motor rotor shaft is double ended; the harmonic drive wave generator is supported on one end of the motor while the optical encoder disc or pulse generator magnet is supported on the other. Thus, the two motor rotor bearings also support two additional driven elements for simplicity, eliminating the need for other support bearings. The second reduction pinion and the Harmonic Drive flex-spline are supported on a common shaft by a second pair of bearings, which again eliminates the need for additional supports and complexity. The output gear bearings also support the clutch hub, which in turn supports the clutch, further limiting the number of bearings required and helping to achieve accurate clutch alignment.

The stepper motor selected is also an extremely simple device in itself, and its use simplifies the overall SADA design, as well. This high-torque stepper has a machined one-piece rotor and an encapsulated wound field structure. No detents, ratchets, pawls, cams, brushes, or commutator - all of which could cause potentially reduced reliability - are used. Stepping is accomplished through the sequencing of drive current to the four-phase winding by switching transistors and the consequent interaction of magnetic fields. The only contacting mechanical parts in the motor are the two precision ball bearings which support the rotor; the space lubrication technology for these is well-known and widely demonstrated.

Besides its inherent internal simplicity and demonstrated reliability, the motor selected simplifies the overall design of the SADA, functionally replacing a conventional 90 degree dc PM stepper or 2 phase ac servomotor and a two-to-four stage gearhead. This motor produces 18 in-oz torque at nominal rate through each of 200 accurate 1.8 degree steps per revolution, without gearing and with simple digital controls. Small (e.g., size 8 or 11) conventional steppers would require reduction gear ratios of 50:1 to 100:1 to produce the high torque and low effective rotational rate of this motor. AC servomotors must normally run

at several hundred rpm for smooth controllable operation and this again would necessitate the use of significant reduction gear ratios to provide the required low output speed which is achieved without additional gearing by the selected stepper motor. The selected motor thus provides both internal simplicity and a significant reduction in gears, bearings, and rate control electronics over more conventional approaches.

The use of the harmonic drive also results in a significant reduction in complexity over conventional spur gear approaches, which would require approximately three times as many parts to achieve the same 100:1 reduction, multiplying the complexity and severity of lubrication and backlash problems. Although other types of single stage high reduction gearing could achieve this ratio, none are as well-suited from a vacuum lubrication standpoint to perform reliably for long life in space. The teeth of the Harmonic Drive come into engagement without significant sliding and unlike spur gears there is no relative motion between the teeth which are carrying the peak load. The elimination of significant sliding friction loads makes it possible to achieve a greater lubricant life and reliability than could be readily achieved in using conventional gearing at this point in the gear train.

The output pinion rotates at one-one hundredth the rate of the HD input. Since it was possible here to utilize very durable 20 pitch, 20 deg pressure angle gears with 15 tooth Nitralloy 135M pinion, and 115 tooth 7075T6, hard anodized gear, an extremely low maximum pitch line velocity of 0.02 cm/sec (.008 in./sec) without incurring an excessive weight penalty, long life is again feasible with conventional boundary lubrication techniques.

To further enhance the reliability of the drive, a dual lubrication system is provided. All gears and bearings of the actuator are lubricated with space-proven liquid lubricants, Krytox AC oils and greases. Wiping lip seals and anti-creep barrier films will be provided at the output shaft of the actuator to retain this lubricant within the actuator housing for flight use. In addition, all surfaces requiring lubrication are coated with compatible space-proven dry lubricants based on plated low-shear strength metallic films or transfer-lubricating polymer film-generating materials. These dry lubricants provide a backup in the event of loss of liquid lubrication. (To verify the efficacy of this dual lubricant approach, the SADA prototype solar array drive actuators were vacuum life-tested; one with Krytox over the plated metallic lubricant films, while the second was lubricated only by the dry film system in the absence of liquid lubricants.)

The wrapspring clutch is the key to providing the desired functional (block) redundancy to increase the reliability of the array drive system. Two or more drive mechanisms may be coupled to the solar array shaft thru these one-piece overrunning clutches. Any or all drives may be operated with additive output torque in the multiple drive case, and any drive can be held in the backup mode without interfering with the operation of any other drive. Each clutch engages automatically when its associated drive operates and disengages automatically when pulsing of the drive's motor ceases. The clutch is lubricated only with a dry lubricant film bonded to the hard anodized hubs which it interconnects.

This lubricant does not interfere with the operation of the clutch during driving; torque of over 135 Nm (100 ft-lb) is required to cause slippage at the clutch, which is 2.5 times greater than the actuator peak/stall torque.

Like the other elements of the SADA, the optical resolver selected is simple and reliable in both its own design and in its application in the drive subsystem. Rotation of the motor is sensed by the resolver, an optical encoder comprised of a light emitting diode, a photosensitive transistor, and a 200 line chopper disc which interrupts the optical path each time the motor steps. This device senses each motor step completed, independent of the motor drive circuit which pulses the motor to "step" in 1.8 degree steps. The motor shaft is geared 605:1 to the output shaft; since each motor step is 1.8 degrees into this 605:1 reduction, then each step of the motor and each output pulse of the encoder = 0.003 deg. This provides both a convenient feedback signal if a position loop is to be closed around the motor and a high-resolution index of array shaft rotation in conjunction with a digital counter.

TYPICAL SPACECRAFT APPLICATION OF SADA SUBSYSTEM

A typical solar array drive subsystem for use in a synchronous altitude communication satellite could operate in the manner described below:

The Solar Array Drive Assembly (SADA) orients the solar array normal to, and steps it to follow, the spacecraft-sun line; and provides array position detection pulses to the Attitude Control System (ACS). Stepping commands are generated by the ACS in response to sun sensor or vehicle clock outputs. Two identical, functionally redundant array drive actuators are provided; a half-system is shown in Figure 1. Although only one drive normally operates while the other is retained as a backup, the functional description of each is identical. The motor drive pulses which originate in the ACS, in clock-triggered bursts of eleven 50 Hz pulses every 8 seconds, cause the drive stepper motor to rotate 19.8 deg every 8 seconds. The output torque of the motor is multiplied by a 100:1 harmonic drive reducer and a 6.05:1 spur gear mesh, so that the array shaft is advanced in an increment of 0.033 degree for each eleven ACS-generated pulses. The drive torque is transmitted from the output of the operating drive to the solar array shaft through a self-energizing unidirectional spring clutch which transmits motion and torque to the array shaft only when the drive is rotating. Rotation of the drive output shaft causes the preloaded clutch spring to tighten with virtually no lost motion about both the driving and driven shafts, locking them together and transmitting the drive motion accurately to the solar arrays.

Motion of the array shaft in the normal direction of array rotation relative to the actuator output hub on each drive disengages the clutch, so that a low but constant frictional drag 0.3 N-m (.25 ft-lb) is present at the non-driving clutch. Either drive may rotate the array shaft while the other remains stationary, and full functional drive redundancy results.

In the highly unlikely event that the required array drive torque exceeds

the capacity of a single drive, both drives can be operated simultaneously and the torque of each actuator will be additively applied to the load. Overshoot of the arrays is prevented by the drag torque of the clutches when the drive is not operating and by the friction of the power transfer slip rings and shaft support bearings. It has been determined through analysis that the momentum in the array when moving is insufficient to overcome these restraining torques when the drive is stopped.

Driving the array in the stepping, or incremental, mode provides two distinct, life and reliability-enhancing advantages to the drive. Power is applied to the motor only during the driving periods (magnetic detenting torque of the motor stabilizes the drive between array "steps"). Although the operating motor power is 9.8 watts, the average power is 0.27 watt; this significantly reduces heating of drive lubricants, and thermal stresses on the drive in general, in addition to saving electrical power throughout the mission. Secondly, since actual drive operation is occurring during only 2.7 percent of the mission, a ten-year flight will require the equivalent of only 100 days of continuous drive operation.

The angular position of the array shaft relative to the vehicle is detected through the combined use of two sensors: the shaft quadrant detector, and the motor step pulse generator (encoder). This information is used by ACS to set up AC and SADA control functions.

PROTOTYPE DRIVE EVALUATION TESTING

Two prototype actuators fabricated for evaluation have been subjected to both bench and vacuum testing. A one-week run-in of each drive followed by teardown, cleaning, inspection, relubrication and reassembly preceded the bench tests, which included rate verification, stall and back-driving torque determinations. Overrunning friction of each clutch was also measured.

The endurance/life-test of the two drives and associated hardware is being performed in a bakeable stainless steel vacuum chamber, having a 500 liters/second ion pump and a 5000 liters/second titanium sublimation pump. The arrangement of the test articles and the vacuum life-test equipment including the chamber are shown schematically in Figure 5. Figure 6 shows the drives installed in the vacuum chamber prior to the start of the life-test. The two prototype array drives are connected to a common output shaft through their wrapspring clutches. Either or both drives may operate to rotate this shaft. Two slip ring assemblies are also attached to the common shaft and rotate with it while their brush assemblies are attached to the fixture baseplate. In addition, a third clutch is mounted on a hub which rotates with the shaft. The "leading" end of the coiled clutch spring contacts a stop fixed to the baseplate of the fixture which causes the clutch to slip on the shaft. The tangential components of the frictional drag force unload each coil of the spring by producing an increase in the inside diameter of each preloaded coil of the spring just adequate to relieve the radial preload, permitting

the spring to slip freely on the shaft. This arrangement simulates the wear conditions which would be seen by the clutch of a drive being held in standby or a drive which had failed. In representing either case the inclusion of the clutch is intended to determine whether its overrunning throughout the life of the test would adversely affect the operation of the drive(s), or the subsequent ability of the clutch to re-engage.

The output end of the common test shaft is connected to a hermetically sealed rotary motion feed through, which in turn couples the drives to a hysteresis brake, which simulates the expected running friction of the array shaft slip rings and bearings.

To verify the adequacy of the dry lubricants to serve as an effective back-up for the liquid lubricants used, it was decided to omit the liquid lubricants from one of the two drives to be tested in 1972. This would simulate the operation of a drive in space which had lost all effective liquid lubrication; and, since the life of the dry lubricant is primarily wear-cycle limited, a reasonably valid long-term accelerated test could be performed on this unit, in compressed time, since no aging effects have been observed in any of the dry lubricants selected.

Test instrumentation includes an oscilloscope to monitor input and output waveforms, a recording thermocouple potentiometer recording the motor temperatures, as well as those of the baseplate and chamber wall. Vacuum pressure is monitored as a function of ion pump filament current. The motors are driven by stepper motor controller at a frequency controlled by a variable rate oscillator. The control circuitry also includes means of automatically and manually driving either or both drives and sequencing them in an alternate mode. Both motors have been driven simultaneously, however, throughout the entire test (except for brief alternate stops to verify performance of the clutches).

The drive operation was accelerated by a factor of 72 to maximize accumulation of life cycles without significantly over stressing the drives thermally or mechanically and without changing the dynamics of drive operation. In flight, the drive will turn at one rev per day; however, it will only operate for 0.22 second every eight seconds (1/36 duty cycle). The 72:1 acceleration was achieved by first eliminating all dwell time between output drive steps (this provided a 36:1 acceleration) and then doubling the probe rate to the motor. The drives were previously tested at this rate for two weeks in laboratory ambient and operated well.

Although it might appear that the severity of the test was reduced by eliminating the repeated start-ups of the drive under load, this is not in fact the case. The mechanical time constant of the motor rotor is less than four milliseconds, while the pulsing rate of 100 Hz produces motor drive pulses of ten

millisecond duration and repetition rate. Therefore, the motor rotor completes each 1.8 degree step in four milliseconds and settles under the electromagnetic damping of the ten millisecond pulse, the effect of the hysteresis brake counter-torque and the friction of the slipring brushes. Therefore, the motor essentially starts and stops with every pulse of the drive circuit. At 30 rpm, which results from the 100 Hz drive frequency, there is no significant momentum development in the system to keep the motor rotor "coasting" between drive pulses.

EVALUATION TEST RESULTS

Bench Tests

The bench tests conducted on the drives were preceded by a ten-day run-in at 100 Hz of each drive. Each was monitored several times daily during this period. Rotational rate and temperature were stable throughout the run-in period for each drive. After run-in each drive was torn down and cleaned. Wear debris, which was slight in both units, was removed. After each drive was cleaned, the liquid lubricants in drive No. 2 were replenished and both drives were reassembled and run for approximately six hours to make certain that they were operating properly. The drives were then installed in the test fixture and bench tested.

In bench testing, each drive delivered a minimum of 58.3 N-m (43 ft-lb) against deadweight torque loading. Clutch overrunning torques were 0.27 to 0.34 N-m (0.2 to 0.25 ft-lb). Combined back driving torque of the two unenergized drives was approximately 37.9 N-m (28 ft-lb). (In prior tests the dry lubricated drive had exhibited 40.7 to 44.7 N-m (30 to 33 ft-lb) back driving torque, while the wet-on-dry lubricated drive required 9.5 Nm to 16.3 N-m (7 to 12 ft-lb) to back drive it. The decrease in the combined torque is attributed to continued bench run-in, cleaning, and relubrication of the drives.)

Vacuum Test

The life-test, originally intended to last five weeks, is continuing beyond its 68th week of operation; since the second week of testing, the pressure has been less than 10^{-7} torr and is currently 3×10^{-8} torr. The drives have operated without significant anomaly throughout the test. More than 34,000 output revolutions have been completed by each unit. At intervals of one to seven days, each drive has been alternately turned off and restarted, demonstrating the continued proper operation of each drive clutch and the reliability of the block redundant system operation. The third clutch continues to offer drag comparable to that seen in the bench test.

The temperature of the hybrid lubricated (No. 2) drive has slowly decreased from 52°C (125°F) to approximately 47°C (116°F). The No. 1 (dry-lubed) unit has remained 1 to 2 degrees warmer than the No. 2 unit. The decrease is partly attributab

to a slight decrease in lab ambient and, possibly, to a continuing run-in of the drives. Load torque has remained constant at 4.1 N-m (3 ft-lb). Speed has tracked the input pulse oscillator properly. The test oscillator (a commercial unit) drifted slowly from 72 to 68 Hz in ten months. It was then raised to 78 Hz, where it is still operating.

The stall torque of the drives cannot be measured as long as they remain in the chamber, since the sealed rotary feed through will not safely transmit 40 ft-lb. These parameters will be evaluated when the test is halted.

The conducted sound through the vacuum chamber frame of the drives operating has been evaluated only subjectively by the writer; in the duration of the test to date it does not seem to have changed significantly, if at all.

The slip rings were energized with load current for a short time, but the high amperage produced significant I^2R heating of the chamber wall electrical penetration, which adversely affected temperature measurement of the drives, so this peripheral activity was halted. No significant change of brush-ring series resistance has been observed. When last measured several months ago the resistance variation during one revolution of the ring averaged 0.001 ohm with very infrequent 0.002 ohm peaks.

There has been no measurable change in motor electrical characteristics, except for current change, as a result of winding resistance change with temperature.

CONCLUSIONS

1. The prototype Solar Array Drive Assemblies have greatly exceeded the original performance requirements in terms of both power and life.
2. The efficacy and reliability of the wrapspring clutches to permit block redundant drive application has been fully demonstrated.
3. Both the hybrid redundant lubrication system and the dry lubricant system have been shown to be adequate for long term space operation. While the mixed lube system provides greater efficiency, the dry lube system alone is capable of long life so it can serve as an adequate backup system or a primary system by itself.
4. While the true validity of the test acceleration method used here will not be verified until real-time flight test data can be obtained, increasing the maximum rate by a factor of only two and gaining major time compression by decreasing dwell time appear to be philosophically sound as a method of evaluating long-life performance in relatively little time, since no major uncontrolled stresses or other dissimilarities are introduced. While the method does not provide real-time aging of the liquid lubricant, it is inherently stable at the temperatures of use with a great safety margin, and the chemical makeup of the liquid used is quite stable.

5. The feasibility of developing a highly reliable, low cost actuator for long-life spacecraft use through the careful selection and application of proven, high margin components, advanced materials, and conscious effort to achieve maximum simplicity has been demonstrated.

These conclusions are valid insofar as the extent and severity of the test operations to date are concerned. Further evaluation testing including shock, vibration, and thermal cycling are planned.

It is hoped that the ultimate proof successful long-term on-orbit operation will be achieved within the not-too-distant future. The possibility of achieving this proof is tangible since the drive is a part of the baseline configurations of a number of future spacecraft in the preliminary design stage.

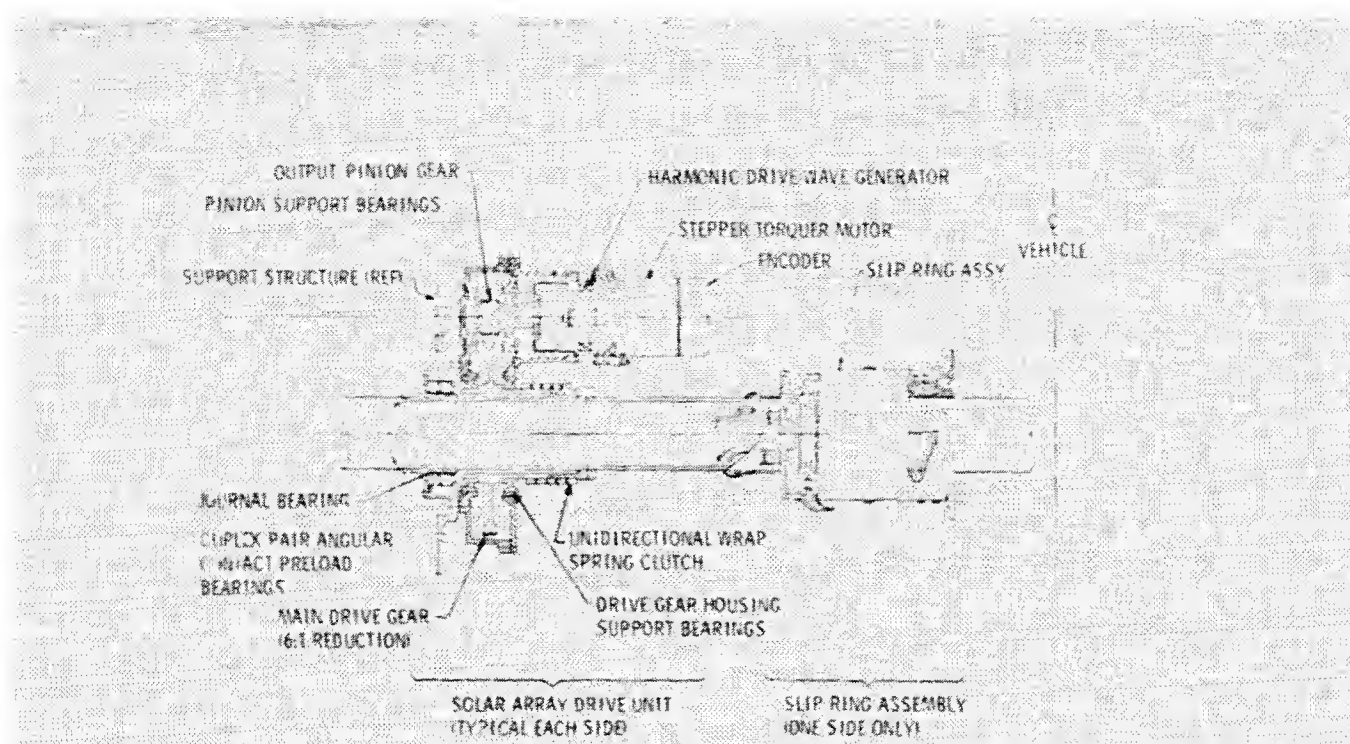


Figure 1.- Layout of advanced solar array drive in typical vehicle installation.

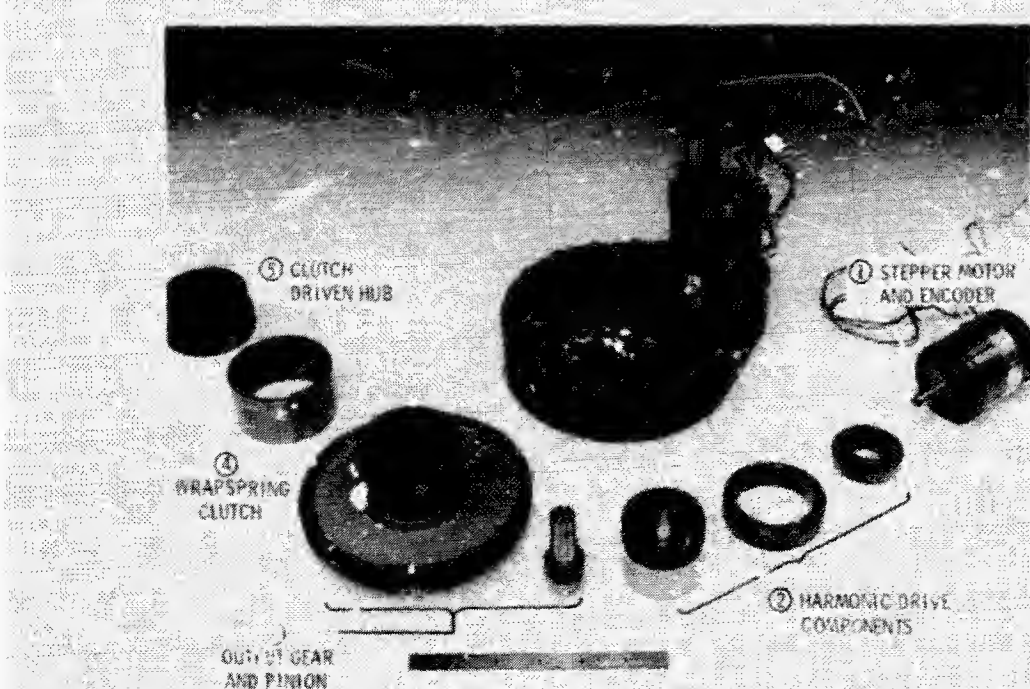


Figure 2.- Major drive train components of advanced solar array drive shown with assembled SAI V prototype unit in background.

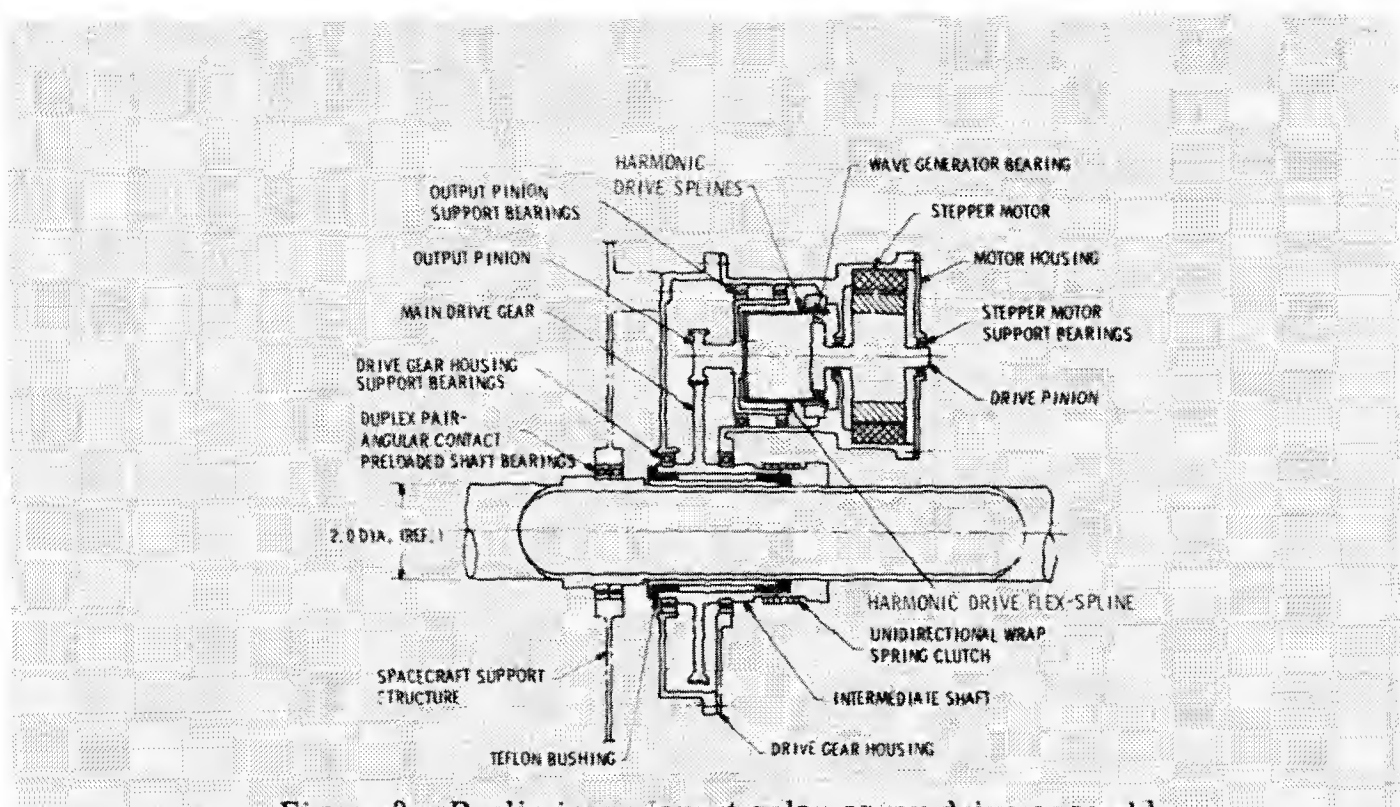


Figure 3.- Preliminary layout solar array drive assembly.

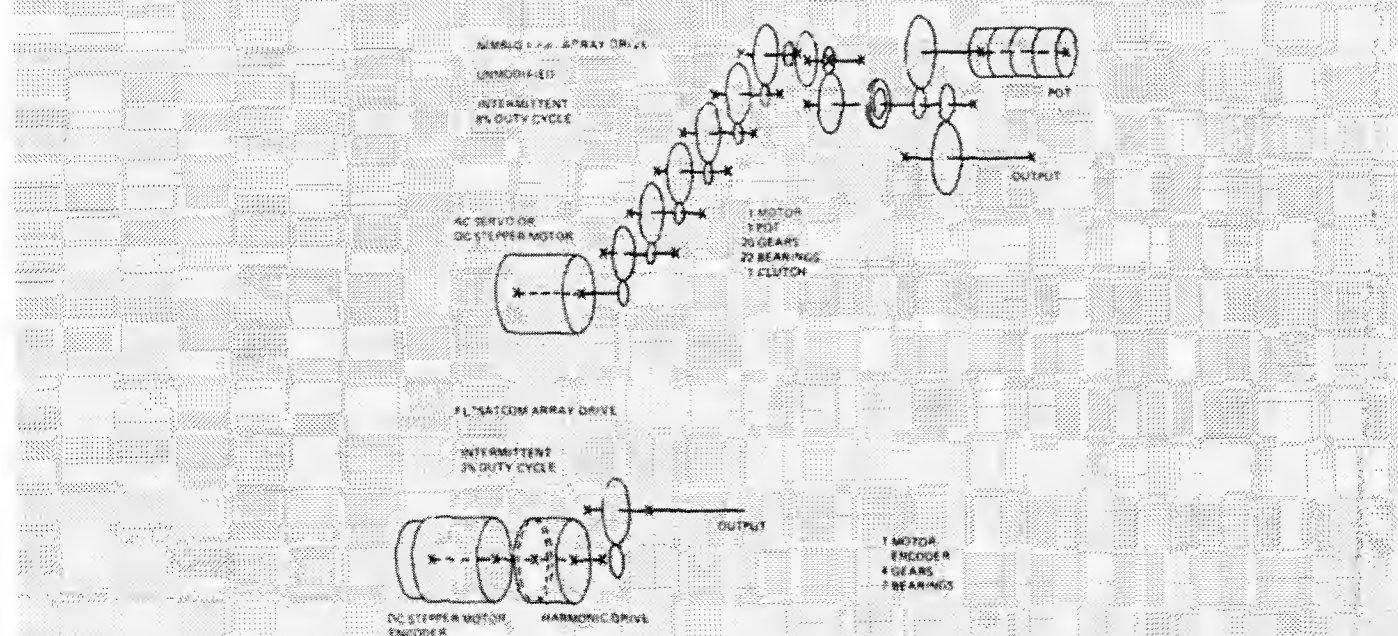


Figure 4.- Comparison of SADA and Nimbus I to III
drive complexity.

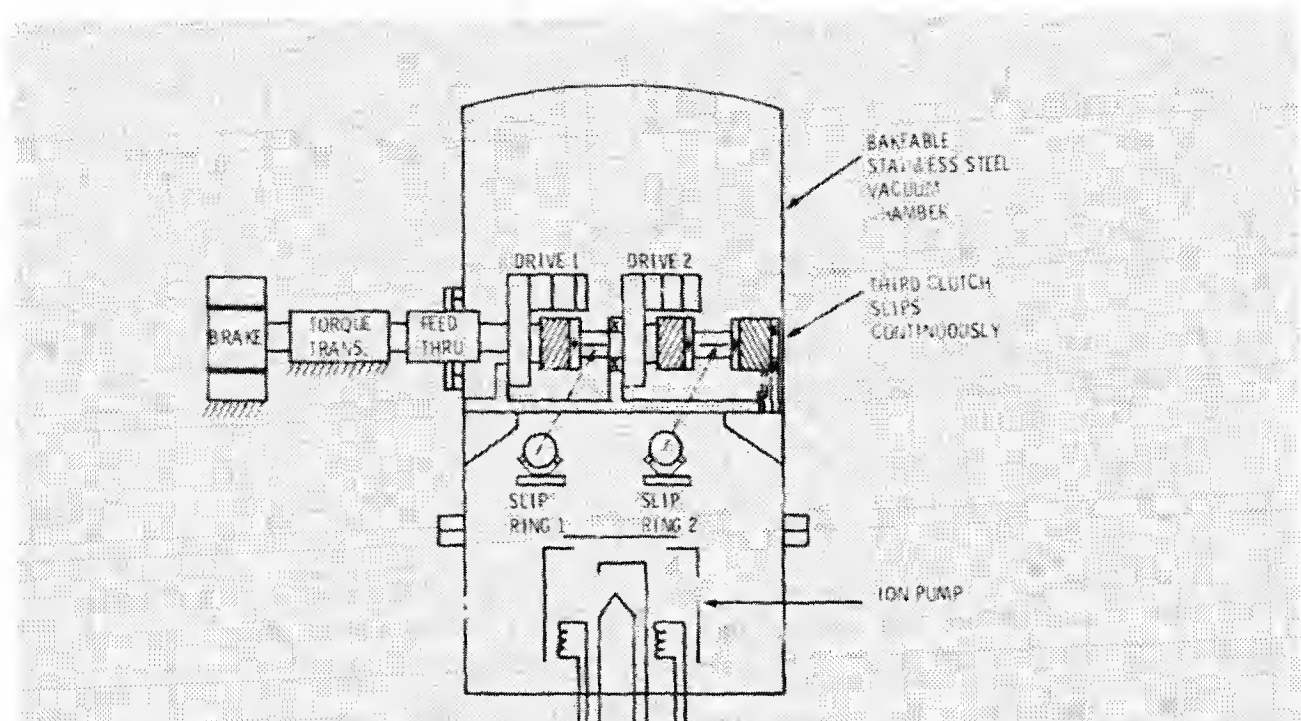


Figure 5.- Schematic layout of SADA vacuum life-test.

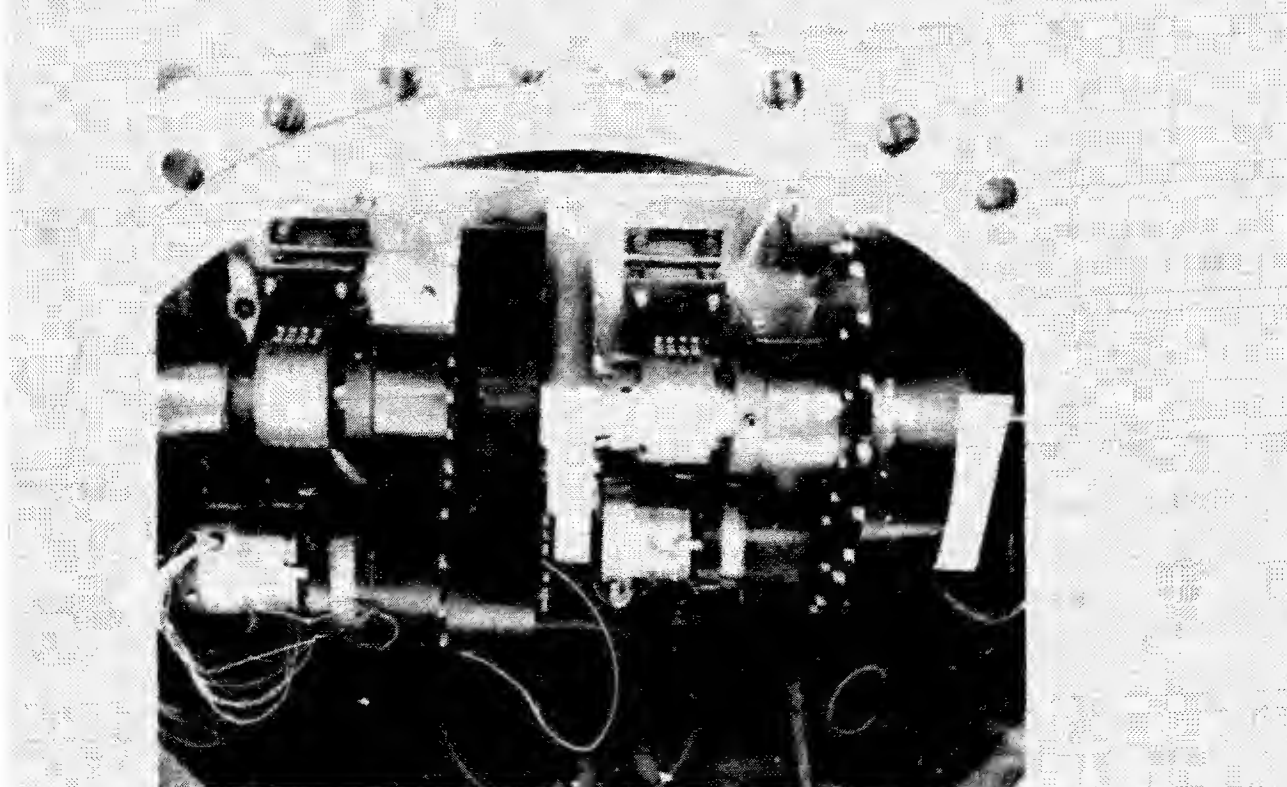


Figure 6.- Prototype SADAs in vacuum chamber prior to life-test.

3. HIGH PERFORMING ACTUATION SYSTEM FOR USE WITH
A LOUVER ARRAY FOR SATELLITE THERMAL CONTROL

by

Peter U. Reusser, Senior Mech. Engineer, Mem. ASME
and
Jan A.F. Coebergh, Mech. Engineer
of

Messrs. Peter U. Reusser Ltd.
Engineers and Management Consultants
25, Gruebstrasse
CH-8706 MEILEN / Zurich, Switzerland

1.0 INTRODUCTION

To meet the more stringent thermal requirements of advanced spacecrafts of the European Space Research Organisation, ESRO, a high performing actuation system has been developed to drive one pair or a set of 9 pairs of louver blades. This under simulated space conditions successfully tested actuation system has, compared with a bimetal or bellows actuator, considerable advantages, i.e.:

high sensitivity, approx. 0.2°C

small ΔT range between opened and closed blades, $5^{\circ}\text{C} \pm 1^{\circ}\text{C}$

faster response for finer temperature control,
approx. 5 sec at a $\Delta T = 5^{\circ}\text{C}$

easy adaption to hot spot sensing for localised high
dissipating equipment

the system can be developed into a moderately high
torque actuator

A bimetal actuator, for instance, is very simple and reliable but it shows the following performance limitations:

sensitivity limited to $\sim 3^{\circ}\text{C}$

ΔT range between fully opened and closed positions of
the blades has to be 15°C or more

no possibility of controlling hot spots

long time constant

2.0 SUMMARY

The high performance actuation system uses a Bourdon spiral as the driving member (see fig. 1).

A tank filled with dimethylether ($C_4H_{10}O$) having a high coefficient of volumetric expansion is used as a temperature sensing and actuating medium. As the tank temperature increases, the pressure of the liquid also increases, and is directly transmitted through a capillary to the Bourdon spiral. Tank, connecting capillary, Bourdon spiral and overpressure compensator constitute a closed system. The angle of rotation of the center of the Bourdon spiral is proportional to the pressure, or the temperature.

The prototype was designed to give an angle of rotation of 90° , with a temperature change of $5^\circ C \pm 1^\circ C$.

(Sensitivity: 18 angular degrees per $1^\circ C$. A bimetal spiral gives approximately 6 angular degrees per $1^\circ C$.)

A mechanical set point variation device permits covering 3 operating ranges of $5^\circ C$ each.

The response time of the liquid expansion of the spiral system is in the order of three seconds. The system can be subjected to very high and low extreme temperatures (freezing point of ether $-116^\circ C$ up to $+70^\circ C$).

An overpressure compensator has been developed; this consists of a spring preloaded bellows (see fig. 2). A change of the spring constant of the spring-bellows assembly allows minimizing the pressure build-up above the operating temperature range. This device extends the upper limit of the non-operating temperature and it increases the overall reliability.

Besides the performance tests, qualification tests have been carried out, demonstrating that the actuation system withstands normal launching conditions. An operating life of 7 years with more than 7000 cycles can be expected because, in other fields, Bourdon tubes have demonstrated a very high reliability. Proper care has been taken not to introduce new materials and techniques. As far as soldering, brazing and welding are concerned, only well-known and tried processes have been employed.

The multiple blade actuator employs the same physical principle as the single blade actuator because it was felt it might be an advantage, with respect to performance and reliability, to employ the same actuation system to operate all 9 pairs of blades. A battery of separate tanks connected by heat conduction through the tank walls was chosen. This configuration gives a good heat conduction through the walls from tank to tank and shows a much better hot spot sensing capability than a mechanically coupled actuator.

3.0 DESIGN AND DEVELOPMENT OF THE ACTUATION SYSTEM

In order to find a suitable actuation system for a louver array as well as alternative solutions with the objective of highest mission success, selection procedures have been carried out to compare some typical configurations, including sensors, actuators, transmissions and bearings. The options were divided into two groups: electrical systems and pressure-expansion systems.

The goal of the study was to find a better system than the bimetal actuator.

The main evaluation parameters of the developed actuation system were:

- performance
- reliability
- cost

Although the rating of the parameters used to compare the various systems may be somewhat subjective, the following conclusions can be drawn:

Because the Bourdon spiral actuator shows a high sensitivity, simplicity and reliability, it seems to be the best choice. The central shaft acts as connection between the two louver blades. It is driven by the inner end of the Bourdon spiral. For the set point variation of the operating temperature, the shaft can be rotated relatively to the inner end of the Bourdon spiral and clamped in place by means of two set screws.

3.1 Actuation characteristics of the Bourdon spiral (see fig. 3)

The angle of rotation of the center of the Bourdon spiral is proportional to the pressure and therefore proportional to the mean temperature of the liquid inside the tank. Because the Bourdon spiral increases its volume under pressure, the tank volume has to be large enough to cover both the compressibility of the liquid and the volume increase of the Bourdon spiral. The tank was considered to be rigid.

The spiral is not able to rotate more than 300 ° but it should withstand a non-operating temperature of 50 °C, with a corresponding maximum system pressure of 36 kp/cm². A special spiral protection device (see fig. 2) is employed (spiral retainer) to prevent the spiral from over-stretching.

Development tests showed that the highest permissible pressure of 36 kp/cm² exists at about 45 °C, depending on the tank rigidity. Because the highest non-operating temperature is

50 °C, an overpressure compensator had to be incorporated. The final overpressure compensator, a spring preloaded bellows, actually extends the non-operating temperature up to 70 °C.

The basic set point temperature of the system can be changed by changing the mechanical preload angle and the corresponding filling temperature of the ether.

3.1.1 Some limiting parameters of the Bourdon spiral

(The calculation of Bourdon spirals is to be seen in ref. 1)

linear range, pressure	0 to 18 kp/cm ²
linear range, angle	0 to 210°
rupture pressure, without retainer	23 kp/cm ²
highest permissible pressure non-operating, with retainer	36 kp/cm ²
max. angle of rotation	300°
max. temperature range	16 2/3 °C
number of set point ranges	$\frac{300}{90} = 3 \frac{1}{3}$
temperature range (operating)	ΔT = 5 °C
corresponding angle	90°
Preloading the system mechanically with 30° at the required undertemperature of 1 2/3 °C, one obtains	3 full operating ranges
typical set point ranges (for a filling at 18 1/3 °C)	20 - 25 °C 25 - 30 °C 30 - 35 °C

3.2 Tank development

The geometry of the tank has been optimized with respect to:

- static and dynamic requirements
- available space
- rigidity
- weight
- ratio between heat transfer surface and tank volume
- short heat path

There exists just enough space between the louver blades to fit a flat rectangular tank (see fig. 1) underneath the Bourdon spiral.

3.2.1 Tank volume V_o

The Bourdon spiral has to rotate 90° for an increase of $\Delta T = 5^\circ\text{C} \pm 1^\circ\text{C}$ (blades from closed to open position). To build up the necessary pressure, the following criterion must be met:

$$V_r = V_{lt} - V_{ltp} > 0$$

The required tank volume V_o for one actuator system is:

$$V_o = \frac{1}{\alpha p} \cdot a \cdot \Delta V_{lt} \cdot \left(\frac{1}{a} - 1\right)$$

V_o	tank volume (cm^3)
α	compressibility of liquid ($1 \text{ cm}^2/\text{kp}$)
p	resulting pressure within the system
ΔV_{lt}	thermal expansion of liquid (cm^3); $p = 1 \text{ kp/cm}^2$
a	ratio of volumes; V_{ltp} / V_{lt}
ΔV_{ltp}	expansion of liquid under temperature and pressure p (cm^3)
ΔV_r	relative expansion of liquid-tank (cm^3)

3.2.2 Stresses in a rectangular tank under internal pressure p

Pressure vessels in general are made of cylindrical or spherical shapes. In our case, the available space and heat flow considerations led to a rectangular tank. To increase the stiffness, a tension pin (see fig. 2) was mounted in the middle of the tank. This pin also increased the heat conduction into the liquid.

The bending stress in the tank wall is:

$$\sigma_b \propto c \cdot \frac{1}{t^2}$$

σ_b	bending stress (kp/cm^2)
c	constant = f (curvature of corners in the tank and ratio of length to width) (see, for example, ref. 2)
t	time

3.3 Mechanical interface problems between actuator, louver shaft and bearing friction

3.3.1 Statement of problem

The louver shaft is held in two end bearings. The bearings consist of a stationary Teflon bushing with a spherical bore and a rotating, straight cylindrical stainless steel bushing, fixed to the louver shaft. This bearing configuration allows even a bent louver shaft to turn freely.

In axial direction, the shaft is not held in these bearings.

The actuator is mounted in the center between the two end bearings, and it has to provide the axial bearing. The actuator forms a third point on the louver shaft, and this constraint gives rise to radial bearing reactions and undesirable friction forces in the bearings of the louver shaft.

The least friction is obtained by leaving the center bearings out. The following force, however, will remain:

The path of the driving end of the Bourdon spiral is not an ideal circle. This, together with the radial spring constant of the Bourdon spiral will give a radial force. However, it is well to note that the radial spring constant of the Bourdon spiral is very small and that the resulting forces will be small, too.

Under excess temperature the actuator would turn more than 90° . Because the pin in the louver shaft hits a stop after a motion of 90° , an excess torque is created in the louver shaft.

3.3.2 Bearing friction and torque characteristics

Under space flight conditions, the only force acting is the radial spring force of the not perfectly centered Bourdon spiral.

Friction radius of bearings	5.7 mm
Thermal deflection	1 mm
Offset of Bourdon spiral	1 mm
Radial spring constant of Bourdon spiral	10 p/mm
Friction coefficient of stainless steel on Teflon in high vacuum	0.2
The above parameters give a friction moment of	1.48 cm-p

The torque characteristics of the actuator are:

Torque	0.8 p-cm/ $^{\circ}$
Angle of rotation per 1 $^{\circ}$ C	18 $^{\circ}$ / $^{\circ}$ C
Minimum sensitivity	< 0.5 $^{\circ}$ C
Resulting torque at 1 $^{\circ}$ C	14.40 p-cm
- Friction moment	- 1.48 p-cm
Excess driving torque	12.92 p-cm

4.0 THERMAL ANALYSIS

4.1 Response behavior and heat flow base-plate - tank

To obtain a good response behavior, the resistance of the heat paths must be as small as possible. The tank bottom area acts as a base-plate. The heat is mainly transferred by conductance and radiation. For the best heat transfer, one has to optimize the values for k , because the contact area A and ($m \cdot c$) can be considered as given and constant.

k total thermal conductivity $\frac{\text{Watt}}{\text{m}^2 \cdot ^{\circ}\text{C}} \equiv \frac{\text{kcal}}{\text{m}^2 \cdot ^{\circ}\text{C} \cdot \text{hrs}}$
(see figures 4 and 5).

4.2 Sensitivity

Tests showed that the shaft of the Bourdon spiral starts to rotate after less than 3 seconds at a ΔT of 5 $^{\circ}$ C. During the first 3 seconds, the liquid receives the following heat quantity Q (cal.):

$$Q = V_0 \cdot \rho \cdot c \cdot \Delta T / \left[1 - e^{- \frac{k \cdot A}{V_0 \cdot \rho \cdot c} \cdot t} \right] \quad \text{Dynamic heat flow}$$

ρ specific gravity of ether

c specific heat of ether

The angle of rotation $\Delta\varphi$ of the Bourdon spiral is:

$$\Delta\varphi = \frac{c_1}{c_2} \cdot Q$$

$$c_1 = \frac{\Delta\varphi}{\Delta Q} \quad ; \quad c_2 = \frac{\Delta\varphi}{\Delta\varphi}$$

$$\Delta\varphi = \frac{1.88}{0.085} \cdot 0.28 = 6.19^{\circ}$$

4.3 Conclusion

The actuator has to overcome friction in the bearings and this friction leads to a phase shift of $3 \text{ sec} \rightarrow 6^\circ$. This delay corresponds to a temperature difference $\Delta T = 0.34^\circ\text{C}$ of the liquid. This calculated sensitivity was confirmed during performance tests.

5.0 PERFORMANCE TESTS

The actuation system was integrated with the louver array and for testing purposes attached to a suitable heating-cooling plate.

To record the angular position, an electrical contact could be made on the end-stop of the bearing-housing. During the tests in the vacuum chamber a pressure of 5×10^{-8} torr was maintained. (See fig. 6.)

5.1 Conclusions

The tests showed:

the response of the actuator is nearly instantaneous

the system reacts at a variation of the sensed temperature of less than 0.5°C

a super isolation blanket covering the actuators is advisable, especially when the louver array is used for hot-spot sensing.

6.0 REFERENCES

1. Wuest, Walter: Die Berechnung von Bourdonfedern
(The calculation of Bourdon tubes). VDI-Forschungshaft 489, Ausgabe B, Band 28, 1962
2. Roark, Raymond J.: Formulas for Stress and Strain,
Mc Graw Hill, 1965, page 117

P.U. Reusser, J.A.F. Coebergh
Meilen/Switzerland
June 14th, 1973

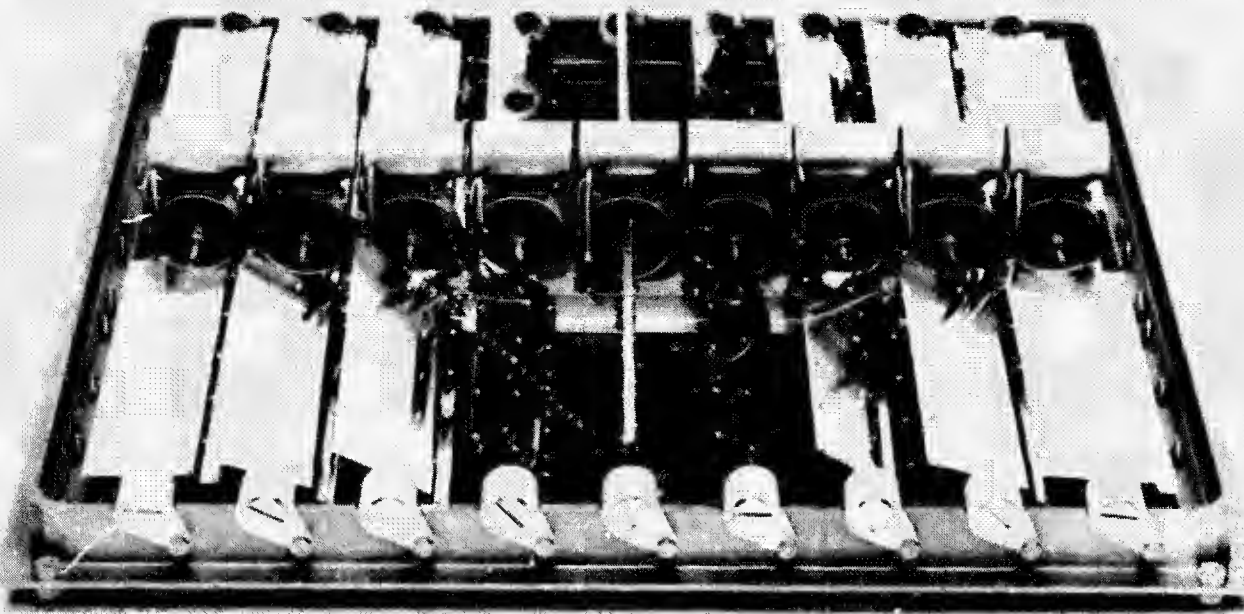


Figure 1.- Complete louver array with a high-performing actuation system.

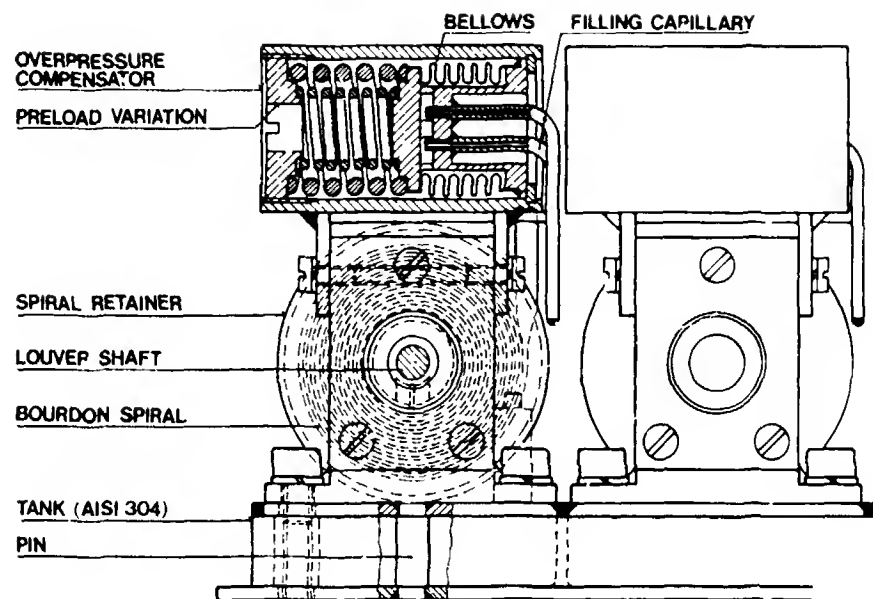


Figure 2.- Section of actuation system.

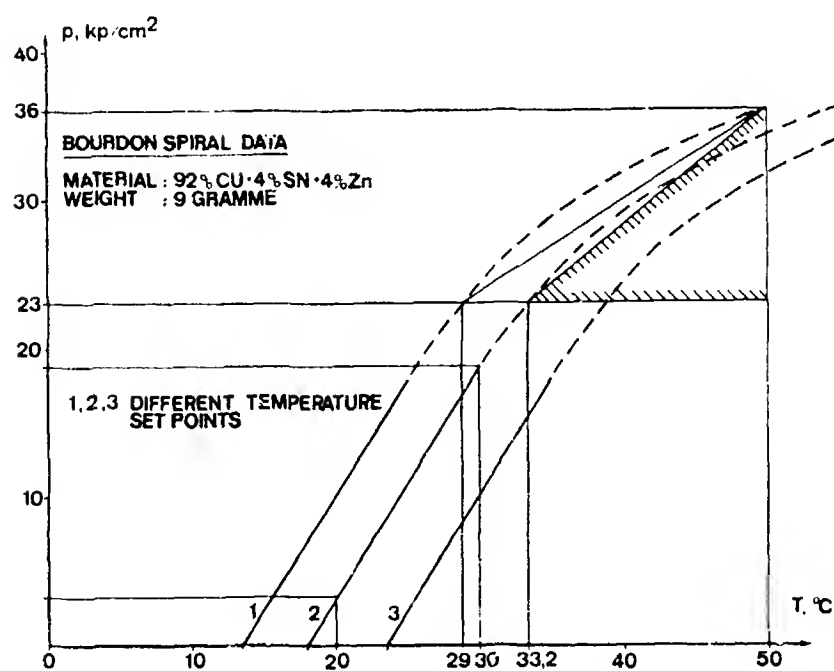


Figure 3.- Bourdon spiral. Temperature-pressure characteristics.

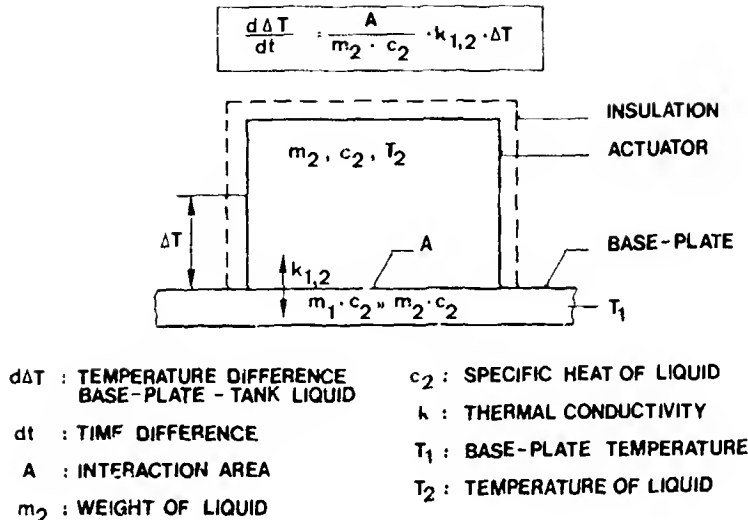


Figure 4.- Response behavior. Base-plate tank liquid.

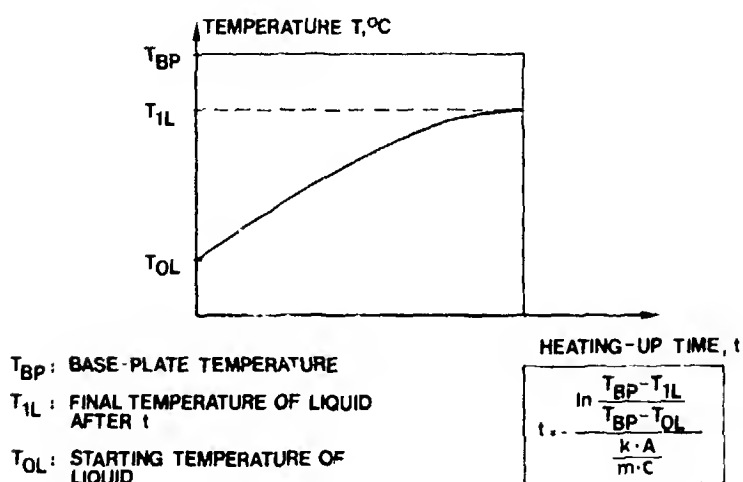


Figure 5.- Heat flow base-plate tank. Heating-up time.

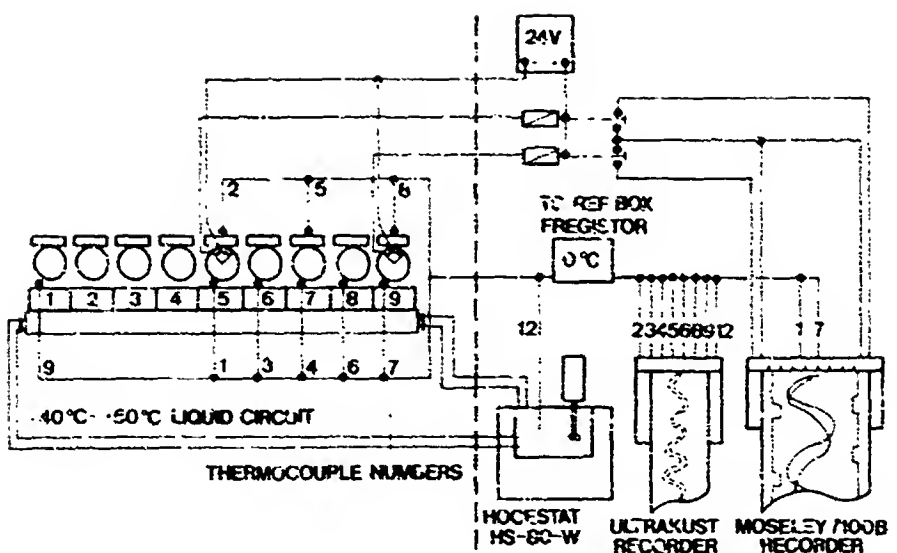


Figure 6.- Schematic diagram of the instrumentation during performance test.

S. DEVELOPMENT OF THE ELEVATION DRIVE ASSEMBLY
FOR ORBITING SOLAR OBSERVATORY I (FYE)

By W. F. Sharpe and M. C. Olson

Hughes Aircraft Co., Space & Communications Group

And B. W. Ward, NASA, Goddard Space Flight Center

SUMMARY

The requirements for pointing accuracy, friction, and power for the elevation drive assembly (EDA) of an orbiting space observatory are discussed briefly. A description of the components making up the assembly is presented. Special features requiring development testing prior to unit fabrication are more fully described together with a review of the test programs conducted and results obtained.

INTRODUCTION

The overall objective of the Orbiting Solar Observatory program is to conduct experiments in solar physics and celestial astronomy above the earth's atmosphere. Purpose of the experiments, in general, is to measure the intensity and variations of radiations from the sun and celestial bodies in the ultraviolet, X-ray, and gamma ray wavelengths. The specific mission of OSO-I, shown in Figure 1, is to investigate the sun's lower corona, the chromosphere, and their interface in the X-ray and ultraviolet spectral regions to better understand the transport of energy from the photosphere into the corona. The elevation drive assembly rotates the sun pointed spectrometers referred to herein as the Pointed Instruments Assembly (PIA).

REQUIREMENTS

Inherent precision pointing capability is provided by closed-loop control utilizing the PIA sun sensor. The primary difficulties experienced in designing a suitable elevation drive mechanism which will achieve the required fine pointing capability are misalignments, bearing, and torque variations. The torque variations occur in the bearings and the flexible cables which cross the gimbal axis. Stiction (breakaway friction) of the bearings is especially

important. Maintaining the inertial position of the PIA in the event of vehicle nutation or platform wobble is facilitated by the inherent stability of the high inertia PIA and the use of a low-friction gearless direct drive. The servo has only to compensate for bearing friction to hold the PIA inertially stationary.

The basic requirements are summarized in Table 1. Meeting the pointing stability requirement and the attendant motion and accuracy requirements depends on the performance of the bearing system. Computer simulation of the vehicle and PIA dynamics has established the maximum acceptable friction torque as eight in-oz to meet the one arcsec jitter requirement. The ability of the EDA mechanism to meet these stringent requirements following the launch environment is the key element in achieving a successful mission.

Power requirements are important for two reasons. These are 1) to minimize the demands on the spacecraft power bus, and 2) to keep the power dissipation in the drive assembly at favorable levels to maintain good thermal balance within the unit and minimize thermal distortion in the structure that would affect the alignment references or the bearing friction.

An important consideration in regard to drive torque requirements is the flexing of wires or cables that must cross the gimbal axis. Since only five degrees travel is required, the use of slip rings is not necessary. The design selected for power and signal transfer to the experiment package uses two flat contour cables, installed in a manner to provide a rolling action as the gimbal rotates.

DESCRIPTION

The elevation drive assembly, shown in Figure 2, consists of the following elements:

- A. Yoke - This is an aluminum structure which provides mounting for the spacecraft solar panel and the azimuth reference assembly. The outer bearing races, the motor housing, the position transducer housing, and one end of the flexible cable assemblies are attached to this structure.
- B. Gimbal Saddle - This U-shaped aluminum part essentially forms the shaft of the rotating gimbal. The experiment saddle, bearing inner races, PIA sun sensor, remote multiplexers, remote command decoders, position transducer and motor rotors, and the other end of the flexible cables attach to this part.

- C. Experiment Saddle - This titanium box-shaped structure mounts on the gimbal saddle. The two pointed instruments are attached to the saddle as are the mechanisms for performing and maintaining the coalignment of the pointed instruments.
- D. Bearings - Two oil-lubricated angular contact ball bearings, preloaded by dual flexure springs, provide low and consistent torque over the limited range of rotation.
- E. Motor - A limited-rotation brushless DC motor produces the torque required to position the pointed instruments assembly.
- F. Position Transducer - A variable reluctance differential transformer signal generator furnishes an output signal proportional to the angular position of the PIA. The input voltage is transformed to either an in-phase or out-of-phase relationship to the primary voltage at an amplitude proportional to the rotation from the null position.
- G. Launch Lock Assembly - This is a mechanism with pyrotechnic separation nuts used to hold the PIA during launch and to release it for in-orbit operation. Two separation nuts are provided; the firing of either or both nuts will release the launch lock.
- H. Flexible Cable Assemblies - These flat cables provide the electrical path for power and signal conductors across the gimbal axis.
- I. Coalignment Adjustment Mechanism - These devices, installed within the experiment saddle, furnish azimuth and elevation adjustments necessary to coalign the pointed instruments. The adjustments are made when the instruments are installed; once adjusted, the instruments are locked in place for subsequent operation.

SPECIAL FEATURES

The elevation drive assembly includes several special features which are of such importance to spacecraft operation that special tests were required prior to assembly of the first unit.

A. Launch Lock Mechanism

During the launch environment the experiments, experiment saddle, and gimbal saddle are caged by two pivoted launch lock assemblies that tie the gimbal saddle to the bottom yoke structure (Figure 3). Squib-

actuated explosive nut assemblies are used to attach the clamp locks to the gimbal saddle base. The tie rod mechanism is designed so that should either one or the two explosive nuts fail to fire both clamps will still be released from the gimbal saddle. The operation is illustrated in Figure 4, which shows the locked position and the unlocked position with one nut or both nuts actuated. After the nuts are actuated, the clamp assemblies are rotated out of the way by means of kickoff springs in the clamp and torsion springs located at the pivot joints. Crushable honeycomb material is used as a clamp stop to cushion the impact as the clamp strikes the clamp stops.

A model of the launch lock mechanism was constructed and tested in order to evaluate the release action. The test sequence consisted of firing one nut, then the other, and then both nuts together. After each firing, the crushable honeycomb material was replaced. Each test sequence was conducted five times for a total of 15 release actuations (20 nut firings, total). High speed motion pictures were taken of each firing.

Results were satisfactory except that in one instance the clamp did not clear the threaded end of the tie rod upon release, causing one clamp to remain partially engaged to the saddle. It was also noted during the tests that the honeycomb shock absorber material did not crush as much as expected so that the clamp did not move far enough to permit full six degrees rotation of the gimbal saddle. These problems were corrected by adding a counterbore in the clamp and by reducing the thickness of the honeycomb material by 0.28 inch.

B. Alignment Mechanism

The alignment mechanism is provided so that both the upper experiment and the lower experiment can be pointed at the same sun position. The mechanism is shown in Figure 5. The experiments must be coaligned within five arcseconds and cannot shift more than an additional five arcseconds as a result of the launch environment and temperature excursions. The Paris experiment is hard mounted to the experiment saddle with no adjustment. The Colorado experiment is adjusted in azimuth and elevation as follows:

1. A tapered, rotatable shim is mounted between the experiment and the experiment saddle. The shim can be rotated 30 degrees to provide an elevation adjustment of two minutes with a taper of $0^{\circ} 4'$. Required shim rotation for a five arcsecond adjustment is therefore 1.2 degrees.

2. Azimuth adjustment is achieved by means of a differential screw which links the experiment saddle to the experiment. The differential threads are 27 per inch and 28 per inch. One revolution of the differential screw results in a motion of

$$\frac{1}{27} - \frac{1}{28} = .0013 \text{ inch per turn}$$

At an arm length of 14 inches, the rotation produced is

$$\frac{.0013 \text{ in.}}{\text{Turn}} \times \frac{1}{14 \text{ in.}} \times \frac{57.3 \text{ deg.}}{\text{Rad}} \times \frac{3600 \text{ sec}}{\text{deg.}} = 19 \text{ arcsec per turn}$$

Alignment tests were conducted to determine the repeatability of the mechanism, the resolution of the adjustment, thermal effects over the expected temperature range of 40° to 100° F, and the effect of the launch induced thrust axis load on the coalignement mechanism.

C. Torque and Torque Variation

The major requirements for the ball bearings are low and consistent friction at slow speeds to minimize control loop errors. A small diameter bearing has minimum friction torque because the rolling friction forces act at a small radius. The desire for consistent friction favors use of a small ball diameter on a large diameter race so that small shaft displacements commanded can cause the ball to roll. Should the ball size be too small, contaminant particles will cause inconsistent torque when encountered. A compromise is therefore required. The 11/16-inch ball diameter is large compared with expected contaminants, but the ball is reasonably small compared with the 2.9-inch pitch diameter. The bearing installation is shown in Figure 6.

The friction level for rolling the pair of bearings is less than three in-oz. The friction torque is almost independent of viscous effects because the velocity is low and the temperature range is limited. The ratio of static-to-rolling friction is of major importance to the control system performance. This ratio is made up of two contributing factors. The constant or reproducible factor inherent to ball bearings is the smaller contributor, while the random torque component due to ball and retainer interaction is more significant. This random component is difficult to evaluate analytically and was therefore definitized through engineering tests.

Breakaway friction tests were conducted using bearings similar to those planned for the flight vehicle. Direct incremental loading of

a beam attached to the bearing shaft was the method used to obtain breakaway torques. Gravity effects positioned the retainer against the balls and the inner race outside diameter to such an extent that test irregularities became a problem. By changing the bearing shaft from horizontal to vertical, the irregularities were eliminated.

Additional tests conducted with the bearing shaft vertical resulted in breakaway torque of less than 50% of the values recorded in the horizontal position. Breakaway torque was 1.6 in-oz with 16 pounds preload and 2.05 in-oz with 30 pounds preload.

To obtain running friction, the fixture was positioned with the bearing shaft vertical with a preload of 16 pounds. Tests were run at rotational speeds of 0.010 and 0.045 degree per second, obtained by using a Genisco rate table and a 20:1 ratio pulley system. Average running torque was 0.80 in-oz through an arc of 30°. Plots of measured torque are shown in Figure 7. The results indicated the following:

1. The torque characteristics of the balls and race are repeatable and can be used as a reference.
2. At the low levels the torque is independent of rate of rotation and viscous effects are not important.

An attempt was made to measure the flexible cable torque, but this torque was so small that it could not be identified within the variations of bearing fixture torque. An estimate of cable torque would be less than 0.5 in-oz.

PROBLEM AREAS

Several problem areas came to light and were resolved during the development program:

1. Shaft stops, as shown in Figure 8, were added to both the microsyn and motor sides of the yoke to prevent the delicate internal portions of the microsyn and motor from making contact during launch or any other time.
2. Although preload springs were included in the original design for proper bearing positioning, the spring rate of the gimbal saddle (and the change in spring rate when the experiment saddle is mounted to the gimbal saddle) was not taken into account. Special fixturing was necessary to take this loading into account when setting the preload.

CONCLUDING REMARKS

The development tests conducted on components of the elevation drive assembly have provided assurance that the pointing accuracy, low friction, and launch lock actuation requirements for proper spacecraft operation will be achieved following the launch environment.

TABLE 1. ELEVATION DRIVE ASSEMBLY REQUIREMENTS

Parameter	Requirement
PIA mass properties	250 pounds, maximum inertia of 17 slug-ft ² about elev. gimbal
Experiment alignment	5 arcsec prelaunch 10 arcsec postlaunch
Angular excursion	± 5 degrees
Experiment Temp. Range	20°C \pm 5°C experiment
Bearing friction	6 in-oz, maximum
Flex cable torque	1 in-oz per degree, maximum
Motor torque	1.0 ft-lb, minimum
Launch Environment	
Sine Vibration	8 g max - sweep 20 to 2000 Hz
Random Vibration	max intensity 0.18 g ² /Hz
Acceleration	10 g along launch axis 3 g lateral to launch axis



Figure 1.- OSO spacecraft configuration.

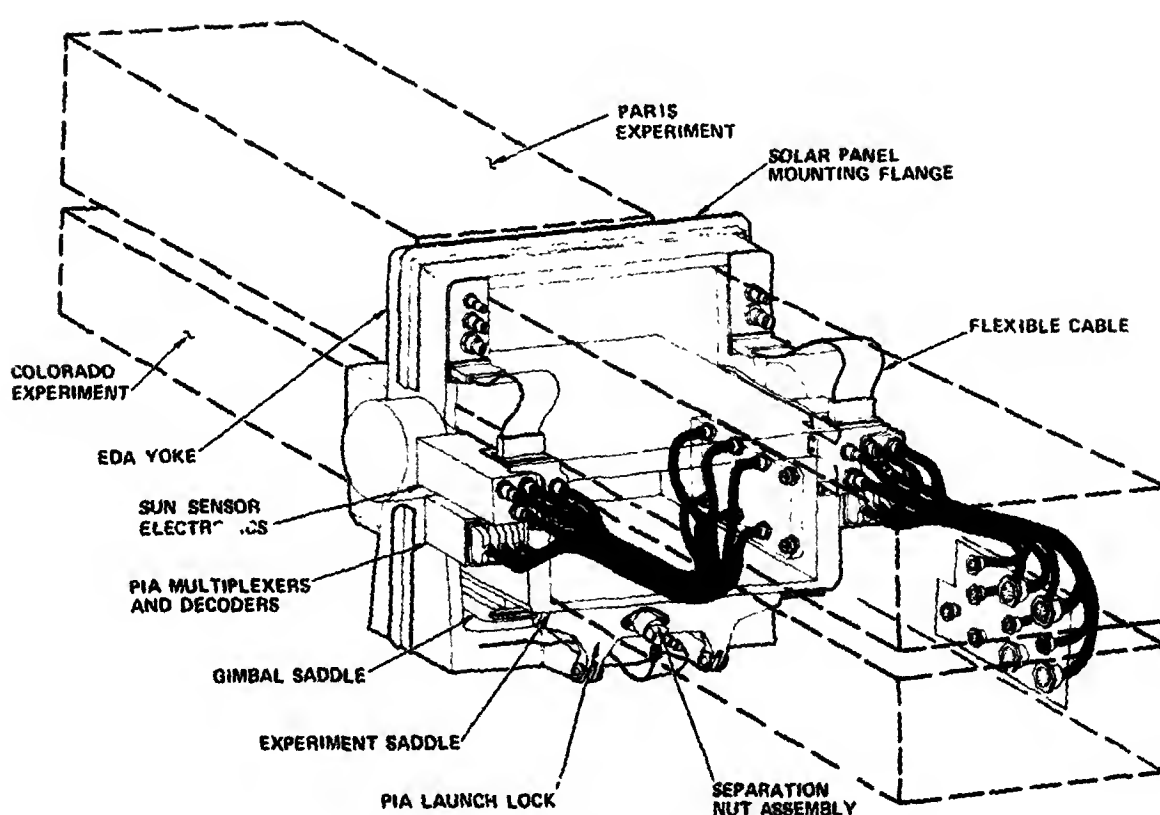


Figure 2.- EDA-PIA general arrangement.

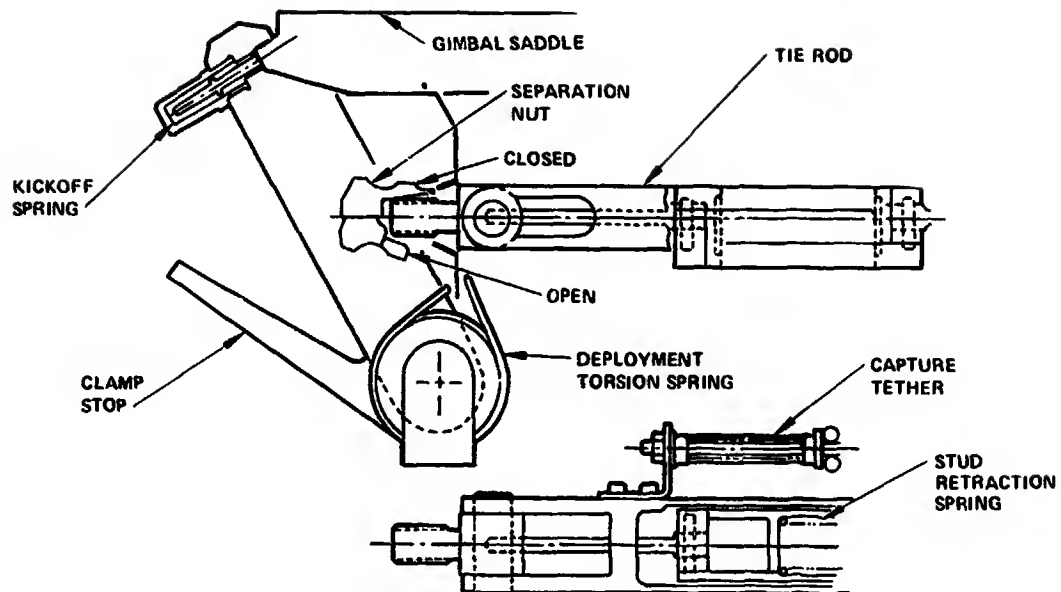


Figure 3.- PIA launch lock mechanism.

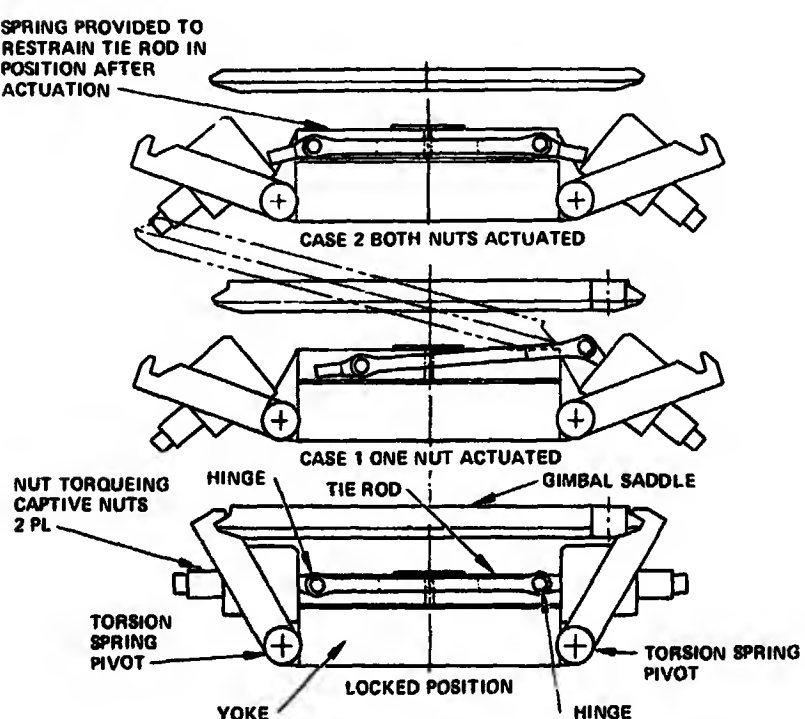


Figure 4.- PIA launch lock captive nut and tie rod.

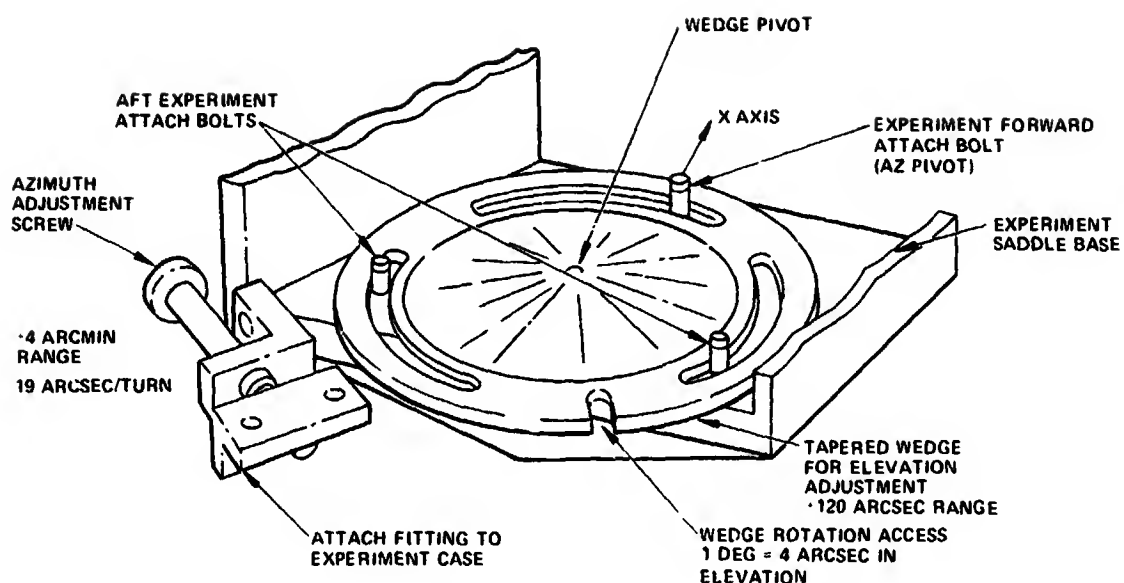


Figure 5.- Coalignement mechanism.

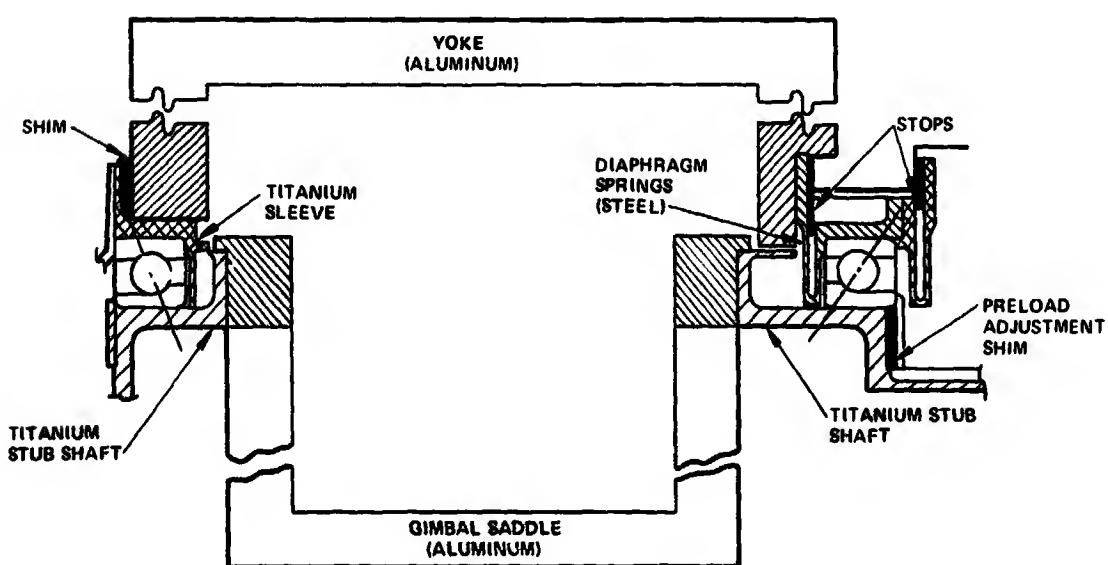


Figure 6.- EDA bearing installation.

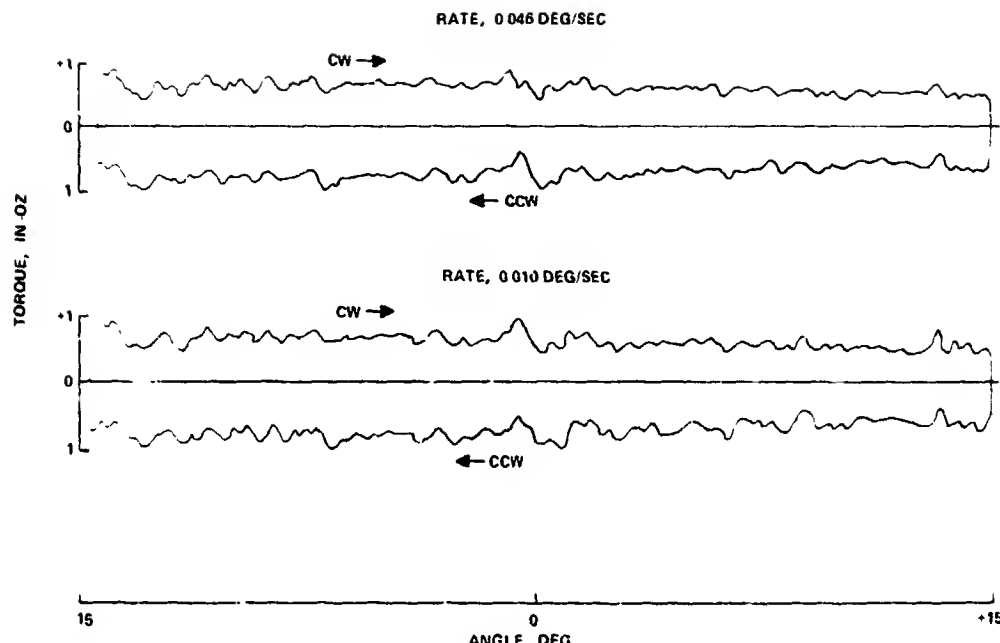


Figure 7.- Running friction test.

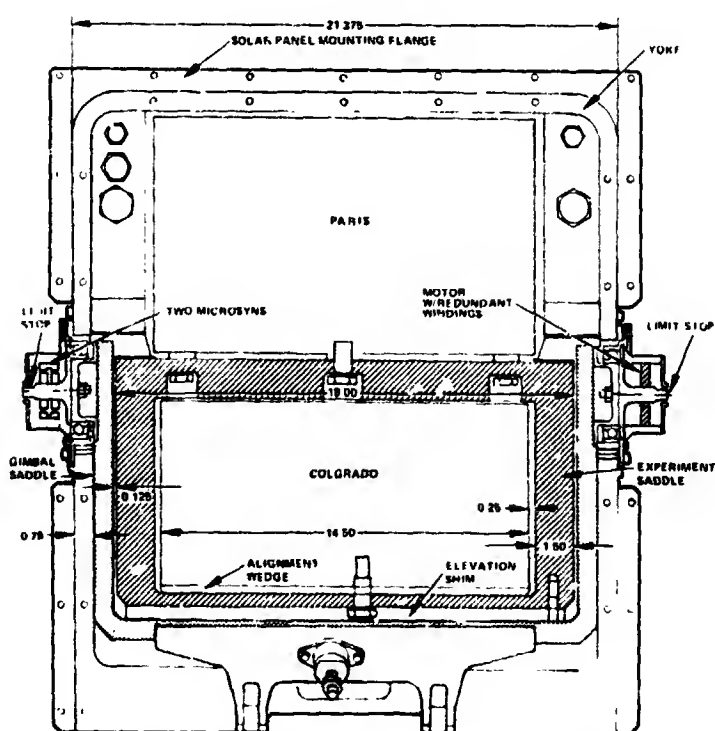


Figure 8.- Cross section of EDA with pointed experiments.
Linear dimensions are in inches.

10. A NEW APPROACH TO LONG-LIFE NONCONTACTING ELECTROMECHANICAL DEVICES

By Edward J. Devine

NASA Goddard Space Flight Center

INTRODUCTION

Development efforts have been underway for a number of years at the Goddard Space Flight Center to improve the life and reliability of electromechanical devices intended for spaceflight applications. This work has progressed to the point where it appears feasible to think in terms of completely noncontacting devices for many applications. These devices are based upon the following technical approaches:

- (a) magnetic suspension of moving elements
- (b) direct drive to eliminate gear reducers
- (c) brushless drive motors
- (d) noncontacting position encoders
- (e) rotary transformers for transfer of power and signals

The purpose of this paper is to discuss the advantages and penalties of this noncontacting philosophy. Following papers will survey the present state of the required component technology and describe an actual hardware application.

WHY NONCONTACTING SYSTEMS?

The prime motivation for elimination of all physical contact is the hazard of operating rolling or sliding members in the space environment. There is at present - and none appears on the horizon - no ideal space lubricant. Fluid lubricants are subject to one or more of the following limitations: poor temperature viscosity characteristic, poor lubricity, outgassing and

contamination, evaporation, creep, shear instability, and radiation damage. Dry films are life limited and tend to be non-self-healing. Sliding electrical contacts have similar lubrication problems, complicated by the requirement of maintaining electrical resistance within some very narrow range of acceptable values.

The next point is that sooner or later the mechanical bearing, brush, or gear will wear out, and it is impossible to predict when this will occur. Many devices are to be designed for lifetimes of several years, or longer, and the problem of testing to establish life expectancy is very formidable. Once the big step is taken to eliminate all contact, all mechanical random and wear out failure modes are eliminated and life expectancy becomes a function of control electronics reliability.

Additional advantages, some of which are not immediately evident, are gained including the following:

(a) Life Independent of Speed:

The life of most conventional bearings is inversely proportional to some power of rotational speed. Noncontact support removes this limitation, which can be exploited to advantage in momentum storage and certain other applications.

(b) Wide Temperature Range:

Noncontact systems can be designed with generous clearances and, being free of lubrication limitations, can be operated at very high and very low temperatures. There are prospects for improved efficiency of magnetic bearings at low operating temperature.

(c) Noise Reduction and Isolation:

Due to irregularities in balls and raceways, even the best conventional bearings generate objectionable noise spread over a broad range of frequencies. Magnetic bearings are expected to markedly reduce the overall vibration level and restrict the disturbance to predictable discrete frequencies.

(d) Torque Perturbations and Breakaway Stiction:

In servo controlled rate and position systems, the breakaway stiction of bearings and brushes and the dynamic perturbations of shaft torque that they produce are major problems. Ultimate pointing accuracy or speed control is frequently limited by this variable. The breakaway friction for a noncontacting magnetically suspended device is extremely low (less than .25 of the best anti-friction mechanical bearing). It is, for all practical purposes, a constant plus a small rate dependent term. This is clearly an ideal characteristic for the servo system designer.

(e) Backlash and Gear Train Windup:

The noncontact approach implies direct drive and the elimination of all forms of gears, belts and traction drives. In addition to eliminating the friction and wear of such devices, backlash and windup are eliminated. These factors, like stiction, are serious limitations to accuracy and bandwidth of high performance servo systems.

LIMITATIONS OF NONCONTACTING SYSTEMS

Looking at the other side of the coin, one must consider the penalties imposed by the noncontact philosophy:

(a) Cost:

Magnetic bearings will be much more expensive. Conventional antifriction bearings, even where exotic space lubricants are applied, cost perhaps 5K dollars per set. Magnetic bearings will start at 10 times this value. Brushless dc motors are also more expensive than ac or brush type motors, but this margin is narrowing and should not represent a major consideration in future systems.

(b) Weight:

With certain exceptions (such as optimized momentum storage systems), there will be a weight penalty incurred with magnetic suspension. In many applications, this will be critical. In the era of the shuttle, however, it is expected that weight constraints will be drastically relaxed.

(c) Power:

Magnetic bearings require power to support shaft loads. In zero gravity, or where the load is essentially static, power consumption can be minimal (2 - 8 watts). Dynamically varying loads require about .3 watt per pound support power. In higher speed applications, support power is at least partially compensated by reduced rotational losses in the noncontact bearing.

(d) Stiffness and Load Capacity:

Magnetic bearings are presently limited in their effective stiffness (deflection under load) characteristics and their load capacity. Stiffness also deteriorates with increasing frequency under dynamic load conditions.

(e) Torque vs. Weight and Power:

Since speed reduction is eliminated, direct drive systems generally suffer a weight and power penalty under high torque and inertia load conditions.

(f) Impact on Structural Design:

At the present state of development, special consideration must be given in the structural design of the device to assure compatibility with the magnetic bearing servo dynamics. One should assure that housing and shaft natural frequencies are high relative to the servo resonant frequency. It is also necessary that bearing servo compensation be optimized for each application. These are not monumental problems, but they do inhibit the ready interchangeability of magnetic bearing designs in various applications.

SOME REPRESENTATIVE APPLICATIONS

Some potential spaceflight applications of the noncontacting approach are:

(a) Momentum Storage:

A following paper discusses the application to an attitude stabilization momentum wheel. Additional application to control moment gyroscopes, bias momentum wheels and, possibly, reaction wheels is predicted. Although performance of these components with conventional bearings has been remarkably good, there have recently been failures that would indicate dependable operation beyond 3 years is questionable. Figure 1 illustrates a rim supported and driven momentum wheel which is under development. This configuration has a very high momentum to weight ratio, particularly at rim speeds approaching one mach. The desirability of noncontacting support at this velocity is self-evident. If, and when, flywheels are applied for energy storage, magnetic suspension will be a strong candidate.

(b) Scanning Radiometer:

Figure 2 shows the conceptual application of noncontacting principles to an image plane scanning radiometer. A requirement here is for precise rate control and stability of the spin axis of the scanning wheel. The low torque perturbation of the magnetic bearings assures attainment of the first goal. Achieving the desired positional accuracy (± 2 seconds of arc) with magnetic bearings has not yet been demonstrated. The closed loop nature of the device is a favorable factor, but improvements in present position sensing techniques will be required.

(c) Mechanically Despun Antenna:

Figure 3 is a conceptual arrangement of a despun antenna, with all physical contact eliminated. Rotational rates range from 15 to 100 rpm, requiring a low speed, low destabilizing force motor. Transfer of radiofrequency (RF) energy is from the stationary feed to the despun reflector. Alternatively, a noncontact choke type rotary joint could be employed.

CONCLUDING REMARKS

Brushless dc motors are finding increasing application in space and it is likely that they will be the predominant type within the next few years. Likewise, with the advent of the light emitting diode, noncontacting encoders are gradually replacing sliding contact types. The direct drive concept has proved its merit and is now the preferred approach for tape recorders and low to moderate torque instrument drives. The final step in this evolution is the magnetic bearing, which now appears feasible for several applications. Where it can be applied in a totally noncontacting system, life and reliability will be a function of the electronic controls, where redundancy, derating, and quality assurance approaches can be applied to virtually assure the desired lifetime and failure rate.

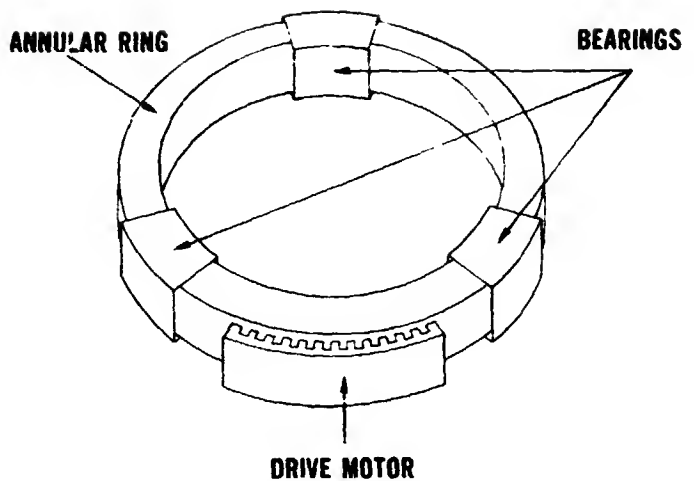


Figure 1.- Annular momentum control device.

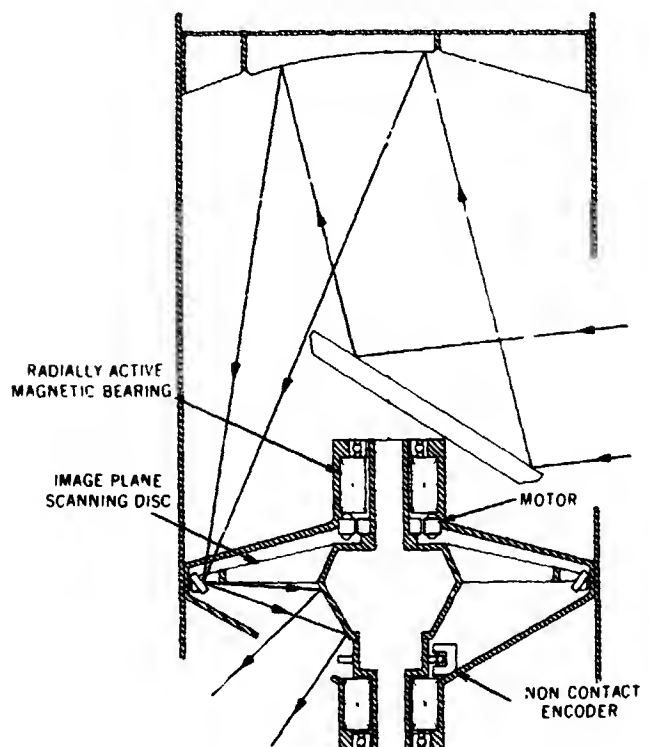
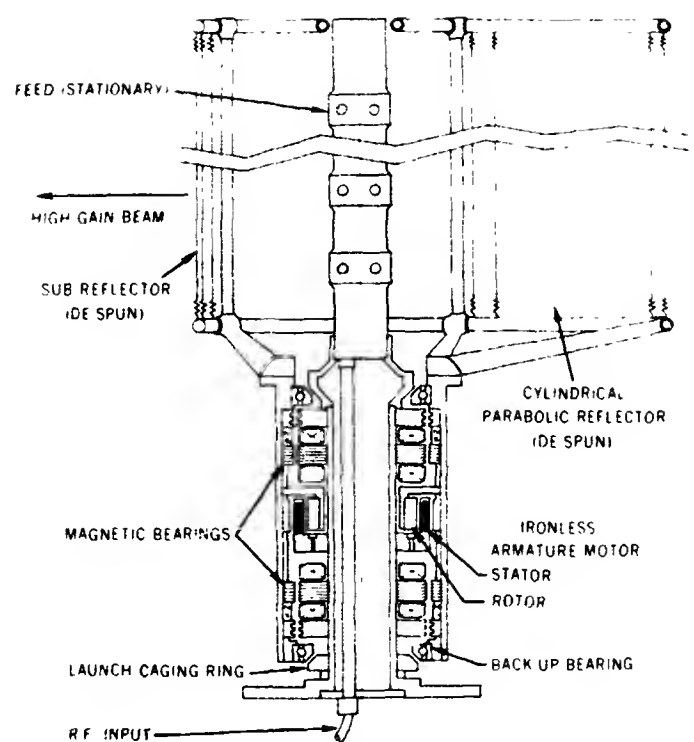


Figure 2.- Conceptual arrangement, noncontacting image plane scanner.



**Figure 3.- Conceptual design, noncontacting
despun antenna.**

II. A REVIEW OF THE TECHNOLOGY

OF NONCONTACTING SYSTEMS

By Philip A. Studer

NASA Goddard Space Flight Center

INTRODUCTION

Advanced components are the fundamental building blocks of advanced systems and spacecraft. Non-contacting elements, including magnetic bearings, brushless and ironless armature motors, rotary transformers and encoders, are discussed. Most of the information presented in this paper has been generated from a continuing program of component development at the Goddard Space Flight Center. The aim of this paper is to identify some of the important design features and provide a perspective on the state of development reached to date.

BRUSHLESS DC MOTORS

Electronic commutation techniques avoiding the problems of sliding electrical contacts in vacuum were developed and flown in the early sixties. Unfortunately, they are still not "catalog items" by any American manufacturer. Their usage in the space program, however, has found gradual acceptance; for example, the latest ITOS weather satellite has seven of various types used in the attitude control system, tape recorders, and in radiometer scanners.

A brushless dc motor consists of a rotor position sensor, commutation circuitry, stationary armature, and a permanent magnet rotor. As a "black box", it is an electrical to mechanical transducer. The developed torque is directly proportional to the armature current, independent of speed. Operated open loop, a linearly decreasing torque with speed characteristic is obtained as illustrated in Figure I.

Operation anywhere within the cross-hatched region is permissible with servo control, requiring only a controller capable of holding the current proportional to the desired error signal. Note that this region is bounded by the terminal voltage (supply voltage less commutator drop - typically 2 volts) at zero speed and decreases linearly as the generated voltage increases with speed. The actual output torque is always less than the developed torque due to the motor's own drag torques, magnetic hysteresis and eddy current losses. While these losses generally represent a small power loss, they must be considered by the servo designer. Operation in both directions is easily obtained simply by changing the switching sequence 180° , a simple digital logic function. Full four quadrant operation is obtainable by providing an alternate path for the generated voltage with diodes, since the motor functions with equal effectiveness as a generator.

Typical of the current state of the art is a tape recorder motor (Figure 2) under development at GSFC. A 2.54 cm (1") high, 5.08 cm (2") diameter package contains integrated circuit hall sensor-amplifier, rotor position sensor, a pancake style torque motor, and a high accuracy optical encoder for precision speed control. The commutation electronics (Figure 3) are modular hybrid integrated circuit packages consisting of a position decoder, amplifier and direction decoder, and a three phase power switching bridge.

The brushless motor represents the most efficient drive component, providing a readily controlled output which can be free of any known wear-out phenomena other than the bearings themselves. One of the early models which was placed on life test in 1963 ran for six and three quarter years at 3000 rpm in a thermal vacuum until the bearings wore out (Reference 1).

Today, any dc motor characteristic obtainable with conventional (brush-type) commutation can be obtained with electronic (brushless) commutation. We are currently working on motors from .03 Nm (4 oz-in.) to 140 Nm (100 lb-ft.).

IRONLESS ARMATURE TORQUE MOTOR

The Ironless Armature Torque Motor was developed to provide a drive element with improved servo characteristics. Both performance and efficiency can be improved by motors using this design concept (Reference 2).

It is, in fact, one of the oldest motor construction techniques which was employed before it was learned that conductors placed in slots perform as effectively as if they were actually in the air gap itself. It is, however, currently in vogue for high performance servo motors for fast response systems since the armature windings can have very low inertia. This latter capability was not a factor in our decision since, when it is electronically commutated, the armature is the stationary element and the permanent magnet field assembly rotates.

What then were the reasons for selecting this motor construction technique? Actually, there are several:

1. Reduction of magnetic drag torques
2. No slot effect, or cogging
3. Fast electrical response
4. Absence of destabilizing forces in the motor air gap

All four of these are of value to the servo designer interested in optimized performance. The elimination of hysteresis and eddy current losses in the normally laminated armature has an obvious benefit in terms of motor efficiency, since these generally account for 50% of the motor losses at the peak of the efficiency curve. There are numerous applications, predominantly in direct drive systems with constant speed requirements, in which the motor losses represent the bulk of the steady state torque requirement. A more significant aspect is that magnetic hysteresis torques represent the greatest nonlinearity in direct drive systems which are free of gearing backlash. Hysteresis torque can become one of the limiting factors in accurate pointing systems, introducing a deadband at the servo null position. Figure 4 illustrates the wider dynamic range provided by the ironless armature motor. It is evident that the uniform slopes of the

conventional motor show that the choice of a larger motor to increase the torque margin and reliability works contrary to the designer's effort to minimize static errors and losses. Only by a different design approach can an improvement in both aspects be obtained.

Figure 5 illustrates the construction of the ironless armature torque motor. There are no cogging torques since the windings are not placed in discrete slots. All torque ripple is not eliminated, however, since groups of conductors forming the three phase delta connected winding vary in effectiveness as the commutation proceeds. One objective of this development, a trapezoidal generated voltage waveform, was not achieved during this development and requires further work before a completely uniform (i.e., not position dependent) torque output is achieved.

The fast electrical response is due to the fact that the armature conductors are not surrounded with highly permeable iron but are cast into an epoxy cylinder projecting into magnetic gap. An order of magnitude lower inductance and a shorter time constant results, moves the electrical time constant in some cases outside the servo bandwidth, or at least reduces its impact on the servo compensation requirement.

There are no static destabilizing forces between the rotor and stator whereas in a conventional permanent magnet motor these represent a significant load on the bearings even in a zero "g" environment. As shuttle launched systems are developed and launch vibration isolation reduces the need for heavy bearing preloads, this aspect will assume still greater significance. In the case of magnetic bearing design, described elsewhere in this presentation, the rotor to stator forces could subtract substantially from the "payload".

The question arises easily that, if these benefits can be achieved, what is the penalty associated with this construction technique and why hasn't it been introduced sooner? The answer to the latter question is easily found if one looks at the permanent magnet assembly (stator) of a commercial moving coil servo motor. Those designed with Alnico magnets have a relatively huge magnet structure. The introduction of rare earth magnet alloys as the result of Air Force research has made the difference. Their tremendous coercive force makes it feasible to drive air gaps almost equal to the length of the magnet itself. A specific comparison to conventional brushless torque motors of similar diameter shows that approximately a two to one weight penalty is imposed by the choice of this design approach.

ROTARY TRANSFORMERS AND NON-CONTACTING ENCODERS

Another functional element required by some, although not all, rotating systems is a means to transfer power and signals to or from the rotating assembly. A non-contacting electromagnetic component well suited to perform this function is the rotary transformer. Matrix Research and Westinghouse Corporations have developed a signal and power transformer of this type as part of an advanced solar array drive system (Reference 3). The illustration (Figure 6) is indicative of the size and volume requirements for a device of this type. It also permits one to visualize the magnetic structure - basically two concentric cylinders - and the coil form. Obviously, the major difference between the rotary transformer and a static type is the necessity of air gaps to permit rotation of the primary with respect to the secondary. The adverse effect of this gap is minimized by the inherently tight coupling of concentric coils and by the superior form factor of circular coils which reduces the I^2R losses. The power transformer, which in this case provided the correct transformation as an inverter, was 99% efficient at the 500 watt level and weighed 1.2 kg (2.6 lb.). Both the signal and power sections were operated at 10 kilohertz with a radial air gap dimension of .01 cm (.004"). The size of the signal transformers was not minimized to electromagnetic requirements but controlled by mechanical considerations. Further effort could result in size reduction; however, substantial signal requirements can be multiplexed into the available channels.

Non-contacting optical and magnetic encoders are commercially available. We have generally used optical encoders because of their high resolution and low inertia and weight. A 2^{14} bit (16,384 line) incremental encoder was used with a 12 cm diameter torquer at 3 rpm and a 1,000 line encoder is being used in the 5 cm diameter motor package mentioned earlier.

The position encoder for motor commutation has a far lower resolution and we are currently using an integrated circuit hall effect sensor activated directly by fringing flux from the motor magnets. This device produces digital logic level outputs with lower power requirements than optical sensors used previously.

MAGNETIC BEARINGS

The elimination of sliding electrical contacts by electronic commutation and rotary transformers, and of sliding mechanical contact by direct drive rather than by use of gearing, can produce long lived systems. Nonetheless, full rotation systems are still not free of a lubrication requirement, nor do they have a life independent of speed, so long as they employ contacting bearings.

For these reasons, we started to look seriously at magnetic suspension as a means to provide the bearing function in a manner not influenced by the environment and with the potential of zero wear.

At that time (1968), considerable work had been done on instrument type suspensions with negligible load capacity, specifically for gyros (Reference 4), and on large gap systems where power and weight were no obstacle, specifically wind tunnel model support. We set out to develop flyable (Reference 5) systems of significant load capacity.

The latest results of this effort will be described in another paper at this conference.

I would like to recount some efforts of the past several years, starting with some of the fundamental characteristics and design problems associated with magnetic bearings, and indicate what progress has been made.

A fundamental aspect of magnetic suspension was proven mathematically by Earnshaw in 1837; simply stated, it is that "no combination of permanent magnets can provide a stable support in all directions". As a practical matter then, a servo (active) system is required for stability in a non-contacting system. The availability of adequate sensors and reliable electronics does not rule out magnetic bearings as a more reliable system. In fact, greater stiffness is generally obtained in the direction of characteristic instability. Early systems, such as that built by Cambridge Thermionic Corporation for GSFC in 1970 (Reference 6), used forty watts and weighed 5.5 kg (12 lbs.) because all of the magnetic flux was supplied by electromagnets (Figure 7). Several successful developments have been made since then, all involving permanent magnets to reduce the power required. At GSFC, a method to differentially modulate the flux in two opposing permanent magnet circuits was invented (Reference 7 & 8) and tested (Figures 8 & 9). At Cambion, a control technique to minimize the average power in the drive coils was also successful (Reference 9) and a prototype momentum wheel was delivered to COMSAT Corporation, which is currently pursuing further development in Europe.

A fundamental problem is weight, since the force per unit area is a function of the square of the flux density, and all of the materials capable of handling high flux densities are of the ferrous group. Fortunately, the development of Samarium Cobalt, a magnetic material of high coercive force by Air Force research has been forthcoming as mentioned previously. While not at all a lightweight material, it can result in shortening the length of the magnetic circuit by nearly a factor of ten. Consequently, a significant payload improvement has been made feasible. Whereas the early model had about 50% of its rotating weight composed of bearing material, the latest device has a payload to bearing

weight ratio of better than 10:1 - the bearing assembly no longer overwhelms the rest of the assembly (Figure 10). An interesting new development occasioned by this same new magnet material is renewed interest in repulsive bearings, in contrast to those mentioned above, all of which have magnetic circuits working in the attractive mode.

An interesting model of a repulsive bearing, with pivots providing axial restraint, was demonstrated at the Naval Ordnance Laboratory in 1971. Hughes Aircraft has also investigated a system using ferrite magnets in repulsion, from which it predicts even more impressive characteristics when Samarium Cobalt is used.

Magnetic bearings, then, have been the subject of some fruitful development, such that they now allow the designer to consider rotating systems which no longer have a life measured in number of revolutions.

CONCLUDING REMARKS

Electromechanical devices are playing an increasingly broad role aboard spacecraft. The reliability of these devices cannot be allowed to fall as application requirements become more demanding and performance tolerances are reduced. Advanced control techniques, improved sensors, and narrower beam-width communication systems have increased the demands on systems performance to the point where fundamental device characteristics limit systems capability. We believe that the component developments which have been undertaken over the past several years will allow a new generation of electromechanical devices to meet future requirements with lifetimes limited only by the failure rates of the control electronics.

REFERENCES

1. TN D-2819, "A Sealed Brushless DC Motor", P. Studer, May 1965, and TN D-5265, "A Brushless Torquer Driven Reaction Wheel", R. Fulcher, July 1969
2. Final Report, NAS5-11481, "An Ironless Armature Torque Motor", R. Fisher, Sperry Marine Systems, July 1972
3. Final Report, NAS5-10459, "A Brushless Direct-Drive Solar Array Reorientation System", R. Jessee, Westinghouse Electric - Aerospace, April 1972
4. 2nd International Symposium on Electromagnetic Suspension, University of Southampton England, July 1971
5. "Survey of Magnetic Bearings", Cambion Inc., J. Lyman, October 1972
6. Final Report, NAS5-11585, "DC Motor With Magnetically Suspended Rotor", July 1970
7. U.S. Patent Application #100,637
8. X-721-72-56, "Magnetic Bearings for Spacecraft", P. Studer, January 1972
9. Final Report, NAS5-21587, "DC Motor with Magnetic Bearing", P. Simpson, Cambion Inc., April 1973

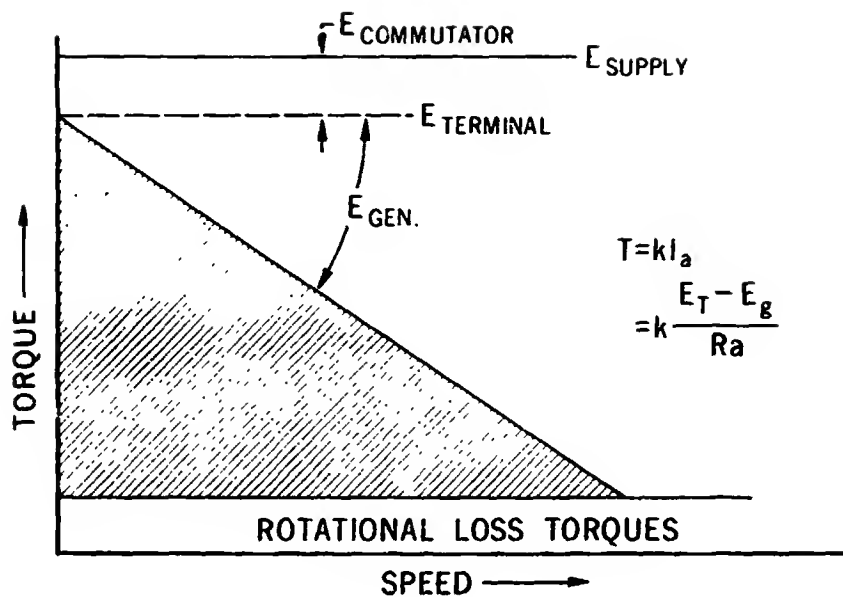


Figure 1.- DC motor torque/speed characteristics.

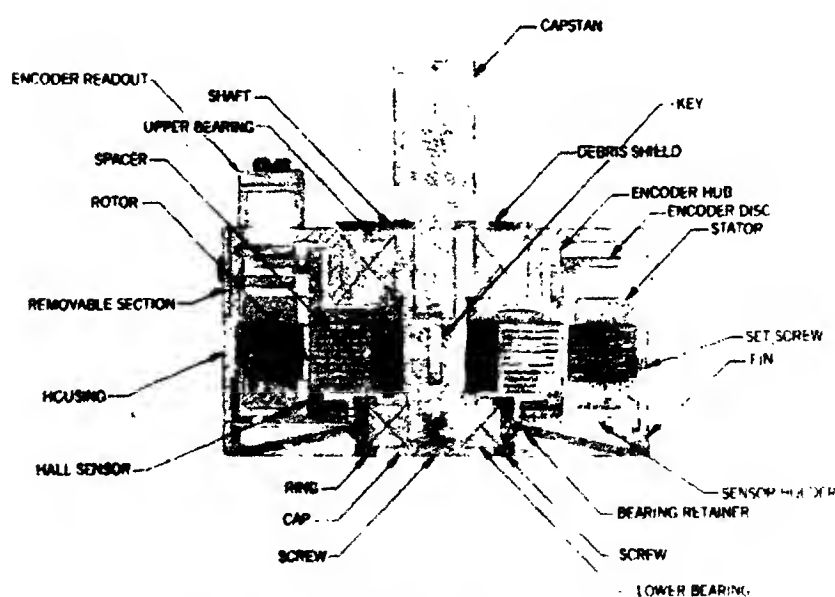


Figure 2.- Tape recorder motor.

REPRODUCIBILITY OF THE ORIGINAL PAGE IS POOR.

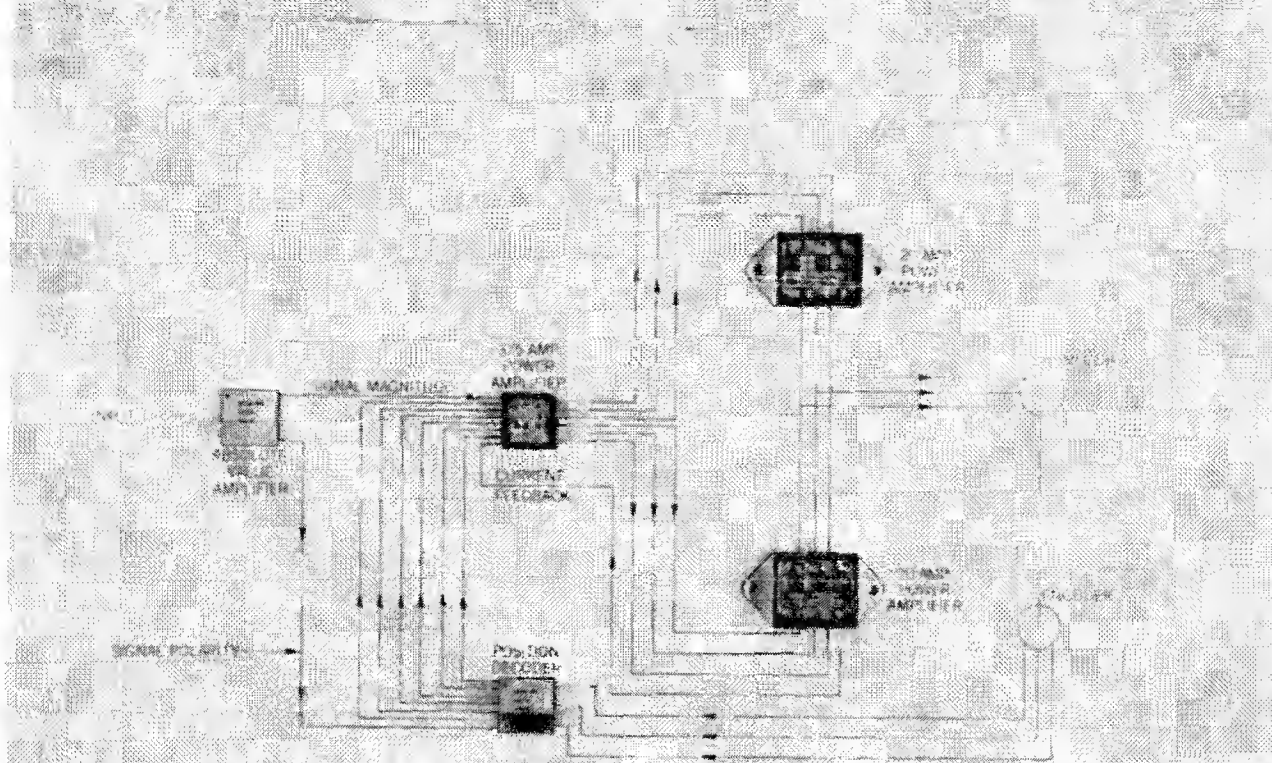


Figure 3.- Hybrid, integrated circuit commutator.

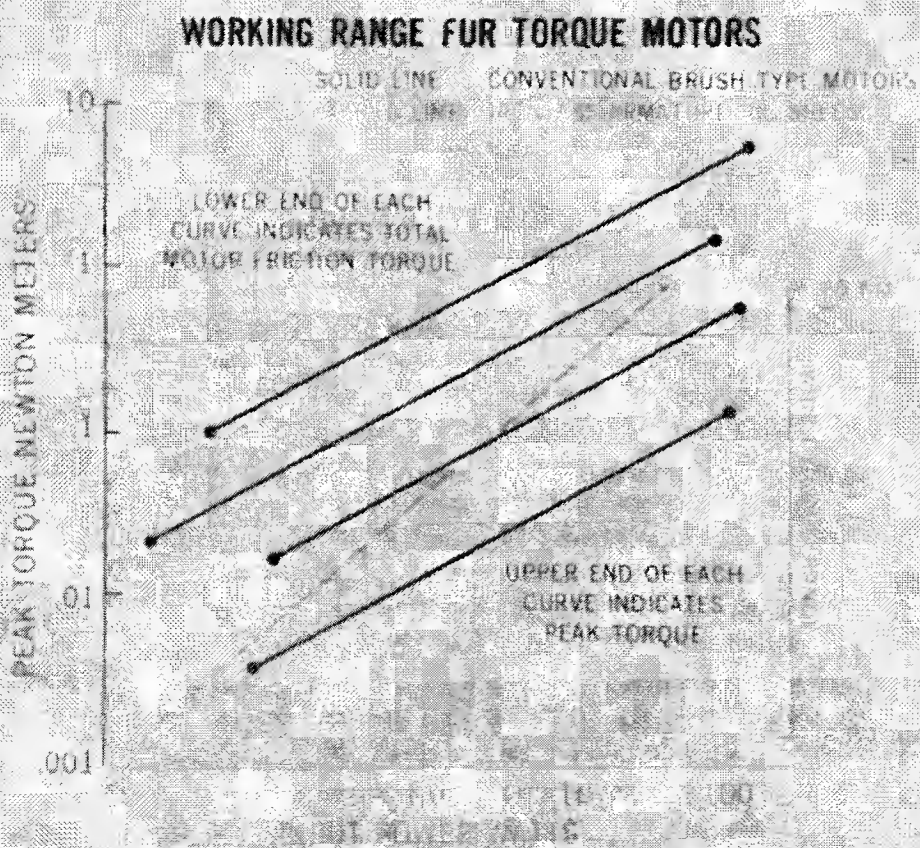


Figure 4.- Ironless armature characteristic comparison.

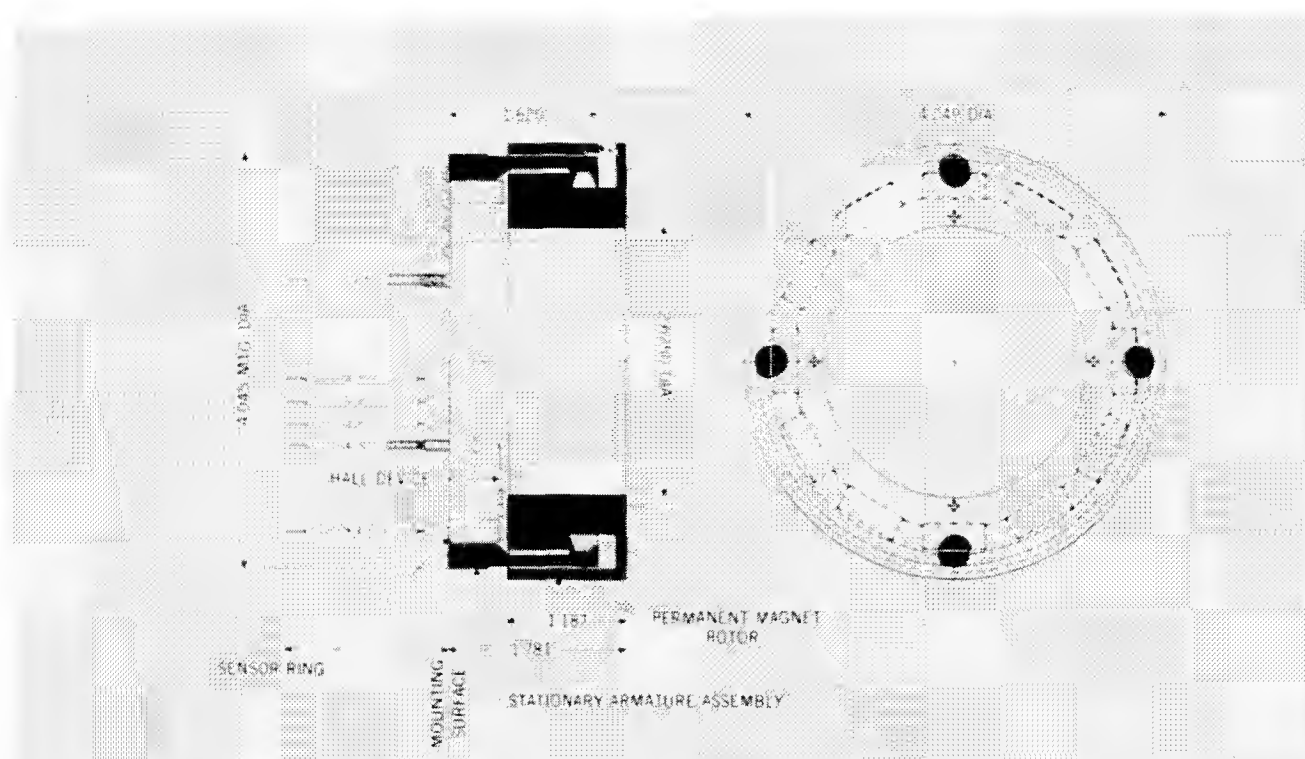


Figure 5.- Ironless armature, cross section.

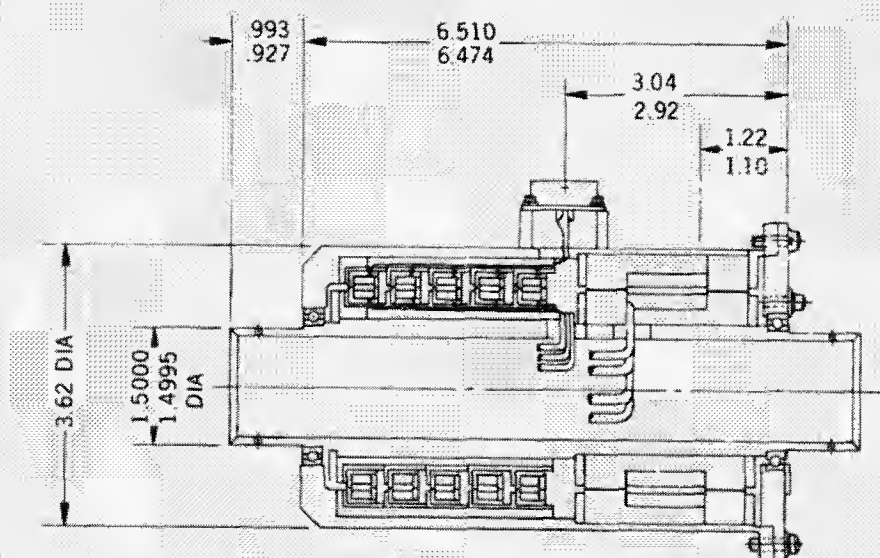


Figure 6.- Rotary transformer, cross section.

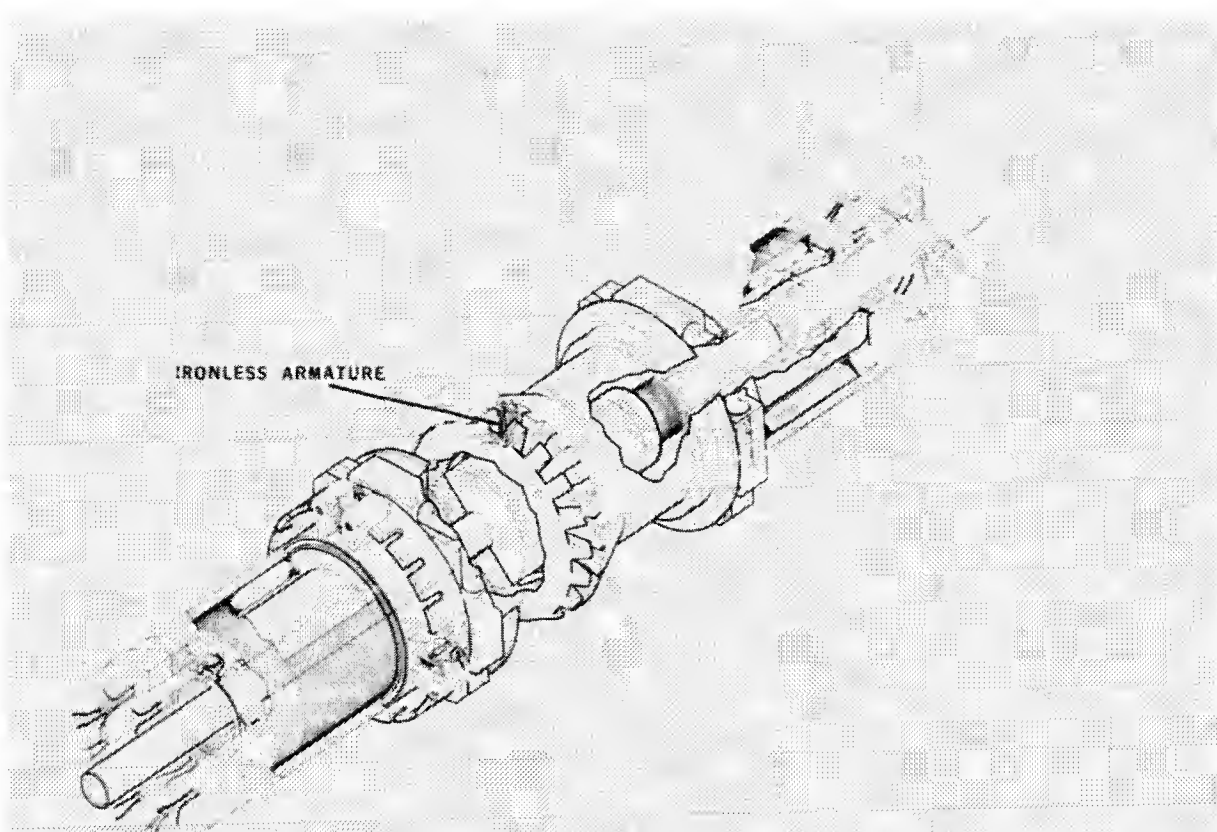


Figure 7.- Magnetically suspended motor.

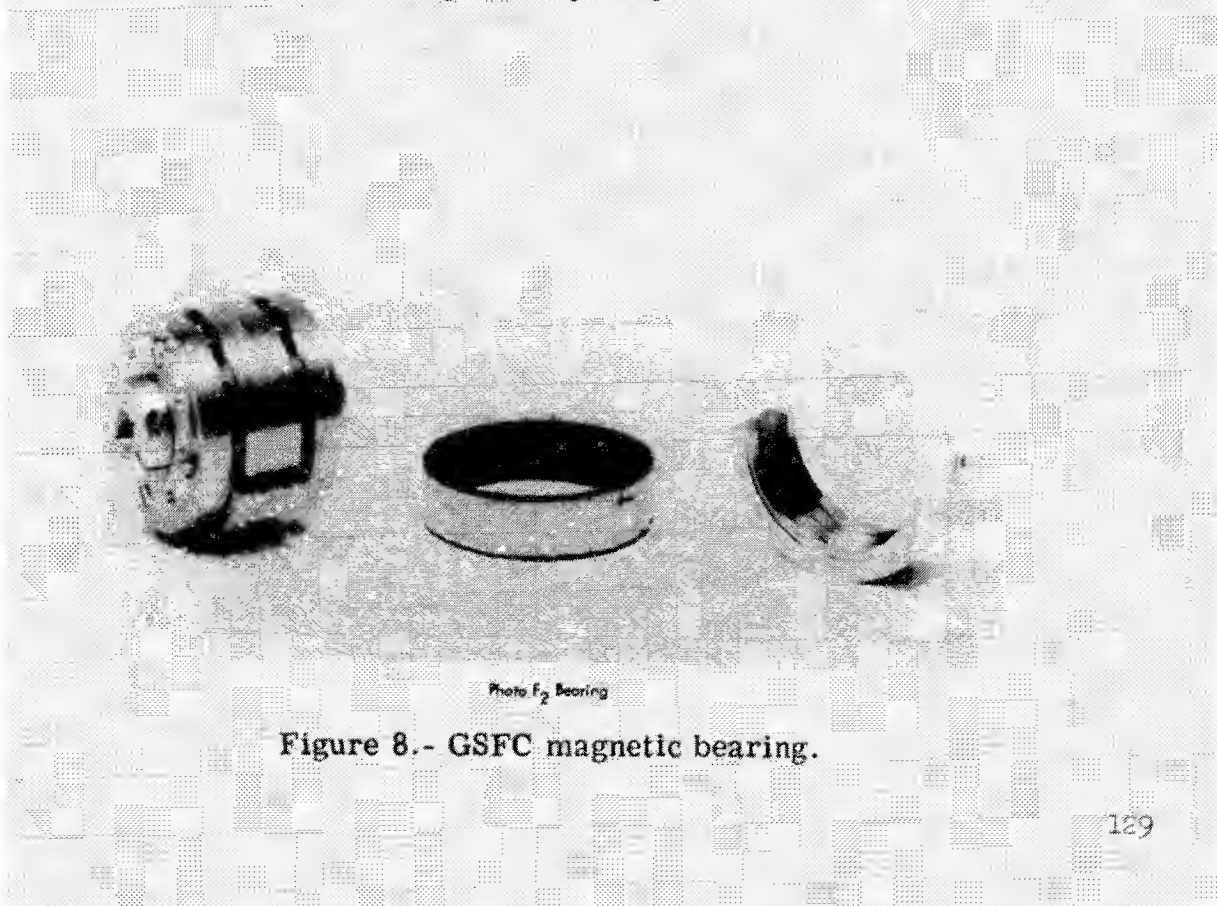


Figure 8.- GSFC magnetic bearing.

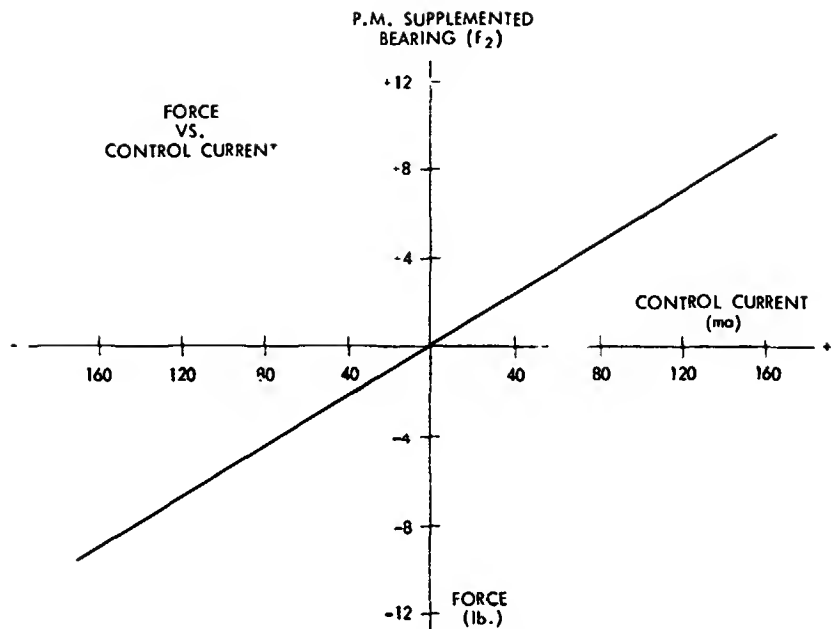


Figure 9.- Characteristics of GSFC magnetic bearing.

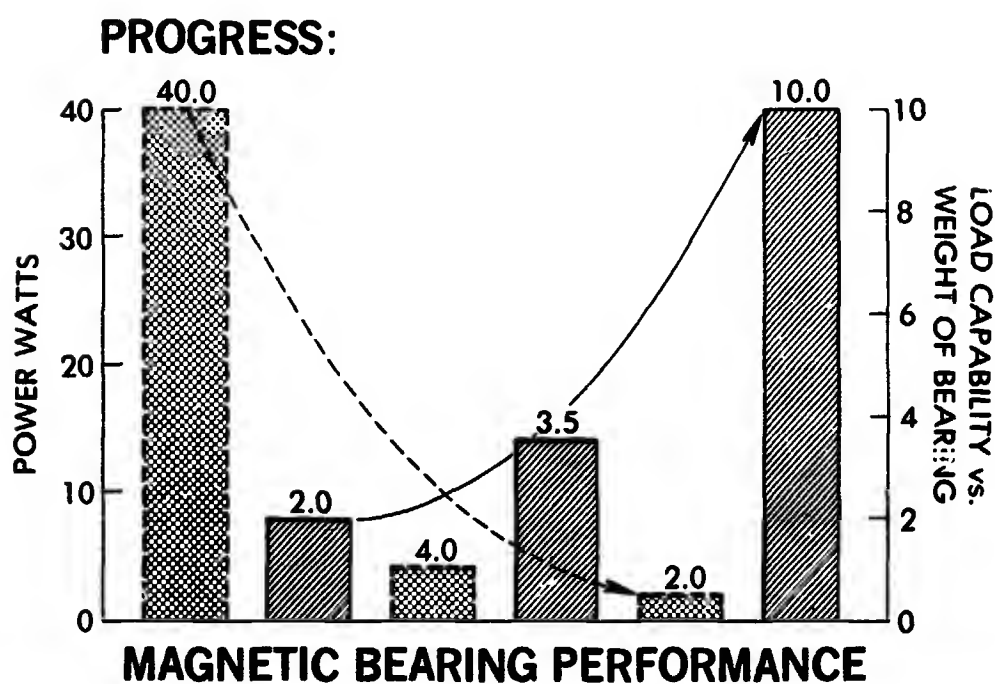


Figure 10.- Progress in magnetic bearings.

12. DESIGN AND DEVELOPMENT OF A MOMENTUM WHEEL WITH MAGNETIC BEARINGS

By Leo J. Veillette

NASA Goddard Space Flight Center

This paper presents the results of a contracted effort to develop a momentum wheel with radially servoed magnetic bearings. The work was performed by General Electric Company, Binghamton, New York, on NASA Contract NAS5-11440.

COMPONENT PARTS OF MOMENTUM WHEEL

A photograph of the engineering model momentum wheel is shown in Figure 1. It consists of a mechanical assembly, suspension circuit and motor drive electronics, and control panel. The mechanical assembly includes (1) the momentum wheel, (2) magnetic bearings, (3) brushless dc spin motor, and (4) base support structure. The momentum wheel is mounted at the center of the rotor shaft and the magnetic bearings are on each end. The physical characteristics of the rotor wheel and shaft assembly are given in Table A.

A cross-sectional view of the magnetic bearing assembly is given in Figure 2. Part A in the figure is a backup ball bearing with oversized inner race diameter. A 0.1 mm (4 mils) radial gap thus exists between the rotor and the inner race of the bearing. This gap defines the normal operating range of the suspension. The axially magnetized ring magnets on the rotor shaft produce a uniform outward field in the radial position sensors (parts B) when the shaft is in the centered position. Magnetoresistors sense the change in gap flux density when the rotor shaft is radially displaced and thus provide the radial position information needed for active bearing control.

The ring magnets also produce inward flux through the 3 concentric rings in each of the axial support sections (parts C). This flux in turn produces an axial restoring force which tends to realign the rotor and stator rings whenever the shaft is axially displaced. Magnetic suspension in the axial direction is thus obtained by passive means.

The magnetic structure of the radial support section (part D) and the active control method used to achieve radial magnetic suspension are described below (Magnetic Suspension Design). The magnetic bearing characteristics are listed in Table B. The electromagnet gradient for each magnetic bearing is the same as for both bearings taken together. The nonrestoring force constant involves the destabilizing effects of both the radial and axial support sections.

Table C gives the characteristics of the brushless dc spin motor (part E).

MAGNETIC SUSPENSION DESIGN

Design of the axial sections of the magnetic bearings is based on the following rules:

- (1) multiple lands increase the axial stiffness proportionally as long as the gap-to-land ratio is maintained
- (2) the lands should be magnetically saturated to obtain high axial stiffness with minimum nonrestoring radial force gradient
- (3) the non-restoring force gradient increases approximately proportional to the axial force gradient (with magnetically saturated lands)

The axial suspension forces depend on the rate of change of gap reluctance with axial position.

Magnetic suspension in the radial direction is active. The radial position of the rotor shaft is controlled by two identical channels. A schematic diagram of one channel of the radial magnetic suspension is shown in Figure 3. It consists of the radial support section of the magnetic bearing, the radial position sensor, and suspension circuit electronics. The magnetic bearing radial section is constructed with 4 poles and associated coils, two along the vertical axis and two horizontal. The vertical coils, C_1 and C_2 , are connected in series as shown, and the winding direction is such that positive coil current produces an upward force on the rotor shaft and negative current produces a downward force.

The vertical position of the rotor shaft is sensed in the radial position sensor by using two magnetoresistors, M_1 and M_2 . The magnetoresistors are connected in a bridge circuit which produces a difference signal, e_1 , which is proportional to the rotor shaft displacement. Signal e_1 is amplified in the suspension circuit preamplifier which has an adjustable gain. The amplified output is then applied to circuits which provide system damping, compensate for rotor structural resonance, and limit saturation of the power output stage. A low frequency integrating circuit is used to give the bearing a very high static radial stiffness. The power amplifier drives the bearing electromagnet in a direction to maintain the rotor shaft suspended at the null or centered position. The suspension circuit parameters and circuit gains are readily changed to provide a wide range of suspension characteristics.

The linearized radial force characteristic of the magnetic bearing is given in Figure 4.

A detailed circuit diagram of the suspension system electronics is given in Figure 5. A Twin-tee notch filter is used to compensate for the rotor structural resonance. The sharpness of the filter notch is increased by using feedback from the low frequency integrator. The increased sharpness minimizes the effect

of the filter in reducing the suspension loop phase margin. System damping is obtained by using a combination of lead-lag and lag-lead compensation. The compensation network design and filter notch frequency are shown in the Bode diagram in Figure 6. The arrangement of lead-lags and lag-leads with respect to voltage saturation points limits the power amplifier phase lag to frequencies above the suspension loop bandwidth.

EXPERIMENTAL RESULTS

Two main problems which were encountered in laboratory work on the engineering model momentum wheel were (1) magnetic suspension instability due to rotor structural resonance, and (2) loss of magnetic suspension at high rotational speeds. Stable magnetic suspension was achieved by (1) stiffening the rotor wheel and shaft, (2) increasing the sharpness of the Twin-tee filter notch, and (3) use of only the inside radial position sensors. These changes served to increase the frequency separation between the rotor structural resonance and cross-over and generally to improve the phase margin of the magnetic suspension loop.

During spin-up tests, the rotor suspension successfully traversed a critical speed at 220 rad/sec., but magnetic suspension was lost at about 380 rad/sec. It is believed that dropout occurred as a result of the rotor shaft hitting the backup bearings. This in turn was caused by increased shaft wobble as the speed corresponding to the suspension servo bandwidth was approached.

Rotor balance and alignment were therefore substantially improved but these improvements resulted in only a small reduction in shaft wobble. The suspension servo bandwidth also was increased slightly as the rotor resonance increased with speed. The maximum rotor speed obtained with these changes was 500 rad/sec.

Self-lubricating Feuralon sleeve bearings were used in the initial design of the backup bearings. They caused severe chattering during even low speed dropout tests, and at high speed they were totally unsatisfactory. The Feuralon bearings were replaced by backup ball bearings and these have performed very well.

The performance characteristics of the engineering model momentum wheel have been measured and the results are listed in Table D. The maximum angular momentum obtained with the engineering model momentum wheel was 83 Nm-sec (62 ft-lb-sec) which is 83% of the design value of 100 Nm-sec (75 ft-lb-sec). The radial stiffness, under static conditions, has been measured as greater than 35,000 N/mm (200,000 lbs/in.) with the integrator included in the suspension circuit. This value compares to a stiffness of 11,000 N/mm (63,000 lbs/in.) for the steel shaft of the rotor. This means that under load, the rotor shaft displacement in the bearing magnetic field is less than 1/3 the displacement at the center of the shaft, due to bending. The radial stiffness under dynamic conditions applies, within the suspension servo bandwidth, to approximately 80 Hz.

The maximum load capability of the system is 356 N (80 lbs.) with the integrator included in the suspension circuit. It appears that the maximum design load is determined by the onset of instability caused by magnetic bearing and suspension circuit nonlinearities. With the integrator removed, however, the maximum load is limited by the backup stops. Also, the rotational losses in the magnetic bearing have been measured at speeds up to about 100 rad/sec. These losses are expected to be about $\frac{1}{2}$ the rotational loss in a ball bearing at maximum operating speed.

SUMMARY AND CONCLUSIONS

An engineering model momentum wheel with radial magnetic bearings has been designed and developed and successfully operated to a speed of approximately 500 rad/sec. This speed corresponds to a maximum angular momentum of 83 Nm-sec (62 ft-lb-sec) which is 83% of the design value. The maximum momentum achieved was limited by the suspension servo bandwidth and this, in turn, was limited by the lowest structural resonance of the rotor. In any future design the maximum wheel speed, and dynamic radial stiffness as well, can be increased by using a stiffer rotor.

Also in this development, radial magnetic bearings have been shown to provide good damping and high load carrying capacity. They offer considerable flexibility in that a wide range of suspension characteristics can be obtained simply by changing some of the suspension circuit parameters.

TABLE A
PHYSICAL CHARACTERISTICS OF THE
ROTOR WHEEL AND SHAFT ASSEMBLY

Rotor Assembly Diameter	=	40 cm (16 in.)
Weight	=	67 N (15 lbs.)
Shaft Length	=	35.6 cm (14 in.)
First Torsional Resonance	=	540 Hz
First Translational Resonance	=	702 Hz

TABLE B
MAGNETIC BEARING CHARACTERISTICS

Outside Diameter	=	8.9 cm (3.5 in.)
Weight (per bearing)	=	28 N (6.3 lbs.)
Electromagnet Gradient	=	75 N/amp (17 lbs/amp)
Non-restoring Force Constant (per bearing)	=	1136 N/mm (6.5 lbs/mil)
Maximum Radial Load (per bearing)	=	177 N (40 lbs.)
Maximum Axial Load (per bearing)	>	89 N (20 lbs.)
Axial Stiffness (per bearing)	=	1748 N/cm (1000 lbs/in)
Position Sensor		
Type	=	Magnetoresistor
Gain	=	1.38 volts/mm (35 mv/mil)

TABLE C
BRUSHLESS DC SPIN MOTOR CHARACTERISTICS

Outside Diameter	=	6.98 cm (2.75 in.)
Axial Length	=	1.5 cm (.6 in.)
Weight	=	2.6 N (.6 lbs.)
Type	=	2 Phase
Number of Poles	=	6
Rotor Magnet	=	Alnico 6
Rated Torque	=	.028 mN (4 in-oz.)
Peak Torque Capability	=	.21 mN (30 in-oz.)

TABLE D
MOMENTUM WHEEL PERFORMANCE CHARACTERISTICS

Momentum

Design Value = 100 Nm-sec
(75 ft-lb-sec)

Actual Max. = 83 Nm-sec
(62 ft-lb-sec)

Radial Stiffness

Static > 350,000 N/cm
(200,000 lbs/in.)

Dynamic = 15,750 N/cm
(9,000 lbs/in.)

Maximum Load Capacity = 356 N
(80 lbs.)

Power

Electronics = 7.6 watts

Bearings (full load) = 22 watts

Rotational Losses = 3.3×10^{-6} Nm/rad/sec.
(.00005 in-oz/rpm)

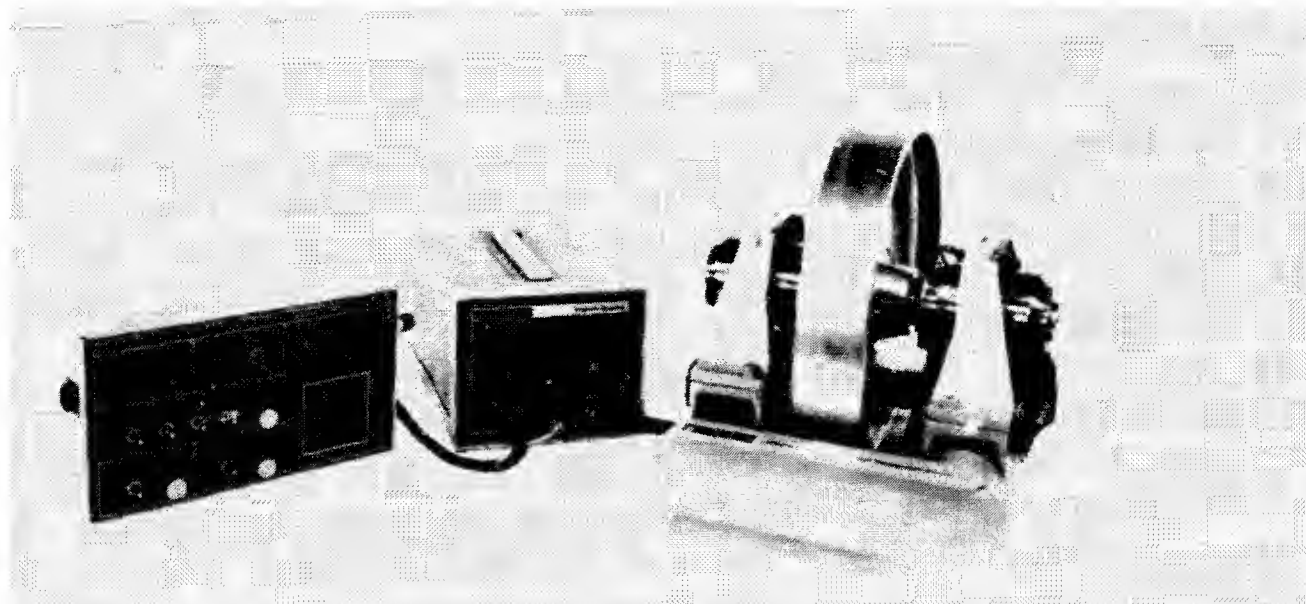


Figure 1.- Magnetically suspended momentum wheel system.

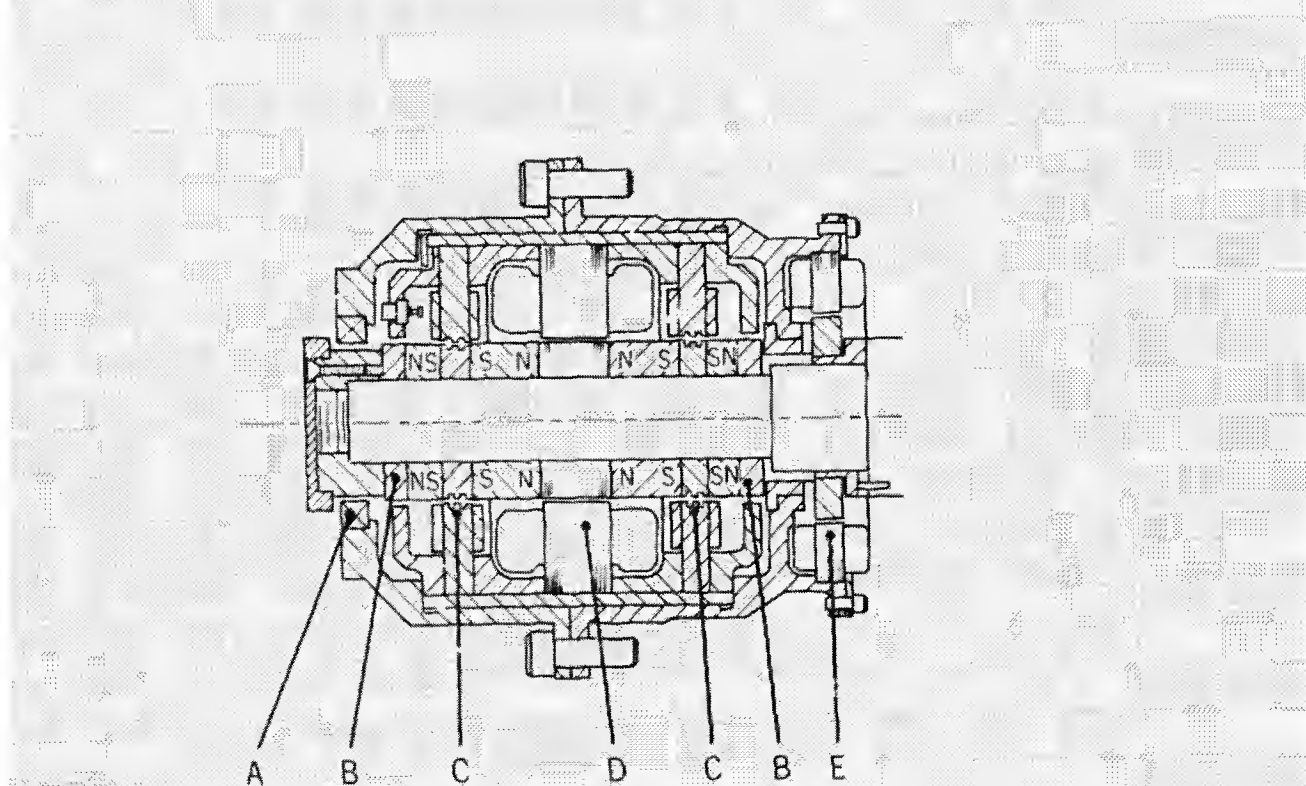


Figure 2.- Magnetic bearing cross-section.

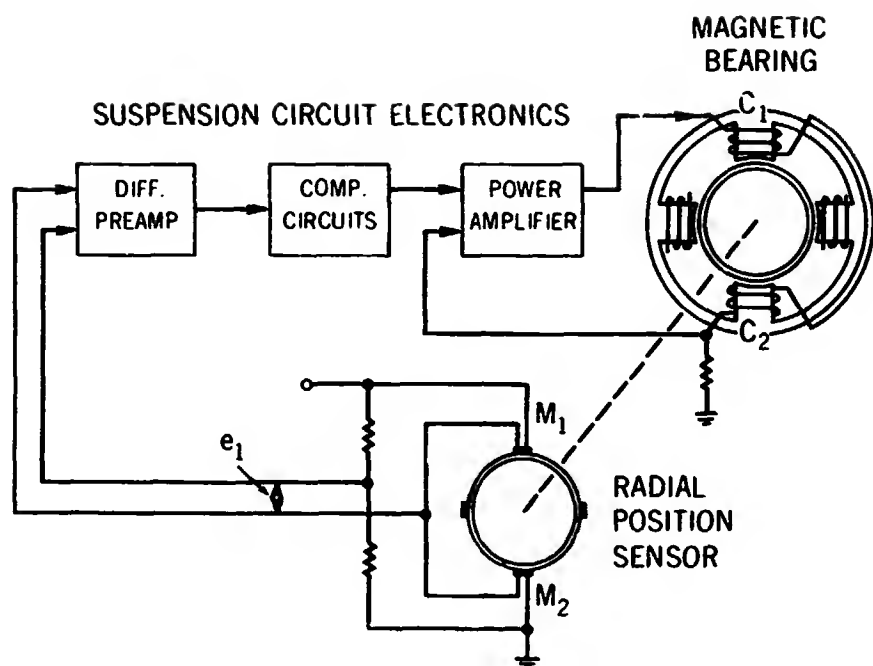


Figure 3.- Schematic diagram of magnetic suspension loop.

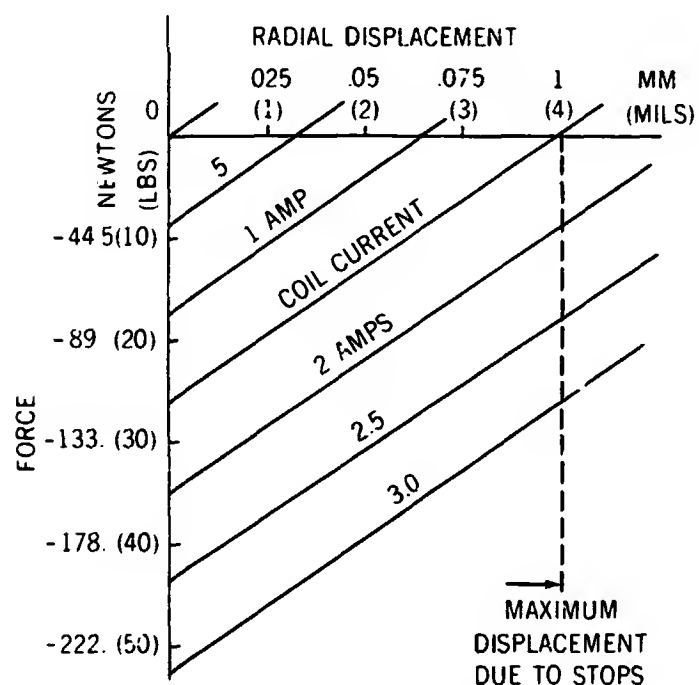


Figure 4.- Linearized magnetic bearing characteristic.

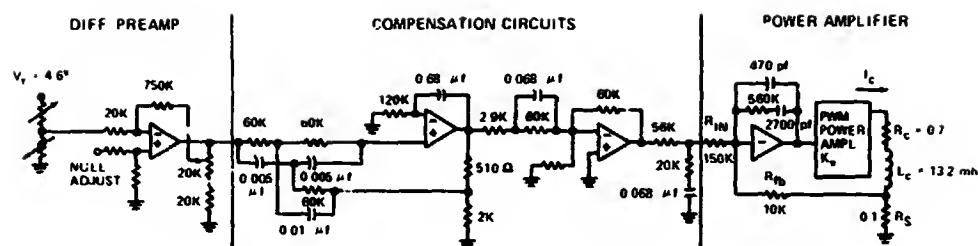


Figure 5.- Magnetic suspension electronic circuit.

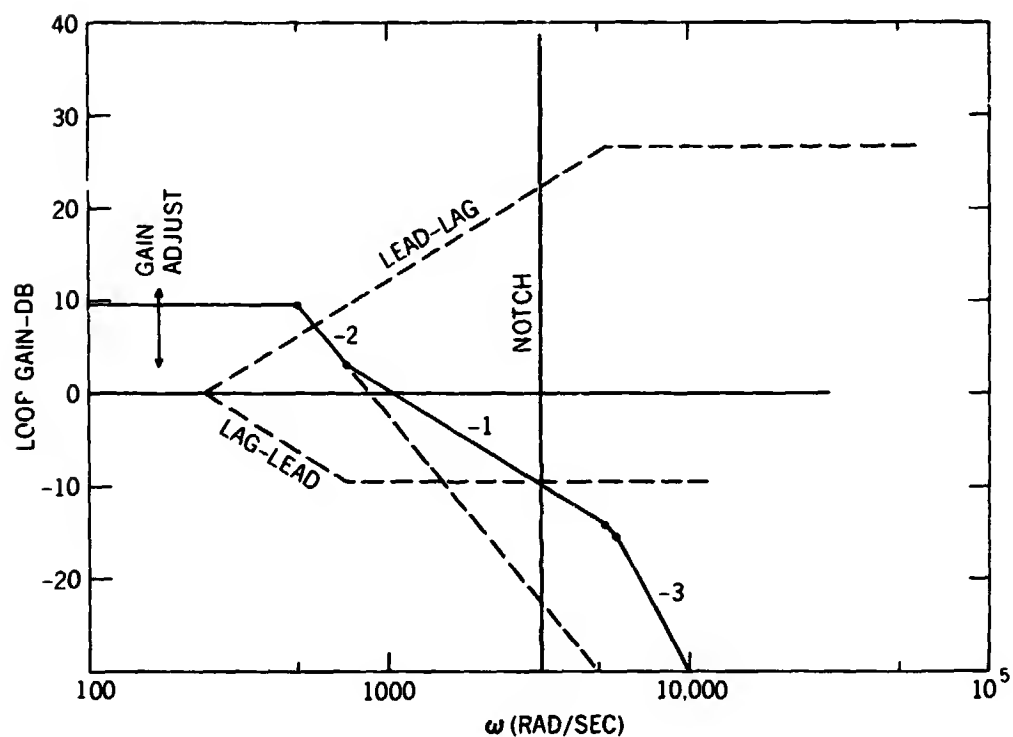


Figure 6.- Bode design of magnetic suspension loop.

13. MODEL STUDIES OF CROSSWIND LANDING-GEAR CONFIGURATIONS FOR STOL AIRCRAFT

By Sandy M. Stubbs and Thomas A. Byrdsong

NASA Langley Research Center
Hampton, Virginia

SUMMARY

An experimental investigation was conducted using a dynamic model to directly compare four different crosswind landing-gear mechanisms. The model was landed as a free body onto a literally sloping runway used to simulate a crosswind side force. A radio-control system was used for steering to oppose the side force as the model rolled to a stop. The four crosswind configurations investigated were subjected to the same test conditions and a direct comparison of the configurations was made although there are several factors that limit a direct application of model test results to a full-scale aircraft. Two of the configurations appeared to be more promising than the others and one of them was clearly the best. The configuration in which the landing gears are aligned by the pilot and locked in the direction of motion prior to touchdown gave the smoothest runout behavior with the vehicle maintaining its crab angle throughout the landing roll. This is not meant to imply that the other configurations could not be used successfully with full-size aircraft where the pilot has aerodynamic control, visual and motion cues, and differential braking. Nose-wheel steering was confirmed to be better than steering with nose and main gears differentially or together. Testing is continuing to obtain quantitative data to establish an experimental data base for validation of an analytical program that will be capable of predicting full-scale results.

INTRODUCTION

Future airports constructed for STOL aircraft operations will have fewer choices for runway headings and have the potential of exposing the aircraft to higher crosswinds than currently encountered. Also, since landing speeds of STOL aircraft are lower than for conventional aircraft, the problems associated with landings in crosswinds are greater. Therefore, a need exists to develop landing-gear systems which will extend the operational capability of aircraft, particularly STOL aircraft, in a crosswind environment. Several crosswind landing-gear concepts were proposed in the late 1940's and early 1950's and some flight tests were conducted, mostly on tail-wheel aircraft. Currently, crosswind landing gear are used on the B-52 and C-5A aircraft; however, these systems are limited to 20° crab angles, and no known comparisons have been made between these and earlier systems.

The objective of the current research is to evaluate various crosswind landing-gear concepts for application on STOL aircraft, landing at crab angles up to 30°. The purpose is to establish those concepts which permit a smooth transition from flight to landing rollout with a minimum of decrabbing, yawing, lateral motions, and steering inputs during rollout.

This paper presents the results from an experimental investigation conducted to study various crosswind landing-gear concepts, utilizing a free body, radio-controlled, dynamic model. Four different crosswind gear configurations were examined and their behavioral characteristics during the landing runout under a simulated crosswind are directly compared. Three steering techniques were evaluated and the effectiveness of each is discussed together with such problems as gear alignment, shimmy, and steering torque requirements.

DESCRIPTION OF MODEL

Figure 1 is a photograph of the radio-controlled model used in the investigation, and figure 2 is a sketch which provides pertinent dimensions. The model, nominally representing a 1/10-scale prototypical STOL aircraft, was designed to minimize aerodynamic effects on vehicle motions so that the effects of a constant simulated crosswind force could be studied. It was decided at the outset of the investigation that the forces needed to overcome the crosswind force must be generated from tire steering inputs rather than from aerodynamic controls since at low speeds, near the end of the runout, aerodynamic controls would be ineffective. The basic body of the model was constructed of solid balsa wood covered with fiber glass. Lead ballast was attached to two aluminum angles shown in figure 1 to provide the desired mass, center-of-gravity location, and mass moments of inertia for the vehicle. The tricycle landing gear used on the model consisted of vertical struts, forks, and wheels equipped with pneumatic model-aircraft tires 11 cm (4.5 in.) in diameter. Mechanical stops were attached to the vertical struts to limit the swiveling action on all gears and the position of these stops was varied until an optimum yaw-angle tolerance was found. Two sets of aluminum forks were constructed to obtain a variation in the amount of trail used for the tests. The pneumatic tires were pressurized to approximately 60 kNm² (9 psi).

Steering Mechanism

Each of the three wheels of the tricycle gear had a separate radio-controlled servo to engage a steering clutch which converted the gear from free swiveling to steerable. Two additional servos were used on each gear to provide steering torque. Separate transmitter control sticks were used for each landing gear and various combinations of the sticks could be operated simultaneously by the pilot through a mechanical linkage. The radio-control system was proportional; that is, the servos displaced proportionally to control-stick displacement.

Configuration Definition

The crosswind gear configurations shown in figure 3 and described below are the configurations as they would operate on a full-scale aircraft. It was necessary during model testing of some of the configurations to modify the free-swiveling feature in order to obtain satisfactory vehicle dynamics during the early part of the landing roll.

Configuration A allows all gears to swivel freely prior to touchdown in order to achieve alinement on contact. After alinement the gears are locked to prevent further swiveling, and steering is initiated. Steering can be accomplished through the nose gear only or by steering the nose and both main gears together or differentially.

Configuration B allows all gears to swivel prior to impact, but mechanical stops are set on the main gears to prevent outward swiveling. The purpose of the stops is to permit steering by developing side forces on the upwind main gear without having to actively lock the main gears as in configuration A. On this configuration, the downwind gear alines with the direction of motion but the upwind gear is held against the stop unless the vehicle decrabs to 0°. Steering is accomplished by actuating and steering the nose gear only.

Configuration C again allows all gears to swivel freely prior to touchdown but, in this case, a crossbar linkage is used to connect the main gears so they will act in unison. The crossbar geometry is such that when the vehicle is running at 0° yaw, there is no toe-out between the main gears; but, at a 30° vehicle yaw, a 3° toe-out is generated. The purpose of the toe-out is to develop a side force with the main gear. It is theorized that the downwind main gear, which is heavily loaded, will aline itself with the direction of motion and the more lightly loaded upwind gear toes out 3° (for 30° crab angles) and produces a small side force to windward. Only nose-gear steering is used with this configuration.

Configuration D is different from the other three configurations in that all gears are alined with the direction of motion by the pilot prior to touchdown. As with configuration A, directional control during rollout can be accomplished by steering the nose gear only or by steering all gears.

APPARATUS AND PROCEDURE

The testing technique involved launching the model as a free body in a crabbcd attitude onto a laterally sloping runway and evaluating the behavior of the model to various steering inputs as it freely rolled to a stop with no brakes. The runway, model, and monorail launch apparatus are shown in figure 4. The runway was 61 m (200 ft) long, 4.1 m (13.6 ft) wide, and inclined 4-1/2° to simulate a crosswind side force. This inclination produced a side force (due to the gravity vector) estimated to be equivalent to that which would occur in a 90° crosswind of one-half the aircraft landing velocity. As shown in the figure, the runway was covered with plywood to achieve a smooth surface and black lines were painted at 1.2 m (4 ft) intervals to aid in analyzing film data.

The model was launched as a free body by a monorail and carriage mechanism. Following acceleration, the carriage was arrested to allow the model to slip free and continue down the runway. Most landings were made with the model preset on the carriage at a crab angle of 30°. This crab attitude corresponded to the attitude assumed by an aircraft flying in a 90° crosswind of one-half the landing velocity. The sink speed for all tests was near zero. No attempt was made to study the impact portion of the landing since aerodynamic forces (wing lift and control-surface forces) were not available for these model tests. The model horizontal velocity was approximately 6.1 m/sec (20 ft/sec) at launch; therefore, the tests more nearly simulated the last two-thirds of the landing runout. Higher landing speeds will be investigated in future tests when brakes are installed on the model.

The only data taken thus far in the investigation have been in the form of motion pictures which are used to study vehicle behavior for the various landing-gear systems. Six cameras were mounted above the runway, each taking only a portion of the runout, and two additional cameras were used to cover the entire runout.

RESULTS AND DISCUSSION

The basic criterion used in comparing the various landing-gear configurations was that the vehicle experience a minimum lateral displacement on the runway. Another requirement was that the vehicle have a minimum, or at least slow, yaw attitude change during runout; that is, a vehicle landing at a 30° crab angle would run out at a 30° crab angle or de crab slowly.

Before the results from studies conducted with each crosswind landing-gear configuration are discussed, several remarks are in order with respect to problems inherent in relating model results to those for full-scale aircraft. One problem is that of pilot response time. Since the model is a 1/10-scale model of a typical STOL airplane, the model pilot's response should be approximately three times as fast as that of the full-scale aircraft pilot. Similarly, the steering response of the model radio-controlled equipment is less than that of a real aircraft whereas it should have been about three times as fast. Furthermore, the control problem for the model is compounded in that its pilot, not physically located in the vehicle, has no cues to motion changes other than visual; and the visual cues are hampered since the model is moving away from the pilot.

Another problem in the simulation of motions is that the model had no aerodynamic controls nor differential braking. An aircraft would have aerodynamic control to balance the crosswind forces at touchdown and during the early portion of the runout until wheel alignment had taken place and the steering system actuated. On the model there was no control until after wheel alignment and steering clutch engagement had occurred and, during the uncontrolled time interval between touchdown and steering clutch engagement, the model started a downwind drift and, at times, a change of yaw attitude. Thus, when the steering is finally attempted, it must first overcome the inertia of a downwind-drift velocity and any yaw angular velocity that has been initiated.

It was soon realized that for configurations A, B, and C (those with free-swiveling gears prior to touchdown) it was necessary to align the gears with the direction of motion and engage the steering clutch before launch so that the initial drift and yaw changes could be minimized and steering could begin immediately. These problems with model testing place limitations on the direct application of the model test results to full-scale aircraft; however, since they apply to the four configurations investigated, a comparison of the relative merits of the various configurations appears to be justifiable.

Configuration A

In the initial tests with configuration A, the landing gears were free to swivel upon ground contact to align themselves with the direction of motion. However, in order to obtain alignment, some amount of trail was needed on the gears which introduced a severe shimmy problem. To eliminate shimmy of the main gear it was found that long trail (1.3 times the tire radius) and a tire inflation pressure of 60 kN/m^2 (9 psi) were needed. On the lighter-loaded nose gear, a trail equal to one tire radius and an inflation pressure of 55 kN/m^2 (8 psi) were required to avoid shimmy. In both cases, lower pressures and/or shorter trail resulted in moderate to severe shimmy. However, the need for long trail to reduce the shimmy introduced severe demands upon the available steering torque. Initial tests of configuration A with the gears free to swivel prior to landing gave poor landing behavior. When landings were made with all gears prealigned with the direction of motion and the steering clutch engaged prior to touchdown, very good crabbed runouts were obtained utilizing only nose-gear steering. When steering of both nose and main gears together was attempted, results were not satisfactory due to either a slight preset misalignment of the gears or misalignment of the gears due to uneven loading. The slight misalignment produced a slow continuing yaw change in the vehicle and, although the vehicle could be displaced laterally on the runway, it would continue yawing until it hit mechanical stops and then diverge off the runway. Steering the nose and main gears differentially with two controls was also unsatisfactory, even though some good runs were obtained. When differential inputs were made (steering nose gear windward and main gear leeward), yawing motions were very rapid and confusing with occasional loss of control. Differential steering was considered an unnecessary complication and could be hazardous.

Configuration B

The landing gear for configuration B was free to swivel on ground contact to align with the direction of motion. To aid alignment, the same trail was used as on configuration A. Configuration B used mechanical stops that allowed the front of the tires to swivel outward only from a 0° stop; thus, when the vehicle landed crabbed into the wind, the nose gear and downwind main gear aligned with the direction of motion whereas the upwind main gear rode against a stop which kept it aligned with the longitudinal axis of the model producing a side force into the wind. Only nose-wheel steering was used on configuration B, and for these tests it was actuated only after touchdown.

No good runs were obtained with stops set at 0° . This was due to a large side force developed by the upwind tire running at a yaw angle of 30° (for 30° crab) with the direction of motion. The large side force acting behind the vehicle c.g. produced a large decrabbing torque and a violent decrab motion. The angular inertia generated by the rapid decrab rendered the model uncontrollable. It was felt that with aerodynamic control during the transition from flight to runout the violent decrab motion could possibly be reduced but not altogether eliminated.

Several runs were made with the stops moved from 0° to 28° and resulted in a reduction of the upwind tire yaw angle with respect to the direction of motion from 30° to 2° when the model was crabbed 30° . Good 30° crab landings were made with the stops relocated but if, for example, landings were made at smaller crab angles the vehicle would have to yaw to the 30° angle in order to develop side forces on the main gear to allow steering with the nose gear.

Configuration C

As with configurations A and B, the landing gear of configuration C was free to swivel prior to contact and, like configuration B, only nose-wheel steering was available. The trail used to achieve alinement was the same as that for configurations A and B. Since the main gear was tied together by a crossbar linkage, it would be expected that the downwind gear, which was more heavily loaded, would align itself with the direction of motion and the more lightly loaded upwind gear would toe out (3° for 30° crab angles) and produce a small side force to windward to facilitate steering.

No good runs were made when the steering clutch was engaged after contact. When the gear was alined with the direction of motion and the steering clutch engaged prior to contact, good runs were obtained at a 30° crab angle. However, it was necessary in those tests to set mechanical stops on the main gear at 30° ; otherwise, during runout the tail would continue to swing downwind. To verify the existence of this problem, several landings were made at 0° yaw but in the presence of the constant side force (sloped runway). Undesirable tail swing was observed for all landings until the main gear hit the 30° stops. Throughout this crabbing maneuver, it was found that the nose gear must be steered or the model would be uncontrollable. Good runs were obtained by first steering into the wind to initiate tail swing, then rapidly steering into the swing until the main gear hit the 30° stops and, from that point, making small corrections with nose steering. In other words, there was no directional control unless the main gear was against a 30° stop and the model was crabbed 30° with a side force strong enough to hold it against the stop.

Configuration D

For a landing with configuration D, it is assumed that a mechanism was provided that allowed the pilot to aline all three landing gears with the direction of motion and lock them in position prior to touchdown. Since the self-aligning feature was not needed, no trail was used on this configuration. With no trail

on the landing gears, the torques required to steer the model were considerably reduced and steering was quite responsive. Thus, in effect, configuration D is essentially the same as configuration A when the gear of A is aligned and locked in the direction of motion, but configuration D lacks the severe steering torque demands that occur on the long-trail configuration A. Good runs were obtained immediately with configuration D when steering was done by the nose gear. The model touched down in a 30° crab and a smooth uneventful runout followed.

An interesting observation with this configuration was that, even though the model was crabbed 30° and the gear was lined up with the direction of motion, the model weather vane or crabbed even farther because of the uneven loading of the main gears. With no steering inputs, the vehicle on touchdown moved leeward slightly, then weather vane slightly, and starts a slow windward drift. Small leeward steering inputs are needed for control and control is relatively easy.

Runs were made with a 5° preset error in the gear alignment with the direction of motion to simulate pilot error. The vehicle was controllable but not without some initial weaving down the runway. When 10° errors in alignment were tried, the vehicle was still controllable, but initial lateral motions were bordering on excessive and some tire squeal was noted. With aerodynamic controls, however, it was felt that landings with even larger alignment errors could be satisfactorily made.

As was observed with configuration A, steering all gears together was unsatisfactory since slight misalignment of the gears would cause a slow ground loop. Steering both nose gear and main gears differentially was tried and a fair run was obtained; however, differential steering increased the sensitivity of an already adequately sensitive steering system and added an unnecessary complication.

CONCLUSIONS

The four crosswind gear configurations investigated were subjected to the same test conditions; thus, comparison of the relative merits of the various configurations can be made even though there are several factors, such as time scaling, only visual cues from a remote position, steering response, and no aerodynamic control, that limit a direct application of these model test results to a full-scale aircraft.

The best crosswind gear system based on subjective results from this investigation was clearly configuration D with nose-gear steering. Configuration A gave good landings when the gears were aligned with the direction of motion and the steering clutch engaged prior to touchdown; however, torque demands were high because of long trail requirements. Configuration C with a free-swiveling main gear had a tail-swing problem that was considered undesirable. No good runs were obtained with configuration B with stops at 0° . These conclusions are not meant to imply that an aircraft could not be successfully landed with configurations B and C as well as A and D; for with aerodynamic control, pilot cues, and differential braking, results from all configurations would be expected to improve.

Testing is continuing to obtain quantitative data on the four configurations to establish an experimental data base with which to validate an analytical program that will predict full-scale results.

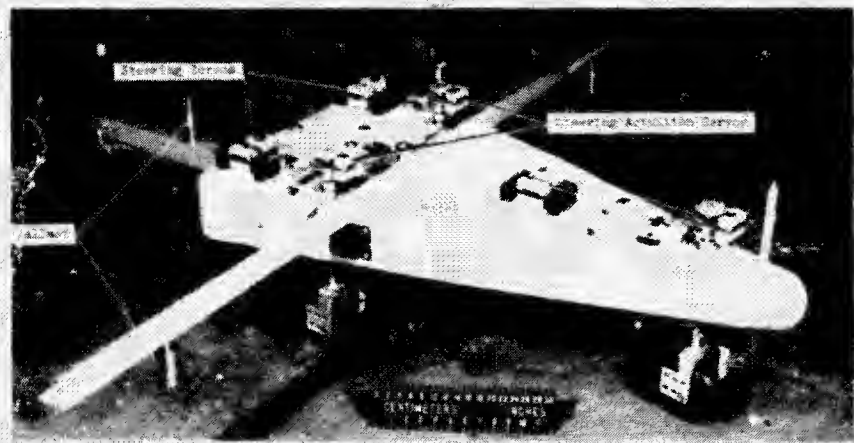


Figure 1.- Photograph of crosswind model with configuration D landing gear installed.

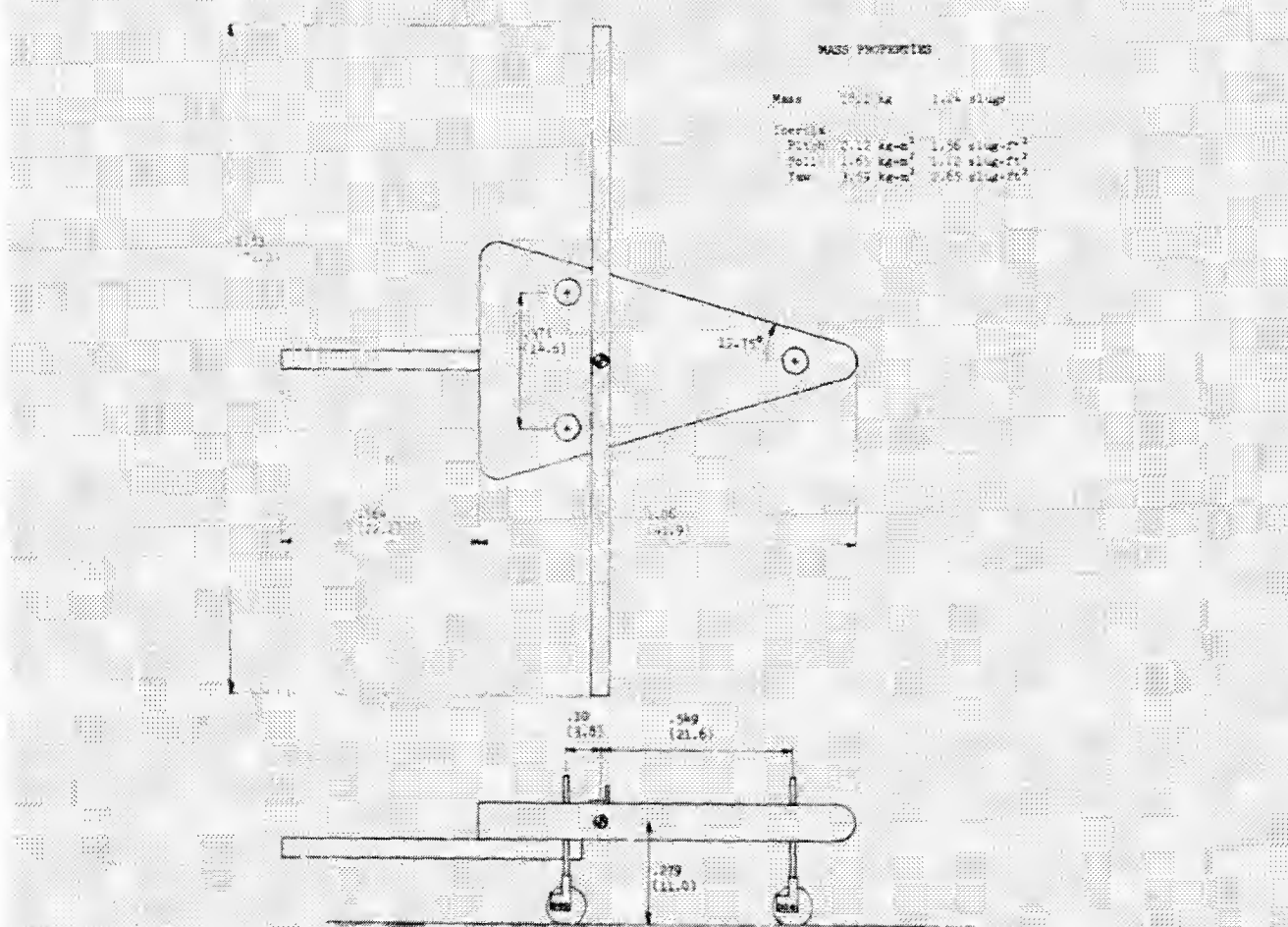


Figure 2.- Crosswind model dimensions for configuration D. Dimensions are given first in meters and parenthetically in inches.

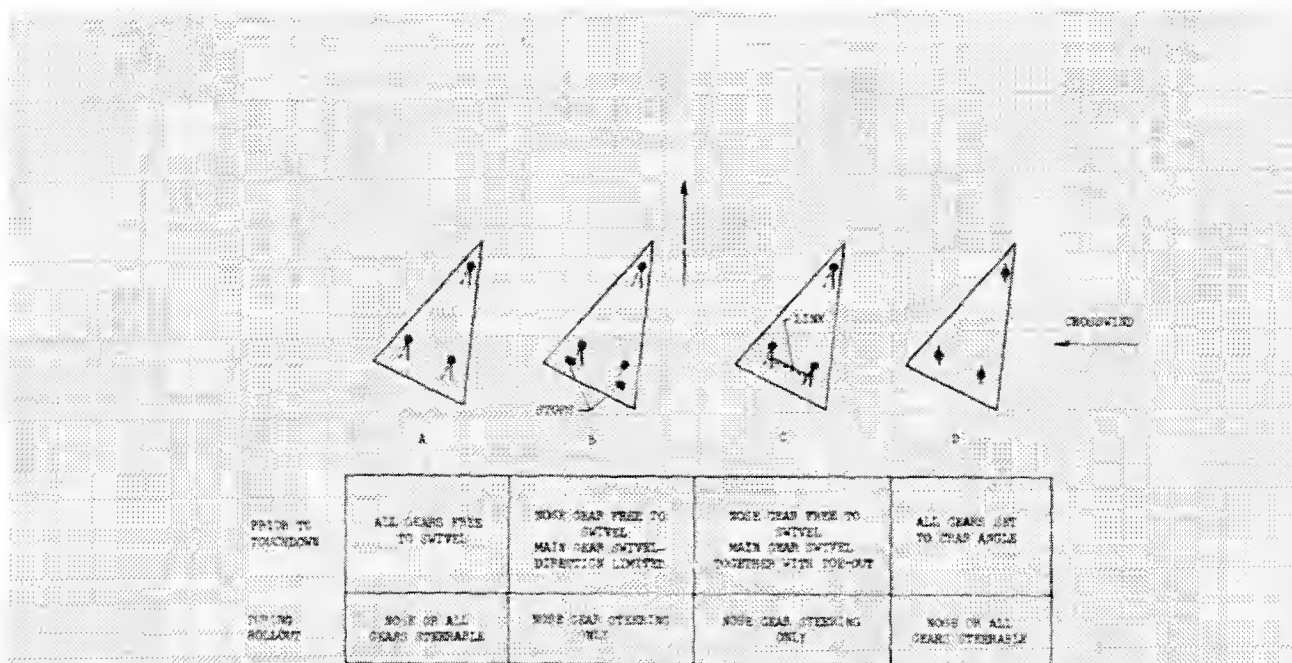


Figure 3.- Crosswind gear configurations.

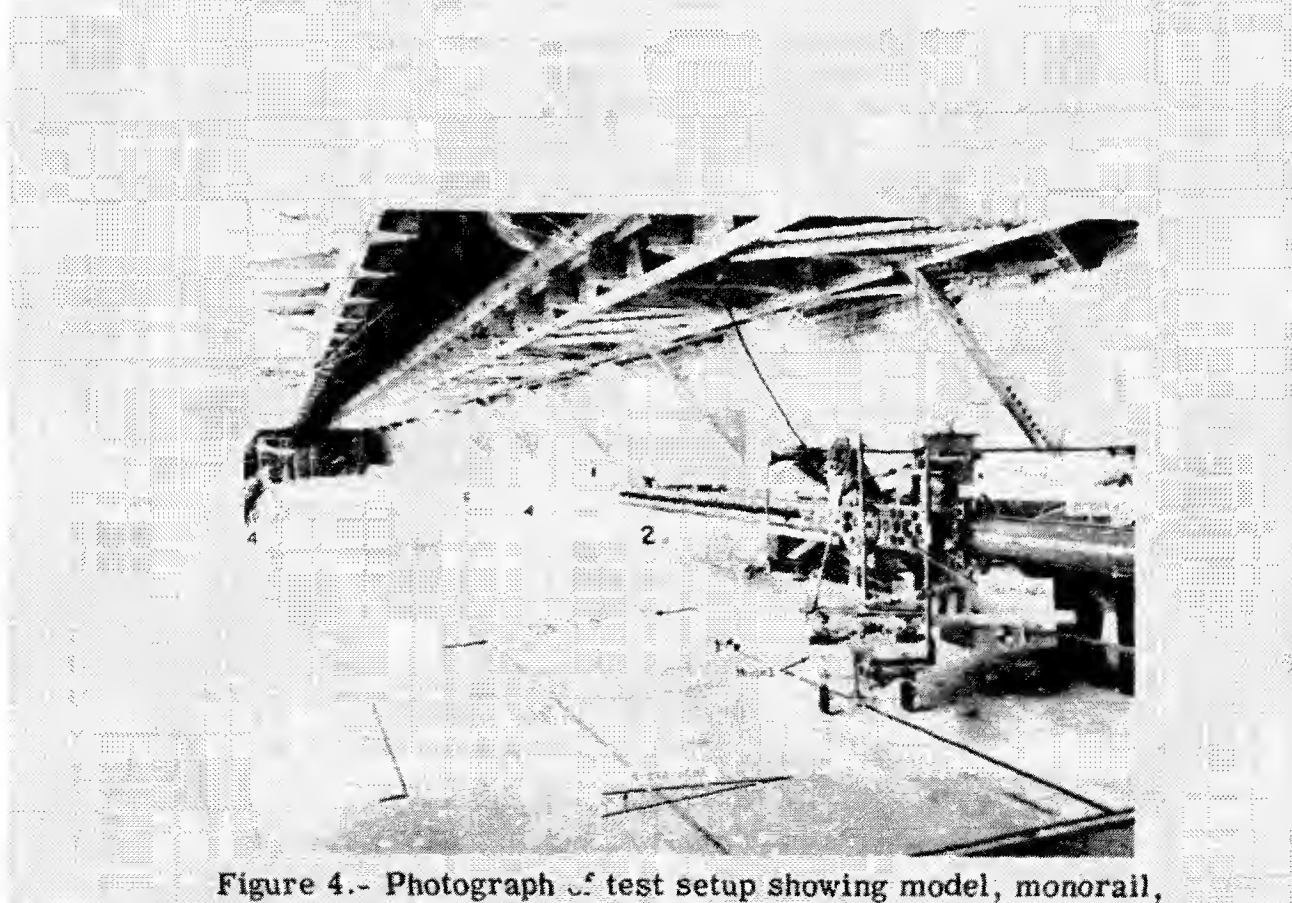


Figure 4.- Photograph of test setup showing model, monorail, carriage, and slanted runway.

14. MODEL SUPPORT ROLL BALANCE AND ROLL COUPLING

By Roy E. Sharpes and William J. Carroll
NASA Langley Research Center

SUMMARY

The design concepts of two specialized wind-tunnel model support mechanisms are described. The forced oscillation roll balance mechanism was designed to meet the specific requirement to measure aerodynamic forces and moments to permit determination of the damping-in-roll parameters of winged configurations. A variable-speed motor is used to oscillate the model by means of an offset crank. The oscillating motion is resisted by a torsion spring to provide a restoring torque and is attached to the section forward of the strain-gage balance. This spring action allows the model to be oscillated at a frequency for velocity resonance, whereby the mechanical spring and any aerodynamic spring balance out the model inertia. The only torque then required to oscillate the model at that particular frequency is equal to that due to aerodynamic damping. The second mechanism, a roll coupling for remotely rotating a model, was designed to invert or roll a model about its longitudinal axis when mounted for testing. The coupling utilizes a small dc gearmotor to drive an integrally designed compound planetary drive system, a potentiometer for remote readout of position, and limit switches to prevent overtravel.

INTRODUCTION

Aerodynamic research in wind tunnels requires specialized model support mechanisms. There are frequent requirements for new designs to permit determinations of aerodynamic characteristics. In response to such a requirement the forced oscillation roll balance mechanism was designed by Mr. Roy E. Sharpes. Aerodynamic testing may also be facilitated by a unique design which permits more efficient operation as provided by the roll coupling for remotely rotating a model. This roll coupling was designed by Mr. William J. Carroll.

FORCED OSCILLATION ROLL BALANCE MECHANISM

This portion of the report will discuss the design and operation of a forced oscillation roll balance mechanism to be used in the study of roll damping and other effects on models in wind-tunnel testing operations.

In figure 1 the operating position of this mechanism is shown in relation to the model and the supporting drive system in a typical tunnel installation. In most installations this balance mechanism will be located as shown, within the fuselage portion of the model, where no tunnel blockage nor airflow disturbance will be created. The drive system shown is typical of two drive systems presently being used to operate oscillating pitch balance mechanisms in tunnels

at Langley Research Center. This oscillating roll balance mechanism has been designed to be interchangeable with the existing oscillating pitch balances. These mechanisms are readily detachable from the drive systems and the models and may therefore be quickly interchanged, as desired, to adapt to either oscillating pitch or oscillating roll operation of the models with a minimum of tunnel shut-down time.

The drive system shown supplies power to the mechanism through the continuous rotation of a drive shaft motivated by a variable-speed, variable-voltage, 2-hp dc electric motor. This mechanism then converts this continuous rotational input movement into a reversing, or oscillating, roll output movement. The input and output movements are maintained about a common axial center line.

One unique feature of this mechanism is that it converts a high torsional continuous revolving input movement into a high torsional oscillating roll output movement, in a very limited space, with a minimum of moving parts. This mechanism has an overall length of about 42.5 centimeters (16.75 inches) and a maximum diameter of about 7.3 centimeters (2.875 inches).

The design and operation of this mechanism will now be explained referring to figure 2.

The means for converting the continuous rotational input movement into an oscillating roll output movement is accomplished by means of a converter yoke. One end of the yoke has a forked sliding connection with a bearing block pivoted on a stationary pin. See figure 2, SECT. D-D. The other end of the yoke has a forked sliding connection with a bearing block pivoted on a drive pin projecting from the part to be oscillated. The yoke has a central bearing to receive an offset crank, driven by the input rotational power drive. As the yoke is actuated by the crank, the yoke making sliding contacts with the bearing blocks will pivot about the stationary pin at one end and will move the drive pin at the other end. Since the drive pin can only move on a radius about its supporting bearings, which are mounted concentrically with the input drive, then the input and output rotational movements will be maintained about a common center line. See figure 2, SECT. A-A and SECT. D-D. The cranking motion, through the actuation of the yoke, will then produce one cycle of oscillation for each revolution of the drive crank. The angle of oscillation is determined by the throw of the crank and is limited by the operating space available for the yoke. Stationary body structure must be provided to bypass the yoke to support the oscillating body, including the forward end of the mechanism to which the model is attached.

Maintaining a minimum overall diameter of this mechanism is very important since the space available for it in most models is extremely limited. Since the loading on models can be extremely high, it is very important to maintain maximum loading capacity. The design feature of keeping the input and output rotational movements about a common center line is imperative in attainment of maximum loading capacity with minimum overall diameter.

A balance beam system is machined into the oscillating body near the forward end to which strain gages are attached to measure the various forces on the model. See figure 2, PLAN VIEW & SECT. A-A. The temperature-control heater

bands maintain uniform temperatures at both ends of the balance beams to insure more accurate strain-gage readings.

The oscillating motion in each direction of roll is resisted by a mechanical spring. The torsion spring is attached to the oscillating body forward of the strain-gage balance section and provides a restoring torque. See figure 2, SECT. A-A. This spring action allows the model to be oscillated at a frequency for velocity resonance, whereby the mechanical spring plus any aerodynamic spring balances out the model inertia. The only torque then required to oscillate the model at that particular frequency is equal to that due to aerodynamic damping. This damping effect of the model can thus be measured through the strain-gage system attached to the balance beams. The torsional spring has been designed to be easily interchangeable with other springs sized as required for optimum operation with various size models.

The portion to which the model is attached is supported on needle bearings to allow it to oscillate freely. A thrust bearing is also provided to take the end loading on the model. These bearings are secured to the supporting shaft portion by retainer rings, as shown in figure 2, SECT. A-A. In order to assemble and retain the oscillating body on the supporting bearings, the housing has been made in two parts. Each part has tapered mating engagements that are securely clamped together by an external nut, thereby effecting a rigid joint.

This roll balance mechanism has been used successfully in conducting tests of a model of the space shuttle orbiter in the Unitary Tunnel at Langley Research Center. The balance oscillating roll angle was $2\frac{1}{2}^{\circ}$ in each direction. Data were recorded at 9 to 11 cycles per second; Mach numbers of 1.6 to 4.6 and pitch angles of 0° to 30° . The oscillating roll balance assembly is shown in figure 3 and the balance parts are shown in figure 4.

A ROLL COUPLING FOR REMOTELY ROTATING A MODEL

The purpose of this portion of the report is to describe a remotely controlled mechanism that will invert or roll a model about its longitudinal axis when mounted for testing.

It is the general practice in most wind tunnels to investigate all models both in an upright and an inverted position to establish the magnitude of the flow-angle correction. At other times it may be desired to test at various roll angles, models of missiles, launch vehicles, pressure instrumented models, or models with survey rakes. For facilities that only have model supports with provision for angular motion in one direction, the roll coupling can be used to obtain angles in a second plane (e.g., if pitch data are obtained ordinarily, yaw data would be easily obtained from roll and angle-of-attack settings).

In the past to roll or invert a model it was necessary to cut power and stop operation of the tunnel, open the hatch or door to the test section and, with the proper tools, disconnect and relocate the model support sting to the next angular position required. These steps resulted in a considerable loss of time, labor, and electrical energy.

Figure 5 shows a solid coupling connecting a typical model sting to the main support system. The primary design requirement was to provide a coupling of approximately the same size and shape for aerodynamic considerations and, in addition, to provide the roll mode of operation. Thus the name, roll coupling. So that this new coupling (fig. 6) could fit to the existing stings and other model support equipment the two tapered ends were not changed. To house the motor and drive system as shown in figure 7, the overall length was changed from 35.56 centimeters (14.00 inches) to 43.18 centimeters (17.00 inches) and the diameter from 10.16 centimeters (4.00 inches) to 12.70 centimeters (5.00 inches). A comparison between the two couplings is shown in figures 5 and 6.

The two major parts, the outer housing, which is fixed to the main model support, and the rotating end or output shaft are machined from heat-treated 17-4PH stainless steel. This output shaft is mounted on two tapered roller bearings and has one end machined with internal gear teeth that mesh with the planet pinions of a compound planetary drive system. Each of these four pinions has teeth machined on one end that mesh with and drive this output shaft. On the other end of the pinion are teeth that mesh with the internal gear teeth of the ring gear that is pressed into the housing. These pinions are spaced equally in the planetary system with no frame nor cage being used to support them. Each pinion is therefore free to float or adjust to any misalignment or irregularity that may be in the system. The driving pinion and shaft of the planetary system are machined integrally. This shaft has a bore through the center and is concentric with the output shaft to allow passageway for the balance leads and other electrical wires that may come from the model. Also machined integrally with this shaft is a spur gear that mates with the initial gear of the transmission system that receives its power from a small commercial dc gearmotor. A potentiometer is geared to the output shaft to transmit the position or amount of roll. Limit switches are also included as a safety precaution to prevent overtravel.

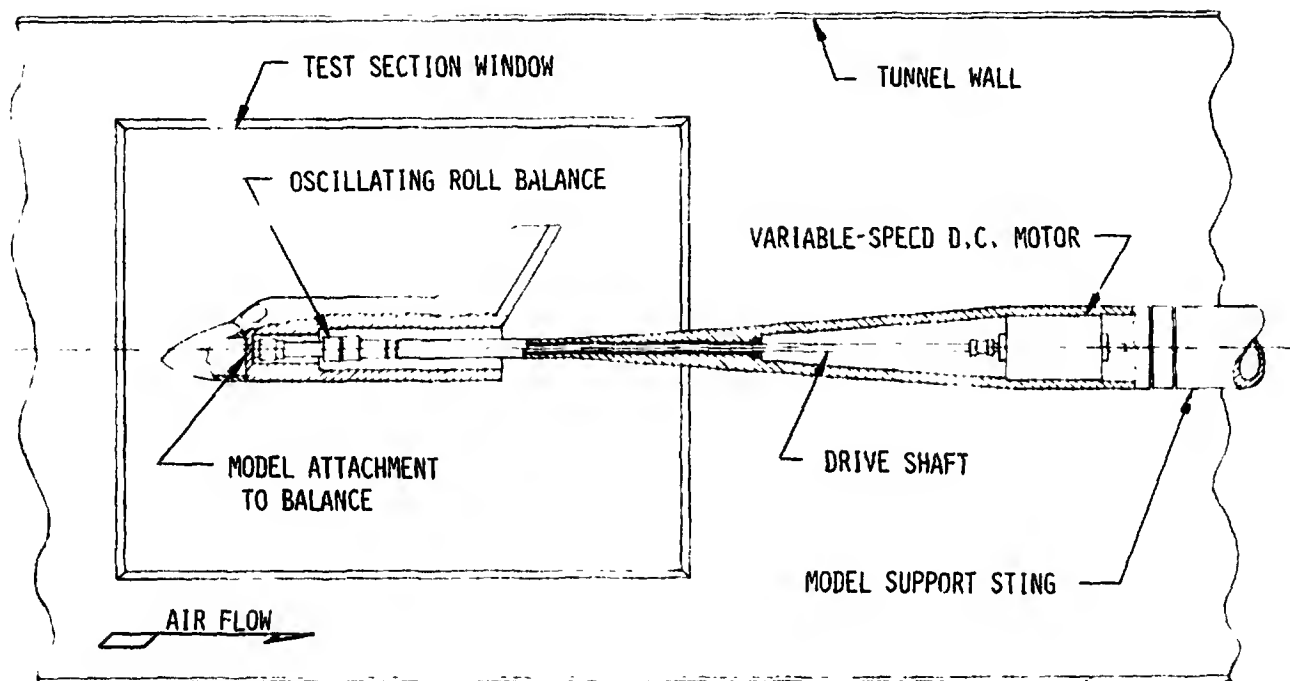


Figure 1.- Typical wind-tunnel installation of roll balance mechanism.

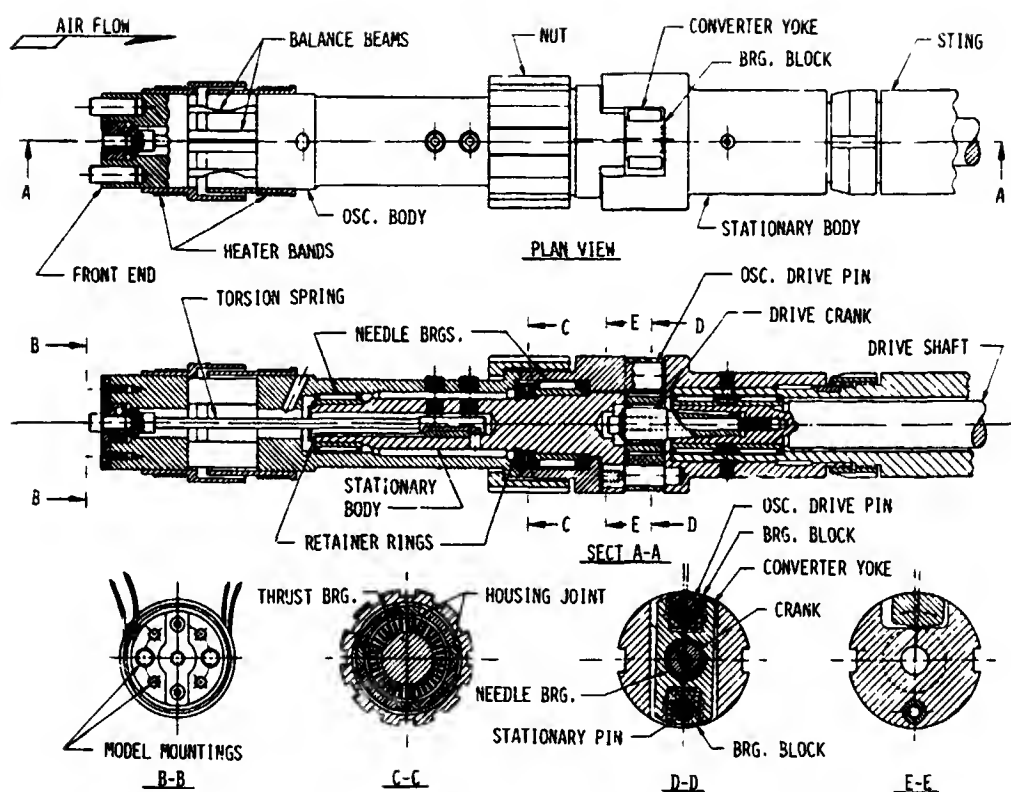


Figure 2.- Forced oscillation roll balance mechanism.

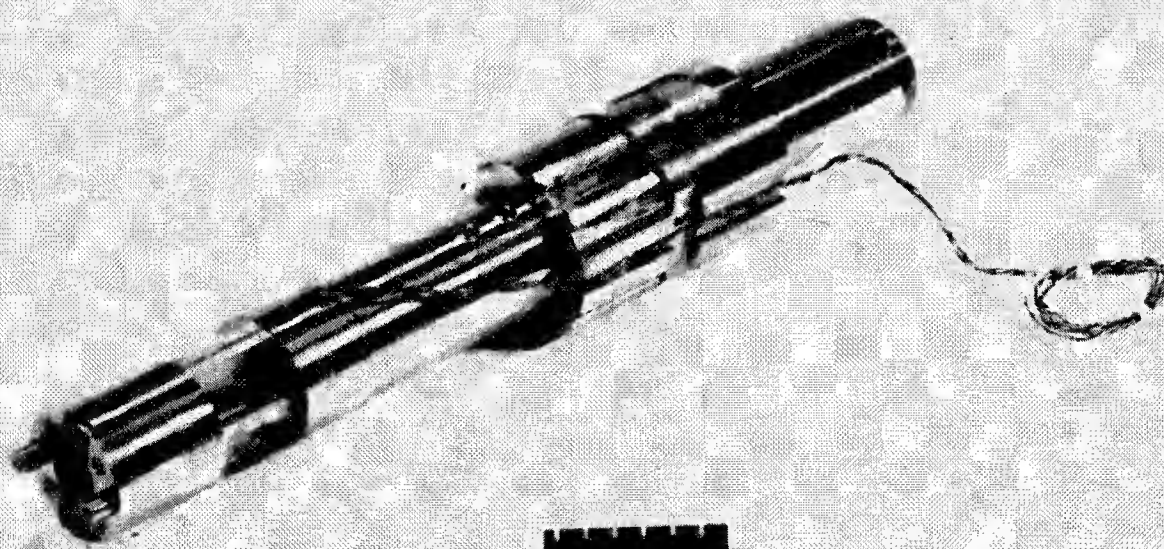


Figure 3.- Oscillating roll balance assembly.

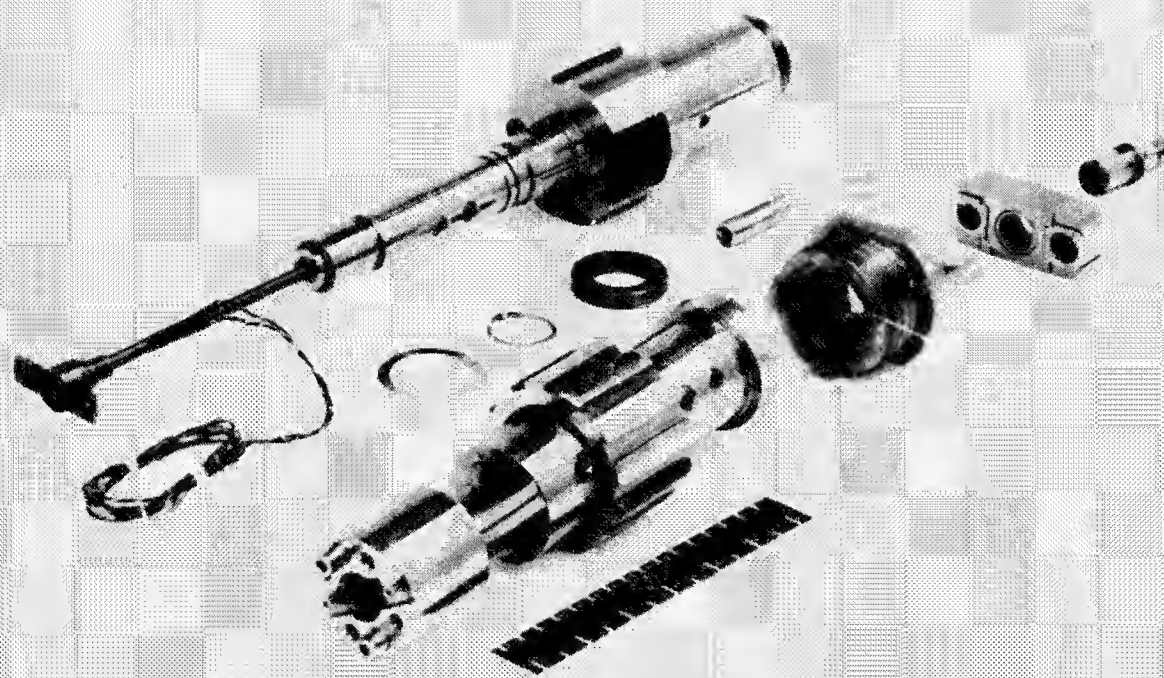


Figure 4. - Components of roll balance assembly.



Figure 5.- Solid-coupling configuration.

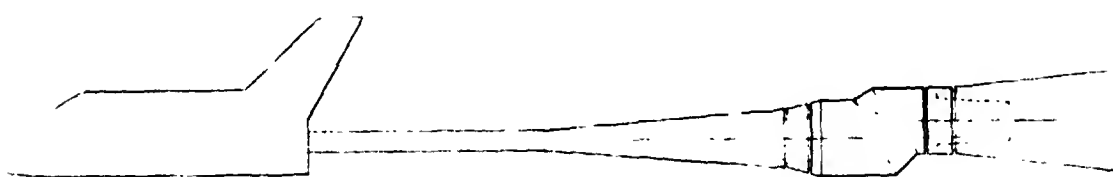


Figure 6.- Roll-coupling configuration.

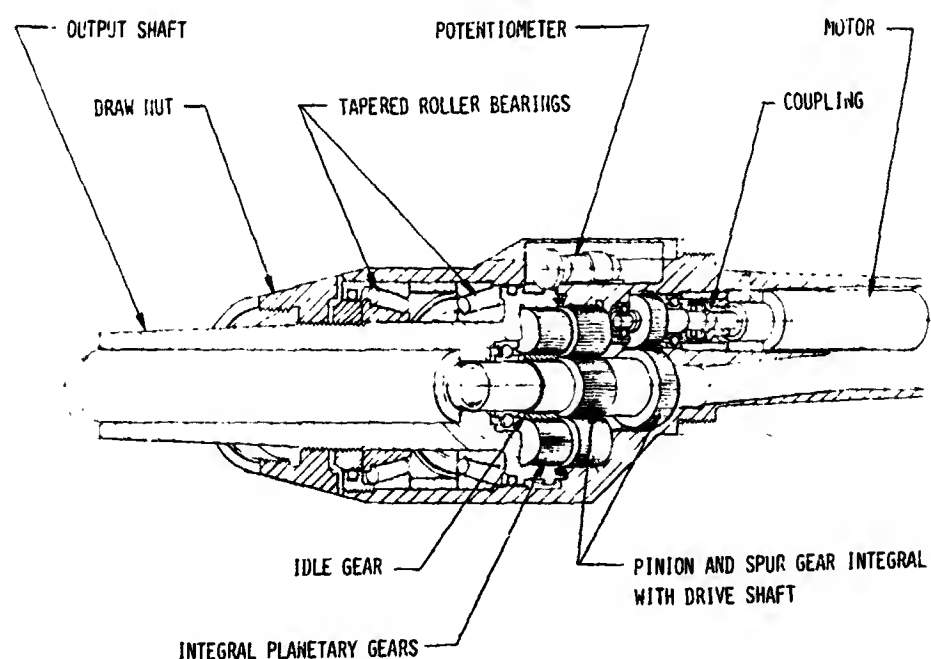


Figure 7.- Cutaway assembly of roll coupling.

15. SPACECRAFT SEPARATION SYSTEMS MECHANISMS:
CHARACTERISTICS/PERFORMANCE DURING HIGH-ALTITUDE FLIGHT TEST
FROM NASA WALLOPS STATION, VA.

By Joseph D. Pride
NASA Langley Research Center

SUMMARY

This paper is concerned with the application of various separation mechanisms to meet flight mission goals within the physical and environmental constraints of a single-stage rocket test vehicle. Each separation concept was selected from the numerous choices available on the basis of its unique requirement and the flight test vehicle incorporated several different concepts. Attention to specific requirements and thoroughness in design and testing were essential to success since there is no specific single answer to separation problems.

INTRODUCTION

In the past few years the National Aeronautics and Space Administration (NASA) has conducted several flight test programs to provide data on the performance of decelerator systems in low-density environments at Mach numbers and free-stream dynamic pressures similar to those expected for an entry vehicle approaching the planet Mars.

One such flight test was conducted on October 9, 1970, at NASA Wallops Station, using a single-stage solid propellant rocket vehicle Castor XM-33E2 motor and two recruit TE-M-29-1 motors. This vehicle is shown on launcher in figure 1. The purpose of this flight test was to determine the opening and stability characteristics of a supersonic disk-gap-band parachute decelerator when opened in the wake of a blunt body aeroshell.

The spacecraft is shown closed in figure 2(a), and in the opened position in figures 2(b) and 3. It consisted of a 10° half angle fiberglass nose cone which served as a heat shield and housed the erection system and its nitrogen supply tanks, the nitrogen supply for the spacecraft attitude control system and the control valves and jets. The aeroshell was an erectable structure with a framework of 24 aluminum ribs (fiberglass caps) attached to a central piston mechanism. The framework of ribs was covered with prestretched nomex fabric (0.285 kg/m^2 (8.4 oz/yd^2)) that was coated with a high-temperature resin to reduce its porosity. The rib caps had tongue-and-groove edges so that the nomex fabric was not exposed to the airstream. The ribs were held secure in the folded position at launch and during powered flight.

The flight trajectory and sequence of events are shown in figure 4. At 90 seconds the Castor rocket motor was separated from the spacecraft. At 225 seconds the aeroshell was erected and the nose cone was released. The parachute was ejected by a mortar firing at 240 seconds. Seven seconds after the mortar fired, or at 247 seconds, the aeroshell separated from the payload parachute. The parachute payload continued to descend until at about 4907.3 m (16 000 ft) altitude and at 1099 seconds a command signal was sent for release of the ballast weight from the payload. The payload and parachute splashed in the water at 1655 seconds of flight time and were recovered from the water surface for inspection and retrieval of the data film.

SEPARATION DESIGN GOALS AND OBJECTIVES, CONSTRAINTS, AND DESIGN SOLUTION

The major separation events and the type of mechanism employed in each separation system are shown in figure 5. The purpose of this section is to discuss the selection of separation mechanisms associated with these events. The goal, the special constraints, and the design solution for each event will be discussed separately.

Event II

Goal.- The rocket booster stage must separate at 3.66 m/sec (12 ft/sec) to have sufficient clearance from the spacecraft at aeroshell deployment

Constraint.-

- (1) No damage to overlapping antennas
- (2) Separation system to stay with booster stage
- (3) Shock limited to spacecraft
- (4) Tipoff disturbance within ($\pm 2^\circ$) deadband of attitude control system

Design solution.- Multisegmented, machined, low profile, V-groove band with redundant, self-contained pyrotechnic release devices, and a gas-pressurized bellows device to effect the desired separation velocities.

Event III

Goal.- To erect the aeroshell during the entry leg of the trajectory at the proper pitch and yaw attitude

Constraint.-

- (1) No damage to spacecraft
- (2) Rib release to be immediate and unconstrained after first rib motion
- (3) Allow aeroshell erection in less than 1.0 sec at dynamic pressures up to 191.5 N/m^2 (4.0 lb/ft^2)

Design solution.- A simple 0.32-cm (1/8-in.) diameter aircraft cable with redundant pyrotechnic cable cutters mounted in a groove at the rib ends. The cable assembly included a small calibrated pretension mechanism.

Event IV

Goal.- After aeroshell erection, to eject the nose cone from the vicinity of the spacecraft to avoid possible aerodynamic wake interference.

Constraint.-

- (1) No ejecta nor flame
- (2) Immediate nose-cone release at aeroshell lock into position
- (3) Limited by shock
- (4) Maximum separation velocity
- (5) Minimum tipoff rates at separation
- (6) Remove erection system and spacecraft attitude control assemblies with nose cone
- (7) Aeroshell after separation to provide a smooth aerodynamic blunt cone profile

Design solution.- Incorporated three self-contained pyrotechnic nuts at the base plate of the nose cone and utilized additional piston stroke from the nitrogen-gas erection system. Also a stud retraction mechanism and container were added to the aeroshell to retract and contain the 1.9-cm (3/4-in.) diameter bolts after release of the nose cone.

Events V and VI

Goal.- At the test condition, to eject the parachute to its proper position behind the aeroshell and deploy the 16.76-m (55-ft) diameter disk-gap-band parachute.

Constraint.-

- (1) No ejecta nor flame
- (2) Limited by shock
- (3) Effect shroud line stretchout in less than 1.0 sec

Design solution.- Provided a 38.1-cm (15-in.) diameter mortar tube for the 56.7-kg (125-lb) parachute package with a high pressure pyrotechnic breech and an eroding orifice for the proper pressure characteristics.

Event VII

Goal.- To release the payload parachute from the aeroshell and separate at the proper velocity to allow the payload parachute to decelerate and descend toward the recovery region.

Constraint.-

- (1) No damage to adjacent aeroshell
- (2) Separation system to stay with aeroshell
- (3) Shock limited to payload

Design solution.- Incorporated a multisegmented, machined, low profile, V-groove band with redundant, self-contained pyrotechnic release devices. An expansion limiter was included to prevent the band segments from contacting the aeroshell ribs.

Event VIII

Goal.- To release the ballast weight (352.89 kg (778.0 lb)) at approximately 4572 m (15 000 ft) altitude to allow for payload flotation after water impact.

Constraint.-

- (1) No damage to payload parachute
- (2) Ballast weight to slide over forward camera housing
- (3) Gravity fall separation

Design solution.- Used a small multisegmented machined, low profile, V-groove band with redundant, pyrotechnic release devices. Allowed the bolt pieces and band segments to fly free from the payload.

Event IX

Goal.- For the parachute payload to survive water impact and the payload to float on the surface to allow for recovery operations and retrieval of the parachute payload.

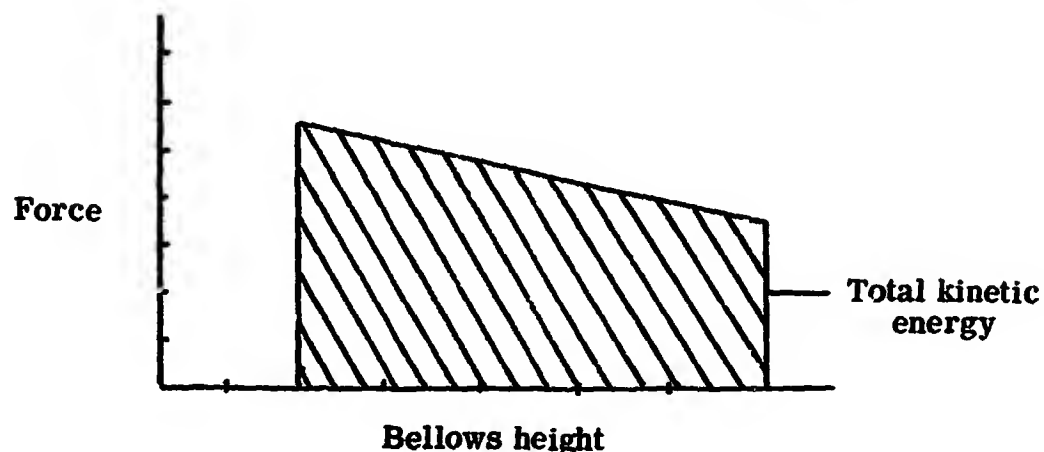
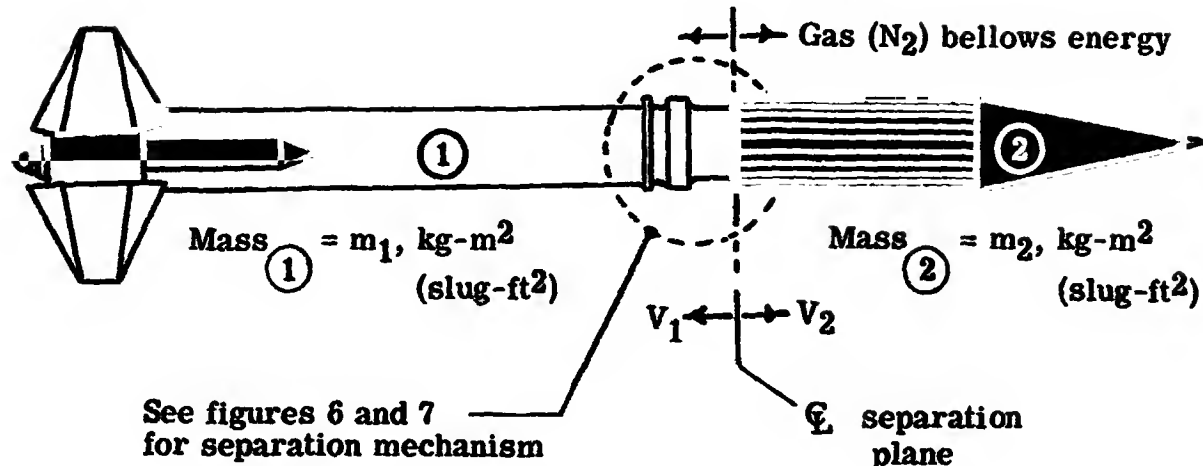
Constraint.-

- (1) Water recovery environment
- (2) Parachute must mechanically detach from the parachute
- (3) Divers, swimming in the water, to effect separation

Design solution.- Incorporated a large, over-center positioned, quick-release pin in the parachute load links.

TYPICAL EXAMPLE: SEPARATION ANALYSIS

1st STAGE SPACECRAFT SEPARATION



Then:

$$v_R \text{ (Relative velocity)} = v_1 + v_2$$

where:

$$v_1 = \sqrt{\frac{2E_K m_2}{m_1(m_1 + m_2)}}$$

and

$$v_2 = \sqrt{\frac{2E_K m_1}{m_2(m_1 + m_2)}}$$

This typical simplified separation analysis technique, where aerodynamic forces are negligible, can be easily parameterized as shown in figure 8 with the resultant separation velocity plotted versus the bellows pressure which determines the kinetic energy.

GROUND TEST PROGRAM

In preparing the spacecraft for flight, a prototype spacecraft was developed for qualification testing (table I) to assure reliability. A test series was conducted to simulate functional flight separation events and to determine the vibration and shock levels at sensitive locations in the spacecraft. These functional separation tests were usually pyrotechnically initiated and often resulted in high shock reactions. The test data established the flight instrumentation component test levels to determine if the electronic and data retrieval equipment would be adversely affected during these flight separation events. The functional characteristics or relative separation velocities were obtained from the prototype test vehicle to evaluate the theoretical calculations. This verification of the separations provided confidence that the system would perform reliably.

FLIGHT TEST RESULTS

Booster Separation (Event II)

The data from the flight test indicate reasonable agreement with the ground test results as shown in figure 9. After Castor burnout the vehicle roll rate was 40 degrees/sec because of fin asymmetries and thrust misalignments. This was taken to zero by the despun system and held until 90.08 seconds when booster separation occurred without any apparent disturbance. The booster was skin-tracked by the SPANDAR radar and indicated an average separation velocity of approximately 3.66 m/sec (12 ft/sec).

Aeroshell Erection (Event III)

The aeroshell was erected by a ground computer signal when the dynamic pressure was estimated to be 191.52 N/m^2 (4.0 lbf/ft^2) at 224.5 seconds. The restraint cable aeroshell was separated and the structure was locked into the blunt cone configuration in 0.70 second after the initiation signal was sent.

Nose-Cone Separation (Event IV)

When the aeroshell was completely erected, a snap ring in the aeroshell engaged and locked the erection mechanism piston. An electrical switch located in the piston snap ring groove sensed engagement and actuated the three pyrotechnic nuts, which released the nose cone. The desired separation velocity was attained by the remaining 6.35 cm (2.5 in.) of pressure stroke in the erection

piston. The initial relative separation velocity was approximately 3.66 m/sec (12 ft/sec).

Mortar Fire: Parachute Extraction (Events V and VI)

To account for deviations from a nominal trajectory, a ground-based computer predicted when to send the signal that would fire the mortar in order to attain the test condition for the fully deployed parachute. The parachute peak load was recorded at a dynamic pressure of 928.88 N/m^2 (19.4 lb/ft^2) at a Mach number of 2.62. The average deployment velocity from mortar firing to line stretch was 38.40 m/sec (126 ft/sec).

Payload Separation (Event VII)

Seven seconds after the mortar fired, the aeroshell separated from the payload parachute. The four explosive bolts in the V-groove band released and the difference in ballistic coefficients of the two bodies provided a large separation velocity, approximately 121.9 m/sec (400 ft/sec). A forward-facing camera in the payload showed there was no damage to the aeroshell during the flight.

Ballast Separation (Event VIII)

When the payload parachute had fallen to 4907.28-m (16 000-ft) altitude, a ground-based command was sent that fired four explosive bolts in a V-groove band. This released the 352.89-kg (778-lb) ballast weight and allowed it to slide cleanly over the forward camera housing and drop clear of the payload.

Payload Water Impact (Event IX)

The payload and parachute impacted the water at 1655 seconds of flight time. The recovery divers mechanically released the parachute from the floating payload and both were recovered from the water for inspection and retrieval of stored data.

CONCLUSIONS

The SPED II separation designs show no single solution that meets all requirements; instead, each system must be selected to meet the unique conditions of the separation. The goals, constraints, and design solution of each event must be defined and an assessment made of the candidate separation mechanisms. To insure reliable separation characteristics a thorough ground test program must be conducted on prototype hardware, where feasible, and correlated with design and analytical programs. The test program showed the adequacy of these designs under simulated conditions. The SPED II flight test results proved that proper separation characteristics could be obtained from a variety of separation mechanisms. These flight test results demonstrate close correlation with ground test results and analytical predictions.

TABLE I.- SPED II GROUND TEST PROGRAM

Prototype qualification and functional tests:

1. Erection system proof pressure
2. Aeroshell functional test - aerodynamic pressure
3. Mortar firings - chute deployment*
4. 1st stage booster/spaceship separation*
5. Aeroshell vacuum erection*
6. Nose cone separation (vacuum)*
7. Spacecraft/mortar firing (vacuum)*
8. Attitude control system functional (air bearing)
9. Spacecraft vibration and shock tests
10. V-groove band/explosive bolt qualification
11. Helicopter drop-water recovery*

Flight spacecraft - assurance tests:

1. Spacecraft vibration
2. Spacecraft shock
3. Aeroshell quick erection (atmospheric) functional*
4. Antenna patterns
5. Spacecraft vacuum

*Functional/separation tests

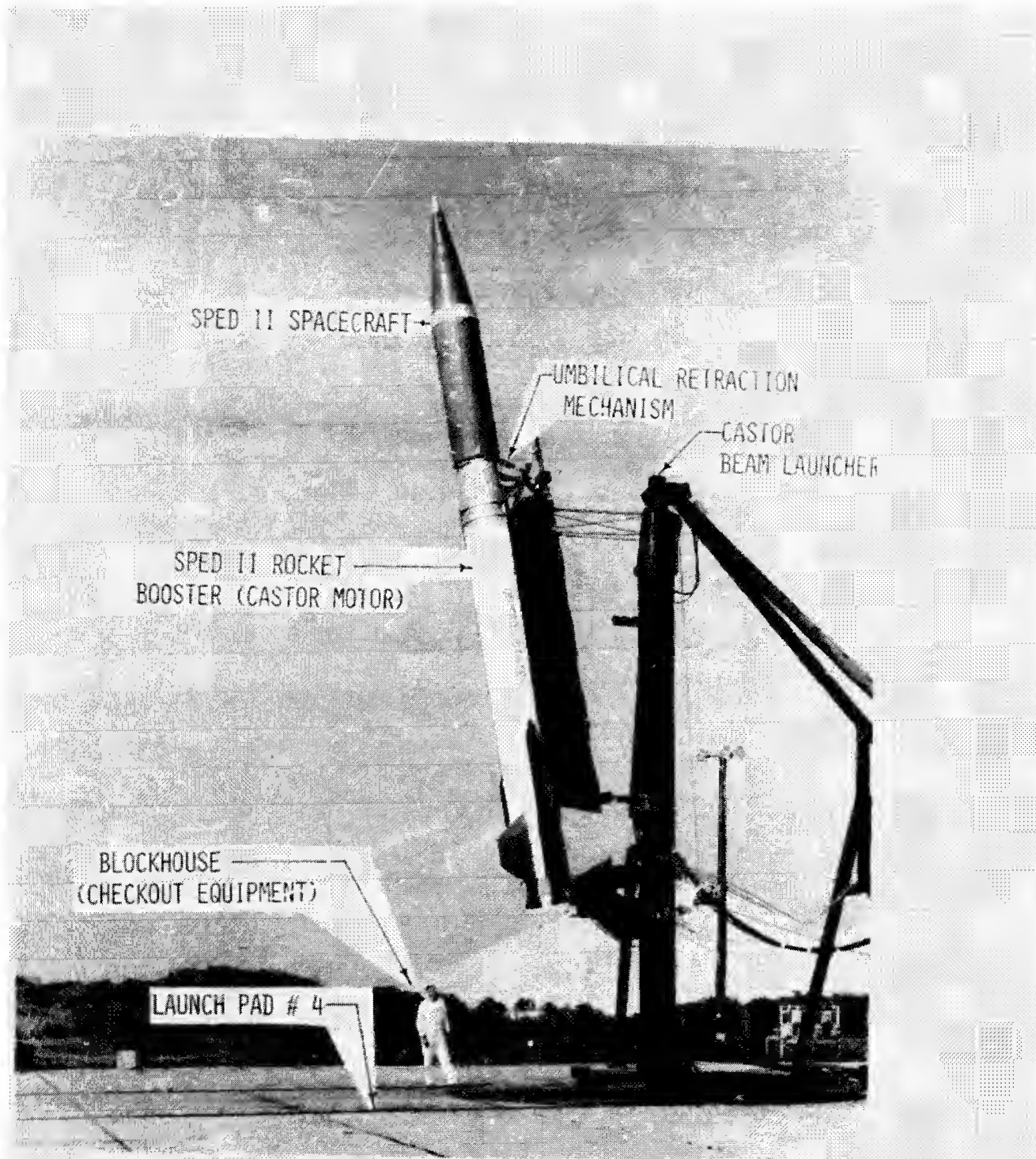
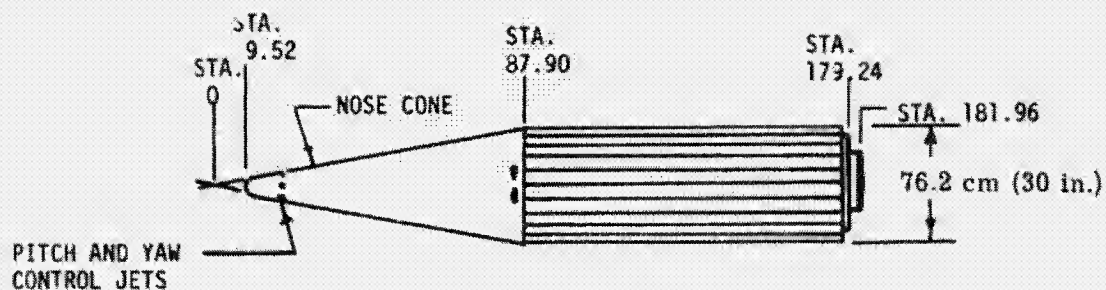
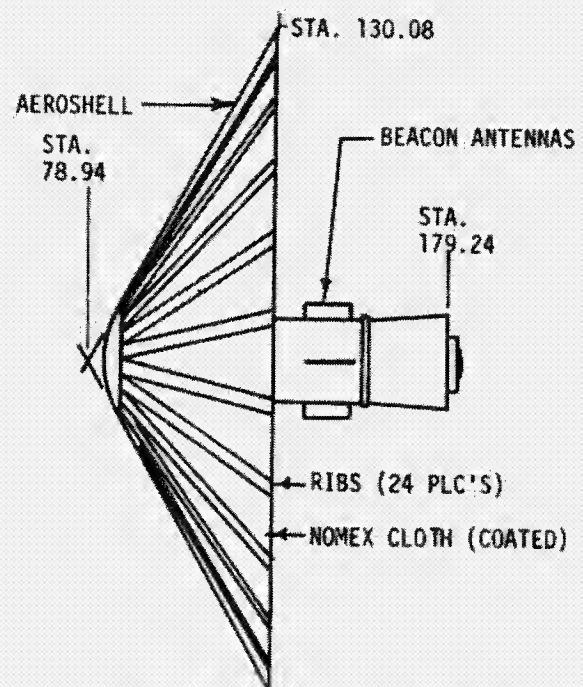


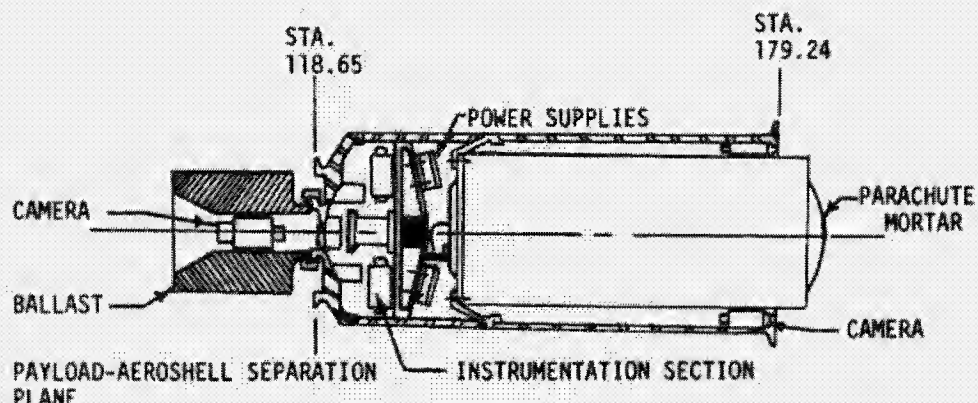
Figure 1.- Vehicle and launch complex.



(a) Folded spacecraft.



(b) Erected aeroshell-payload.



(c) Payload.

Figure 2.- SPED II spacecraft dimensions.



Figure 3.- Erected spacecraft interstage.

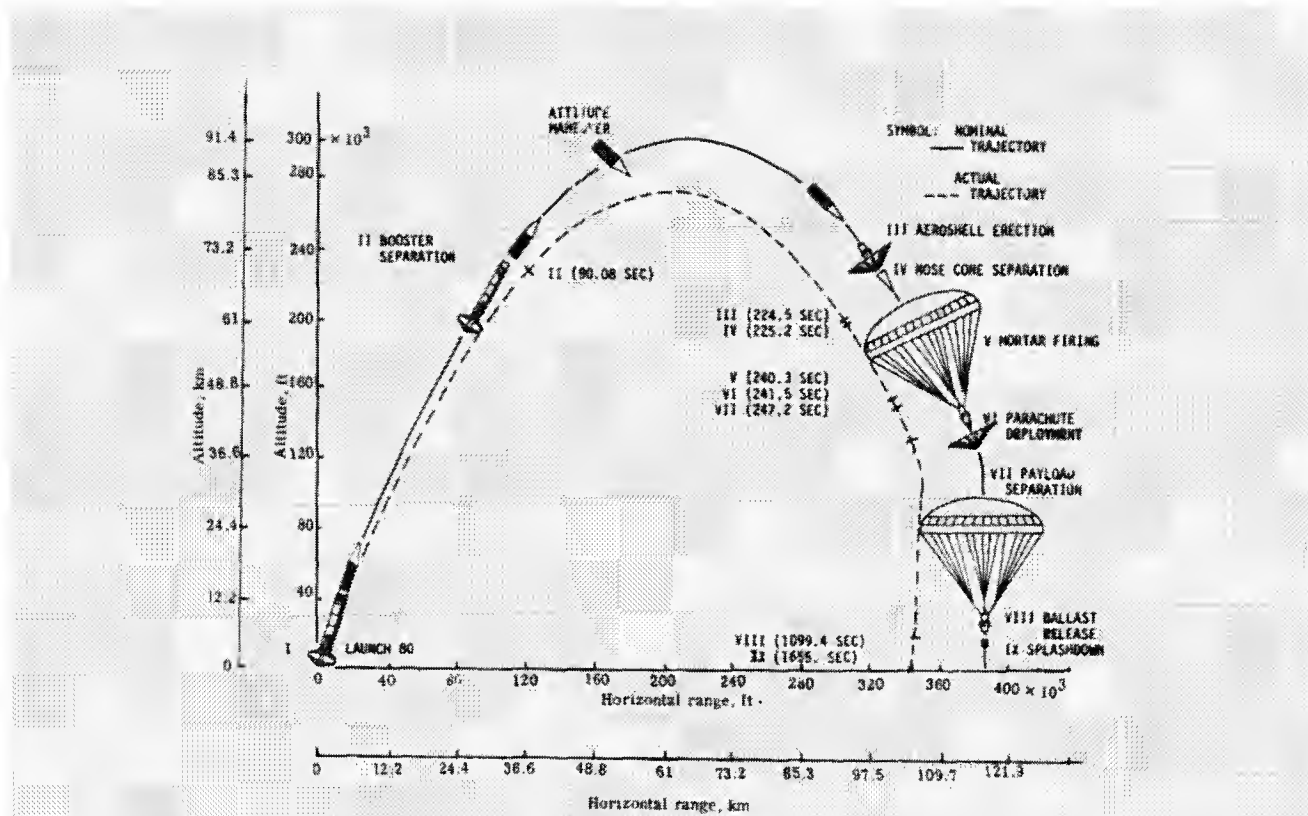


Figure 4.- Illustration of events, nominal and actual trajectory.

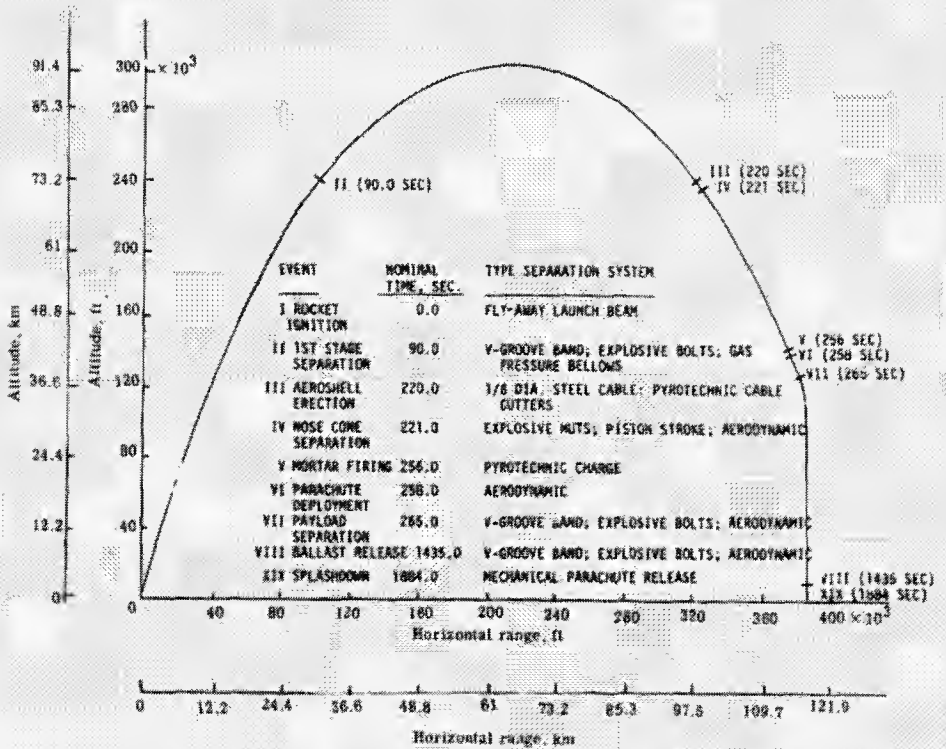


Figure 5.- Nominal trajectory, events, and separation systems.

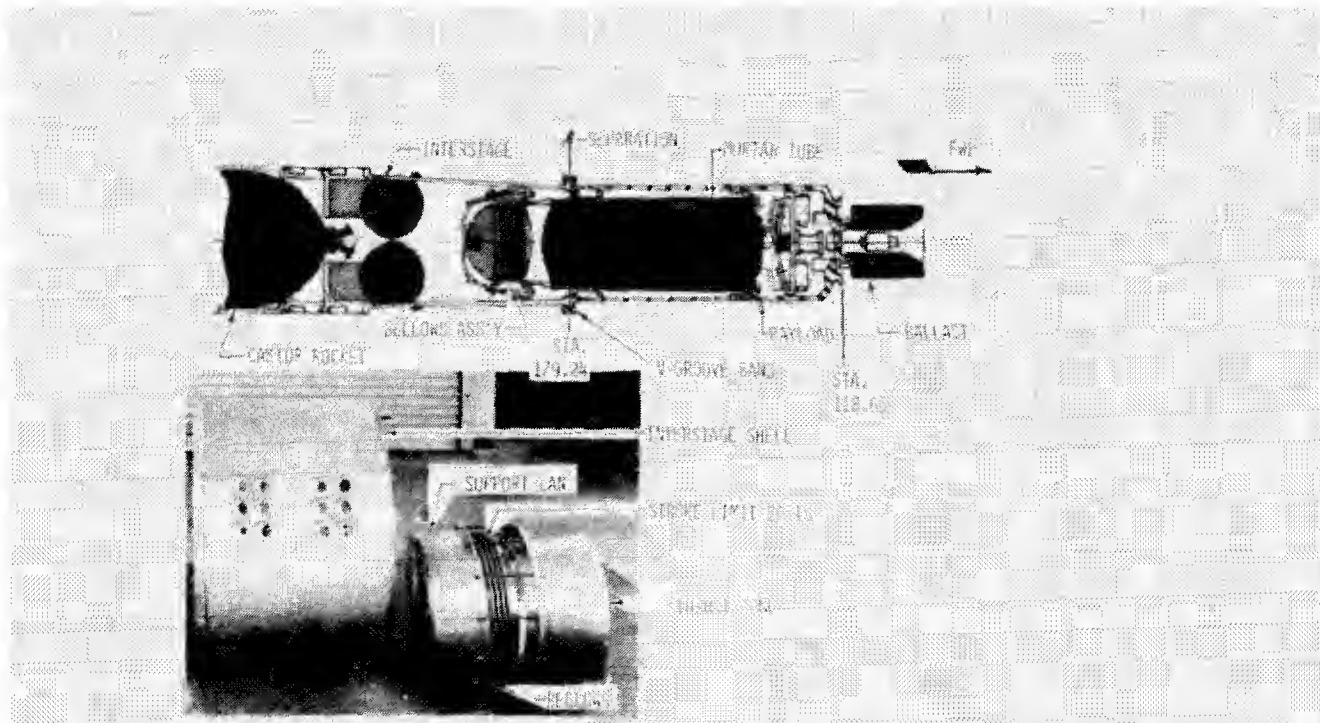


Figure 6.- Rocket booster/spacecraft separation system.

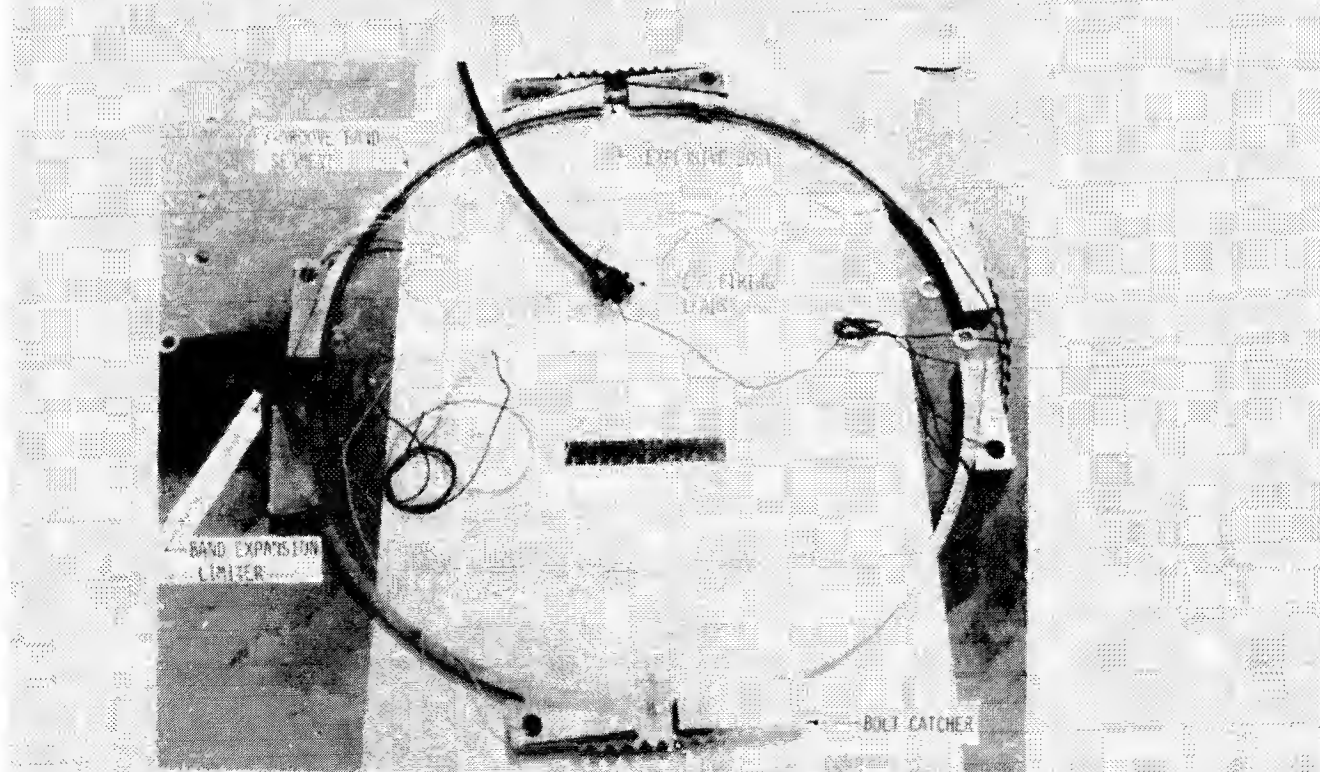


Figure 7.- 1st stage separation, V-groove band assembly.

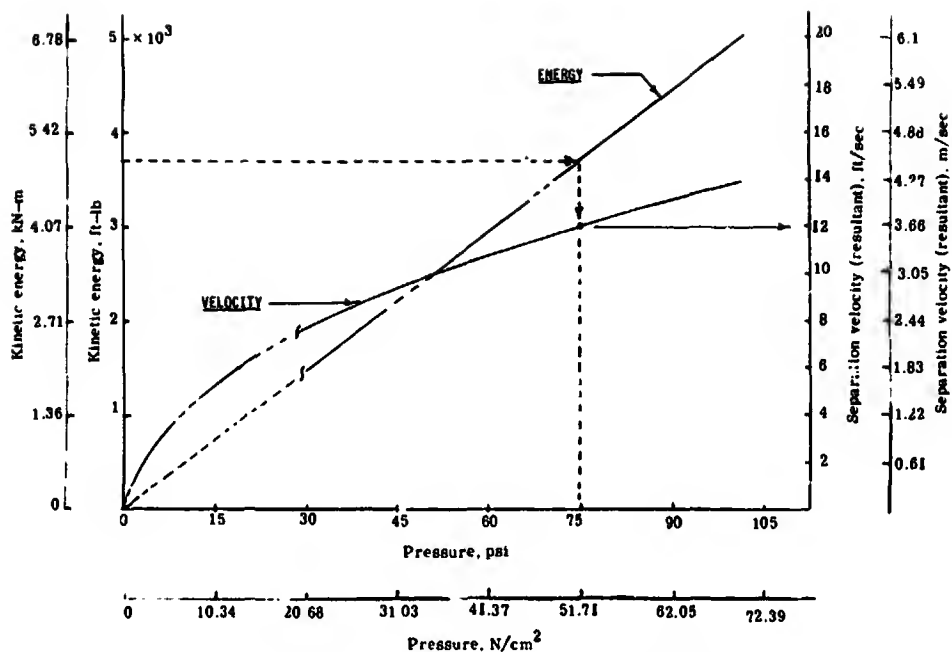


Figure 8.- 1st stage/spacescraft separation.

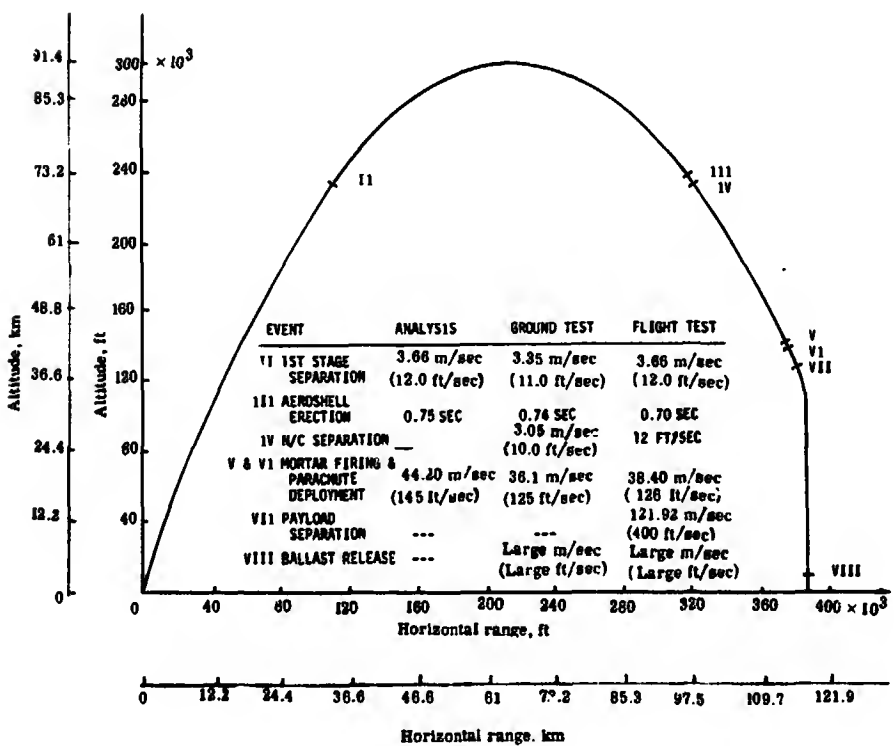


Figure 9.- Flight test results; correlation with analysis and ground test.

16. DEVELOPMENT OF LOW-SHOCK PYROTECHNIC SEPARATION NUTS

By Laurence J. Bement

NASA Langley Research Center
Hampton, Virginia

and

Dr. Vernon H. Neubert

Pennsylvania State University
University Park, Pennsylvania

SUMMARY

"Pyrotechnic shock," a relatively unknown environment generated by the actuation of pyrotechnic devices, has been an increasing concern to aerospace systems designers as system complexity increases. This study has expanded the understanding of pyrotechnic shock in three areas: pyrotechnic separation nuts, a relative idea of their input into structure, and performance monitoring systems. Performance demonstrations and comparisons were made on six flight-type pyrotechnic separation nut designs, two of which are standard designs in current use, and four of which were designed to produce low shock on actuation. Although the shock performances of the four low-shock designs are considerably lower than the standard designs, some penalties may be incurred in increased volume, weight, or complexity. These nuts, and how they are installed, can significantly influence the pyrotechnic shock created in spacecraft structures. A high-response monitoring system has been developed and demonstrated to provide accurate performance comparisons for pyrotechnic separation nuts.

INTRODUCTION

Pyrotechnic shock, the name given to the mechanical pulses created by the actuation of pyrotechnic devices (separation nuts, valves, pin-pullers), has been a poorly understood environment throughout the years of pyrotechnic applications. As spacecraft have become more sophisticated and delicate, the concern caused by this environment has increased. Few anomalies have been directly attributed to these short-duration, high-force, high-frequency pulses; electrical relays chattered on the Apollo program and Titan vehicle, and a commutator failed on a spacecraft prior to a NASA Wallops launch. The unknowns in this pyrotechnic-shock environment have been: How is it generated and transmitted; how is it measured; what are its shapes; what are its effects on spacecraft systems; what can be done to minimize its generation; and can systems be "qualified" under this environment?

The objective of this study was to provide a better understanding of the pyrotechnic-shock environment by demonstrating the performance of four "low-

shock" pyrotechnic separation nut designs, comparing their shock performances to two standard nuts currently in use, relating the mechanical output of all six nut types to their internal mechanisms, and considering their application on aerospace systems. The pyrotechnic-shock performance comparisons and analyses were based on a monitoring system utilizing high-response strain gages, as well as conventional accelerometers, mounted on simple, cylindrical bars.

APPARATUS

The experimental apparatus consists of the monitoring system and seven separation nuts, six flight-type and one nonflight type.

Monitoring System

The main elements of the monitoring system shown in figure 1 are the two cold-rolled steel bars, 3.66 m (12 ft) long and 2.54 cm (1 in.) in diameter. Each was hung by 152.4-cm (60-in.) cables with elastic cords contacting the bars. The shock waves generated by the separation nuts travel in a uniform plane wave down the bar at sonic velocity. Therefore, a time period of 1.44 milliseconds is required for a wave to traverse the 3.66-m (12-ft) length and return to its source, allowing a pulse within that duration to be viewed as a single pulse.

Several adapters were machined to accommodate the stud thread sizes, thread nomenclature 7/16-20 or 1/2-20, and lengths. Also, a cylindrical adapter with a half-inch wall was machined to allow the monitoring of shock waves through the flange of the separation nuts. All separation nuts, except Low-Shock Design 4, utilized this adapter. Low-Shock Design 4 had no mounting flange and the bar was threaded into a tapped portion of the nut's cap. This technique considerably improved the coupling of the nut's generated shock over the flange mounted approach. A 0.32-cm (1/8-in.) flat washer, 8.1 cm (3.2 in.) in diameter, was installed at the nut-to-stud interface to provide a method of containing the internal components of two of the nut designs, Standard Design 1 and Low-Shock Design 1.

The shock waves were monitored by strain gages and accelerometers at positions indicated in figure 1. The strain gages were mounted at diametrically opposing positions on the bars and were wired within the Wheatstone bridge of the amplifier to cancel the effects of longitudinal bending of the bars. The gages, Baldwin Model FAB1235S13, and the amplifiers, Ellis Model BAM-1B, have a frequency response flat to at least 100 kHz. The accelerometers, Endevco Model 2225C, have a resonant frequency of 80 kHz and a mounted resonant frequency of approximately 50 kHz, yielding a monitoring capability that is flat to 10 to 16 kHz. The accelerometer amplifiers were Endevco Model 2718.

The dynamic pulses were recorded on an FM magnetic tape recorder Minneapolis Honeywell 7600 with a frequency response flat to 40 kHz (capable of measuring rise times to 6 μ sec). The equivalent paper speed of the permanent records, achieved by reducing playback speeds, was over 5588 cm/sec (2200 in./sec), or 0.19 millisecond/cm (0.48 millisecond/in.).

Separation Nuts

One nonflight and six flight-type separation nuts were tested in this program: a noncaptive design which was historically the first and simplest release nut concept, two "Standard" designs that have been utilized considerably in present and past aerospace programs, and four "Low-Shock" designs that were specifically designed toward reducing the mechanical shock generated on actuation. Although each nut could contain two cartridges for redundancy, only one cartridge was used for each functioning.

The following explanations describe only principles. Physical designs and performance margin: are beyond the scope of this presentation.

Noncaptive (see fig. 2).- The bolt is retained by the threaded portion of the steel collet which is in four segments. The segments are, in turn, held in position by a retaining ring. Electrical ignition of the gas-generating cartridge, which produces 6.8948 kN/m^2 (1000 psi) in a 10-cc closed volume, pressurizes the volume formed by the bolt end and the housing. The housing is forced to the right, stripping back the retaining ring and releasing the collet segments. No effort is made for confinement of gases, housing, nor collet segments.

Standard Design 1 (see fig. 3).- This release mechanism is similar to that of the noncaptive nut; the retaining cylinder holds the collet assembly at its base and is withdrawn. The collet in this design has four deep incisions, instead of being segmented. The SBASI (Single Bridgewire Apollo Standard Initiator), which produces 4.4816 kN/m^2 (650 psi) in a 10-cc volume, pressurizes the volume formed by the piston and the retaining cylinder, causing the cylinder to stroke to the right. The piston holds the nut segments in position. As the restraining ring strokes over the collet, the flared portion of the collet is compressed, forcing the base of the collet to petal open, hinging at the base of the incisions, and releasing the bolt. The restraining piston is decelerated by the O-ring as it impacts against the housing.

Standard Design 2 (see fig. 4).- The retaining cylinder holds the segmented collet at two circumferential points of increased diameter. The spreader piston is spring loaded to restrain and spread the segmented collet on its release. The cartridge, which produces 9.6527 kN/m^2 (1400 psi) in a 10-cc volume, pressurizes the volume formed by the housing and the top of the restraining cylinder. This forces the restraining cylinder to the left, allowing the four collet segments to fall into the cylinder's recessed areas, releasing the bolt. The restraining cylinder then impacts against the bottom of the housing.

Low-Shock Design 1 (see fig. 5).- This nut is a modification of Standard Design 1 and utilizes the same release mechanism; the restraining cylinder strokes to the right : pressurization from the output of a SBASI, compressing the incised collet. The shock-reduction principles were to use an increased mass for the pistons, to minimize their acceleration and to maximize the restraining cylinder's acceleration, and to use crushable honeycomb to reduce the peak load forces on the piston and retaining cylinder from the brisant output of the SBASI. This would reduce the pressure-induced loads through the collet into the bolt. The outer honeycomb provides for a longer period of deceleration on impact.

Low-Shock Design 2 (see fig. 6).- The output of the SBASI cartridge is ported into the body of the nut to force the restraining cylinder to the right, releasing the three-segmented collet. The deceleration of the retaining cylinder/spreader piston/collet combination is achieved by the force produced by the residual gases from the output of the cartridge.

Low-Shock Design 3 (see fig. 7).- The output from the SBASI cartridge is ported through the body of the hinging piston to force the retaining cylinder to the right. As the retaining cylinder strokes, the three-segment collet is first released at its base and is then forced to rotate open about the hinging piston by contacting the lower lip of the recessed area in the retaining cylinder. Again, the motion of the retaining cylinder/hinging piston/collet combination is decelerated by the residual gas from the output of the cartridge.

Low-Shock Design 4 (see fig. 8).- The output of the cartridge, which produces 16.272 kN/m^2 (2360 psi) in a 10-cc closed volume, is ported to the annular ports at each end of the nut body. The two retaining cylinders are forced inward, allowing the three-segmented collet to fall into the recessed areas under the force of an expansion spring (not shown). The shock-reduction principles were to avoid loading the bolt from the cartridge output and to have the low-mass retaining cylinders dissipate their energy on impacting together rather than against the housing.

PROCEDURE

The experimental program was divided into six major divisions. establish monitoring apparatus, function the six flight-type separation nuts, analyze the performance records and compare nut performances, determine the housing performances with only a standard bolt (no stud monitor), determine the effects of bolt torque on shock performance, and consider the possible effects on a typical spacecraft system. In the course of this program, 35 separation nuts were functioned; the number and type of nuts tested are summarized in Table I.

Monitoring Apparatus

To evaluate the response and linearity of the monitoring system, the bar was impacted with a steel ball and was used to monitor the noncaptive nut, shown in figure 2. The bar impacts were accomplished by a 0.24-kg (0.54-lb) steel ball, 3.18 cm (1.25 in.) in diameter, on a 152.4-cm (60-in.) pendulum at horizontal displacements of 30.48 cm (12 in.), 60.96 cm (24 in.), and 91.44 cm (36 in.) from the bar's end, at heights of 3.048 cm (1.2 in.), 12.7 cm (5.0 in.), and 30.48 cm (12 in.). Several flat-ended cylindrical and conical adapters were threaded to the bar and impacted with the ball to determine the effect of interfaces and possible internal reflections. All interfaces were coated with silicone grease to maximize shock coupling. The noncaptive nut was torqued to 11.298 Nm (100 in-lb) on the monitoring bar for functioning.

Nut Performance

The six separation nuts were functioned under as nearly identical conditions as possible; each nut was torqued to 11.298 Nm (100 in-lb) on the stud monitoring bar, and the housing flanges (except for Low-Shock Design 4, see Apparatus) were bolted to the housing monitoring bar. Several nuts of each nut type were functioned in this arrangement: Six each of Standard Designs 1 and 2, and six each Low-Shock Designs 1 and 4, and one each of Low-Shock Designs 2 and 3. An effort was made to associate the mechanisms of the functioning with the force-time history obtained from the stud and housing monitoring bars. The motion of the monitoring bars was observed with a 400-pps framing camera to estimate the impulsive loading on functioning. This motion was equated to energy by multiplying the displacement height by the weight of the bars.

Performance Analysis

For comparison the force and acceleration time histories of one representative record of each nut type were plotted on the same scales. Also, the impulsive loads produced by the actuation of each nut type were compared.

The acceleration time histories of the representative records were analyzed on a shock spectrum analog analyzer (MB model 980) to 40 kHz with a Q of 10. Only the first pulse produced by each channel was analyzed and only for the duration of the pulse to produce a primary spectrum; that is, the reflected pulses were disregarded in the analysis, and the spectra produced represent the absolute response of a mass within a single-degree-of-freedom system only within the time period of the pulse itself, a maximum time of 1.34 milliseconds. In like manner, the acceleration response of a single-degree-of-freedom system to the force pulses could be calculated and presented in spectral form.

Stud Performance

To simulate the mounting normally used in separation systems, in which the nut housing is secured to the structure and the stud is allowed to move, five nuts (all except Standard Design 2) were functioned with a free stud and were monitored only on the housing side. The force time histories of the housing were compared to the performance utilizing both monitoring bars. Also, the stud ejection velocities produced on actuation of the nuts were observed with a 400-pps camera. This velocity was related to kinetic energy $1/2 mV^2$.

Effect of Torque

To determine the effect of torque on shock generation, four additional nuts were functioned at torque levels greater than 11.298 Nm (100 in-lb) (45.194 Nm (400 in-lb) to 101.686 Nm (900 in-lb)) using both bars: Noncaptive nut, Standard Design 1, Low-Shock 1, and Low-Shock 4. Their force time histories were compared to the corresponding tests at 11.298 Nm (100 in-lb).

Effects on Spacecraft

Based on the force time histories produced by these low-shock nuts, the general effect on spacecraft systems was considered. Under consideration were relative shock loads, effects of mounting, and relative displacements on actuation.

RESULTS

Monitoring Apparatus

Several observations can be made from the force and acceleration records obtained from impacting the 3.18-cm (1.25-in.) steel ball against the bar's end shown in figure 9. There is a 1.34-millisecond period from the beginning of the initial compression wave, until the arrival of the reflected wave which is first tensile, then compressive. According to theory, the acceleration is proportional to the first derivative of the force signal. Consequently, if the input force pulse is not a true sine wave, the derivative will be a complex wave, requiring up to twice the input's frequency to reproduce. In the examples in figure 9, the input force is evidently a haversine pulse, since the acceleration pulse indicates two acceleration peaks, producing a pulse that is equivalent to twice the frequency of the input pulse. Also, since the accelerometer is mounted on the bar's end, the acceleration is twice the level that would be recorded at a point along the bar. The amplitudes of these simple impact-generated pulses provide a basis of comparison for the loads induced by the function of the separation nuts; that is, at a 91.44-cm (36-in.) displacement the impact velocity of the steel ball is 4.24 m/sec (13.9 ft/sec), producing a 11.076-kN (2490-lb) force, 118-microsecond pulse.

No appreciable losses nor internal reflections were produced by the straight cylindrical adapters; this was also observed for a 45° expansion conical adapter (from 2.54 cm (1 in.) to 5.08 cm (2 in.) diameter, the angle used in the housing adapter).

Typical performance plots for the noncaptive nut are shown in figure 10. The initial tensile pulse is produced by the force required to shear a pin at the retaining ring to collet interface and to overcome friction. (See cross section, fig. 2.) The pressure within the cavity then loads the stud into compression until the stud is released. The oscillating acceleration pulse bears little visual correlation to the input force pulse. The impulsive load on the stud caused the monitoring bar to swing approximately 25.4 cm (10 in.), equivalent to 2.99 Nm (26.5 in-lb) of energy. The remaining energy in the nut housing was not recorded.

Separation Nuts

The functional performance of each nut type will be explained individually in this section through representative performance curves. In general, the performances produced by several units of each type of nut were highly repro-

ducible. The performance curves could be exactly overlaid from nut to nut with only small variations in amplitude.

Standard Design 1.- See figure 3 for the cross section and figure 11 for the functional histories. As the retaining cylinder is forced to the right, a momentary tensile wave is created in the bolt. This is followed by a strong compressive force produced by the piston against the collet. The major tensile spike is produced by the retaining cylinder stroking the flared portion of the collet. The housing first experiences a tensile wave as a reaction force to the acceleration of the retaining cylinder applied through the collet. As the retaining cylinder impacts against the O-ring and housing, a strong compressive pulse is produced. The monitoring bars were observed to swing apart by approximately 15.24 cm (6 in.) on functioning.

Standard Design 2.- See figure 4 for the cross section and figure 12 for the functional histories. The initial tensile load in the stud appears to be produced by the housing reaction in loading through the collet which exceeds the compressive loading produced by shearing the shear pin between the retaining cylinder and the collet. The large compressive spike is produced by the impacting of the retaining cylinder, bottoming against the housing. The housing load first exhibits a compression corresponding to the reaction to the initial tensile load of the stud. The major shock of the impacting retaining cylinder is apparently transferred efficiently into the stud mass and not the housing. The second compressive load of the housing can be attributed to the bottoming of the spring or spreader piston against the retaining cylinder in ejecting the stud. The positive pulse could be related to the seating of the spreader piston in the then-expanded collet sections. The monitoring bars swung apart approximately 20.32 cm (8 in.) on functioning.

Low-Shock Design 1.- See figure 5 for the cross section and figure 13 for the functional histories. The initial tensile pulses on the stud can be related again to the shearing of a shear pin and friction when the retaining cylinder begins its motion. The major compressive indication is caused by the loading through the piston and honeycomb. The retaining cylinder impacting the flared portion of the collet produces the sharp tensile pulse. The loads into the housing are apparently well isolated from the stud; the reactionary forces are low, reduced by the crushable honeycomb and the acceleration of the high-mass piston. A small tensile load is coupled through the washer at the interface, followed by a compression produced by decelerating the retaining cylinder against the housing. No separation of the bars was observed on functioning.

Low-Shock Design 2.- See figure 6 for the cross section and figure 14 for the functional histories. The initial stud compressive load is produced by the force of the spreader piston on the collet on pressurization. The tensile pulse is produced by the friction of the retaining cylinder withdrawing over the collet. The subsequent compressive pulses are then created by the piston-loaded segments sliding outward and bottoming into the cavity to release the bolt. The stud is abruptly off-loaded when the piston is stroked to the right by the internal shoulder of the retainer cylinder. The housing experiences the small compressive pulse due to a pressurization force to the right, followed by the tensile pulse produced by the reaction to the friction resistance in forcing the retaining cylinder to the right. The next compressive pulse is the reac

tion to the loading of the collet by the piston. The remaining compressive pulse can be attributed to the deceleration of the retaining cylinder and piston within the housing by the residual gas from the cartridge. The bars swung apart approximately 10.16 cm (4 in.) on functioning.

Low-Shock Design 3.- See figure 7 for the cross section and figure 15 for the functional histories. The initial tensile indication on the stud is due to the movement of the retaining cylinder to the right. The hinging piston applies the major compressive load, which is quickly converted to tension when the retaining cylinder's recessed area impacts the projection of the collet. The second compressive pulse can be attributed to the forcing of the combination of hinging piston, retaining cylinder, and collet to the left, and applying a compressive load against the stud. The initial tensile load produced by the housing can be attributed to the reaction to the retaining cylinder's motion to the right. The compressive pulse is the reaction to the loading of the collet. On release of the bolt, the housing load would remain compressive during the deceleration and reversal of the piston/cylinder. A positive pulse would be produced on the impacting of the piston/cylinder against the bottom of the housing. The bars were observed to swing apart approximately 20.32 cm (8 in.) on functioning.

Low-Shock Design 4.- See figure 8 for the cross section and figure 16 for the functional histories. The loads by the converging retaining cylinders coupled into the collet, and transferred into the stud, are essentially balanced. The compressive load may be attributable to the relaxation of the long-length stud on release. The major identifiable load produced by the housing is compressive, possibly caused by a pressurization of the port volumes. The force is appreciably higher as compared to the other nuts, due to the mounting of the bar into the nut cap rather than in a flange at its base. No separation motion of the monitoring bars was observed.

Performance Analysis

The functional performance comparisons are shown in figures 17 to 19. The shock spectral analyses are shown in figures 20 and 21.

The stud force and acceleration levels of the low-shock designs, as shown in figure 17, are appreciably lower than the levels produced by the standard designs. The contrasts in force levels are not reflected in the acceleration comparisons. The housing loads, shown in figure 18, of the low-shock designs are lower than for the standard units except for Low-Shock Design 3. However, the acceleration levels of the low-shock designs were considerably lower as shown in figure 19.

The impulsive loading performance for each nut type is compiled in table II. The highest impulse was produced by the noncaptive nut, since a single 14.33-kg (31.6-lb) bar was swung 25.4 cm (10 in.) (a height change of 2.13 cm (0.84 in.)). The impulse produced by the remaining nuts was delivered to two bars, producing considerably less height change. The total impulse delivered by the nuts can be directly related to the integral of the force-time curves delivered into each bar. Although the peak stud loads of Standard Design 2 are more than 16 times those of Low-Shock Design 3, the total impulsive loads are the same. Obviously,

the least-shock-producing method of delivering an impulse to achieve a desired separation of interfaces is to apply lower level loads over a longer time interval.

The stud performance spectra in figure 20 indicate that energy levels are present to 40 kHz. The highest response was produced by Standard Design 2, particularly at high frequencies. The lowest response was produced by Low-Shock Design 4 whose primary content is above 4 kHz.

The housing performance spectra (fig. 21) are not so clearly differentiated as the stud performance (fig. 20). The acceleration spectra indicate Low-Shock Design 1 to produce the highest levels at frequencies to 1000 Hz.

Stud Performance

The force performances of the five separation nuts using a free stud, compared to using a two-bar monitoring system, are shown in figures 22 to 26.

The initial tensile loads, produced by pressurization of the nut body and the forces necessary to overcome friction in the retaining cylinder withdrawal, were considerably increased for all nuts; the increases ranged from two to six times the loads observed in the two-bar system. Although the amplitudes were higher, the performance histories from the free-stud functionings are very similar to the performances from the two-bar systems.

The secondary loads of Standard Design 1 and Low-Shock Designs 1 and 4 produced by the actuation of separation mechanisms or decelerating masses were appreciably increased. However, the secondary loads produced by Low-Shock Designs 2 and 3 in the free-stud setup, although somewhat different in shape, were essentially the same as for the two-bar system.

The force-performance differences and similarities can be attributed to the manner in which the nuts' internal components couple loads to the surrounding structure and dissipate their energy. The increased loads were caused by a lack of coupling into the stud monitoring bar. The lack of increased loads indicates that the mechanisms of internal energy dissipation were not appreciably changed.

The velocities of the studs achieved on functioning the nuts varied from zero to 2.80 m/sec (9.2 ft/sec) and are shown in table II.

Effect of Torque

The force-performance histories of the four separation nuts torqued to higher levels are shown in figures 27 to 30. The performances of the noncapitive nut, Standard Design 1, and Low-Shock Design 1 are essentially the same within normal functional variations. However, the loads in the Low-Shock Design 4 were considerably increased. Since the only force required to achieve separation in Low-Shock Design 4 is that of moving the small-mass retaining

cylinders, an increase in friction caused by an increase in torque level would significantly affect the force to initiate and stop this motion.

Effects on Spacecraft

This study has produced several significant points of information for consideration by a spacecraft systems designer in the application of pyrotechnic separation nuts.

Pyrotechnic separation nuts can be produced that generate low-shock outputs on functioning. The low-shock nuts evaluated in this study are in various stages of development and have yet to be applied to any aerospace program. Some penalties may be introduced in these low-shock nut designs in increased weight, volume, and complexity of the release mechanism over the existing commonly used pyrotechnic separation nuts. Also, each of the nuts can be designed to contain two gas-generating cartridges as an approach to redundancy. Should both cartridges be functioned simultaneously to achieve actuation, considerably higher shock loads would be produced, since internal pressures could be doubled, yielding considerably higher forces. To maintain minimal shock loading, the second cartridge should be functioned only if the first failed to achieve separation. Further, care should be taken to avoid sympathetic ignition between cartridges; that is, the second cartridge should be sufficiently protected to prevent ignition by the hot gases produced by the first cartridge.

Due to relative loads induced into the stud and housing on actuation of these low-shock nuts, some decisions should be made on physical mounting and attachment. Peak shock loads are reduced significantly on rut actuation by providing maximum coupling of loads to structure on both sides of the separations plane; that is, with the housing and stud rigidly attached to the structure. Shock loads are increased in the nut housing by a freely moving stud. Little or no impulsive loading is introduced into a rigidly mounted stud by Low-Shock Designs 1 and 4 to accomplish separation. The impulsive loads in Low-Shock Designs 3 and 4 are insufficient to eject a stud that is free to move. The impulsive loads produced by the remaining nut designs can produce a desired separation of structure or stud ejection in a well-controlled manner. Also, lower-level shock loads are introduced into the stud side of the separation plane, as compared to the housing side, for Low-Shock Designs 3 and 4. The reverse is true for Low-Shock Designs 1 and 2. Finally, only Low-Shock Design 4 of the four tested (noncaptive, Standard 1, Low-Shock 1 and 4) exhibited any increase in shock levels due to an increase in torque level of the mounting stud.

Although the peak shock loads of the complex high-frequency pulses produced by these low-shock nuts are considerably less than for the standard designs, the question still remains as to what part of a spacecraft is affected, and to what degree. These shock loads are well below the elastic limit of metals and should have little effect on primary structure. The total impulsive load is small, since the pulse width is generally 1 millisecond or less. However, high-frequency shock loading of small-mass, flexible items, such as electronics, can produce significant effects. The high-frequency content of these pulses can be significantly decoupled and amplitudes lowered by interfaces, bolted or riveted joints, and low-density mounting pads on the electronic chassis, according to

current investigations accomplished by the Viking Project Office (NASA Langley Research Center). Experiments to investigate shock isolation of the nut body and interfaces have been unsuccessful, since the use of low-density materials prevents adequate mechanical linkage.

The dynamic analysis of spacecraft structure can be appreciably enhanced through the use of actual force time histories as well as through the current practice of using acceleration histories. However, the theoretical prediction of dynamic response of spacecraft to these high-frequency inputs is still a difficult problem area, because of the limitations of most computer programs for structural analysis. Spectral analyses of acceleration pulses do not compensate for phase and time relationships. The integration of acceleration signals to produce more useful force signals is difficult to accomplish electronically. Also, the dynamic response of strain-gage monitors is considerably better than that of acceleration monitors for this high-frequency environment. Finally, strain gages can be directly attached to a structure without modifying the structure or significantly increasing the mass of the structure as compared with the use of accelerometers.

CONCLUSIONS

The conclusions drawn from this study can be categorized into three areas: low-shock separation nuts, their relative effect on a spacecraft system, and monitoring systems.

Pyrotechnic separation nuts that generate a low mechanical shock on actuation can be produced. Four different separation nut designs were evaluated in this study, demonstrating a reduction in shock forces by factors from 10 to 100, as compared to a commonly used pyrotechnic separation nut. However, some penalties may be introduced in increased volume, weight, or complexity. The performance and physical characteristics of each nut are unique, each having its own advantages and disadvantages. Examples are: One type produces no separation forces but has a high weight; another produces low impulsive loads into a fixed stud but requires an increase in volume to function; and a third produces low impulse into a free stud but produces a higher level shock pulse. The selection of a particular nut on a spacecraft system must be predicted on the system-unique requirements.

To minimize the effects of the functioning of these nuts on the spacecraft system, their location and how they are installed should be predicated on the performances described above. Although the peak shock levels have been significantly reduced over commonly used designs, the short-duration, high-level, high-frequency shock pulse still remains complex. The shock output should have little or no influence on primary structure, but the effect on electrical or flexible components remains unknown. Fortunately, these high-frequency pulses can be effectively attenuated or reflected through the use of interfaces and low-density isolation materials.

The use of strain-gage monitoring systems offers several advantages over the use of conventional acceleration monitoring techniques. Strain gages can

monitor the shock pulses more accurately, have less effect on the structure, and produce information that is more useful for structural analyses than do accelerometers. However, this is not a recommendation to exclude the use of accelerometers. Within the limitations of accelerometers, the data produced are complementary to that produced by strain gages, particularly in complex structures. The simplified-structure monitoring system used in this study has been demonstrated to be an accurate performance-comparison technique for separation nuts. The performance data can be related to actual spacecraft systems.

TABLE I.- NUMBER AND TYPE OF NUTS TESTED PER CATEGORY

Nut type	Performance comparisons	Stud performance	Torque effect
Standard Design 1	6	1	1
Standard Design 2	6	1	1
Low-Shock Design 1	6	1	1
Low-Shock Design 2	1	1	
Low-Shock Design 3	1	1	
Low-Shock Design 4	6	1	1
Noncaptive nut			1

TABLE II.- IMPULSE PERFORMANCE COMPARISONS

Nut type	Two-bar system		Single-bar, free-stud system	
	Displacement, cm (in.)	Energy, Nm (in-lb)	Ejection velocity, m/sec (ft/sec)	Energy, Nm (in-lb)
Noncaptive	*25.4 (10)	2.99 (26.5)		
Standard Design 1	15.24 (6)	.27 (2.4)	2.80 (9.2)	0.136 (1.2)
Standard Design 2	20.32 (8)	.47 (4.2)		
Low-Shock Design 1	None	None	1.34 (4.4)	.031 (.27)
Low-Shock Design 2	10.16 (4)	.12 (1.1)	2.07 (6.8)	.073 (.65)
Low-Shock Design 3	20.32 (8)	.47 (4.2)	**1.27 (.5) motion	None
Low-Shock Design 4	None	None	**.635 (.25) motion	None

*Single-bar displacement.

**Not ejected.

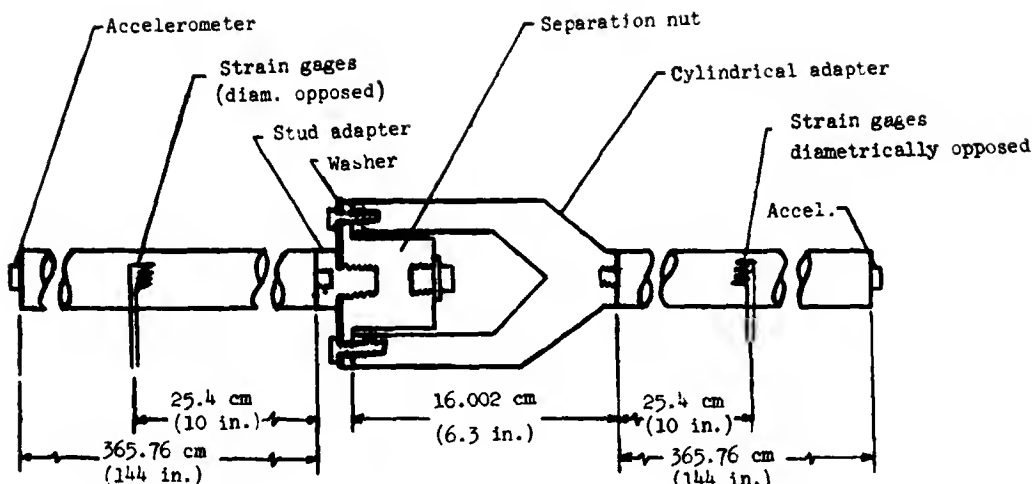


Figure 1.- Cross section of shock monitoring apparatus.

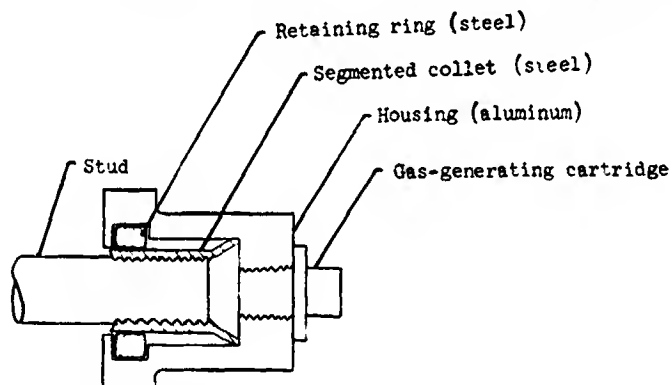


Figure 2.- Cross section of noncaptive separation nut.

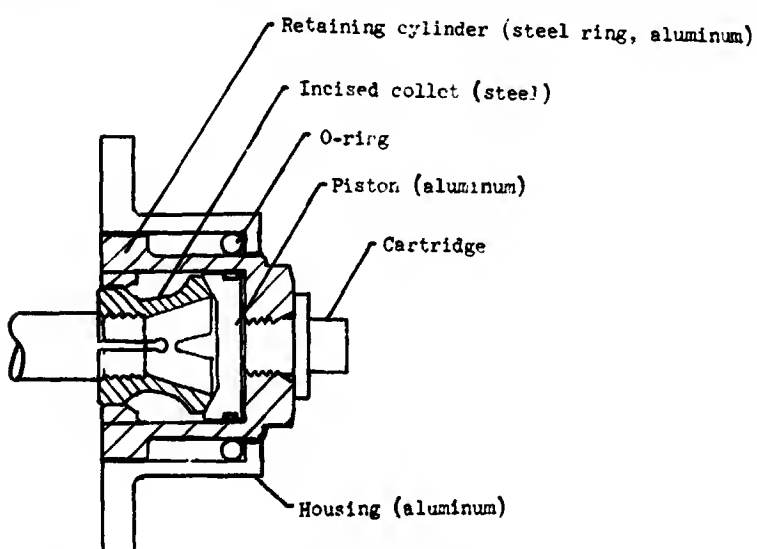


Figure 3.- Cross section of Standard Design 1.

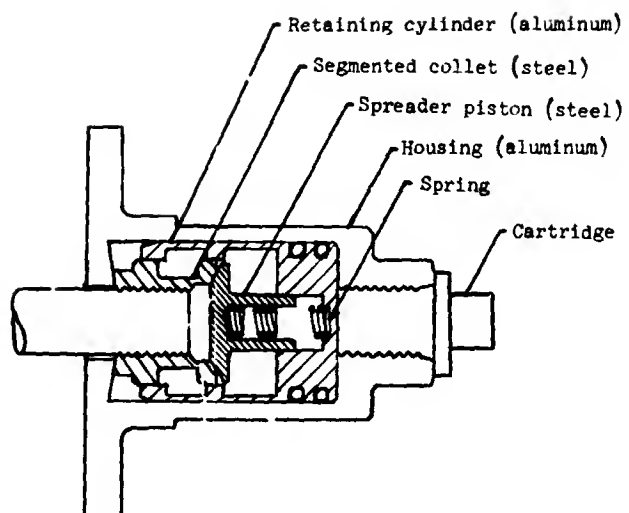


Figure 4.- Cross section of Standard Design 2.

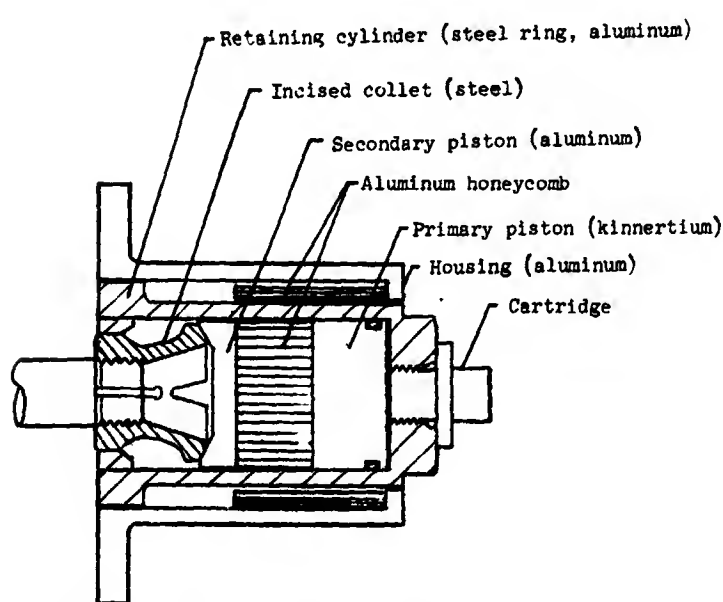


Figure 5.- Cross section of Low-Shock Design 1.

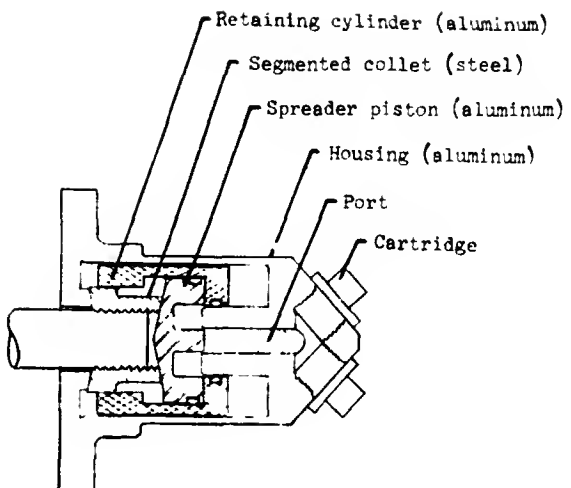


Figure 6.- Cross section of Low-Shock Design 2.

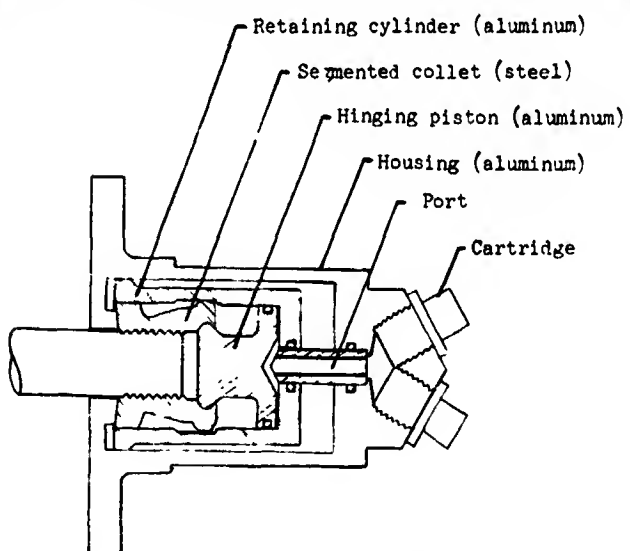


Figure 7.- Cross section of Low-Shock Design 3.

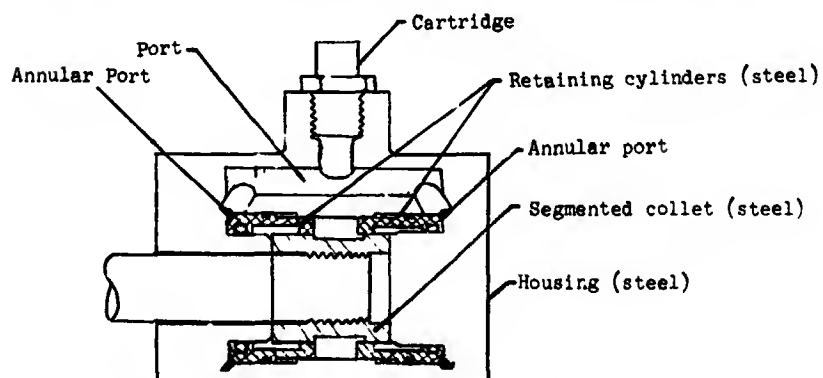
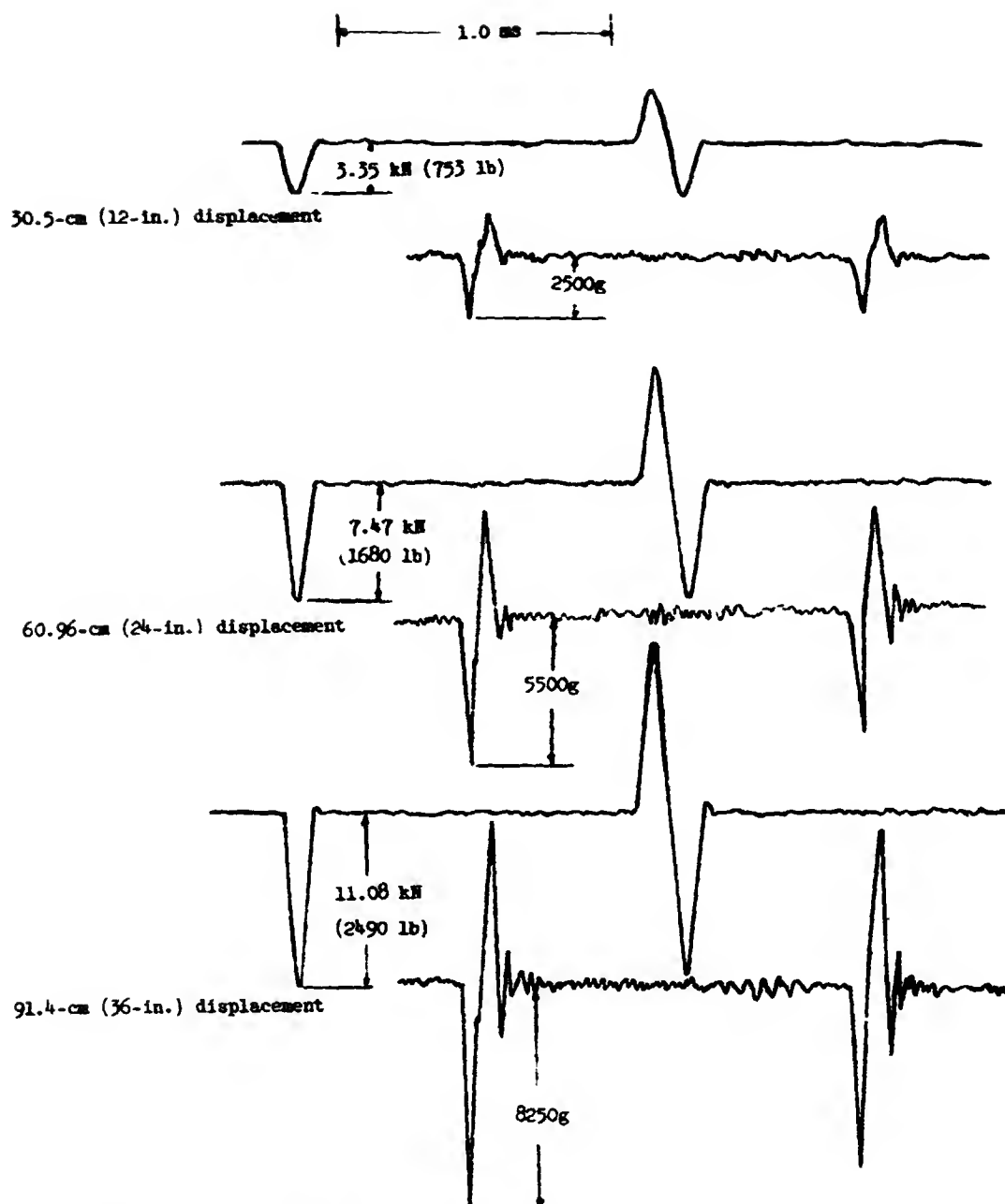


Figure 8.- Cross section of Low-Shock Design 4.



**Figure 9.- Force and acceleration performance of 3.18-cm (1.25-in.) steel ball; impacts at horizontal displacements indicated.
($1g = 9.807 \text{ m/sec}^2$.)**

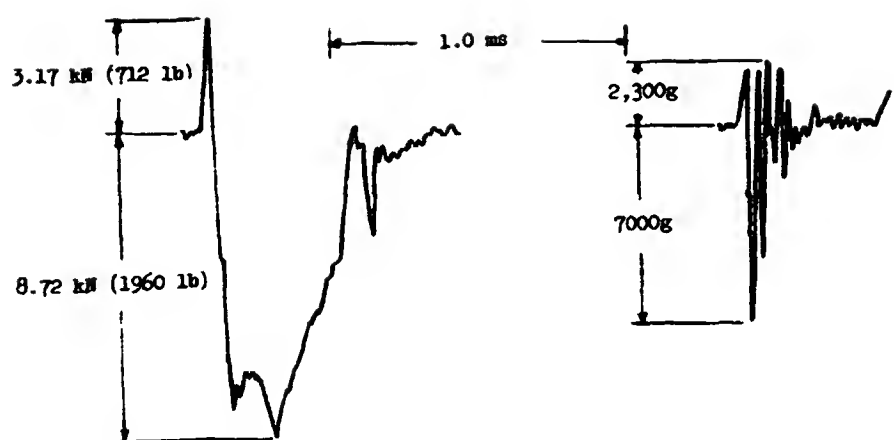
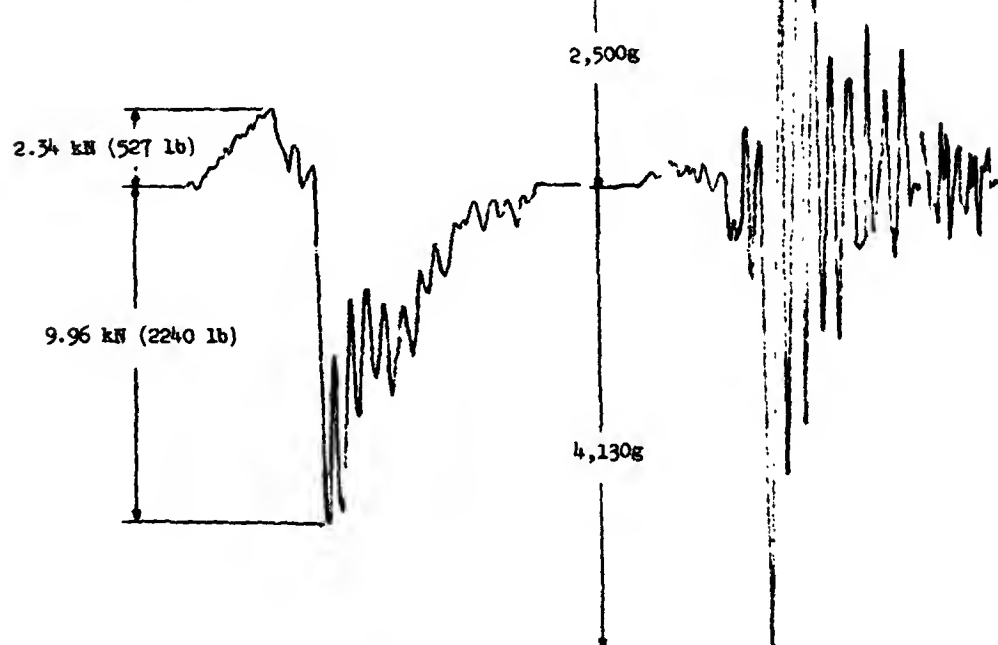
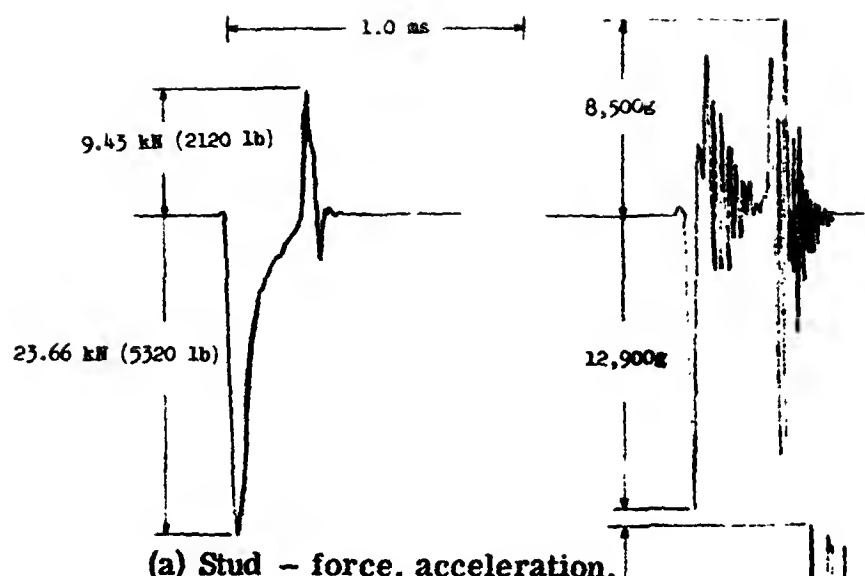


Figure 10.- Force and acceleration performance of noncaptive nut.



(b) Housing - force, acceleration.

Figure 11.- Force and acceleration performance of Standard Design 1.

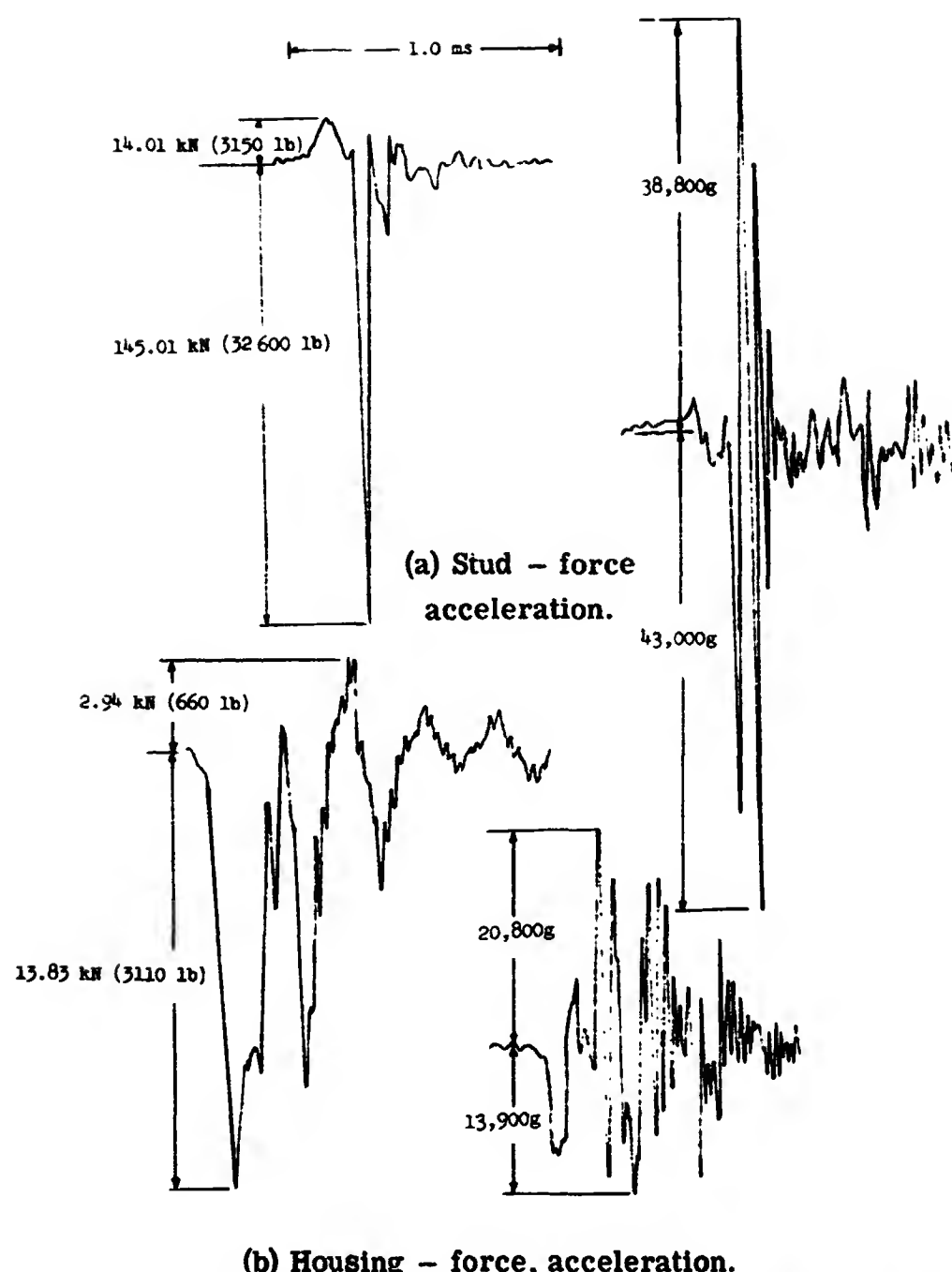
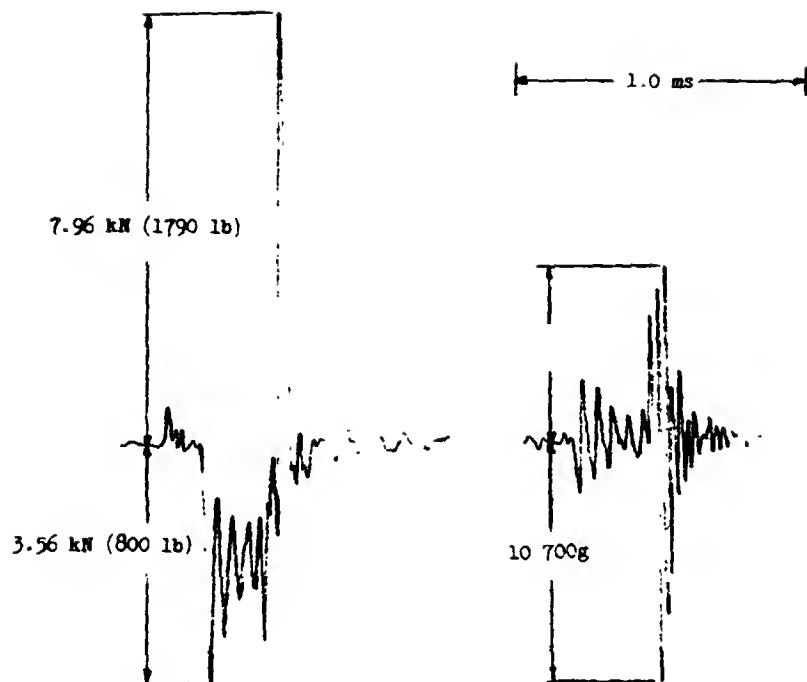
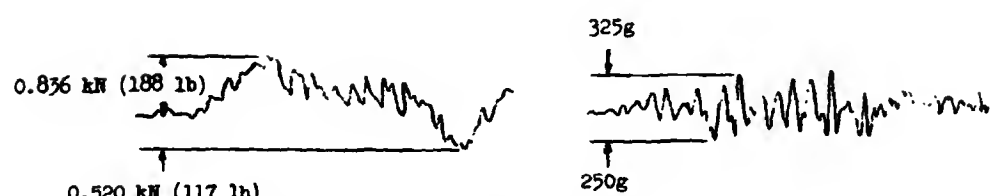


Figure 12.- Force and acceleration performance of Standard Design 2.

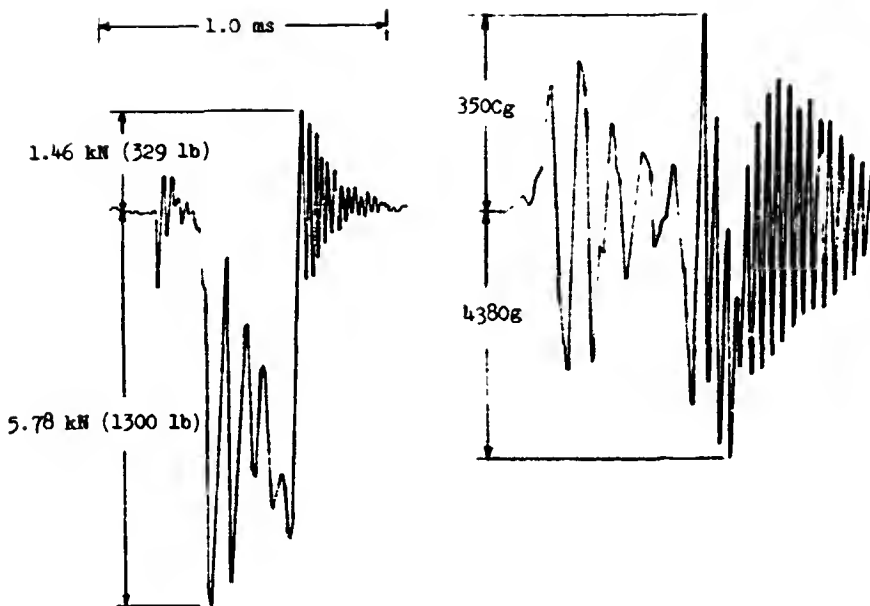


(a) Stud - force, acceleration.

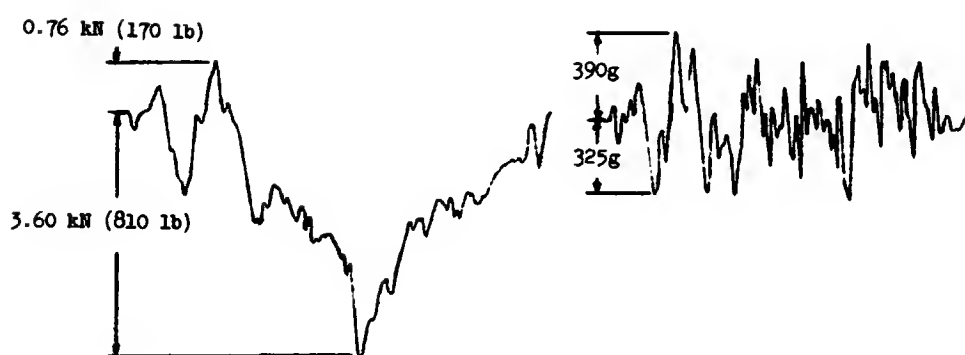


(b) Housing - force, acceleration.

Figure 13.- Force and acceleration performance of Low-Shock Design 1.



(a) Stud - force, acceleration.



(b) Housing - force, acceleration.

Figure 14.- Force and acceleration performance of Low-Shock Design 2.

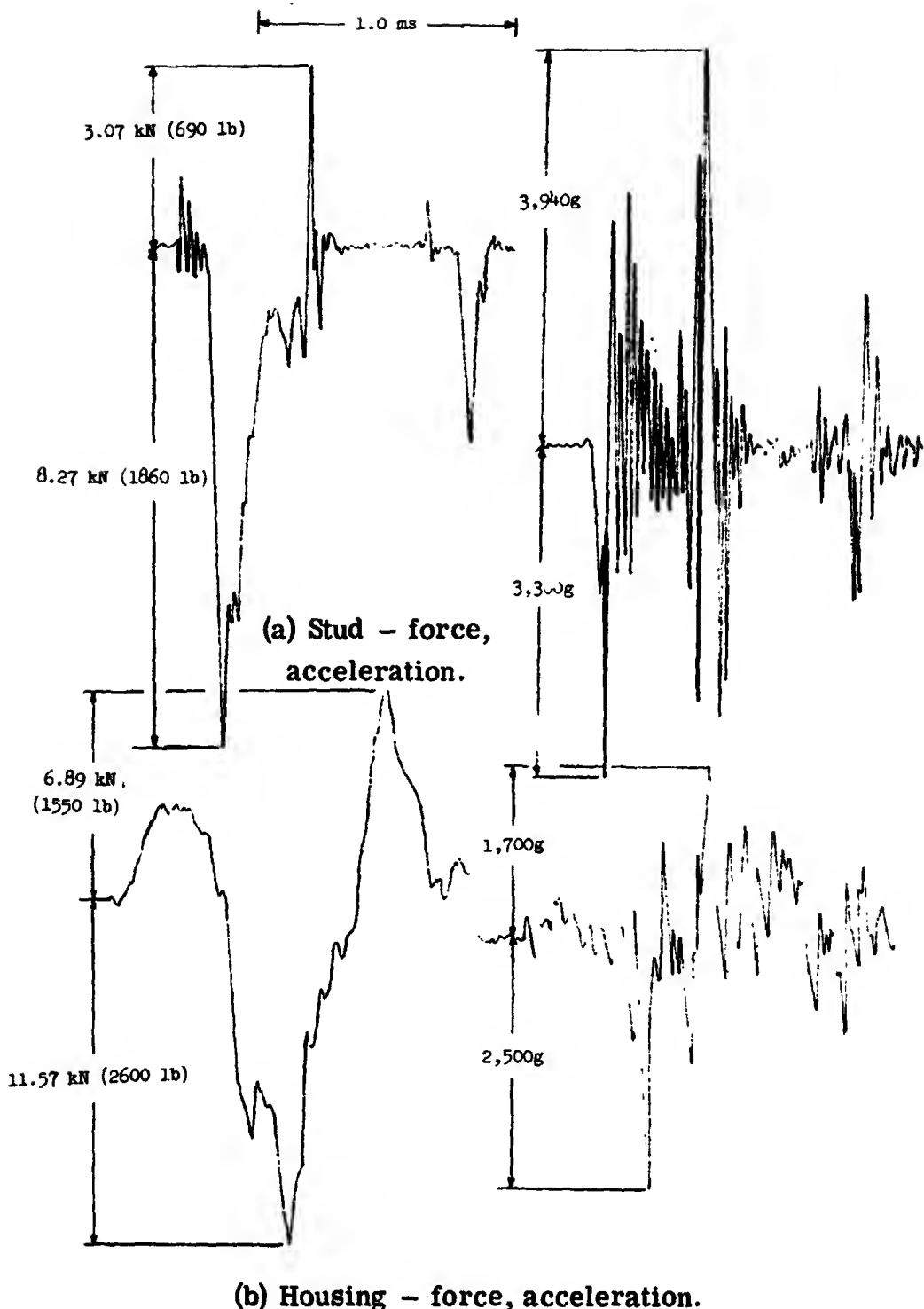


Figure 15.- Force and acceleration performance of Low-Shock Design 3.

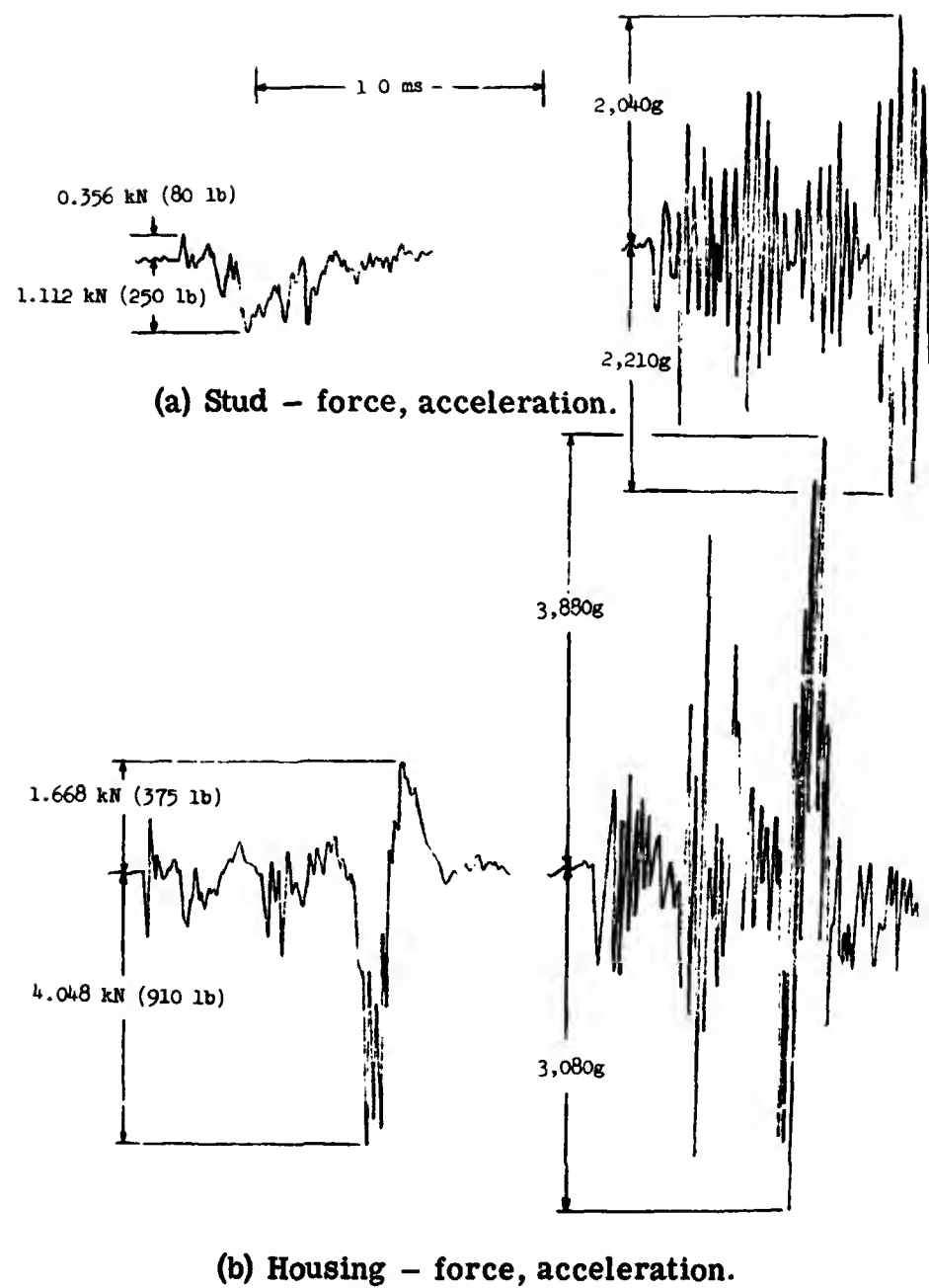


Figure 16.- Force and acceleration performance of Low-Shock Design 4.

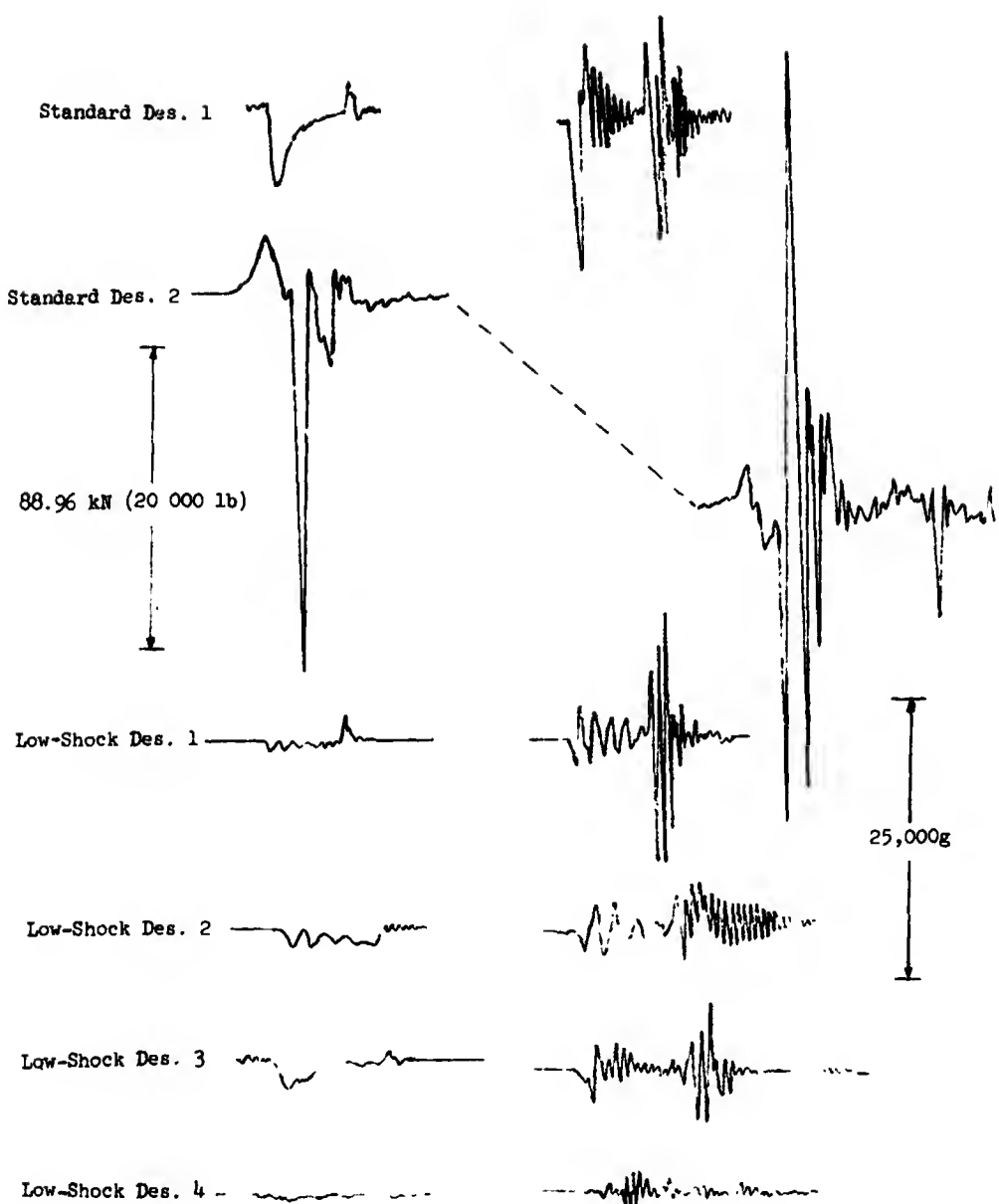


Figure 17.- Stud force and acceleration performance comparison of six separation nuts.

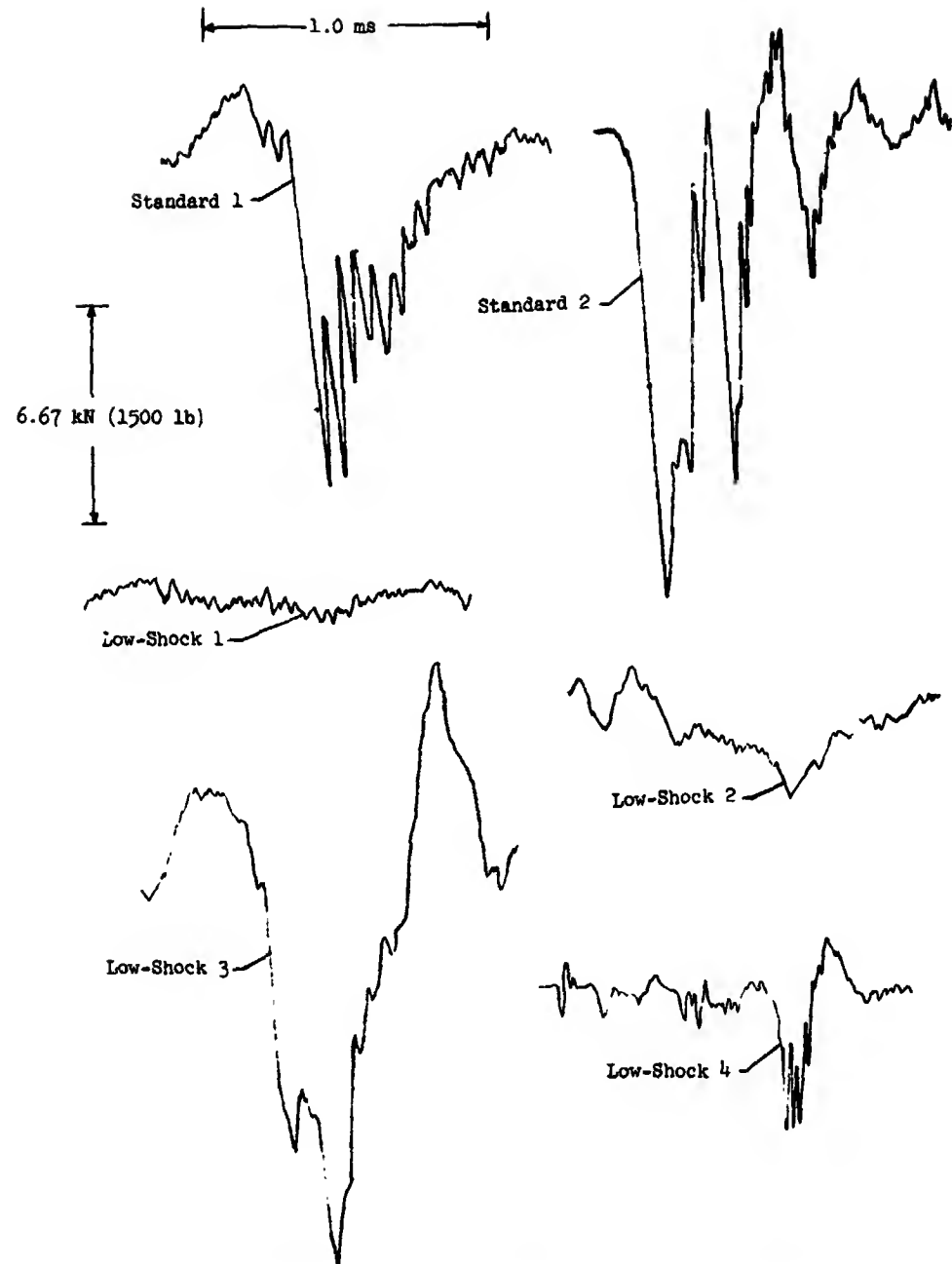


Figure 18.- Housing force comparison of six separation nuts.

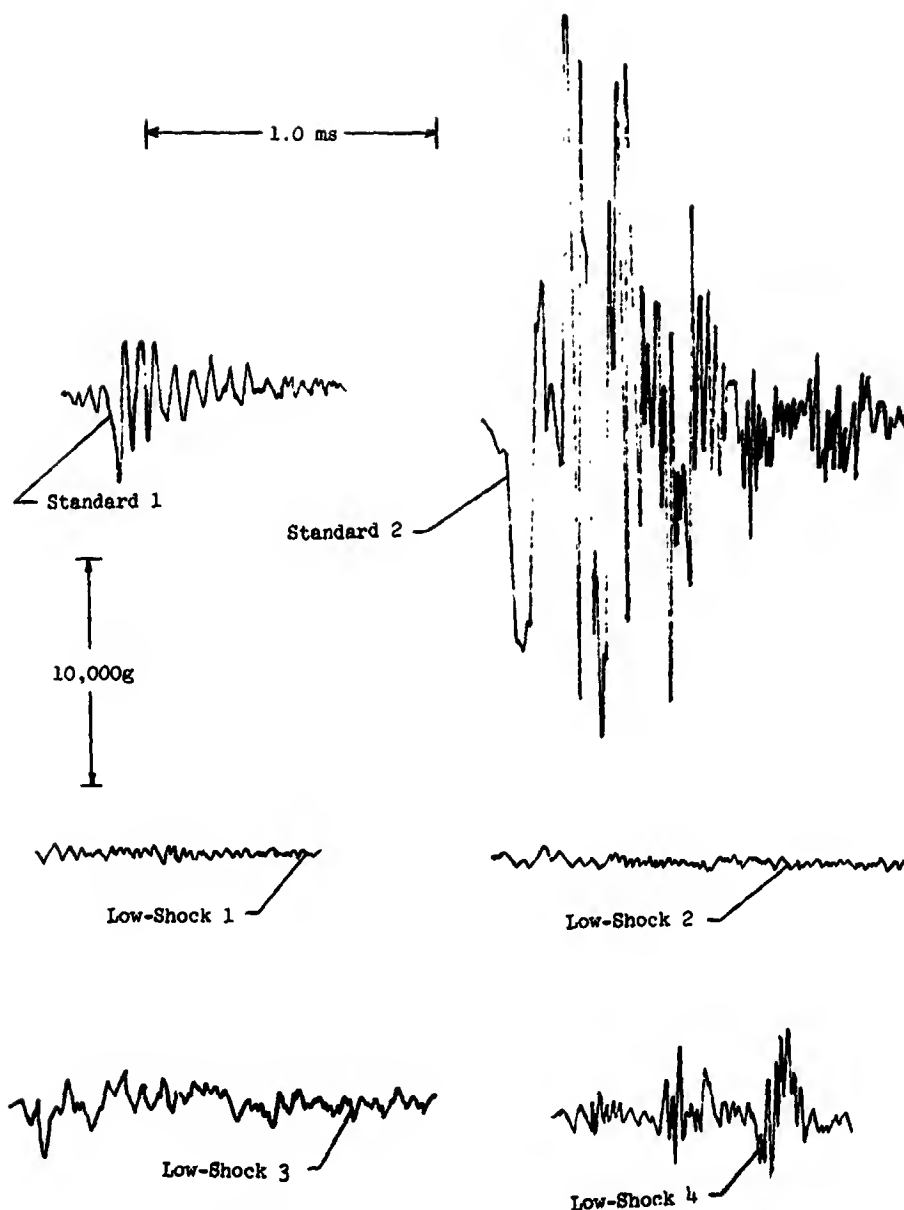


Figure 19.- Housing acceleration comparison of six separation nuts.

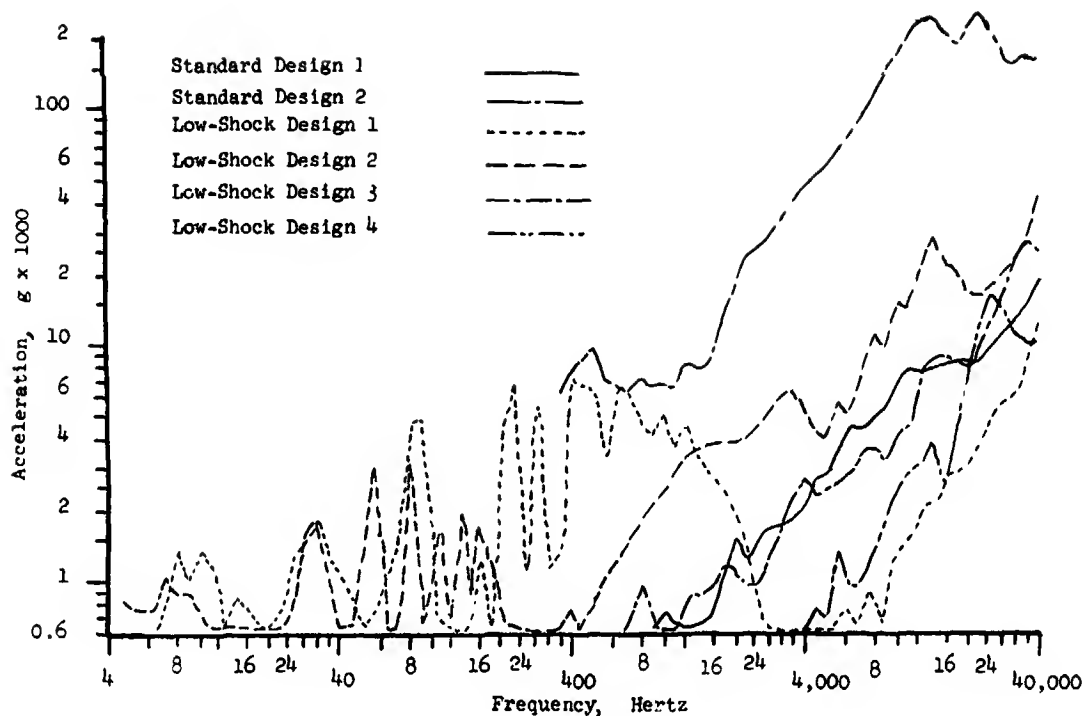


Figure 20.- Stud performance spectra comparison.

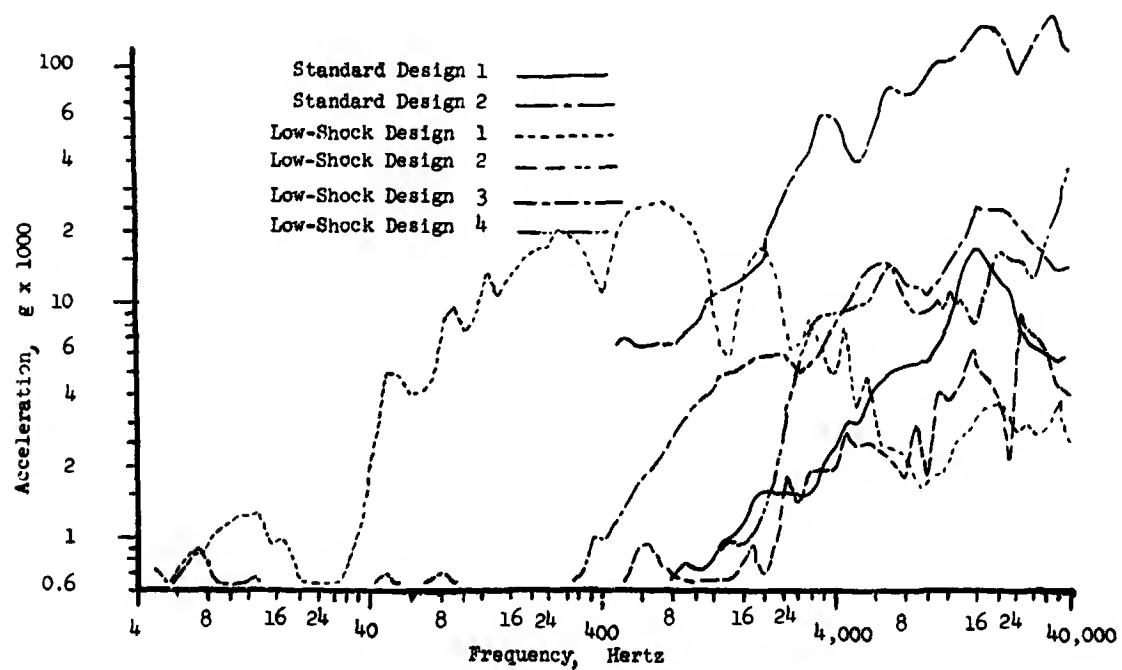


Figure 21.- Housing performance spectra.

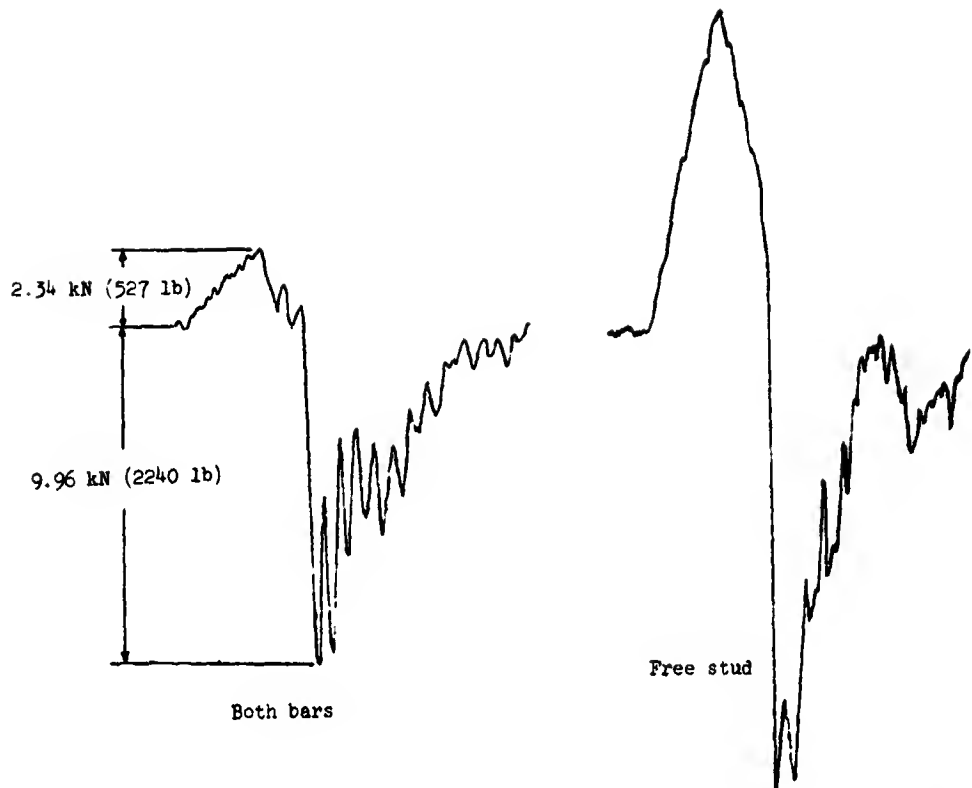


Figure 22.- Housing force performance comparison between using both bars and a free-stud (single bar) of Standard Design 1.

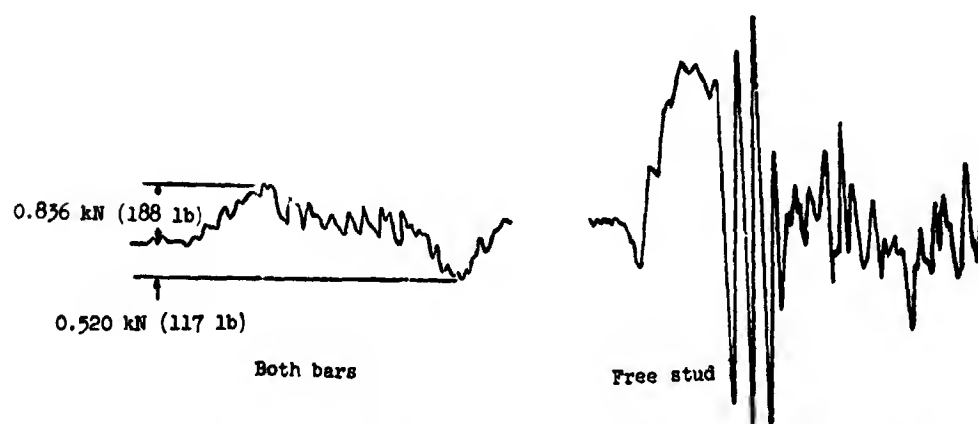


Figure 23.- Housing force performance comparison between using both bars and a free-stud (single bar) of Low-Shock Design 1.

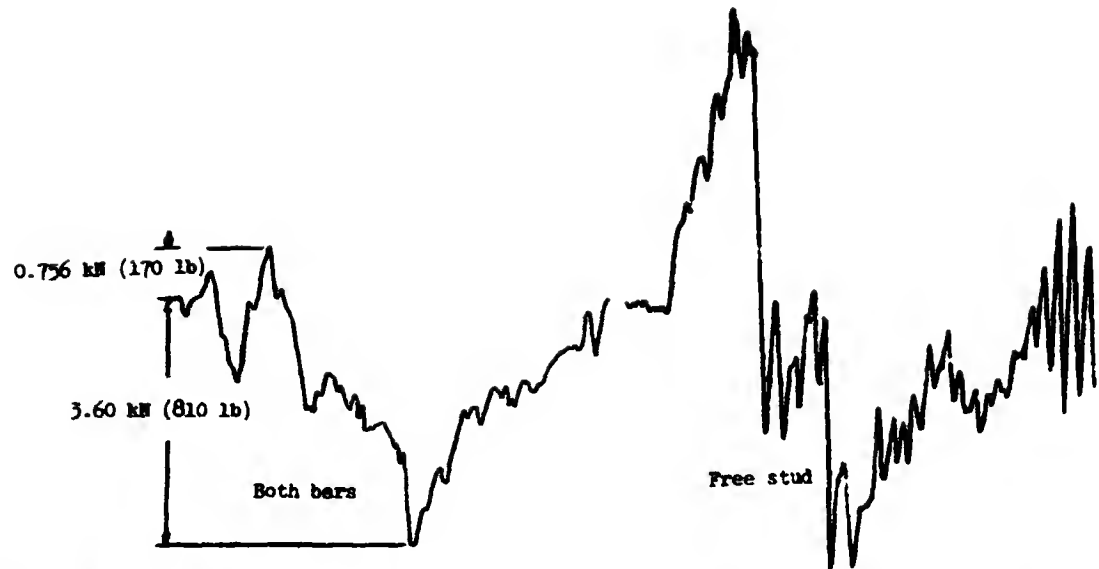


Figure 24.- Housing force performance comparison between two bars and a free-stud (single bar) of Low-Shock Design 2.

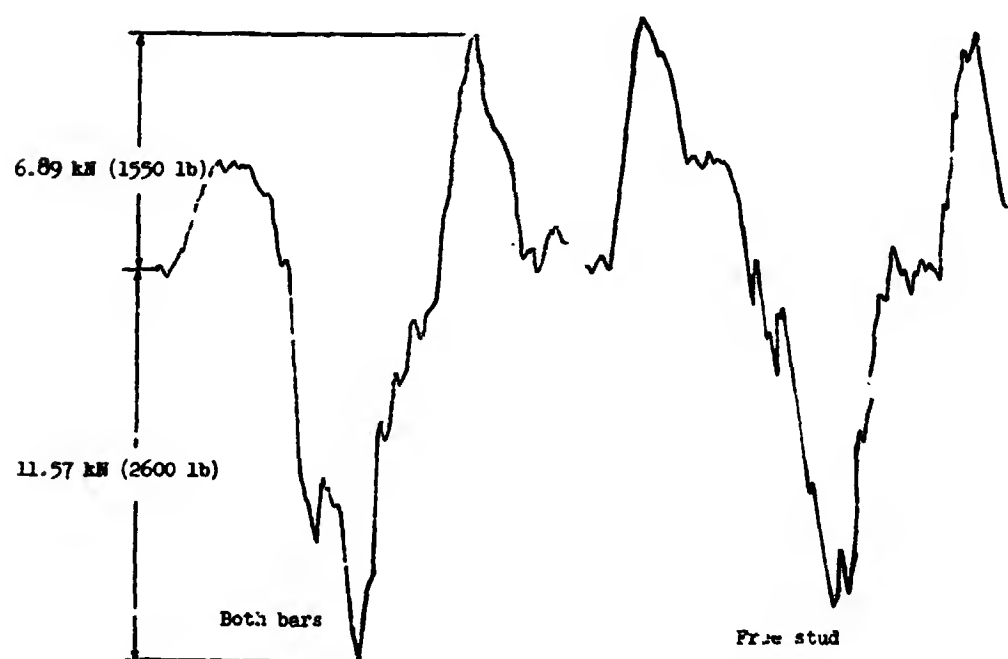


Figure 25.- Housing force performance comparison between two bars and a free-stud (single bar) of Low-Shock Design 3.

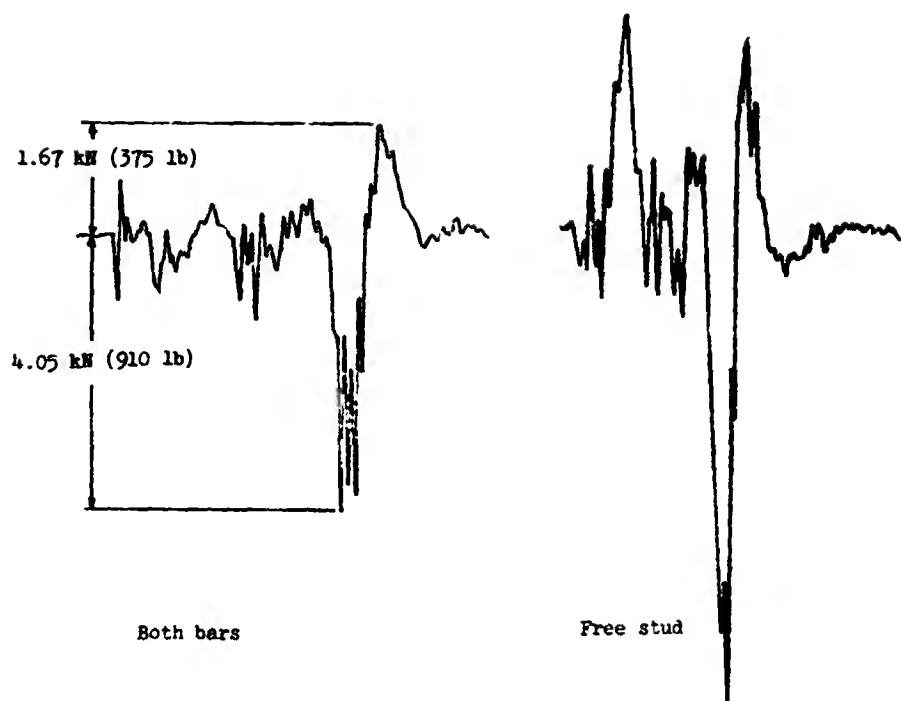


Figure 26.- Housing force performance comparison between two bars and a free-stud (single bar) of Low-Shock Design 4.

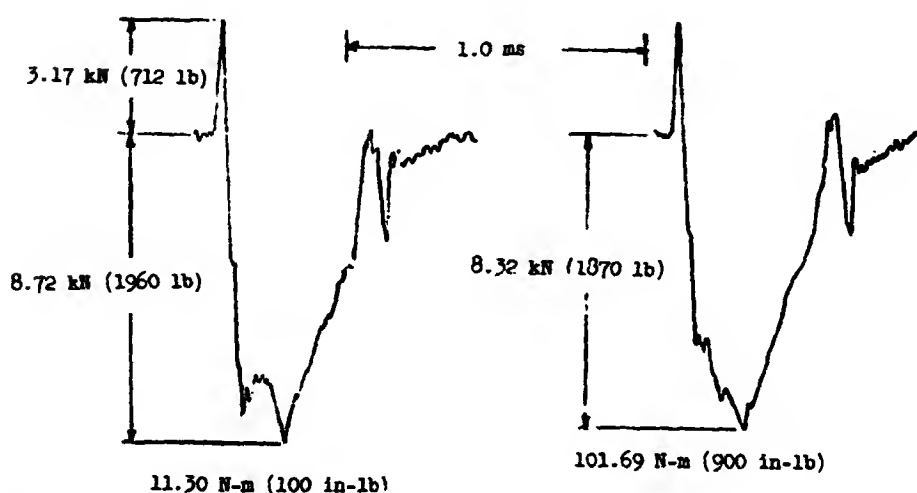
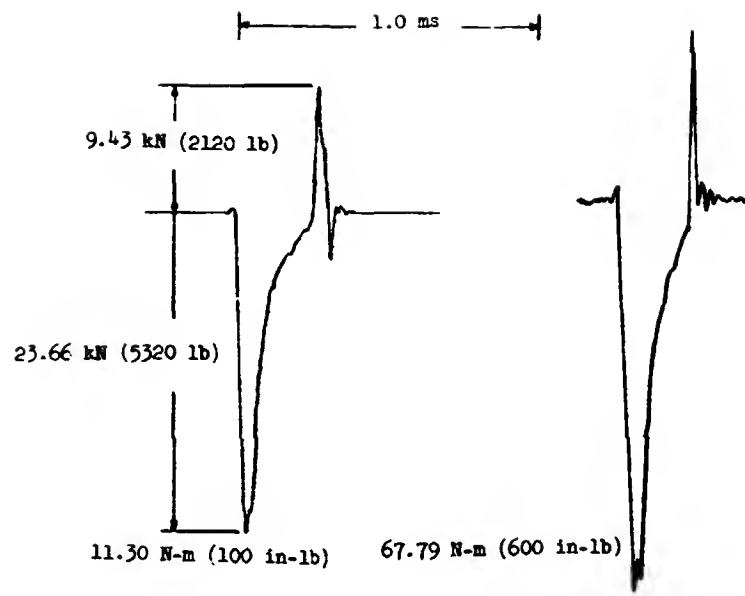
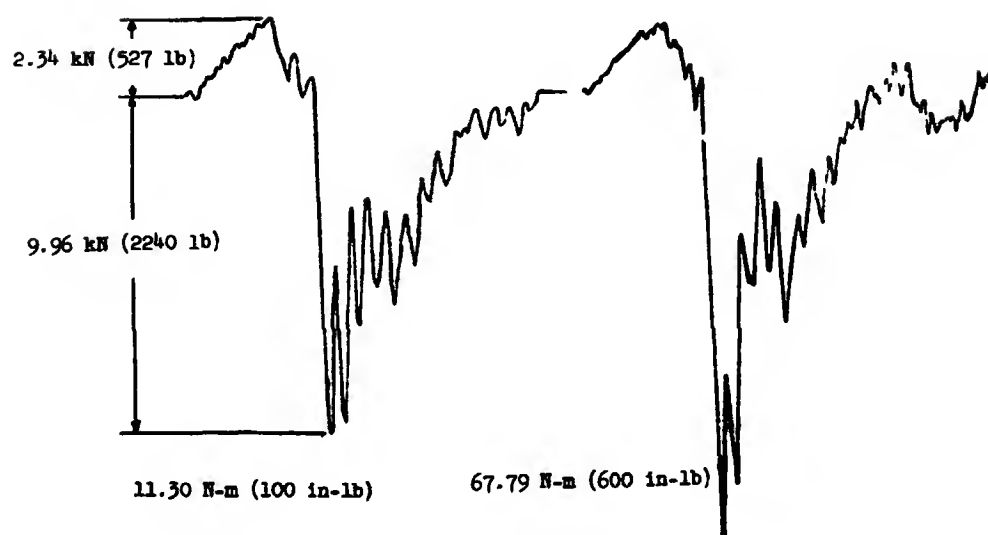


Figure 27.- Comparison of stud force performance for noncaptive nut at torque levels of 11.30 N·m (100 in-lb) and 101.69 N·m (900 in-lb).

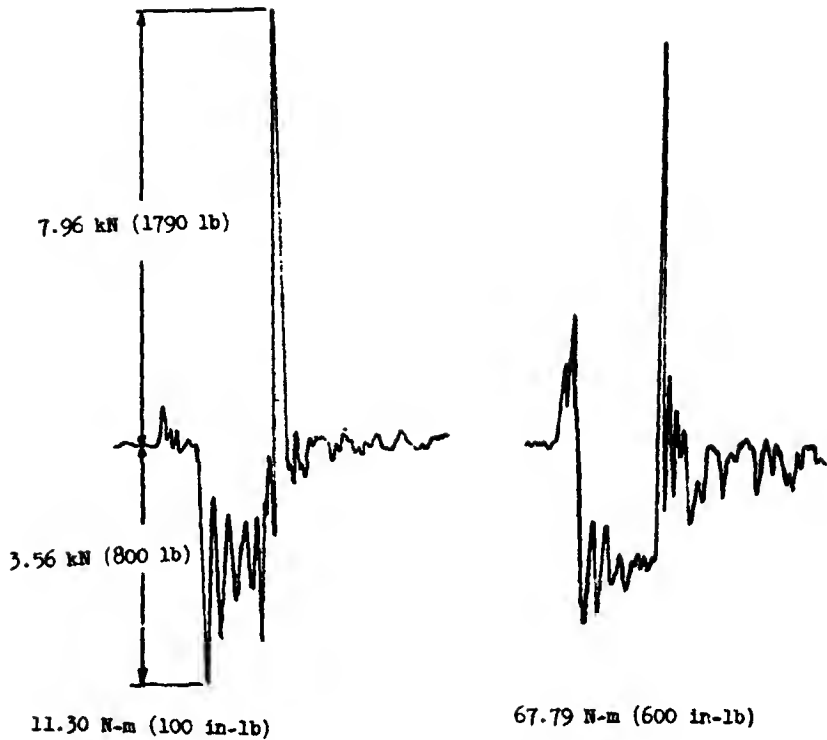


(a) Stud monitor.



(b) Housing monitor.

Figure 28.- Comparison of force performances for Standard Design 1 at torque levels of 11.30 N·m (100 in-lb) and 67.79 N·m (600 in-lb).

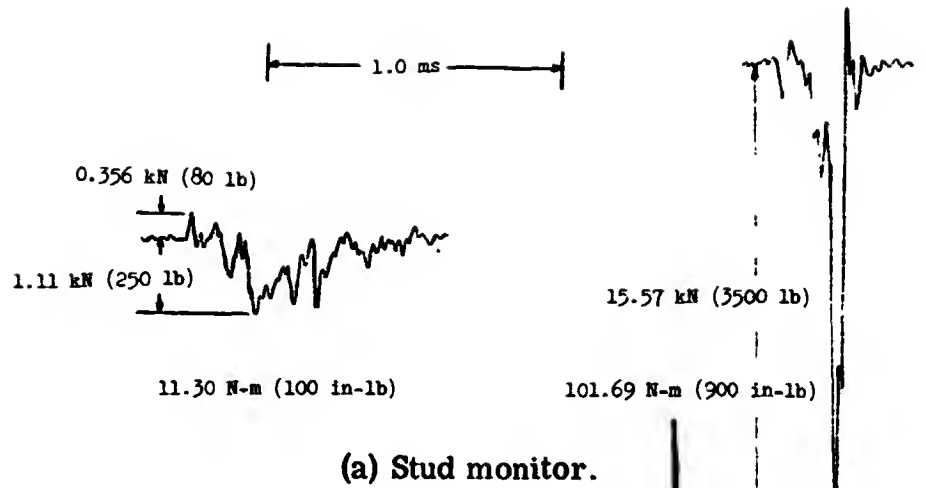


(a) Stud monitor.

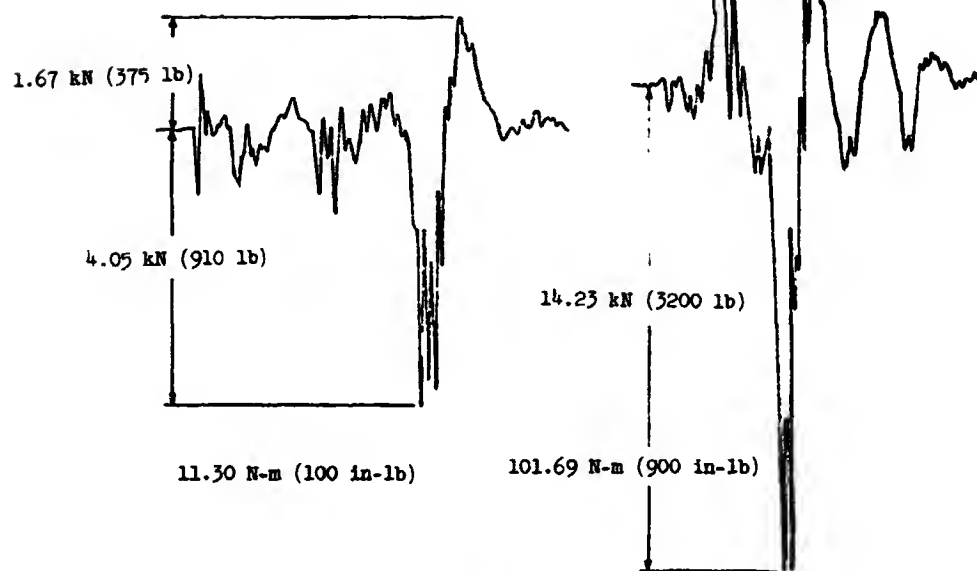


(b) Housing monitor.

Figure 29.- Comparison of force performances for Low-Shock Design 1 at torque levels of 11.30 N·m (100 in-lb) and 67.79 N·m (600 in-lb).



(a) Stud monitor.



(b) Housing monitor.

Figure 30.- Comparison of force performances for Low-Shock Design 4 at torque levels of 11.30 N·m (100 in-lb) and 101.69 N·m (900 in-lb).

17. ROCKET ENGINE BIPROPELLANT VALVE PROBLEMS AND CURRENT EFFORTS

by Joseph Fries

NASA Johnson Space Center

SUMMARY

In developing the highly successful bipropellant valves for the Apollo primary propulsion engines, a variety of developmental problems were encountered and resolved. These problems and the new technology that is being pursued to eliminate or minimize these problems on the Space Shuttle Orbital Maneuvering Engine are discussed. The Space Shuttle, being a reusable system, has new requirements of the valve. The potential effects of these requirements on valve design and potential solutions are also discussed.

INTRODUCTION

The bipropellant valves, developed for the Apollo primary propulsion engines (Ascent, Descent, and Service Propulsion Systems) were quad-redundant ball valves. The Ascent and Descent engine valves were actuated with fuel and the Service Propulsion System engine valve was pneumatically actuated. The propellants used are earth storable and hypergolic. The fuel, Aerozine 50, is a 50% blend by weight of unsymmetrical dimethylhydrazine and 50% anhydrous hydrazine. The oxidizer is nitrogen tetroxide (N_2O_4). Problem areas in these valves included the actuation system², shaft seals, primary seals, filters, position indicators, wiring harness, housing, material incompatibility, lubricants, contamination sensitivity and formation of salts. While these problems were eventually solved and the valves performed well during the Apollo missions, the long life, reusability and maintainability requirements of the Space Shuttle place additional stress on the valves. Several companies are investigating improved valve designs.

Apollo Valve Development Problems

The Apollo primary propulsion system valves shared many similar development problems. These problems can be categorized into a few broad areas. First, there were the failures due to sliding seals. The sliding seals are in three areas: the ball element seal or primary seal; the shaft seal or secondary seal; and the actuator piston seal.

The primary seal in each of the valves was in contact with the ball at all times; subsequently, when the ball was rotated to open or close the valve, the seal would slide on the ball. The continuous sliding resulted in excessive leakage due to wear of the seal, contamination generated by the wear process, scratching of the seal by deposits on the element, and nipping of the seal as the flow bore passed the seal.

The primary seal on each of the valves was TFE Teflon. The wear of these seals was most evident when the valves were dry cycled. When the valves were cycled dry, the Teflon would abrade and abraded particles would lodge between the ball and the seal. The mechanisms responsible for the wear of the Teflon are not fully understood but it is generally thought that adhesion and freeing of the transferred fragments, either in terms of surface energy or by virtue of fatigue, are of major importance. It is known that when the TFE Teflon is rubbed against other materials, a transfer of layers of materials takes place. It is believed that the wear process involves the laying down and subsequent removal of such transferred layers.

To minimize this problem, the rate at which the valves were dry cycled was reduced. The reduced cycle rate did not eliminate the problem but did minimize it.

Scratching of the seals occurred because of salts forming on the ball element. The salts that formed on the balls were aluminum and ammonium nitrates and were found only in the oxidizer system. Several factors that influence the formation of salts in the oxidizer system are: moisture in the system, where the moisture emanates from both the atmosphere and from the N_2O_4 ; aluminum used in the N_2O_4 system; the absorption and subsequent outgassing of the N_2O_4 from the Teflon seals; and the migration of fuel vapors to the oxidizer system. The scratching of the seal by the salts occurs after the salts form on the ball and the ball is rotated.

Nipping of the primary seals occurred because of sharp edged flow bores and extended lips of the primary seals. This problem was eliminated by redesigning these areas. The redesigns minimized the lip length of the seals and made larger radii on the flow bores.

The shaft seals used in the Apollo primary propulsion system valves were Teflon lip seals and Teflon Omnisseals. In one system the Teflon lip seal was backed by a redundant KEL-F lip seal.

Problems encountered included leakage caused by contamination, incompatible materials, and permeation. A majority of these problems occurred in the N₂O₄ system. In one system contamination was generated by corrosion²⁴ of an aluminum shaft seal vent line on the N₂O₄ side of the valve. This contamination subsequently damaged the shaft seal. The KEL-F lip seal presented a problem because KEL-F is incompatible with N₂O₄. The permeation of N₂O₄ through Teflon shaft seals resulted in failure of one of the Apollo valves to actuate due to the reaction with the lubricant in the actuation system drive train and subsequent jamming of the drive train. The permeation occurred during a long term compatibility test and was not considered to be an operational problem.

The actuator piston seals in the Apollo primary propulsion system valves were sliding seals which were a source of problems. One problem was caused by differential expansion between a plastic headed actuator piston and its aluminum housing. This resulted in excessive leakage past the piston. Another problem was the scoring of the actuator piston cavity due to cocking of the piston. In one system, an o-ring intended to be used in a static application was used as the dynamic actuator piston seal. Movement of the piston, for actuation, caused the o-ring to twist. The twisting of the o-ring resulted in excessive checkout fluid (gaseous nitrogen) leakage; however, the actual operating fluid (fuel) did not leak past the seal.

Other categories of development problems encountered were pilot valve leakage, erroneous position switch output, low electrical resistances, sluggish operation, hang-up, filter collapse, and disconnect leakage. A summary of these problems is presented in table 1.

SPACE SHUTTLE ORBITAL MANEUVERING ENGINE VALVE TECHNOLOGY

BACKGROUND

The OMS (Orbital Maneuvering System) of the Space Shuttle is similar to the Apollo propulsion systems and will be a pressure fed rocket propulsion system utilizing helium pressurant and nitrogen tetroxide and hydrazine base earth storable propellants. The existing Apollo propellant shutoff valves and actuation systems were designed for single mission usage and, along with less serious deficiencies, are not sufficiently contamination tolerant or propellant compatible to economically and reliably satisfy the Space Shuttle requirements for reusability and extended life.

REQUIREMENTS

Requirements were established for the valve technology of the OME (orbital maneuvering engine). These requirements are not considered to be firm but are to be used as design goals with emphasis on establishing realistic requirements. Table 2 presents the requirements, or design goals, as defined for the OME valve and actuation system.

The impact of these requirements as related to the long life and reusability of the Space Shuttle is summarized in table 3.

APPROACH TO ELIMINATE PROBLEMS

From the discussion of the Apollo valve development problems and the potential problem areas imposed by the long life and reusability requirements of the Space Shuttle, a fresh approach must be taken in the OME valve design. Recommended design practices are presented in table 4.

TECHNOLOGY CONCEPTS

As a result of the current technology efforts, two primary concepts for the OME valve and actuation system have evolved. The first, as shown in figure 1, is referred to as a "moving seat" poppet valve. The actuation system is a brushless direct current motor. In this concept, the valve poppet is stationary. The valve is opened by deflecting the seat. The actuator is located outside of the flow path and connects to the outside of the seat housing. The bellows, as incorporated in the design of this valve, have three purposes. First, to open the valve, they allow the seat to be deflected with respect to the poppet. Second, they provide a hermetic seal between the propellant and actuator. Third, they pressure balance the poppet valve. This minimizes the forces required for actuation.

Key features of this concept are as follows:

1. Streamlined flow path, which is easily decontaminated.
2. Inherent hermetic seal between the actuator mechanism and propellant.
3. Low operating force due to inherent pressure balance, thereby reducing actuation force and power requirements.
4. No sliding parts, so that no wear can occur and no lubrication is necessary.
5. No sliding contact of sealing surfaces.

The electromechanical actuation system eliminates the problems associated with the pneumatic and hydraulic actuation systems used on Apollo by its very nature of being different. However, it is realized that this system will have its own set of problems. It is felt that it is a step in the right direction.

The second concept, as shown in figure 2, is referred to as a "dual" poppet. In this concept the seats are in parallel with respect to flow. The actuation system is also electromechanical. The dual poppet acts to pressure balance the valve, minimizing the actuator force requirements. The only actuation force required is that needed to overcome the spring forces of the axial

guidance flexures and bellows dynamic seal which are sized to provide the necessary sealing closure interface forces. The dual poppet concept has the capability of sealing as reliably as a single poppet valve since the total seal area of a single poppet valve is nearly identical to the combined sealing areas of the dual poppets. Simultaneous sealing of both poppets in the dual poppet concept is assured by making the carrier of one of the seats a spring element. The poppets are fully flexure-guided and the shaft seal features a hydroformed redundant bellows assembly. Thus, frictional forces have been eliminated. Utilization of the dual poppet concept results in a smaller valve envelope because the two poppets are smaller in diameter than a single poppet and the overall diameter of the poppet housing is reduced.

While both of the above described valve concepts would be expected to utilize electromechanical actuation systems, both concepts are capable of being actuated by pneumatics or hydraulics.

CONCLUDING REMARKS

The problems encountered in the development of the Apollo primary propulsion system valves were resolved by design modifications, procedural changes, and the relaxation of some requirements resulting from a better understanding of program requirements with time. While this led to highly successful operational valves for Apollo, valve designs must be developed for the Space Shuttle which enhance the life, reusability, and maintainability aspects over those used on Apollo.

TABLE 1
APS, DPS, AND SPS VALVE FAILURE SUMMARY

FAILURE		TOTAL		
		No.	%	Causes
Total Failures		206	-	-
Sliding Seals	Ball Seal Leakage			Contamination, Wear, Scratches, Salting, Corrosion, Teflon Flaking, Galling, Seal Shrinkage
	Piston and Shaft Seal Leakage	109	53%	
Poppet Seals	Pilot Valve Leakage	26	13%	Contamination, Motion of Solenoid, Assembly Error
	Erroneous Position Switch Output	16	8%	Solder Joints, Environ. Cond., Adjustment Sensitivity
	Low Electrical Resistance	10	5%	Damaged Wire, Faulty Diode, Propellant Fumes, Moisture, Dirt
	Sluggish Operation	8	4%	Unknown Causes
Hang-Up		7	4%	Leaking Oxidizer, Rusted Needle Bearings, Leaking Oxidizer Reacts with Gear Lubricant
	Filter Collapse	6	3%	Inadequate Support
	Disconnect Leakage	4	2%	Seal Handling Damage
Miscellaneous		20	10%	

TABLE 2
OME VALVE DESIGN REQUIREMENTS

Parameter	Design Criteria
<u>Compatibility</u>	
1. Fluids	N ₂ O ₄ , MMH, 50-50 as liquids and vapors; H ₂ O at outlets; Freon TF
<u>Performance</u>	
2. Pressures	
Nominal	1413.4 kPa (205 psia N ₂ O ₄) 1434.1 kPa (208 psia MMH)
Operating Range	1185.1 to 1827.1 kPa (172 to 265 psia)
Max Surge	2757.9 kPa (400 psia)
Proof	2757.9 kPa (400 psia)
Burst	4619.5 kPa (670 psia)
3. Flow Rates	5.40 kg/s (11.91 lb/sec N ₂ O ₄) 3.27 kg/s (7.22 lb/sec MMH)
4. Pressure Drop	34.5 kPa (5 psid) max (normal) "balanced" (fail close)
5. Response Time	100 - 1000 ms open 100 - 1000 ms close
6. Response Repeatability	Important
7. Propellant Simultaneity	Design for simultaneous propellant delivery
8. Internal Leakage	10 std cc/hr GHe per seat (0 to 1827.1 kPa (265 psia))
9. External Leakage	1.66 x 10 ⁻⁷ std cc/sec GHe per joint
10. Electrical Supply	24 to 30.5 Vdc (27.25 Vdc nom)
11. Electrical Power Limits	To be determined

TABLE 2 (CONT.)

Parameter	Design Criteria
<u>Life</u>	
12. Cycles	4000 wet/pressurized, 6000 dry
13. Missions	100 missions
14. Time	10 years
15. Propellant Throughput	15,526 kg (34,230 pounds per mission)
<u>Environmental</u>	
16. Temperature	
Propellant	4.4°C to 51.7°C (40 to 125°F)
OMS Structure	4.4°C to 48.9°C (40 to 120°F)
Engine Soakback	93.3°C (200°F maximum)
Transport/Storage	-48.3°C to +87.8°C (-55°F to +190°F)
17. Random Vibration	20 to 2000 Hz, 15.3 g rms, 231 hours
18. Shock	1.5 g maximum for 2.60 ms
19. Acceleration	Up to 4 g
<u>Maintainability</u>	
20. General	Easily maintainable
21. Accessibility	To be determined
22. Filter Replacement	To be determined

TABLE 2 (CONT)

Parameters	Design Criteria
<u>Checkout</u>	
23. General	Minimize valve actuations
24. Position Indication	Open and closed positions
<u>Decontamination</u>	
25. General	Easy to decontaminate
26. Fluid	Hot GM ₂ purge
<u>Contamination</u>	
27. Self generated	Minimize
28. Propellant	Particle size (microns) Number of 0-25 particles Sample 25-50 Not defined size 50-100 1000 part. 500 ml 100-250 100 part. sample 250 10 part. 0
29. Filter Rating	Consistent with valve tolerance
<u>Construction</u>	
30. Lubricants	Avoid if possible
31. Dribble Volume	Not critical
32. Failure Position	Close with loss of power
33. Gas Pressure Source	Must be included in valve if used
34. Motors	Brush type not allowed
35. Force Margin	To be determined

TABLE 2 (CONT)

Parameter	Design Criteria
<u>Installation</u>	
36. Envelope	Minimize
37. Mounting Provisions	On side of engine
38. Porting	Parallel or counterflow
39. Port Size	To be determined
<u>Weight</u>	
40. General	Minimize
<u>Duty Cycle</u>	
41. Maximum on-time	870 seconds
42. Actuations per mission	20 maximum

TABLE 3
POTENTIAL VALVE PROBLEMS
RELATED TO LONG LIFE AND REUSABILITY OF THE SPACE SHUTTLE

Long Life/Reusability Parameter	OME (Orbital Maneuvering Engine) Potential Valve Problems
<u>High Cycle Life</u>	(4000 wet/6000 dry cycles) Seal deterioration due to wear; seat deterioration due to impact; gear, stop, and bearing failure due to stop impact loads; fluid hammer fatigue failures.
<u>Long Vibration Time</u>	(231 hours, 15.3 g rms Vibration) Fatigue failure of springs and other flexing or rattling elements; seat scuffing; bearing failure; electrical wire and solder joint failures; micro-switch failures; generation of contamination.
<u>Long Life Time</u>	(10 years) Propellant caused corrosion, nitric acid caused corrosion (at N ₂ O ₄ valve outlet); limited life materials (elastomers); cold flow, swelling or permanent set of non-metals; decomposition of MMH; propellant reacting with lubricants.

TABLE 3 (CONT)

Long Life/Reusability Parameter	Some Potential Valve Problems
<u>Large Number of Missions</u>	
(100)	Filter clogging or excessive size needed; bellows fatigue due to flow inducing vibration.
<u>Avoidance of Liquid Flushing</u>	
(Use GN ₂ Purge)	Inadequate removal of propellants in crevices, seals, or stagnant areas.
<u>Ease of Maintenance</u>	Excessively "high" maintenance level; excessive maintenance time; parts not 100% interchangeable; introduction of contamination.
<u>Ease of Pre-Flight Checkout</u>	Complex checkout requiring long time; inability to isolate fault.

TABLE 4

RECOMMENDED DESIGN PRACTICES TO AVOID OR
MINIMIZE PAST AND POTENTIAL VALVE PROBLEMS

Past and Potential Valve Problems	Design Approach to Avoid or Minimize
Sliding seal leakage	Avoid sliding seals to minimize wear
Poppet valve leakage	Use elastomer seats for contamination tolerance
Short life of impacting and sliding parts	Reduce inertia; use shock absorbers; avoid sliding fits
Vibration fatigue failures	Replace sensitive mechanical parts with electronics; provide adequate holding forces; design for vibration resistance; design for easy maintenance
Incompatibility with propellants and nitric acid	Use best proven materials; avoid lubricants; design for easy maintenance
Problems with flushing liquids	Design for propellant removal by gas purging (avoid crevices, stagnant areas)

TABLE 4 (CONT)

Past and Potential Valve Problems	Design Approach to Avoid or Minimize
Filter clogging	Design adequate dirt holding capacity; use high micron rating; design for easy maintenance
Field maintenance difficult or impossible	Design for easy maintenance at low level; avoid contamination sensitive construction
Difficult checkout	Design for ease of checkout and isolation of fault to level of maintenance

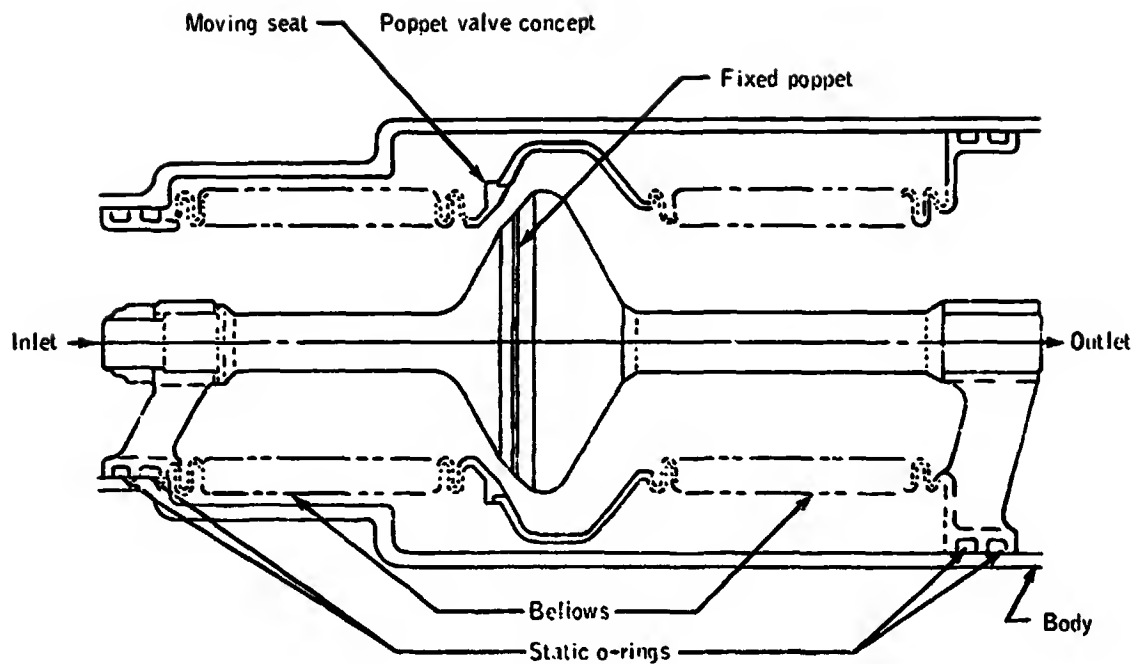


Figure 1.

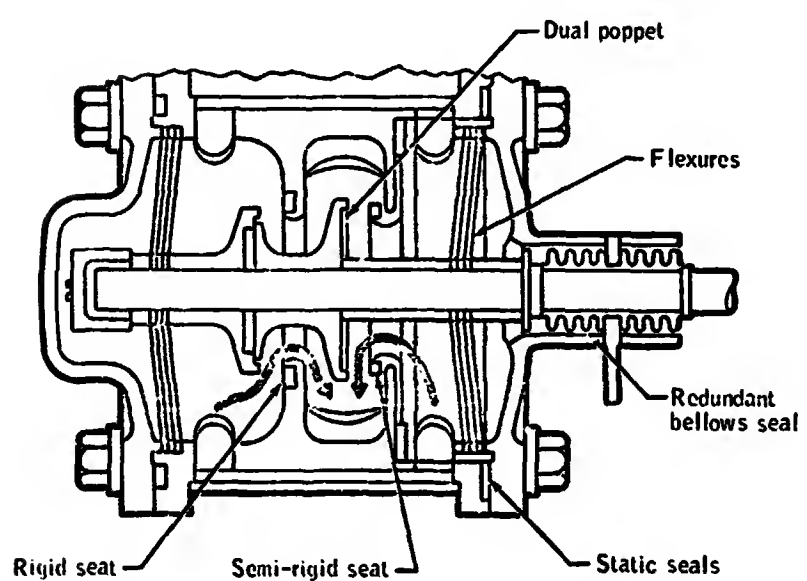


Figure 2.

18. METEOROID-DETECTOR DEPLOYMENT AND PRESSURIZATION SYSTEMS

By H. C. Halliday
NASA Langley Research Center

SUMMARY

The Explorer 46 Meteoroid Technology Satellite (MTS) launched from Wallops Island, Va., on August 13, 1972, was configured to fit within the Scout heat shield, 86.36 cm (34 in.) in diameter. In order to package within this envelope, the meteoroid bumper detector panels had to be rolled up unpressurized and secured to the spacecraft main structure. After the spacecraft was placed in orbit the panels were unrolled by a deployment system and inflated by a pressurization system.

INTRODUCTION

The Explorer 46 Meteoroid Technology Satellite (MTS, fig. 1) was designed to collect data on the near-earth environment and its effect on spacecraft structures. The data will be utilized to evaluate the meteoroid protection provided by a typical bumper-protected multisheet spacecraft structure.

The spacecraft in its launch configuration (fig. 2) was designed to fit within the Scout heat shield, 86.36 cm (34 in.) in diameter. In order to do this the bumper detector panels were rolled up on spools, the telemetry system was packaged in two containers that were hinged down against the spacecraft structure, and the aft-facing solar cells and impact detectors were mounted on the flip-out panels. The Scout fourth stage motor case and upper "D" section were retained as part of the spacecraft.

The bumper detector panel consisted of two stainless-steel bumper target sheets 0.025 mm (0.001 in.) thick attached to the bumper detector panel, which is 0.051 mm (0.002 in.) thick, with belt loops, restraint bars, and standoffs (fig. 3). The standoffs were tack welded to the detector panel in the void areas between detectors. A restraint bar was passed through the loops in the ends of the standoffs and tack welded to the standoffs on the center line of the panel only. The same restraint bar also passed through belt loops tack welded to the bumper sheet. Along the panel center line the belt loops were attached to the bumper sheet on alternate sides of the standoffs as shown in figure 3. This method of attachment allowed the bumper sheet to float above the detector panel while being restrained along the center line of the panel.

The total bumper-protected area was 27.87 m^2 (300 ft^2). This area was subdivided into 12 panels 48.92 cm (19.26 in.) wide and 3.20 m (10.5 ft) long. Each detector panel had eight detectors, 5.03 cm (1.98 in.) wide by 3.20 m (10.5 ft) long, giving a total of 96 bumper-protected detectors. A pressurized-depressurized pressure sensing device utilizing two single-pole double-throw switches monitored the condition of each of the 96 detectors (fig. 4).

DEPLOYMENT SYSTEM

Two Spar Aerospace Products Ltd. "Bi-Stem" motorized actuator assemblies were used to deploy 12 rolled-up detector panels. Each assembly (see fig. 5) deployed six panels, two groups of three diametrically opposed.

Each of the two actuator assemblies had a master and a slave actuator coupled together with a shaft to insure synchronous extension of the booms 2.18 cm (0.86 in.) in diameter. The master actuator was motorized to provide an extension rate of 17.78 cm (7 in.) per second under a tip load of 11.12 N (2.5 lb) per boom.

The spreader bar was attached to the tip ends of the booms and carried three detector spools. A drag device was built into the spools to provide a tension load to eliminate any premature unrolling of the detectors as they were deployed.

Straps restrained the detector-spool assemblies and spreader bar to the cradles during launch. One end of the strap was pinned to the cradle with a tensioning device, which was secured by dual pyrotechnic pin-pullers. Release of a strap required only one pin-puller to function.

After the straps were released the motor was energized and the panels deployed. When the panels were fully deployed stops dropped into slots in the booms to limit the boom extension. Limit switches operated by the stops on the master actuator boom opened the motor circuit. The detector panels were then ready to be pressurized.

PRESSURIZATION SYSTEM

Since the detector panel had to be rolled up unpressurized during launch, it was necessary to provide a means for pressurizing the detectors after deployment. To do this a reservoir, with a valve to contain the pressurization gas in the reservoir, and a pressure sensing device to indicate the pressurized or depressurized state of the detector were designed. These two units made up the switch-reservoir assembly (see fig. 4). There was an assembly for each detector in a panel. The eight assemblies serving a panel (see fig. 6) were located in its cradle. Eight small-diameter tubes projected from the root end of each panel and were coupled to the switch-reservoir assembly detector pressurization tubes.

The valve in the switch-reservoir assembly was closed by pressurizing the bellows to 48.26 N/cm² (70 psig) through its pressurization tube. This seated the valve seal plate on an O-ring in the reservoir base, isolating the reservoir from the detector and switch.

The eight-valve-bellows pressurization tubes for a detector panel were manifolded together with two additional tubes. One of the additional tubes was used to pressurize the valve bellows. The other tube had a break-off element soldered to the end of it. This element was inserted in a pyrotechnic device that when

fired would break off the end of the element, thereby venting the gas in the valve bellows and allowing the bellows to open.

After all the valves were closed, each reservoir was pressurized individually to 44.32 N/cm² (65 psig) and its pressurization tube crimped and sealed with solder. After the detector panels were deployed and the valves opened, the gas from the reservoir pressurized the detector to between 6.21 N/cm² (9 psia) and 11.38 N/cm² (16.5 psia), depending upon the detector temperature.

When the valve was opened gas also passed into the pressure sensing device, deflecting the belleville spring to the position shown in figure 4 and causing the switch contacts to transfer and indicate a pressurized condition. When the detector was punctured by a meteoroid the gas leaked out, the belleville spring returned to its normal position and allowed the switch contacts to transfer back and indicate a no-pressure condition.

REPRODUCIBILITY OF THE ORIGINAL PAGE IS POOR.

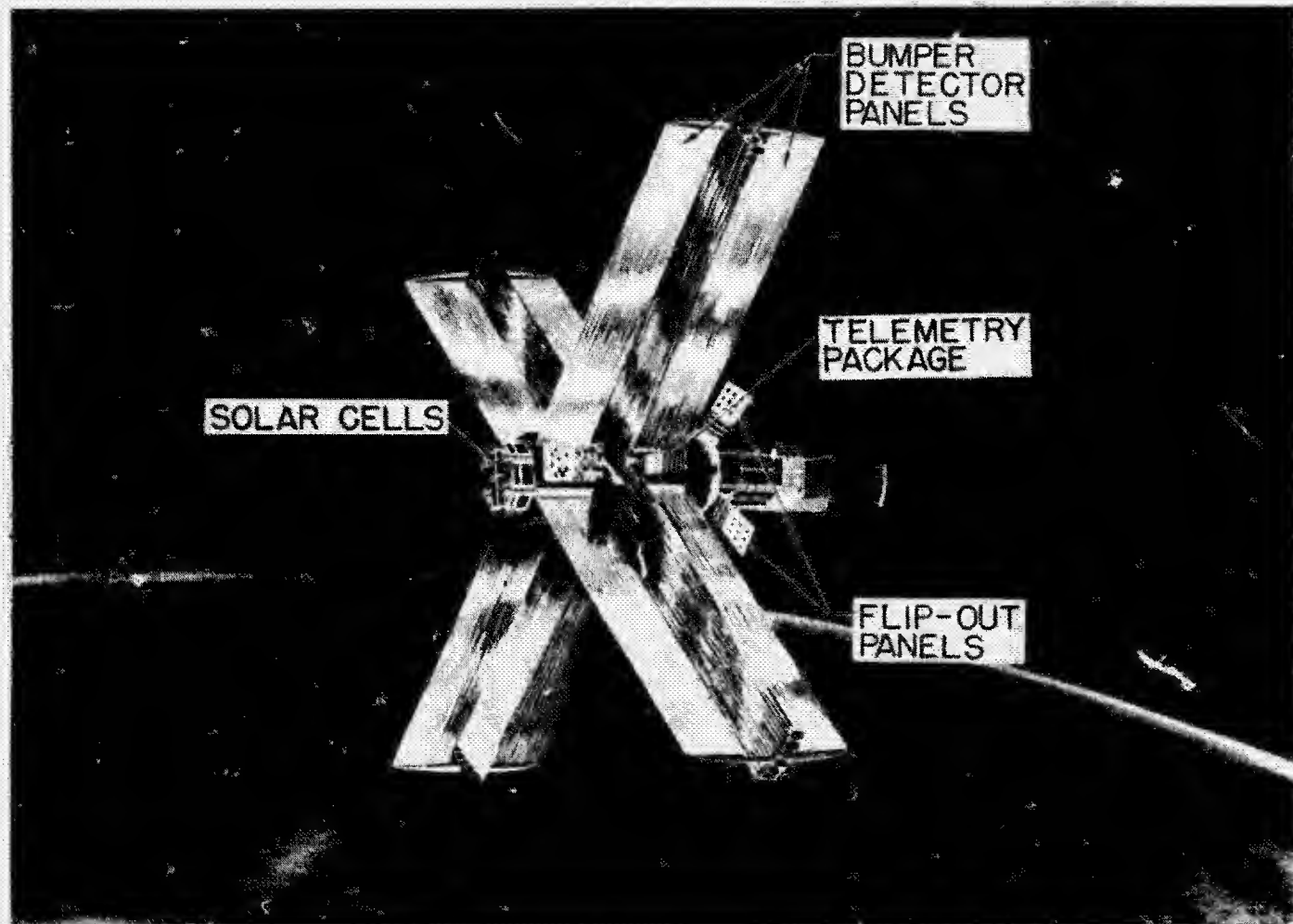


Figure 1.- Meteoroid Technology Satellite (MTS). Explorer 46.

REPRODUCIBILITY OF THE ORIGINAL PAGE IS POOR.

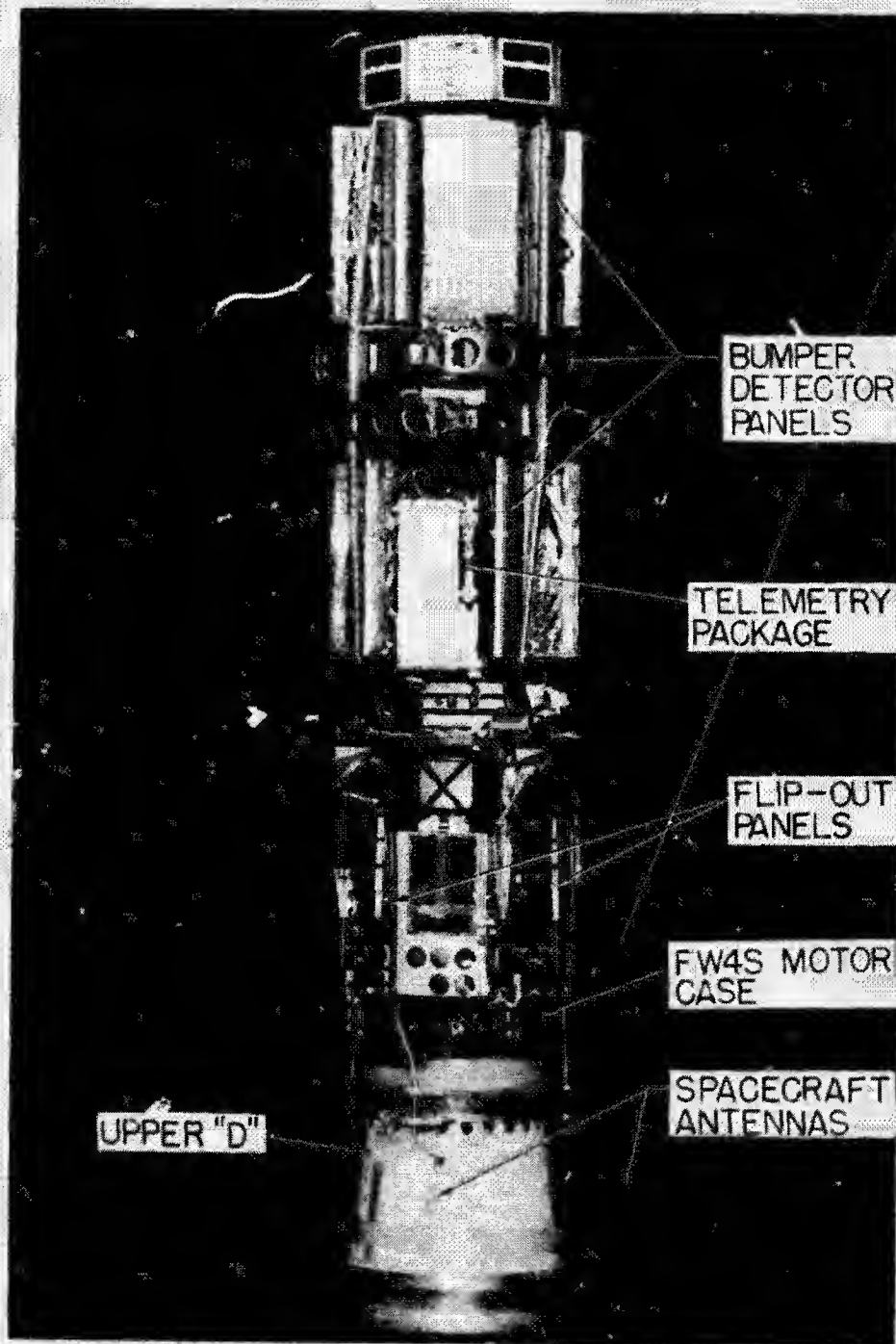


Figure 2. - MTS launch configuration.

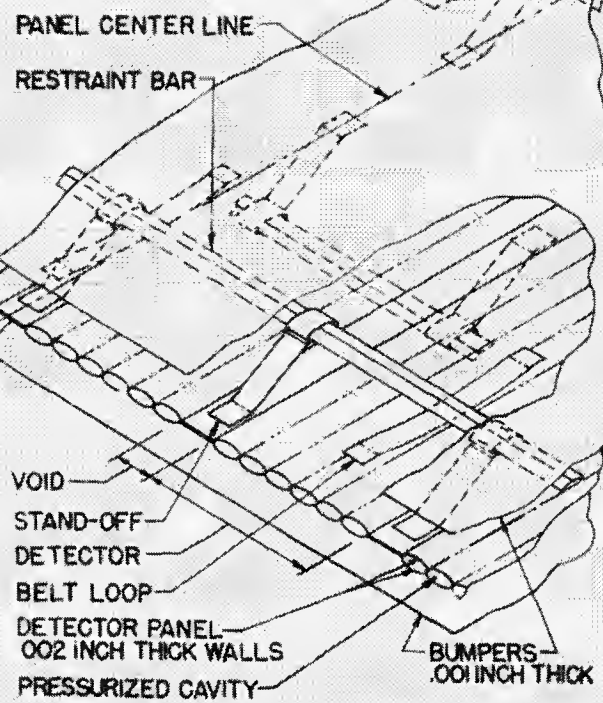


Figure 3.- Bumper detector panel.

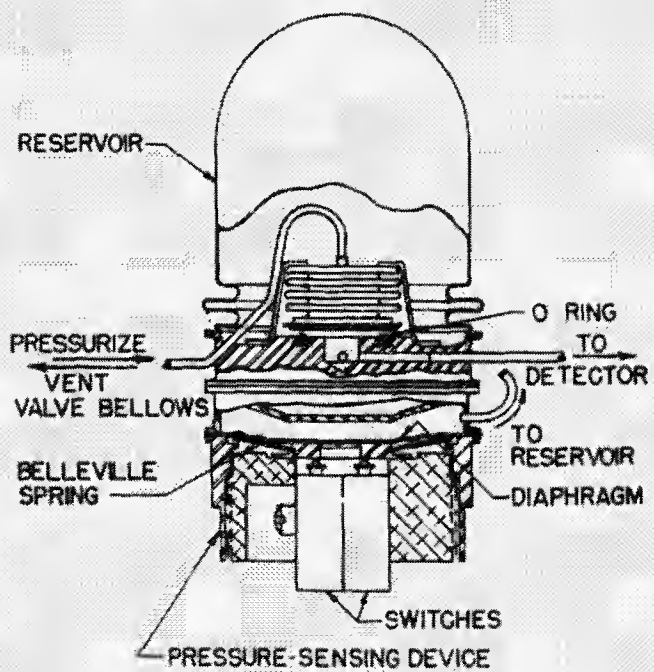


Figure 4.- Detector switch-reservoir assembly.

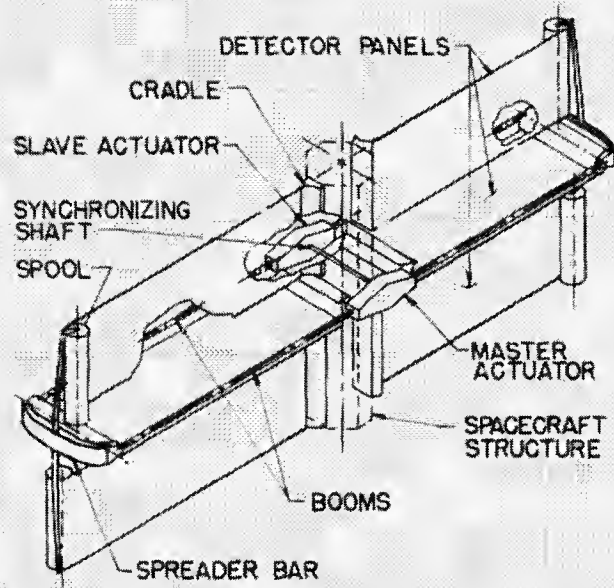


Figure 5. - Detector panel deployment system.

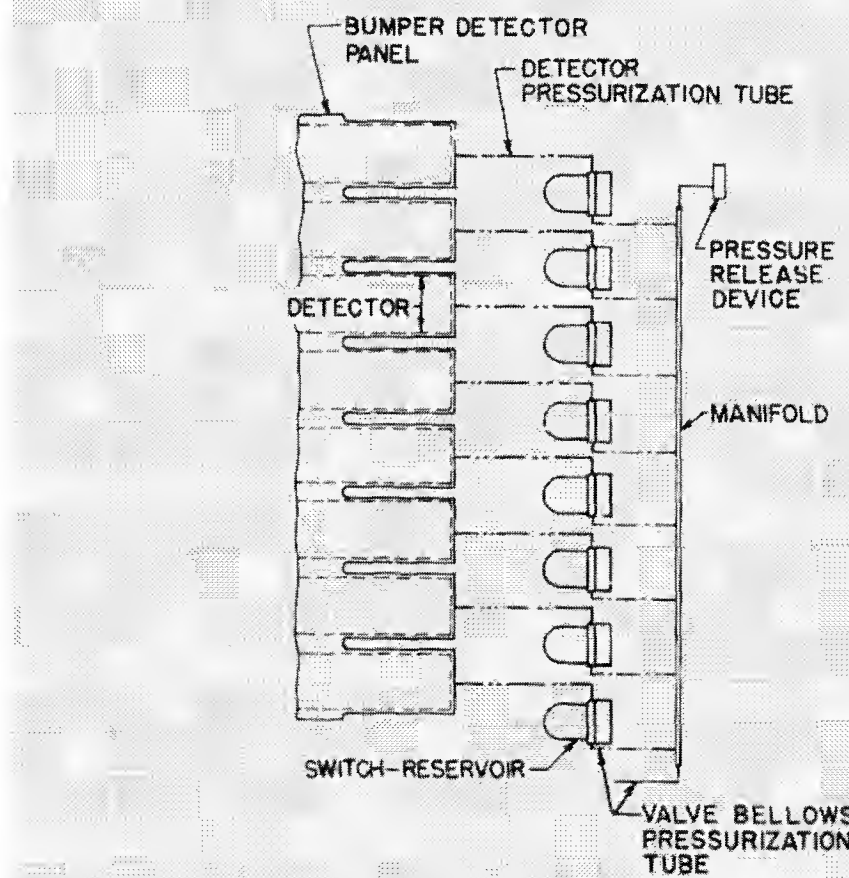


Figure 6. - Detector panel pressurization system.

19. CONTROL VALVE: HOT GAS FAST RESPONSE

**J. T. Hollis, A. B. Killebrew, and J. M. Smith
McDonnell Douglas Astronautics Company-West
McDonnell Douglas Corporation**

ABSTRACT

This control valve was a key component in the jet interaction (JI) control of the UpSTAGE missiles which were flown in 1972. The vehicle was an elliptic cone which provided space at the extreme aft end for the JI control system. This system was mechanized to provide maneuverability of the vehicle. The moments necessary for pitch, yaw, and roll control were provided by a fast-response system of 10 nozzles located around the aft periphery of the vehicle. Each nozzle was fitted with a control valve which regulated the flow of gases from a solid propellant gas generator to the nozzle.

The control valve functioned in an on-off mode. The prime requirement on the valve design was the 10-millisecond response time. However, the most difficult problems in the development resulted from the vibration and acceleration effects on the valve operation and also from the particulate matter in, and the chemical composition of, the propellant exhaust, which the valve controlled and by which the valve was operated.

This paper, after briefly describing the valve's physical configuration and presenting a pictorial schematic of its arrangement, discusses several of the more interesting and challenging problems encountered during the development testing.

The discussions include the effect on valve performance and integrity by the material and shape of the upstream gas manifolds. Some do's and don'ts for designing valves for very severe vibration and high acceleration environments will be presented. A description of the destruction which resulted from internal parts impacting their stops at a hundred thousand g's, as well as the solution for this problem, also will be presented. Interesting and novel solutions to the anticipated erosion and thermal problems associated with the hot gas will be included.

Several performance oddities are disclosed along with their reasons, such as why the valve's response time decreased when rapidly cycled several times.

SUMMARY

Design of a warm gas control valve is reviewed outlining the problems posed by the requirement for extremely fast response combined with a severe environment and a hot, dirty, and corrosive operating fluid.

INTRODUCTION

The jet interaction (JI) models of the UpSTAGE vehicle are controlled by a set of 10 nozzles, 4 or 5 of which are discharging warm gas from a solid propellant gas generator into the boundary layer to provide large control forces. The flow through the nozzles is controlled by three-stage, warm gas control valves operating in a bistable mode. In addition to controlling the thrust vector, the valves regulate the gas generator pressure by the number of valves open at any time. In order to satisfy the response and stability requirements of the vehicle, the valves were required to have a response time of 10 milliseconds or less.

Acknowledgement is made to Moog Inc., Western Development Center, Monterey Park, California, who developed this valve under subcontract for the UpSTAGE program.

The J1 control valve is an electrically commanded three-stage valve consisting of a pilot, an intermediate, and a main stage. A schematic of the valve is shown in Figure 1. The first stage is operated by a flat-faced magnet, and the second and third stages are operated by gas pressure. Each stage is a poppet-type stage, balanced for poppet areas and utilizing a 2:1 area ratio for operation. Springs are provided to insure proper poppet position at startup but are unnecessary for actual operation of the second and third stages. A novel feature is the provision for operation of the valve with cold gas by pressurization through the vent port. This enables each stage to be exercised without application of pressure to the normal inlet port.

Stringent requirements with regard to valve response, weight, high pressure, leakage, valve position indication, and restricted envelope dictated a careful analysis of the available schemes to accomplish the task of designing the valve. The response of the valve was considered to be the most important specification parameter. A reliable, fast-acting position indicator, minimum weight, low peak wattage demand, and low leakage rates were other essential prerequisites governing valve design. The severe valve response requirements over a broad spectrum of operating conditions were achieved by a three-stage valve.

A summary of valve specification requirements is given in Table 1.

The pilot stage is a conventional solenoid-operated poppet. The poppet is of balanced design, biased by a spring to port the incoming gases to the intermediate stage. The construction of the intermediate stage is essentially identical to the pilot stage. Gas pressure is used to shift the poppet spool of the intermediate stage to either fill or dump the main stage pintle control cavity. Amplification effect of the intermediate stage allows use of a relatively small pilot stage solenoid, with low power demands, to operate the valve. The pilot and intermediate stages were arranged on the valve structure to be in the axis of least g-sensitivity.

The main stage of the valve is balanced by use of an integral pintle support and a guide member. There are many advantages to this approach, the most significant being that the control cavity volume back of the pintle is reduced to the minimum allowable in this design. This small control volume contributes directly to the fast valve action. The pintle support reduces very effectively the variation in forces on the pintle due to the wide excursion of operating pressure range. The valve body is made from a titanium alloy, primarily for weight considerations. This material, however, is not an ideal material for sliding applications and therefore the pintle support member is used for guiding the pintle. The clearances of the parts are arranged to insure that the pintle slides on the support and not on the housing. In addition, the hollow support provides a space isolated from the warm gas, for packaging of the pintle closing spring, electrical suppression circuits components, and the indicator switch system.

In the pressure off, power off, or solenoid deenergized condition, the valve is closed and the main pintle is pushed against the seat by a spring. The intermediate stage poppet for the initial no-pressure case is shifted to close its vent port by a small bias spring so that the incoming pressure is directed to the main stage control cavity, insuring its closed position. The deenergized pilot stage is in the vent closed position ready to admit the gas to the large end of the intermediate stage.

With the solenoid energized, the armature overcomes the spring and friction forces to shift the poppet to close off the incoming pressure source and vent the large end of the intermediate stage overboard. With this end of the intermediate stage vented, the pintle shifts position due to the pressure acting on the opposite end of the intermediate poppet. This closes off the valve inlet pressure and connects the main stage pintle control cavity to the overboard vent. As soon as the control cavity pressure decays sufficiently, the pintle starts opening the main valve cavity.

Table 1
VALVE SPECIFICATION SUMMARY

Operating Fluid	Solid propellant GG combustion gas Temperature – 2,650° F (1,460° C) maximum Specific heat ratio – 1.29 Molecular weight – 19.3 No heavy abrasives or magnetic particles
Flow	7.4 lb/sec (3.36 kg/sec) at 3,250 psi (2,240 N/cm ²) inlet
Inlet pressure	2,050 to 4,600 psi (1,410 to 3,160 N/cm ²)
Pressure drop (inlet or outlet)	500 psid (345 N/cm ²) at full flow
Operating duration (flight)	1.5 sec minimum
Response time	0.010 sec maximum, 0.005 sec minimum
Cycle rate	50 Hz
Leakage at 4,600 psi (3,160 N/cm²)	
External	0.001 sccs maximum
Main stage internal	0.05 lb/sec (22.6 gm/sec) maximum
Pilot stages internal	0.02 lb/sec (9.1 gm/sec) maximum
Shelf life	1 year
Cycle life	
At 0 psi (0 N/cm ²)	2,000 cycles
At 4,600 psi (3,160 N/cm ²)	300 cycles
At flight conditions	75 cycles
Weight	3.43 lb (1.56 kg) maximum
Electrical inputs	
Minimum	2.0 amp at 25 vdc
Maximum	2.4 amp at 30.3 vdc
Burst pressure	9,200 psi (6,320 N/cm ²) minimum

The selection of materials for all components of the assembly was based on engineering practice and backed up by past experience. Material combinations used in this design have been successfully applied in previous designs and are compatible with the valve operating media. Titanium alloy, Ti-6AL-4V, in the annealed condition was selected for the valve housing because it offered light weight, high strength, and low thermal conductivity. Due to the short valve operating duration, minimal temperature rise in the body was expected; however, based on test results it was determined that a zirconia coating would be required inside the body to insulate it from the high temperatures.

The main stage pintle is made of Hastelloy-C and 17-4 which were inertia-welded together. Dry film lubrication Microseal is applied to all surfaces of the pintle. The intention here is to reduce friction on the inside diameter of the pintle where it runs on the chrome-plated pintle support surface. The pilot stage and intermediate stage of the valve are constructed of identical materials except the pilot stage has a Rene 41 poppet and the intermediate stage has a 440C stainless steel poppet. These poppets seat on Monel K500 material. The bushings that support the seats are 416 stainless steel. The springs used in these stages are of 302, 17-4, or 304 stainless steel and are sufficient for the duration of the valve operation. Hydrogen-annealed C-1018 carbon steel is used in the solenoid construction. The solenoid is encased by a cover and for additional corrosion protection both the armature and the electromagnet are nickel plated. The solenoid coil is wound with a heavy coated magnet wire on a bobbin. By using epoxy, the coil is potted into the steel core of the solenoid body.

The main seat material and configuration are identical to those of several other warm-gas valves. The seat material used is tantalum tungsten which is a ductile material with a high melting point of 5,550°F (3,030°C) and a very low coefficient of thermal expansion. Dimensional changes induced by heating are insignificant because of the low thermal expansion coefficient. This material is compatible with the specified propellant. The seat is pressed into the outlet passage of the plenum chamber against a shoulder. In addition to this press fit, the seat is also held at all times either by the pintle or the inlet pressure forces. The available force margin to translate the pintle is large enough to overcome the environmentally induced loads and still provide a comfortable design margin of safety. The minimum available pintle opening and closing forces are 430 lb (195 kg) and 630 lb (285 kg), respectively, at 1,800-psia (1,240 N/cm²) inlet pressure.

The position indicator on the valve is a single-pole switch which indicates the position of the main pintle. This switch is electrically closed when the valve main poppet is in the open position and is electrically open when the valve main poppet is in the closed position. The switch is located in the free volume behind the main pintle and is not subjected to hot gas conditions. Basically, the switch is constructed of a rod connected to the main pintle which slides on stationary flexible beryllium copper springs. Sections of the moving rod are appropriately coated with nonconductive materials in order to make or break contact as required. The concept was selected over other schemes for speed of operation, minimum bounce time, and good vibration and shock capabilities.

The ammonium perchlorate base propellant used to supply the operating gas poses some problems to valve design. Initially, the gas generated is of the order of 2,600°F (1,430°C) which will melt or soften many materials. Secondly, there is a high percentage of hydrochloric acid generated which, at the high temperatures, not only can attack valve materials but also will form undesirable compounds on reaction with system materials. Finally, there is a high carbon content especially at the lower temperatures which can clog passages and bind moving parts. All these problems were encountered in the valve development.

Early in the development testing, the valve performance was to suffer from a large amount of contamination. The contamination appeared to be particulate carbon bound together with a sticky material and was of a sufficient consistency to stop the first stage movement. Chemical analysis of the binder material showed it to be ferric chloride. It seemed likely that this was being generated by

the reaction of the hot hydrochloric acid in the grain combustion products with the steel gas generator case and the manifolds. These surfaces were subsequently protected with a coat of flame sprayed zirconia which reduced the generation of the ferric chloride to acceptable levels. Although considerable amounts of carbon remained in the valve after the test, it was presumed that this was largely generated during the tailoff as it had little effect on performance. As a precaution, fine mesh screen filters were installed at the inlets to the first and second stages.

An unexpected source of difficulties was the impact load generated when the third stage impacted on its stops. This impact, resulting from the pintle moving 0.25 in. (0.64 cm) in approximately 2 ms caused failure of position transducer attachments, buckling of the pintle itself, and even a tension failure of a stainless-steel 1C-32 screw from the inertia of the screw head when undergoing the deceleration of the pintle. It was necessary to redesign the pintle to incorporate an inertia-welded 17-4 stainless-steel skirt to the Hastelloy-C poppet to prevent buckling of the skirt. The original switch configuration with the contact fingers mounted on the moving part had to be redesigned to put these fingers on the stationary part since the impact loads neatly sheared off the fingers from their own weight. Significantly, the self-induced shock loads on the valve body were more severe than the environmental criteria.

The unusually high environmental acceleration and vibration loads (see Figure 2) on the valve posed some interesting problems. Magnet forces had to be high, not only to overcome the g loads and friction effects induced by these loads but also because of the high spring return forces. Consideration had to be given to deflections, particularly if the parts became warm. Initially, the vibration problem was considered secondary and only normal good design practice was considered necessary. On testing, however, problems developed, particularly with the magnet stage. The armature of the magnet, being cantilevered on its shaft, broke, moved on its press fit, gouged the aluminum cover, and exhibited other undesirable actions until tamed by a new design incorporating a large press fit area and support around the armature periphery by the cover. An indication of the level of vibration, again self-induced by the jet interaction process, was that the testing facility was not able to supply the environment with its largest equipment in one pass, having to split the spectrum into three parts which were run separately. The high acceleration levels caused test equipment problems as well as some unexpected instrumentation anomalies due to the high g forces. For example, a few inches of grease in an instrumentation pressure line was enough to offset the line pressure under acceleration until the grease burned out, resulting in some perplexity during data reduction until the phenomenon was identified.

The magnet design, which had been used successfully on other components, allowed the armature to tilt in the housing. While the force levels and response were adequate during the initial testing, the armature failed under vibration. In an attempt to correct this failure, the armature shaft was strengthened and the armature was constrained so as to move parallel to the magnet face. It was then discovered that the available magnet force had diminished substantially. Testing of the original configuration revealed that the original armature motion consisted of a tipping sequence in which one edge of the armature would contact the magnet first, followed by the opposite side. This mode yielded substantially higher magnet forces than the constrained motion. In the final version, the armature shaft diameter was increased and the armature supported by its edge on the inside of the housing. This configuration successfully passed the vibration testing. A number of problems were encountered with the armature shaft attachment. Swaging and electron-beam welding were both tried unsuccessfully to preclude shifting of the armature on the shaft and finally the original press fit with larger bearing and interference areas solved the problem.

The original design, allowing the warm gas to impinge directly on the titanium body, proved inadequate, the first test resulting in a burn-through on the inlet neck and enough softening to allow body distortion. A 20-mil coating of zirconia, flame sprayed on the interior of these passages, proved adequate to keep body temperatures within acceptable levels. The main stage pintle had to be

thickened to prevent its distortion and five of six vent holes in the top of the pintle had to be removed to keep circulation of the warm gas from destroying the seal inside the pintle. The other seals performed quite well and in most cases were intact after operation and the inevitable heat soak after test completion.

Although the Viton seals performed quite well in the elevated temperature regimes, some difficulty was experienced with the slipper seals which protected these seals. The U cross-section seal on the main pintle trapped gas pressure underneath itself and bound up the main pintle. This was alleviated by grooving the sides of the seal to allow pressure to escape. A more obscure problem developed with the slipper seal on the first stage pintle nearest the magnet. When the magnet was energized, the poppet moved forcing the slipper seal against the side of the groove. At the same time, the poppet was unseated allowing pressure to build up in the adjacent chamber. Since the slipper seal was blocking flow into the O-ring groove, gas was able to leak past the slipper into the magnet chamber and blow the armature away from the magnet, resulting in anomalous operation of the valve. This condition was cured by venting the magnet chamber.

In spite of the testing problems, the valve development was very successful. A measure of this was the necessity to impose a minimum operating time on the vendor of 5 ms from the original requirement of 10 ms or less. Both vehicle flights were successful and the valve subsequently is being used in another test program where fast response is a prime requirement. A photograph of the valve is shown in Figure 3.

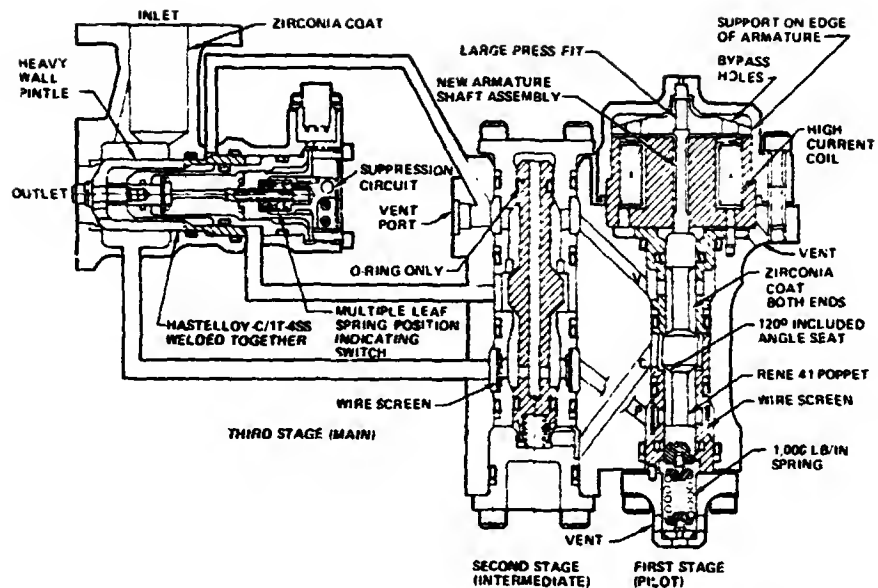


Figure 1.- Jet interaction control valve final configuration.

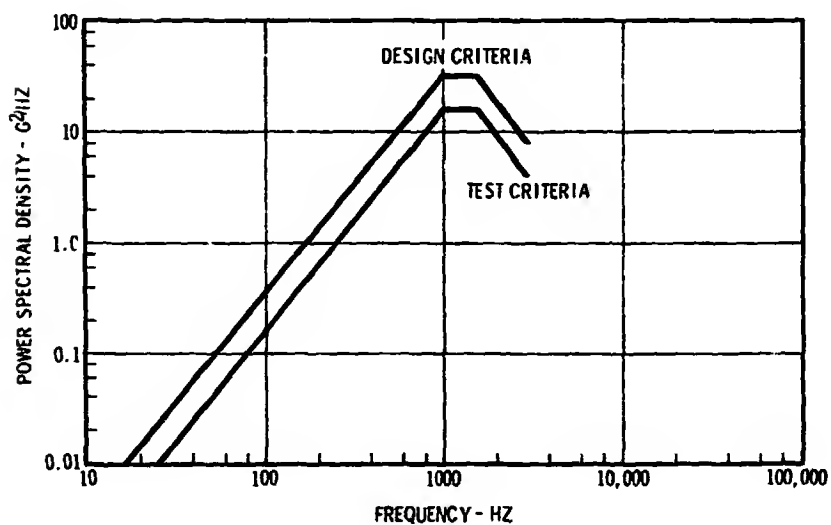


Figure 2.- Random vibration criteria for valve design and test.

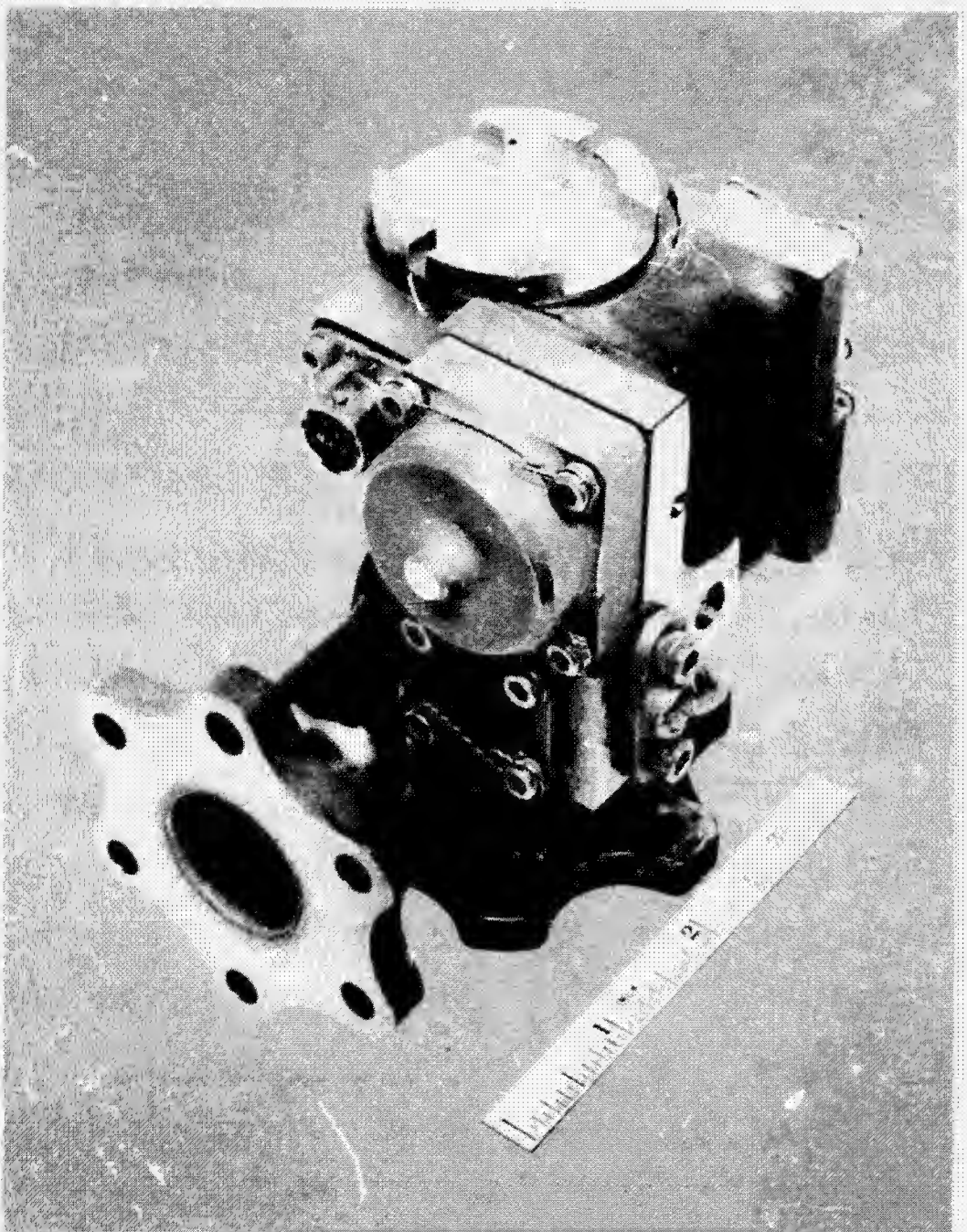


Figure 3.- Warm-gas valve.

2C. THE VIKING SURFACE SAMPLER

By Robert B. Seger, Martin Marietta Aerospace
and Vernon P. Gillespie, Langley Research Center

INTRODUCTION

During the 45 day launch window starting August, 1975, twin Viking Spacecraft will be launched from Kennedy Space Center toward the planet Mars. The second craft will follow the first by about 30 days, being launched in series from the same complex. The 3400 kilogram (7500 lb) Viking Spacecraft, consisting of both an Orbiter and a Lander, is encapsulated in a fairing above the Titan III E/Centaur Launch vehicle. Nearly a year later and 330 million kilometers (206 million miles) from Earth, Viking will approach and orbit the Red Planet. The Spacecraft then separates into an Orbiter and a Lander. The Orbiter performs visual mapping and upper atmospheric investigation. The Lander descends to the surface of the planet, depending upon its ablative aeroshell, its 16.8 meter (55 foot) diameter disc gap band parachute, and finally its three descent engines. Once safely down, the Lander Science Instruments will collect data for transmission to Earth, including panoramic stereo color pictures; organic, inorganic, magnetic and physical analyses of the surface; and seismic and meteorological characteristics. Also the Mars surface material will be investigated for evidence of biological activity. The subject of this paper is the Surface Sampler Subsystem which will help make possible the investigation of the Martian surface.

THE SURFACE SAMPLER SUBSYSTEM

Figure 1 is a photograph of a prototype Viking Lander, taken near the Martin Marietta plant. Figure 2 shows the relative placement of the Surface Sampler Subsystem to some other subsystems on the vehicle. The Surface Sampler Subsystem consists of the acquisition assembly, the biology processing and distribution assembly (Biology PDA), the gas chromatograph/mass spectrometer processing and distribution assembly (GCMS PDA), and the electronics control assembly. The system interfaces with the Biology PDA, the GCMS PDA, and the X-Ray Fluorescence instruments. It also supports many Physical Properties experiments. (The mirrors mounted on the side of the acquisition assembly support some of the Physical Properties experiments.) The magnets mounted on the collector head backhoe, the magnet cleaning brush, and the magnet magnification mirror support the Magnetic Properties Investigations. The primary sample field is made up of an 120° arc with a minimum radius of three feet and a maximum radius of ten feet, a total area of approximately 90 square feet. It is designed to acquire a

sample from a variety of soil models as specified in the Viking Mars Engineering Model. The Surface Sampler transports, processes, meters, and delivers the samples to the science instruments in accordance with strict scientific requirements such as cleanliness and cross-contamination. Digital commands are received by the Surface Sampler Control Assembly (SSCA) from the lander Guidance Control and Sequencing Computer (GCSC) for controlling the operations of the subsystem. Position, temperature and other data are collected by the Surface Sampler and transferred to the lander data acquisition unit for transmission to Earth. It should be emphasized that all operations of the Surface Sampler must be performed by onboard sequences and logic because of the transmission time from Earth to Mars.

TYPICAL SEQUENCE

Before the individual components of the subsystem are discussed, a typical acquisition cycle is presented. This will aid in the understanding of the purpose and requirements of the individual assemblies.

Shortly after landing, the pyros fire, and release the covers on the two PDA's. Automatically the wind spoilers deploy and the PDA's are ready to accept their first sample. Sometime later the furlable boom is extended about 1-1/2 inches, releasing the boom mechanism from the support post. The boom mechanism then elevates about 45° and rotates about 180° in azimuth. At this point, the collector head is rotated 45° inside the protective cover (shroud), and the boom element is extended approximately 4 inches. This additional extension mechanically releases the shroud and four springs propel the shroud through the thin atmosphere about eight feet. The collector head is returned to the upright position and is ready for its first digging sequence.

Although it can be completely changed or altered through a ground update capability, the first sequence is stored in the Lander GCSC. It must be emphasized that the sequence presented here is a typical sequence anticipated for acquiring the first samples for the biology and GCMS experiments. First, the boom unit rotates in azimuth to a predetermined position, elevates "down" to a position approximately horizontal and then extends to a length of approximately nine feet. Note that each motion is performed singularly; that is, it does not rotate and extend at the same time. This is done to improve the system accuracy and to increase the system safety. After extending, the boom unit elevates "down" until it is stopped by the actuation of the ground contact switch located in the gimbal mechanism of the collector head. At this point in time, the jaw opens and the connector head is extended forward with a force of thirty pounds, gathering a scoop full of surface material. If the desire would have been to acquire sub-surface material, upon ground contact the furlable boom would be retracted a short distance. The backhoe would have positioned itself and would have made a furrow about three inches wide and a foot long. The collector head would then open and the forward movement

of the collector head would have obtained a scoop full of material from the bottom of the furrow. After the jaw closes to retain the sample, the boom is again elevated to the horizontal position and retracted. The collector head is now rotated to the inverted position, in which position most surface material lodged in the "nooks and crannies" will fall off. The inverted collector head is rotated in azimuth to a position over the GCMS PDA. It is extended so as to center over the PDA screen, and is lowered to a position over the screen that allows adequate room for collector head vibration (one-half inch) but is well protected from the Martian winds by the spoilers atop the processor. After activation of the processor a delivery sequence is initiated. The collector head is vibrated; that is, the lid is pulsed in very short strokes at 8.8 hertz. The sharp teeth inside the cover break up any loosely bound clods and the 2000-micron holes sift the material onto the primary screen of the PDA. The PDA grinds, sieves and meters the material. A level sensor in the metering tube indicates whether or not an adequate sample has been obtained. If an adequate sample has not been obtained, the collector head will vibrate again for a few seconds and, after permitting time for grinding and sieving, the level sensor will again check for adequate material.

When adequate material is obtained, the acquisition assembly will elevate to clear the spoilers, rotate in azimuth, retract and lower itself to be correctly positioned over the Biology PDA. A similar delivery sequence will ensue.

In the ninety day lander mission, this will be repeated four times for the Biology PDA and three times for the GCMS PDA. (All Biology samples should be common to GCMS samples.) If insufficient material is obtained, however, it is permissible to collect a second sample at the same sampling site to complete the sampling cycle.

THE ACQUISITION ASSEMBLY

The acquisition assembly consists of a furlable articulated boom and the collector head. This boom shown in figure 3 stands about 14 inches high, 8-1/2 inches wide, and 24 inches long and weighs about 28 pounds.

Wound around a single six-inch-diameter drum is about twelve feet of furlable boom. It is forced flat when it is wound on the boom through guides and forms a column when it is extended. Attached to the tip of the boom element is the collector head, shown in figure 4. It was primarily designed to dig or scoop material. The rotation motor is located in the cylindrical section immediately behind the jaw. The lower jaw housing is the largest single piece and makes up the primary structure. The upper jaw can be opened and shut by the solenoid attached to the housing directly behind the upper jaw. This solenoid can be used to open and close the jaw and also to vibrate the jaw. The solenoid is energized by a square wave signal of 8.8 hertz.

The switch adjacent to the jaw monitors the jaw movement and "chops" the signal. This creates a short sharp vibration conducive to passage of material. If, however, the jaw hangs open due to excess load or material causing it to stick, the full square wave is exercised and the jaw motion is much more violent. As a secondary function, the collector head is involved in many physical properties and magnetic properties experiments.

The backhoe, which was designed primarily to get a sub-surface sample, can also make trenches. These trenches, placed at different positions, can be used to study the effects of the wind on the soil and the angles of repose which are of major interest to the physical properties scientists. The backhoe also contains two magnet arrays. These samarium-cobalt magnets may be viewed from the back with the cameras directly. Also, there is a magnifying mirror which allows a close look of the front side of magnet arrays.

The lower surface of the jaw has a temperature probe to record the temperature of a jaw. With the aid of the grid pattern painted on the upper surface of the lander, onto which material will be deposited, color, size, angle of repose and wind action may be observed.

GCMS PDA

It was mentioned earlier that GCMS PDA was opened by a pyrotechnic device soon after landing. This device allows the lid of the pressurized instrument to swing open, freeing the wind spoilers and allowing them to "pop" in place. The processor is now ready to accept its first sample.

The collector head sifts 2000-micron size material onto the primary screen, as shown in figure 5. An agitator vibrates the underside of the screen to increase the acceptance of this material. The agitator is basically a spring wire shaped like a question mark. The top of the agitator rubs the underside of the 2000-micron primary screen. The stem of the agitator extends down the funnel and into the grinder. A lobe on the grinder severely agitates the spring. This keeps the material flowing and prevents compaction in the funnel. The material flows through the funnel and collects in the comminutor. The comminutor acts much like an auger and a grinder. Allowed to position itself freely within the housing, its eccentric action tends to grind the material. At the same time the flutes tend to reject the material, much the same action as the flutes on a drill forcing the chips back away from the cutting surface. The material then circulates until it is ground down to a size that permits it to fall through the 600-micron "gap" around the periphery of the auger. As the material falls into a plenum chamber, it is stirred over a sieve covering a one cubic centimeter metering tube. Most of the material falls through the 300-micron sieve and collects in the metering tube.

A level sensor, easily a symposium subject within itself, is electrically pulsed and it is determined whether or not the metering tube is full. As mentioned earlier, this sequence can be repeated as many times as desired. The metering tube is located in a sliding shuttle. Once it is determined that the metering tube is "full" the material is transferred to the GCMS experiment. The shuttle then is translated to the "dump" position. The vibrator on the shuttle is activated and the comminutor is run in reverse. A linear cam causes the auger to lower, increasing the gap to 4000 microns. The flutes then force the excess and oversized material into the plenum chamber, through the dump tube, and into a self contained dump box. The PDA is now ready to accept the next sample.

BIOLOGY PDA

The Biology PDA (figure 6) is functionally similar to the GCMS PDA. The Biology PDA, however, does not have a grinding unit; rather it utilizes the material directly as it is sifted through the 1000-micron primary screen. The volume processed for the Biology experiment is seven cubic centimeters. Unlike the GCMS PDA, the Biology PDA is not pressurized. Rather this component has a bio-filter in the upper cover which allows the Biology experiment to "breathe" through the PDA. The Biology PDA also has an integral dump box for excess material.

CLEANING

After manufacturing and acceptance testing, the Biology PDA is organically cleaned to 1 ppm of total organics at the Martin Marietta plant. The GCMS PDA and the collector head/shroud assemblies are sent to the NASA White Sands Test Facility (WSTF) to be organically cleaned to less than 1 nanogram per square cm with the procedures developed for the Apollo Moon Missions. This is required by the extreme sensitivity of the GCMS instrument. After the assemblies are broken down as far as possible, each and every part is cleaned and flushed. The parts are then reassembled and vacuum baked. The parts are so clean that a screw will not thread into an insert and new screws using a silver plating for their lubricant are used for the reassembly procedure. The motors are hermetically sealed to maintain their lubricants. The assembly is now pressurized to protect it from the ingress of contaminants prior to flight. The assemblies will remain pressurized during any further testing, transportation and assembly onto the spacecraft. Prior to the final "buttoning up" procedures, the auxiliary tanks used to maintain positive internal pressure will be removed and the pressurized system will depend upon its own sealed construction to maintain cleanliness until landing on Mars.

CONTROL ASSEMBLY

The Surface Sampler Control Assembly (SSCA) located inside the lander body receives 16-bit digital commands from the Viking lander

computer (GCSC), decodes the command, and activates the appropriate motor or solenoid to perform the commanded function. In the case of boom movements, the command word contains 9-bit position information. As the boom moves, potentiometers inside the boom send analog information to the SSCA and, after an A/D conversion, the position words are compared. When comparison is of the commanded position and actual position agree, power is removed from the boom. Each command is timed to assure completion prior to performing the next command.

A block diagram of the software required to operate the Surface Sampler is shown in Figure 7. Each table contains a group of detailed digital commands for specific operations. Features of the software are the decision elements associated with level detectors, and the flexibility to deliver a sample to support any investigation, or any combination thereof.

SUBSYSTEM PERFORMANCE

A Surface Sampler Subsystem for the Viking lander has been designed, fabricated, cleaned, and successfully tested. To date, testing has included component level tests to qualification environment and subsystem level tests. This development hardware has also been integrated into a System Test Bed (STB) for the lander system. In addition to the normal dynamic and thermal environments the Surface Sampler hardware has been tested in the NASA/USAF KC-135 aircraft to simulate the effects of the reduced Martian gravity. Although problems have been encountered with the "first-build" and integration, theasic design appears to be sound and hardware qualification is scheduled for late 1973.

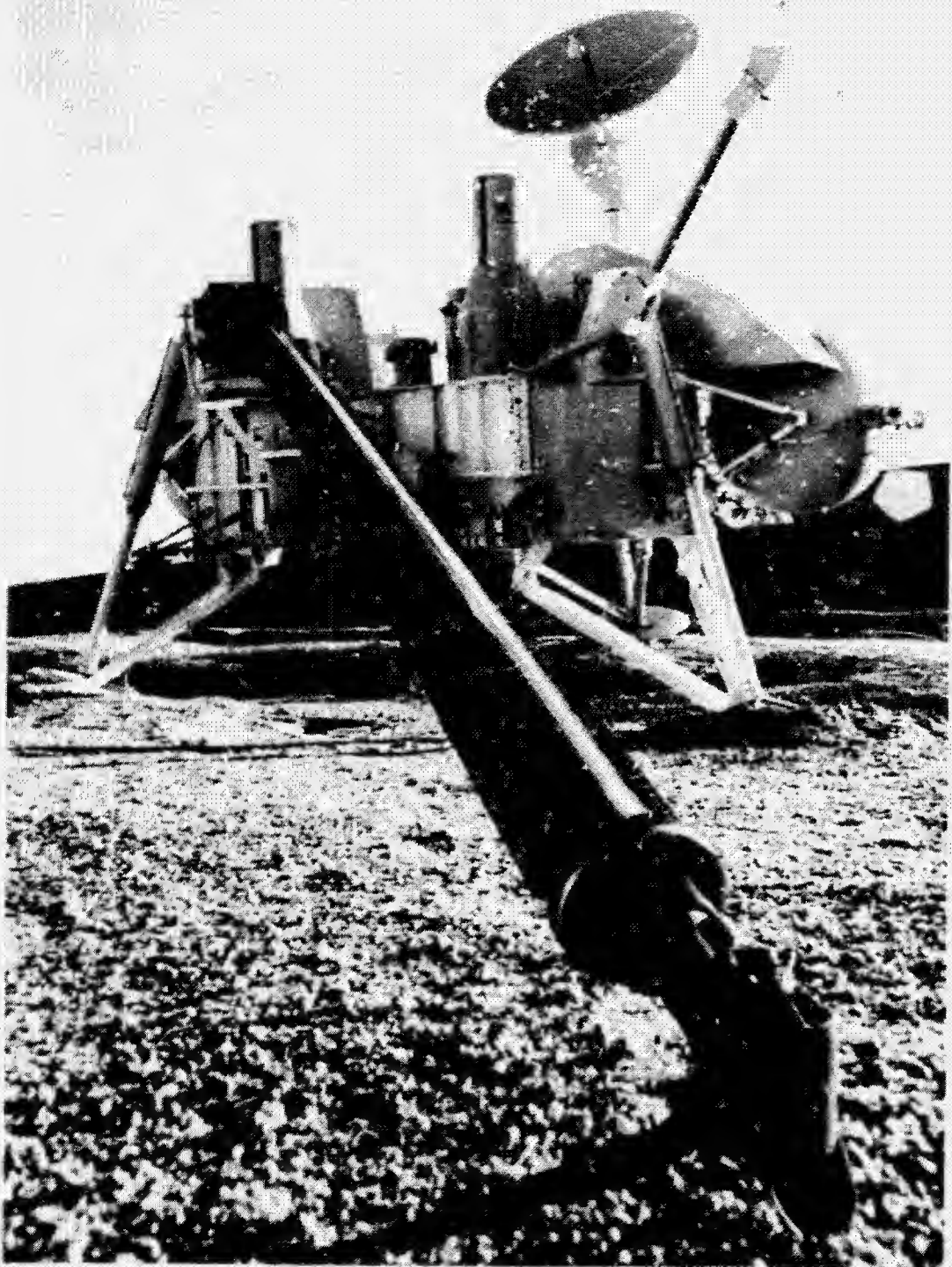


Figure 1.- Viking lander.

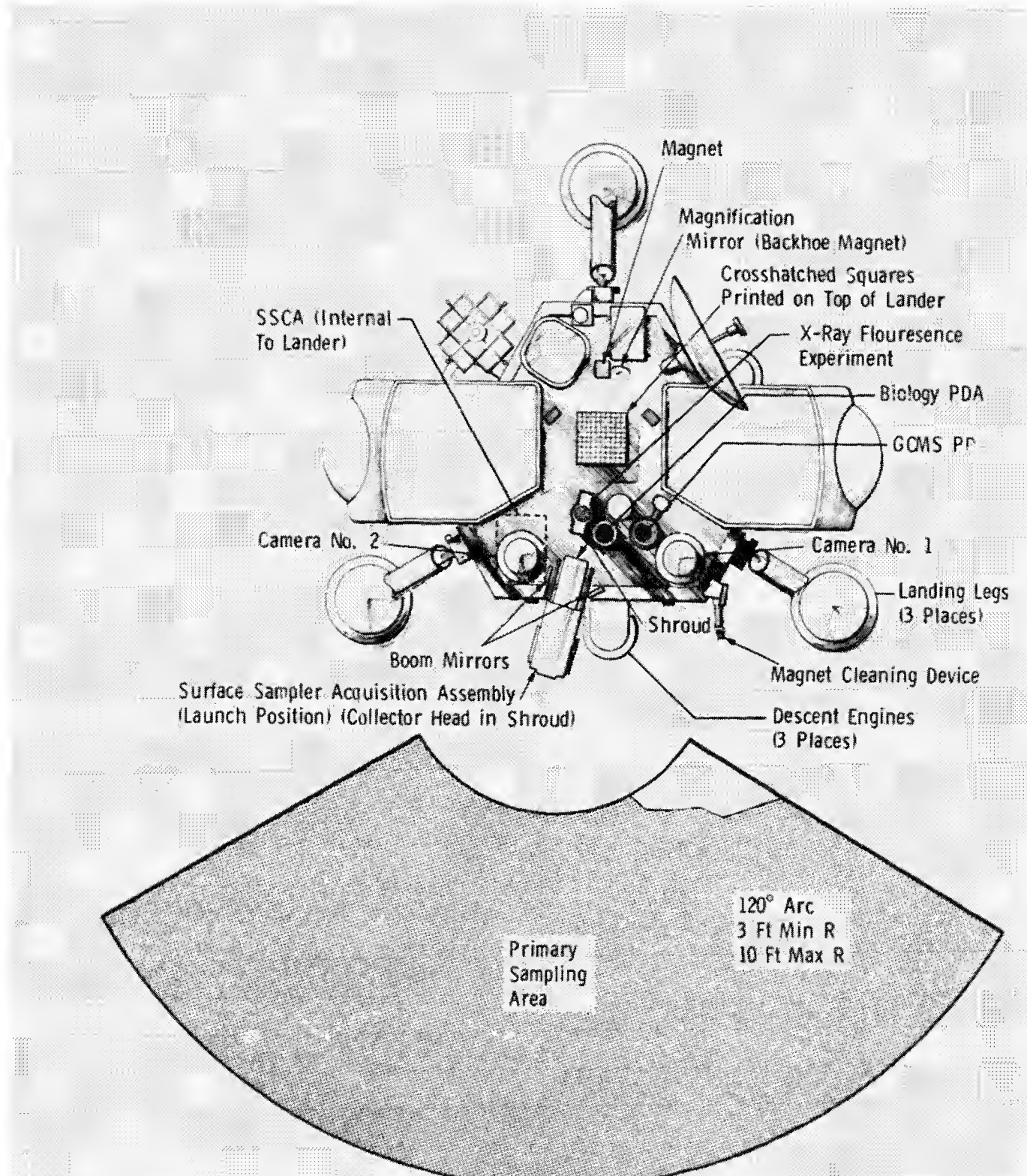


Figure 2.- Lander configuration.

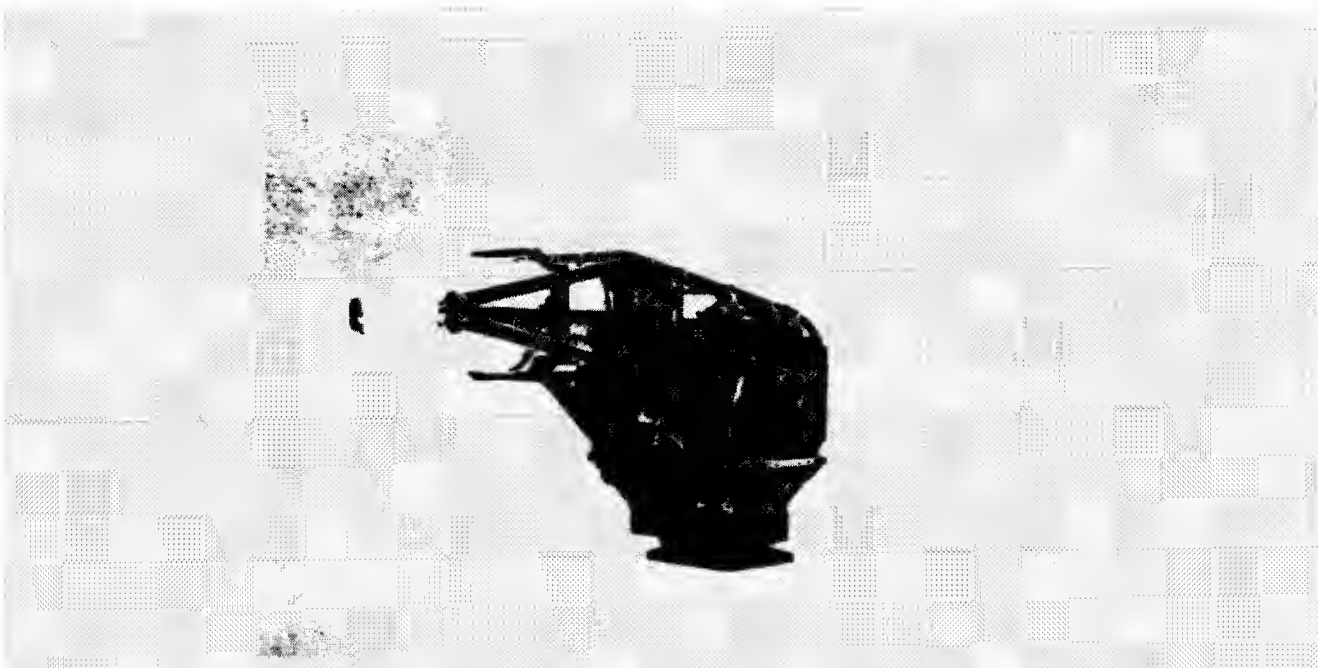


Figure 3.- Acquisition assembly.

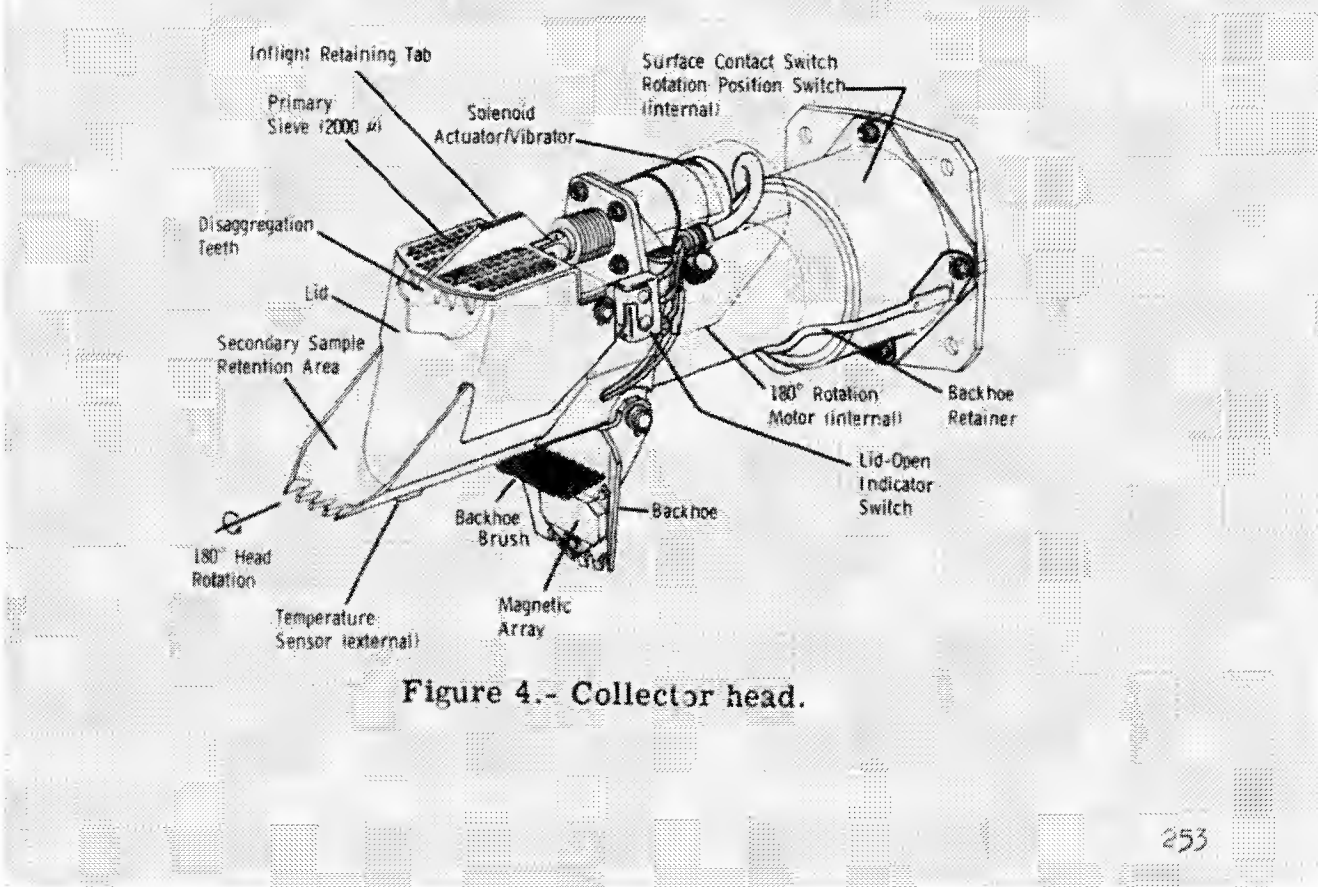


Figure 4.- Collector head.

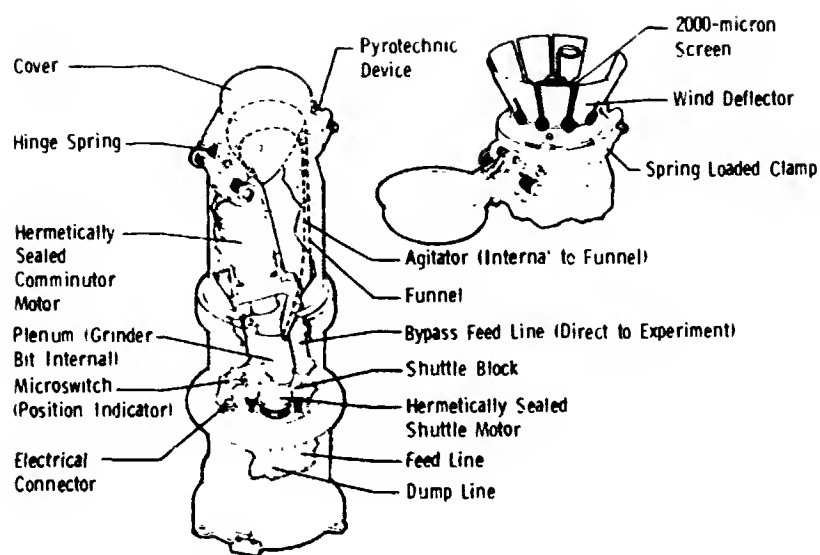


Figure 5.- GCMS PDA.

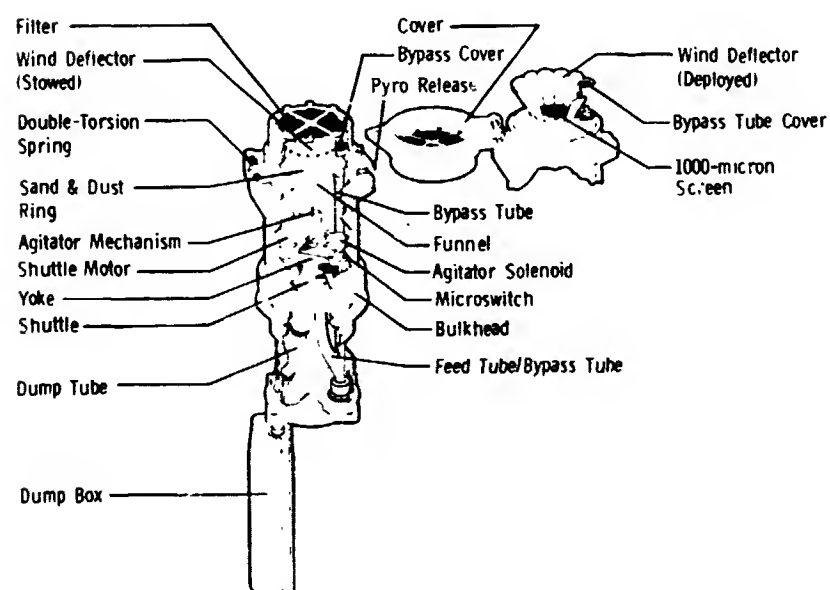


Figure 6.- Biology PDA.

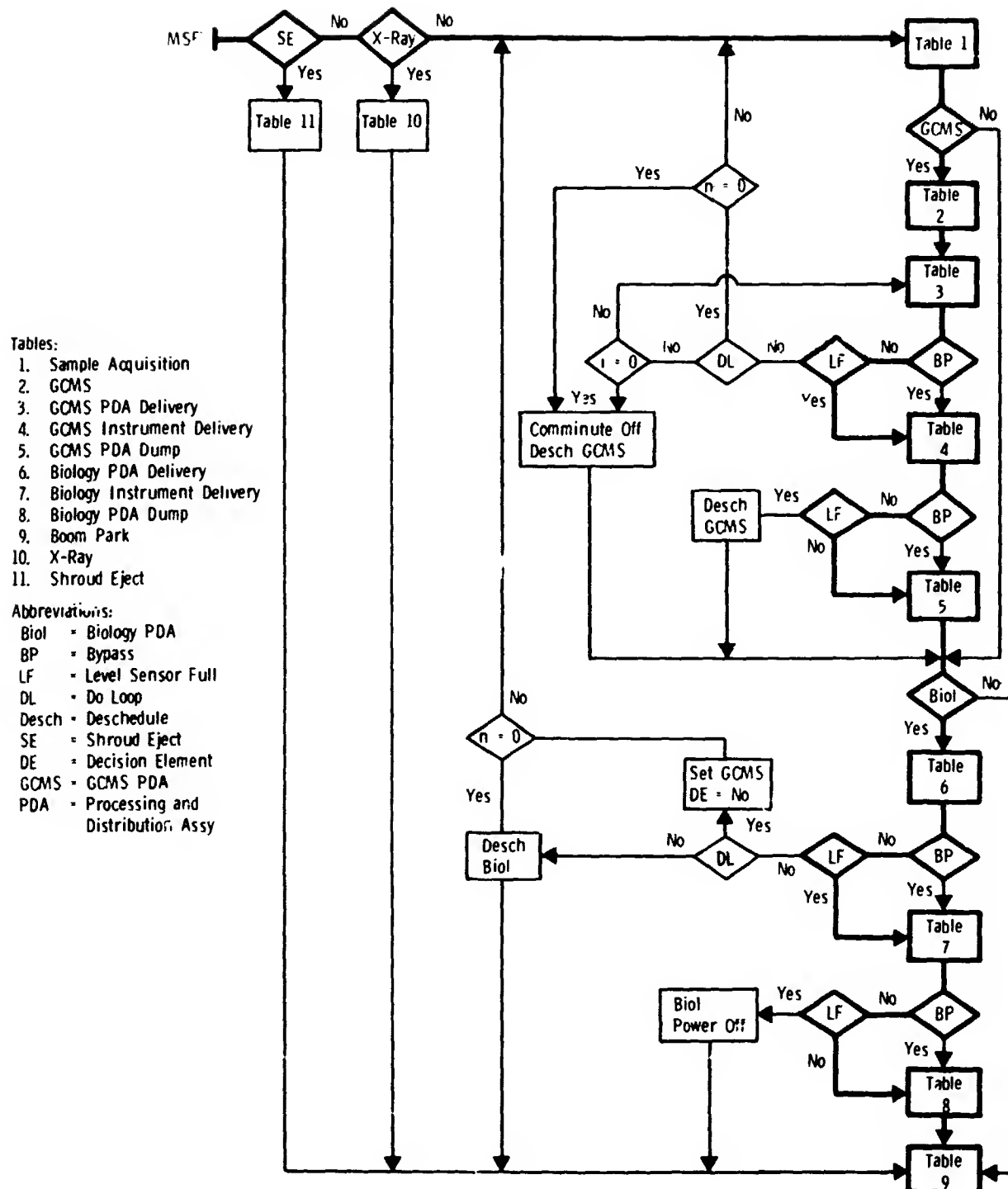


Figure 7.- Surface sampler operational capability diagram.

21. VIKING LANDER
ANTENNA DEPLOYMENT MECHANISM

By Kenneth H. Hopper and Dean S. Monitor
Martin Marietta Aerospace Corporation

SUMMARY

A Mars lander is currently being designed and built by Martin Marietta Aerospace as part of the Viking Project, under contract to the Viking Project Office of NASA Langley Research Center.

One of the mechanisms that is included in the configuration of the Viking Mars Lander is an antenna dish deployment mechanism which utilizes a mechanical escapement device for controlling deployment. The criteria require that the mechanism be capable of deploying the antenna under a wide range of aiding and retarding winds after landing on Mars but must limit the acceleration during deployment and latching of the antenna. Adding to the complexity of the design are the requirements for very accurate alignment after erection and heat sterilization prior to launch. This mechanism has been designed, fabricated and successfully tested to qualification test levels for usage on the Viking mission.

INTRODUCTION

One of the requirements of the Viking Project is that the Mars Lander have the capability of direct lander-to-Earth communication as well as relayed communication through the Mars Orbiters. This requirement resulted in the selection of a 30-inch-diameter parabolic dish antenna with the capability of being pointed at the Earth. The size of this antenna and the

need to locate it high enough above the lander to avoid interference, coupled with the spacecraft volume limitations, established the need for a deployment mechanism. See Figure 1 for a definition of the spacecraft envelope restrictions and the deployed relationship of the antenna to the lander.

DESIGN SELECTION

The integrated arrangement of all systems on the lander dictated the storage envelope and operational envelope following deployment. This then indicated that the deployment mechanism design would be a pivoted arm to swing the antenna through approximately 145° rotation from the stowed position to fully deployed position. A summary of the design criteria is presented in Table 1.

The main deployment loads result from the Mars surface winds. The results of wind tunnel tests upon a 45% scale model of the parabolic dish combined with gravity, cable bending and friction effects established the total maximum deployment load of 400 in-lb torque with the head wind. An aiding wind produces 200 in-lb of torque. A summary of the torque requirements is presented in Figure 2.

Trade-off studies of alternate means of powering the deployment mechanism included pyrotechnic gas generation, electric motor, clock spring drive, torsion spring, compression spring, constant-force spring, and stored gas systems. Due to the resulting minimum lander weight and overall simplicity, dual constant-force springs of laminated construction, similar to those for the Apollo lunar excursion module landing legs, were selected to power the deployment mechanism.

Studies of several means of controlling the rate of deployment and shock limitation included electrodynamic braking, hysteresis braking, centrifugal braking, deformable member shock attenuation, viscous damping, magnetic particle braking, mechanical escapements, and shock mounted limit stops. A mechanical escapement was selected as the design approach affording the best chance of success.

Since there was no need for precise control of the rate of deployment, the anchor-recoil type of escapement was selected over the balance-wheel type. It also has inherent self-starting performance, fewer mechanical elements, and the capability to operate over a wide range of torque loads. See Figure 3 for a schematic of the escapement device.

DESIGN DESCRIPTION

The deployment mechanism consists of a welded aluminum fixed support, a pivot-mounted support elbow, the power spring subassembly, a spring-loaded uplock latch subassembly, and the governor subassembly. The mechanism is shown in Figure 4 and its weight is 8.3 pounds.

The fixed support is a three-piece weldment consisting of a base plate, support tube, and hub and is made of 2219-T87 aluminum alloy. After rough machining, this assembly is stress relieved and then final machined. The base plate is pinned to the lander body for accurate angular alignment.

The support elbow, made of 2024-T851 aluminum alloy, is mounted on angular-contact, torque-tube type ball bearings within the hub of the fixed support. Fixed stop pins in the elbow contact integral limit stops in the hub to accurately position the support elbow at the end of its rotational travel. The support elbow terminates in a mounting flange which interfaces with the antenna mounting base. This mounting flange is required to be positioned within 16 arc minutes cone angular error but is typically within 1 arc minute upon completion of the elbow support travel.

The power spring subassembly consists of dual constant-force springs laminated of Elgiloy, a cobalt-chromium-nickel alloy, which together produce 400 in-lb of torque. One end is anchored to the hub and the other rolls over a spool on the elbow support.

The uplock latch is attached to the elbow support with a hinge pin. A torsion spring causes the opposite end to engage the outer diameter of the hub, drop into a pocket, slide up a ramp machined in the hub, and then lock the elbow support upon completion of the deployment rotation.

The governor subassembly, shown in Figure 3, includes a two-piece gear box, a three-pass gear train of a 300:1 ratio, the escapement, torsion pendulum, two R-4 ball bearings, six R-3 ball bearings, and a cover. The first gear mesh is driven from the end of the elbow support. The gear box is fabricated from 2024-T851 aluminum alloy, the gears are made from A-286 stainless steel, and the escapement from 17-4PH stainless steel. The escapement is the anchor-recoil type which produces an oscillation frequency:

$$f = K \sqrt{\frac{T}{I}}$$

Where - T is input torque and
I is pallet axis inertia

The escapement wheel also includes a ratchet clutch to provide for retracting the mechanism to the stowed position without a rate governing function. The active pallet faces and escapement wheel teeth are machined to 32 microinch finishes.

Dry film lubrication of bonded molybdenum disulphide types are incorporated in the ten ball bearings, the gears, the escapement, and within the laminations of the drive springs. A Teflon filled hard anodize coating serves to lubricate the spool upon which the power springs roll and the surfaces of the uplock latch.

Since the surfaces of the deployment mechanism reflect sunlight which may affect the lander cameras, a low reflectance coating is applied over Iridite surfaces on the mechanism.

DEVELOPMENT PROBLEMS

The design of the mechanism, with the exception of the escapement device, utilized technology that is well within the current state of the art and presented no particular problems during development testing. This application of an escapement device is rather unique, however, and required several iterations during test before the current design was finalized.

The major problems encountered were related to material selection, surface finish and lubrication, the detailed geometry of the pallet and wheel, and the stiffness of the pallet and its shaft. The initial configuration of the pallet and wheel is shown in Figure 5(a). After a few

operating cycles the mechanism would hang up because of brinelling of the aluminum pallet. A change to A-286 stainless steel pallet and wheel tended to correct this problem; however, hang-ups still occurred short of the desired operating life.

Under the assumption that a reduction in the impact load, obtained by reducing the stiffness of the pallet, would increase the operating life, the pallet and wheel geometry shown in Figure 5b was tested. This configuration eliminated the hang-ups but proved to be too flexible, resulting in a run-away failure mode when subjected to the simulated maximum aiding wind. It was concluded that the stiffness of the pallet could probably be fine-tuned to solve the run-away problem and still avoid the hang-up mode; however, in the interest of economy and schedule, a stiff pallet with a revised contact surface geometry was tried and, since it worked well enough to meet the life cycle goal of 100 cycles, no further development of the pallet stiffness was considered to be warranted. The final geometry is illustrated in Figure 5c.

The materials used in the final configuration are 17-4PH H900 hardness for the pallet and 17-4PH H950 hardness for the wheel. This selection was made to provide a harder material on the pallet than on the wheel since the pallet is impacted 24 times for each impact on a given wheel tooth. Also, a chrome plating was applied to the pallet; nickel plating, to the wheel; and as Lubco 905 dry lube, on both surfaces.

The development test article was retrofitted with the updated escapement hardware and the qualification level test program was reconducted. (See table 2.) After completing the vibration, pyro shock and landing shock tests, with approximately 36 operating cycles, the escapement mechanism again experienced a hang-up. A failure analysis concluded that the chrome plating on the pallet was breaking down and chipping off, resulting in sharp edges that cut into the softer wheel and causing the hang-up. Consequently, the chrome plating was removed from the pallet design. However, the Lubco 905 was retained. Retesting of this configuration has verified its adequacy for its intended purpose.

CONCLUSIONS

The constant force spring system proved to be lightest of the candidate drives examined. The escapement type of rate governor provides adequate rate control throughout the large temperature range combined with the large torque variation in a simple, reliable manner. Although only one deployment on the Mars surface is required, the design goal of 100 deployments under worst case loading has been successfully demonstrated with this mechanism.

TABLE 1
DEPLOYMENT MECHANISM DESIGN CRITERIA

Deployment with 40 m/sec Restraining or 70 m/sec Aiding Wind

Up-Latching During Deployment That Prevents Back Travel

No Erection Velocity Required to Engage Uplock

Governor Life 20 Cycles With 40 m/sec Aiding Wind

Governor Life Goal of 100 Cycles

Erection Time - <5 Minutes With No Wind

Acceleration of High Gain Antenna Center of Gravity Less Than 2 G

Angular Error Mast/High Gain Antenna Interface - <16 Arc Minutes
Root Sum Square

TABLE 2
DEPLOYMENT MECHANISM DEVELOPMENT TESTS

Environmental Effects

Heat Compatibility	Five Cycles of 40 Hours at + 267°F Two Deployments
Vibration	Resonance Survey Sinusoidal Vibration Sine Vibration Requirement 5 to 19 Hz at 0.4 Double Amplitude (DA) 15 to 50 Hz at 7.5 G's Peak Rolloff at 20 dB/Octave from 50 to 100 Hz 100 to 250 Hz at 0.75 G's Peak Sweep Rate - 1 Octave/Min
	Random Vibration Normalized Spectrum 20 to 250 Hz: + 3 dB/Octave 250 to 100 Hz: at 0.75 G ² /Hz 1000 to 2000 Hz: -6 dB/Octave Overall Level: 10g rms 5 Minutes per Axis
	Six Deployments
Landing Shock	30 G 1/2 Sine Pulse Three Times Each Direction in Each Axis
	Six Deployments
Surface Thermal	Two-Hour Exposures at + 145°F Two-Hour Exposures at - 195°F Two Deployments at Each Temperature
Sand and Dust	Six-Hour Exposure Two Deployments
<u>Operating Pyro</u>	Six Deployments with Flight-Type Pyrotechnic Pin Puller Release System
<u>Deployment Life</u>	3/8 G Attitude With 70 Meter/Sec Aiding Wind 74 Deployments Total deployments under all environments is 100.

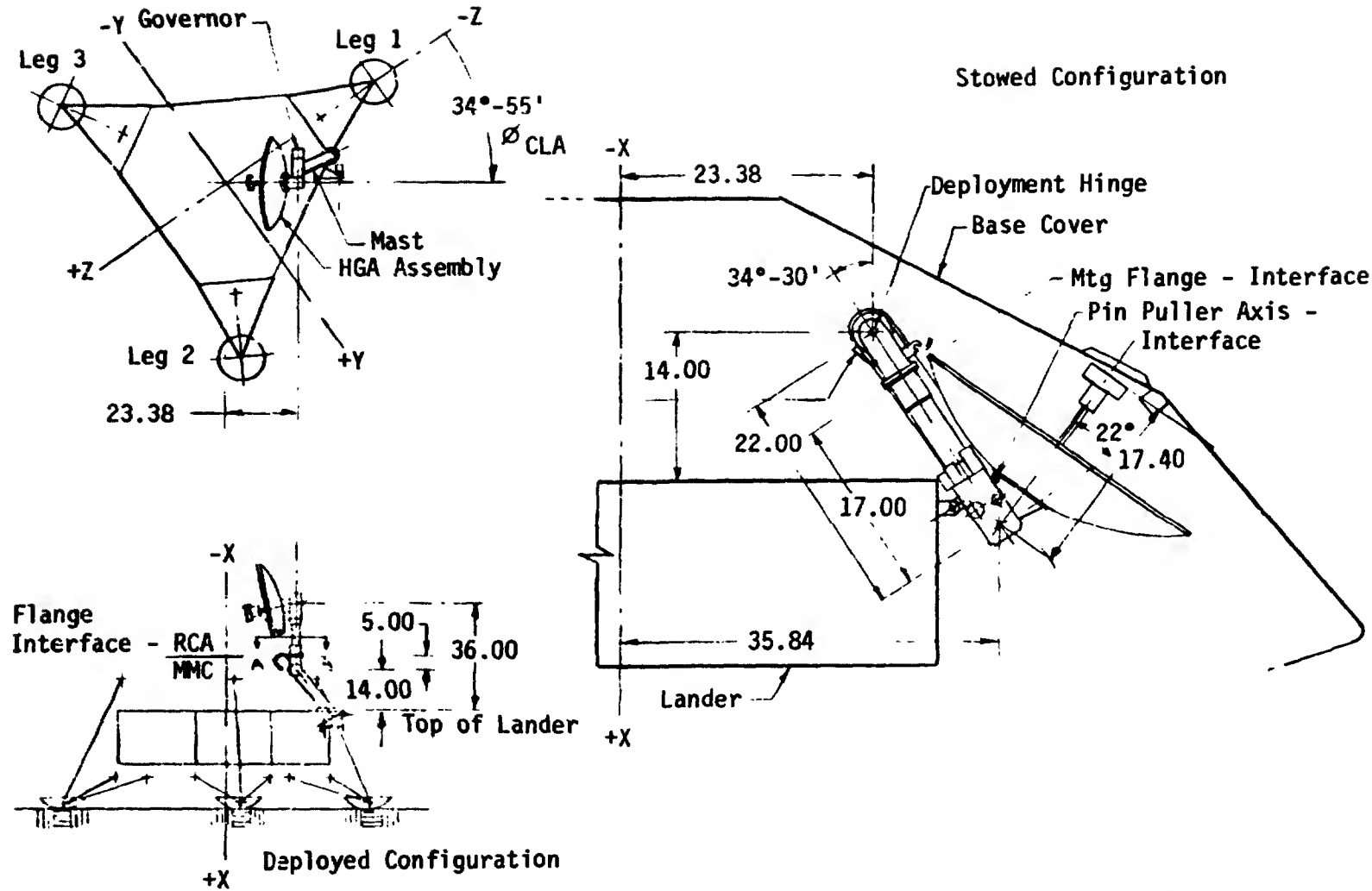


Figure 1.- Antenna deployment mechanism arrangement on Viking Lander.
All linear dimensions are in inches.

NOTES:
 Curve A - Retarding 70 m/sec wind
 Curve B - Aiding 70 m/sec wind
 Curve C Is a Composite, Assuming Wind Direction Reversal and A
 10% Factor for Friction, Bending of Cables, Sand in Dish, etc
 & 40 m/sec retarding wind
 $\rho = 10.38 \times 10^{-5} \frac{\text{lbf}\cdot\text{sec}^2}{\text{ft}^4}$

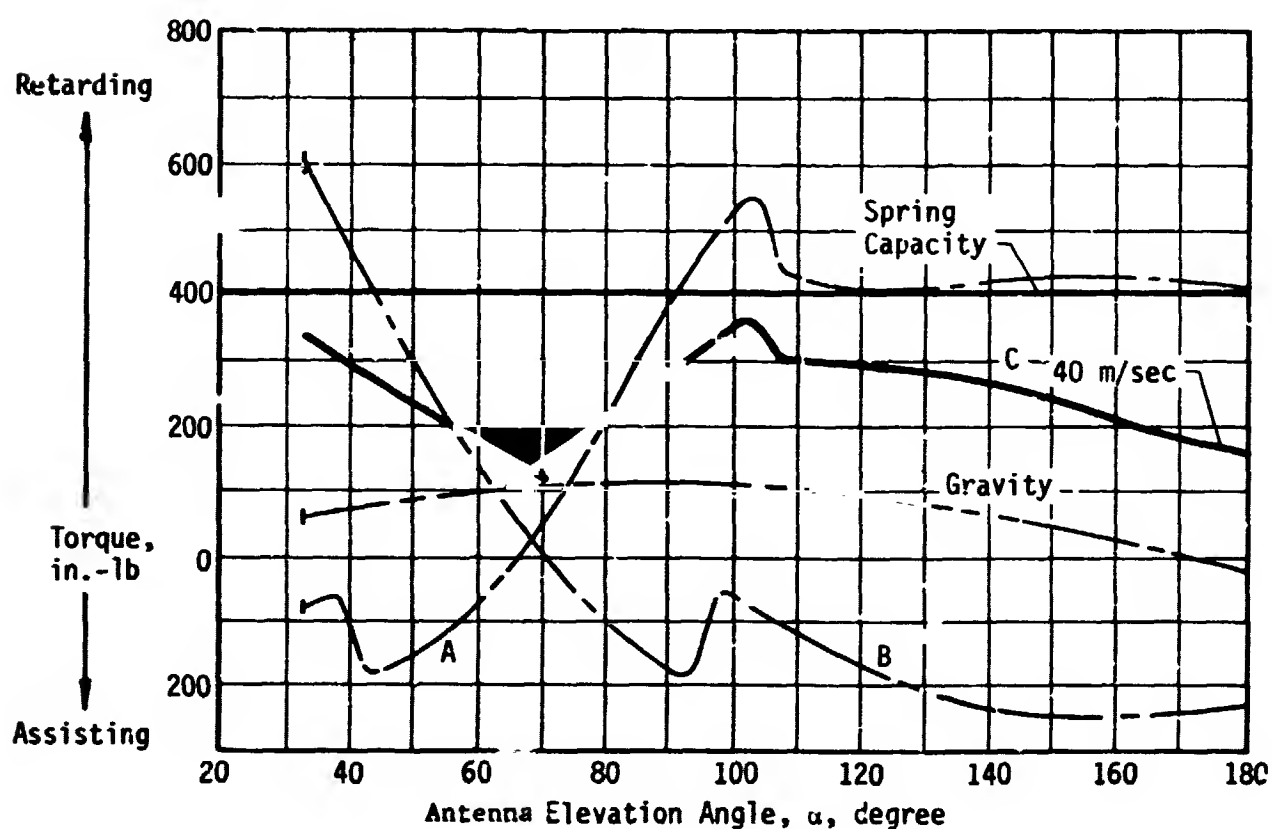


Figure 2.- Deployment loads.

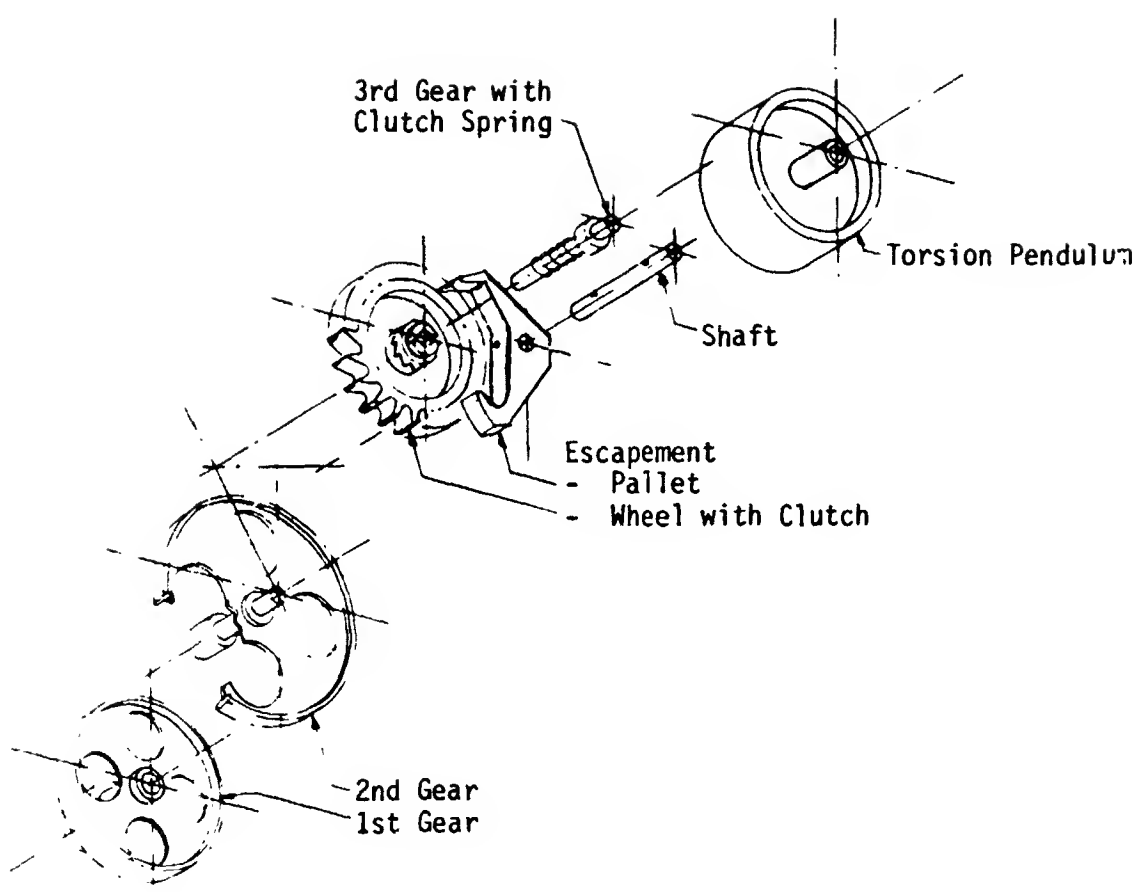


Figure 3.- Governor subassembly.

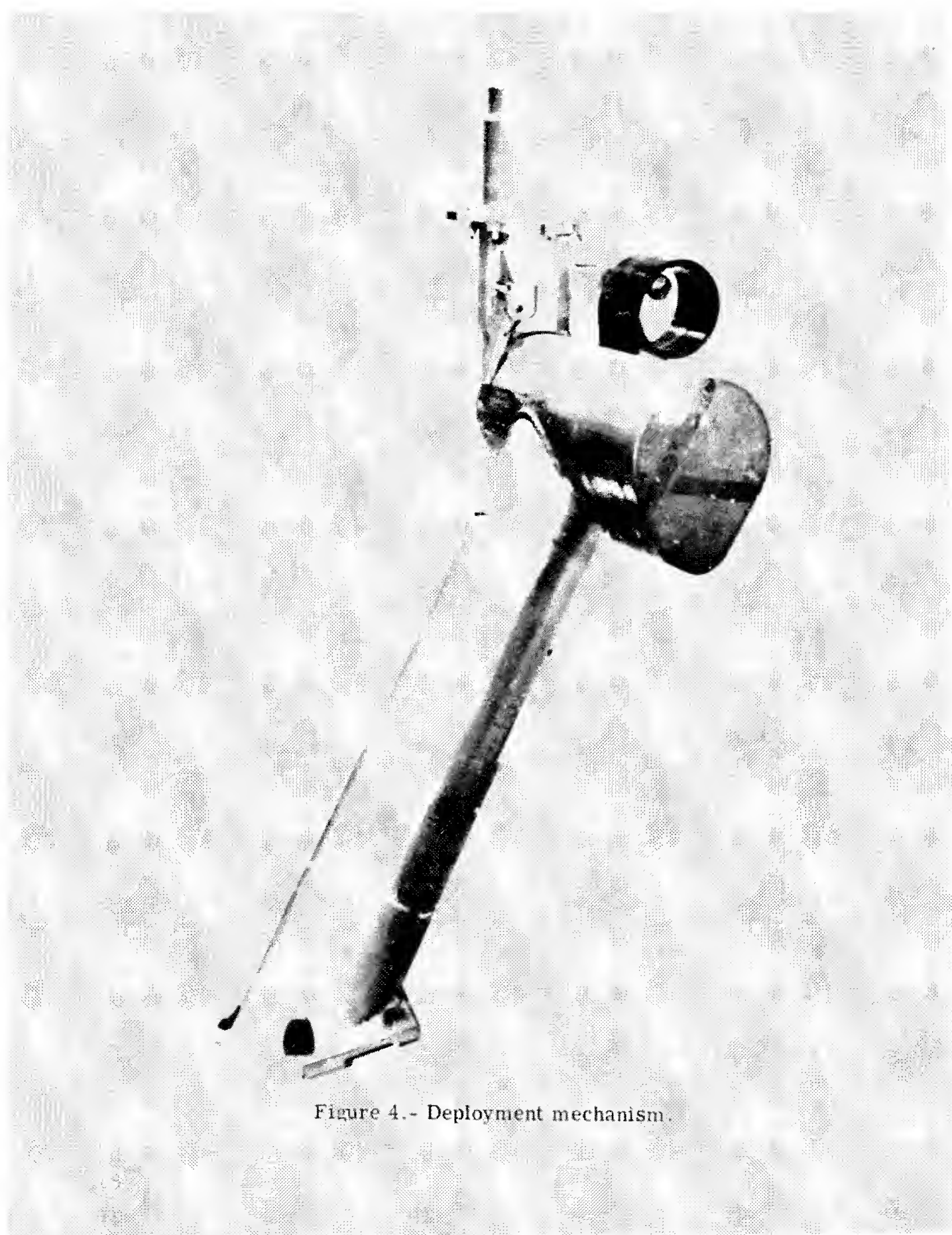


Figure 4.- Deployment mechanism.

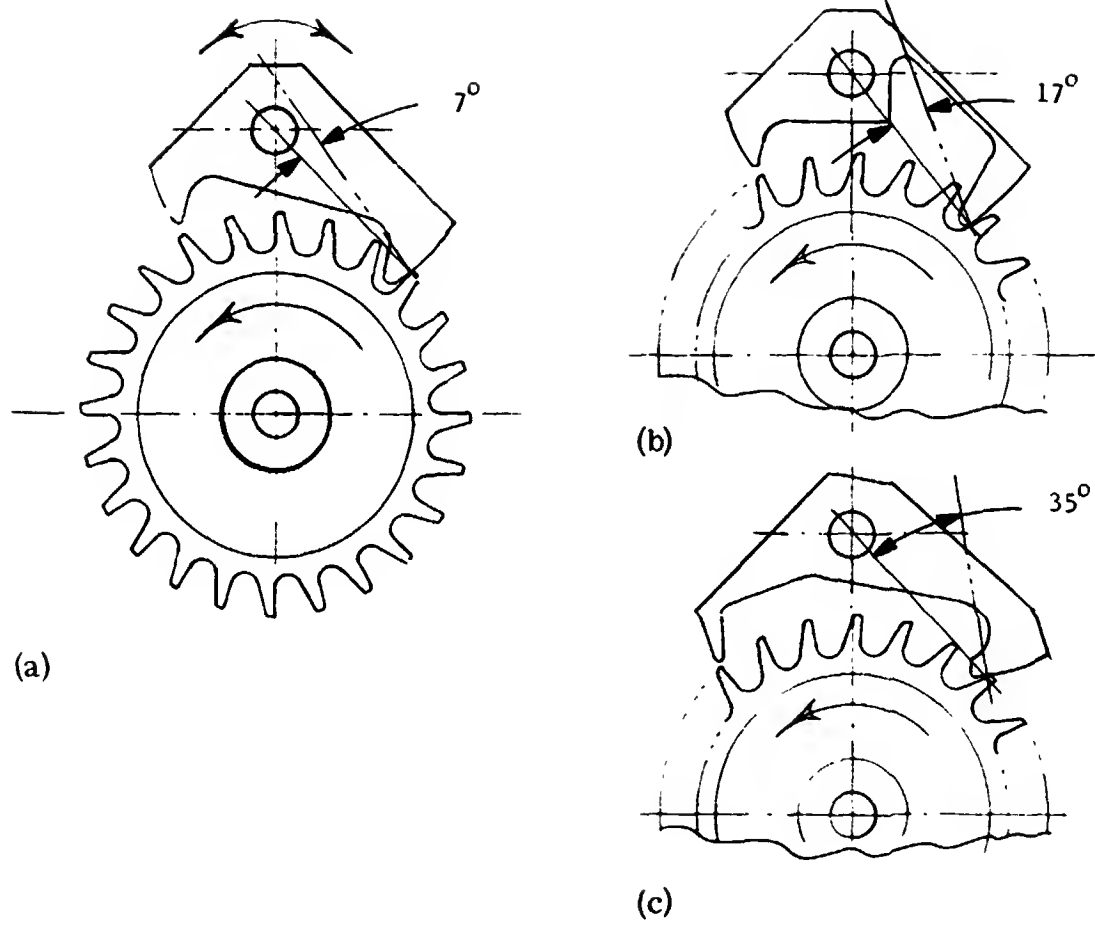


Figure 5.- Escapement geometry.

22. OPTICAL MODULE FOR THE INTEGRATED REAL-TIME CONTAMINATION MONITOR*

E.H. Wrench

**Convair Aerospace Division of General Dynamics
San Diego, California**

SUMMARY

This paper describes the concept of a real-time contamination monitor and traces the evolution of the optical module component from laboratory model through the engineering evaluation model. Mechanisms employed and problems experienced are described. Current efforts are directed toward a major simplification of design in a unit intended for flight.

INTRODUCTION

With the current and projected use of optics in space, consideration must be given to the possible degradation of optical components by contaminants evolving from the spacecraft. The potentially severe consequences of such degradation have led NASA to the philosophy that "contamination is an engineering environment just like shock or vibration and, as such, must be measured." Beginning in 1966, NASA has maintained a continuing program to develop contamination monitoring equipment and, in 1971, undertook development of an Integrated Real-Time Contamination Monitor (IRTCM).

The integrated module (Figure 1) consists of four independent instruments and an experimental active cleaner. The independent instruments include a quartz crystal microbalance (QCM) for measuring mass accumulation, a residual gas analyzer to identify the contaminant, a particle size analyzer, and an optical module for measuring the degradation of optical properties. This paper describes the evolution of the optical module design.

LABORATORY FEASIBILITY VERSION

In 1970, Convair Aerospace Division of General Dynamics undertook to design and develop a laboratory feasibility version of an optical module for measuring reflectance, transmission, and scattering of optical surfaces in a contaminating environment. The feasibility model (Ref. 1) uses a pair of monochromatic ultraviolet sources to illuminate the sample. To eliminate effects of source and detector gain change, a single photomultiplier sequentially measures incident and specularly reflected beams. Scattered radiation from the sample is collected by a hemiellipsoidal reflector and reimaged onto the same photomultiplier. Figure 2 shows the optical elements and photomultiplier positions for the various measurements.

*Work described in this paper was performed for the Thermal Environment Physics Branch, Space Sciences Laboratory, George C. Marshall Space Flight Center.

Since the ultraviolet radiation employed (1.236A and 1.849A) is absorbed in air, the instrument must be operated in a vacuum. The mechanical design problem thus becomes one of physical manipulation within a vacuum chamber. For manual operation of the feasibility model, magnetic motion feedthroughs were employed. Rotary motions, which included sample and light source selection, used Varian magnetic rotary feedthroughs and conventional CRES ball bearings lubricated with molybdenum disulfide. Both rotary and translational motions were required to move the phototube between the transmission, reflectance, and scattering measurement positions. A push-pull-rotary magnetic feedthrough from Huntington Mechanical Laboratories was used. A soft iron slug on the output shaft of this feedthrough is supported on a rotary bearing which, in turn, is mounted to a wheeled carriage riding on the inside of the sealing tube. An external magnet slides on the exterior of the tube and is free to rotate or translate. Both feedthroughs worked well, although the push-pull operation is mushy when operating with appreciable loads.

In the feasibility model shown in Figure 3, the rotary and push-pull feedthrough can be seen to the right of the vacuum chamber flange; the light source housing, photomultiplier mount, hemiellipsoid, and sample mount wheel are at left.

ENGINEERING EVALUATION MODEL

In 1971, Convair Aerospace began development of an engineering model version of the optical module. It was specified that this instrument employ the same optical system, including the sources and photomultiplier, but that the instrument be fully automated and capable of unattended operation and data printout under computer control. The instrument was to incorporate provisions to electrically heat and monitor the temperature of the samples. Further, since the instrument was intended for use in ATM testing, a rigid material selection criterion was established (Ref. 2).

Since the optical design and sequence of operations were fixed, the task became one of automating the manual manipulations to occur in a specified sequence. The requirement manipulations are:

Open or close doors to expose samples to contaminants, either on command or as part of the measurement sequence. On command, move sample wheel to bring any one of three sample groups to a contaminant exposure position. Rotate sample wheel four positions to bring contaminated group to the measurement station, advance wheel one position for each of four measurements, and return wheel eight divisions after measurement.

Move photomultiplier in both translation and rotation, dwelling for measurement at the transmission, scattered, and reflectance positions. Return to initial position.

Change light source from krypton to mercury source and back after each measurement cycle.

All of these motions can be produced by a clockwise and counterclockwise rotation or by a forward or aft translation, which can itself be produced by a rotating screw. Initially, it was proposed to use the module shown in Figure 4, which consists of the geneva mechanism and segmented gear reverser described in Ref. 3. A breadboard of this device encountered a number of difficulties. Note that the teeth that drive in the forward direction must be completely disengaged before the reverse drive teeth can engage. When the geneva reaches the dwell point, the load is completely decoupled from the drive. If the load shifts even a fraction of a tooth, re-engagement may occur with the teeth meeting tip-to-tip rather than tip-to-valley. Further, even when properly phased the first tooth takes the full lead only at the tip and at an angle considerably displaced from the line of centers. Since smooth operation could not be achieved, this approach was abandoned.

An alternative drive module for producing intermittent and reversing motion consists of a pair of

geneva mechanisms coupled through a differential (Figure 5). This combination, which operated smoothly and efficiently when breadboarded, was adopted for the engineering model. After assembly of the complete unit, a basic deficiency was discovered: prohibitively high torques were required to move the load. Since ball bearings were used for the shafts and the drive stud, we initially suspected improper gear centers and went so far as to dress the genevas to increase clearance. Still, the effect persisted. The input turned freely until an output load was introduced; then it bound up. The source of the binding is now understood. In Figure 5, note that when Geneva A is being driven through the low-friction ball bearing stud, the torque is transmitted not only to the load, but back through the differential to the locked Geneva B. The binding is produced by friction between the drive wheel and the stationary geneva, which is under load. Note that this effect will occur whenever a geneva is used to support a load and will occur during the dwell interval rather than when the load is being moved. We eliminated this binding by fabricating new geneva drivers having a double row of miniature ball bearing rollers around the periphery of the locking cam (Figure 6). The technique worked very well with the loads involved, though it should be noted that each roller must be capable of withstanding the full torque load and that the roller rather than the drive stud bearing may become the critical component.

A mechanical schematic of the full gear train is shown in Figure 7. With the demise of the mechanical calculator and the poor repute of the cuckoo clock, this may well be the last of the gear train sequencers. The doors for sample exposure and the initial position of the sample wheel, which are under operator command control, employ separate motors with electrical limits. The remainder of the mechanism employs a single motor and automatically sequences the position of the photomultiplier, selection of the light source, and incremental advancement of the sample wheel. The train employs eleven geneva motions and five differentials.

The sequence consists of 32 unique steps which are then repeated. Four sequences are performed to measure each sample group. Completion of the fourth group electrically initiates repositioning of the sample wheel to the contaminant exposure station and opens the contaminant doors. Figure 8 shows the gear train, while Figure 9 shows the complete instrument and Figure 10, the control console with manual controls and the computer for automatic operation and data printout.

OPERATIONAL EXPERIENCE

One major failure was encountered with the instrument and the history of events leading to the failure is instructive. One requirement for the instrument was incorporation of QCMs and sample heaters into the sample wheel. Electrical connections to the wheel used a ribbon wire wrapped into a jellyroll configuration (Figure 11). The ribbon worked properly for the 1-1/3 revolution reversible movement required. End of travel was electrically sensed.

A second requirement of the program was to demonstrate cleanliness of the vacuum rated system by measuring the vacuum obtainable at elevated temperature. While we had rigidly adhered to the material selection criteria of Ref. 2 and had specified and used nylon wire ties, a few ties were inadvertently made with waxed tie cord.

The unit was placed in a vacuum chamber, pumped down to approximately 10^{-6} torr, and the exterior of the chamber heated to 250°F with electrical heater tape. The unit was energized to use the temperature sensors incorporated into the instrument.

Since heat transfer was primarily by radiation from the walls, the temperature rise of the instrument was only a few degrees per hour and the bakeout cycle extended over 72 hours of continuous operation. As luck would have it, it reached the melting point of the waxed cord at

3 o'clock in the morning. The pressure, which had been gradually decreasing, suddenly surged up, causing the ion pump to arc. We valved off the ion pump, restarted the roughing pump, and attempted to cycle the instrument. The arcing had destroyed electronic components used to sense the sample wheel position and the end-of-travel sensor failed. The wire ribbon jellyroll continued to wind up, eventually failing the ribbon. Unfortunately, we did not have a spare ribbon and were faced with a delivery deadline tied to the schedule for testing the Apollo telescope mount at Chamber A in Houston. In desperation, we fabricated a substitute wheel harness by bundling wires into a heat-shrinkable sleeve and winding into a helix (Figure 9). The improvised fix worked during the remainder of the tests in San Diego; however, after installation and pumpdown in Chamber A, the instrument failed to operate. Post-test inspection revealed that an upper coil of the helix had expanded when the wheel was unwinding and had dropped over a lower coil. Upon reversal, the helix attempted to tighten but the overlapped loop cinched up on the inner loop, resulting in binding. The conscious application of motor overvoltage in an attempt to break loose the bind eventually burned out one motor and apparently caused insulation damage in the second.

Fortunately, we were not the only ones to experience difficulties during the test. Water cooling lines in the chamber ruptured, producing a rare Texas blizzard and the test was terminated. We were able to return the unit to San Diego and, by then, had obtained additional ribbon wire. We rebuilt the wheel harness to the original configuration and replaced the shorted motor. During the second test at Chamber A the instrument operated for approximately 40 hours under computer control, producing hundreds of print outs. About eight hours before conclusion of the test, the instrument failed while operating unattended. Post-test inspection revealed a failure of the second original motor, presumably due to abuse when subjected to overvoltage during the aborted test. Thus, all failures encountered resulted not from the proverbial horseshoe nail but from a piece of string or – more exactly – from the wax on a piece of string.

FLIGHT ARTICLE SIMPLIFICATION

We are currently performing a study to achieve a major reduction in complexity for a flight article. This simplification is based upon our experience with the previous configuration. Originally, it was feared that the intensity of the ultraviolet sources might be marginal when measuring scattered radiation and that the number of optical surfaces in the light path should be minimized. In practice, we have found it necessary to use a perforated screen with a transmission of only 7% to prevent saturation of the photomultiplier when viewing the impinging beam. By taking advantage of the available intensity, we can introduce an optical crank and eliminate the necessity of moving the photomultiplier. The conceptual design of the optical train for measuring the impinging and specular beam is shown in Figure 12. The sole moving part is the optical rotor, which advances stepwise to each of four positions. No reversal of rotation is required since no electrical leads are needed on the rotor.

Scattered radiation is collected and reimaged on a second stationary photomultiplier. A double-paraboloid collection system (Figure 13) is currently under study as a replacement for the hemiellipsoid. The paraboloids permit positioning of the photomultiplier above the plane of the sample. This allows the samples to be mounted on a drum where electrical connection can be made with the hardwire rotating coupling described in Ref. 4. The coupling permits unidirectional continuous rotation of the sample drum and eliminates the possibility of the overtravel failure encountered on the current model.

An inexpensive demonstration breadboard of the optical train has been fabricated employing filament sources and photodiodes. Figure 14 shows the optical module alone and as assembled into a housing with analog outputs displayed on meters. The conceptual design of the flight unit is shown in Figure 15.

REFERENCES

1. "A Module for Measuring Optical Degradation," AIAA Paper 71-461, AIAA 6th Thermophysics Conference, Tullahoma, Tenn., April 1971.
2. "ATM Material Control for Contamination Due to Outgassing," 50M02442
3. "Ingenious Mechanisms for Designers and Inventors," Volume III, Industrial Press, 1951, pp 143-145.
4. E.H. Wrench and L. Veillette, "A Hardwire Rotating Coupling," 4th Aerospace Mechanisms Symposium, May 1969.

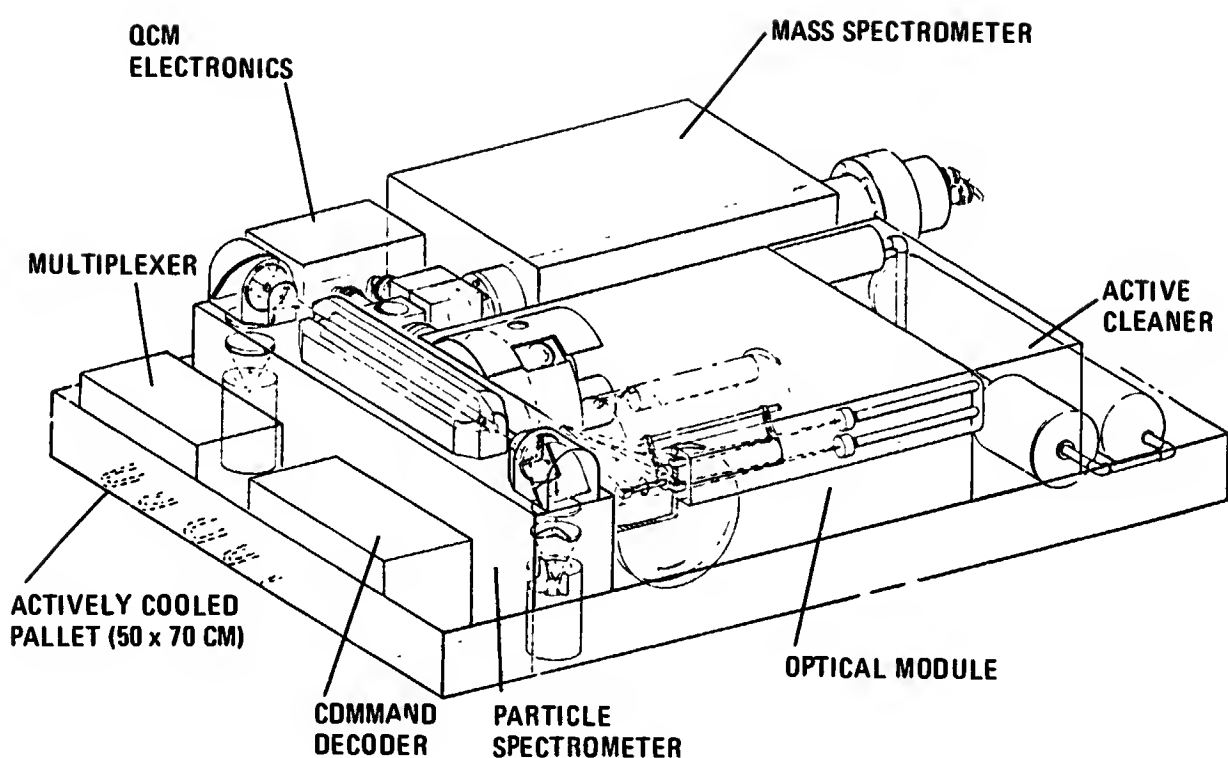


Figure 1.- Integrated real-time contamination monitor.

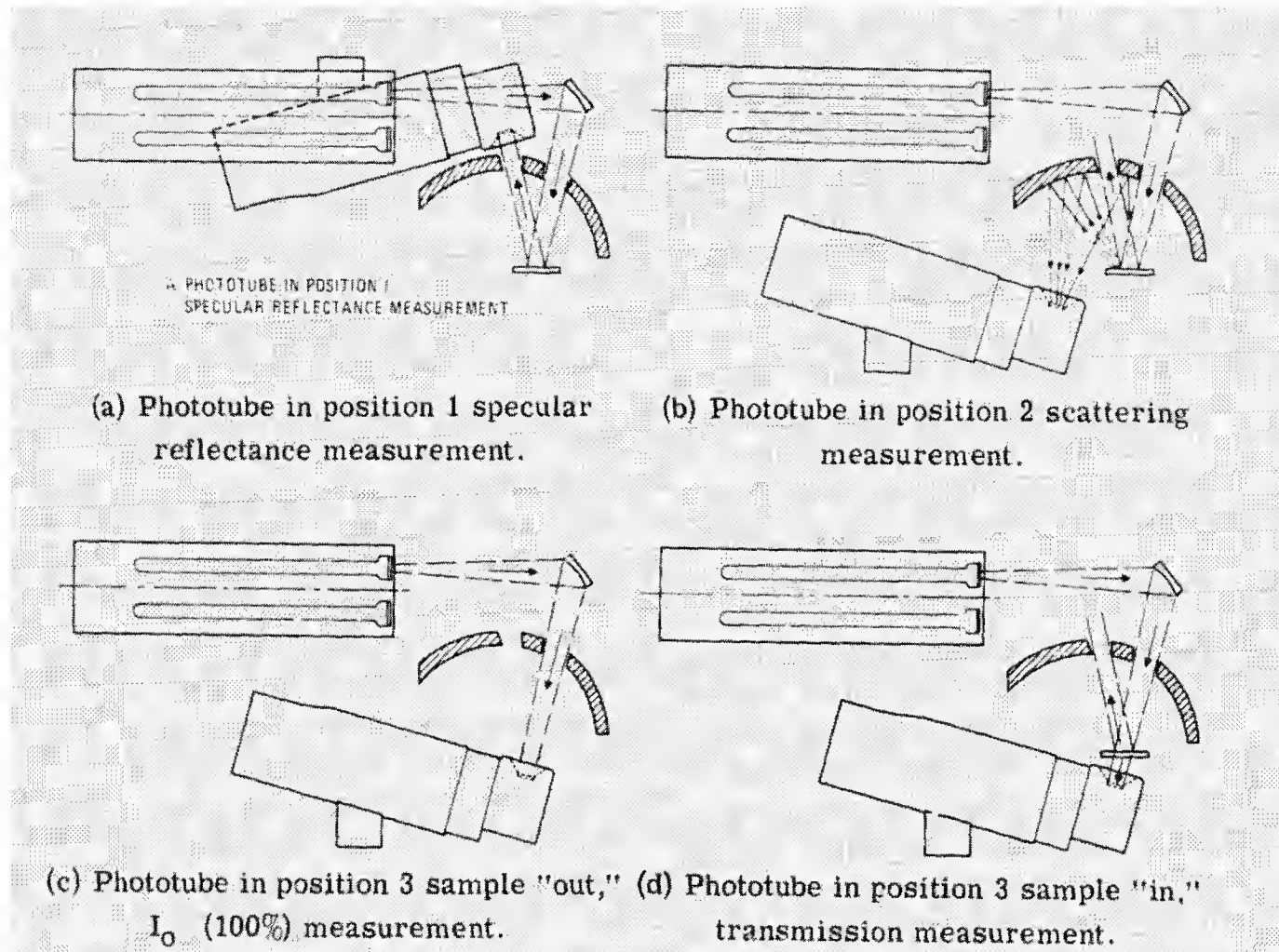


Figure 2.- Optical design.

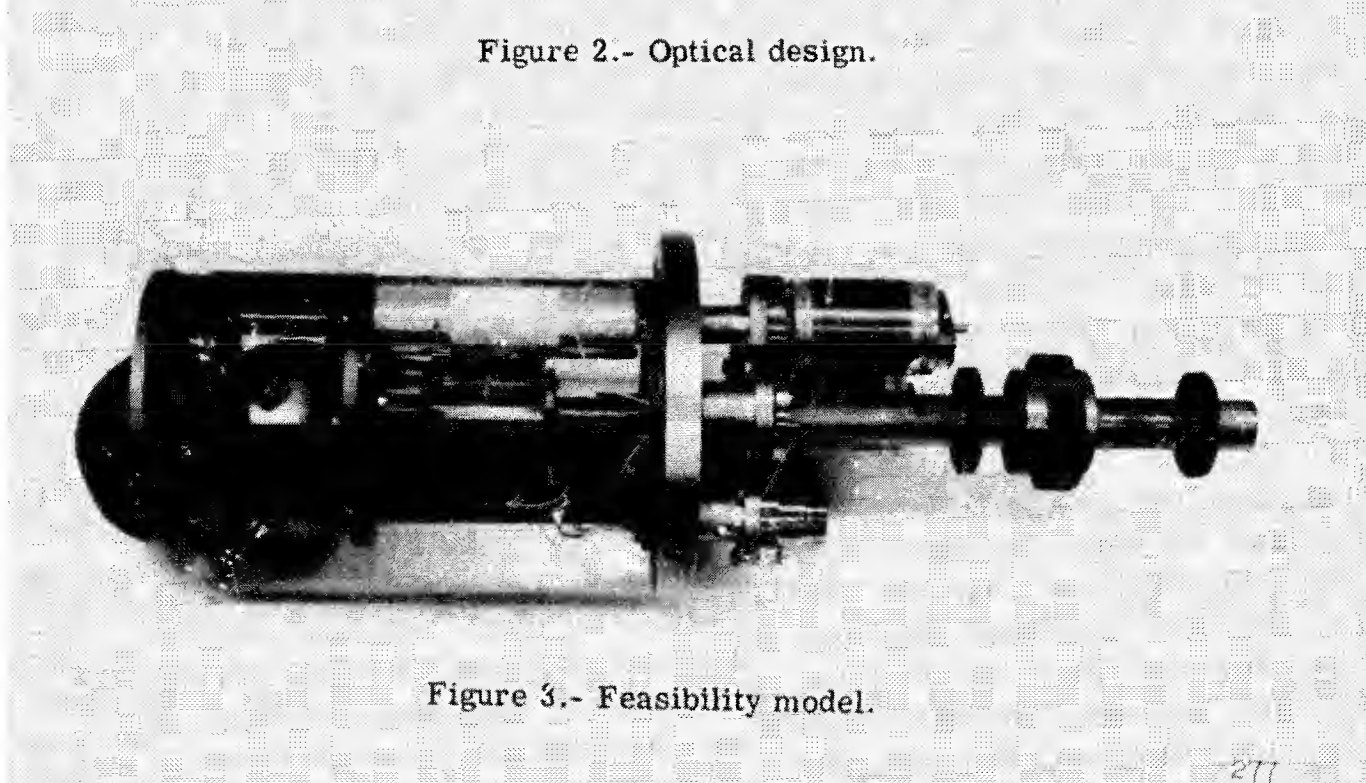


Figure 3.- Feasibility model.

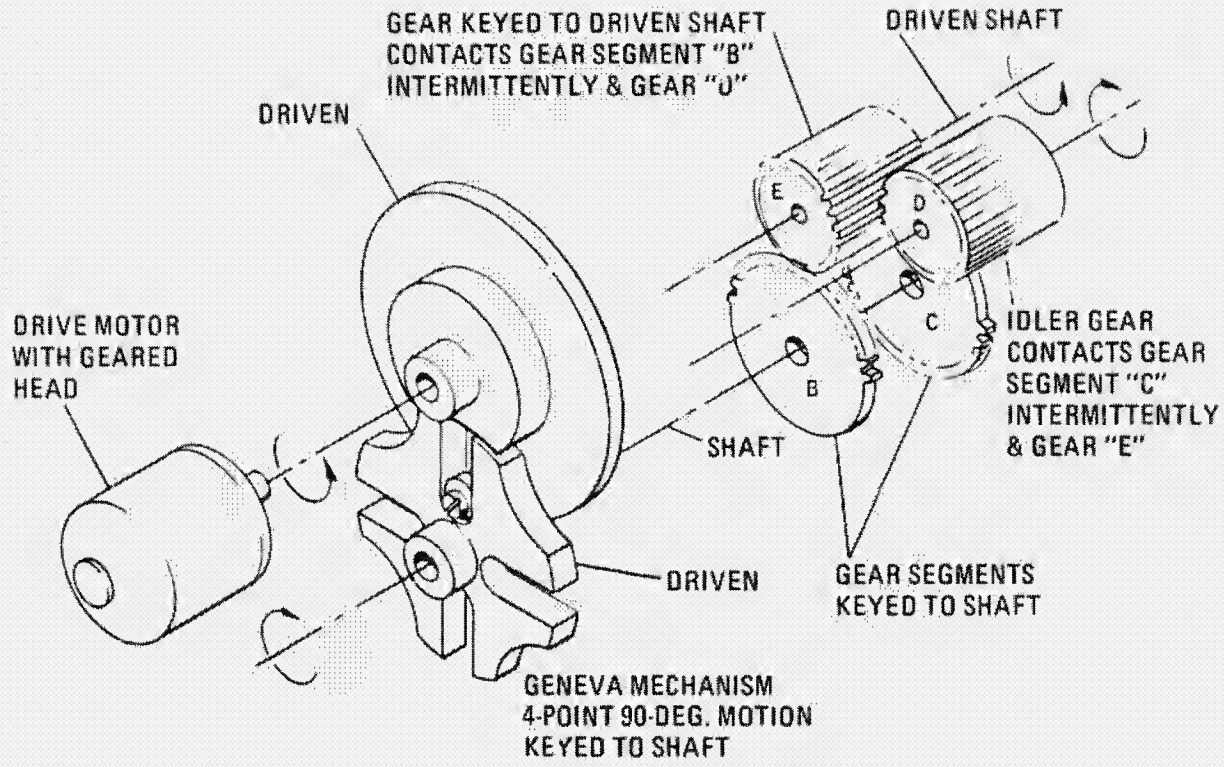


Figure 4.- Module with geneva mechanism and segmented gear reverser.

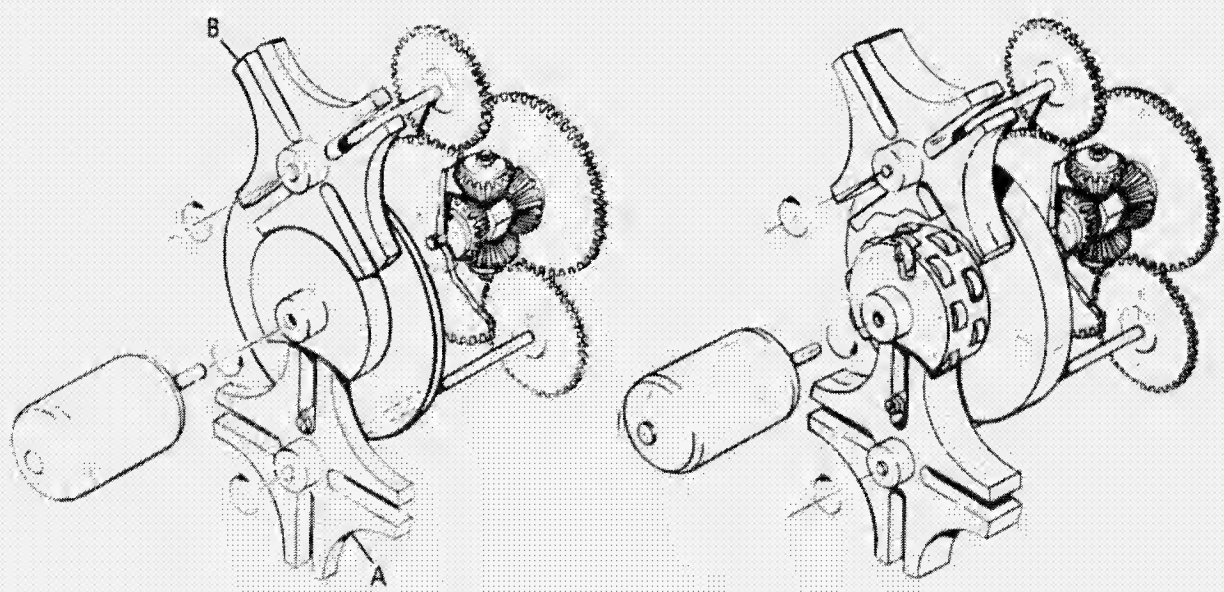


Figure 5.- Genevas with differential.

Figure 6.- Ball bearing geneva cam.

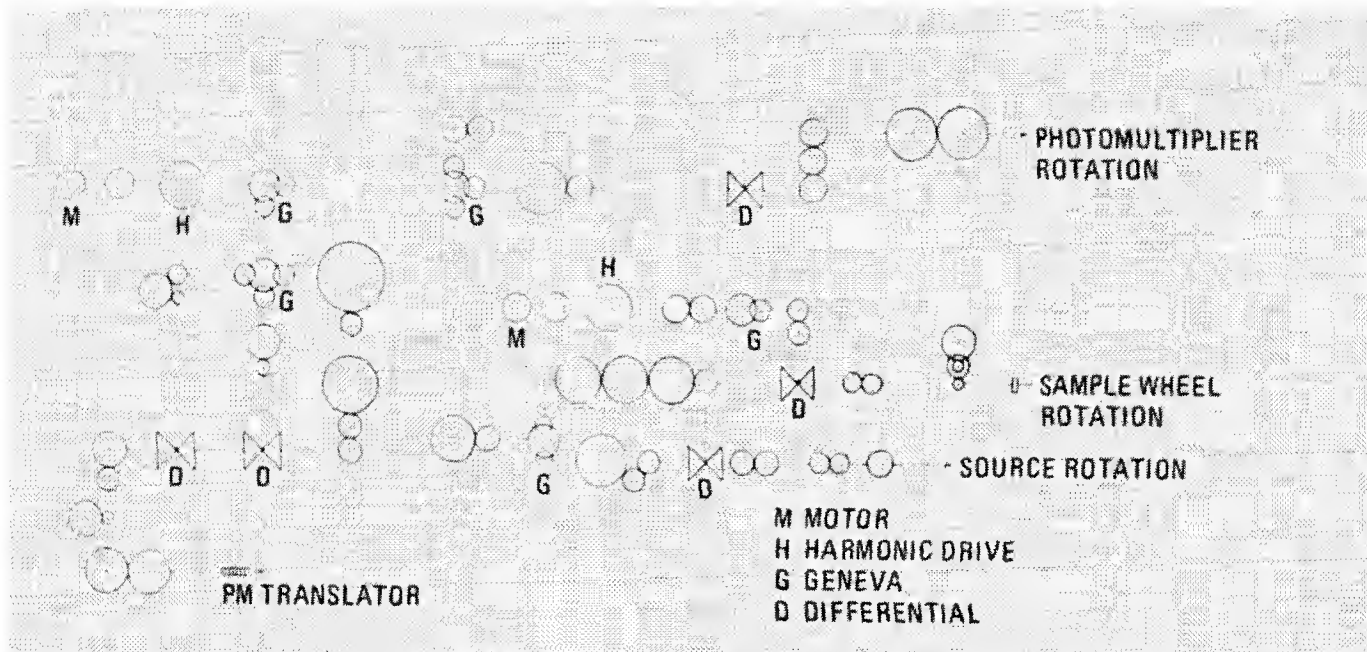


Figure 7.- Mechanical schematic.

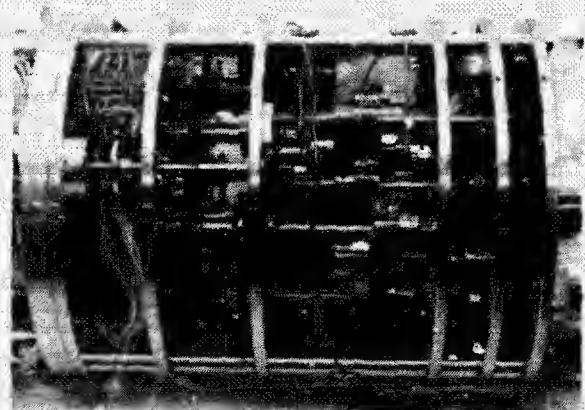


Figure 8.- Gear train.

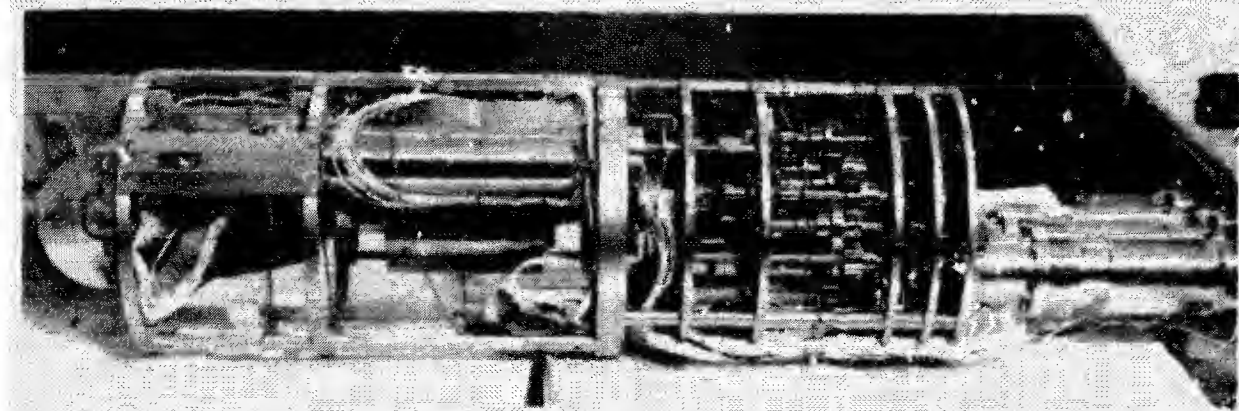


Figure 9.- Engineering model.

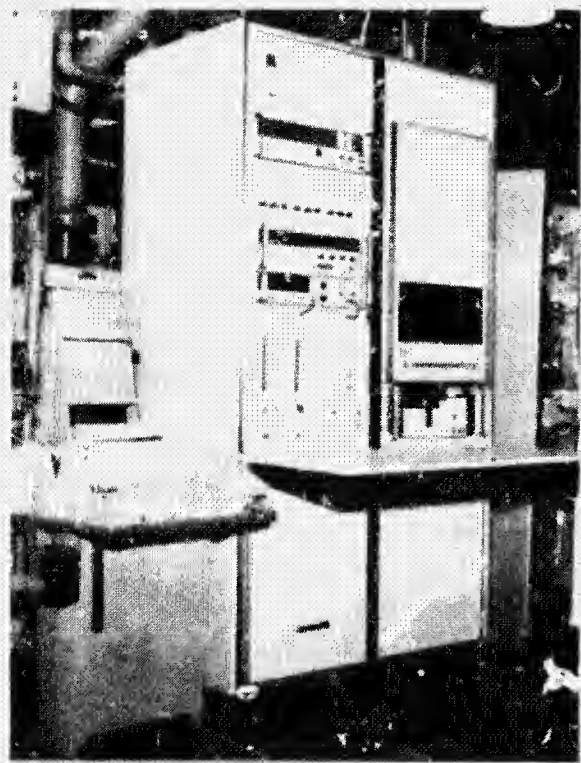


Figure 10.- Control console.

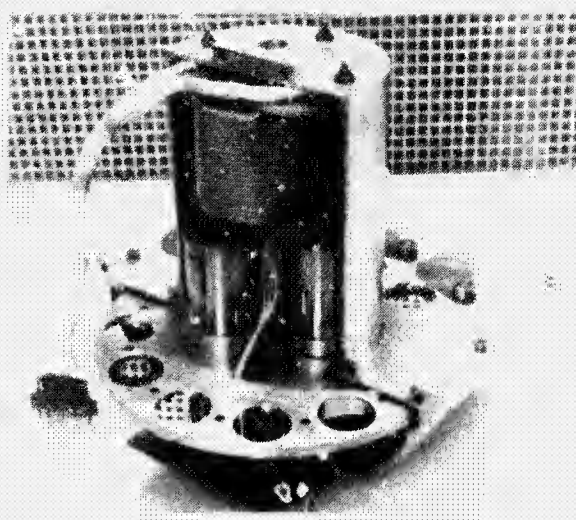


Figure 11.- Sample wheel.

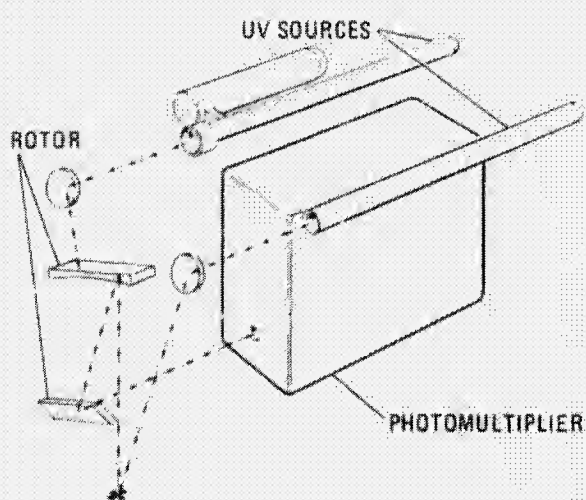


Figure 12.- Specular reflectance measurement.

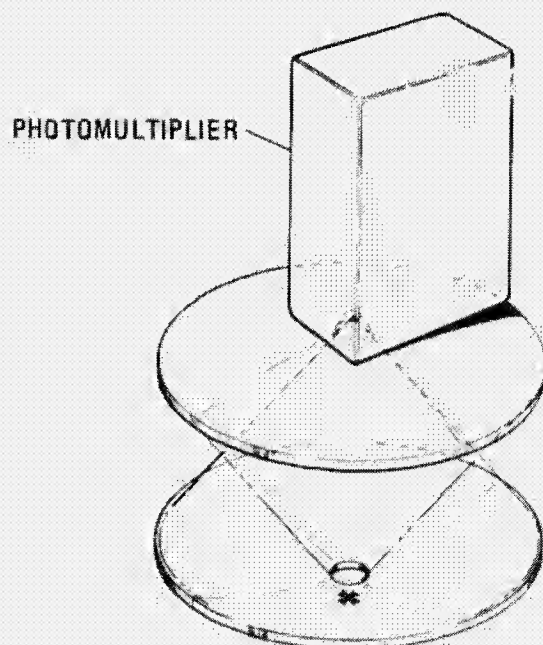


Figure 13.- Scattering measurement.

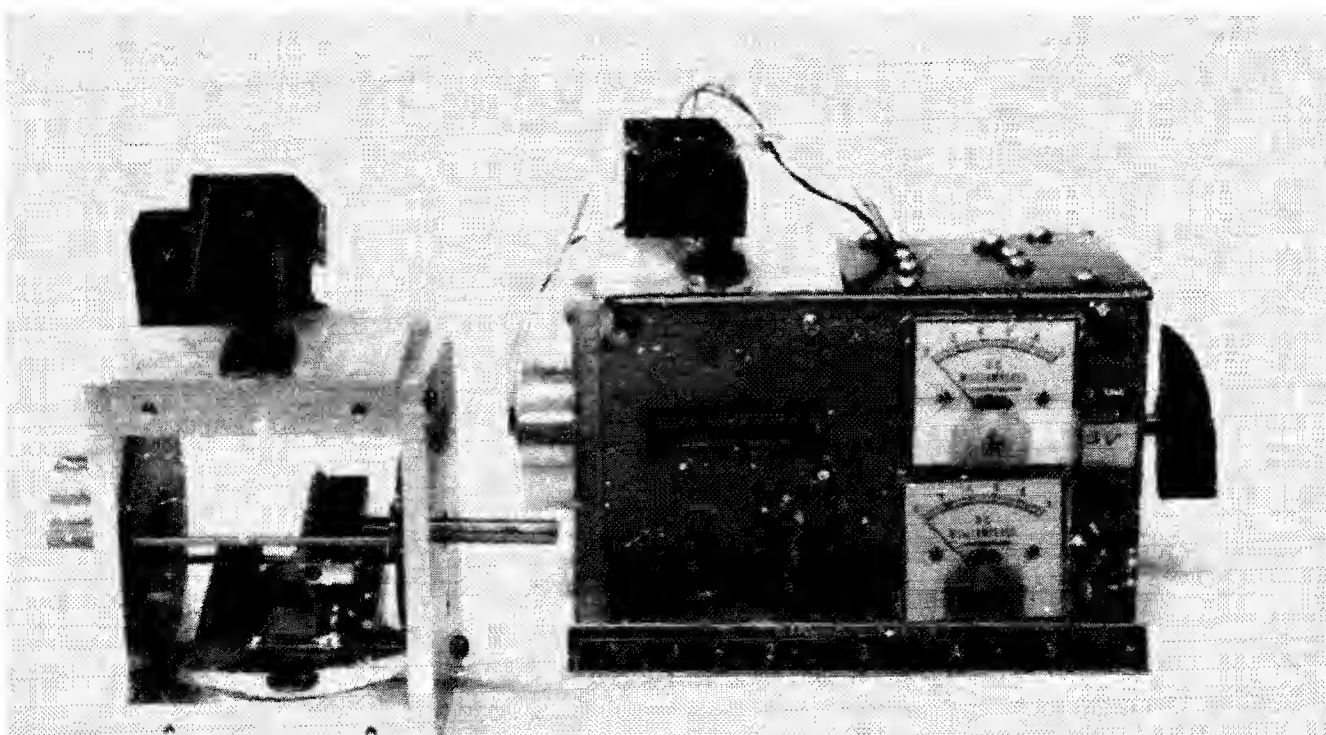


Figure 14.- Breadboard of conceptual design.

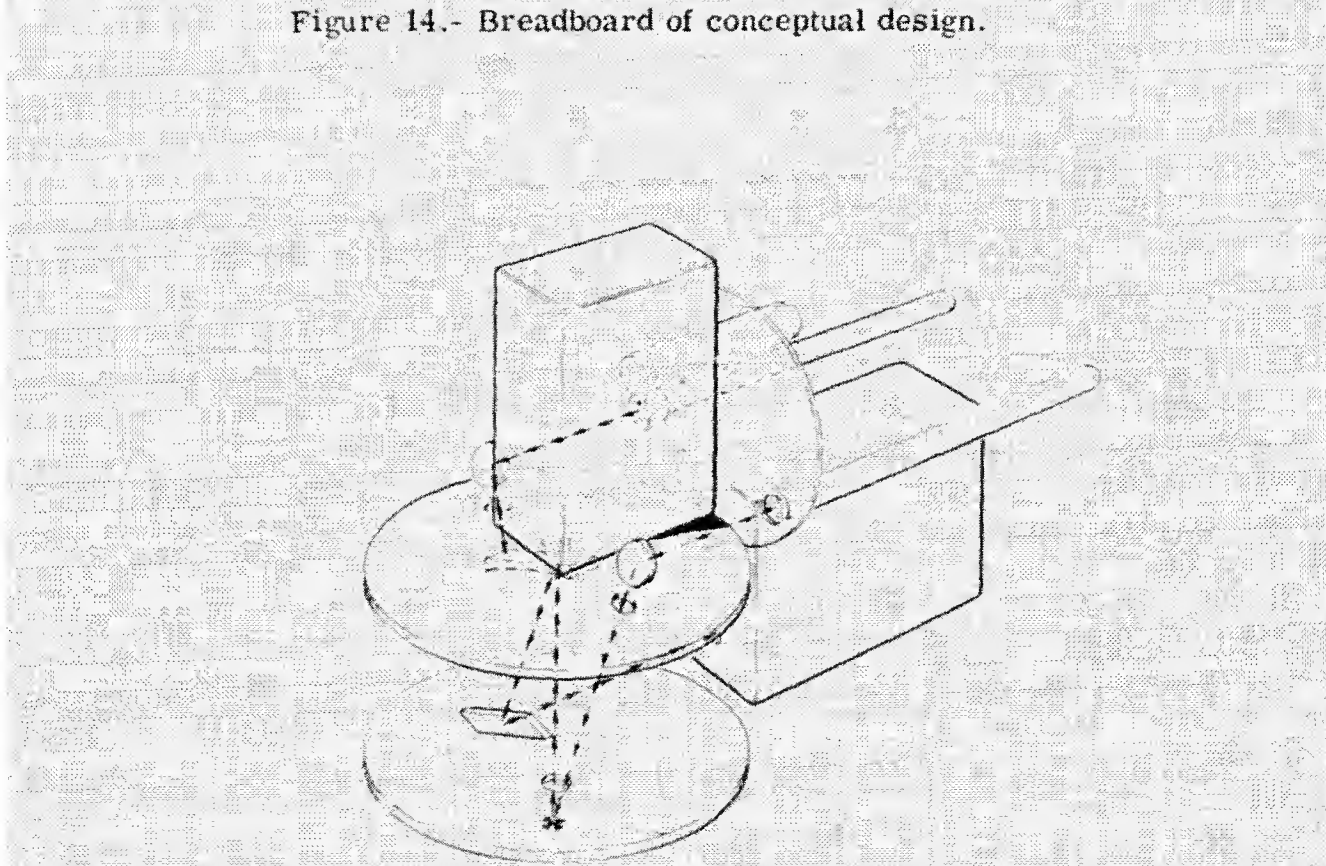


Figure 15.- Flight article preliminary design.

23. TRANSDUCER TECHNOLOGY TRANSFER
TO BIO-ENGINEERING APPLICATIONS*

E. N. Duran, G. W. Lewis, C. Feldstein
Jet Propulsion Laboratory, California Institute of Technology

E. Corday, M.D., S. Meerbaum, Ph.D., Tzu-Wang Lang, M.D.
Cedars-Sinai Medical Center

ABSTRACT

The results of a technology transfer of a miniature unidirectional stress transducer, developed for experimental stress analysis in the aerospace field, to applications in bio-engineering are reported.

By modification of the basic design and innovations in attachment techniques, the transducer was successfully used in vivo on the myocardium of large dogs to record the change in contractile force due to coronary occlusion, reperfusion, and intervention.

BACKGROUND

As part of the experimental stress analysis program in the Propellant Mechanical Behavior Group of the Jet Propulsion Laboratory's (JPL) Polymer Research Section, a Miniature Stress Transducer (MST) was developed to aid in the design of proposed solid propellant rocket motors (refs. 1,2,3,4). As conceived, the MST (fig. 1) was intended to be embedded in a solid propellant grain to measure the stress parallel to the gage axis.

The transducer was first used operationally in connection with the Surveyor Project. In order to achieve a maximum level of confidence in the structural integrity of the main solid propulsion motor used for retrograde propulsion in the Surveyor Spacecraft (fig. 2), a complete grain stress analysis was carried out. Boundary conditions and load definitions were consistent with the motor duty cycle as specified in the Surveyor Mission Profile. The state-of-the-art Redundant Force, finite element, elastic analysis was carried out by Douglas Aircraft Company. Concomitantly, an experimental program was undertaken to verify the predictive accuracy of the theoretical work. The MST's provided the backbone of the experimental program. Two quarter-scale Surveyor model motors were constructed and five

*This paper presents the result of research carried out at the Jet Propulsion Laboratory, California Institute of Technology, under Contract No. NAS7-100, sponsored by the National Aeronautics and Space Administration. Work at Cedars-Sinai Medical Center was partially sponsored by HE14943-01 and HL14644-02.

locations within the grain, corresponding to critical stress fields, were selected. In one motor, thermocouples were embedded at the five sites. In the second motor, fifteen MST, arranged in five rosettes of three orthogonally oriented MST each, were embedded at the locations which corresponded to the positioning of the thermocouples in the first motor. Both motors were subjected to a complete simulated Surveyor duty cycle, and the measured stress and temperature fields were satisfactorily compared with analytical predictions (ref. 5).

The MST is basically a force or stress sensitive device, constructed as shown in figure 1. The construction details are discussed at length elsewhere (refs. 1,4) but, simply stated, the MST consists of a p-type silicon piezoresistive element grown and cut so that the horizontal axis has the highest, or most sensitive, piezoresistive coefficient or gage factor. Care is taken to insure that the piezoresistive coefficients in the transverse directions approach zero, while the coefficient in the sensitive horizontal axis exceeds 100. The sensing element is packaged in a protective, force condensing and amplifying medium such as Teflon, whose design aids in calibration and mounting.

MEDICAL APPLICATIONS

In 1971, an opportunity presented itself to explore the possible uses of the MST in medical applications. The Cedars-Sinai Medical Center Cardiovascular Research Group (CS) was conducting research in the progressive changes in cardiac function and myocardial alterations associated with coronary occlusion and subsequent reperfusion. The objectives of the mechanical and metabolic measurements were to assess the extent and functional significance of regional ischemia, to develop data on myocardial viability and coronary revascularization, and to provide a baseline for evaluation of the effectiveness of pharmacological, surgical and circulatory assist interventions.

During this period CS personnel were attempting to measure myocardial wall forces on an intact, viable canine heart. The Walton-Brodie gauge (fig. 3) which was the prime candidate for use in this study is basically a resistance wire strain gage packaged to allow its attachment, via sutures, to the ventricles of a relatively large animal (refs. 6,7). The bulk and mass of this gauge, which is representative of other presently used medical gauges (refs. 6,7), hampered the efficient measurements of physical parameters in vivo. Since the MST provided a much smaller size and mass than presently available medical gauges, exploratory tests were conducted to determine if the MST was presently usable or adaptable to medical applications.

In the first test an attempt was made to suture the MST onto the myocardium. Due to the small size and lack of appendages on the MST this initial effort was not successful. It was concluded that the MST had to be modified in order to facilitate suturing. At that time several changes were

made and a second in vivo test was conducted with the modified MST. These modifications tripled the MST overall length (from 0.212 cm to 0.700 cm) and increased the weight (0.0123 gm to 0.0810 gm) but still presented a package that was suturable by the surgeon with less than half the size and weight of the smallest available medical gauge (fig. 3).

ATTACHMENT PROBLEMS

Sutures are commonly used in medical research as a method of attaching a transducer to the surface of a viable myocardium. Initially we wanted to study the adaptability of two aerospace techniques, adhesives and embedment.

1. Adhesives

Aerospace technology has long relied upon adhesives as means of bonding, joining, and attaching dissimilar materials. The usefulness of strain-gage technology lies in the development of a class of adhesives which transmit strains from the part under study to the transducer with minimal re-enforcing and perturbation. When the experimentalist considers the surface of a viable myocardium one is faced with a high compliance, continuously moving organ which is always perfused with blood and other body fluids. Adhesives which readily bond to this type of surface are the ethyl, propyl, and isopropyl 2-cyanoacrylates (ref. 8). Tests were performed in vivo and MST were attached to the epicardium by use of the isopropyl 2-cyanoacrylate adhesives. The resulting bonds appeared to be satisfactory and the type of data recorded was similar in shape and magnitude to that recorded by other attachment methods.

This means of attachment, while presently in the development stage, shows promise since the MST is only attached to the surface of the heart and the question of pretension encountered with suturing is avoided. The future uses of adhesives in this research depend upon the future development of stronger adhesives, which bond quickly in the presence of body fluids.

2. Embedment

Initially the MST was constructed to be mounted within solid propellant motors to measure the magnitude of the stresses which exist in a point region within a material. This was accomplished by positioning the MST, by means of removable positioning wires, within the motor case before the propellant is cast and cured.

In medical research this method of introducing the MST within the myocardium is not feasible. Since it is desirable to measure the state of stress within the various layers of the myocardium, a study was conducted on methods of introducing the MST below the epicardium. Tests were conducted on the possibility of placing an MST in an incision in the myocardium and using sutures to close the incision. While some success was noted, a better method of embedment was developed when the overall size of

the original MST was reduced in length by 30%, to 0.106 cm. This smaller MST was embedded within the myocardium through a small puncture in the epicardium, made by a needle approximately 0.1 cm in diameter. Results for this test indicate that an embeddable MST is feasible and, while much work remains to be undertaken, an embeddable MST will answer many questions dealing with the force distribution throughout the layers of myocardial tissue.

CALIBRATION

The MST is calibrated for use in aerospace applications in tension, compression, and side loading. In these calibrations loads are directly imposed on the MST and the change of resistance measured as a function of the loading.

Medical applications required the innovation of new calibration techniques. One new calibration technique is shown in figure 4. This method imposes a variable load, recorded by a load cell, as a function of time and the MST output. This method has the capability of imposing loads at rates from 0.1 Hz to 4 Hz. Calibrations of the MST at frequencies up to 2 Hz have not shown any rate or frequency dependence.

Other calibration techniques have also been explored, e.g., static tension and compression directly on the MST, and future work will exploit dynamic in vitro calibration.

RESULTS

Regional effects of local coronary occlusion and subsequent reperfusion have been studied in anesthetized, open chest dogs with assisted respiration. Occlusion was accomplished by the ligation of the proximal left anterior descending coronary artery (LAD). Reperfusion was later achieved by releasing the ligature. Cardiac output and coronary flows were measured by means of electromagnetic flow probes on the aorta and LAD. The MST were attached to the epicardial surface, within the LAD occlusion region, and also on a lateral wall in an unoccluded zone.

The type of data collected is shown in figure 5. Measurements include: (A) a standard Lead II ECG; (B) aortic flow; (C) LAD flow; (D) lateral wall MST; (E) anterior wall MST, i.e., occluded area; (F) aortic root pressure; (G) left ventricular pressure (LVP); and (H) maximal rate of rise of the left ventricular pressure (LVP).

In this test, baseline control data were obtained for all parameters and continuous data were recorded on an oscillograph during the time of occlusion and reperfusion of the LAD coronary artery. Figure 5 shows representative data for the control period, five minutes after occlusion, one hour after occlusion, and thirty minutes after reperfusion. It can be seen that the MST in the area of the occluded myocardium (E) exhibited an

almost immediate (<1 minute) and large increase in its output. At the same time, the local myocardium lost contraction and showed visual evidence of local outward bulging. This increased output, which remained relatively unchanged during the remaining period of occlusion, was therefore interpreted as a loss of the contractile force component in the area beneath the MST. This condition increased both the force acting on the MST by the surrounding myocardium and the possible effects of local myocardial bulging subsequent to LAD occlusion. Reperfusion after relatively short periods of LAD occlusion appeared to cause at least a partial return of the contractile force and hence reduced the anterior wall MST output in the direction of pre-occlusion control.

The viability and return of contractility of the previously occluded myocardial wall were verified by direct observation and are evidenced by the similarity in the outputs thirty minutes after reperfusion. The lateral wall MST (D) output remained essentially unaffected throughout the entire test.

CONCLUSIONS

Function and dysfunction of the heart as a pump, which supplies vital oxygen and nutrients to all parts of the body, have been the subject of intensive investigations, particularly within the past decade. Much clinical data have become available, but research into myocardial mechanisms, modes of heart disease and methods of their treatment require very extensive measurements which generally cannot be performed in the human body. Hence, controlled animal experimentation is resorted to, with great emphasis on appropriate physiological simulation. Among the common global myocardial measurements are hemodynamic, metabolic and electrophysiological indices. Recently, developments in the field of cardiology and cardiovascular surgery, exemplified by coronary bypass and circulatory assist treatment of the failing heart, have focused attention upon the mechanical performance of the ventricles of the heart and, more specifically, upon the localized and regional response of the left ventricular wall to various insults and interventions. Thus, a new era has opened up requiring the development and experimental qualification of advanced approaches to sophisticated mapping of the forces, stresses and strains which are characteristic of normal and deficient functioning of the heart.

The measurements of local myocardial wall mechanics is of extreme importance in studies of coronary disease, because regional coronary occlusion is reflected perhaps best in the immediate loss of regional contractions, dyskinetic movement and frequent outward bulging of the non-contractile wall. The gauges employed in past attempts to map the myocardial forces and stresses have not been satisfactory because of their relative size, weight and inadequate sensitivity. Also, insufficient progress has been made in the mathematical and structural modeling of the mechanical behavior of the left ventricle, partly because of the great difficulties in devising gauges which could be satisfactorily coupled to the myocardial muscle for valid quantitation of forces.

The Jet Propulsion Laboratories and Cedars-Sinai have joined hands in overcoming the above problems. The vehicle is the NASA-developed MST. The first direct application was the measurement of wall force in normal and deliberately coronary occluded zones of the left ventricle. First results (fig. 5) appear very encouraging in that occlusion of the coronary artery was reflected in (almost) immediate and large changes in gauge output, which were again reversed upon reperfusion of the coronary. Similar results were obtained with several other interventions. The gauges appear well suited to further research along the above lines, particularly for the solution of the usual problems of mapping and coupling.

It is expected that the future work, which includes further modification and testing of the MST, will go far to increase both the medical researcher's understanding of myocardial wall mechanics and the role of the aerospace experimentalist and analyst in transferring technology to this civil sector.

REFERENCES

1. San Miguel, A., and Silver, R. H.: On the Construction and Theory of a Miniature Stress Transducer to Measure Radial Stress in Propellant Grains. JPL Technical Report No. 32-643, Pasadena, Calif., Feb. 1965.
2. San Miguel, A., et al.: On the Practical Application of a Miniature Stress Rosette to Solid Propellant Grain Design. ICRPG Working Group on Mechanical Behavior, CPIA Publication No. 94U, Silver Spring, Md., Oct. 1965.
3. San Miguel, A., and Silver, R. H.: A Transducer to Aid in the Structural Design and Application of Plastics. Polymer Engineering and Science, Vol. 7, No. 1, Jan. 1967.
4. U.S. Patent No. 3,350,929 granted to NASA as assignee from A. San Miguel and R. H. Silver.
5. Duran, E. N., and San Miguel, A.: On the Measurement of Stress in Solid Propellant. Exper. Mech., Vol. 10, No. 12, Dec. 1970.
6. Boniface, K. J., Brodie, O. J., and Walton, R. P.: Resistance Strain Gauge Arches for Direct Measurement of Heart Contractile Force in Animals. Proc. of the Soc. of Exptl. Biology (N.Y.), Vol. 84, 1953, pp. 263-266.
7. Walton, R. P., et al.: Factors Influencing Measurement of Contractile Force of Heart Muscle in situ. Am. J. Physiol., 161:489, 1950.
8. Matsumoto, T., et al.: Cyanoacrylate Tissue Adhesives: An Experimental and Clinical Evaluation. Military Med., 134:247, 1969.

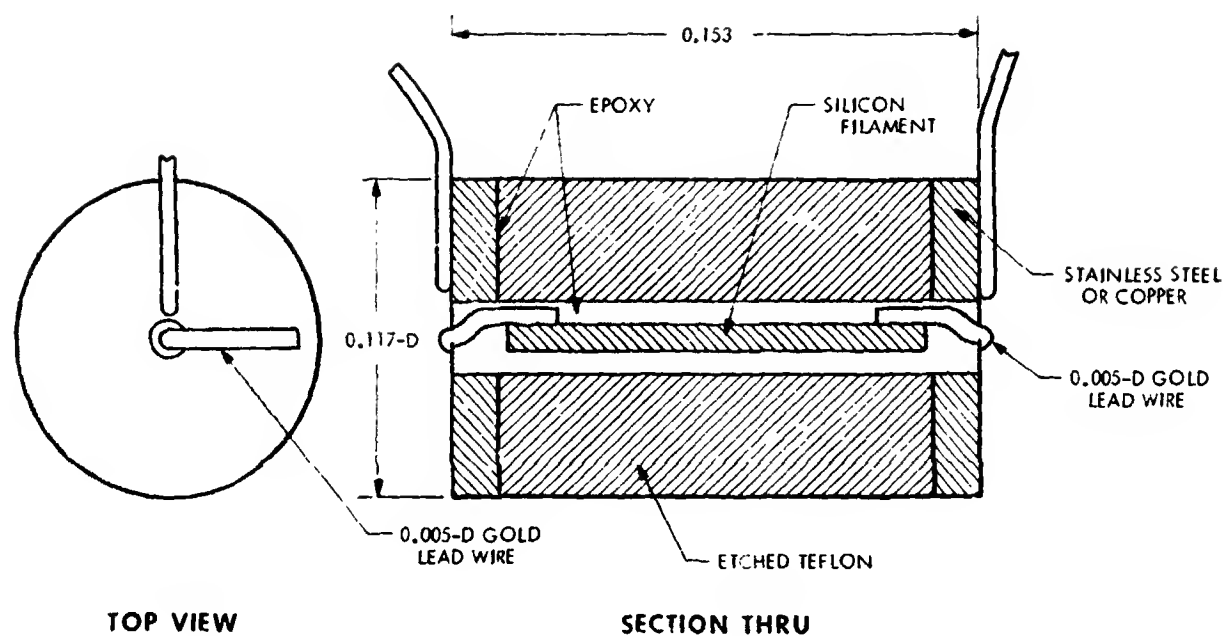


Figure 1.- Construction of miniature stress transducer (MST).
Dimensions in centimeters.

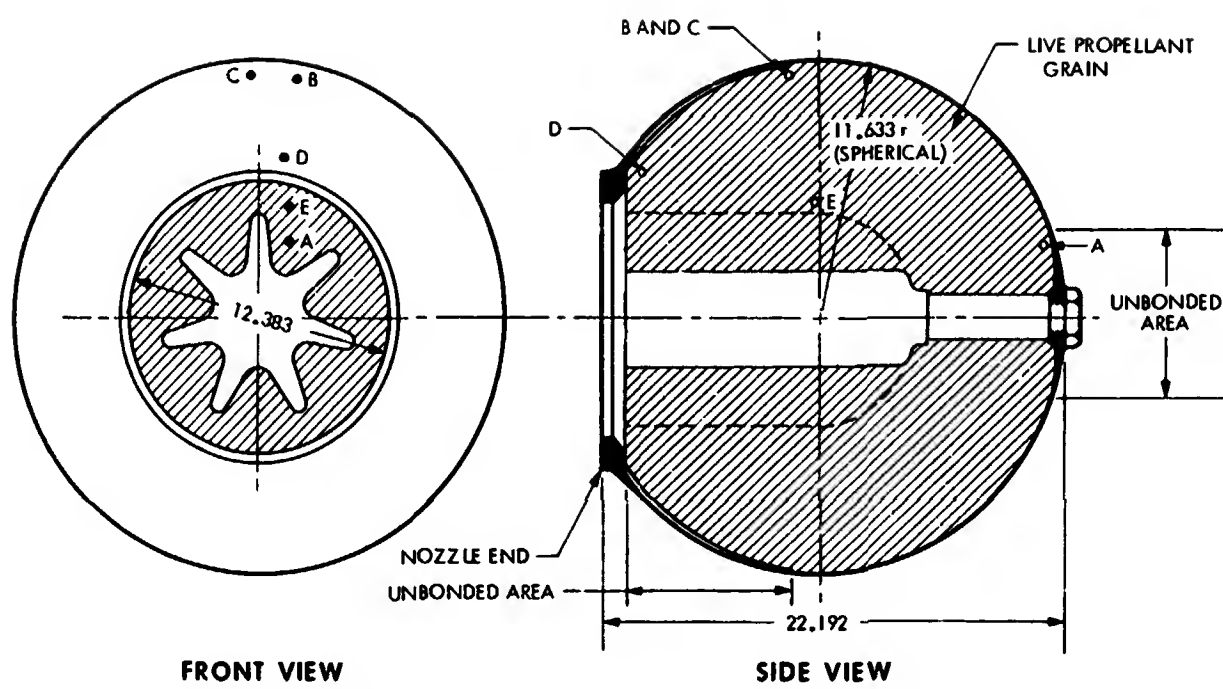


Figure 2.- Quarter-scale Surveyor main retrorocket motor. Dimensions in centimeters. Letters (A-E) denote locations of MST rosettes.

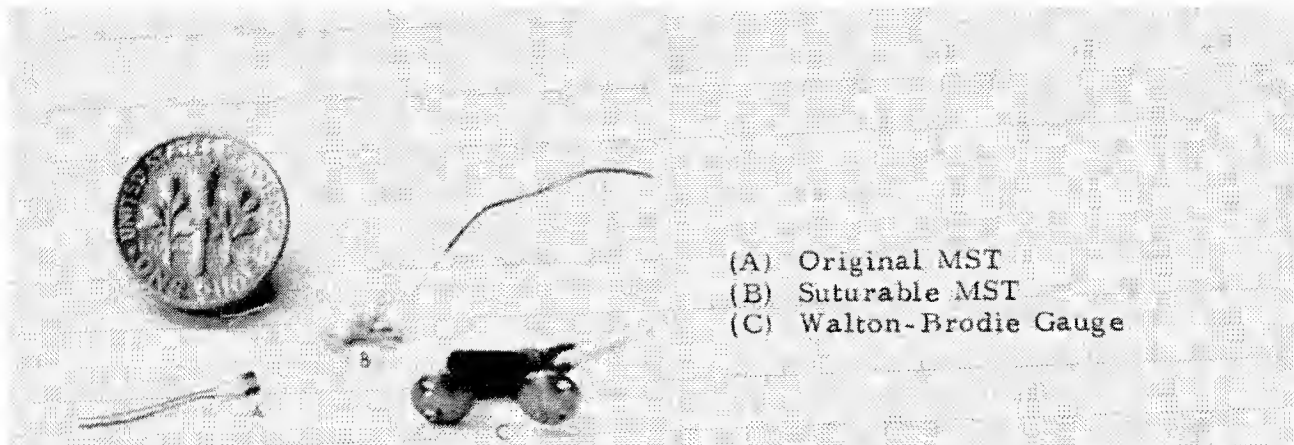


Figure 3.- Size comparison of MST and recent Walton-Brodie gauge.

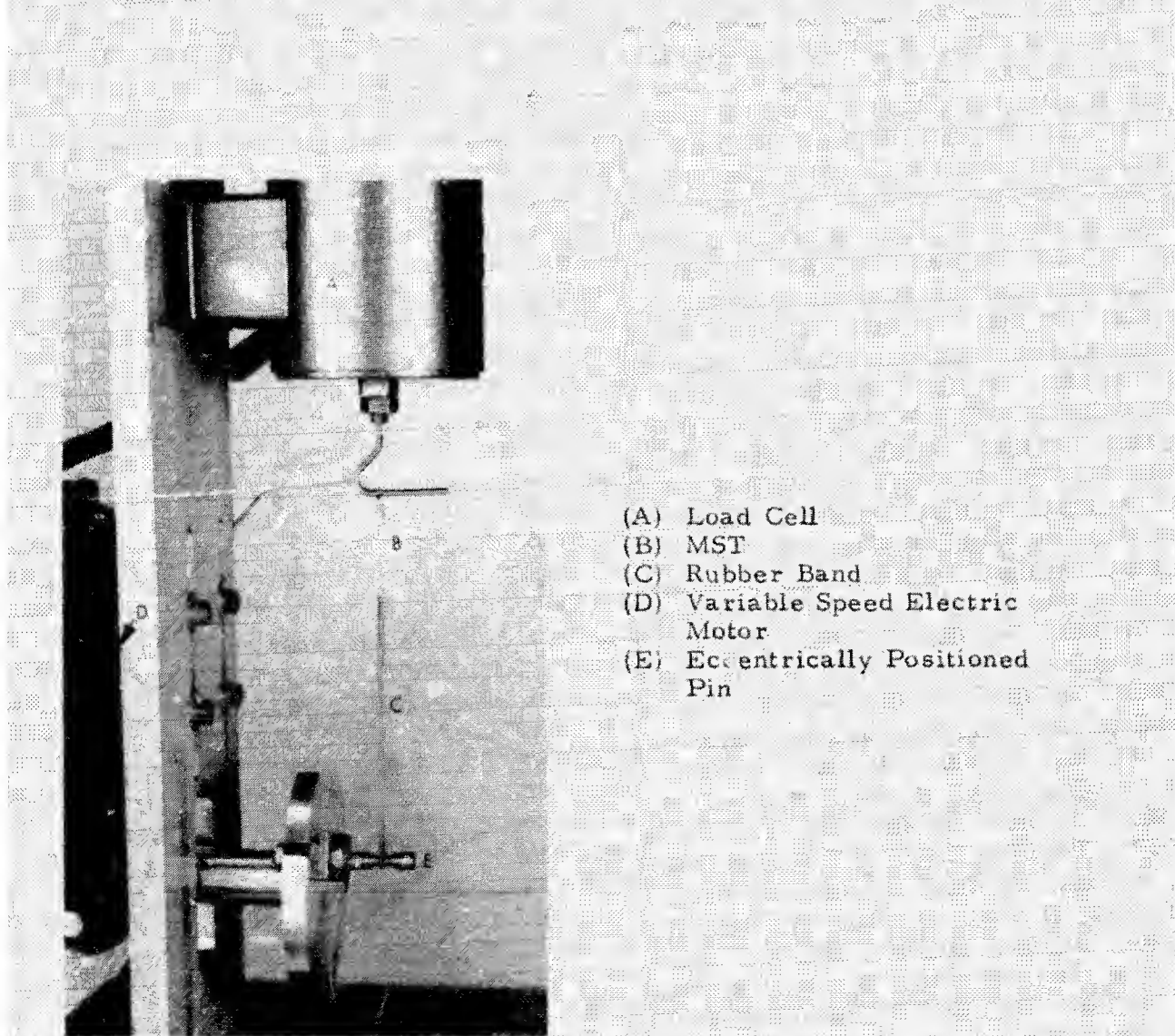


Figure 4.- Dynamic calibration of MST.

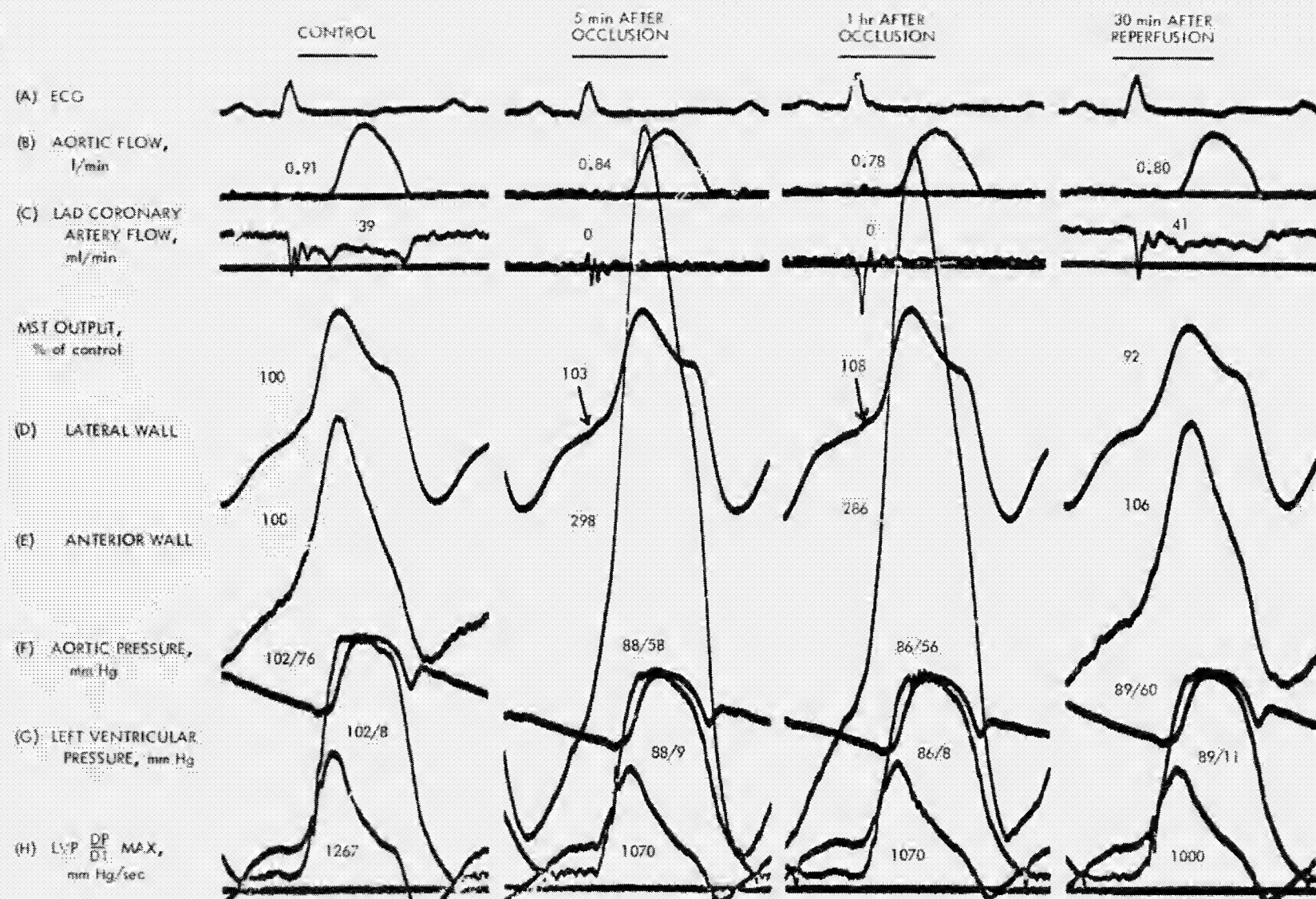


Figure 5.- Regional myocardial mechanics following acute LAD coronary artery occlusion and reperfusion.

... HELICOPTER VISUAL AID SYSTEM

By Ronald L. Baisley
NASA Jet Propulsion Laboratory

SUMMARY

The results of an evaluation of Police Helicopter effectiveness revealed a need for improved visual capability. A JPL program developed a method that would enhance visual observation capability for both day and night usage and demonstrated the feasibility of the adopted approach.

This approach, the Helicopter Visual Aid System, incorporated three interesting mechanisms as solutions to design and development problems. These mechanisms contributed greatly to the successful operation of the Helicopter Visual Aid System.

INTRODUCTION

Background

Recently many law enforcement agencies have integrated helicopters into their patrol activities, and the trend toward their use is continuing to increase on a national scale. Experiences with these aerial patrols led to recognition of the limitations of the basic observation system. The initial system consisted of the helicopter, the observer, and sometimes minimal visual aids such as binoculars or a camera. This minimal amount of support equipment for the full range of police missions, conducted both at night and during the day, limits the potential value of the helicopter system. Many attempts have been made to adapt equipment designed for other purposes to use on police helicopter patrols. Little effort has been made, however, to design equipment specifically for the police helicopter in its performance of the patrol function.

In response to this need, the Jet Propulsion Laboratory has developed a Visual Aid System for helicopters that is based on a set of requirements derived from law enforcement agencies (Ref. 1).

Problem Definition

The initial definition of the problem was based upon a previous Civil Systems task at JPL. In this task, the Los Angeles Police Department's helicopter patrol program was evaluated, with one element of this effort being the assessment of various means by which patrol effectiveness could be increased. A major item identified was improved visual capability.

To confirm some of these observations, and to provide a broader base of understanding of the range of missions and their requirements, a nationwide survey was conducted involving ten law enforcement organizations. This survey confirmed the pressing need for improved visual capability.

From this, the functional requirements for a visual aid system were established to be:

- (1) An increased field-of-view, coupled with the capability to see at night without visible illumination. Minimum resolution should be equivalent to that of the unaided eye under conditions of daylight illumination.
- (2) An improved capability to see during normal conditions of daylight illumination through an increased field-of-view as above and with increased resolution.
- (3) Evidence-gathering capability through airborne photography.

Requirements and Constraints

Based on the functional requirements, physical constraints and technical requirements were established for a visual aid system and are outlined below.

- (1) Physical Constraints: Bounded by the characteristics of the Bell 47 G-5 helicopter, chosen to be the test vehicle.
- (2) Mode of Operation: Daytime operation under ambient light conditions and nighttime operation using either visible illumination or non-visible infrared illumination.
- (3) Fields-of-View: The field-of-view centerline shall be pointable from the horizon to at least 45° below the horizon and from a forward position to at least 90° right azimuth. In addition, it shall be capable of variable magnification.
- (4) Visual Resolution: Daylight resolution capable of resolving line pairs on a 1951 Air Force resolution chart, which are separated by 50 µrad and which have typical brightness values equal to or greater than 1000 ft-L. At night, have the capability to distinguish line pairs separated by 250 µrad and have typical brightness due to ambient illumination of 0.001 ft-L.
- (5) Display Characteristics: The image shall be erect and non-reverted and shall have a minimum brightness of 1 ft-L. It shall also incorporate an indicator that shows the orientation of the line of sight relative to the vehicle. A similar indicator shall be provided for the pilot.
- (6) Searchlight: The searchlight shall be slaved in azimuth and elevation to the turret subassembly and shall be capable of remote control by the observer. The capability shall exist to remotely control the filter elements required for both visible and covert illumination of a target.

SYSTEM DESCRIPTION

The breadboard Visual Aid System consisted of five modular elements: the optical turret, the optical display, the searchlight, the control console and the auxiliary generator.

The Visual Aid System optics and electro-optics were packaged into two separate modules; the turret, located underneath and forward on the "chin" of the vehicle and including the front objective lens and turning mirrors, and the display that contained the balance of the optics. A flexible, image-carrying fiber-optics bundle connected the two modules. A description of the optics, keyed to Fig. 1, is presented below.

One of the two objective lenses (3 and 4) alternately provided a focused image upon the end of the fiber-optics bundle (7), the selection depending upon the orientation of the switching mirror (6). Each of the objective lenses "looked out" through a flat glass window (1). Turning mirrors (2) and windows were coupled in rotating housings to form optical scanning heads. These heads are mechanically coupled together and rotate as shown about the common axis of the objective lenses providing an elevation scan. Rotation of the entire turret about the centerline shown at the left of Fig. 1 represents an azimuth scan.

Objective lens (3) and (4) were 21-inch and 3-inch focal length, providing 7-power and one-power magnification.

The four-foot-long fiber-optics bundle (7), comprised of 3 million flexible optical conduits, each 10μ in diameter, transmits the image from the turret to the display without transmitting mechanical motions from one to the other.

The first relay lens pair (8) collected the visible or infrared light from the fiber-optics bundle and reformed the image at the photocathode of the intensifier (11), or at the field lens (12), for further relay through the display module.

The filter wheel (10) contained, in one position, a multilayer filter to pass near-infrared and exclude visible light and, in a second position, a clear piece of glass of appropriate thickness to correct for visible light focal length of the first relay lens pair (8).

The image intensifier (11) was a cascaded three-stage, electrostatically imaged intensifier with photocathode and phosphor screen diameters of 40 mm each. Light gain through the tube is typically increased by a multiple of 100,000.

Relay lens (13) was mounted in a turret with the image intensifier and could be rotated into position to relay a visible image from the first relay pair (8). Field lenses (12) were located at the input and exit image locations to minimize vignetting.

Display switching mirror (14) had two operating positions: one directed light from the image intensifier or second relay lens to a 35 mm recording camera (16) and the other, to a projection lens (17), which forms the final image at the viewer end of the display.

The projections lens (17), the viewing field lens (23) and pupil splitter (22) provided a pair of exit pupils imaged approximately 16 in. beyond the viewing field lens. The exit pupils were approximately 1 in. in diameter and spaced on center by an average adult interpupillary separation of a little less than 3 in. It was at this location that an observer positioned his eyes to look into the display.

Items (18) and (19) are a light-emitting diode (LED) and a projection lens, respectively, which are incorporated into a position indicator. The LED was mounted onto a torquer-driven assembly which was gimballed to allow reproducing the azimuth and elevation angles of the turret assembly. The combining mirror allows an image of the LED to be formed at the pupil splitter and viewing field lens. The red dot was seen with both eyes as superimposed upon the presented scene.

Optical Turret

The major functions of the optical turret illustrated in Fig. 2 were to provide azimuth and elevation scanning for the objective lenses; focusing of the optics; selection of magnification; a mechanization to maintain the horizon level at the display; image motion stabilization; support structure to maintain alignment of the elements; and a housing to provide a protective enclosure against weather conditions.

Servo-driven, the turret rotated in azimuth through 180°, from straight forward clockwise to straight backward. In elevation, the pointing limits of 0° (horizon) to 75° below horizon were achieved. The skew rate of the turret was measured to be 22.5°/s in azimuth and 26°/s in elevation.

The details of image motion stabilization combined three techniques. First, vibration isolators were used between the helicopter and the suspended portion of the turret. Second, large stabilizing gyros were added to the isolated member to increase the rotational inertia. Third, rate gyros were mounted on the turret to sense angular motion and, through the control system, the elevation and azimuth servos were driven to directly compensate for that motion.

Magnification changes were accomplished by rotating a diagonal mirror to direct the optical axis from a one-power (1X) objective lens to the seven-power (7X) objective lens. Accurate indexing was achieved through a motor-driven Geneva mechanism. The development of this mechanism is one of the subjects of further discussion later in this paper.

One feature that is familiar to us is the level horizon at the top of a scene whatever direction we may turn our head. To help maintain orientation it was decided to present a display with the horizon at the top, which would be fixed with respect to the observer even though the helicopter should roll and pitch. The concept used in the turret utilized rotating mirrors for scanning and as a result caused unwanted image and horizon rotation that required compensation. This compensation was achieved through rotation of the fiber-optics rope in response to each of these turret functions. This fiber-optics mechanism is also the subject of additional discussion later in this paper.

Rotation of the fiber optics required a mechanism capable of summing the variables that affect image rotation. This was accomplished by utilizing a combination of summing differentials and a servo-driven phasing mechanism. The development of this mechanization is also discussed in further detail.

Optical Display

Several functions were provided in the display module. These were, principally, display of the image (day or night), conversion of infrared to visible light (night), intensification of the visible or infrared image (night), and display of the turret-pointing position indicator. Certain ancillary functions were also mechanized.

Figure 3 shows the display module mounted on a supporting stand prior to installation in the helicopter. The upright drum housed the day-night turret. The fiber-optics rope entered the display module from bottom far side as seen in this photograph. The viewing field lens is shown located in the diagonal housing at the upper left of the module.

Searchlight

The searchlight used for the breadboard Visual Aid System was the commercially available SX-16 "Nightsun" manufactured by Spectrolab of Sylmar, Cal. The light is in wide use by law enforcement agencies for nighttime airborne search and tactical operations. It has a 1600-W xenon short arc lamp that supplies 21,000 lumens in a beam that may be varied in flight from 4° to 10° in width. It is servo-driven and slaved to the look vector of the optical turret.

As procured from Spectrolab, the searchlight had either of two windows mounted in a light-baffled, air-ducted shell (Fig. 4). One was a clear window that passed essentially all visible and near-infrared radiation. The other had a multilayer interference filter that passed the near-infrared but reflected essentially all visible radiation back to the bulb. The transmission characteristics of the infrared beam reduced the visibility of the direct searchlight beam to an appearance similar to that of the helicopter running lights when viewed from a distance.

Control Console

Figure 5 is a photograph of the control console in its breadboard configuration. It was located between the pilot and observer, in a position where controls were conveniently operated by the observer's left hand. It provided control over the system as indicated by the functions on the control panel. Pointing of the turret look vector was accomplished by a control stick mounted to a floor pedestal in front of the observer.

Helicopter Installation

Installation of the Visual Aid into the police helicopter (Bell 47 G-5) is illustrated in Figure 6.

MECHANIZATION PROBLEMS

The design and development of the system required the application of several mechanisms, three of which are discussed in this text. They have been highlighted in the description of the system and will be discussed in detail below.

GENEVA MECHANISM

Background

As was pointed out, magnification changes in the optical system were accomplished by rotation of the turret switching mirror, directing the optical axis from the 1X to the 7X objective lens. Accurate indexing of this mirror was required at two discrete positions, the optical axes of the 1X and 7X lens. In addition, the mirror is coupled through a geared assembly to a fiber-optics rope. The fiber-optics rope, when twisted, exhibits a torsional spring rate, which through the geared assembly is fed back to the same mechanism that indexes the mirror.

A motor-driven Geneva mechanism was selected for this application because of its accurate indexing characteristics. In operation, the choice of image magnification (use of 1X or 7X objective lens) is accomplished by applying DC power of selected polarity (dependent upon choice of 1X or 7X lens), to the Geneva drive motor. Upon reaching the selected index position, actuation of a micro-switch interrupts the applied power. Motor coasting, thus, overshoot of the index position, is prevented by the application of dynamic braking on the motor.

In the specific design, the Geneva driver wheel, Figure 7, is rotated by a DC motor through a double reduction spur drive.

In operation the star wheel is driven through one 90° increment for each revolution of the driver wheel. This sequence is illustrated in Figure 8.

The star wheel is directly connected to the mirror and, through a geared assembly, to the fiber-optics rope. The torsional spring rate of the rope appears (Fig. 7) as a torque on the star wheel applied in the direction of star wheel rotation.

Problem

Initially, the design and fabrication of this Geneva assembly was straightforward. When tested, both as a subassembly and later installed in the turret module (less fiber-optics rope), no operating difficulties were encountered. Upon assembly of the turret module with the display module, including the interconnecting fiber-optics rope, problems with the Geneva operation were encountered.

When actuated in one direction (1X to 7X) the Geneva operated properly. However, when operated in the opposite direction (7X to 1X), full rotational travel could not be attained and binding occurred at the beginning of travel. When the rope was disconnected, the Geneva operated properly in both directions. With the Geneva set in the 7X position, the rope was reconnected. This resulted in the reverse situation, proper operation from 7X to 1X but incomplete travel from 1X to 7X. This confirmed that restoring torque, resulting from rope torque, was causing the star wheel and driver to bind when actuated in the direction of restoring torque. Installing the rope with preload equivalent to one-half the restoring torque, thus, having the total restoring torque, did not correct the problem.

It was determined that, near the start of return rotation, where binding occurred, the area of contact between the star wheel and the driver was extremely small, resulting in very high unit loading at that point. This was enough to inhibit the necessary sliding motion; thus, rotation of the Geneva could not continue.

Solution

The problem was corrected by a modification to the Geneva driver. Rollers were inserted in the driver at the points of high unit loading to eliminate the frictional bind condition. This modification is illustrated in Figure 9 along with a segment of the Geneva operating sequence. With the fiber-optics rope installed no binding in the mechanism occurred and it continued to operate without malfunction throughout the flight program that followed.

FIBER-OPTICS ROPE

Background

A fiber-optics rope was selected to be the optical link connecting the turret and display modules. This approach was selected to minimize transmission of vehicle vibration to the stabilized optical turret.

The fiber-optics rope used in this application is 25 mm in diameter and contains approximately 3 million flexible glass optical conduits (single fiber elements) each 10 μ in diameter. The rope length is 7 ft.

In use, an image is focused at the input surface of the rope, with each of the 3 million fibers "seeing" a discrete segment of the image, or picture element. Each fiber acts analogous to a wave guide, wherein the entering rays will be reflected off the sides of the fiber and conducted until it appears imaged at the other end of the fiber. Each glass fiber is clad with a glass coating approximately 1 μ thick and having a lower refractive index than the core glass. This cladding functions to maintain a high reflectance (near total) at the side of the fiber, thus minimizing end-to-end losses in the fiber.

The fabrication of the rope is illustrated in Figure 10. The processing provides for the necessary end-to-end coherence in the two-dimensional arrangement of all glass fibers. This arrangement is necessary if the image at the rope exit is coherent with or duplicates the image at the input to the rope.

The fiber-optics rope provides a flexible link that can optically transmit an image over several feet with excellent resolution.

Problem

In the design of the turret module, the mechanization of the optical path (rotating mirrors, etc.) resulted in an unwanted image and horizon rotation. A usual method used for correction of image rotation is the insertion of a rotating Dove prism in the optical path. This prism when rotated will cause the image to rotate. Because of size and weight constraints, a prism could not be installed without seriously compromising optical performance.

Solution

The problem was approached by utilizing the flexibility of the fiber-optics rope, which permits the rope to be twisted about its optical path. With the ends being structured coherently, rotation of one end of the rope relative to the other will cause a rotation of the image at the output end of the rope.

By mechanizing one end of the rope (in this system, the input end was chosen, for convenience) to rotate in response to those parameters which cause image rotation, the rotation which appears at the input to the rope will be corrected or "taken out" at the other end of the rope. With the fiber-optics rope output connecting to the display module, no image rotation will appear in display.

DIFFERENTIAL MECHANISM

Background

Rotation of the fiber-optics rope required a mechanism capable of summing the variables that affect image rotation. These variables are turret azimuth and elevation scan positions and position of the switching mirror (selecting 1X or 7X objective lens). The following outlines the required relationship between rope rotation and the above variables.

Angular rotation of rope must track angular rotation of turret during azimuth scan, maintaining the same angular displacement both in magnitude and phase. The magnitude and phase of this rotation is 0° to 180° clockwise, as viewed from above.

Angular rotation of the rope in response to switching mirror position is the same as for azimuth scan except the magnitude and phase are 120° counter-clockwise from 1X to 7X position, also as viewed from above.

Elevation scan from horizon to 75° negative requires a like magnitude of rope rotation. The phasing of rope rotation is where the problem developed.

Problem

In establishing the relationship between elevation scan and image rotation the optical system was evaluated on the basis of viewing through the 1X objective lens. In this situation, elevation scan from horizon to negative 75° requires a clockwise rotation of the rope (viewed from above) for proper phasing. In the initial appraisal, the same relationship appeared to exist for viewing through the 7X objective lens. It was on this basis that the mechanism design was established. (Details of the mechanization will be discussed later.)

During testing of the turret module (as viewed through the 1X lens), the differential mechanism had summed the variables as intended and there was no image rotation. Upon switching to 7X viewing, the problem appeared. Elevation scanning resulted in image rotation. A reassessment of the conditions revealed that, when viewed through the 7X lens, the relationship between elevation scan and rope rotation was 180° out of phase although proper in magnitude. Summarizing, an elevation scan for horizon to negative 75° requires a clockwise rope rotation (viewed from above) for 1X viewing and a counterclockwise rope rotation for 7X viewing.

Solution

This situation was corrected by supplementing the existing design with a phasing mechanism with an output equal in magnitude to the input but either in phase or 180° out of phase, depending upon a second variable, switching mirror position, i.e., 1X or 7X viewing.

Implementation of the modified differential mechanism is described as follows. The phasing mechanism, input-coupled to the elevation heads, drives one input of a geared differential. The other differential input is coupled to switching mirror position (1X or 7X). The outputs of the differential and azimuth scan positions are summed in a second geared differential with its output driving the fiber-optics rope to the proper angular position.

The phasing mechanism itself operates in the following manner. The input shaft drives a pair of mechanical stops. These stops, driven differentially, rotate in opposite directions (out of phase) and in angular magnitude equal to the mechanism input, elevation head position. The output shaft and coupled tab are driven by a DC torquer in either direction, maintaining the tab in contact with either stop depending upon whether an in-phase or out-of-phase output is required (corresponding to 1X or 7X viewing).

Subsequent testing of the turret module disclosed that the modified mechanism successfully combined all influencing variables and corrected image rotation under all circumstances encountered during ground and flight testing.

CONCLUSIONS

The Helicopter Visual Aid System described in this text has been built and flight-tested by the Los Angeles Police Department in situations representative of actual flight missions. The mechanisms discussed contributed greatly to the successful performance of the System throughout the 160 hours of flight testing.

It has demonstrated that the visual aid concept can provide improved daytime visual capability, greatly improved nighttime capability, surveillance from greater distances and/or altitudes, covert operation at night through the use of the IR searchlight, and a photographic recording at the scene being viewed.

A proposal is being prepared, seeking funding for continuation of activity in this area.

REFERENCE

1. Baisley, R. L., Helicopter Visual Aid System, Vols. I and II. Document 650-155, Jet Propulsion Laboratory, Pasadena, California.

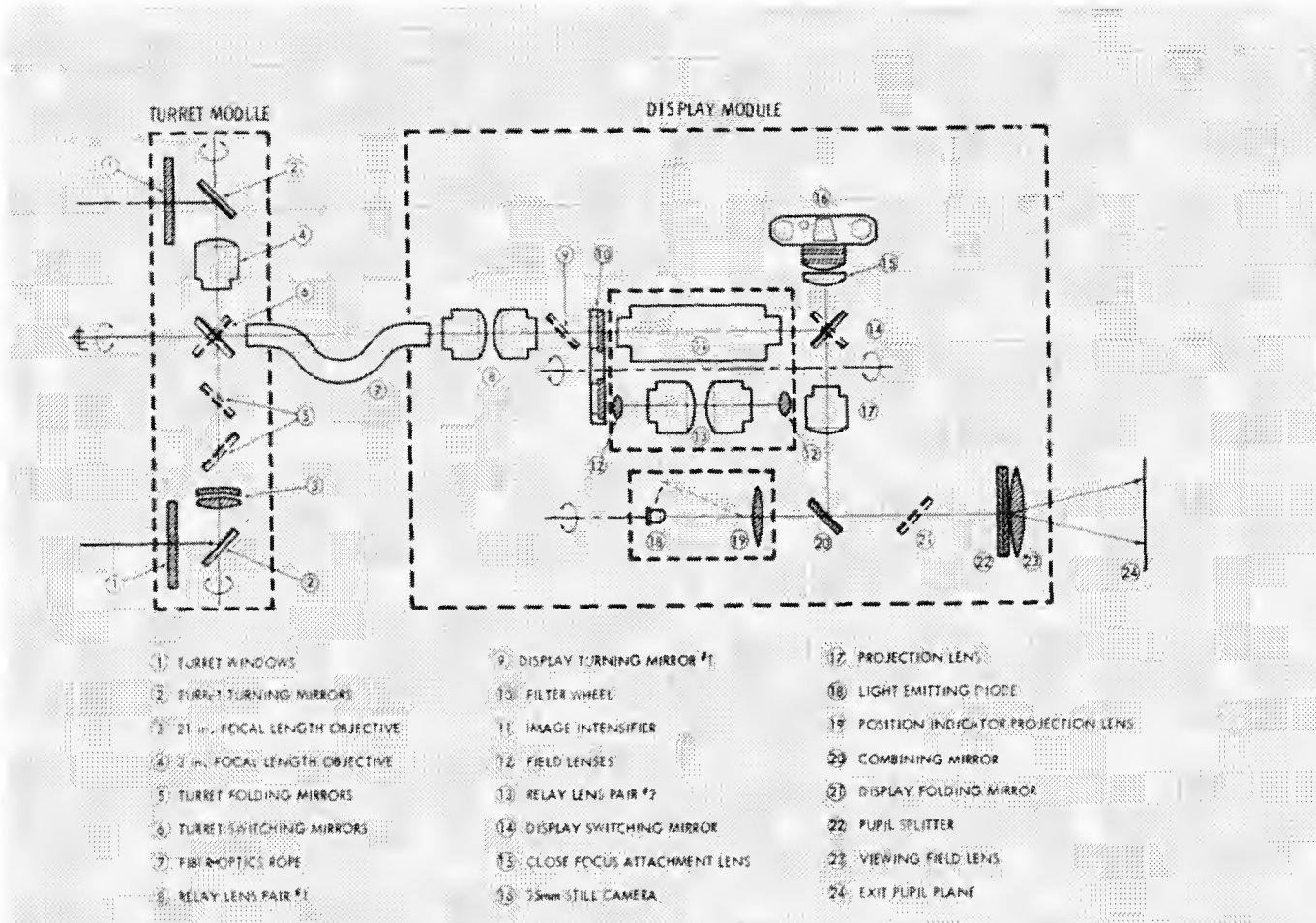


Figure 1.- Visual aid optical block diagram.

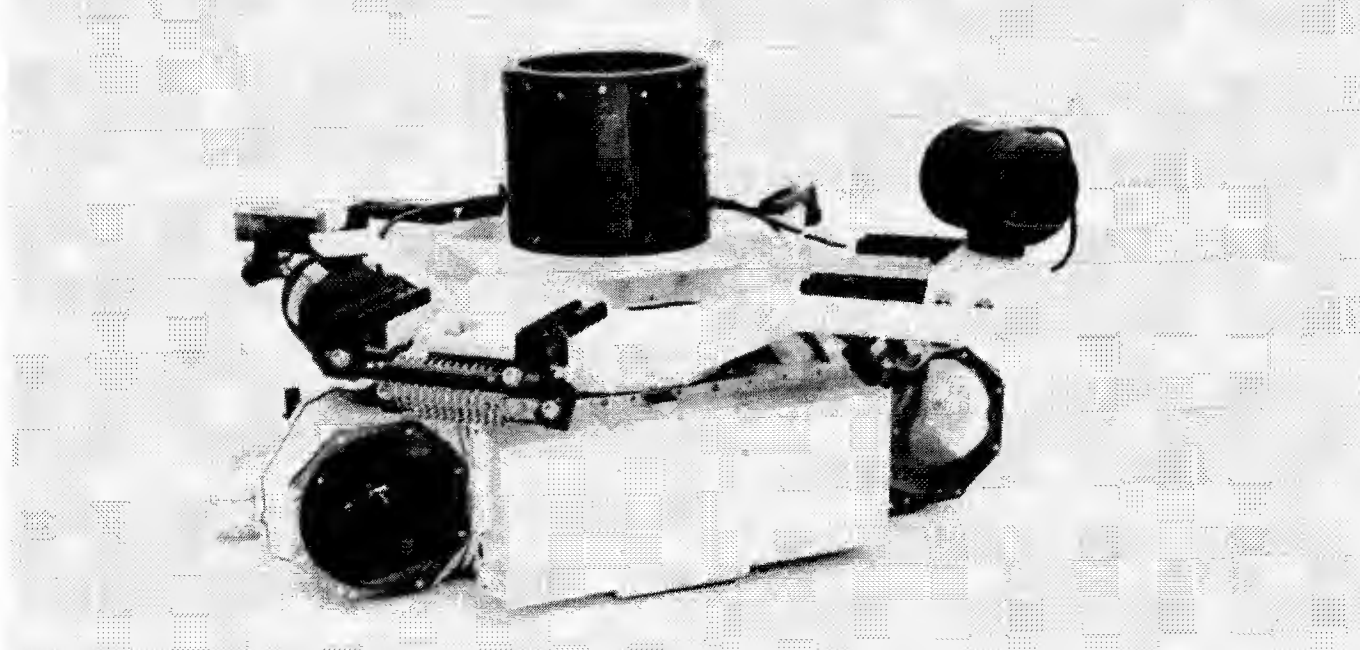


Figure 2.- Turret module.

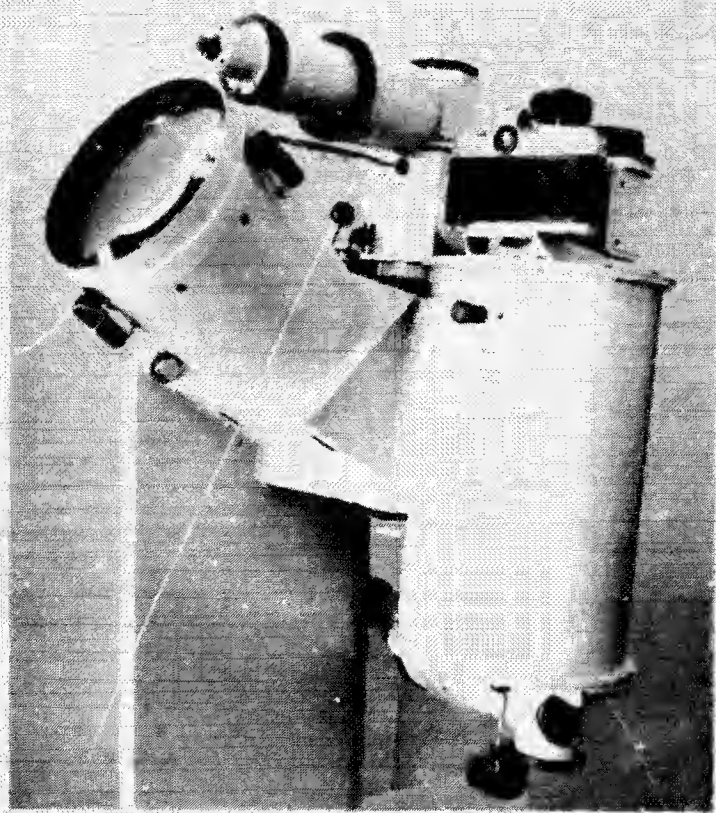


Figure 3.- Display module.

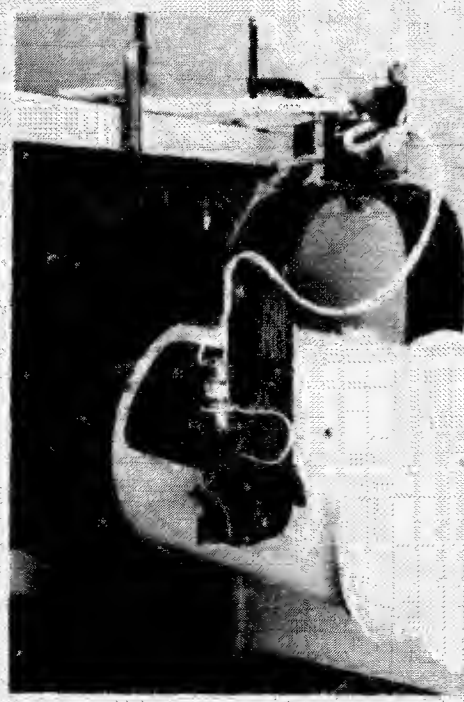


Figure 4. - Searchlight.

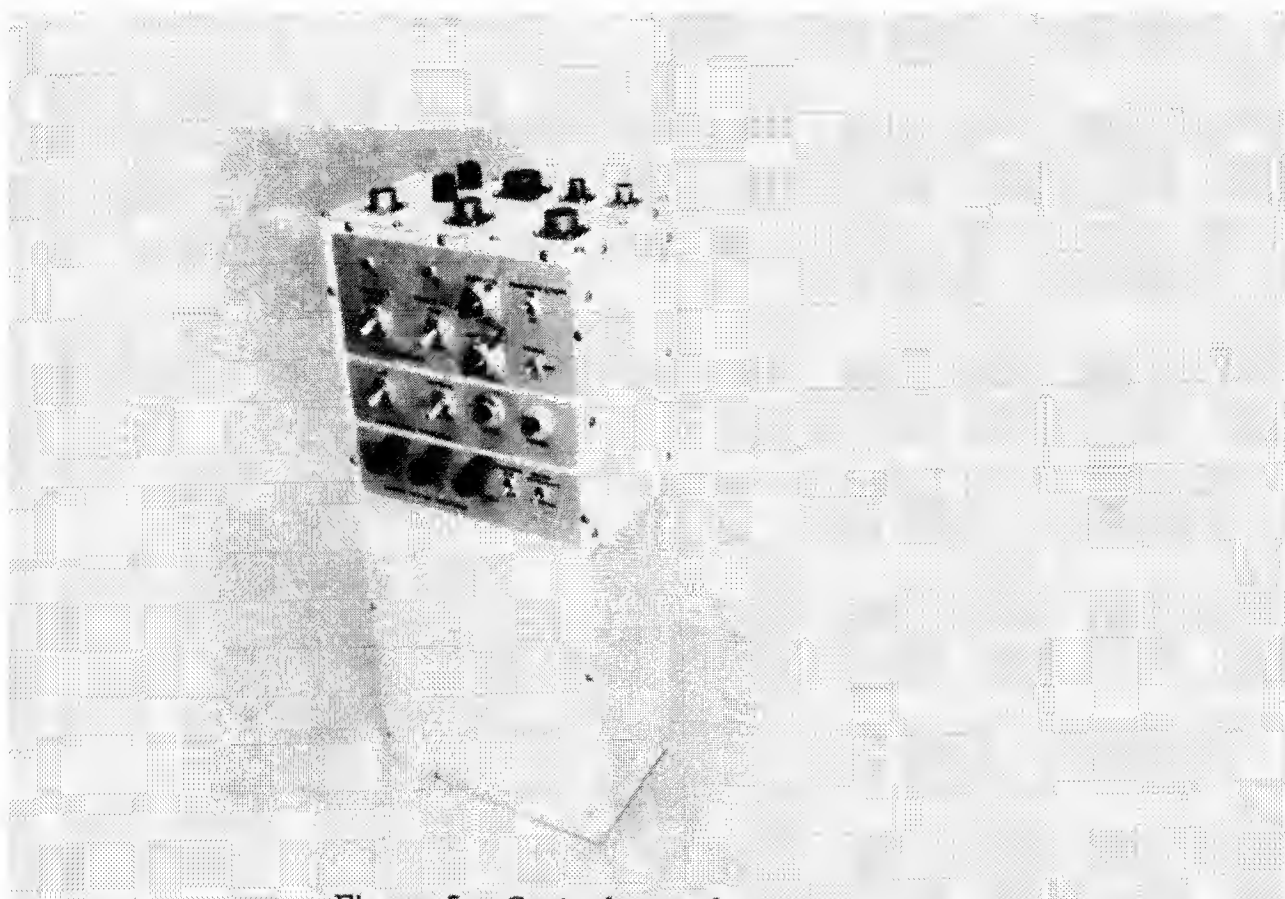


Figure 5.- Control console.



Figure 6.- Helicopter installation.

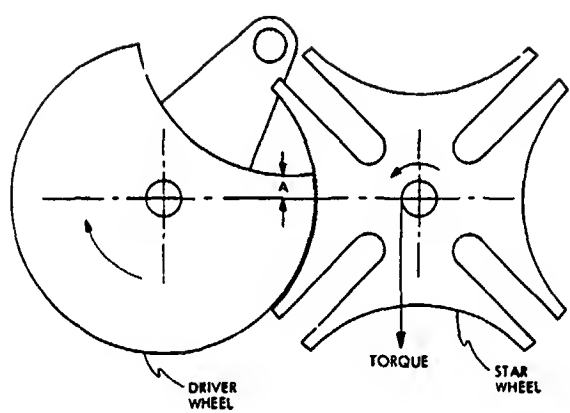


Figure 7.- Geneva mechanism.

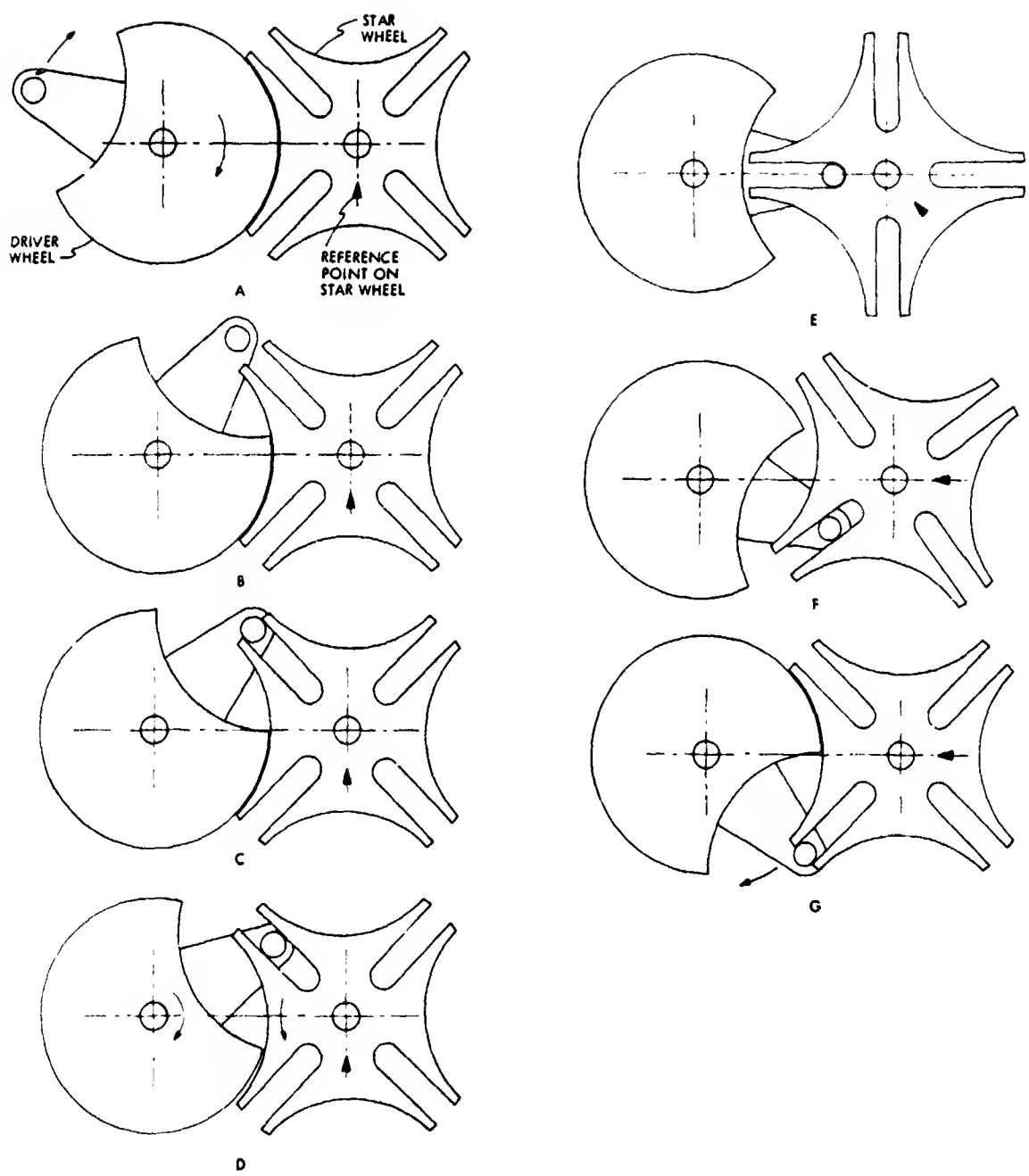


Figure 8.- Geneva operating sequence.

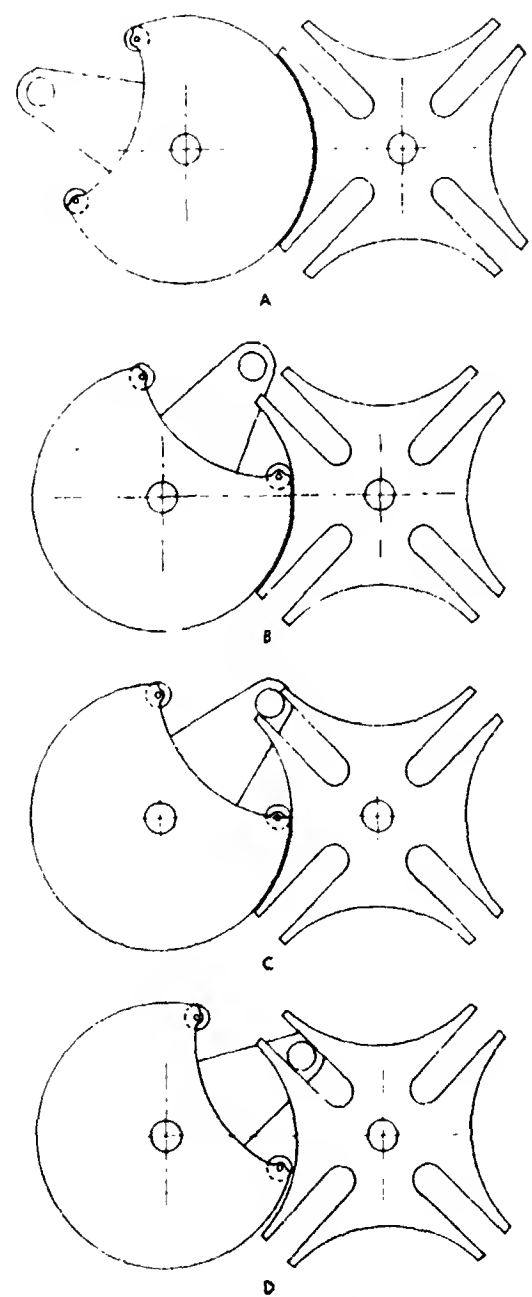


Figure 9.- Modified Geneva mechanism and operating sequence.

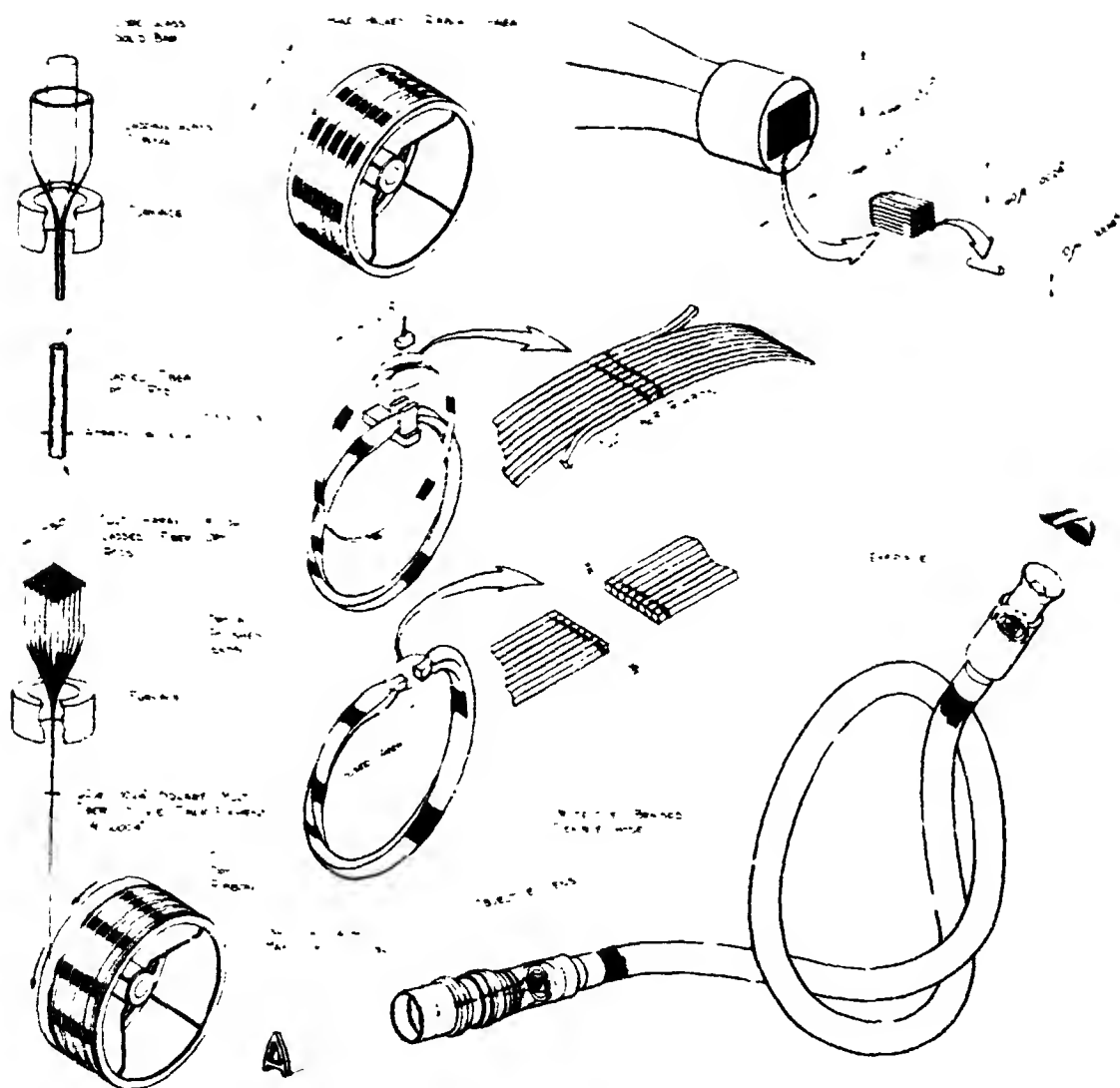


Figure 10.- Fiber-optics rope and fabrication process.

25. A GRAVITY EXERCISE SYSTEM

By William E. Brandt
and Allen L. Clark

Gyrotrim Corporation, Santa Clara
California

INTRODUCTION

The authors' interest in the possibility of employing gravity in a more efficient manner as the basis for a muscle conditioning exercise system stems from early findings of the space program regarding exposure to weightless environment. With the elimination of gravity, the normal loading of muscles during the conduct of routine activities is removed with an attendant muscular deconditioning and deterioration of muscle bulk. With a protracted period of weightlessness, the deterioration increases to potentially create a problem of cardiovascular pooling of the blood. Even inactive individuals within earth's gravity generally do not suffer these problems, or if they do, only mildly.

In other words the natural body gravitational stresses related to relatively simple natural activities have an extremely beneficial effect upon the body's muscular system even without a specific program of exercise. Simply resisting the ever-present gravitational pull in the most basic activities, such as keeping one's equilibrium, standing or sitting, walking, etc., forms a significant part of maintaining the muscular system at a minimum acceptable level of condition and tone.

With this perspective in mind the authors sought to determine ways to maximize the benefits we already receive in so many natural ways. The objective was to extend the localized stresses obtained naturally to the full body, if possible, and to do it more efficiently. Additionally, it was hoped to evolve a more effective method of muscle conditioning than is derived from ordinary unconscious reactions to a relatively inactive daily routine.

WHAT IS GRAVITY EXERCISE?

Gravity exercise is the sum total of muscular tone and conditioning that derives from the controlled reactions of the major body of muscles to the body's own weight in a gravitational field.

Here on earth in the presence of gravity we experience (both consciously and unconsciously) a process of weight transfer that is continually taking place. This process occurs consciously when we sit down or stand up or unconsciously when we sleep. It can occur when we suddenly react to the movement of a street car or the floor boards under our feet or upon being bumped off balance in a crowd. In all of these instances one common occurrence is taking place -- the

reaction of the total body weight as transferred through the structure of the body is being redistributed between the bony or skeletal structure and the various major muscle groups. The most recognizable load path, which traces the reaction of the body's weight from the head to the pressure of the foot on the floor, is that of a compressive stress acting directly through the skeletal frame. Almost everyone has experienced lower back pain from muscle reactions involved in the transfer of the body's trunk weight through the hips and down the leg structure. In order to transfer weight directly from the bone structure, it becomes necessary to selectively tension the major muscle groups of the body. The muscles are not designed for remaining in a tension condition for anything but relatively short periods of time. Hence we notice the continual shifting from one foot to the other during a lengthy period of standing — the welcome feeling of relaxing at ease versus standing at attention — the feel of the easy chair after a long walk; all of these actions decry the relative inability of the body's muscles to react to sustained loads.

Once this relatively simple property of the human body is acknowledged, it becomes clear that if weight transfer can be (accurately) regulated, then the corresponding muscular reactions will become equally regulated. Thus, the basic principle of gravity exercise is to periodically displace the human body upon reactionless rollers so that spacial equilibrium can only be maintained by the proper tension and relaxation of the body's muscles. This full body reaction constitutes an isometric exercise.

MECHANICS OF GRAVITY EXERCISE SYSTEM

The basic GES apparatus consists of a rotating platform to support a standing individual. The platform is mounted upon two-degrees-of-freedom rollers so as to obviate the formation of any lateral reactions by means of the feet. By arranging the platform to tilt away from the vertical, the body's mass can be variously unloaded from the skeletal bone structure onto the muscle structure in direct proportion to the angle of tilt. If now we introduce a rotation of the tilted platform, the full body muscular system is exposed to a condition of gravitational reaction stress throughout each 360° of rotation. This condition is depicted schematically in Figures 1(a) through 1(d). For example, at any given point of rotation, certain groups of muscles are stressed to maintain spacial equilibrium, while other groups are relaxed. As the rotation progresses, the stresses within any muscle group must correspondingly shift to succeeding muscle groups and thereby allow the previously stressed muscles to relax. The period or frequency of this cycle of stress/relaxation is exactly set by the speed that the platform is driven.

It was stated above that the combined body structural reaction maintained equilibrium against the force of gravity. It is easily recognizable that the gravity component of weight in the platform plane would cause the two-degrees-of-freedom support to translate in the down-hill direction as indicated in Figure 1 unless an equal and opposite reaction were provided. A simple analysis of the mechanics of the situation shows that, for the body supported upon 2-D rollers to apply a reaction force in the plane of the support, an equivalent force and moment must be applied by the hands and arms (and the full body) at the upper supports. Figures 1(a) through 1(d) show that the

mechanics of the body reaction as described above for each of the positions of rotation (at a finite angle of tilt) would require a different equilibrium stress condition throughout all of the muscle groups of the body. As the platform rotates, the body muscles cyclically stress and relax at the platform rotational speed. This speed can be suitably adjusted to a value known to produce optimum isometric muscle conditioning.

GRAVITY EXERCISE SYSTEM RESULTS

The process of evaluating the conditioning effects of a particular exercise routine are difficult, to say the least. One can resort to certain extremes to obtain qualitative bounds of the effects. For example, if persons of extremely limited physical capabilities can be taught to employ the routine, then the results of physical conditioning and muscle tone are usually quite dramatic.

However, a quantitative evaluation of normally active bodies is generally difficult. Such a test was conducted at Palo Alto V.A. hospital in the course of a research endeavor involving normal adult males of approximately middle age. Data were obtained by using the electromyograph (EMG) to measure the reduction of EMG mean voltage output as a gage of the reduction in motor units required to produce the same amount of work. (NOTE: This assumes that an increase in the size of muscle fibers due to a conditioning effect, and associated with an increase in contractile strength of a given motor unit, would require fewer motor units to produce a given amount of work). Results of Reference 1, representing the EMG voltages obtained from the pectoral muscles of a typical 40 year old male subject, are shown in figure 2 as illustrative of the significant and linear decrease in myoelectric output throughout a program of one 200-second exercise per day conducted at a rate of 5 days per week for a period of 12 weeks.

This work of Carlson, et al, is cited primarily as a quantitative indication of the efficiency of the Gravity Exercise System to provide muscle conditioning and toning under normal gravity conditions. The authors have had considerable experience with the dramatic physical improvements wrought with a number of physically deficient subjects ranging from a child having cerebral palsy, to a middle aged stroke victim, to routine geriatrics.

CONCLUDING REMARKS

The muscle system of the human body is an amazing adjunct to the skeletal structure; it can take all kinds of punishment and hard use during the course of a lifetime with little or no signs of wear. This is because it is designed for walking, lifting, climbing, and working in our earth's environment. In fact, it can adjust to almost any situation - except inactivity. The muscular system rapidly loses its natural tone during any protracted period of disuse; this would, of course, include the gradual effects of lack of a gravitational pull upon our bodies.

In order to maintain a healthy and natural body tone, all of the major muscles of the body will have to be reacted periodically whether under the influence of gravity or not. We believe that the Gravity Exercise System as

proven on earth is a logical candidate for weightless (zero g) environment by simply replacing the gravitationally induced body stresses with mechanically induced stresses. That is to say, we would require a subject to maintain upon center a spring-loaded two-degrees-of-freedom plate that is forced to rotate eccentrically. In our estimation, the subject's body reactions to overcome the spring tension force would provide an exercise that is quite similar to that of overcoming gravity in our present machine.

REFERENCE

1. Carlson, Karl E., M.D., Montero, Jose C., M.D., Gerontinos, Evangelo M., and Kerrins, Robert K.: The Use of Gravity in Isometric Exercise. The American Corrective Therapy Journal, vol. 25, no. 1, Jan.-Feb. 1971, pp. 19-22.

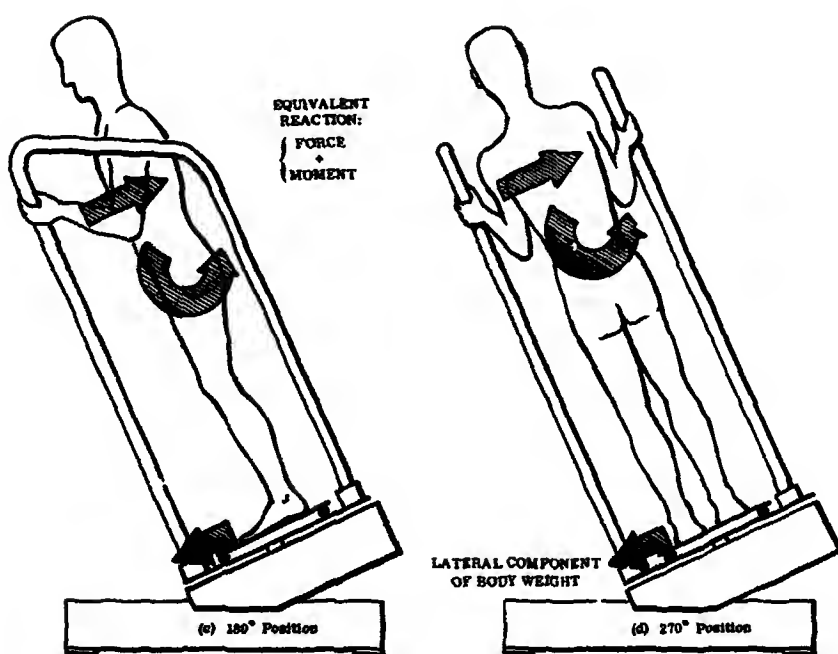
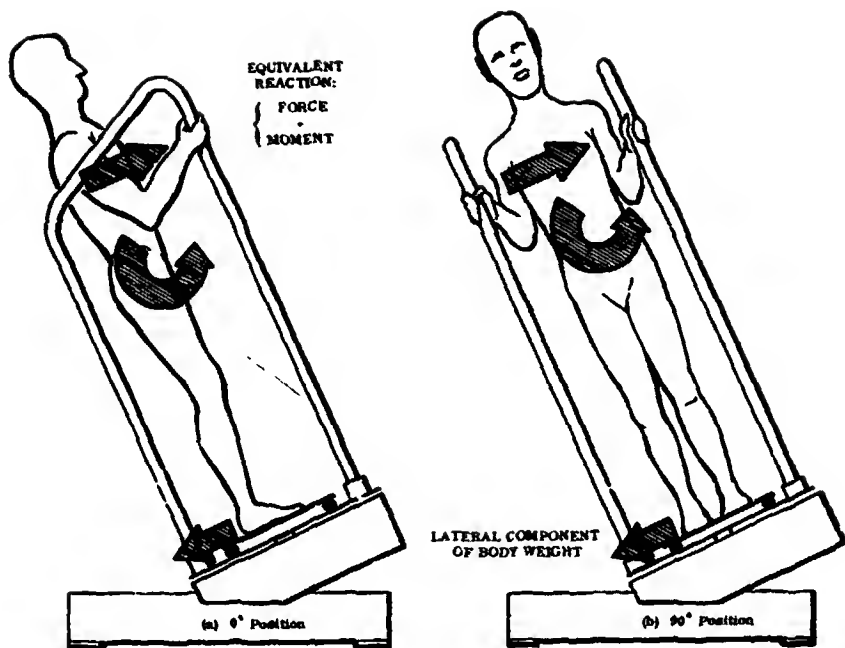


Figure 1.- Gravity exercise system.

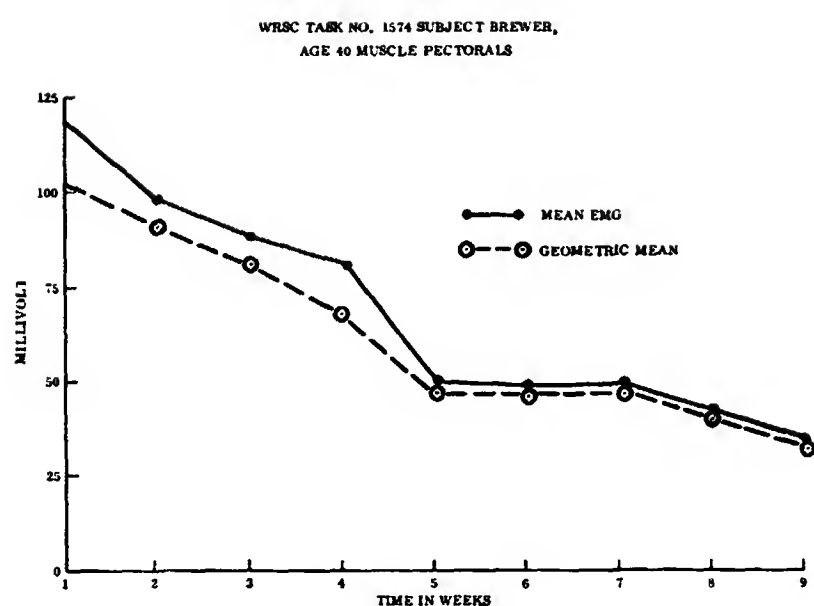


Figure 2.- Composite plot of voltage decrease against time in weeks.

26. POLYURETHANE RETAINERS FOR BALL BEARINGS

by

R. I. Christy
Hughes Aircraft Company

SUMMARY

Evaluation of a new ball bearing retainer material is reported. A special composite polyurethane foam ball retainer has been developed that has virtually zero wear, is chemically inert to hydrocarbon lubricants, and stores up to 60 times as much lubricant per unit volume as the most commonly used retainer material, cotton phenolic. This new retainer concept shows promise of years of ball bearing operation without reoiling, based on life testing in high vacuum.

INTRODUCTION

The life and performance of spacecraft ball bearings are dependent on reliable operation of the ball retainer. For many bearing applications, where the lubricant supply must be sealed in during assembly, the retainer should serve as a lubricant reservoir as well as a ball-holding and separating device. Retainer selection, therefore, must be based on:

- High oil-holding capacity (absorptivity)
- Good oil retention and feed characteristics
- Physico-chemical inertness and stability
- Low friction and wear
- High strength, but good resiliency
- Low cost with good machinability

The most widely used porous ball retainer material is laminated cotton cloth base phenolic tubing. Although many other materials have been tested and a few achieved limited usage, cotton-reinforced phenolic is still the workhorse in a ball bearing design. Because only part of the oil impregnated into such a retainer will transfer to the bearing balls, ultra-long-life oil supply is limited by low absorption retainers. (For example, a typical 90 mm bore, light series angular contact bearing retainer of 1 percent porosity phenolic will hold only 0.4 gram of hydrocarbon oil.)

RETAINER DEVELOPMENT

Because of the difficulties in applying commercial phenolic, a search for alternate materials for bearing retainers has been conducted. Materials evaluated include sintered bronze, sintered aluminum, sintered polyimide, polyurethane composite foams, and laboratory-fabricated cotton phenolic laminates.

Numerous bearings have been tested using laboratory-fabricated phenolic and polyurethane foam. Bearings using polyurethane composite foam retainers have been operated successfully for periods up to 1 year in vacuum at 100 rpm. Polyurethane composite foam retainers have shown extremely low

wear compared to cotton phenolic, sintered bronze, and sintered aluminum and are capable of storing up to 60 percent by volume of lubricant. The oil transfer characteristics are good in that oil is rapidly transferred from the retainer to the balls and races when an insufficient oil film exists and the transfer stops as soon as an adequate oil film is reestablished. Chemical tests and accelerated high temperature aging tests indicate the retainer is inert and does not react with nor degrade hydrocarbon lubricants and that the retainer maintains adequate mechanical properties for long-term applications (longer than 3 years).

The composite foam is a special high porosity material with controlled pore size to accurately control oil storage and capillary flow rate. Vacuum outgassing tests have shown very low volatility ($< 6 \times 10^{-10} \text{ gm/cm}^2/\text{sec}$ at 50°C). Because the foam is a flexible material, designs using a rigidizing frame are necessary. This type of design achieves more favorable thermal expansion match with the bearing metal parts. Bearing retainers in sizes from R-4 to 150 mm bore have been built and tested (see Figure 1). Bearings equipped with these retainers have survived vibration up to 12 g at frequencies from 20 to 2000 Hz, temperatures from 30° to 150°F , and speeds from 60 to 3600 rpm. Running torque of composite foam retainer bearings can be somewhat higher than that of cotton phenolic (approximately 10 percent) and torque variation (i.e., torque noise) is about the same as for cotton phenolic.

RETAINER DESIGN USING POLYURETHANE FOAM

Because of the high flexibility of the polyurethane composite material (Shore A 30 hardness), a rigid frame is necessary to maintain the shape of the retainer. Various designs of metal frames have been used successfully. Figure 1 illustrates two sizes of composite metal frame retainers.

The polyurethane composite foam has inherent properties that make it ideal as a ball bearing retainer material for many applications. It is a tough material with fairly good tear strength (22 pli) and an extremely low wear rate. The pore size, shape, and distribution provide a large lubricant storage area with a feed rate that varies favorably according to the oil film thickness. Table 1 summarizes some of the properties of interest.

TABLE 1. POLYURETHANE COMPOSITE FOAM PROPERTIES

<u>Property</u>	<u>Value</u>
Density (dry)	0.398 gm/cm ³
Density (oil impregnated)	0.994 gm/cm ³
Oil per unit volume	0.597 gm/cm ³
Oil per unit volume for phenolic (for comparison)	0.046 gm/cm ³
Pore size (diameter)	10 microns
H- ^d ness	30 Shore A
Tensile strength	115 psi minimum
Tear resistance	22 pli minimum
Operating temperature range	0 to 70°C

Accelerated aging tests of the oil-impregnated foam (Apiezon C oil with 5 percent lead napthenate EP additive) and unimpregnated foam done at 250°F in vacuum for 408 hours showed no significant changes from aging except for a hardness increase from Shore A 30 hardness to Shore A 35-40. Infrared analysis, carbon hydrogen elemental analysis, and thermogravimetric analysis results showed no difference due to aging of the foam or the oil.

The steady-state weight loss rate of the foam was measured at 50°C in vacuum and was found to be $5.5 \times 10^{-10} \text{ gm/cm}^2/\text{sec}$.

POLYURETHANE COMPOSITE FOAM MATERIAL PERFORMANCE

A series of material performance tests evaluated performance of the foam material prior to fabrication of retainers for ball bearings. Wear tests compared friction, wear, and oil transfer rates of the urethane material with phenolic and other candidate retainer materials. These tests were run in air at laboratory ambient conditions in a Class 10,000 laminar flow room. Wear test samples were run on a half-inch diameter stainless shaft driven at 300 rpm. A 3 pound force was applied by the coil springs in the specimen holders, pushing each wear test sample against the shaft. All test samples were impregnated with Apiezon C oil with a lead napthanate EP additive. Barrier coatings were applied in bands around the shaft between the samples. The tests were run for 1 month with the results as follows:

<u>Sample</u>	<u>Results (after 1 month)</u>
Sintered aluminum, standard	High wear, catastrophic failure in 8 days
Special alloy sintered aluminum	Unacceptable wear by end of test
Phenolic	Small wear scar and debris, shaft discolored
Sintered polyimide	Less wear than phenolic, shaft discolored
Sintered bronze	Wear comparable to phenolic, no discoloration of shaft
Composite urethane foam	No detectable wear, no shaft discoloration

A notable result of this initial test was the complete absence of wear, debris, or shaft discoloration for the polyurethane foam sample. Tests were continued for a second month with the same result.

Friction Tests

A series of friction coefficient measurements was made on the specially constructed friction test apparatus shown in Figure 2. Friction coefficient was measured between the rotating ball (19/32 inch diameter) and a fixed flat block of polyurethane foam over a range of speeds, normal forces, and oil quantities, and for two block thicknesses. The friction force was measured by using a force transducer consisting of a cantilever spring and differential transformer displacement transducer. This was calibrated against a Chatillon spring type force gauge. The results are shown in Figure 3.

The high values of friction coefficient and the higher coefficient for low normal forces may be due in part to the method of measurement. The 19/32 inch diameter ball penetrated on the order of 0.005 inch into the foam with 0.1 pound normal force applied. This penetration leads to a surface under tension in the contact region and may result in higher friction. (See ref. 1.)

Oil Transfer Tests

Lubricant transfer characteristics were measured on blocks of foam impregnated with Apiezon C oil mixed with a lead naphthanate additive. A special fixture was constructed to continuously remove the oil film transferred from an impregnated foam block to a large 440C stainless ring. Successive weighings of the foam block provided data on oil transfer rate as the oil was depleted from the block. Other measurements were also made without removal of the transferred film to evaluate oil transfer versus already transferred film thickness. A foam wheel in a freon bath was used to remove the transferred oil film. The oil transfer test apparatus is shown in Figure 4.

As shown in the oil transfer data (Figure 5), the transfer rate is highest for the fully impregnated condition and then decreases with running distance. This decrease may partially result from the abnormally high oil transfer rate imposed on the test sample to provide data in a reasonable time interval. In a ball bearing, the transfer rate would be far less because of the established oil film, as shown in the following experiment.

The same apparatus used for measuring oil transfer with continuous removal was used to measure oil transfer as a function of previously transferred oil film thickness. Results have shown that after three or four revolutions of the stainless ring, an equilibrium oil film thickness is established and that continued rotation up to thousands of revolutions results in no further measurable oil transfer. The equilibrium film thickness was found to be on the order of 33 microinches for a test block almost fully impregnated (surface oil removed) and this decreased to 20 microinches after about one-third of the oil had been transferred out of the block by continuous removal of the oil from the ring. The interesting characteristic of the polyurethane foam was the very rapid transfer of oil to a dry surface followed by an abrupt end of oil transfer once the equilibrium oil film was established.

RETAINER/BEARING PERFORMANCE

A number of short-term performance evaluation tests such as oil transfer, vibration, torque noise, and thermal aging have been conducted on bearings equipped with polyurethane composite foam retainers. In parallel with these tests, 20 bearings with polyurethane composite retainers are currently operating in thermal-vacuum life tests.

Oil Transfer Tests

Various oil transfer measurements were made on a 2.362 inch diameter bore by 3.740 inch outside diameter bearing (440C material) and a polyurethane foam retainer. Oil transfer from the retainer to the balls and races of the bearing was measured by successively weighing the retainer. The test procedure was as follows:

- 1) Freon-rinse balls and races to remove oil
- 2) Weigh retainer
- 3) Assemble bearing
- 4) Run bearing 100 rpm, 45 pound axial preload, laboratory ambient conditions, various time intervals from 1 minute to 17 hours

- 5) Disassemble bearing
- 6) Go back to step 1 above

At one point, the freon rinse was not done for several cycles to evaluate oil transfer as a function of amount of oil on the metal surfaces. The total amount of oil transferred per run appears to be independent of run duration. Both the 1 minute and the 15 hour, 49 minute runs resulted in the same amount of oil transfer from the retainer to the balls and races, as shown in Figure 6. This suggests that the transfer mechanism is dominated by the oil film thickness on the balls and races and that oil transfer stops after a given oil film is established.

Bearing Torque Test Results

Bearing torque and torque noise were measured in air over a speed range of 45 to 150 rpm on nine bearings with urethane foam retainers. Figure 7 shows torque and torque noise measurements on a typical bearing. The measurements were compared to similar data on phenolic retainers and the torque values ranged from the same to 20 percent lower on the bearings equipped with phenolic retainers.

Vibration Test

A vibration test was run on a polyurethane foam equipped bearing. The test was run from 1.5 to 25 g at frequencies of 5 to 2000 Hz. Inspection of the bearing and retainer after vibration showed no damage nor problem with the polyurethane foam retainer. There was no evidence that vibration caused oil loss from the foam. The test was repeated on 16 other bearings of three sizes with polyurethane retainers, and no damage, oil loss, nor degradation of performance was found after vibration.

Wettability Tests

A 90 hour vacuum test on one 3.543 inch diameter bearing with a polyurethane foam retainer lubricated with Apiezon C oil with a lead napthanate additive was conducted. The bearing was run at 60 rpm and with a 60 pound axial load. The test pressure was 1×10^{-5} Torr and the test was done at ambient temperature. The bearing metal parts had previously been run in vacuum without a retainer and were 100 percent wetted with the same oil. Inspection of the bearing after the 90 hour vacuum test with the polyurethane foam ball riding retainer installed showed no evidence of nonwetting of balls nor races. The oil quantity in the bearing was also normal.

Temperature Test Results

Eight bearings with foam retainers were subjected to simulated storage and transportation exposure for approximately 3 hours at each temperature extreme of -50° and $+150^{\circ}\text{F}$. Subsequent performance of these bearings in life tests was normal. Torque on a pair of bearings operating in vacuum was measured over a temperature range of 40° to 115°F , with results comparable to a similar phenolic-equipped bearing, as shown in Figure 8.

Life Test Results on Polyurethane Foam Retainers

Twenty-two bearings equipped with polyurethane retainers are currently under life test in high vacuum. There have been no failures and no indications of degradation in any of the tests, some of which have been operating for over a year. Figure 9 shows the duration of the various tests. These bearings are mounted and preloaded to simulate despin bearing applications for communication spacecraft antennas. Figure 10 shows torque versus time for various test bearings. One test was interrupted after 1 year of operation and visual inspection showed no damage nor degradation and no evidence of retainer wear. The bearings were coated with thick oil films, and weight measurements indicated that over 97 percent of the initial oil in the bearing remained after 1 year of vacuum operation.

CONCLUSIONS

Experimental work on composite polyurethane foam as a ball bearing material has demonstrated certain characteristics that are superior to metal ribbon, cotton phenolic, and certain other types of retainers.

Tests of composite polyurethane foam have shown:

- 1) Lower wear rates than cotton phenolic, sintered bronze, sintered aluminum, and sintered polyimide.
- 2) Very low outgassing in vacuum (5.5×10^{-10} gm/cm²/sec at 50°C).
- 3) Good chemical stability and minimum physical properties change when aged in hydrocarbon oil at 150°F.
- 4) Rapid lubricant transfer until a film is established followed by diminished transfer, thus minimizing the risk of flooding.
- 5) Good performance in bearing high vacuum life tests for up to 12 months.

The friction coefficient is higher than for metal retainers or phenolic and ranges from 0.27 to 0.37.

Fabrication of this material to very close tolerances suitable for ball bearing retainers is difficult but attainable and, by using the metal backup structure, good dimensional control can be achieved.

The inherent high porosity and oil storage capacity make this material attractive as a bearing retainer material for long life, zero maintenance systems. Continuation of life tests currently in process will establish a test data matrix upon which to estimate the reliability of this concept.

REFERENCE

1. Nazarenko, P.V. et al., "Investigation of the Deformation and Sliding Friction of Polyurethane in the Presence of Lubrication," Kievskii Institute Inzhenerov Grazhdanskoi Aviatsii, Kiev, Ukrainian SSR, Mekhanika Polimerov, Vol. 5, March-April 1969, A69-35362.

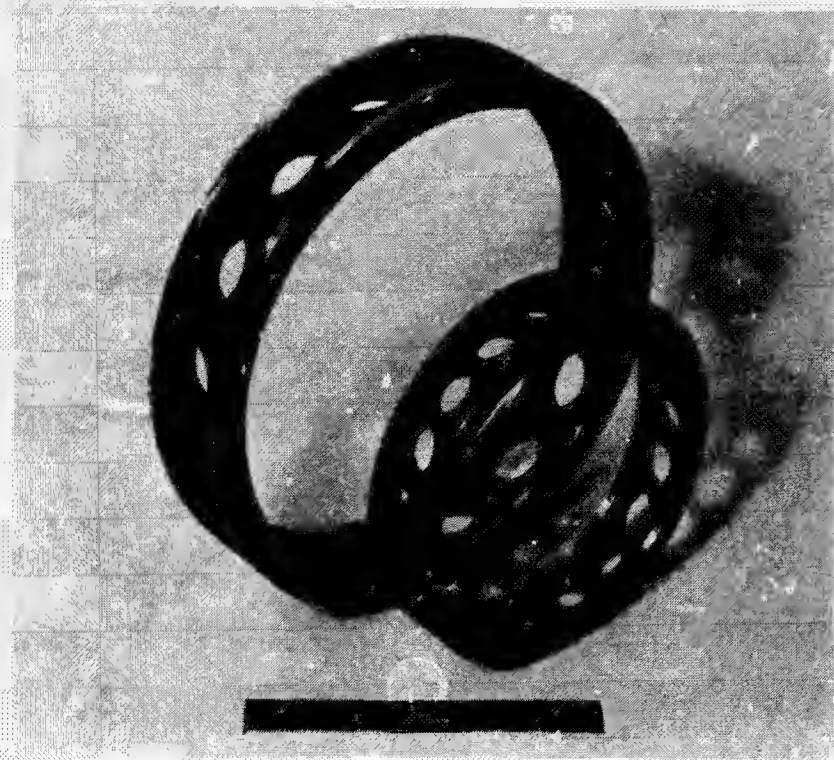


FIGURE 1. POLYURETHANE COMPOSITE BALL RETAINERS
(PHOTO 4R24412)

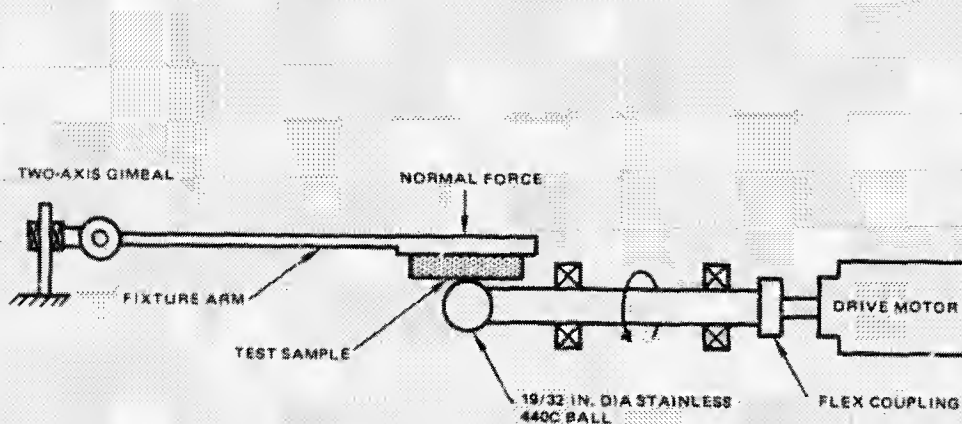


FIGURE 2. SCHEMATIC OF FRICTION TEST APPARATUS

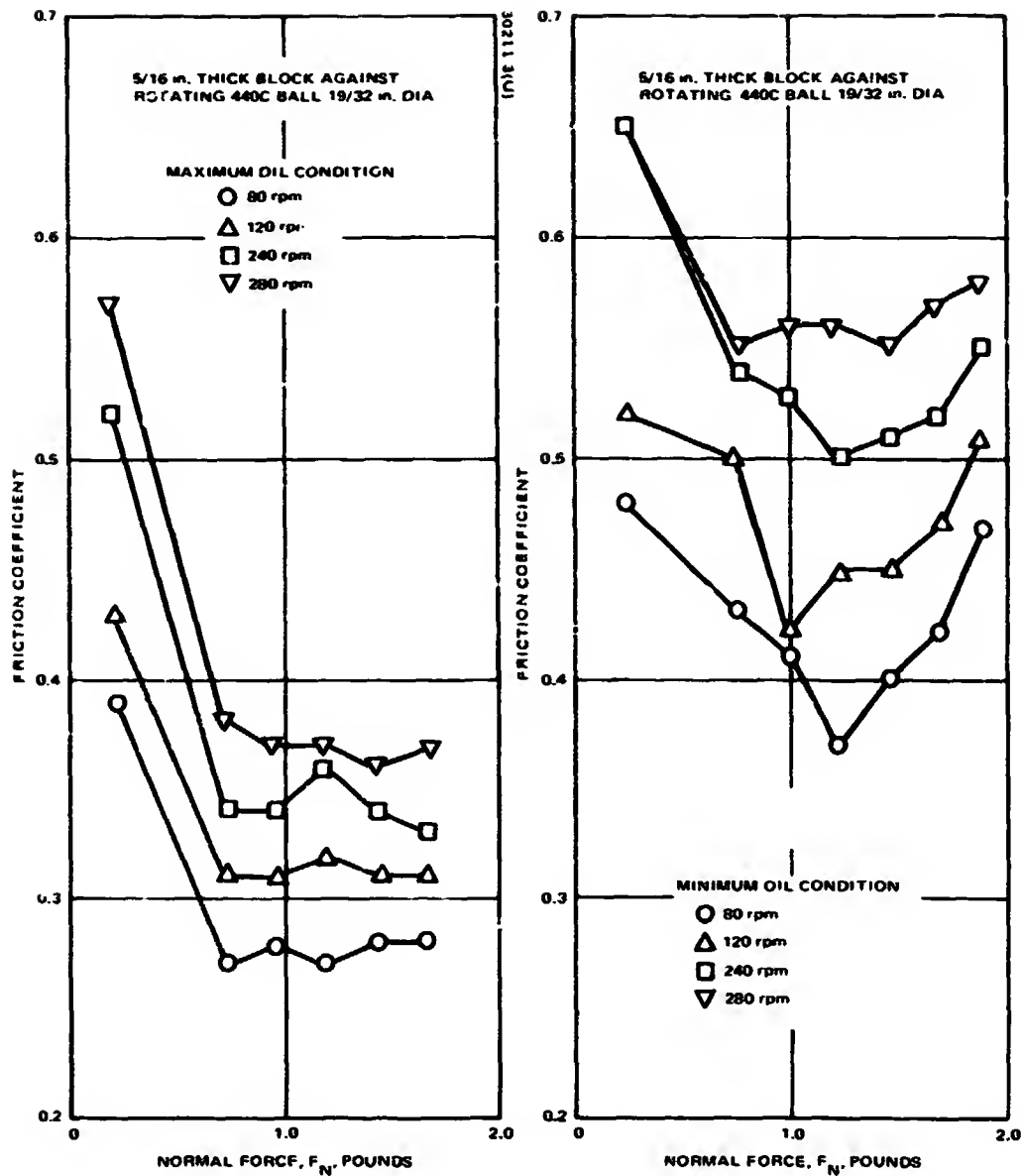


Figure 3.- Friction coefficient for polyurethane foam against stainless steel.

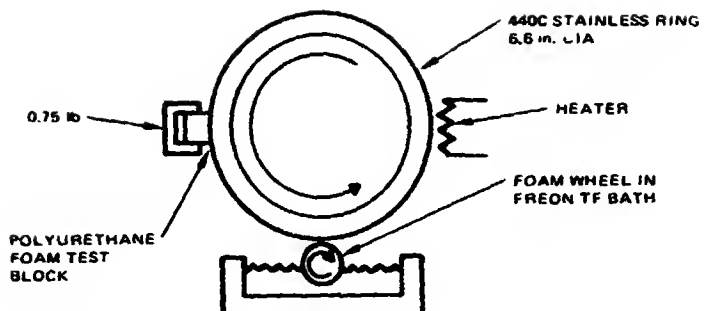


Figure 4.- Oil transfer test apparatus.

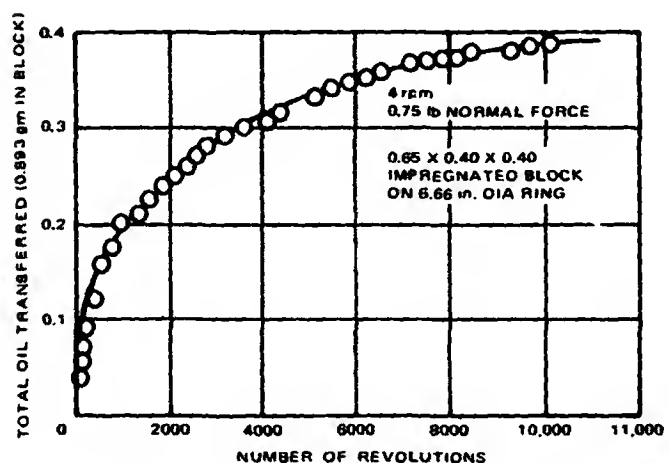


Figure 5.- Total oil transferred versus number of revolutions.

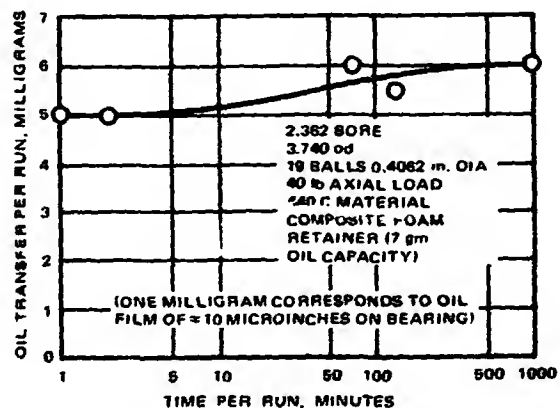


Figure 6.- Amount of oil transferred to dry bearing from composite foam retainer as function of running time.

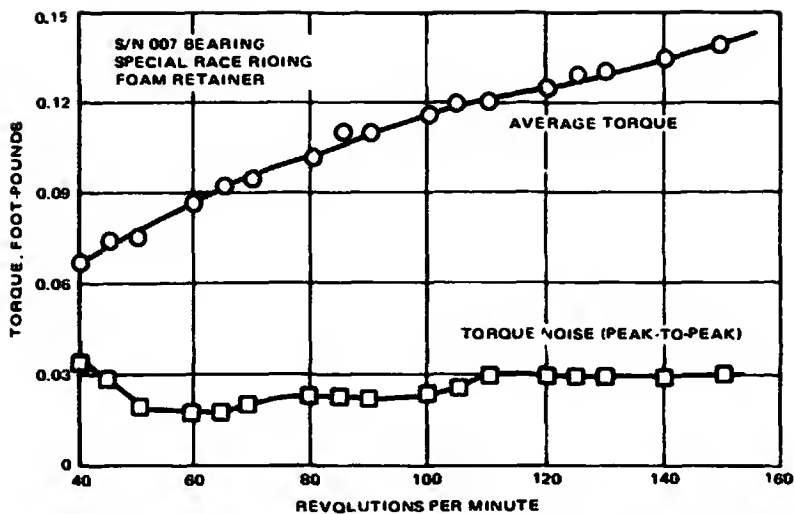


Figure 7.- 3.543 inch diameter bearing torque data.

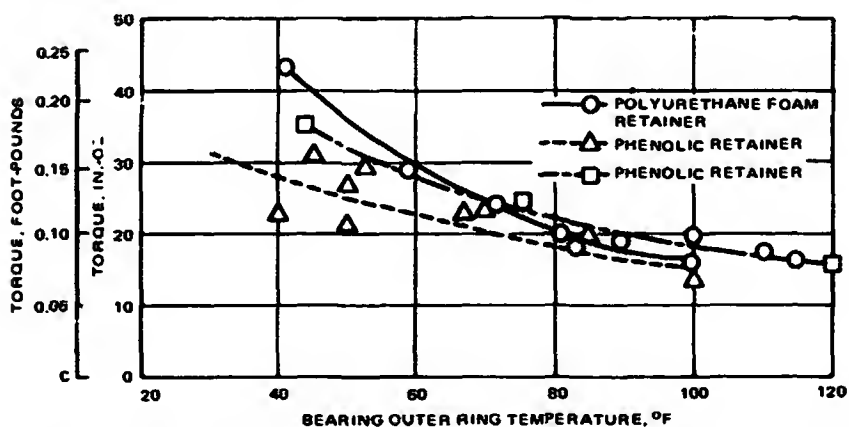


Figure 8.- Hot and cold temperature cycle 3.543 inch bore bearings (torque of two bearings) at 60 rpm.

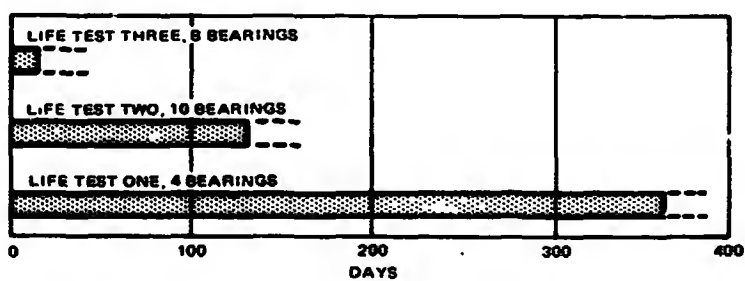


Figure 9.- Life test history chart (as of 10 May 1973).

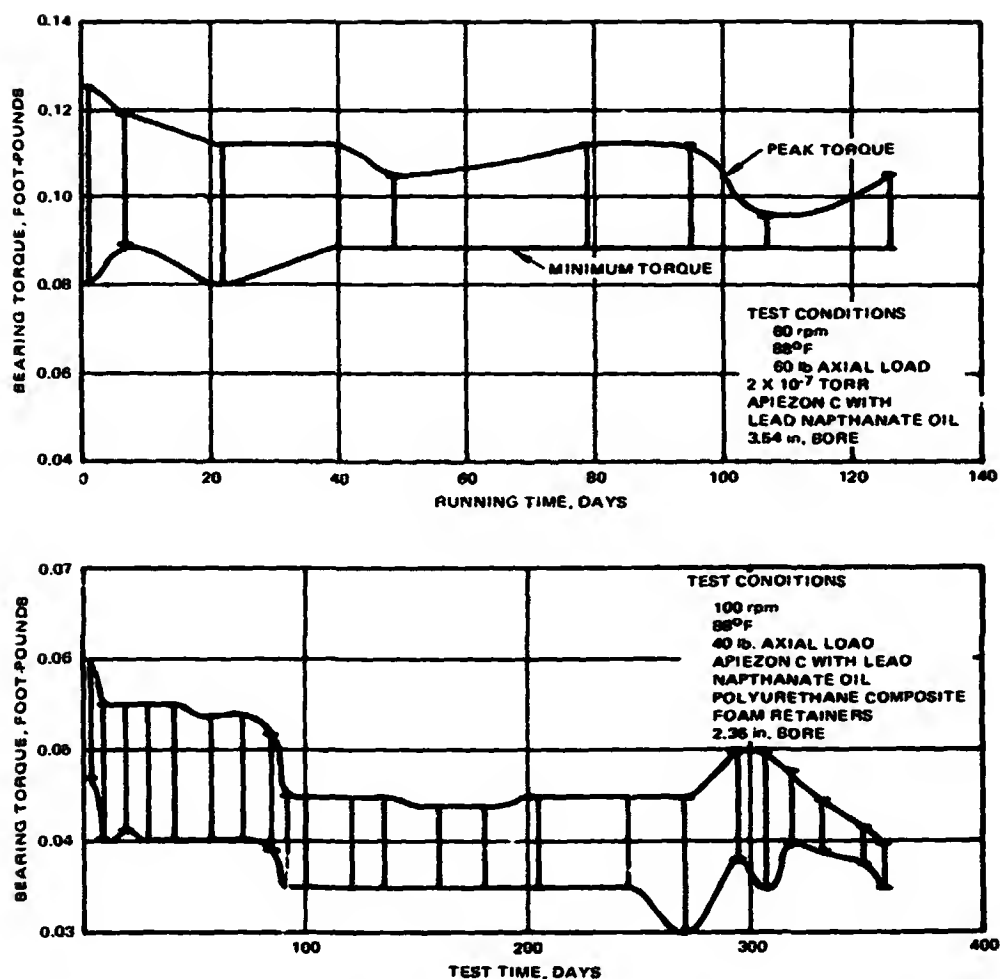


Figure 10.- Test bearing torque versus time for two bearings.

27. MULTI-POINT RELEASE MECHANISM

By E. Groskopfs

Spar Aerospace Products Ltd.

SUMMARY

The purpose of this paper is to present the design of a multi-point release mechanism used on the Communications Technology Satellite (CTS). This spacecraft is designed and being built by Spar under a contract from the Communications Research Centre in Ottawa, Canada.

The mechanism is designed to jettison one large panel (Jettisonable Body Solar Array - JBSA) and to release a second panel (Pressure plate). Both panels have independent multi-point attachments to the spacecraft and require to be released in sequence. In addition, the outermost panel, or JBSA, is easily removable without any special tools to permit quick access to the pressure plate, which retains the stowed flexible solar array. The solar array is stowed concertina fashion under 2 psi pressure to ensure that no movement occurs between the stowed folds of the array during the launch. One pair of linear pyrotechnic-actuators releases both the JBSA and the pressure plate via the release mechanism.

This release mechanism has successfully passed qualification level vibration launch and thermal environment tests and has accumulated to date close to 30 successful releases.

INTRODUCTION

With the advance of spacecraft having large flexible solar arrays and the general need to release large structural members, there is a common problem of the simultaneous or phase releasing of multi-point attachments usually spaced many feet apart. Many multiple attachment release systems have been used in the past; however, none of these systems met the basic requirements of the CTS deployable solar array system. Therefore, an unusual release mechanism was developed, where the firing of a pair of pyrotechnic-actuators releases 8 tie-down points on the pressure plate and 4 tie-down points of the JBSA. The release mechanism is designed such that both or either of the linear pyrotechnic-actuators can release all 12 points.

SOLAR ARRAY

The Communications Technology Satellite has two flexible solar arrays, each 52 inches wide and 276 inches long mounted on opposite faces of the S/C and stowed concertina fashion, for launch, between two honeycomb panels, and is shown in Figure 1.

To protect each array fold from damage during the launch, thin foam interleaves are laid between the folds from each side of the array with additional protection being provided by means of 5/8" thick foam pads attached to the inside surfaces of the honeycomb panels. These pads isolate the stowed array from local deformations created by the stowage pressure and the reactions from the spacecraft mounting face during launch and apogee motor burn. The array stowage pressure of nominally 2.0 psi is achieved by compressing the folded array and interleaves through 8 strain gaged tie-down points. Since the compressed area is approximately 400 sq. inches (giving a total of 800 pounds force) it is, therefore, very important to "free" all tie-down points simultaneously to prevent serious structural damage.

PRESSURE PANEL AND RELEASE MECHANISM

The pressure panel is required to cover the stowed array and to apply the stowage pressure. Mounted on the top surface of this panel is the tie-down and release system for both the pressure panel and the Jettisonable Body Solar Array (JBSA).

The release system, see Figure 2, is such that either one or both linear pyrotechnic-actuators can initiate the required movement of the tie-down release cable, therefore creating the required redundancy in the release system. A pair of Holex pyrotechnic-actuators mounted in a support bracket is shown in Figure 3. A compression spring opposing the pyrotechnic-actuators is mounted to remove any possibility of premature release during vibration.

The release cable is made from standard .125 in. diameter aircraft cable. In the tie-down point areas tubular metal sections are swaged onto the cable to give a rigid support for the latch beams and to provide a smooth sliding surface for the cable movement.

In addition to four latch beam supports, two "L" shaped brackets are attached to the release cable. These brackets are

positioned such that when the release cable moves, approximately .1 of an inch, the JBSA release mechanism plunger is contacted. Additional release cable movement then releases the two pairs of ball-lock retainers holding the JBSA assembly to the spacecraft. The release mechanism is designed such that JBSA release occurs before any of the pressure plate tie-down points are released.

JETTISONABLE BODY SOLAR ARRAY

A honeycomb panel completely covers the total stowed solar array subsystem. It serves a two-fold purpose; firstly, it provides thermal protection to the folded array, and its associated mechanisms; secondly, it provides additional electrical power to the S/C from solar cells mounted to its outer surface, prior to the extension of the main solar arrays.

The release mechanism consists of two pairs of cable connected ball-lock attachments as shown in the Figure 4.

The four interface feet holding the JBSA to the space-craft have "Uniball" type seats, thus assuring that no jamming can occur during the ball-lock release. Each JBSA support leg contains an ejection spring of adequate force to give the JBSA the required 7 ft. per second separation velocity. An "exploded" view of the JBSA release mechanism is shown in Figure 5.

The JBSA is easily removable to provide access to the stored solar array. This facility is needed to permit the "last-minute" adjustment of the stowage pressure (there is a tendency for the stowage pressure to drop slightly after long periods of time) and to provide access to the pyrotechnic-actuators.

DESIGN CONSIDERATIONS

In selecting this release mechanism a number of design trade-offs were made. Many existing release mechanisms were evaluated with special emphasis on performance, weight and cost. A study for both panels was made to arrive at the optimum number of tie-down points. It is desirable that the number of pressure panel tie-down points be sufficient to assure a uniform pressure distribution within the stored array while, on the other hand, for simplicity and weight reasons, the number of attachment points should be a minimum. By using a computer assistance, an 8 point attachment mechanism for the pressure plate with 4 points for the JBSA was selected.

The initial release mechanism design used a light weight release rod. However, the bread board mechanism tests showed that the use of a rod created very difficult alignment problems of the support brackets. In addition, when pressurized, the pressure plate deflected, causing a complete jam-up which was solved by changing the rod to a cable with swaged fittings in the support bracket area.

ACKNOWLEDGMENT

The author wishes to thank Communication Research Centre in Ottawa for permission to publish this paper and particularly to acknowledge the contributions of D. G. McFarlane, who designed the mechanism discussed above.

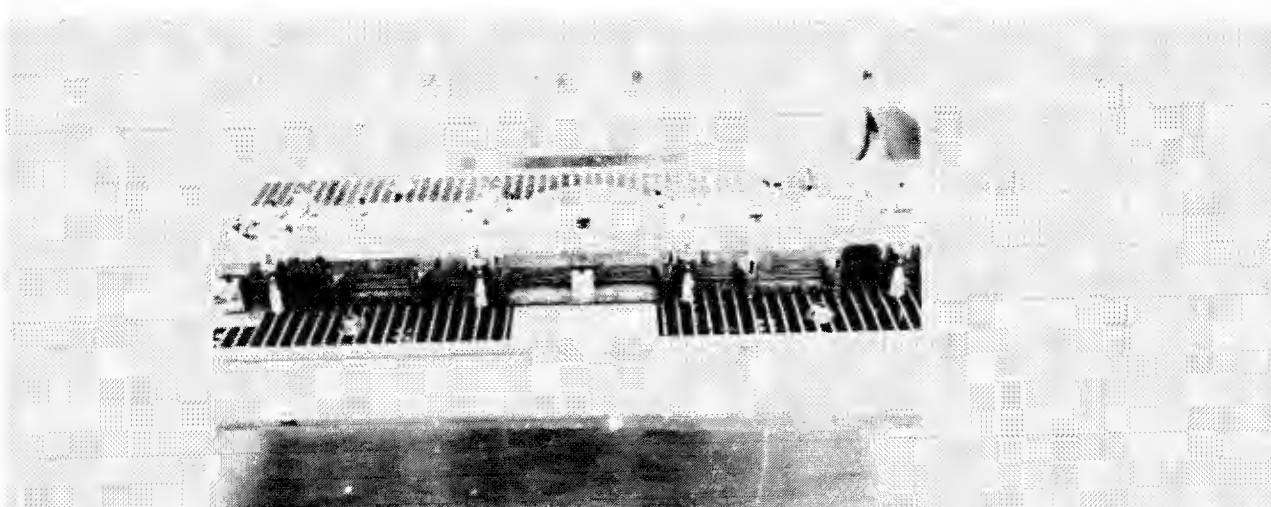


Figure 1.- Stowed solar array with JBSA removed.



Figure 2.- Pressure plate assembly.

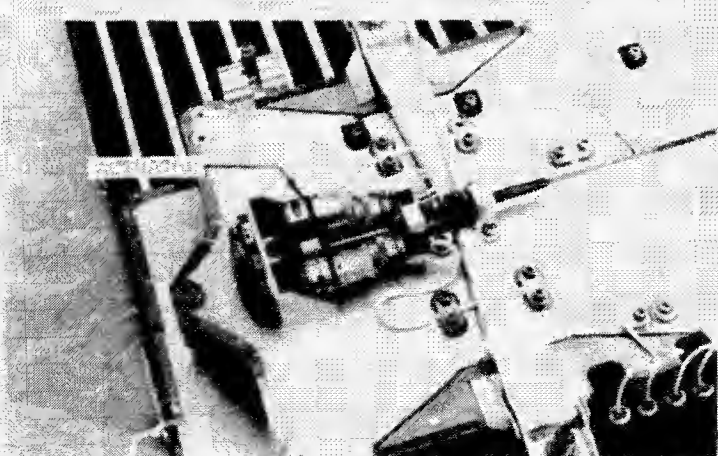


Figure 3.- Redundant pyrotechnic-actuator assembly.

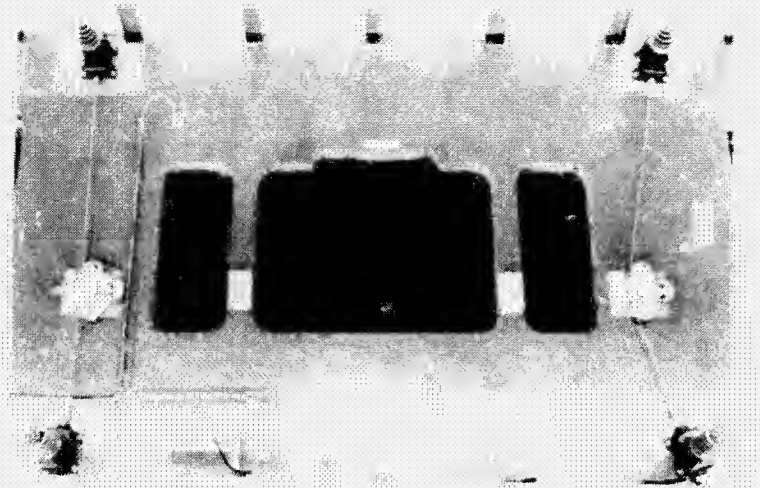


Figure 4.- JBSA assembly.

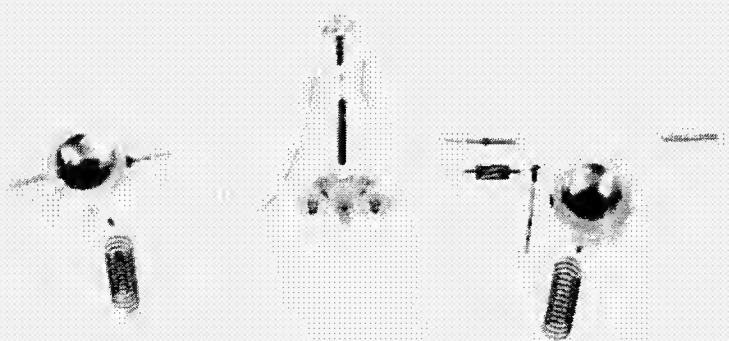


Figure 5.- JBSA release mechanism details.

28. VIKING ORBITER 1975 ARTICULATION CONTROL ACTUATORS*

By G. S. Perkins

Jet Propulsion Laboratory
California Institute of Technology
Pasadena, California

ABSTRACT

A series of three (3) digital actuators will drive the scan platform, the high gain antenna, and the solar energy controller assembly on the VO'75 Mars orbiter spacecraft. The scan platform is a two (2) axis device for carrying and pointing the science instruments on the spacecraft. Motion for the two (2) axes (clock and cone) is provided by separate identical and interchangeable actuators. The high gain antenna also a two (2) axis (azimuth and elevation) device is kept pointed at the earth for the purpose of maintaining spacecraft control and communication. The antenna azimuth axis is driven by a scan actuator; the elevation axis is driven by an antenna actuator. The solar energy controller (SEC) is a louvre covered reflector assembly used for maintaining temperature control of the vector propulsion engine fuel tanks by regulating the sun radiation to the interior of the spacecraft. There are four (4) SEC assemblies on the spacecraft; each is driven by one actuator. All three (3) actuators have identical electrical schematics and identical electrical connectors. In the control system, one drive logic is used to drive each of the three (3) actuators. The control system is multiplexed in order that it can be time shared by all of the eight (8), two (2) scan, two (2) antenna, and four (4) SEC, articulation control subsystem actuators used on the spacecraft. Each actuator is a geared actuator using a stepper motor as its prime mover. Position feedback information (shaft angle) is provided by a potentiometer. The scan and antenna actuators have high precision low backlash gear trains. In order to do this, a beryllium metal gear housing is used. The beryllium housing closely matches the thermal coefficient of expansion of the gears. There are multidisk slip clutches in the scan and antenna actuators for the purpose of providing overload protection through the dynamic environment of launch and in ground handling during spacecraft test activity. Design experience is described and test results are discussed. Overall Viking Project management is the responsibility of NASA/Langley Research Center; the Jet Propulsion Laboratory is developing the orbiter.

* This paper presents the results of one phase of research carried out at the Jet Propulsion Laboratory, California Institute of Technology, under Contract No. NAS 7-100, sponsored by the National Aeronautics and Space Administration

INTRODUCTION

The articulation control subsystem on the Viking Orbiter spacecraft will use eight actuators of three different sizes in order to perform its function. Each actuator will use a stepper motor as a prime mover and potentiometers for feedback control. The articulation control subsystem will have dual redundant channels and will be capable of multiplexed operation. The devices to be controlled are the platform containing the science instruments, the high gain antenna for earth communication and spacecraft control, and the solar energy controller used for temperature control of the vector engine fuel. The multiplex feature of the system will allow the control electronics to be time shared by all of the eight actuators. The dual redundant capability will allow any two axes to be articulated simultaneously and will allow any actuator to be driven by either one of its two command loops. Figure 1, a simplified subsystem diagram, will illustrate these features.

The scan (figure 2) and antenna (figure 3) actuators are very similar, both having identical gear reductions from motor to output shaft and two speed fine-coarse potentiometer shaft position readout capability. Each of these actuators will perform with constant low backlash throughout a large temperature range (-40°C to +85°C). The solar energy controller actuator (figure 4) does not have this precision requirement nor the two speed shaft position potentiometer readout capability; however, it must operate over the same temperature range. All of the actuators have identical electrical schematics and identical electrical connectors. A multidisk clutch (figure 5) is used for overload protection in the scan and the antenna actuator. The solar energy controller actuator does not have a clutch. This paper presents the design requirements, describes the actuator construction and gives the results of performance, life and environmental testing. Overall Viking Project management is the responsibility of NASA/Langley Research Center; the Jet Propulsion Laboratory is developing the orbiter.

DESCRIPTION

The actuators provide the controlled rotary motion for positioning and pointing the articulated devices on board the Viking Orbiter spacecraft. The articulated devices are the scan platform which mounts the science instruments, the high gain antenna which transmits data to earth from the science instruments and receives commands from earth for the control of the spacecraft or its science instruments, and the solar energy controller which regulates the solar energy in order to control the temperature of the vector propulsion engine fuel tanks. Each of the three actuators consists of five major parts. They are listed as follows:

1. A potentiometer for feedback control and telemetry data
2. A 90° per step permanent magnet stepper motor
3. A gear train
4. A gear train structure
5. An O-ring sealed housing

The housing is pressurized in order to protect the mechanism from corrosive gasses and to preserve the lubrication in the space vacuum environment. The gas used for pressurization is a mixture of 90% nitrogen and 10% helium by volume. The helium trace makes it possible to measure the actuator housing leak rate with a mass spectrometer leak detector since the leak is in the molecular flow regime. A resistance heater is mounted in the actuator on the gear structure to prevent damage due to low temperatures that will be encountered during the mission. A box mounting glass to metal hermetically sealed electrical connector is mounted on the actuator housing in order to provide for electrical inputs and outputs. The actuator's rotary motions are coupled to the articulated devices through either a bar linkage in the case of the SEC or an Oldham coupling as are the scan platform and high gain antenna. Mechanical stops are provided, by either the articulated devices or the actuator itself, that will limit the actuator shaft rotation in order to preserve position readout continuity from the potentiometer.

DESIGN REQUIREMENTS

The performance requirements may be generally described as motor voltage and power limits, gear train backlash, output torque, slewing speed, detenting torque, clutch slip torque, shaft angular range, and housing leak rate. The actuators must also be able to perform over a large temperature range and after being subjected to environmental testing. Specific values of Design Requirements are listed in the appendix.

GEAR STRUCTURE

In the scan and antenna actuators, the requirement for maintaining low backlash in the gear train over a large temperature range is satisfied by matching the thermal coefficient of expansion of the gears and gear train structure. In order to do this beryllium metal is used for the structure and precipitation hardening stainless steel is used for the shafts and gears.

The differential expansion rate for these materials is 4×10^{-7} inch per inch per degree Fahrenheit. This differential rate is not sufficient to either bind the gears at the low temperature or cause undesirable backlash at the high temperature end. Beryllium metal was selected for the gear housing for the following reasons:

- Light weight
- Beryllium lends itself to precision fabrication very effectively
- The near match of the thermal coefficient of expansion of beryllium to that of the stainless steel gears which will keep the backlash within limits throughout the temperature range

The SEC actuator can function with a larger backlash allowance. This will allow the use of aluminum for its gear structure. Greater clearances in the gear meshes will accommodate the differential expansion. Its value is 6×10^{-6} inches per inch per inch per degree Fahrenheit.

GEARS

Spur gears were selected for the precision gear train because they are the least sophisticated to use. The simple straight spur gear is the best for precision application unless other requirements rule out its use. The spur gear mesh does not produce shaft axial thrust and is more efficient than helical, bevel, or worm gear meshes. Spur gears may be spring loaded in order to virtually eliminate backlash. This technique is used in the actuators in order to couple the potentiometers to the output shaft for angle readout information.

For maximum precision in the spur gear train 20° pressure angle gears have been selected. Minimum pitch size gears are used within the constraints required by load in order to maximize the contact ratio. Contact ratio may be described as the number of teeth simultaneously in contact in a pair of mating gears. The advantage of the high contact ratio is that it produces greater tooth-to-tooth error averaging which results in smoother tooth action and decreased tooth-to-tooth variable backlash and less position error. For this reason contact ratio with precision meshes should be maintained higher than those in commercial quality gears. A ratio of 1.4 or higher is desirable. The contact ratios used in these actuators are all above 1.6.

In selecting the best functional gear train for the actuators the gear ratio n is defined as the input angle divided by the output angle. The gear train performance parameters are described as follows:

1. The torque available at the output shaft, neglecting friction, is equal to the torque at the input multiplied by n .
2. The shaft speed of the output shaft is equal to the speed at the input shaft divided by n .
3. The angular acceleration at the output shaft which is a direct reduction of the speed variation is equal to the input acceleration divided by n .
4. The moment of inertia as reflected at the output shaft is a direct function of torque and an inverse function of acceleration; therefore, it is equal to the input moment of inertia multiplied by n^2 .

GEAR STRESS

In order to determine the gear tooth stress, the Lewis gear formula modified ¹, consider K_c the stress concentration factor, M_c the gear tooth contact ratio, P the gear pitch, T the torque applied, and N the number of teeth on the gear will be used:

$$S = \frac{2TP^2K_c}{NFYM_c}$$

Where F = face width, $Y = \pi y$, and y = tooth form factor

GEAR TRAIN BACKLASH

The gear train backlash was calculated by the use of an Root Sum Square (RSS) summation of gear and gearing worst case tolerances

$$\Delta\theta = \frac{360 \times 60 \tan \phi}{\pi R n} \left\{ x + \left[\Delta\bar{R}^2 + \Delta\bar{r}^2 + \Delta\bar{C}^2 + \left(\frac{\Delta\bar{D}}{2} \right)^2 + \left(\frac{\Delta d}{2} \right)^2 \right]^{\frac{1}{2}} \right\} \text{minutes}$$

Where:

x = gear mesh center distance clearance

ΔR = tolerance on gear pitch radius

Δr = tolerance on pinion radius

R = gear pitch radius

$\frac{\Delta D}{2}$ = radial clearance in bearing - gear shaft

$\frac{\Delta d}{2}$ = radial clearance in bearing - pinion shaft

ΔC = tolerance on center distance

n = gear ratio from output shaft to mesh being evaluated

ϕ = gear pressure angle

BEARINGS

Journal bearings are used generously throughout the three actuators. The solar energy controller and the antenna actuators use all journal bearings except in their motors and potentiometers where ball bearings are installed. This is done in order to provide greater precision, maximum reliability, greater simplicity and reduction in cost. The friction loss in the actuator through the use of journal bearings is found to be not greater than 5% more than the friction losses in a similar actuator making use of ball bearings

whose friction is 100 times less than that of a journal bearing. The friction torque losses in the journal bearing equipped actuator were calculated by the following equation:

$$F = \frac{T}{R} f_c r \lambda, \text{ torque loss}$$

Where:

T = torque
 R = gear radius
 f_c = coefficient of friction
 r = shaft radius
 λ = gear efficiency

The friction losses may be computed for each shaft and summed.

ACTUATOR TORQUE

The pull out torque capability of a stepper motor is closely related to the inertia of the load being driven by the actuator and the pulse rate of the input voltage (figure 6). It is also indirectly related to the temperature of the motor windings. Since the dc resistance of the windings increases with rising temperature, constant voltage input to the motor will result in a reduction of current in the windings linearly proportional to the rise in temperature. It is an inherent characteristic of the permanent magnet stepper motor that through one step it is analogous to a dc torquer. Considering this fact, the torque loss will now be linear and directly proportional to the current reduction caused by the increased temperature of the motor windings.

The relationship between load inertia and step rate is illustrated by typical performance data shown in figure 6. In the case of the actuators the inertia portion of the driven load plus the gears is reflected back to the motor and is inversely proportional to the square of the gear ratio. Since the gears have typically small mass and inertia values, the inertia of gears beyond the second stage from the motor can be neglected. In the stepper motor actuator at constant temperature and driven at a constant stepping rate, torque and inertia appear as dependent variables whose limiting sum will inhibit the motor from stepping. The relationship between torque and inertia is typically linear.

SLIP CLUTCH

The multidisk slip clutch (figure 5) used in the scan actuator and in the antenna actuator was tested by using a lathe as a test device (figure 7). A thermocouple was placed on the clutch, the load cell was calibrated and its

output was recorded on a strip chart recorder. Three lubricants were tested in the clutch. They are listed: Versilube G300, Krytox 240AC, and Versilube F50 plus MoS₂. The Versilube F50-MoS₂ combination lubricant provided the best results and was specified for use in the actuator clutches. This lubricant was also used in other clutches in the Mariner '69 and Mariner '71 scan platform actuators.

The clutch is set at 40 inch-pound slip torque and slipped in the lathe at 10 rpm with direction of rotation reversed every five minutes at room temperature. This procedure was used to evaluate the lubrication. The Versilube F50 plus MoS₂ in the clutch allowed it to have: 1) lower temperature rise; 2) longer slip time before torque change; 3) operation over a larger temperature range with lower torque change. In this condition driven at 10 rpm the clutch showed no change in torque to 1,600 turns. After 3,000 turns the torque increase was 25% to 50 inch-pounds. The test was terminated at 4,000 turns. The clutch torque was then at 60 inch-pounds. The clutch was cleaned, re-lubricated, and readjusted to 35 inch-pounds and its temperature raised to 100°C. Over a two hour period the clutch torque was 38 inch-pounds. The temperature was then lowered to -45°C. The clutch torque at that temperature was 48 inch-pounds.

The multidisk slip clutch used in the actuators is designed to be a high efficiency slip device with loads comparable to those experienced in journal bearings. The coefficient of friction in this clutch is of the order of 0.1. The clutch disks are made of through hardened, brittle hard 440C stainless steel hardened to Rockwell C 62 working against beryllium copper half hard disks.

There are two methods of calculating the clutch friction torque. One, a classical method, is the uniform pressure method where the integration of the clutch torque equation will yield an average radius where force applied puts uniform pressure over the face of the disk. The other method is the uniform wear method where the average of the internal diameter and outside diameter of the disk divided by two yields the effective radius. Test results indicate the uniform wear analysis method being closer to the results obtained.

SUMMARY

The articulation subsystem actuators were rigorously tested in severe environments. They were operated through temperature ranges from -73°C to +121°C. In each case the temperature rate of change was at maximum. The actuator under test at room temperature was put into a pre-chilled or pre-heated chamber. Satisfactory performance was obtained throughout this full temperature range and under the temperature shock conditions above. However, at temperatures below -78°C some leakage was experienced through the O-ring seal around the shaft. The actuators were subjected to severe vibration tests at the qualification levels, both random noise and sinusoidal vibration. In addition to vibration, they were subjected to 500 g shock test with a time

duration of 0.0007 second. The scan actuator was life tested by operating it from stop to stop through 2,000 cycles with 20,000 start-stop procedures randomly distributed through the 2,000 cycles.

CONCLUDING REMARKS

At the conclusion of the test program the actuators met the performance requirements listed earlier in this report. The use of beryllium in the gear structures for the scan and antenna actuators represents an ideal application of beryllium. These actuators have now been qualified and will be used on the Viking Orbiter Spacecraft for the purpose of controlling the articulated devices on board. Overall Viking Project management is the responsibility of NASA/Langley Research Center; the Jet Propulsion Laboratory is developing the orbiter.

APPENDIX

Design Requirements

The actuators are designed to meet the following performance requirements:

- (1) Motor voltage 28 VDC \pm 10%
- (2) Motor power limited to 10 watts
- (3) Performance over temperature range -40°C to $+85^{\circ}\text{C}$
- (4) Gear train backlash
 - Scan < 6 arc minutes
 - Antenna < 10 arc minutes
 - SEC < 30 arc minutes
- (5) Actuator pullout torque at 25°C while being driven at 100 pulses per second step rate
 - Scan > 160 inch-pounds
 - Antenna > 45 inch-pounds
 - SEC > 70 ounce-inches
- (6) Driving speed at 100 pulses per second step rate
 - Scan 1° per second
 - Antenna 1° per second
 - SEC 14° per second
- (7) Detenting torque with motor unexcited
 - Scan > 250 inch-pounds
 - Antenna > 75 inch-pounds
 - SEC > 2 inch-pounds

APPENDIX
(continued)

(8) Clutch slip torque

Scan 250 to 400 inch-pounds

Antenna 80 to 160 inch-pounds

SEC no clutch installed

(9) Shaft angular range

Scan 250°

Antenna 200°

SEC 90°

(10) Actuator leak rate all actuators

< 0.08 standard cc per hour mixture

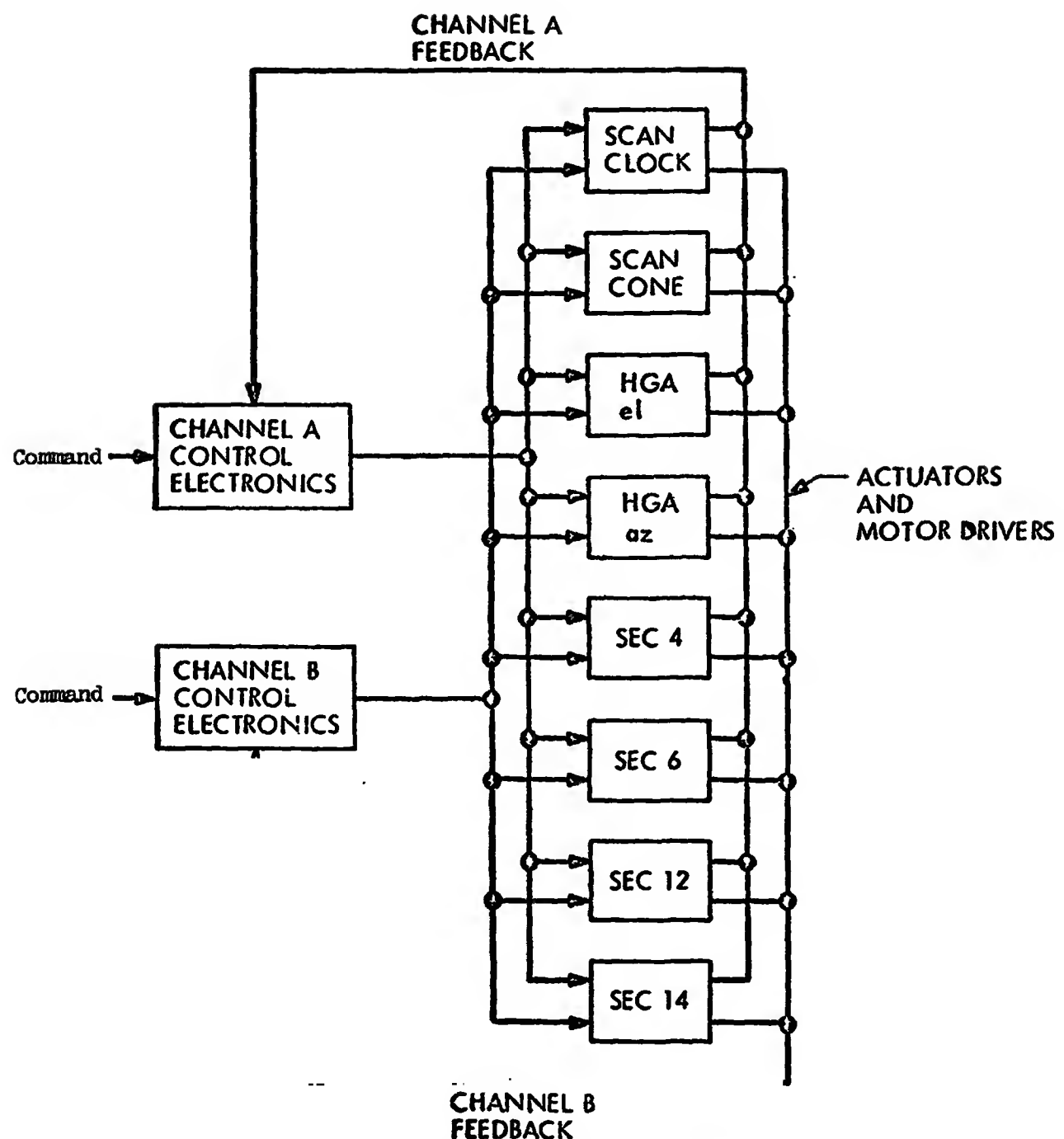


Figure 1.- Articulation control subsystem.

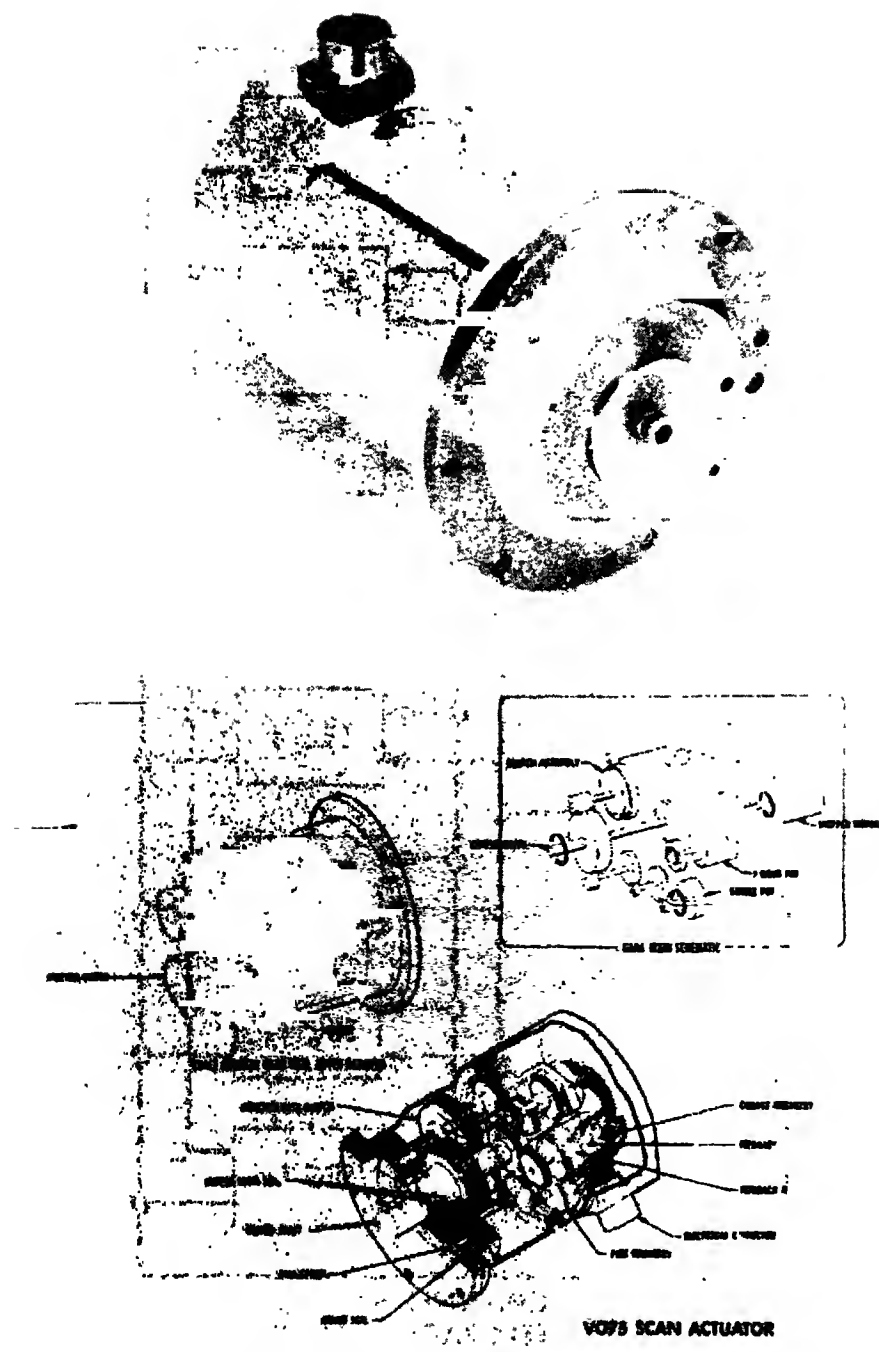


Figure 2.- VO'75 scan actuator.

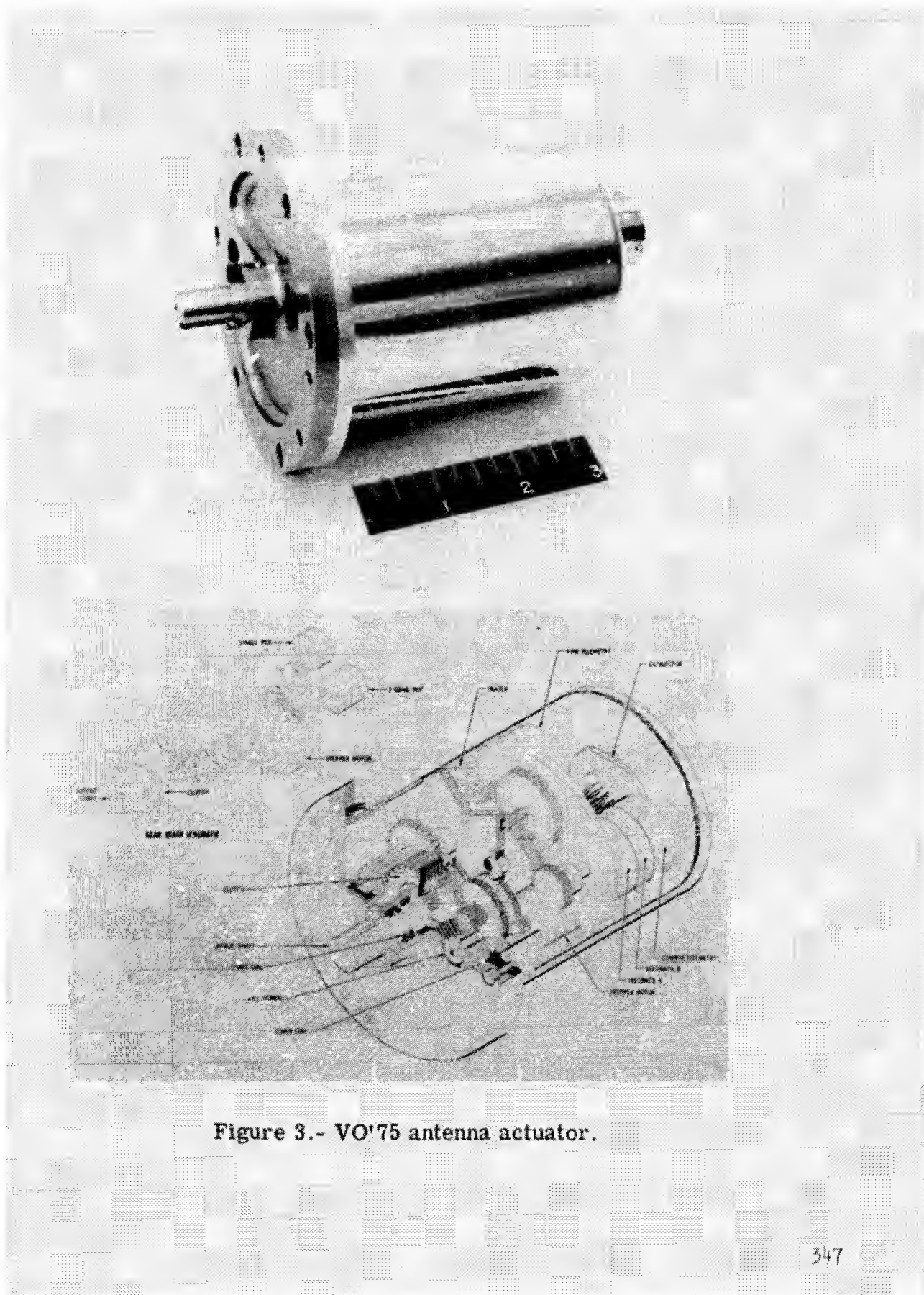


Figure 3.- VO'75 antenna actuator.

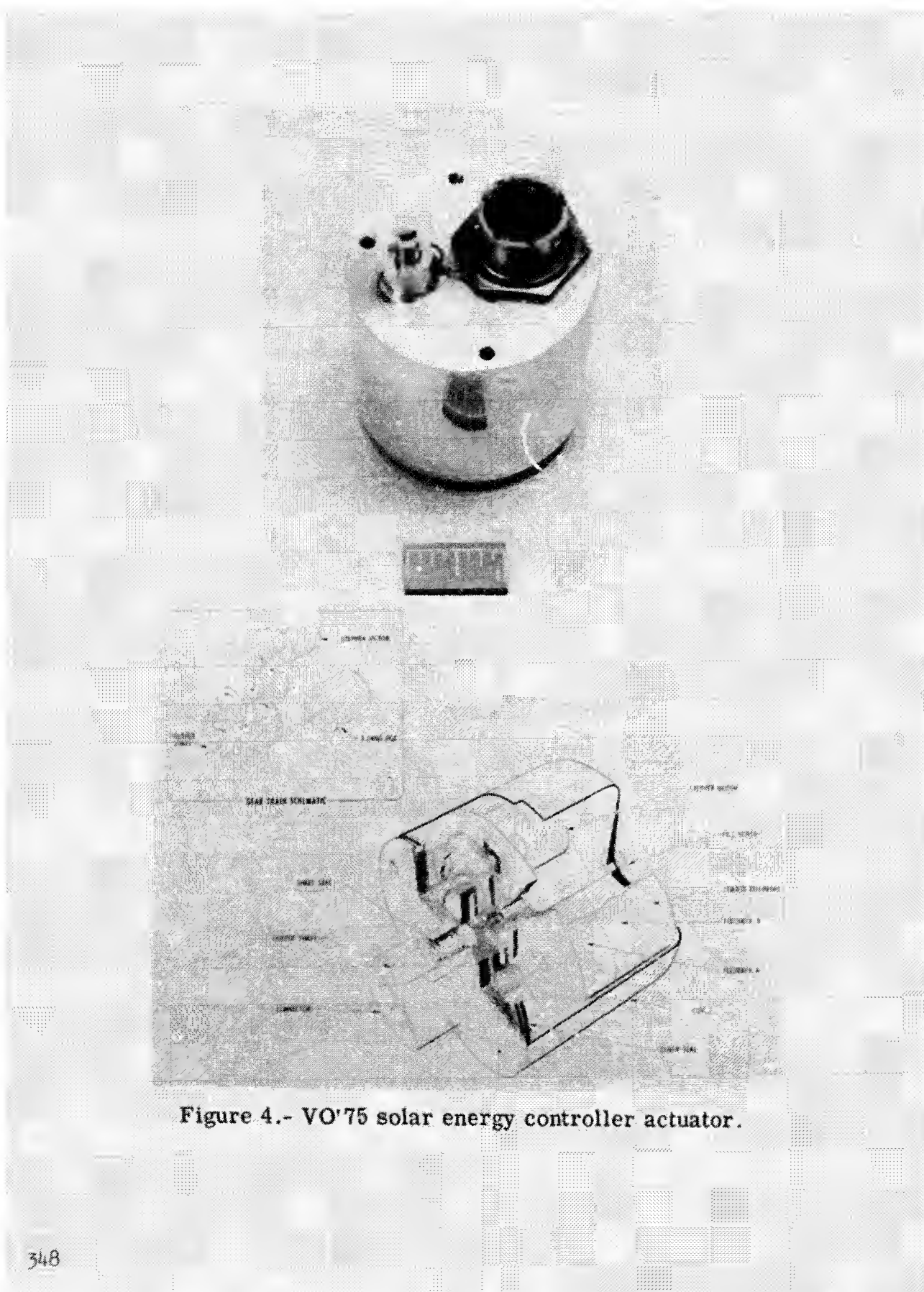


Figure 4.- VO'75 solar energy controller actuator.

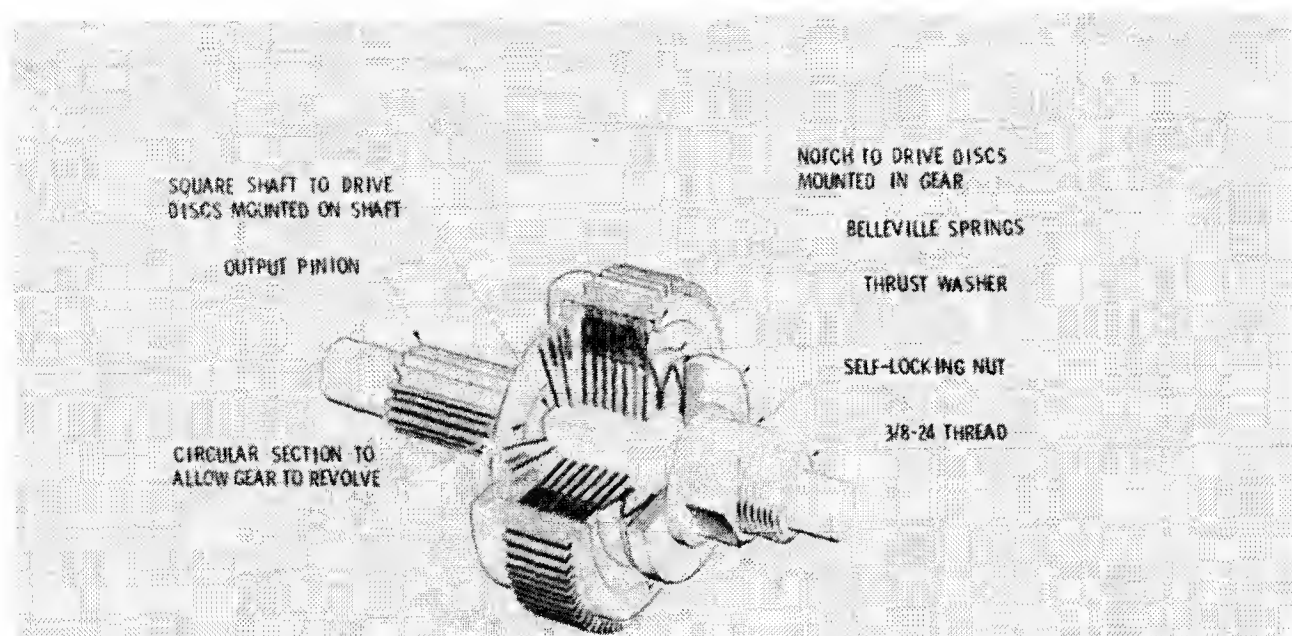


Figure 5.- Clutch assembly scan actuator.

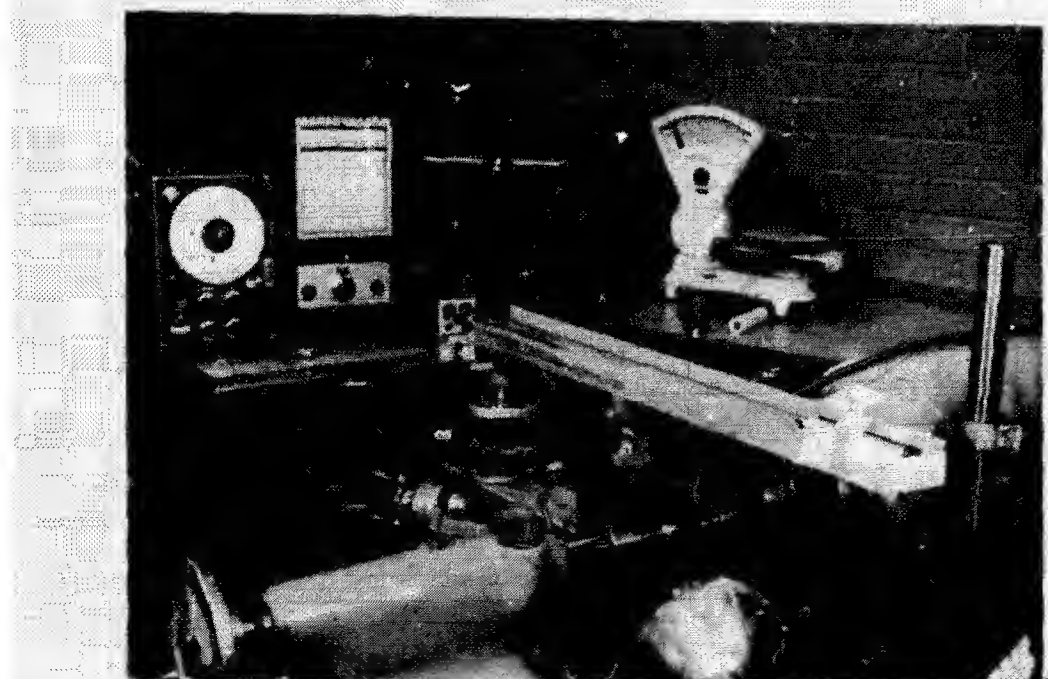


Figure 6.- Stepper motor performance characteristics (scan actuator).

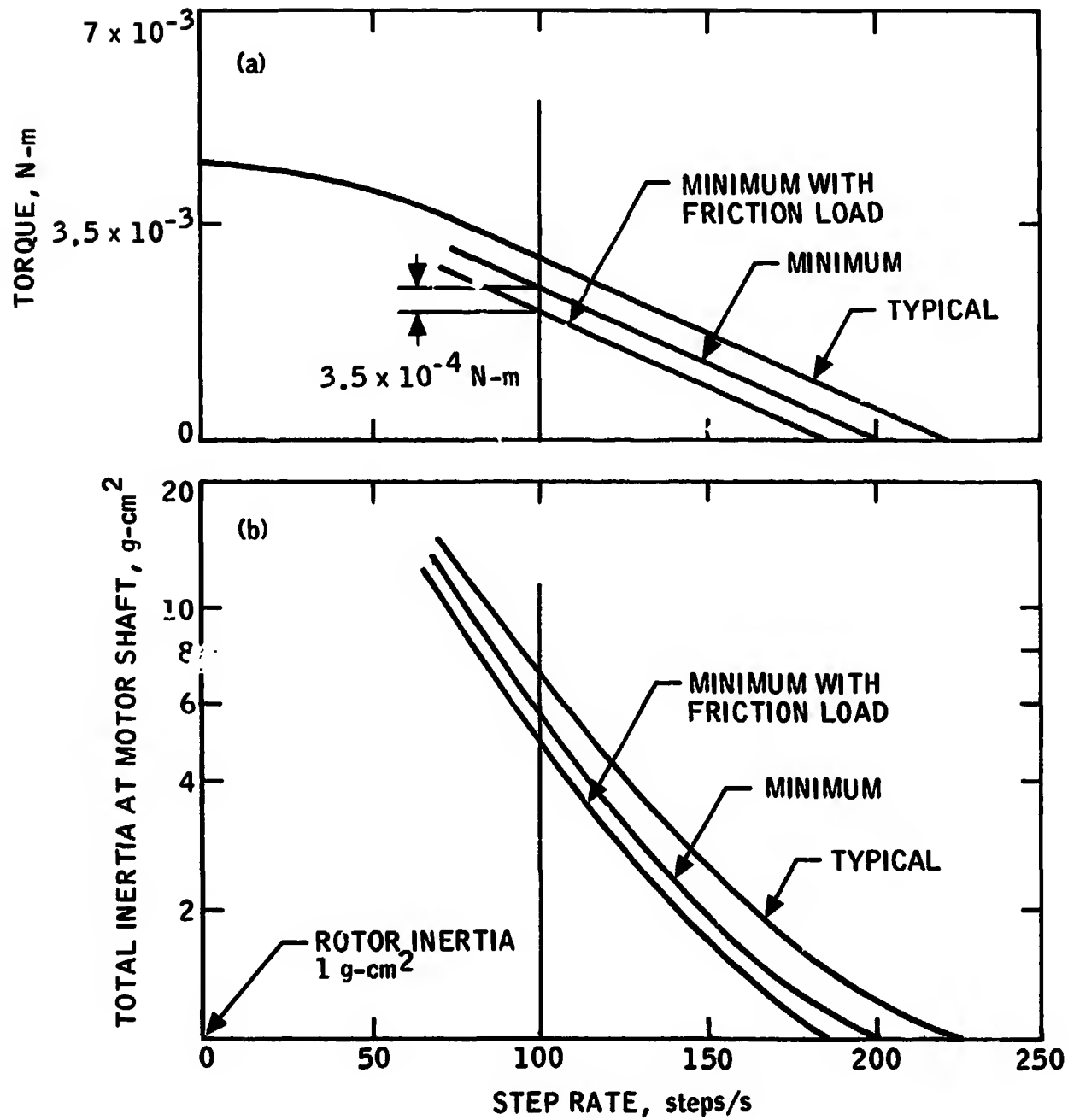


Figure 7.

29. THE REQUIREMENT FOR DESIGNING ANALYZABLE SPACE DEPLOYABLE STRUCTURES

By Arthur A. Woods, Jr.

Lockheed Missiles and Space Company, Inc.

SUMMARY

The Applied Technology Satellite Parabolic Reflector Subsystem is one of the first systems designed for space environment with limited terrestrial environmental ability. As a result, the complete performance of the system could not be demonstrated in a terrestrial environment without unacceptable design compromises. This problem was circumvented by developing a test philosophy which relied heavily on analysis to qualify and accept the flight hardware. Such a solution avoids the design compromises and costly test aids that are required for full terrestrial demonstration. The test program was successfully concluded and an optimized, low cost structure resulted. It is felt that this test and analysis philosophy can be applied to future space systems, resulting in substantial cost and schedule savings and a mission optimized system.

INTRODUCTION

Designs for large, space deployable, high positional accuracy structures have evolved over the last decade. A primary area of implementation of these structures is the area of communications. With the desire for large aperture reflectors comes the problem of launch constraints, both size and weight. Since the subject structures are intended for functional use only in space and are designed to maximize booster payload effectiveness while maintaining minimum weight, the optimum design is one which will not perform in the terrestrial

environment. In order to achieve this optimum design some of the normal ground test requirements must be deleted from the test program and heavy reliance on analysis must be substituted. This places new requirements on the design: that the analysis must be qualified, or verified, and that the structure itself must be as simple and straightforward to analyze as is possible, to provide additional confidence in analytical assumptions.

In a space deployable antenna system the reflector surface distortions and alignments are as critical to the system as ascent and deployment integrity. As a result the Applied Technology Satellite (ATS) test program was provided with the additional problem of qualifying orbital radio frequency performance which encompassed thermal, structural and electrical analyses.

This paper presents the ATS test program which evolved to qualify the parabolic reflector subsystem hardware and analyses. The significant test and analysis results are presented and the design simplifications for analytical modeling are also discussed.

DESIGN DESCRIPTION

The ATS parabolic reflector design (Figure 1) approximates a parabolic reflector by providing a reflective surface of forty-eight parabolic cylinders or gores of a woven dacron substrate, coated with copper and overcoated with silicone. These gores are sewn to forty-eight semi-lenticular, chem-etched sculptured and contoured ribs. The ribs are attached through hinges to a central hub weldment which in turn is attached to the spacecraft. The deployed reflector diameter is 9.144 meters; the focal length to diameter ratio is 0.44. The reflector weighs 83.9 kg and stows in a 1.47 m inside diameter by 1.98 m outside diameter by 20.32 cm thick torus.

To stow the reflector for ascent the ribs are rotated about their hinges until they are tangent to the hub. After this rotation the ribs are elastically buckled or collapsed and the ribs and mesh are then wrapped around the hub between the upper and lower hub covers. While the ribs and mesh are held in the hub structure, twenty-four doors are closed and a restraining cable is placed around the periphery. When the reflector is deployed, redundant pyrotechnic cable cutters are used to sever the cable; the stored energy in the ribs causes a reversal of the above process and the ribs and mesh deploy to form the parabolic surface.

DESIGN SIMPLIFICATIONS

The most critical requirements for a space deployable reflector are that it deploy reliably and maintain the desired surface contour. The deployment of the ATS reflector is accomplished with only one active element, a pyrotechnic cable cutter. There are redundant cutters. The remainder of the mechanisms are passive and consist of rib stored energy, rib hinge springs and door springs. Rib hinge springs were necessitated by a requirement to achieve a full deployment in a reflector cup up orientation in air. For a vacuum deployment the rib stored energy is more than sufficient to achieve a full deployment. The door springs were required to meet spacecraft stability requirements. The rib hinges rotate on spherical bearings which can rotate in their outer race or about the hinge pin. The door hinge has a large clearance hole through which the hinge pin is placed.

The reflector contour is dictated mainly by the rib/mesh interaction which essentially is a membrane loading of a cantilever beam. The mesh can be modeled structurally as a membrane with thermal and edge loads; the rib, by a standard beam with offset shear center finite elements. Thermally the mesh can be modeled as semi-transparent cylindrical section elements. The ribs

employ only thermal surface coatings as opposed to multi-layer insulation to avoid dependence on reliable, repeatable shape for insulation effectiveness and to avoid concerns associated with identifying and eliminating or attempting to model joints and leaks.

A further source of contour error is associated with hub top to bottom differential expansion. This type of distortion causes a rotation of the rib in a direction normal to the reflector surface. The hub consists of two rings welded together with spacers. A fixed thermal blanket is used for insulation purposes. This provides a relatively simple design for thermal and structural analyses.

Contour repeatability is also of concern since the contour to which all performance is relative is of significance. To provide a reliable, repeatable deployed contour, rib rotation normal to the reflector surface is eliminated since this direction is perpendicular to the hinge axis. Rib position is set by a stop at the hinge and position is maintained by a tapered plunger which is released by a cam on the hinge when the rib has rotated to the radial position. The only repeatability error is then in the rib radial angular position which produces negligible surface errors.

TEST PROGRAM

Even though the reflector itself was inherently simple in design and simple to analyze, a test program demonstrating performance was necessary. The qualification test program for the ATS reflector is shown in Figure 2. It represents a normal test program with the exception that final acceptance of the test article was contingent on analyses since it was required to demonstrate conformance of the deployment envelope, contour repeatability and radio frequency performance with analytical requirements to obtain qualification certification.

The reflector can be and was designed to deploy to a stable contour under gravity loading; however, the weight impact associated with making that contour the ideal orbital contour was unacceptable. As a result it was decided to measure the deployment envelopes and reflector contours at each of the deployments, both in the cup up and cup down attitude, and then analytically to calculate zero gravity contour. This calculated contour was then compared to the desired zero "g" manufacturing contour. The measured distortions were also used to compare to the structural model analysis results for analytical correlation and verification of the structural model. The analytical one "g" distortion correlation with the measured data is presented in Figure 3. In a similar manner the zero gravity deployment envelope was determined and the resulting analytical envelope was used to show compliance with the requirements. A total of ten deployments was used to provide demonstrations of compliance in these areas.

The final requirement on a reflector is to show compliance with the r.f. performance specification for the entire orbit. The reflector contour in one "g" could not, however, be achieved without a test aid to hold the contour. Since this contour was being artificially induced it was extremely important that the information used to derive the contour be shown to be accurate. It was decided that two contours would be used to demonstrate compliance, the orbital predicted "best" and "worst" contours. These contours are dependent on the proper prediction of the thermal loadings and their resulting structural surface distortions. If these analyses are correct, then the complete orbital radio frequency analyses would be correct; this was verified by correlation of the test predictions with the test measurements from the two test contours.

The verification of the thermal analysis predictions necessitated an additional test on a reflector model in a solar simulator. This model consisted of a full scale 5-rib sector of the reflector with the flight thermal control system.

Three positions of the test model were investigated during the test so that the full effects of mesh transparency and rib/mesh shading were experienced. The data obtained from these tests were then compared to the analytical predictions for the test model. This provided verification of thermal analysis modeling assumptions and temperature predictions. Figure 4 presents the analysis predictions and the test results obtained for the absolute temperatures occurring on the center rib at test position one. The data presented in Figure 5 present the analysis/test prediction comparison for the rib top to bottom gradients for test position number 3. These results were typical of those obtained and show excellent correlation of absolute temperature predictions with the test results. The correlation of predicted rib depthwise gradient with test results was also excellent since the gradients predicted were always larger than the measured data. For this type of reflector design, this leads to conservative surface distortion predictions.

The thermal distortion, or structural, model was, in addition to the aforementioned gravity loading certification, verified by an isothermal test of the full reflector. The contour change from 20^oC to 110^oC was measured during a thermal test in the NASA/MSC test chamber and this measurement compared to predictions to achieve correlation.

GENERAL TEST RESULTS

The ATS test program was extremely successful considering the developmental nature of the hardware program. There was however, one major failure that occurred and this resulted from overconfidence in expected performance stemming from the simplistic design. As stated earlier, if the cable cutter cuts the cable, there is nothing that can stop the reflector from opening since the ribs seek their original shape and a considerable amount of force is required

to hold them closed. There was apparently no mechanism in or on the reflector which could generate the required force. This was not true and a failure occurred during a low temperature (-110⁰C) vacuum deployment test.

The failure mode appeared just after the cable was cut. Sections of ribs started to peel off the wrap (Figures 6, 7 and 8) and tear the mesh as they were opening. The result was a deployed reflector with two torn mesh panels. This was an unacceptable condition. A failure investigation was started immediately to determine the cause of and corrective action for the failure. The failure mechanism discovered was the mesh overcoat of silicone.

The silicone (CVM DC 6-1104) is applied to the mesh as a protective coating for the copper and as a thermal surface coating. Silicones have a characteristic phenomenon in that they stick together. It was determined during the failure mode testing that the silicone blocking force is highly dependent on temperature. At temperatures above -45⁰C there is relatively little force required to unstick the surfaces; however, at temperatures below - 73⁰C there is an increase in blocking force by several orders of magnitude. This force at -110⁰C was proven to be sufficient to hold the ribs within the hub structure so that when a rib started to unfurl, the rib adjacent to it was held sufficiently within the hub by the silicone that forces in the mesh were developed to the point that the mesh failed in tension.

Since the reflector was deployed at -110⁰C for reasons of test convenience rather than as a result of pre-deployment thermal analysis predictions, the test temperature was changed to a deployment temperature consistent with predictions of -18⁰C. However, since the failure did occur, a solution to the problem uncovered no aging or curing of the silicone coating which would reduce

the low temperature blocking forces to acceptable levels. As a result a strip was added to carry the load which the blocking could produce. In addition, the strip had to be designed so that it would be ineffective once the deployment was achieved so that it would not cause surface distortions due to orbit thermal loading. The design solution was to install the strip so as to be always slack during the orbit conditions and to use a material with a high modulus of elasticity relative to the mesh so that it would unload the mesh and carry the blocking loads if the situation reoccurred.

The modifications were implemented and the test re-run. The coldest temperature at time of deployment was recorded as -50°C occurring on the reflector doors. The reflector deployed successfully with no sticking due to silicone blocking apparent.

CONCLUDING REMARKS

The Applied Technology Satellite Parabolic Reflector Subsystem development program was faced with a unique problem. That was: How do you space qualify a reflector system that is designed optimized for operation in the orbital environment? The solution to the problem was to derive a test program which eliminated terrestrial test conditions that would cause design compromises. This required the qualification of analyses used in conjunction with the derived test program. This resulted in a qualification of the reflector based on the combined analysis/test program. The solution led to a very satisfactory design with a minimum of ground test compromises and provided the necessary confidence to certify the flight worthiness of the reflector. It is felt that this is a valuable approach for future programs where a mission optimized design is desired.

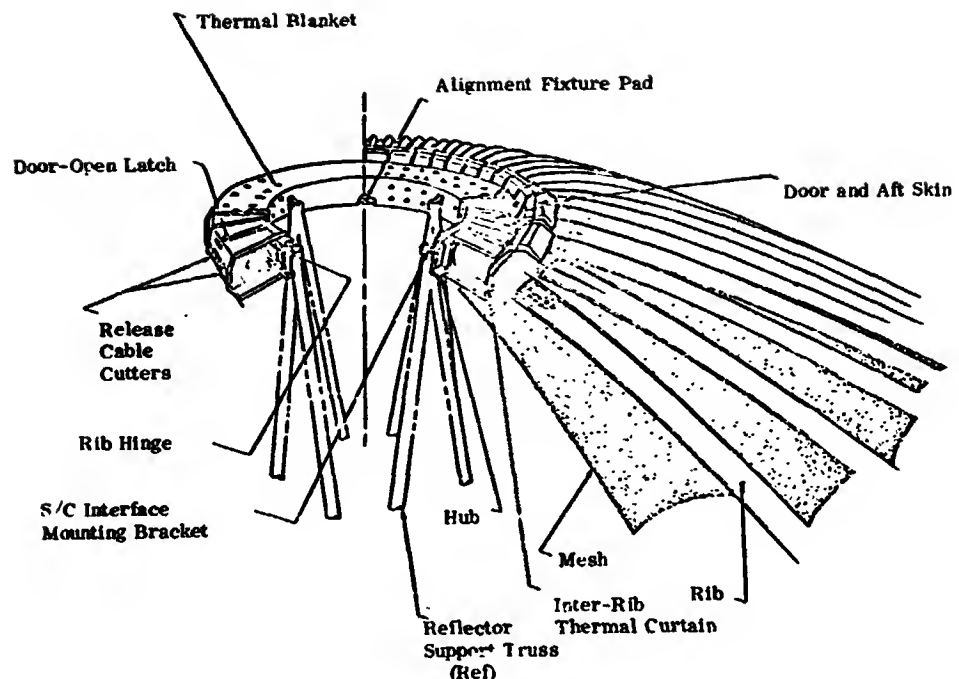


Figure 1.- Applied Technology Satellite parabolic reflector subsystem.

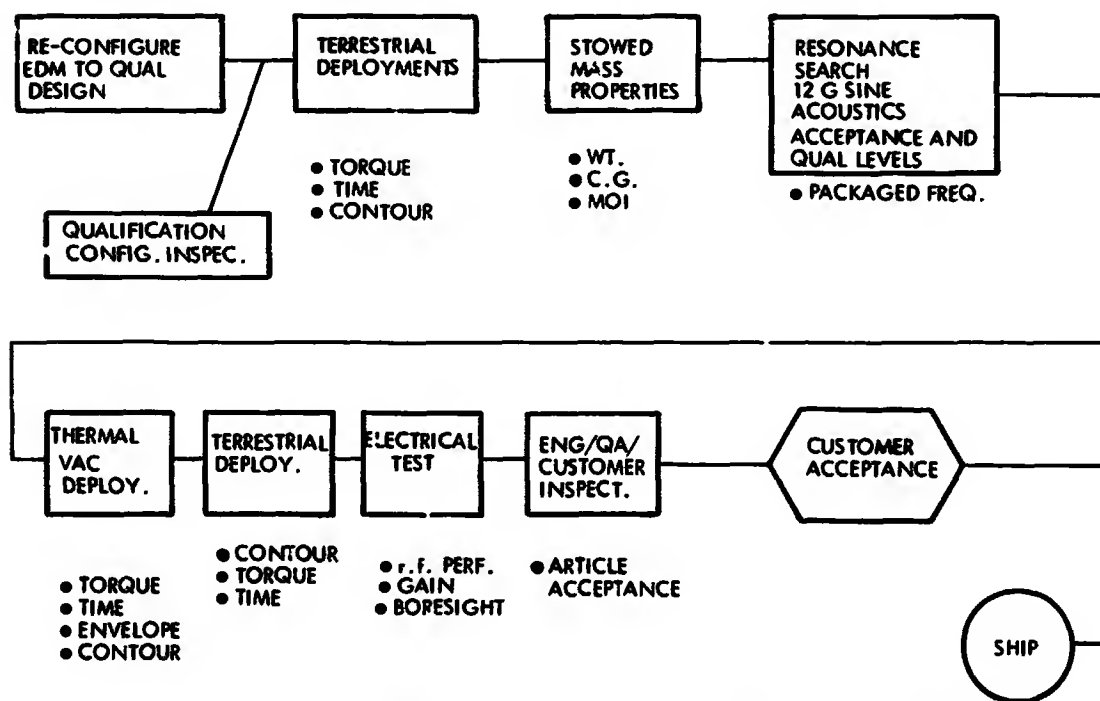


Figure 2.- ATS parabolic reflector subsystem test program.

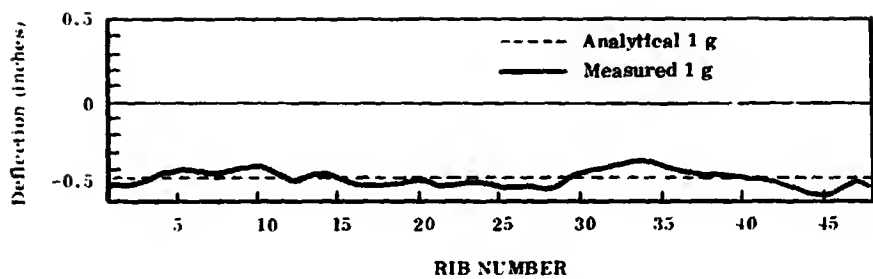
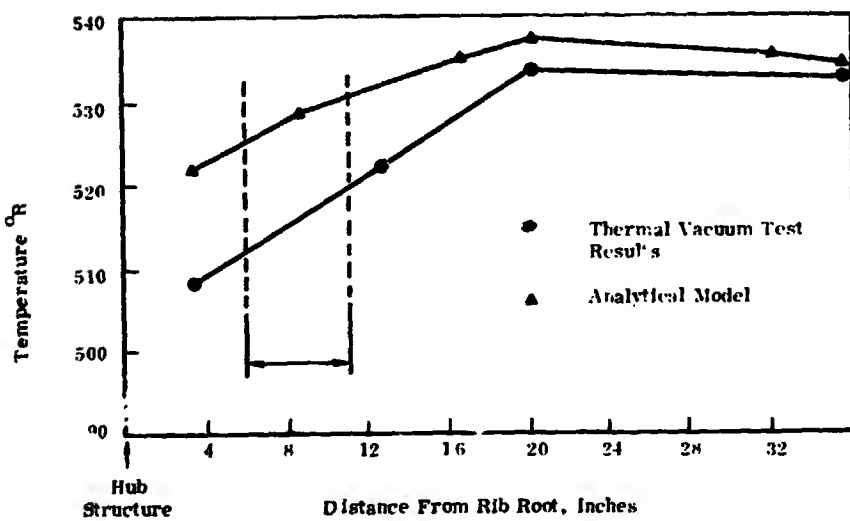


Figure 3.- One g analysis/test results.



**Figure 4.- Average temperature analysis/test results,
position 1.**

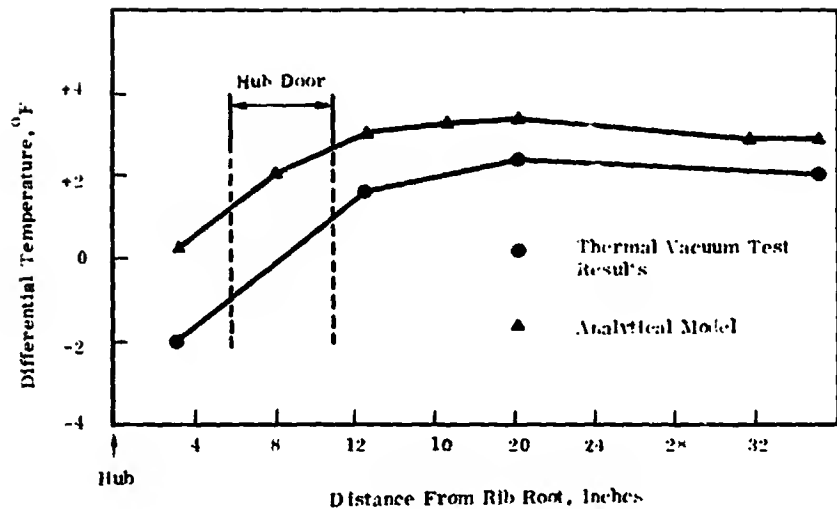


Figure 5.- Depthwise temperature gradient analysis/test results,
position 3.

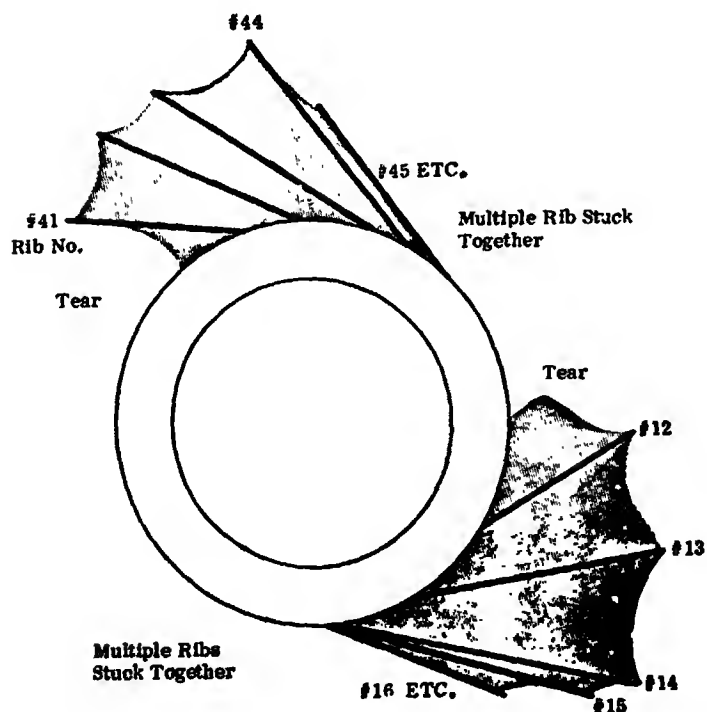


Figure 6.- Partially deployed reflector at deployment
plus 0.335 second.

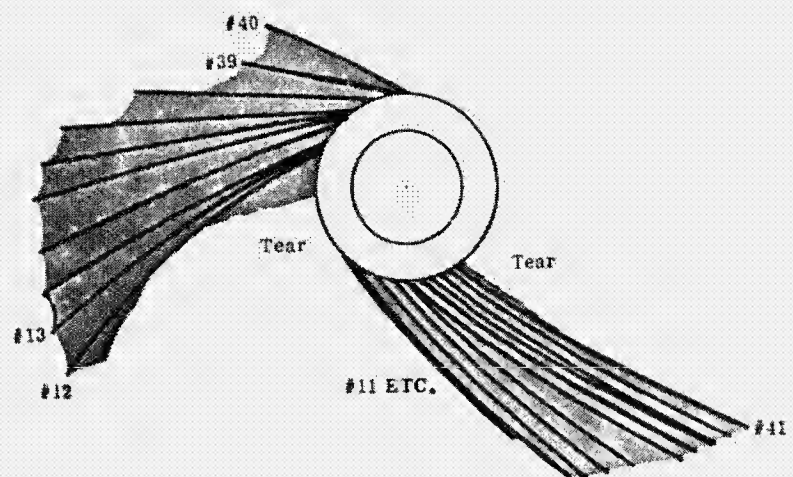


Figure 7.- Partially deployed reflector at deployment plus 1.36 seconds.

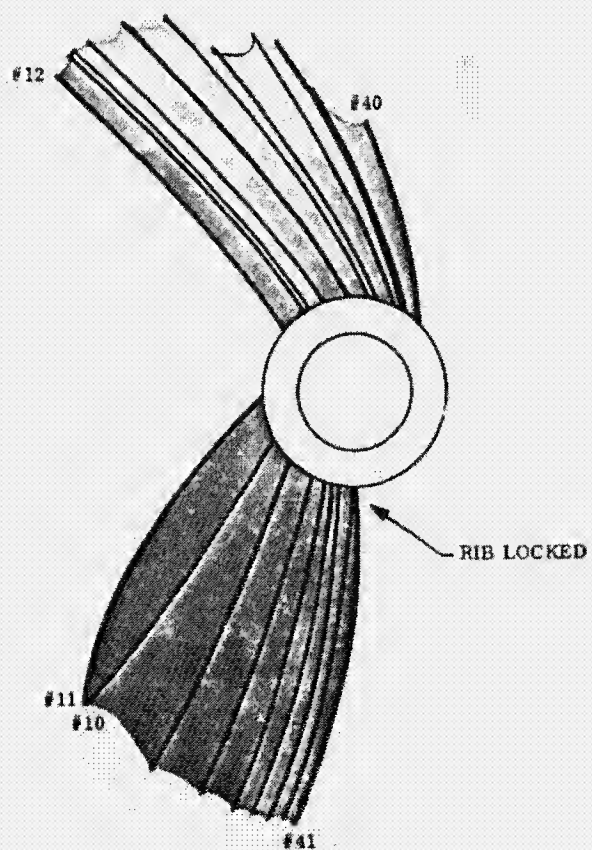


Figure 8.- Reflector at time of full deployment plus 1.9 seconds.